RAL-87-041

Science and Engineering Research Council
Rutherford Appleton Laboratory
CHILTON, DIDCOT, OXON, OX11 0QX

Science and Engineering Research Council Central Laser Facility

Annual Report to the Laser Facility Committee 1987

Laser Division
Rutherford Appleton Laboratory

RAL-87-041

Science and Engineering
Research Council

PREFACE

Research and facility development work carried out in association with the Central Laser Facility (CLF) in the year to 31 March 1987 is reported.

The CLF is funded by SERC through its Science Board and Subject Committees and operated by the Laser Division of the Rutherford Appleton Laboratory (RAL) to provide advanced lasers for use by UK University and Polytechnic research workers. Access to the facilities is through a competitive peer review system and demand for facility use for α rated research projects is heavily oversubscribed.

The high power Nd:glass laser (Vulcan) and KrF laser (Sprite) are the major installations of the CLF and their scientific applications and development are reported in Section 'A'. This has been a very productive year in which the trend to greater diversity of science has continued. XUV laser research has been especially successful with the demonstration of laser amplification at the shortest wavelength ever of 8.1nm. The line focus facility developed for the XUV laser work has also been adapted to study laser plasma interactions in plasmas of scale length relevant to laser fusion. Single pulse X-ray sources have produced new results in microscopy of living cells, the first EXAFS of dense plasma and absorption spectroscopy of ions in plasmas. A new plasma instability, attributed to a Bénard convection mechanism, has been discovered and novel measurement techniques have been developed in the ongoing study of energy transport in laser irradiated targets. The KrF laser, Sprite, has been operated for the first time with 6 beam optical angular multiplexing to extract its energy in a 6-fold reduced pulse length. Tests of picosecond pulse amplification in Sprite suggest it has unique potential for high power output in this mode.

The work of the Laser Support Facility, which provides smaller lasers both at RAL and on loan for multidisciplinary research in chemistry, biology and physics is reported in Section 'B'. The LSF has been expanded this year to provide more frequency tunable lasers in the loan pool and very productive and cost effective work in photochemistry has been accomplished with them. The highlight of the year however has been the large number of successful experiments conducted with the new picosecond laser. Among these the study of multiphoton ionisation on femtosecond timescale from Coulomb explosion of molecules is particularly interesting.

The successes achieved by visiting users of the facilities have depended on their own ability and enthusiasm on the skills of their many international collaborators and on the dedication and professionalism of the staff of the CLF. I am pleased to record here my sincere appreciation of all their efforts.

M H Key

CONTENTS

PART I

INTRODUCTION

P T Rumsby (RAL)

The Central Laser Facility (CLF) is funded by the Science Board of the Science and Engineering Research Council and in the year covered by this report, April 1986 to April 1987, its allocation was £3.07 M.

The Science Board has provided the Facility for research whose major themes are:

- A High Density Plasma Physics
- B High Intensity Laser Plasma Interactions
- C Energy Transport in Laser Produced Plasmas
- D Laser Driven Implosions
- E X-Ray Lasers
- F Other Applications of Laser Produced Plasmas (eg as X-Ray sources)
- G Applications of Short Pulse Frequency Tunable Lasers

The programme is managed by the Laser Facility Committee (LFC) whose membership is given in Table 1. The LFC delegates responsibility to the Rutherford Appleton Laboratory for the operation of the Facility.

The Laser Division of RAL used 58 man years of effort. Staff costs and overheads used 47% of the allocation while facility operations and minor development costs used another 44%. The remaining 9% of the total allocation was spent on the Phase 1 programme of capital facility development.

The major facilities provided by the CLF and a brief indication of their principal scientific applications is given in Table 2.

The Nd glass laser VULCAN is the major facility and about 45% of resources was used to support its programme of research by UK Universities.

The high power UV gas laser SPRITE has now been developed to the point that at least 50% of its time is used to provide UV picosecond pulses of ultra high intensity and X-ray source facilities for University work. About 20% of total operating resources were committed to this work.

Multidisciplinary scientific applications of excimer lasers and excimer pumped dye lasers by UK Universities are catered for by the Laser Support Facility using 25% of resources. This also operates a picosecond laser system for photobiological applications at the CLF and a laser loan scheme for University based experiments.

A target preparation service and a small group giving theoretical support by maintaining computer codes support all CLF activities.

Use of the CLF by UK Universities is free of charge to those successful in a peer review process. Research grants of typically three years duration covering expenditure in University Laboratories and research assistants' salaries may be obtained from the LFC by application to SERC. LFC Grant holders are entitled to bid for time on the CLF's lasers through a procedure described below.

A few percent of the time may also be allocated to bids for short trial experiments from University researchers working in the Science Board area who do not hold LFC grants.

The SERC encourages use of the CLF by industry or other organisations on the basis of payment for the full cost of laser time. Such use is limited to not more than 10% of available laser time.

International collaboration in the research programme is particularly welcomed, either through collaborative participation in approved experiments of UK University groups or through agreements negotiated with the CLF and SERC.

Selection and scheduling of University experiments using the VULCAN glass laser and SPRITE UV laser is via proposals to one of 4 informal specialist scientific groups which anyone may join. Each has a University Chairman and an RAL secretary (Table 3). Each group discusses the experimental proposals and makes modifications, improvements and collaborative suggestions. More formal proposals based on these discussions are then submitted to an expert panel

which places scientific priorities on the proposals. This panel is chaired by the Scientific Programme Chairman and its secretary is the Scientific Programme Coordinator. Its members include the five Scientific Group Chairman, the Chairman of the High Power Laser Scheduling Committee (HPLSC) and a representative of the LFC. A draft schedule which includes as many of the high priority proposals as possible (typically ≤50% of proposals), is then prepared, discussed and modified at a meeting of the more formal High Power Laser Scientific Programme and Scheduling Committee (HPLSPSC). All University staff members involved in the programme have voting rights, together with the group secretaries and programme coordinator. The Committee is chaired by the Division Head of Laser Division and is formally advisory to him.

Scheduling of Laser Support Facility lasers is performed in a different way. The LFC has delegated LSF Management duties to a panel whose membership is given in Table 4. Selection of experiments requiring loan pool lasers or use of the lasers based at the CLF is carried out by this panel and scheduling is performed by an ad hoc committee of users chaired by the Laser Division Head.

Scheduled experiments are supported by the operating budget of the CLF which covers travel and subsistence costs for University users and minor engineering work and other costs of experiments.

The experimental programme is linked to theoretical work in Universities which is supported by grants from the LFC and coordinated by the Theory and Computation Scientific group.

There is a large and diverse community of University researchers participating in the programme. They number over 150 staff and research students. Most are physicists and chemists, but recently there has been a rapid growth of participation from biologists.

TABLE 1

Membership of the Laser Facility Committee 1986/87

Professor G J Pert (Chairman)
Dept of Applied Physics
University of Hull

Dr E H Evans *
School of Sciences
Preston Polytechnic

Professor M G Haines
Imperial College of
Science and Technology
London

Dr T A Hall
Department of Physics
University of Essex

Dr M H R Hutchinson *
Imperial College of
Science and Technology
London

Dr T A King
Schuster Lab
University of Manchester

Dr C L S Lewis *
Department of Pure and
Applied Physics
The Queen's University of
Belfast

Professor D Phillips
Department of Chemistry
Royal Institution of Great Britain

Dr D Robinson +
UKAEA Culham Laboratory
Abingdon

Prof W Sibbett +
Department of Physics
University of St Andrews

Professor J P Simons
Department of Chemistry
University of Nottingham

Dr M Vaughan
Procurement Executive
Royal Signals & Radar Est, MOD,
Gt Malvern

Dr C W Wharton +
Department of Biochemistry
University of Birmingham

* until 31 August 1986
+ from 1 September 1987

TABLE 2

Major Facilities at the CLF

Nd glass Laser facility	Laser Support Facility	High power KrF laser facility
VULCAN	LSF	SPRITE
Plasma Physics X-ray laser Research Applications of intense X-ray and particle sources	Photo chemistry Photo biology Materials processing Non linear optics Plasma diagnostics Laser loan pool Tunable VUV source	Facility utilising the high X-ray brightness of UV laser produced plasmas Ultra high intensity sub picosecond laser source
Target Preparation Service Theoretical support service		

TABLE 3

High Power Laser Scientific Groups

Groups of the HPLSPSC	Chairman	Secretary
Laser plasma Interaction and Energy transport	Dr A E Dangor* Dr O Willi+	Dr R G Evans* Dr A Cole+
Laser Driven Compression and dense plasmas	Dr T A Hall	Dr A J Cole* A Ridgeley+
XUV lasers and applications of laser produced plasmas	Dr C L S Lewis	S Rose* M Grande+
Theory and Computation	Dr R A Cairns	Dr D Nicholas* Dr S J Rose+
Facility Development	Dr P T Rumsby	Mr J E Boon
Scientific programme coordinator	R G Evans‡	

* Until October 1986
\+ From October 1986
‡ until March 1987

TABLE 4

Laser Support Facility Panel (1986/87)

Professor J P Simons - Chairman
Nottingham University

Professor R E Hester for Chemistry Committee
York University

Dr P B Davies for Chemistry Committee *
Cambridge University

Dr C W Wharton for Biological Sciences Committee
Birmingham University

Dr C Webb for Physics Committee
Oxford University

Dr H Evans for Laser Facility Committee *
Preston Polytechnic

Prof M C W Evans +
University College

Prof I W M Smith +
Birmingham University

* until 31 August 1986
+ from 1 September 1986

A HIGH POWER LASER SCIENTIFIC PROGRAMME

Experiments using the high power laser facilities, Vulcan (Nd:glass laser) and Sprite (KrF laser) are reported here together with related theoretical work.

The report is subdivided into the programmes of the five scientific groups of the High Power Laser Scheduling Committee which received 41 proposals for experiments of which 27 were eventually scheduled, though often with less time than that bid for.

Vulcan was used solely for experiments by University groups and their collaborators from RAL and overseas. Three different target irradiation laboratories were in use and experiments were run in two laboratories in parallel at all times, using automated switching of laser beam paths on alternate laser shots.

Target Area East supported experiments using multibeam line focus irradiation and particularly important results were obtained in X-ray laser research. Scaling from earlier success with C VI, laser amplification was recorded on the 8.1nm F IX Hα transition from a LiF coated fibre target, giving the CLF a world first in the shortest wavelength of laser amplification. Collaboration with colleagues from France established a promising new line of XUV laser research using Li-like ions, with observations of gain at 15.4 and 10.6nm in Al XI. The line focus facility was also adapted for study of laser plasma interactions in plasmas of long scale length by producing plasmas through explosion of a thin ribbon target in a two sided line focus and directing the independent 7th beam of Vulcan along the axis of the plasma to study Raman and Brillouin scattering and self focussing. An interesting unforeseen result of this work was the discovery of a new kind of plasma instability in the heated targets tentatively attributed to a Bénard convection mechanism.

TAW provided 12 beam irradiation of spherical targets and opposed cluster beams for colliding shock studies. A notable result, in dense plasma studies with colliding shocks, was the first EXAFS probing of the transition from order to disorder in correlation between ion positions, as the internal energy of dense matter is increased in the transition from cold solid to a dense strongly coupled plasma.

Sophisticated energy transport experiments were features of the 12 beam studies with novel results obtained from two different methods giving measurements resolved in space to circumvent problems arising from non uniformity of irradiation.

The auxiliary target area, TA2, supported a major experiment to study beat wave acceleration in which a promising advance was made through the demonstration of precise control of preformed plasma density using multiphoton ionisation. Successful applications of X-ray sources included biological microscopy of living cells and absorption spectroscopy to analyse the ionic composition of plasmas.

The major theme of work on Sprite was its ongoing development as a test bed for high power laser facilities of the future, and two significant milestones were reached. The first was the implementation of six beam angular multiplexing to shorten the pulse from 60nsec in one beam to 10nsec in six beams and the second was the preliminary study of injection of picosecond pulses into the multiplexed system demonstrating amplification to 500mJ. The system now has the potential for power generation in picosecond pulses greatly exceeding that of Vulcan and it is planned to produce 2-3J pulses in each of the six beams.

The high repetition rate of shots on Sprite (every few minutes) was of value for the 40% of time dedicated to experiments which was equally divided between commercial contract use and University experiments, notably in spectroscopy.

Theoretical work advanced significantly during the year particularly in the modelling of XUV lasers, beatwave acceleration and energy transport.

Editor: M Grande

A1.1 EXPERIMENTAL STUDY OF RECOMBINATION PUMPED XUV LASER ACTION IN C VI

C Chenais-Popovics, R Corbett, C J Hooker, M H Key, G P Kiehn, C L S Lewis, G J Pert, C Regan, S J Rose, S Sadaat, R Smith, T Tomie, O Willi, J E Boon, C Brown, A R Damerell, P Gottfeldt, M Grande, D A Pepler, I N Ross, P T Rumsby, W Shaikh,
Ecole Polytechnique Laboratoire PMI, F91128, Palaiseau, Cedex France
Electrotechnical Laboratory, 1-1-4 Umezono, Sakura-Mura, Nihari-Gun, Ibaraki Japan
University of Hull, Hull HU6 7RX England
Imperial College of Science and Technology, London SW7 2BZ England
Queens University, Belfast BT7 1NN Northern Ireland
Rutherford Appleton Laboratory, Chilton, Didcot, Oxfordshire OX11 0QX UK

The development of XUV lasers is progressing rapidly through a variety of schemes using laser produced plasmas as the amplifying media[1].

Strong exponential behaviour was first reported for 3p-3s transitions in Se XXV,[2]. High gain on C VI Balmer α has been observed with a solid target in a strong magnetic field[3]. Smaller gain has been seen in Li-like Al XI with solid targets[4] and in C VI with thin film targets[5]. Our work has concentrated on recombination to C VI[6] including the use of short carbon fibre targets[7][8].

The present experiment was designed to produce significant amplification by irradiating longer fibres under optimised conditions. The six beam neodymium glass laser facility, Vulcan, at the SERC Rutherford Appleton Laboratory, was used to generate up to 10^{12} W, 70 ps, 0.53 μm pulses. A new target irradiation facility was devised, combining focussing via an f/2.5 aspheric doublet lens with 13° off-axis reflection at an f/2.5 spherical mirror to produce a 7 mm long 25 μm wide aberration free line focus[9]. Six laser beams were focussed in opposed pairs[9]. Two beams, suitably masked, were used for line focus lengths from 1 to 7 mm, and by axial displacement of the line focii, a further two beams extended the length to 14 mm. Carbon fibre targets up to 14 mm long, supported at one end, were positioned with ∿ 5 micron spatial accuracy and angular accuracy of 10^{-3} rad[9].

A time-resolving XUV spectrometer observed the axial emission from the unsupported end of the fibre[10]. The instrument used a variable periodicity grazing incidence diffraction grating to focus the XUV spectrum to a flat field at the transmission photocathode of an XUV streak camera. Spectral resolution was 0.5Å and the temporal resolution was 0.4 nsec. An XUV pinhole camera image, filtered to $h\upsilon$ = 500eV, recorded images of the plasma and the absorbed energy was measured with plasma calorimeters.

Optimum conditions were calculated to be 2Jcm^{-1} of absorbed energy, fibres of 7 μm diameter and 70 psec pulse duration at 0.53 μm wavelength. A model description[11] was used for semi-quantitative optimisation and was supplemented by detailed numerical simulations.

For a laser heated plasma cylinder of uniform temperature, the relationship of optimum energy content E to mass M and laser pulse duration τ is given by[6]

$$E = 1.7 \times 10^{6}\, M^{17/11} \tau^{-6/11}\ \text{Jcm}^{-1} \qquad (1)$$

Adiabatic cooling of a plasma of bare nuclei and free electrons creates inversion in hydrogenic C VI ions between n = 3 and n = 2. The inversion originates in the collisional population of n = 3 in the recombination cascade and the radiative decay of the n = 2 level.

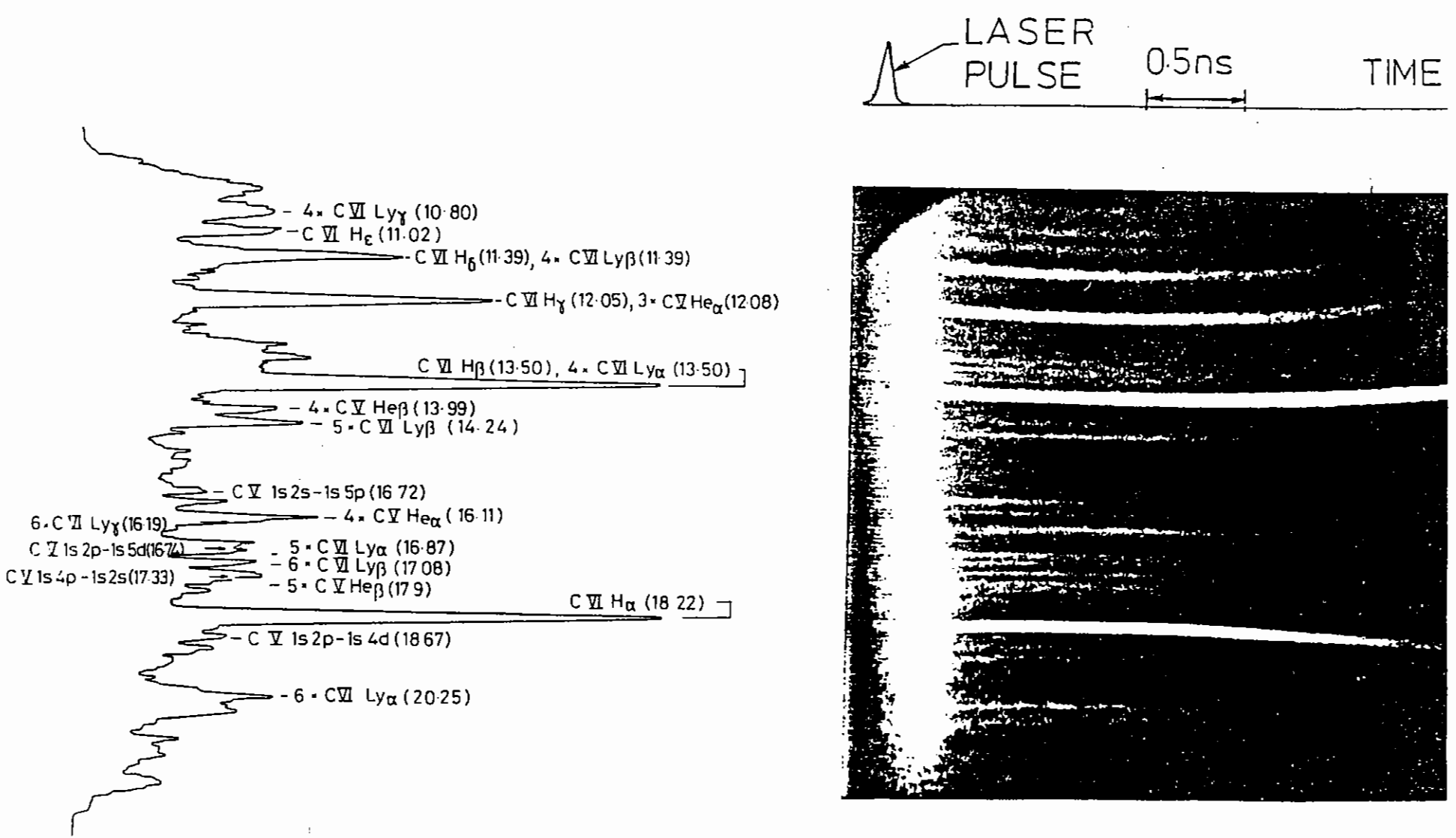

Fig A1.1 (a) Streak camera record of the emission spectrum along the axis of a 7 μm carbon fibre target with 8 mm irradiated length and 2.5 Jcm⁻¹ absorbed energy.
(b) Densitometry from (a) 975 psec after the peak of the laser pulse, with wavelengths labelled in nm.

For lower than optimum energy the inversion is quenched by trapping of Lyα emission. For higher than the optimum energy, the population density n(3) and gain are reduced because of less recombination.

The model approximates the behaviour of the plasma produced by laser irradiation of a solid fibre, where a surface layer is raised to high temperature at a density close to the critical density.

An analytic description of the ablation of fibre targets of radius r by 0.53 μm laser radiation gives,

$$M = 3.9 \times 10^{-3}\ r^{2.9}\ E^{5.9}\ \tau^{4.9}\ \text{gcm}^{-1} \qquad (2)$$

The simultaneous solution of equations (1) and (2) for a fixed laser wavelength gives for optimum gain,

$$E/1\text{Jcm}^{-1} = 0.11\ (r/1\ \mu\text{m})^{2.4}\ (\tau/100\ \mu\text{m}) \qquad (3)$$

relating radius and pulse duration to absorbed energy.

Because smaller mass reduces radiation trapping, allowing lower temperature and higher n(3) population, the scaling of optimised gain with mass and laser pulse length is of the form,[6], $G \sim M^{-17/22}\ \tau^{-8/11}$ with smaller plasma mass and shorter pulse duration giving higher gain.

Constraints for the present work were laser pulses no shorter than 70 psec, the lower limit for the Vulcan system, and minimum fibre diameter of 7 μm limited by bending under gravity of a 14 mm length supported at one end. The optimum energy indicated by equation 3 for these conditions is 1.6Jcm^{-1}. Numerical modelling refined these analytic conclusions, showing that gain is produced in an expanding annular region, and suggesting an optimum energy of 2J cm^{-1} and peak gain of $15\ \text{cm}^{-1}$.

The absolute and relative intensities of the Balmer lines were determined by calibrating the detector using synchrotron radiation[12]. Line blending of H_β with $4 \times Ly_\alpha$ was assessed by recording spectra showing simultaneously $H_\beta + 4 \times Ly_\alpha$ and $3 \times Ly_\alpha$, both with and without a 1000Å Aℓ filter to cut out the Balmer lines. The results showed that the fraction of the observed intensity due to the Balmer lines was 100% for H_α and 75% for H_β.

An experimentally recorded streak spectrum is shown in Fig A1.1. The main spectral features are the C VI Balmer α, β and γ lines. Weaker lines are C VI and C V resonance lines in higher orders and some C V 1s2ℓ to 1snℓ transitions .

Figure A1.2 shows H_α and H_β intensities for a range of lengths from 1.5 to 9.5 mm, 975 psec after the peak of the laser pulse. In Figure A1.2 the exponentially increasing H_α intensities are fitted to the function exp(gℓ)-1, (appropriate for small values of gℓ where gain

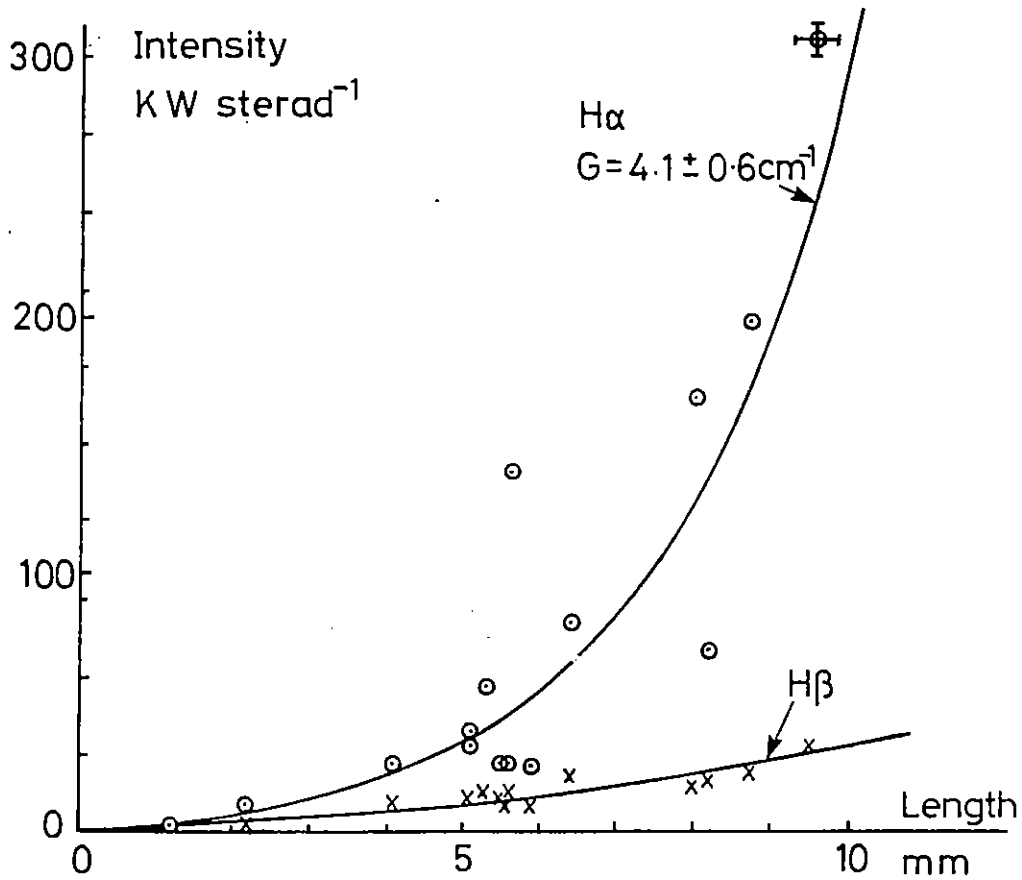

Fig A1.2 (a) Ordinate absolute intensity of axial H_α and H_β emission measured from streaked spectra 975 psec after the peak of the laser pulse. Abcissa irradiated length. A typical measurement error bar is shown for H_α. Theoretical fits to the experimental data are also plotted.

narrowing of amplified spontaneous emission is not important). The method used was linear least squares fitting for data points $\ln(I(\ell)/C+1)$, using C as a free parameter to obtain a fit passing through the origin, for which the slope g gave the gain. The resulting best fit is $g = 4.1 \pm 0.6$ cm^{-1} corresponding to maximum $g\ell = 3.9$ or single transit gain of 49. Lengths ℓ were taken from the X-ray pinhole camera images of the irradiated fibres. The data have average absorbed energy per unit length E/ℓ of of 2.6J cm^{-1} with RMS variation $\pm$ 0.6 cm^{-1}. The incident energy was 10 times the absorbed energy. Least squares fitting showed no systematic change in E/ℓ with ℓ.

The H_β data have a best fit g value of 1.57 $\pm$ 0.17. A similar conclusion is obtained for H_γ. These lines are not expected to show gain and the small non linearity is attributed to systematic error in the data set, though there was no statistically significant variation in E/ℓ with ℓ as noted earlier. If the H_α data are scaled by a factor $g\ell/(\exp(g\ell)-1)$ with g = 1.57, which gives zero gain if applied to the H_β and H_γ data, the resulting g value for H_α is found to be g = 3 $\pm$ 0.5 cm^{-1} giving a lower bound on the gain.

The temporal variation of H_α and H_β is plotted in Figure A1.3 for short (2.2 mm) and long (8 mm) plasmas. Line intensities can be measured from about 130 psec when the lines emerge from the continuum. The intensities for 2.2 mm have been scaled by the length ratio $\ell_1/\ell_2 = 8/2.2$, showing clearly that H_β has very similar pulse shape for both lengths with intensity scaling almost linearly with length at all times. The H_α pulse shape is similar to that of H_β for 2.2 mm but for 8 mm length the intensity rises rapidly relative to the other lines with a ratio peaking after about 1 nsec.

The temporal variation of amplification was assessed by measuring the time dependent ratio of the H_α intensity for the two lengths. This ratio has the form $S_1(\exp(g\ell_1)-1)/S_2(\exp(g\ell_2)-1)$ enabling determination of g provided the ratio of the source function brightnesses S_1 and S_2 is known. In this case $S_1/S_2 \approx 1$ as evidenced by the similarity of the scaled H_β intensities in Figure A1.3.

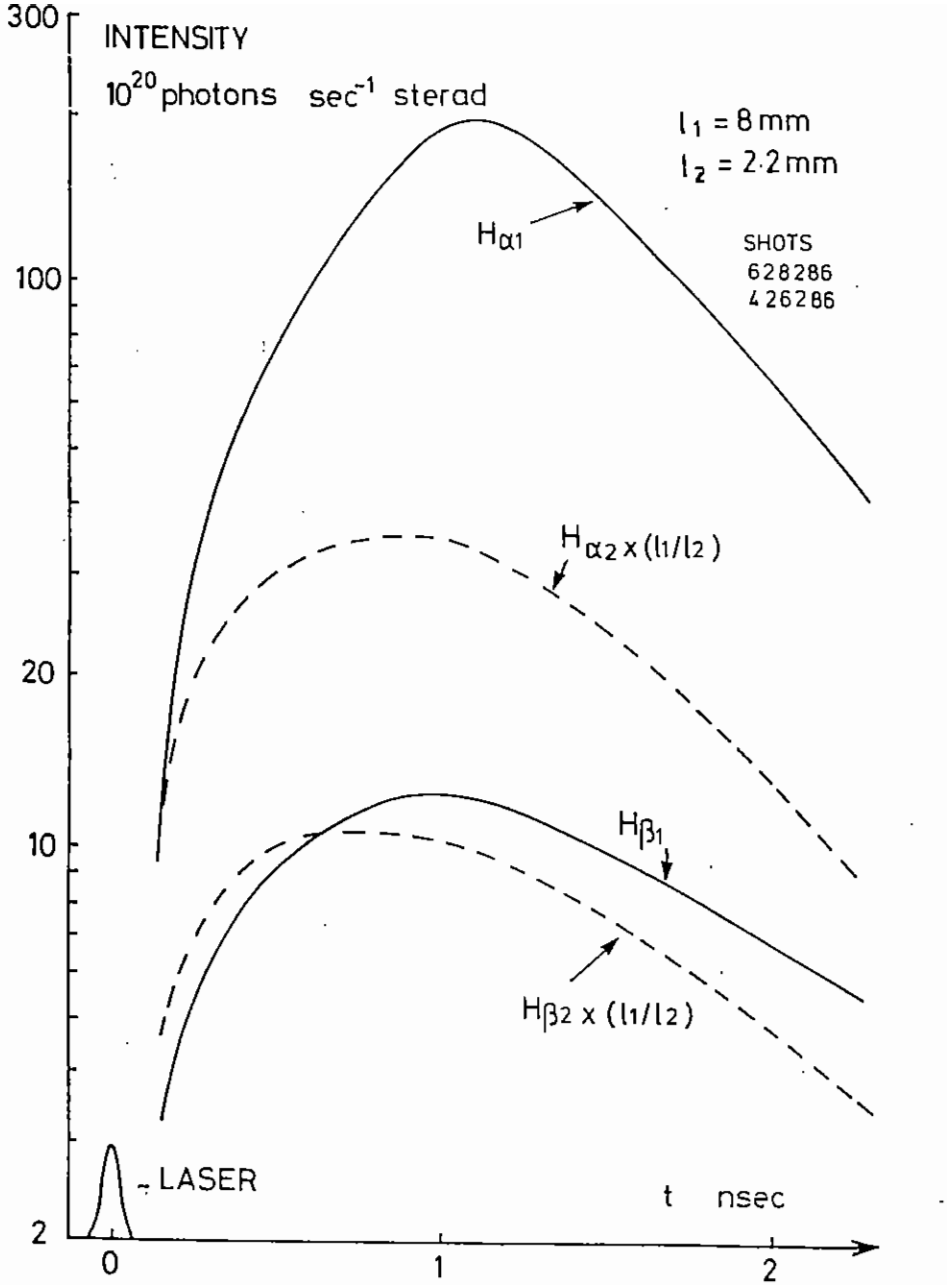

Fig A1.3 Time history of the absolute intensity of H_α and H_β from two streak spectra. H_{α_1} and H_{β_1} are for length ℓ_1 = 8 mm and H_{α_2} and H_{β_2} are for ℓ_2 = 2.2 mm.

Figure A1.4 presents the variation of gain with time. For times later than 1 nsec a systematic error becomes important as the radius of the expanding short plasma becomes comparable with its length, leading to a spherical expansion and more rapid cooling. Some evidence of this is seen in Figure A1.3 in the different late time slopes of H_β emission for the two lengths. The estimated gain at late times therefore becomes systematically too high. At early times (< 400 psec) the 400 psec temporal resolution in the streaks masks any sudden change of intensity ratio.

Various numerical simulations of the experiment were carried out. A one-dimensional Lagrangian hydrodynamic code was used involving a collision-radiative model for ionisation. This model included the Sobolev[13] approximation to describe the effect of Doppler-decoupling on the trapping of C VI Lyman radiation. The results gave radial profiles of emission and gain as a function of radius and time, from which the total emission along the axis was computed as shown in Figure A1.5. The computed values of absolute intensity of H_β for long and short plasma lengths agree well with the experimental values except that the peaks occur 300 ps earlier and decay more rapidly. The computed H_α emission for long lengths is much greater than is observed because the observed amplification is smaller. The H_α:H_β ratio at late times when gain is low is the same in both theory and experiment.

The apparent H_α gain was deduced by treating the computed intensities in the manner used in analysing the corresponding experimental data. The finite (400 psec) temporal resolution of the streak camera was included in the simulation by a convolution procedure giving a significant modification to the apparent gain. Instead of an initial 150 psec period of -ve gain the apparent gain starts at zero and rises sharply. Comparing this apparent gain with experiment shows qualitative similarity, ie initially zero gain followed by a sudden rise of gain which reaches a maximum and then decays. The calculated peak of 15 cm^{-1} is however much higher than the 4 cm^{-1} deduced from experiments and it decays more rapidly. No full explanation of the difference between experiment and theory has been obtained yet but investigations are continuing. Non-uniformities seen in X-ray and Schlieren images of the plasma suggest inhomogeneity of the plasma early in the expansion which may reduce the early gain, while at late times the spherical expansion of the short plasma length leads to an over estimate of gain.

In conclusion, we have successfully used new optical and diagnostic systems to measure moderately large laser gain on the 18.2 nm Hα transition of C VI.

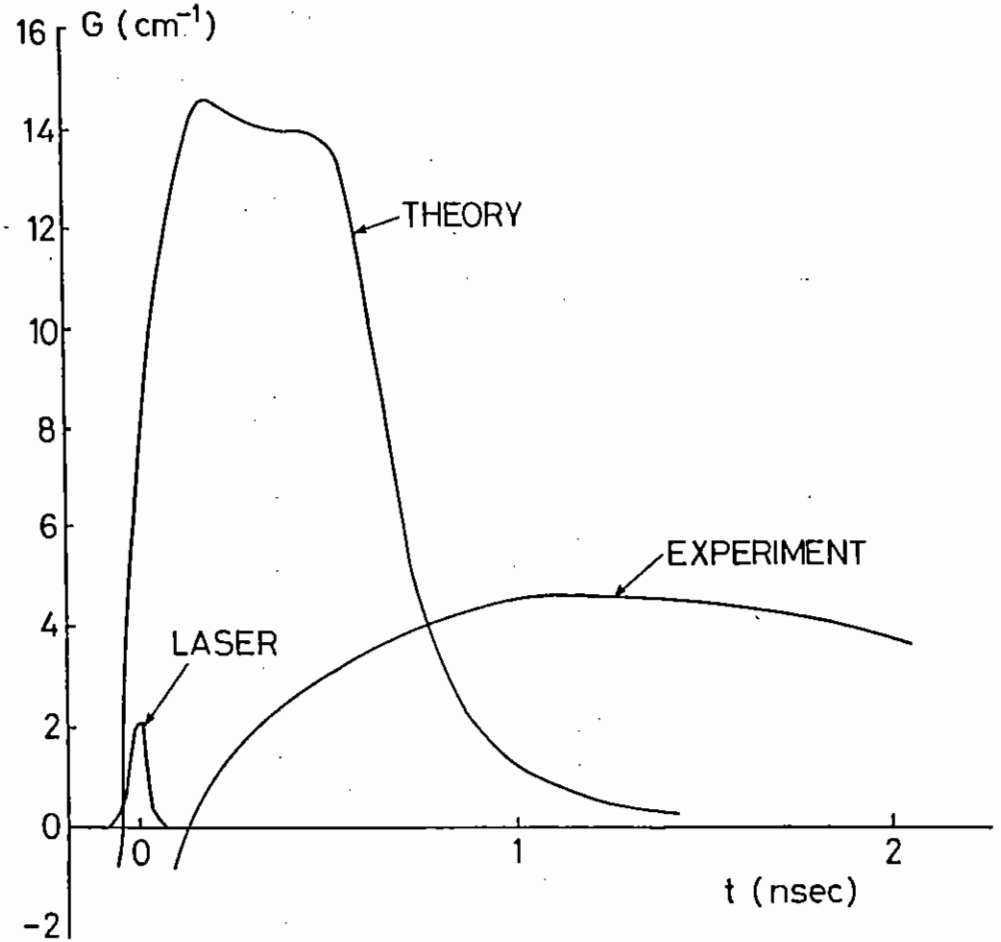

Fig A1.4 Gain coefficient as a function of time deduced from Figures 3 and 5 as explained in the text.

A1.2 EXPERIMENTAL STUDY OF RECOMBINATION PUMPED XUV LASER ACTION IN F IX

C Chenais-Popovics, M Grande, R Hawkins, C Hooker, M Key, S Rose,
W Shaikh, T Tomie (Rutherford Appleton Laboratory)
G Kiehn, R Smith, O Willi (Imperial College, London)
R Corbett, C Lewis, C Regan (Queen's University, Belfast)
G Pert, S Ramsden (Hull University, Hull)

Introduction

Isoelectronic scaling of the hydrogenic Balmer α transition and of the XUV laser mechanism is discussed in Section A4.9 and Section A4.15 ibid.

The objective of the present experiment was to demonstrate laser action at the shortest wavelength possible constrained by the limits of the Vulcan laser facility for short pulse generation (70 psec) and power (1 TWatt) at λ = 0.53 μm and also by the availability of a target material suitable for coating on a carbon fibre.

It was important to choose a material which could, in principle, operate at a gain length ≥ 3,sufficient for measurement of laser amplification. The scaling arguments and numerical calculations presented in Sections A4.9 and A4.15 suggested that flourine would meet this criterion; additionally it could be readily coated as LiF. For 7 μm fibre diameter and 70 psec pulse duration the modelling suggested an absorbed energy requirement of 11Jcm^{-1}. This is just at the limit of the target irradiation facility with all six beams irradiating the same 7 mm length, transmission through the optical system of 70% and coupling of 10% to the target.

The numerically predicted performance of the targets is summarised in Figs A1.6 and A1.7 which show a time history of plasma parameters for a Lagrangian element of the target material originating from a depth of 390 nm and radial profiles of parameters at the time of peak gain.

Gain is predicted when the resonance transition becomes optically thin within the Doppler decoupling range, as illustrated in Fig A1.7, with gain coefficient up to 5 cm^{-1}.

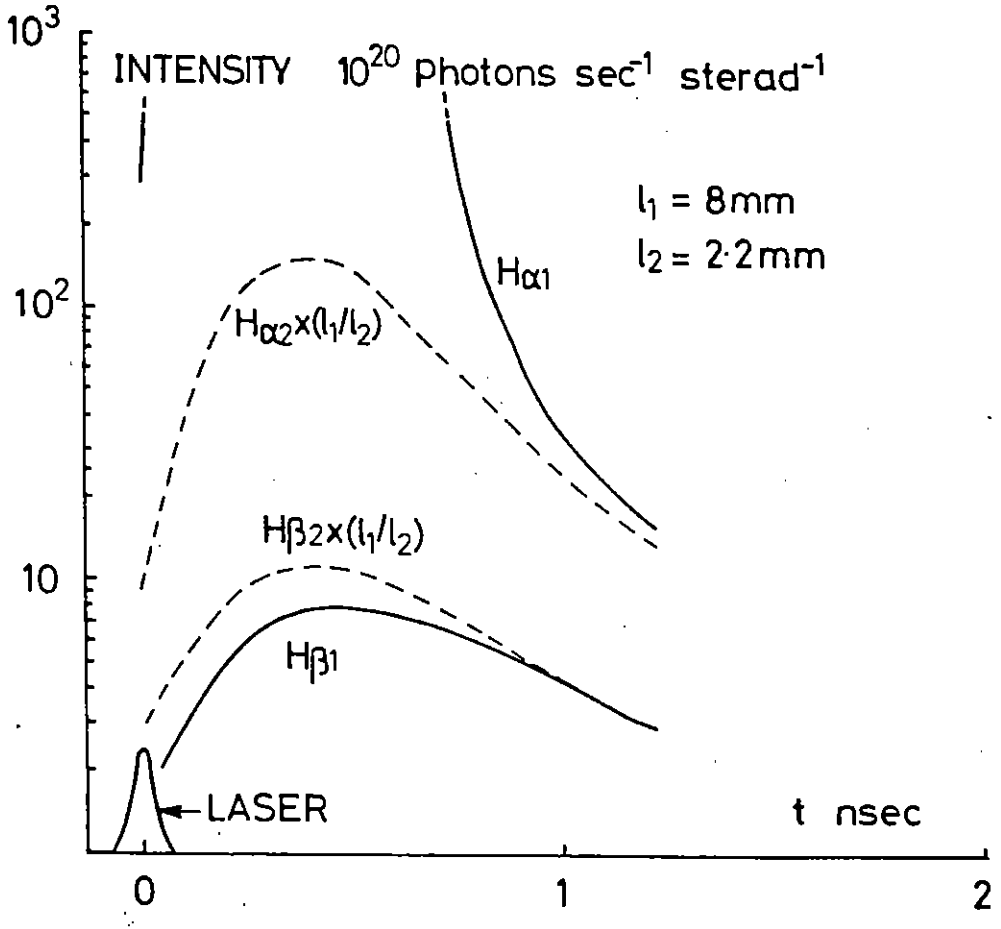

Fig A1.5 Computed time history of absolute intensity of H_α and H_β for plasma lengths of 2.2 and 8 mm corresponding to the experimental data in Figure A1.3.

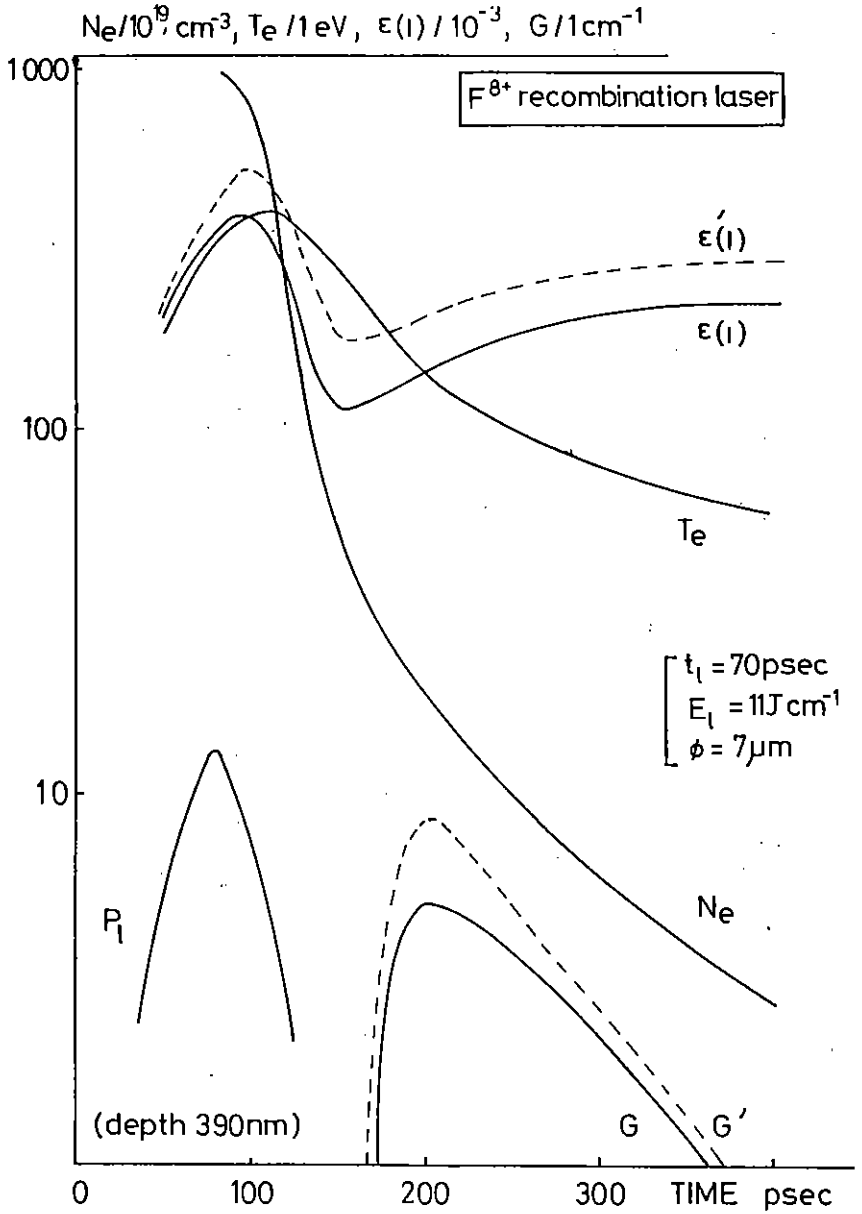

Fig A1.6 Predicted time histroy of plasma parameters in the recombination pumped hydrogenic fluorine X-ray laser scheme.

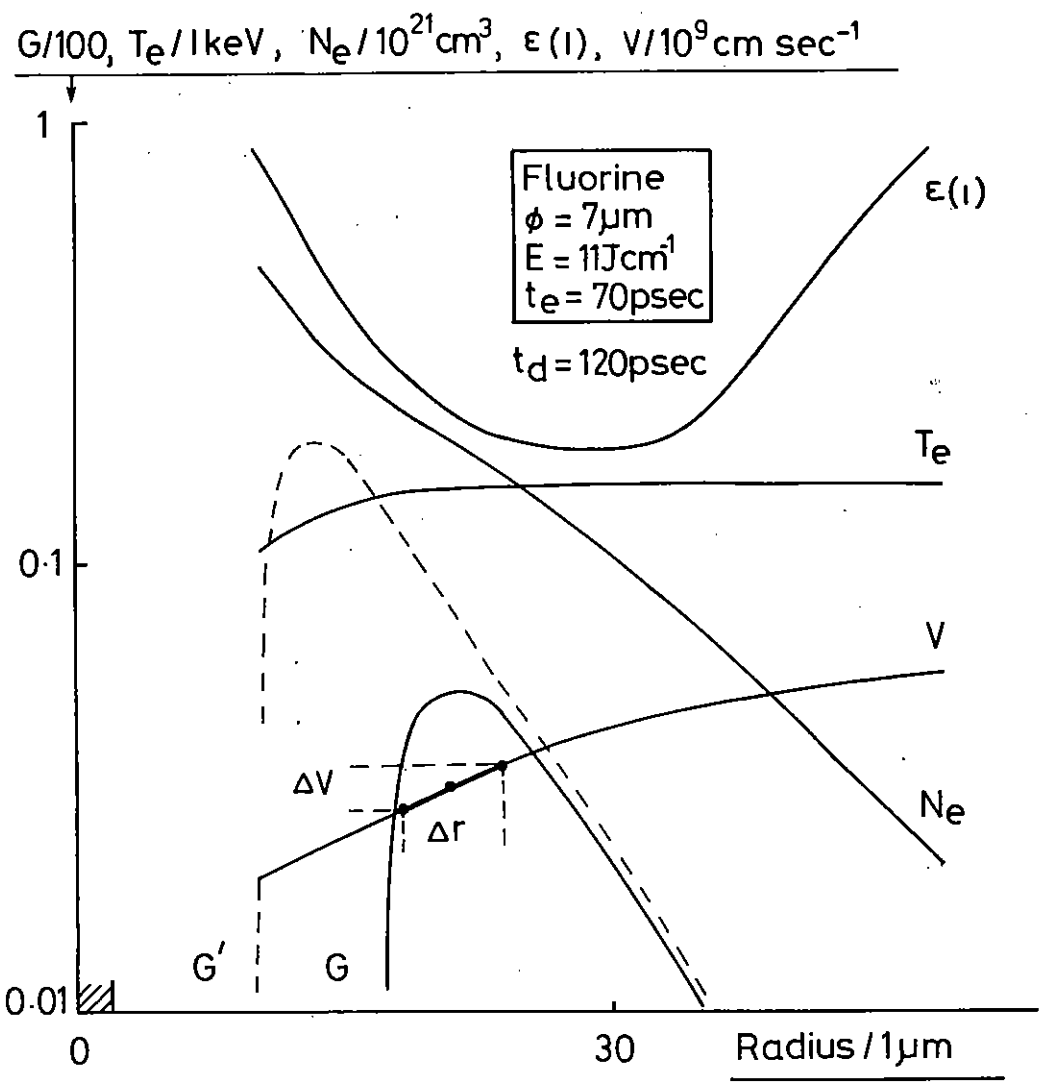

Fig A1.7 Predicted radial behaviour of plasma parameters in the recombination pumped hydrogenic fluorine X-ray laser scheme.

The peak temperature is about 370 eV at 4 x 10^{21} electrons cm^3 expanding to 2 x 10^{20} cm^{-2} and 140 eV at the time of peak gain. A lower temperature would ideally be obtained as discussed in Section A4.15 but more cooling cannot be obtained because the density at peak temperature cannot be made greater than the critical density.

Experimental Method

The experimental facility shown in Fig A1.8 was similar but enhanced relative to that used for the C VI experiments, (described in A1.1). A second flat field time resolving spectrometer was added to record off-axis emission, with as before, an axial flat field instrument, X-ray pinhole camera and plasma calorimeter array.

A further diagnostic measurement was a temperature monitor giving one dimensionally space resolved images along the fibre at several different filtered X-ray energy bands. The device supplemented the normal X-ray phc in providing data on the effective irradiated length of the fibre. The F IX resonance spectrum was space resolved transversely to the fibre with a 1-D penumbrally imaging X-ray crystal spectrometer to assess how inversion develops in the radial expansion (see Fig A1.9).

Results

Data were recorded for a range of irradiated lengths from 1.5 to 6 mm with the free end of LiF coated fibres positioned towards one end of the line focii and with the six beams all irradiating the same region of nominal 7 mm length. The beams were masked to reduce the irradiated length.

For energies a few times less than the calculated optimum, spectra recorded in the F IX Balmer spectral region (40-100Å) showed strong F VIII features as well as F IX with Balmer α not prominent relative to other lines and not showing any temporal peak of ratio relative to other lines.

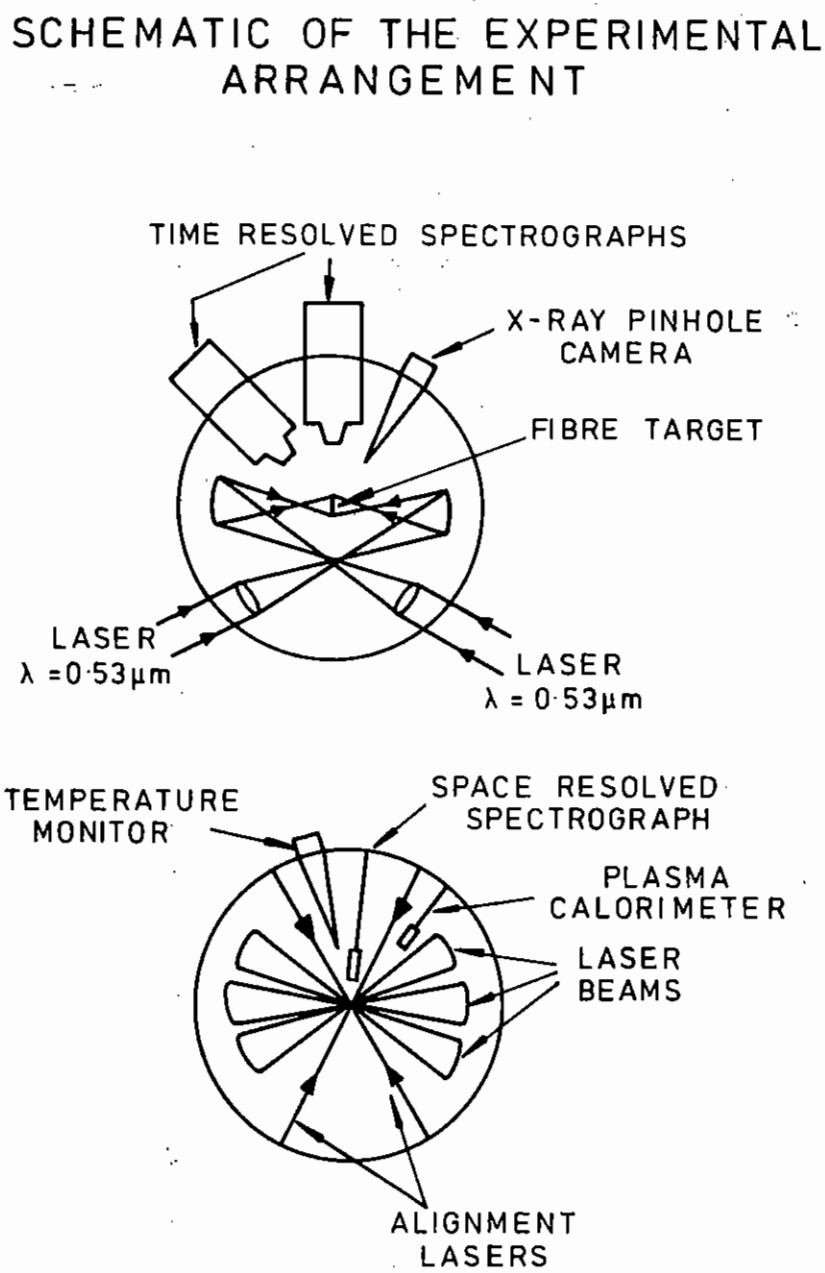

Fig A1.8 Schematic of the experimental arrangement showing plan and axial views.

Increased energy up to the computed optimum level gave an obvious change illustrated in Figs A1.10 and A1.11 (for axial and transverse emission with 6 mm irradiated length). F IX Balmer α is the dominant line in the axial spectrum and the Balmer series is mixed with weaker F VIII lines with identification shown in Fig A1.12. In the transverse spectrum F IX Balmer α is less prominent and the F VIII spectrum is strong (Fig A1.13). No F VIII or F IX resonance lines are seen in higher order, in contrast with the C VI spectra. The reason is that the 3° grating angle is too large to reflect the circa 10Å F IX and F VIII resonance spectra.

The time dependence of the ratio Hα/Hγ is of interest. For short length there is a steady decrease with time, Fig A1.14, while for the largest length there is a marked temporal peaking suggesting a gain peak as shown in Fig A1.15.

The main test of gain is the axial to transverse intensity ratio. The two instruments were cross calibrated using plasma formed on a plane target with surface normal bisecting the angle between the two instruments to give an equivalent view of the plasma for both.

The ratio is of the form $(\exp g\ell-1)/g\ell$ (for small gain and negligible spectral narrowing). Lengths ℓ were measured both from the X-ray pinhole camera (filtered to 0.6 KeV) and from the temperature monitor images, eg Fig A1.16.

Fig A1.17 presents the results with two length estimates for each data point from the two instruments and a cross calibration point shown at zero length.

The data clearly indicate a gain coefficient $g \sim 3cm^{-1}$ and single transit amplification of about 7. Data from the space resolving spectometer show a population inversion at a distance of 100μm from the axis (Fig A1.18).

This result is important as it is the shortest wavelength for which XUV laser amplification has been reported to date.

Work is continuing to analyse the results in more detail and to make further comparison with theory. It is already clear that the

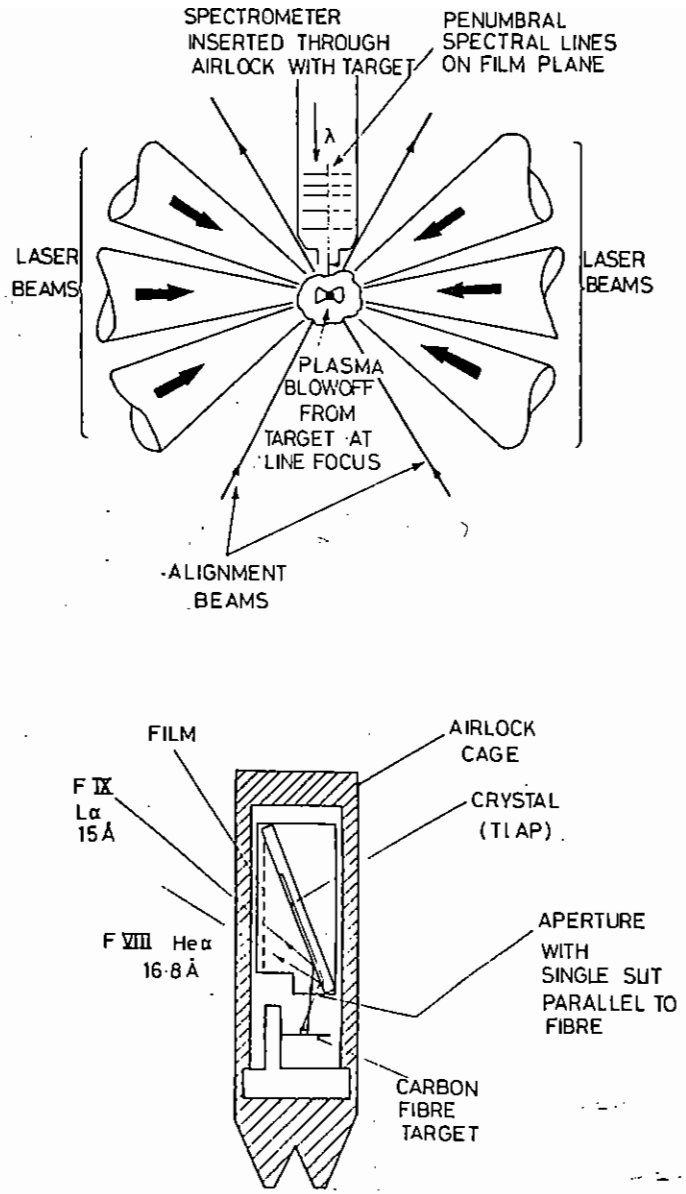

Fig A1.9 Schematic diagrame of single slit 1-D penumbral imaging X-ray crystal spectrometer showing axial and transverse views.

observed gain occurs later and is lower than expected theoretically. The reason is thought to lie in inhomogeneity of the plasma at early times as evidenced by structure in X-ray images, temperature monitor images (Fig A1.16) and Schlieren pictures (see Section A1.4).

Further experiments will seek to obtain laser action at shorter wavelength, with higher gain-length and using XUV optics to increase the effective gain-length.

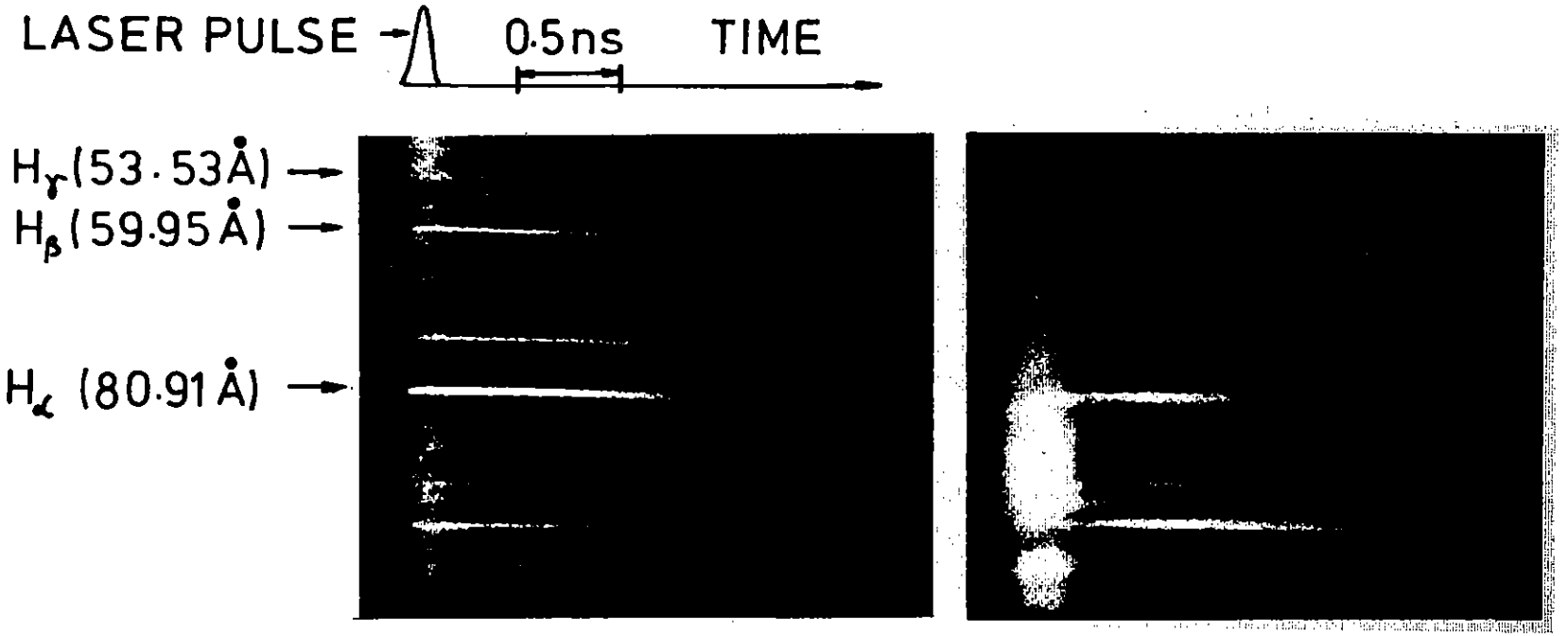

Fig A1.10 Axial time resolved spectrum for 6mm fibre.

Fig A1.11 Transverse time resolved spectrum for same 6mm fibre as A1.10.

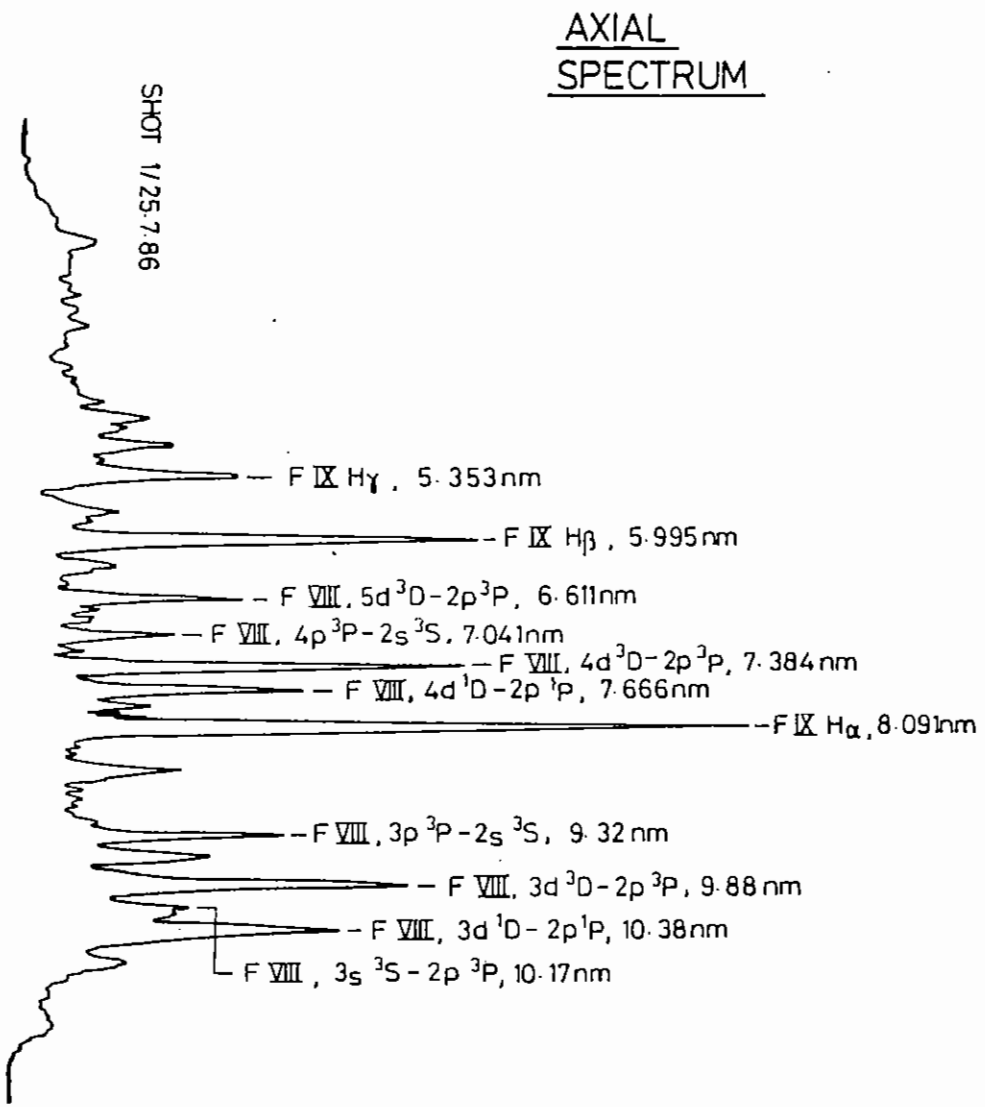

Fig A1.12 Detailed assignment of spectral features in Fig A1.10.

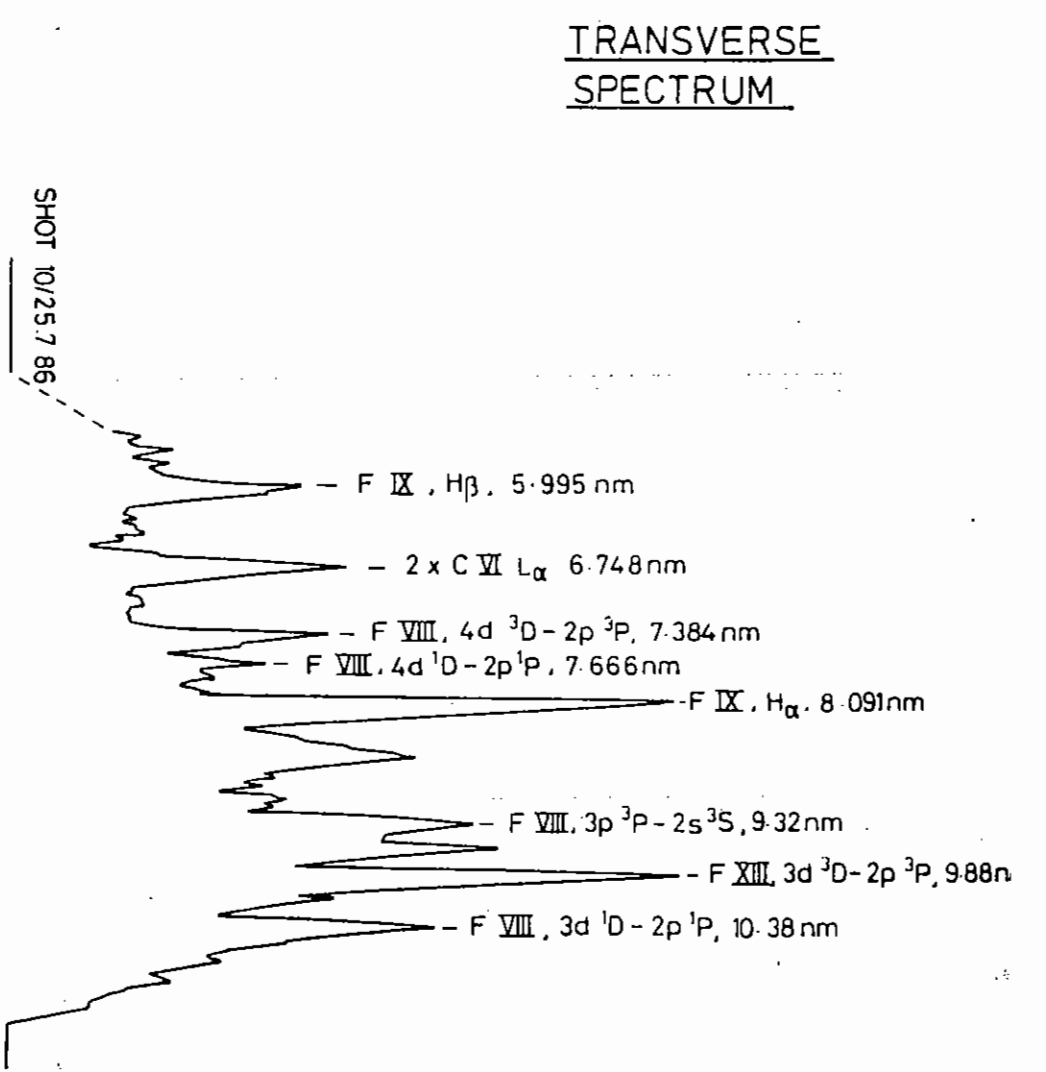

Fig A1.13 Detailed assignment of spectral features in Fig A1.11.

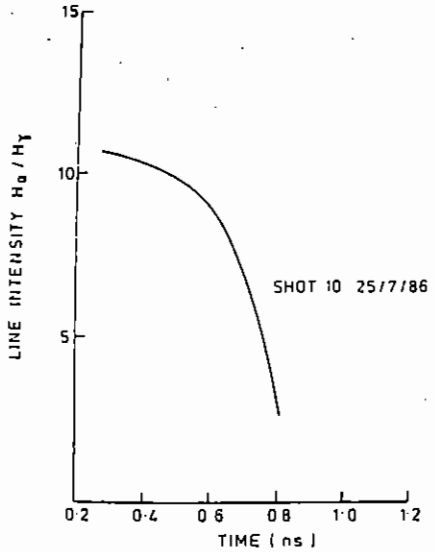

Fig A1.14 Time variations of H_α/H_γ line ratio for a short pulse.

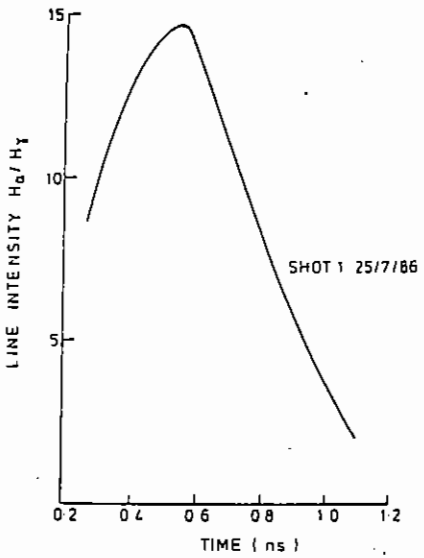

Fig A1.15 Time variations of H_α/H_γ ratio for the longest fibre, showing marked temporal peaking.

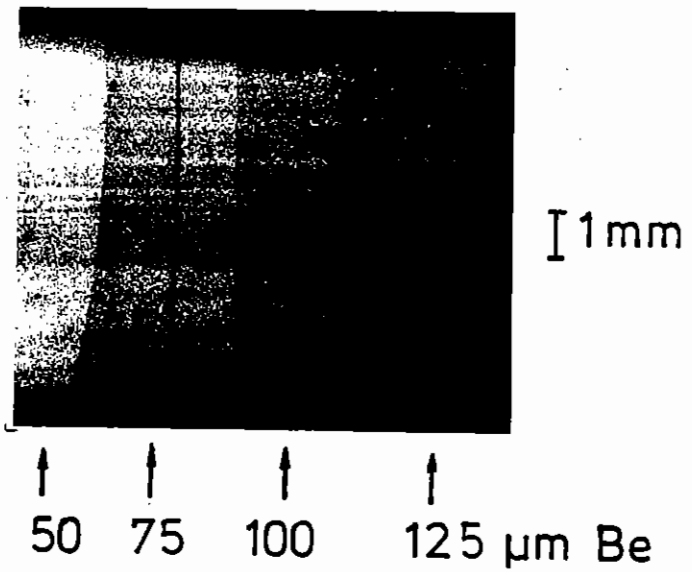

Fig A1.16 Temperature monitor image of a long length fibre, showing marked inhomogeneities along the length of the fibre, shown vertically. The horizontal variaton in intensity is due to varying thicknesses of Beryllium filter allowing the temperature to be inferred.

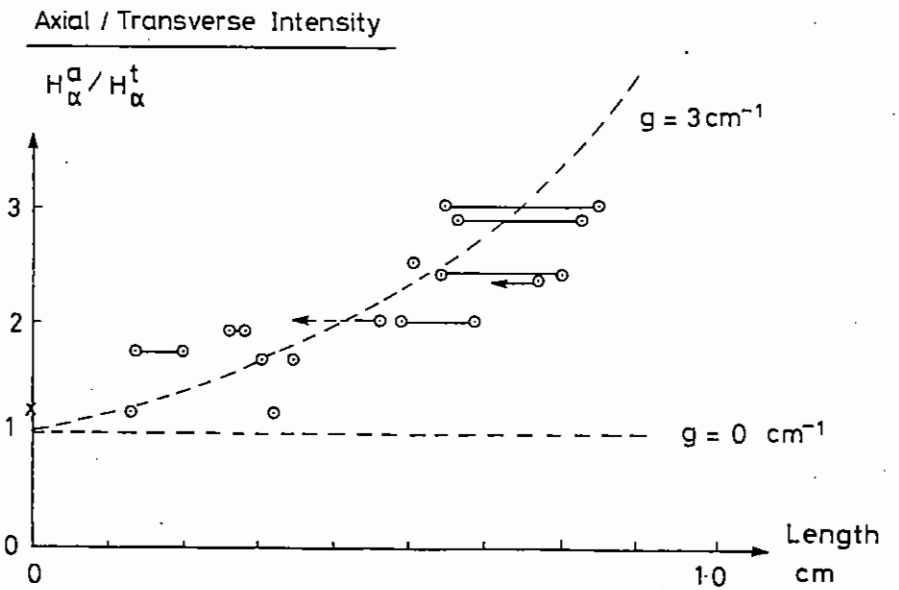

Fig A1.17 Variation of axial/transverse intensity at H_α with fibre length, showing exponential behaviour indicative of a gain on the order of $5cm^{-1}$.

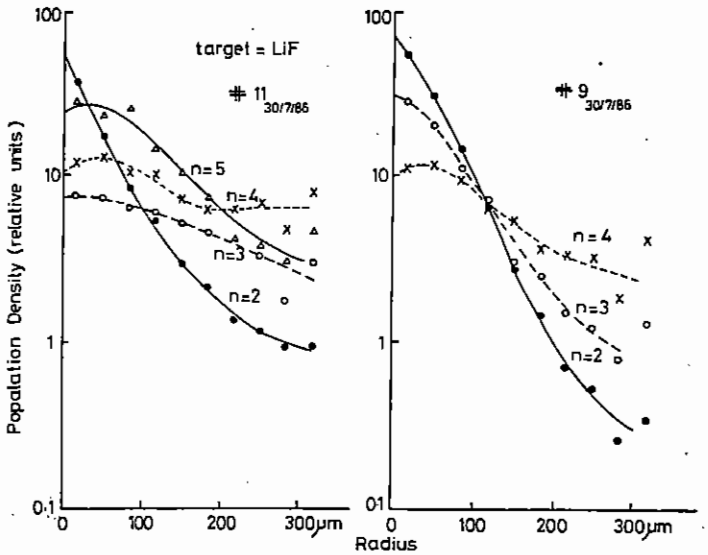

Fig A1.18 Variation of population density with radius for two shots as inferred from the Hydrogenic Fluorine Lyman series emission observed with the 1-D ??? imaging X-ray crystal spectrometer.

A1.3 EXPERIMENTAL STUDY OF A RECOMBINATION PUMPED LI-LIKE Al XI XUV LASER SCHEME

A Carillon, M Guennou, P Jaegle, G Jamelot, A Klisnick, A Sureau (LSAI, Orsay, France)
C L S Lewis, C Regan (Queen's University of Belfast)
O Willi, R Smith, J Edwards (Imperial College London)
M H Key, G Kiehn, M Grande, S J Rose (Rutherford Appleton Laboratory)
T Tomie (Elect Lab, Japan)

Introduction

The basic principles of recombination laser schemes which have been most extensively considered in terms of hydrogen-like ions can be extended to any ion state but most interestingly to any ion having a closed shell configuration with electrons recombining into high lying valence states. Bare nuclei He-like and Ne-like ions form the most interesting set with recombination leading to potential XUV lasing transitions in H-like, Li-like and Na-like ions respectively. Li-like schemes, being the simplest system to model after H-like, have been most extensively considered by the French group led by Jaegle at Orsay. Most of their experimental work has previously dealt with the irradiation of slab targets by 1-20 nsec laser pulses (eg Ref A1.14). To capitalise on French experience with Li-like systems and RAL/UK University experience with small mass target irradiation and diagnostics a collaborative experiment on Li-like Al XI laser action was carried out at the CLF.

Background

The term diagram for a Li-like ion derived from an atom of atomic number z closely resembles the hydrogenic term diagram of an ion with atomic number z-2, apart from term splitting (fig A1.19). Now however the ground state is $1s^2 2s(^2S_{1/2})$. The recombination principles well-known for H-like ions now apply with the requirement that resonance 3-2 transitions are optically thin and that the collision limit is near n = 4 at the time of inversion during recombination. Inversion is established between n = 4 and n = 3 levels and, as shown by experiment, also between n = 5 and n = 3. A major difference between Li- and H-like systems is that dielectronic recombination becomes an additional pumping mechanism.

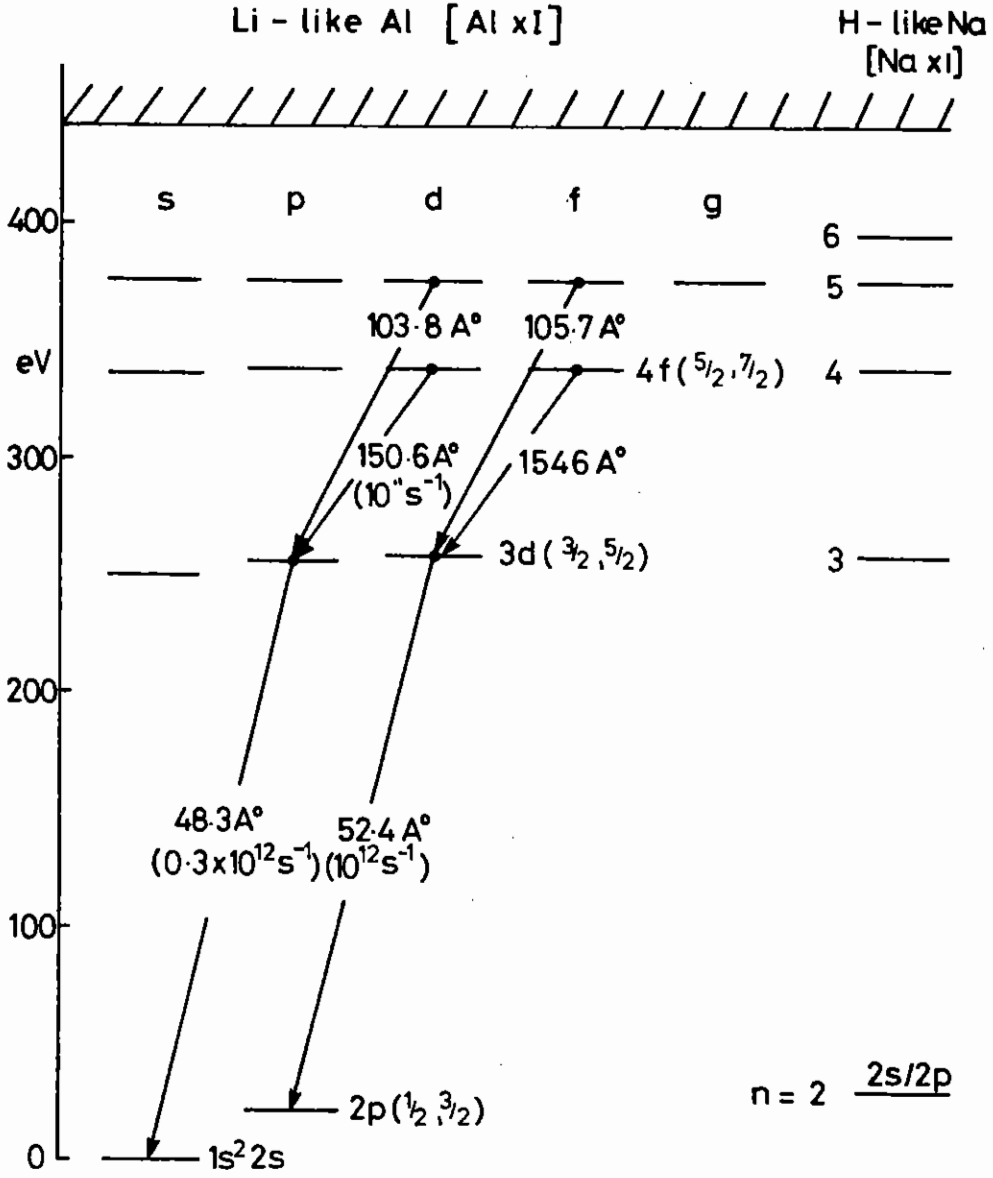

Fig A1.19 Term diagram of Li-like Al and the related terms of excited states of H-like Na. The three dominant doublets observed in emission are indicated.

It is possible to gain an insight into the relative merits of Li-like and H-like schemes by treating them both as essentially hydrogenic. To achieve laser action at a given λÅ on a 3→2 transition in H-like ions requires a target with atomic number $z(H-) \approx (6563/\lambda)^{\frac{1}{2}}$. To achieve the same λ on a Li-like transition requires $z(Li-) \approx 2 + fz(H-)$ where f = 1.7 and 1.4 for 4→3 and 5→3 transitions respectively. The ionisation energy to ionise the last electron to form He-like ions is then $\approx f^2/4$ times the ionisation energy of the corresponding H-like scheme for the same λ, ie $^3/_4$ or ½ depending on whether a 4→3 or 5→3 laser can be operated. Assuming all other factors to be equal this represents the advantage of Li-like schemes as it is easier to reach the required excitation temperature. Furthermore, when crudely estimating the pump energy required (assuming all electrons and ions produced require a thermal energy comparable to the ionisation energy of the last ionisation stage and summing ionisation energy over all stages) it appears that the required absorbed energy per unit mass in the initial plasma is also approximately a factor $f^2/4$ lower in the Li-like scheme. This is illustrated in Fig A1.20. The pump power requirements will depend on how this energy can be coupled on the right time scale (determined by the ionisation rates) to the right mass (determined by energy transport mechanisms appropriate to the laser power) and in such a way that the subsequent hydrodynamics and recombination lead to maximum gain. To assess these factors properly and in particular the z-scaling implications of Li-like versus H-like schemes requires more analytic and numerical modelling.

Experiment

As an initial experiment in gaining experience in Li-like recombination laser Al was chosen as the material with potential lasing action at 154.6 Å (4f→3d) and 105.7 A° (5f→3d). Targets were 8 μm diameter Carbon fibre coated with ≈ 3500 A° of Al and were irradiated with 120 ps, 2ω pulses in the normal line focus mode using off-axis mirrors. Two sets of data were taken using a) four out of the six beams superimposed with a 7 mm long common focus and b) two pairs of beams displaced giving ≈ 14 mm long plasma columns. In each

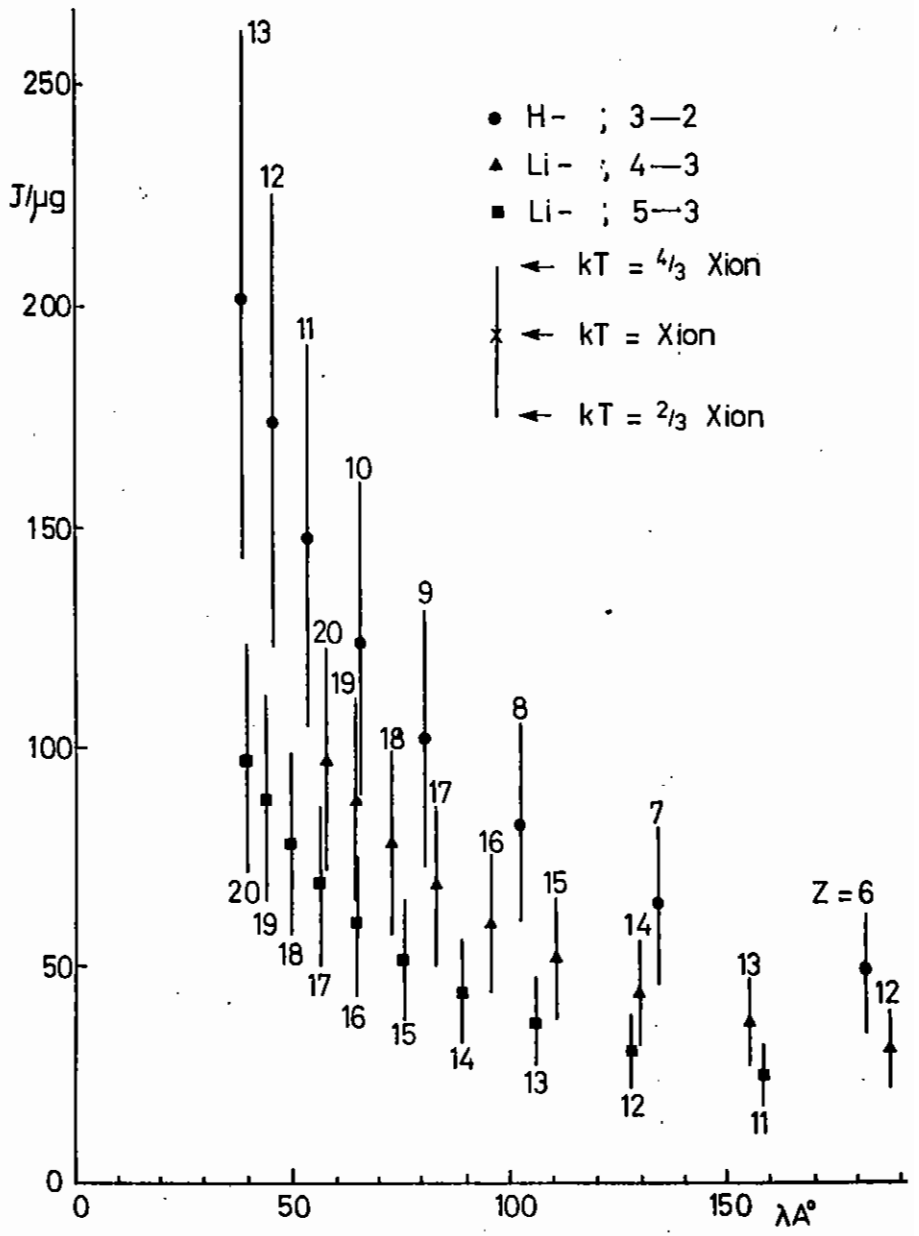

Fig A1.20 Estimate of the scaling of absorbed energy per unit plasma mass (J/μg) required to achieve specific lasing wavelengths, λ Å, in H-like and Li-like ions of various atomic number targets (z).

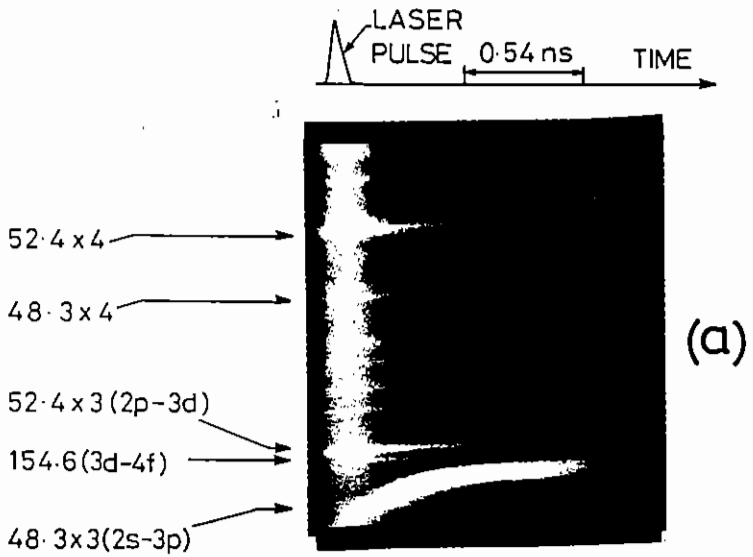

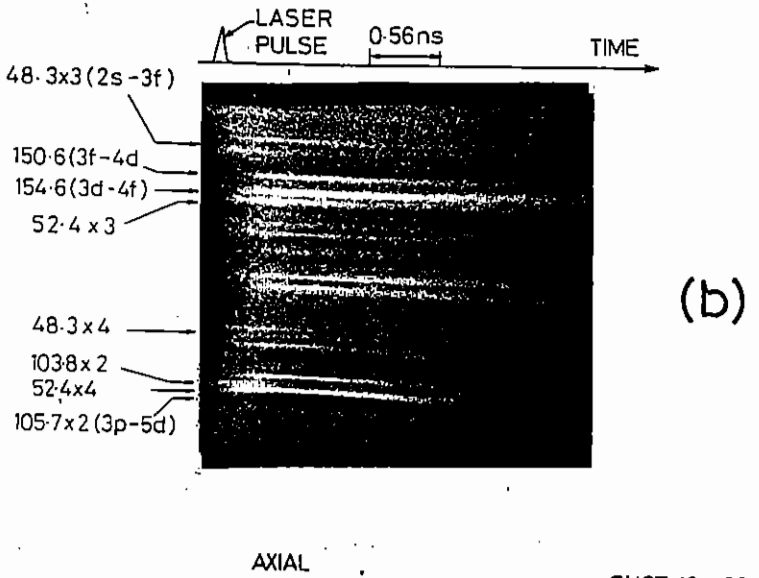

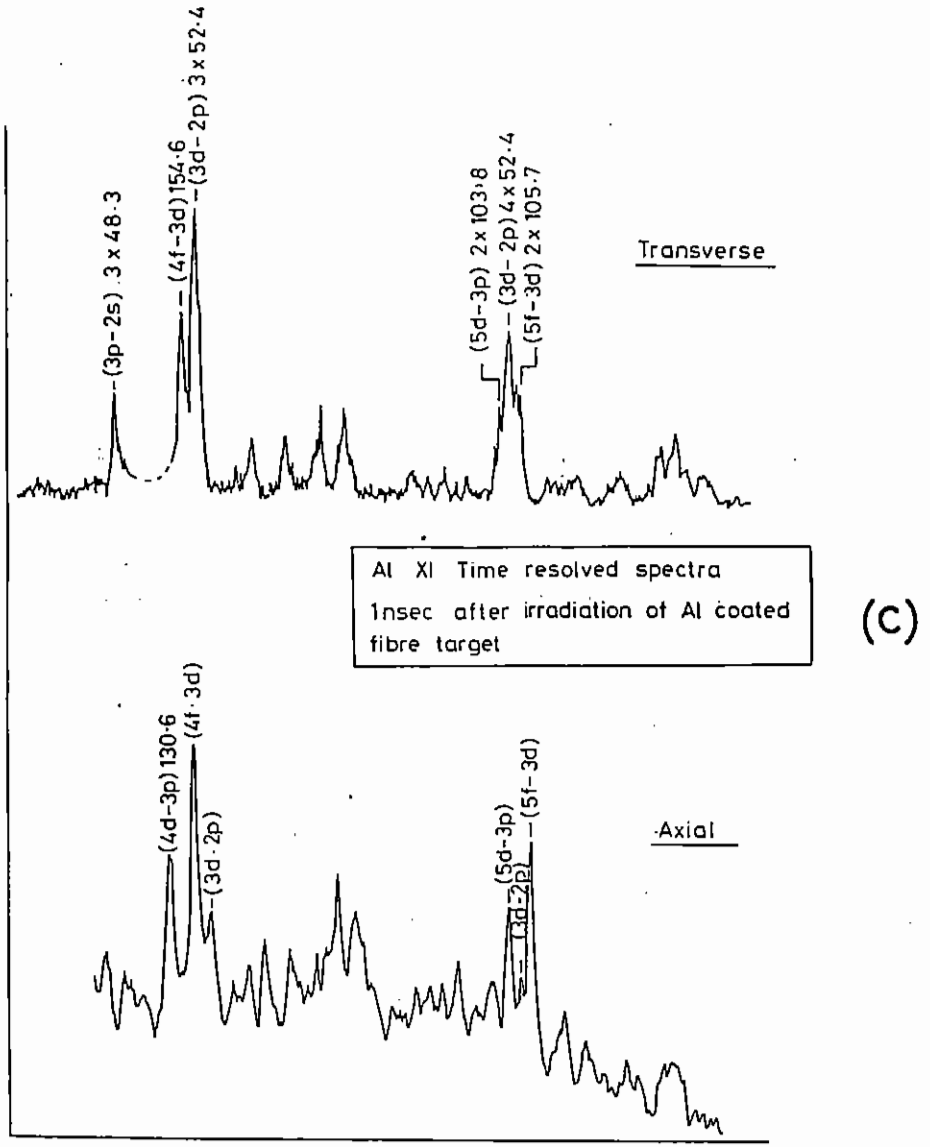

Fig A1.21 Transverse (a) and axial (b) streaked emissions from an Al coated carbon fibre, 11 mm long and with 80 J energy at 2 ω incident in 120 ps.

case effective plasma length was controlled by aperturing the input beams. Typically 10-15 J was incident on the aperture per beam. In configuration a) this corresponded to ≈ 5 J/cm absorbed energy in the fibre with 10% coupling efficiency and resulted in a burn depth on the target surface less than the Al thickness. Standard diagnostics were used to monitor the plasma formed and included active and passive pinhole cameras, plasma calorimetry and axial and transverse time-resolving flat-field spectrometers looking at a spectral window 100-250 A° approx.

A typical pair of streaks from axial and transverse streak spectrometers is shown in Fig A1.21 and the main spectral features can be understood with reference to the term diagram for Al XI shown in Fig A1.19. The spectra are essentially dominated by three doublets, ie resonant 3→2 transitions at 48.3 A° and 52.4 A°: 4-3 transitions at 150.6 A° and 154.6 so and 5→3 transitions at 103.8 A° and 105.7 A°. The transverse spectrum is dominated by the resonance doublet seen in 3rd and 4th order while the axial spectrum is dominated by the 4→3 and 5→3 doublets seen in the 1st and 2nd orders respectively. This trend becomes stronger as the length of plasma is increased. A second feature of the spectra is that the temporal history of the doublets are different although they all generate from the same parent ion. In particular the 4→3 and 5→3 lines peak in brightness after the laser pulse has terminated, ie they increase in brightness during the plasma recombination phase.

These trends provide circumstantial evidence that population inversion and gain has been attained. Although a detailed analysis is in progress a preliminary conclusion is illustrated in fig A1.22. Here the peak intensity (above continuum) of the 5f→3d line at 105.7 A° is plotted against plasma length over the range 1.5 to 6 mm for the case of four superimposed beams. A fit to the line growth curve of the form $I\alpha(e^{Gl}-1)$ indicates a gain coefficient G ≈ 3 cm-1 which is somewhat larger than observed with massive targets and longer pulses (G ≈ 2 cm^{-1}). In contrast the intensity of the resonance line measured at the same time shows a linear growth. Although this line is optically thick a linear growth is not totally unexpected from geometrical effects as the line plasma is viewed by the grating in a slitless configuration.

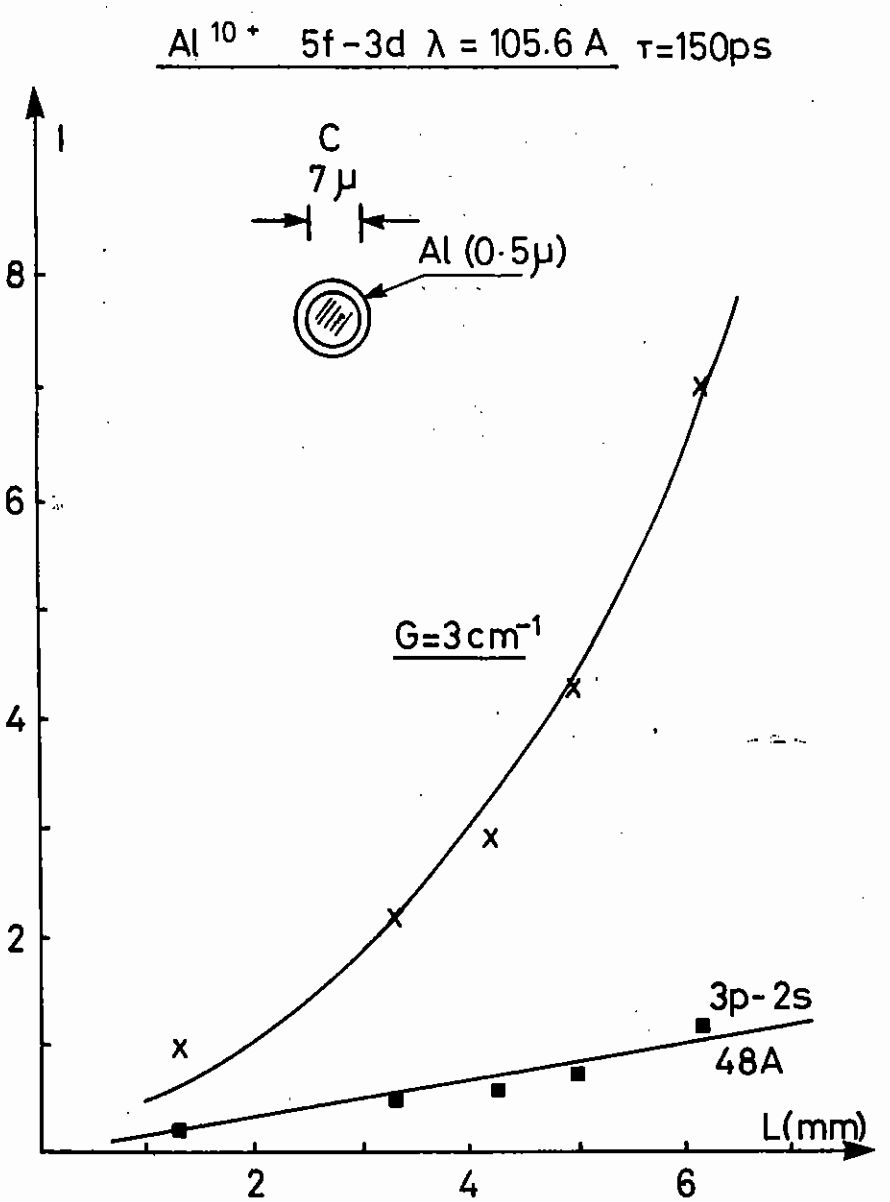

Fig A1.22 Axial intensity of 5f-3d (106 A°) and 3p→2s (48 A°) emissions as a function of plasma length at a time when the 106 A° line is maximum. The 106 A° line is fitted to an exponential, e^{Gl} - 1, indicating a gain coefficient G - 3 cm^{-1}.

Conclusion

Although a detailed analysis is still in progress it appears that our first attempt at generating gain in a Li-like ion has been successful. However details of the scheme are not yet properly understood and require more modelling. For example, why are the gains observed on the 5→3 and those on the 4→3 transition comparable? Nevertheless since we have now seen gain at 81 A° and 182 A° in H-like schemes and at 106 A° in Li-like schemes the prospects of scaling to $\lambda \approx 40$ A°, near the water-window region, appear promising with Li-like systems (cf Fig A1.3(2).

A1.4 HYDRODYNAMICS OF X-RAY LASER TARGETS

D Bassett, O Willi (Imperial College), T Afshar-rad, M Grande and W Shaikh (RAL)

Recent experiments in X-ray laser research have clearly demonstrated gain at wavelengths below 100Å. Thin fibres, coated with Lithium Fluoride are irradiated with the 70 ps frequency doubled (0.53μm) pulse from the Vulcan Laser System. Energy of the order of 150 J cm^{-1} creates population inversion in an annular region where densities present are about 10^{20} cm^{-3}. Gain was observed in the Balmer alpha 3-2 transition of Fluorine at 81Å. The maximum observed gain, though, appears at few hundred picoseconds later than that predicted by simulations. The value of that gain is also considerably less than expected. For this reason an experimental investigation into the hydrodynamics of the fibre targets was carried out.

The experimental arrangement was similar to that used in the X-ray laser runs. Four beams were focussed onto the fibre via the off-axis spherical mirrors used to generate the line focus, which was set at 1.5mm long.

The ablating plasma was diagnosed with a synchronous short pulse optical probe. Raman backscatter of the frequency doubled beam generated single pulses of 15 ps in length and with a wavelength of 622nm. The probe was split into five components, and five separate images were obtained separated by a few hundred picoseconds. A mixture of schlieren photographs and interferograms were taken.

The results demonstrated clear unstable elements in the cylindrical expansion early in time visible in fig A1.23. The severe structural breakup of the expanding plasma is similar to previously observed thermal instabilities. Longitudual modes with wave numbers of 1-5 x 10^3 cm^{-1} can be seen stretching nearly 150 μm into the plasma. These irregularities in the fluid flow obviously seriously affect the ability of the medium to produce lasers with a large effective gain length if the line integral through the regions of gain has been significantly reduced. The net result is that lower gain is recorded early in time.

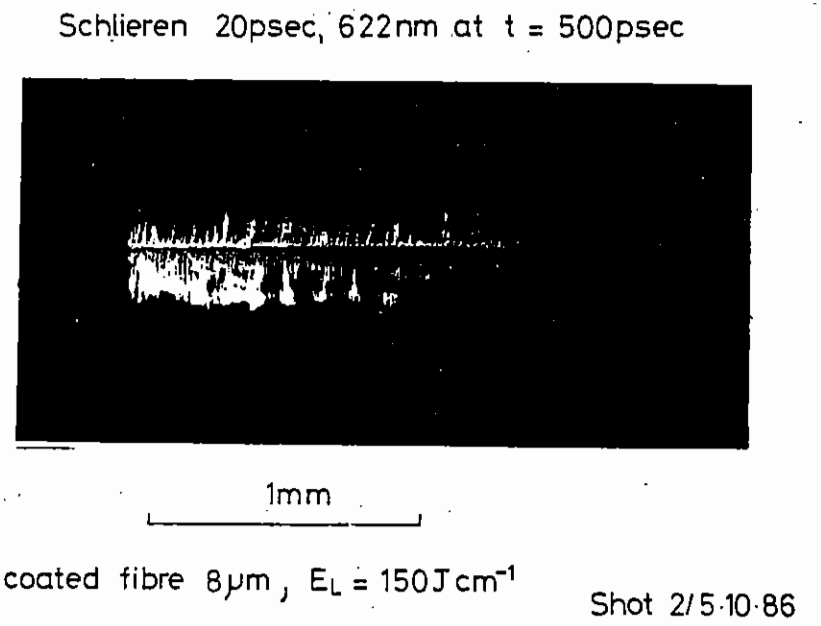

Fig 1.23 Schlieren image of a LiF coated fibre, under 190Jcm^{-1} illumination, showing apparent filamentary structure.

A detailed programme of experimental analysis should prove whether a method of induced thermal smoothing can reduce these instabilities. These experiments are planned for the near future.

Recent interest has also been shown in generating X-ray lasers from a coated stripe type of target. Exploding a Lithium flouride stripe of some 25 μm width is expected to generate the temperature and density necessary for laser action. Although the atomic physics is identical, what is hoped is that using lower initial laser intensities the central region of the generated plasma will lase. The advantages of this scheme come not only in the lower laser irradiances but also from the fact that the gain region is cylindrical and central to the expanding plasma, easing the route for any multipass systems which may be developed.

The hydrodynamic studies were performed on a stripe of 173 nm x 25 μm of Aluminium coated onto a 1000Å Former substrate. These targets were exploded using either two or four short pulse (70 ps) green (0.53 μm) laser pulses from the Vulcan laser. Line foci of 1.5 mm x 25 μm were used and the energies on target varied from 15 J cm^{-1} to 150 J cm^{-1}. The five frame diagnostic probe previously described was used to gain a time resolved insight into the plasma flow. Two frames were also added to investigate the radial expansion.

Preliminary results, however, showed that the targets did not behave quite as expected. Laser energy spilling over onto the plastic substrate seems to create two large regions of cold overdense plasma on either side of the expanding stripe. This restricts the cylindrical flow causing slower rate of expansion and cooling. In addition to this, fluid instabilities have been noted as a consequence of the hot Aluminium - cold plastic interface. (See Section A2).

A1.5 K-SHELL ABSORPTION SPECTROSCOPY

C L S Lewis, R E Corbett, E Robertson, D O'Neill, M J Lamb, S Saadat, Queen's University of Belfast
T Afshar-rad, S Rose, RAL
J P Mosnier, E Kennedy, Nat Inst of Higher Education, Dublin

Introduction

We have developed and successfully demonstrated a technique to record keV absorption spectra in the coronal region of a laser produced plasma which provides spatial information in the corona at the ≤ 10μm level and can freeze the motion of the expanding plasma at the ≤ 100 psec level. Analysis of an absorption spectrum should allow a high resolution (temporal and spatial) history of the absorbing ion population density to be determined which can be compared to hydrodynamic simulations which include an atomic physics package. Inner shell absorption processes can also yield data for line classifications and comparisons with ab initio atomic physics calculations.

System Description

The experimental geometry is illustrated in Fig A1.24. The target material of interest initially forms a target in the shape of a foil typically 5 mm x 1 mm x 50 μm. The target may be melinex coated with the appropriate material. This target is irradiated by a laser pulse on the 5 x 1 mm surface and the resultant plasma blows off on one side. A second synchronised laser pulse of short duration irradiates a thin wire or coated fibre target of diameter 10-20 μm at its tip and the resultant quasi-point source plasma backlights the main plasma by projection. X-rays from the backlighter can propagate on either side of the foil target before Bragg reflection of a plane crystal and detection on X-ray film (DEF). Different Bragg matched wavelengths follow slightly different paths through the plasma and all detected wavelengths probe all distances in front of and behind the foil target limited by the spectrometer entrance aperture. Typically we have used a 1 nsec, 2ω pulse at ≈ 10^{12} W cm^{-2} to irradiate a ≈ 1 mm diameter spot or a 1 x 5 mm line on the foil (Al or Si) and a 100 psec, 2ω pulse of ≈ 20 J in tight focus (≈ 30 μm spot) to irradiate ≈ 15 μm ϕ W wires or 8 μm carbon fibres built up to ≈ 15 μm ϕ by CH coating and a top coating of ≈ 0.5 μm thick Yb. The quasi-continuous M-band emission from these hi-z backlighters are

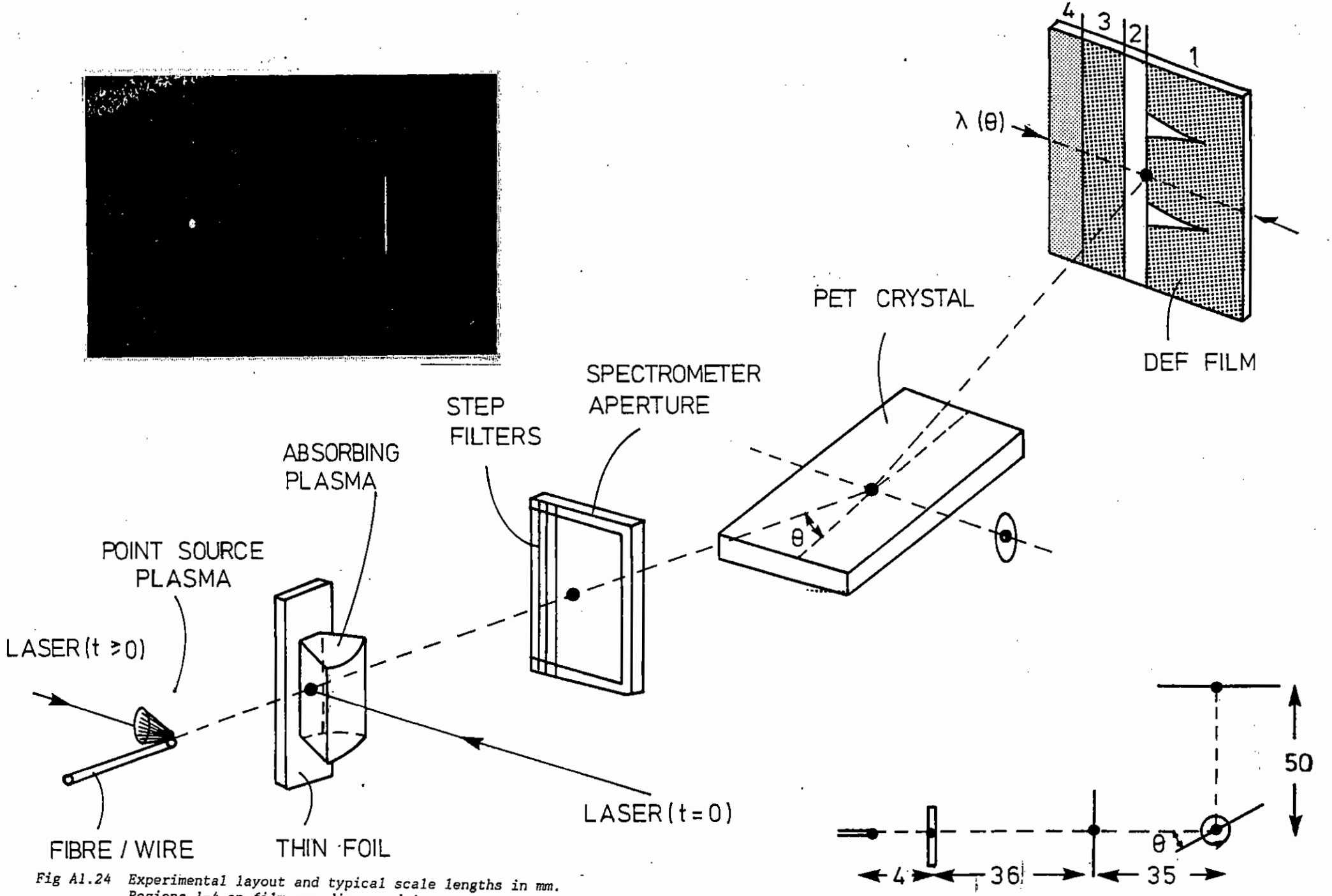

Fig A1.24 Experimental layout and typical scale lengths in mm. Regions 1-4 on film are discussed in text. Insert shows pinhole picture of backlight and main plasma separated by 4 mm.

suitable for backlighting low-z, k-shell absorbing ions. Typically the projection magnification to film is x 30 with the two plasmas separated by ≈ 4 mm.

Each piece of film provides four pieces of information on each shot and are recorded in regions 1-4 as indicated in Fig A1.24. Region 1 records the absorption spectrum over a spectral range typically 4.5-7.5 A° for a PET crystal (40 x 30 mm in area). Region 2 is the edge-on shadow of the foil but records the background level on film due to either self-emission from the main plasma or fluorescence from the crystal and filters. It also provides an alignment check as the shadow width is calculable. Region 3 is a record of the source spectrum and can be divided into the absorption spectrum to provide opacity estimates at each frequency. Region 4 is a step wedge filtered source spectrum (typically in 25 μm Be or 10 μm melinex steps) which provides a film calibration at each wavelength. The filters are located along one edge of the spectrometer entrance aperture. The crystal can rotate so that a particular line seen in absorption and self-emission can be brought to the same position on the film. In this condition that wavelength probes the central zone of the main plasma.

The spatial resolution of the system is illustrated in Fig A1.25 where a Cu grid with 30 μm wide bars and 120 μm period has been backlit by a 20 μm diameter W wire irradiated by a 600 ps pulse. In regions of continuous emission the spatial resolution is <10 μm whereas in regions of line emission it is worse and depends on the particular line. This indicates the source plasma is effectively smaller for continuum emission and line emission is from a larger expanding plasma. This was also supported by the streaked spectroscopy which showed continuum emission to closely follow the laser pulse profile with line emission generally lasting for longer times. Correspondingly the spectral resolution is also better for continuum emission with the effective source size in the dispersion plane clearly ≥30 μm for some line emissions. For continuum spectral regions spectral resolution is largely determined by the crystal rocking curve.

Experimental Results

Absorption spectra of the AlXl 1snp → $1s^2$ resonance series and SiXII 1s2p → $1s^2$ resonance line region have been observed. Irradiation of the Al and SiO_2 targets has been kept below ≈ 3 x 10^{12} W cm^{-2} in 1 nsec, 2ω pulses to minimise self-emission on the same He-like transitions. For Al targets the backlighting plasma has been formed with various targets Al, W or Yb irradiated with 600 ps or 100 ps pulses at ≤ 10^{15} W cm^{-2}. Absorption spectra have been recorded with the two pulses synchronised at their peaks (t = 0) and with the backlighting delayed in 0.25 nsec steps. Fig A1.26 illustrates typical data for backlight/plasma combination of Al/Al (i.e., resonant line absorption with frame time ≥ 600 ps), W/Al with ≤ 600 ps frame time and Yb/Si with ≤ 100 ps frame time. In the latter we see ≈ 15 satellite-type inner shell absorption features on the long wavelength side of the He_α line as well as evidence of Al impurities in the glass target (He_β). Fig A1.27 is a Yb/Al combination with a ≤ 100 psec frame time and shows clearly ≈ 10 satellite features close to the target surface (≤ 20 μm) which have been lost in the temporal smearing of the 600 psec case. This shot also shows the effect of decreasing oscillator strength through the resonance series in that the higher series members become optically thin closer to the target surface. The 1s6p → $1s^2$ (He_ϵ) only appears in absorption at ≥ 20 μm from the surface, presumably because reduced Stark-broadening at lower density has raised the Inglis-Teller limit to a level at which the line can be resolved.

Preliminary Analysis of Ion Density Profiles

Using the film calibration, the source spectrum and the absorbed spectrum intensities above background an opacity at each line centre (τ_o) can be measured for each line at various distances (z) from the target surface corresponding to the absorption frame time. With a knowledge of absorption path length from pinhole camera images an estimate can be made of the ground state ion density, n_A, at each z. This simple procedure assumes the spectral line width is well resolved and can be measured. Fig A1.28 illustrates the effects of poor resolution and indicates some factors to be optimised when

accurate density measurements are to be made. Assuming the crystal rocking curve is Gaussian with a fwhm, $\Delta\theta_R$, equivalent to a spectral resolution $\Delta\nu_R$, that the absorption line is Doppler broadened with a fwhm of $\Delta\nu_A$ and that the source spectrum is flat in the region of the line the expected observable transmission at line centre (ν_o) can be calculated from:

$$T(\nu_o) = \Delta\nu_R^{-1} \int_{-\infty}^{\infty} \exp(-\tau(\nu^1)) \exp\left(-(\nu_o-\nu^1)/\Delta\nu_R)^2 4\ln 2\right)$$

where the opacity $\tau(\nu) = \tau(\nu_o) \exp\left(-(\nu_o-\nu^1)/\Delta\nu_R)^2 4\ln 2\right)$ and $\tau(\nu_o) \approx 1.53 \times 10^{-16} f\, n_A\, \lambda_o(A°)\, 1(Z/T(eV))^{1/2}$. Fig A1.5(5) shows how

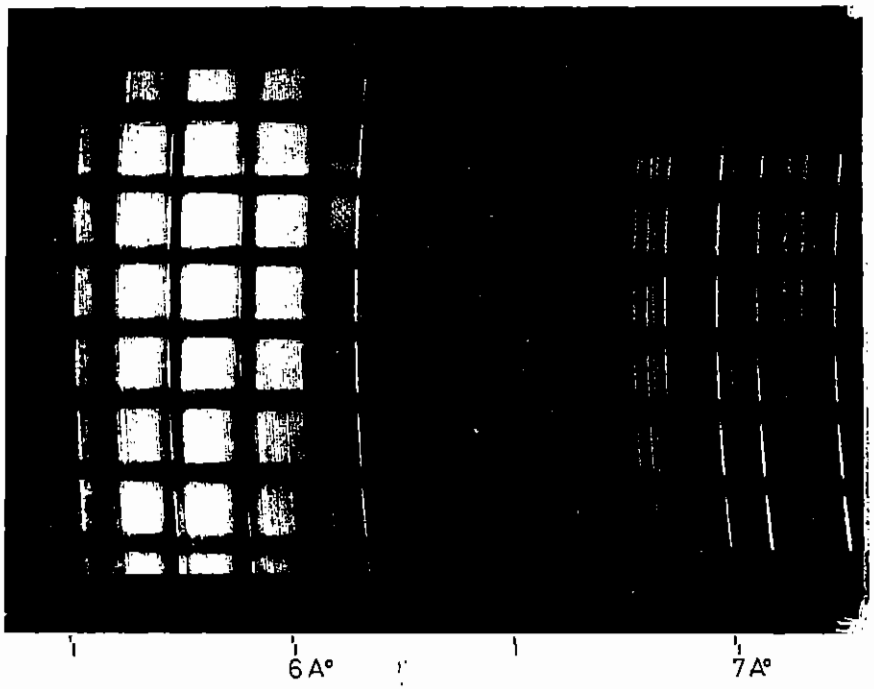

Fig A1.25 – Tungsten spectrum from quasi-point source shadowing Cu grid with 30 μm bars and 120 μm period.

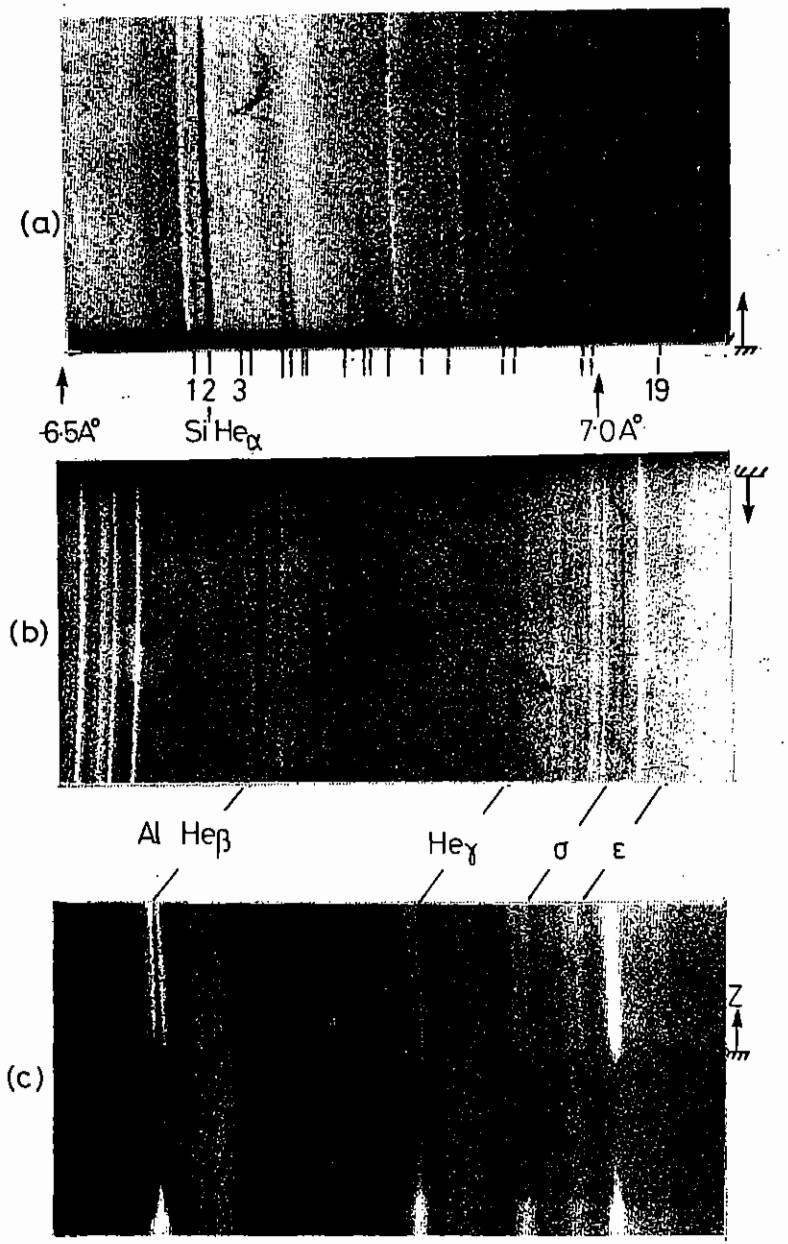

Fig A1.26 (a) *SiO_2 plasma backlit by Yb. He-, Li-, and Be- features are marked and labels refer to Table A1.5(1).*

(b) *Al plasma backlit by W.*

(c) *Al plasma backlit by Al.*

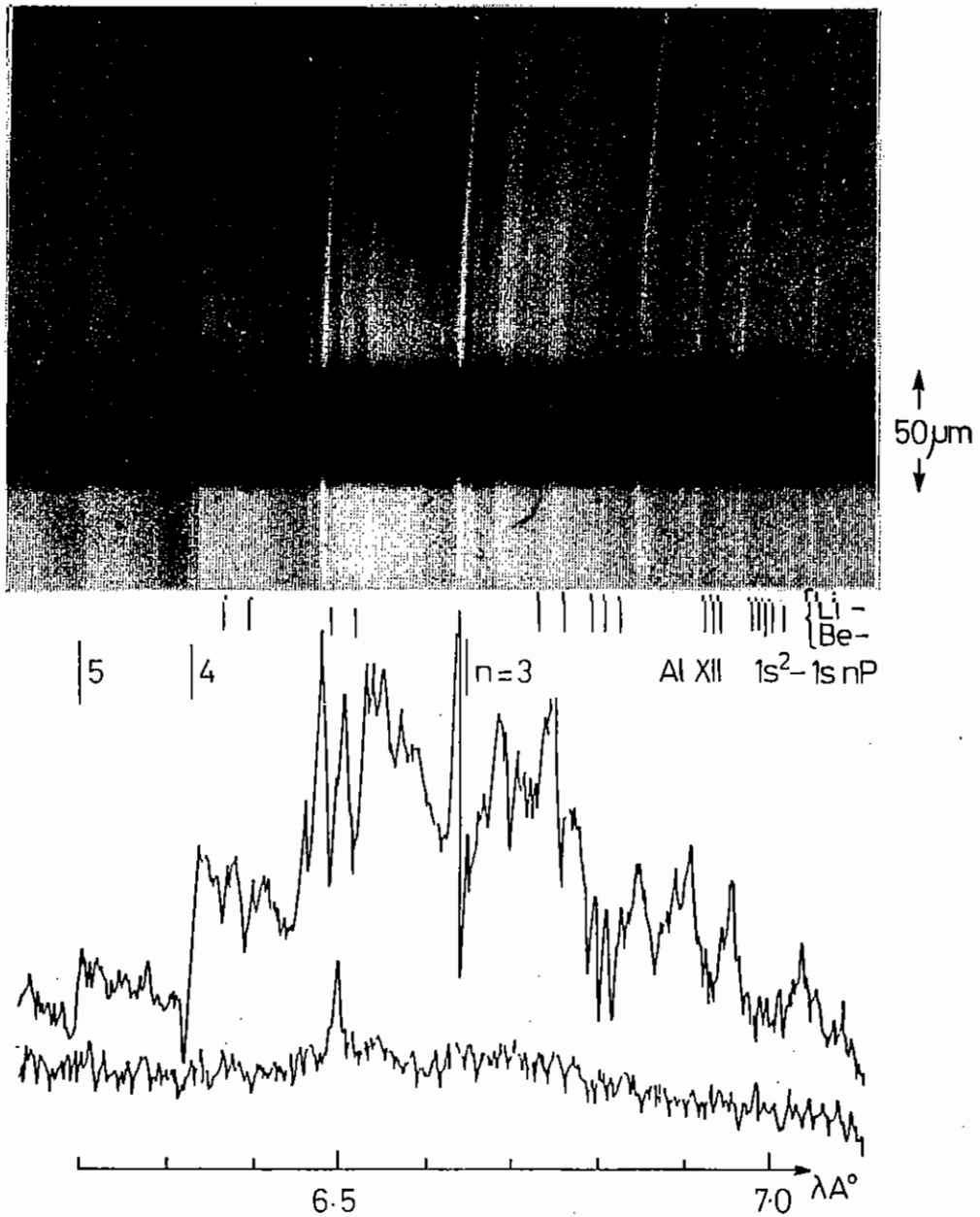

Fig A1.27 Al plasma backlit by Yb showing some of the He-like resonance series and several Li- and Be-like satellite features.

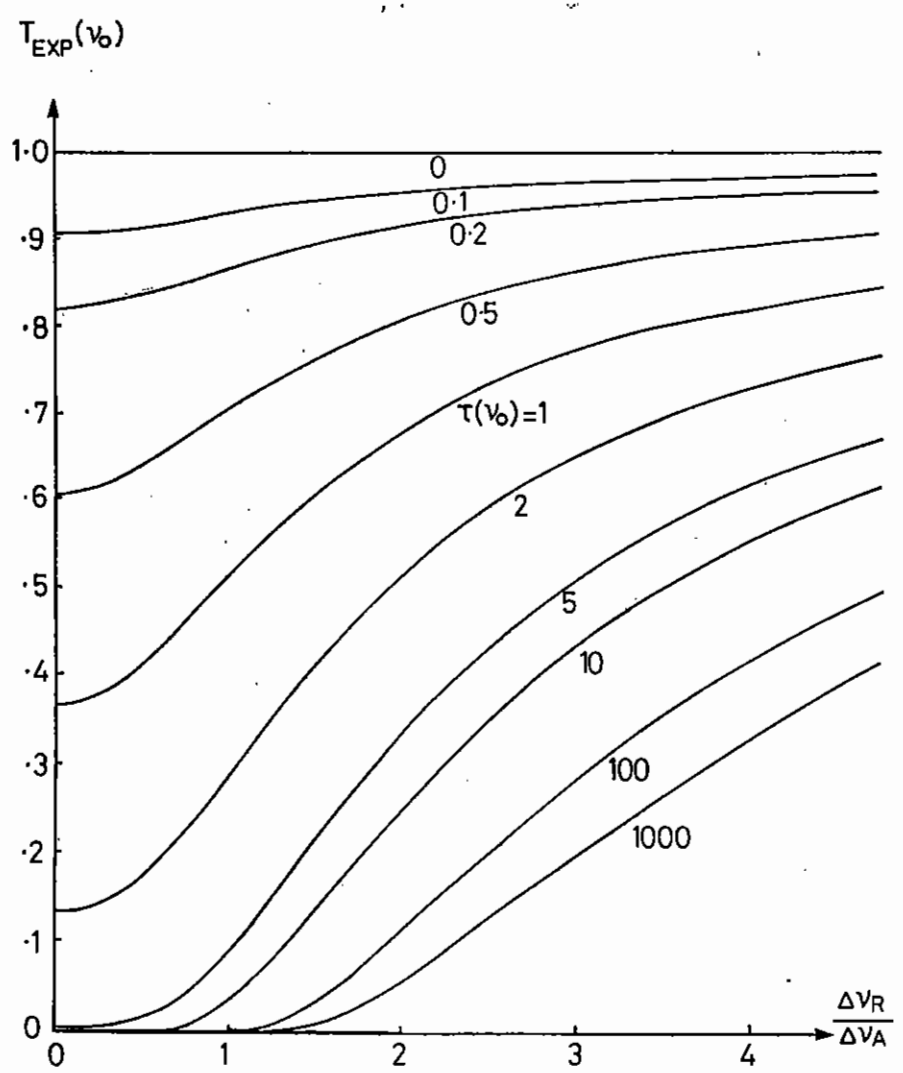

Fig A1.28 How the experimentally measured line centre transmission $T(\nu_o)$ depends on the instrumental and line profile half widths, $\Delta\nu_R$ and $\Delta\nu_A$, under different conditions of actual line centre opacity $\tau(\nu_o)$.

the measured transmission $T(\nu_o)$ varies with the real $\tau(\nu_o)$ as a function of $\Delta\nu_R/\Delta\nu_A$. In the limit of a well resolved line, $\Delta\nu_R << \Delta\nu_A$, $T(\nu_o) = \exp(-\tau(\nu o))$. In practice we can expect $\Delta\nu_R/\Delta\nu_A \sim 1.8 \times 10^4\ \Delta\theta_R (Z/TeV)^{1/2}/\tan\theta$. For Al Heβ (6.635 A°) and a PET crystal Z =13, θ = 49°, $\Delta\theta_R \approx 3 \times 10^{-4}$ rads and $\Delta\nu_R/\Delta\nu_A \approx 17/(TeV)^{1/2}$. Thus for ion temperatures ≥ 100 eV in the corona we should be able to make reasonably accurate estimates of the true opacity and hence ion density n_A to a factor of x 2 provide the measured transmission is ≥0.3. The value $\Delta\theta_R$ was estimated from an ability to clearly resolve the fine structure splitting in Al Lyα (5mA°) at 7.2 A°.

Fig A1.29 shows such an analysis applied to the 1s4p -$1s^2$ Al transition at different time delays and the comparison with a Medusa hydro simulation using an average ion atomic physics approximation. The simulation data has been post processed to allow for the 600 psec time-frame spatial smearing. (Improved data with 100 ps backlighting has not been analysed yet). The broad agreement between theory and experiment is encouraging. Improved data analysis may eventually allow us to test the accuracy of full atomic physics codes treating ionisation and recombination kinetics.

Since we can simultaneously record a large number of absorption lines in the same resonance series it is possible to accurately measure a relative absorber ion density profile. Since for all lines the absorption length is constant (especially in a line focus plasma) and the coronal plasma is approximately isothermal then at each line centre $\tau(z)$ a $f\lambda\ n_A(z)$. Since the effect of poor resolution is less pronounced at low opacities we can specify an arbitrary low value and find the experimental distance into the plume where this value is observed in each line. The ratios of ion densities at these points is then α $1/f\lambda$ and the relative profile can then be fitted to any reliably measured absolute density. Such an analysis is illustrated in Fig A1.30 where the highest relative density data point has been normalised to the average of two code predictions spanning the typical frame time.

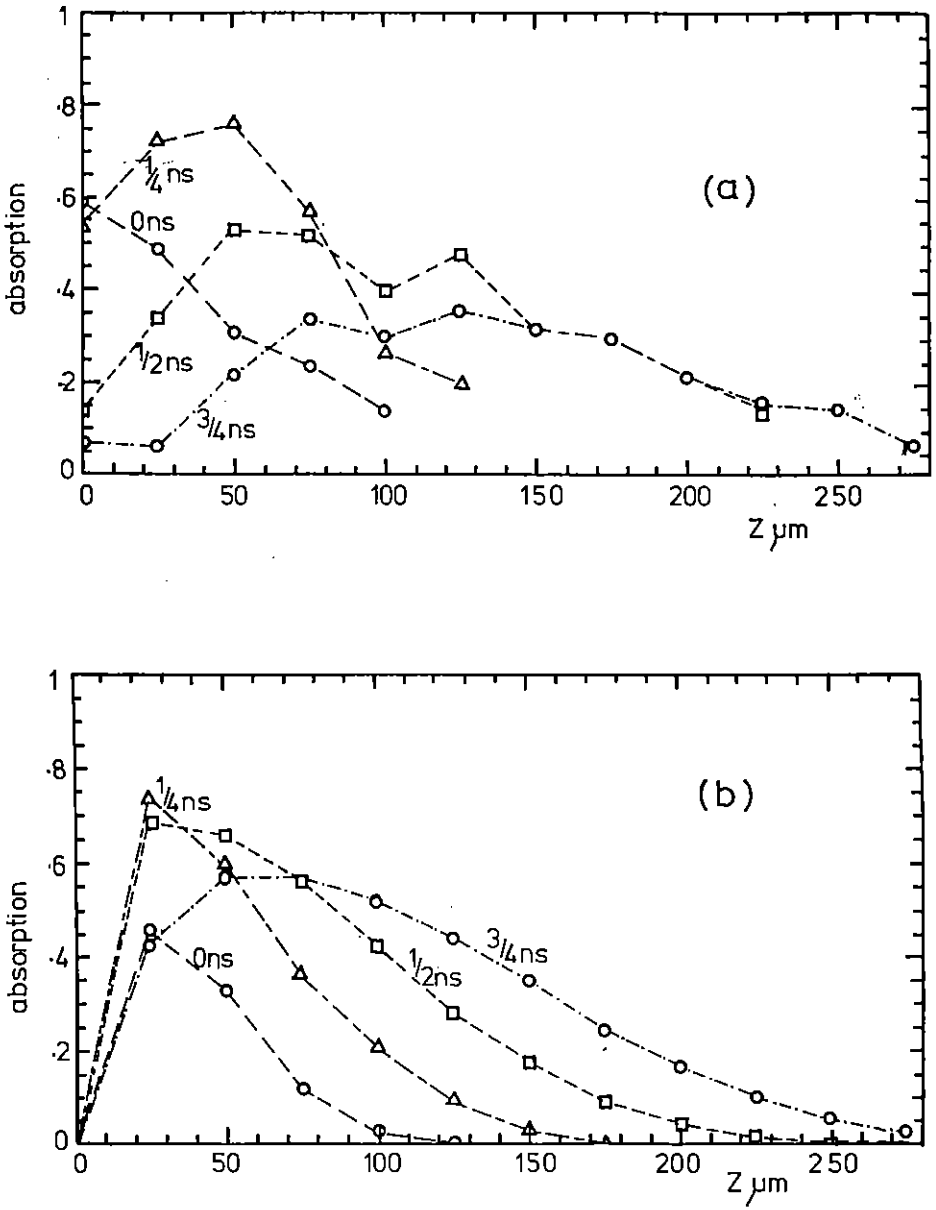

Fig A1.29 (a) Line centre absorption at 6.314 A° (Al $1s^2$ - 1s4p) as a function of distance, z, from the target surface at four time delays wrt the peak of the 0.6 nsec laser pulse.

(b) Post-proceed Medusa simulation using average atom model for the same shots at I ≈ 10^{13} W cm^{-2}.

Preliminary Analysis of Absorption Line Classification

In the case of a glass target backlit by Yb we see ≈ 15 satellite-type inner shell absorption features on the long wavelength side of the Si Heα line as well as evidence of Al impurities in the glass target. The positions of 19 absorption features are indicated on Fig A1.26a and the corresponding wavelengths are listed in Table A1.5(1) together with some preliminary line identifications. Ab initio values of wavelength for Li-like and Be-like satellites were calculated using a Hartree-Fock-Relativistic program-package and these are also listed in the table. Close agreement with observed values allowed lines 3 and 5-8 to be provisionally identified as Li-like and lines 9-12 as Be-like. Lines 13-19 have not yet been identified but are possibly satellite lines due to lower ionisation stages. The presence of a large number of ionisation stages is probably due to a variation of temperature along the 'line of sight', for this shot where a small angle scatter plate was used in front of the focussing lens in an attempt to smooth out hot spots in the normal irradiance distribution on the target surface.

Conclusions

We have demonstrated the feasibility of recording X-ray absorption spectra with high spatial, spectral and temporal resolution. Future analysis of such spectra will be improved by generating more homogeneous plasmas with better defined absorption path lengths. This can be achieved with ISI techniques and using targets constructed by evaporating known width stripes of absorber material onto the foil substrates. A survey of brightness and spectral composition available in Yb to Bi backlighters indicates that spectra can be recorded for K-shell absorptions for z ≈ 12-17 and L-shell absorptions for z ∿ 34-44.

TABLE A1.5(1)

Key	λ observed	λ theory	Identification			Comments
1	6.634	6.634	Al XII	$1s^2\ {}^1S_0$	- $1s3p\ {}^1P_1$	Al resonance line
2	6.648	6.648	Si XIII	$1s^2\ {}^1S_0$	- $1s2p\ {}^1P_1$	Si resonance line
3	6.677	6.674	Si XII	$1s^2\ 2P\ {}^2P_{\frac{3}{2}}$	- $1s2p^2\ {}^3P_1$	Li-like satellite
4	6.686	6.687	Si XIII	$1s^2\ {}^1S_0$	- $1s2p\ {}^3P_1$	Intercombination line
5	6.713	6.715	Si XII	$1s^2\ 2s\ {}^2S_{1/2}$	- $1s2p\ 2p^3P_{3/2}$	Li-like
6	6.724	6.723	Si XII	$1s^2\ 2p\ {}^2P_{3/2}$	- $1s\ 2p^2\ {}^2P_{3/2}$	
7	6.736	6.733	Si XII	$1s^2\ 2p\ {}^2P_{1/2}$	- $1s\ 2p^2\ {}^2D_{3/2}$	satellites
8	6.741	6.736	Si XII	$1s^2\ 2p\ 2P_{3/2}$	- $1s\ 2p^2\ {}^2D_5/_2$	
9	6.780	6.781	Si XI	$1s^22s2p\ {}^1P_1$	- $1s2s\ 2p^2\ {}^1P_1$	Be-like
10	6.795	6.793	Si XI	$1s^22s2p\ {}^3P_2$	- $1s2s\ 2p^2\ {}^3P_2$	
11	6.800	6.804	Si XI	$1s^2\ 2p^2\ {}^1D_2$	- $1s\ 2p^3\ 1D_2$	satellites
12	6.817	6.817	Si XI	$1s^22s2p\ {}^1P_1$	- $1s\ 2s2p^2\ {}^1D_2$	
		6.818	Si XI	$1s^2\ 2p^2\ {}^1D_2$	- $1s\ 2p^3\ {}^1D_1$	
13	6.851	-	Si X?	-		possible
14	6.873	-		-		satellite
15	6.924	-	Si IX?	-		transitions in
16	6.938	-		-		Boron-like and
17	6.982	-		-		Carbon-like
18	6.998	-		-		Silicon
19	7.052	-		-		

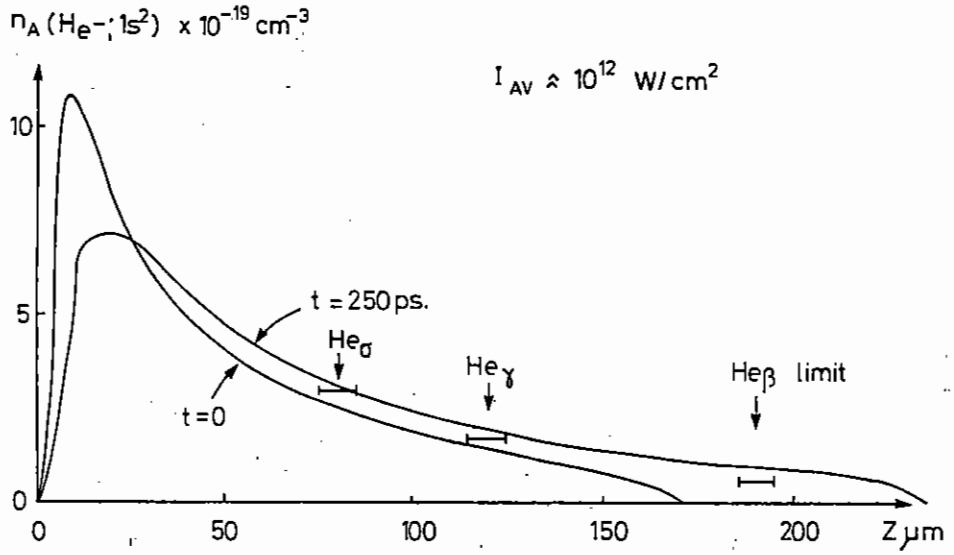

Fig A1.30 He-like ion density profile for Al plasma deduced from spatial extent of three resonance lines and normalised to Medusa simulation.

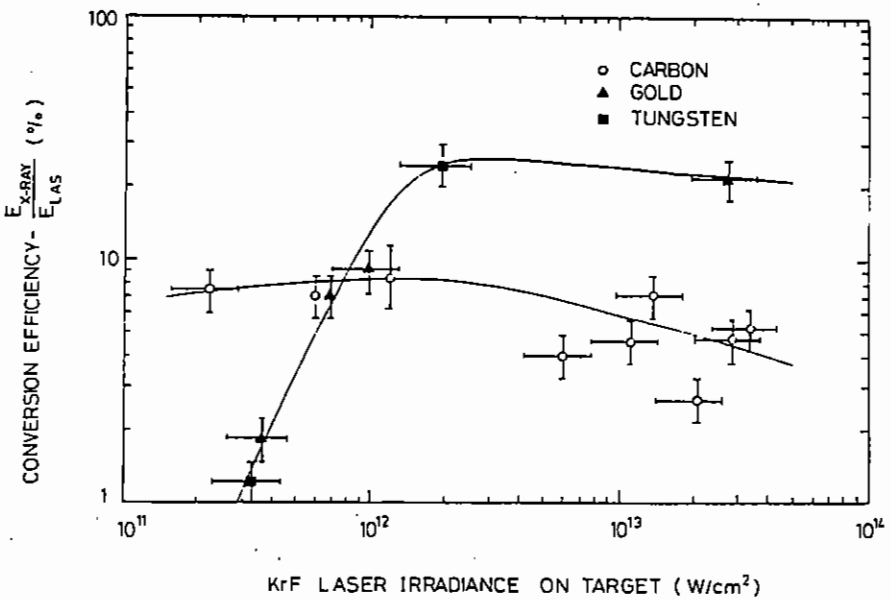

Fig A1.31 Conversion efficiency from KrF laser light to water window X-rays as a function of laser irradiance for carbon, gold and tungsten targets.

A1.6 CHARACTERISATION OF A KrF LASER-PLASMA X-RAY SOURCE IN THE 280eV-530eV PHOTON RANGE

I C E Turcu, F O'Neill, U Zammit (RAL)
Y Al Hadithi, R W Eason (Essex University)
A M Rogoyski, C P B Hills, A G Michette (Kings College)

A preliminary description of this experiment was presented in Sect A4.2 of the 1986 Annual Report to the Laser Facility Committee. In brief the experiment involved using a 50ns pulse from the Sprite KrF laser to generate a laser-plasma X-ray source for application to contact X-ray microscopy. A filtered vacuum X-ray diode (XRD) was used to make quantitative measurements of the X-ray emission from the source and thus obtain the conversion efficiency from laser light to X-rays. In this past year the sensitivity of the XRD has been measured using the SERC synchrotron radiation source at Daresbury Laboratory and the plasma source X-ray results have been reanalysed in light of the calibration. Details of the XRD calibration work are described below in Section C4.7.

The main reanalysis work has been performed on the measurements of conversion efficiency from KrF laser light to water window X-rays ($280eV \leq h\nu \leq 530eV$). Fig A1.31 shows the variation of conversion efficiency with target irradiance for carbon, gold and tungsten targets. Carbon was chosen as a water window X-ray source because its K-shell emission falls in the required spectral range as does the N-shell emission from gold and tungsten. The results taken with gold (Z=79) and tungsten (Z=74) targets have been plotted together on the same curve because the X-ray spectra are expected to be similar because of the closeness of atomic numbers.

The results displayed in Fig A1.31 show that the optimum irradiance for carbon targets is 1.2 x 10^{12}W/cm^2 which gives a conversion efficiency to water window X-rays of 8.5%. For any irradiance between 2 x 10^{12}W/cm^2 and 4 x 10^{13}W/cm^2 the conversion efficiency from gold and tungsten is $\geq$ 20%. At high irradiance the gold and tungsten targets were however found to produce a considerable amount of X-rays of energy $\geq$ 530eV which could reduce image contrast in microscopy experiments unless they are filtered out. For example XRD measurements show that at an irradiance of 2.6 x 10^{13}W/cm^2 the gold plasma conversion efficiency to X-rays at $h\nu \geq 700eV$ is 13.5% whereas at an irradiance of 3.4 x 10^{13}W/cm^2 the conversion efficiency for carbon is only 1.1%. At an irradiance $\sim$ 3.0 x 10^{12}W/cm^2 the component at $h\nu \geq 700eV$ from both targets is essentially zero.

The conclusion from the above results is that an irradiance $\sim$ 2-3 x 10^{12}W/cm^2 is optimum for the targets tested (and probably for other target materials as well). At this irradiance the X-ray conversion in the range 280eV $\leq h\upsilon \leq$ 530eV is maximised and the conversion to X-rays at $h\upsilon \geq$ 530eV is minimised.

A1.7 TIME-RESOLVED STUDIES OF NEON LIKE IONS USING THE SPRITE KrF LASER

R A Smith, G Kiehn, O Willi (Imperial College)
J C Gauthier, J P Geinde (Ecole Polytechnique, Paris)
E Turcu (RAL)

1. Introduction

We report an experiment on the time-resolved atomic physics of laser-produced neon-like ions, involving the first successful use of time-resolved VUV and X-ray spectroscopy on Sprite.

Neon-like ions are of interst as possible amplifiers in the VUV and soft X-ray spectral regions. Lawrence Livermore National Laboratory has recently demonstrated gain in laser-produced Se, Y and Mo plasmas[15].

The initial aim of this experiment was to study the atomic physics of neon-like ions produced by laser irradiation of foil, wire and solid targets of various elements from Zn to Ag in both point and line focus geometries. The time dependence of several ionisation stages adjacent to the neon-like state was to be investigated.

One week of the experiment was to be devoted to the study of the atomic physics of a strontium photopump X-ray laser scheme, as a collaborative venture undertaken between the Ecole Polytechnique, Paris, and the team from Imperial College.

2. Experimental

This experiment was one of the most heavily diagnosed to be carried out on Sprite. The following diagnostics were used to observe the plasmas produced by laser irradiation of targets with = 50 ns, 100 J pulses from the Sprite laser:

i) A time-resolved "flat field" VUV spectrometer[16] (developed by Imperial College and RAL for X-ray laser studies) with a spectral range of = 40-350 Å in a 100 Å window. This instrument was used to observe VUV lines from 3-3 transitions of neon-like ions.

ii) A time integrated high resolution VUV spectrometer (GML5). This is a diffraction grating Rowland circle instrument, used to help identify time-resolved VUV spectra. Due to its size, GML5 was set up outside the Sprite target chamber, with light from the target being imaged onto the entrance slit of the spectrometer using a focussing toroidal mirror.

iii) A time-resolved curved crystal X-ray spectrometer, recording the time evolution of 2-4 resonance transitions at 4-7 Å.

iv) A time integrated mini-crystal spectrometer to observe 2-4 transitions in the 4-10 Å region, and to help identify time-resolved spectra, as this instrument covered a larger spectral range than the time-resolved X-ray spectrometer. The arrangement is shown in Fig A1.32.

3. Target Design

Thin foil targets consisting of a 1000 Å thick formvar substrate coated with target materials of interest were used. At high irradiance (eg 10^{12} W/cm^2 in this case) such targets explode, rather than ablating away as do thicker targets. Targets were designed to burn through at 4-5 ns after the start of the laser pulse. This is at the peak of the 50 ns Sprite pulse. Foil thickness was calculated using approximate scaling laws derived from the hydrodynamics of an exploding foil[17] which have been shown to be in good agreement with "MEDUSA" hydrocode simulations. From the exploding foil model, the

burn through time T_{bt}/ns is given by

$$T_{bt} = 2.2\times10^{-1}\text{ns}\ (1/10^{14})^{-2/3}\ (\lambda/0.53)^{2/3}\ (A/80)^{-7/6}\ (Z/25)^{3/2}\ \Delta^{1/3}$$

where

T_{bt} = burn through time in ns
I = irradiance W/cm² in two beams of I/2 (correction factor of $2^{2/3}$ for one beam
λ = laser wavelength in μm
A = atomic number of target material
M = target mass per unit area in g/cm²
Z = charge of ions produced
Δ = coulomb logarithm

Putting in the parameters for the Sprite laser system gives:

T_{bt} = 4.5 ns for I = 10^{13} W/cm², λ = 0.249 μm (KrF laser wavelength), Z = A-10 (to give neon-like ions) and the coulomb log Δ = 5.

and so the target thickness h is given by:

$$h/\mu m = \frac{2.1\ A^{7/8}Z^{-9/8}}{\rho}$$ where ρ is the target density in g/cm³.

4. Results

All the diagnostics were found to work well, and the first streaked VUV and X-ray spetra were recorded on Sprite. Time-resolved VUV spectra from selenium foils supported on a formvar substrate showed that the foil targets were indeed burning through after the 4-5 ns required.

Time integrated X-ray and high resolution VUV as well as time-resolved VUV and X-ray spectra of the following elemenets of interest were obtained:

Zn, As, Ge, Se, Br, Sr, Rb, Y, Mo, Ag

Incidental spectra of Na, C, O, F, and Al were also recorded, either for calibration, or as they were combined with elements of interest for target manufacture.

Initial analysis of the hard X-ray spectrometer results suggests that neon-like ions were not being produced by targets of Z > 39 (ytterium) with point focus irradiation. This was thought to be due to insufficient irradiance, as a result of the unexpectedly long rise time (≈ 10 ns) of the Sprite pulse.

A number of interesting results were obtained. In particular, the temporal behaviour of three different ionisation stages (Na, Ne, Mg) of a bromine plasma was recorded and is shown in Figure A1.33.

Figure A1.34 shows the corresponding time-integrated X-ray spectrum from a Rb Br target plasma, with neon-like transitions being the dominant feature. Initial analysis also suggests that neon-like transitions were observed in the VUV at the same time as the X-ray signals were observed. Figure A1.35 shows a time-resolved VUV spectrum from a 0.3 μm thick Se foil target demonstrating the 4-5 ns burn through time, and showing neon-like transitions. The detailed analysis of the data is still in progress.

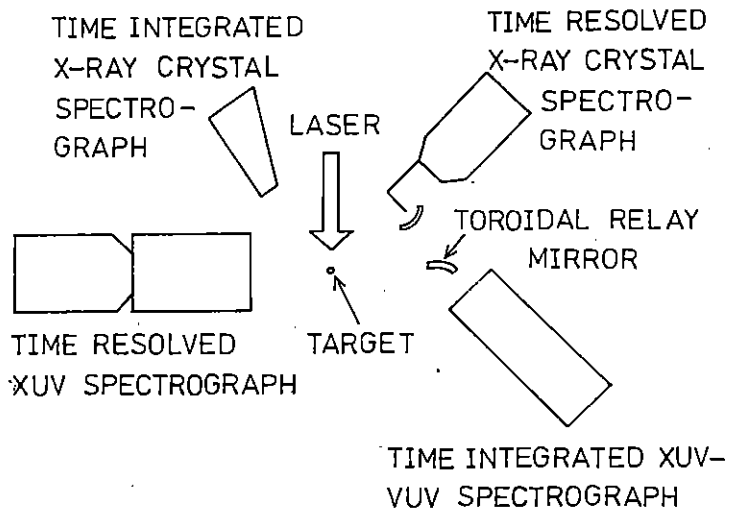

Fig A1.32 Arrangement of diagnostics

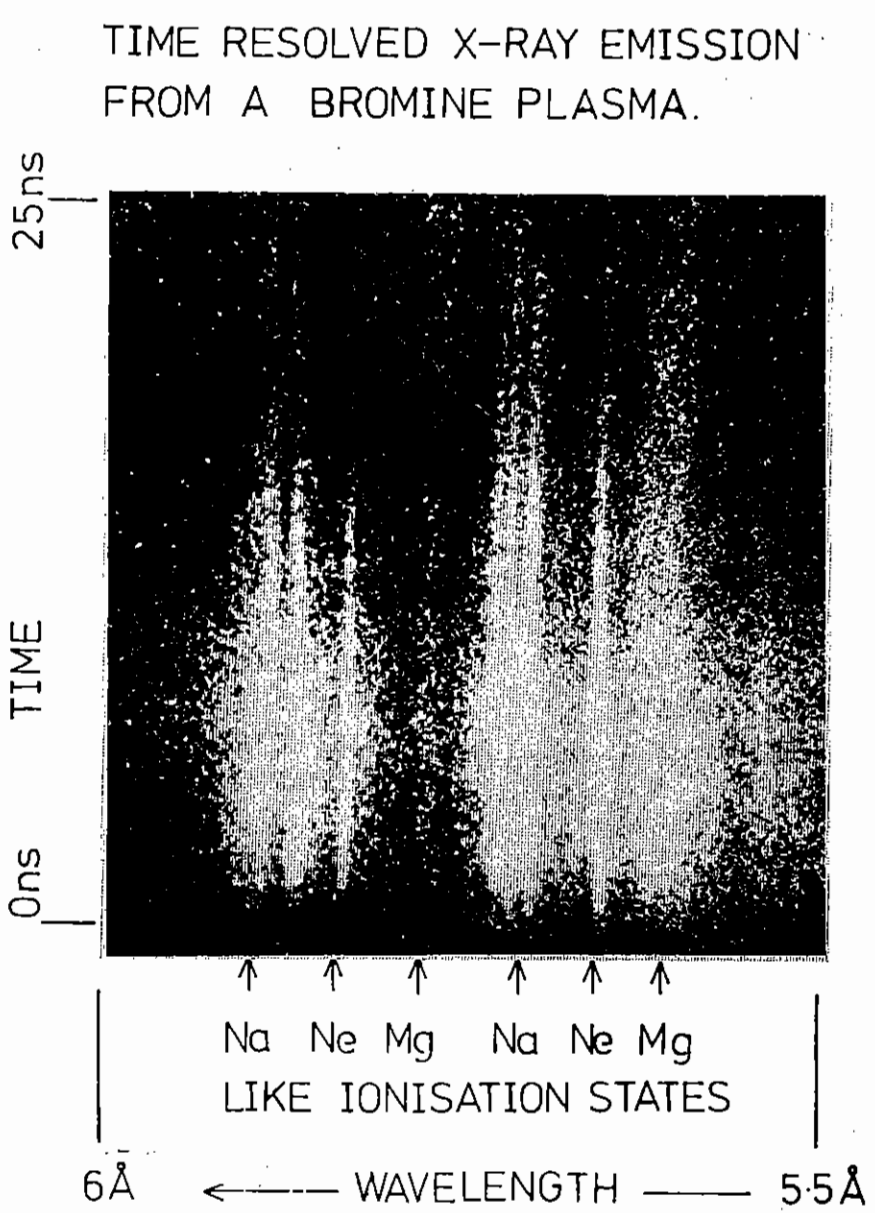

Fig A1.33 Time-resolved X-ray emission from a bromine plasma

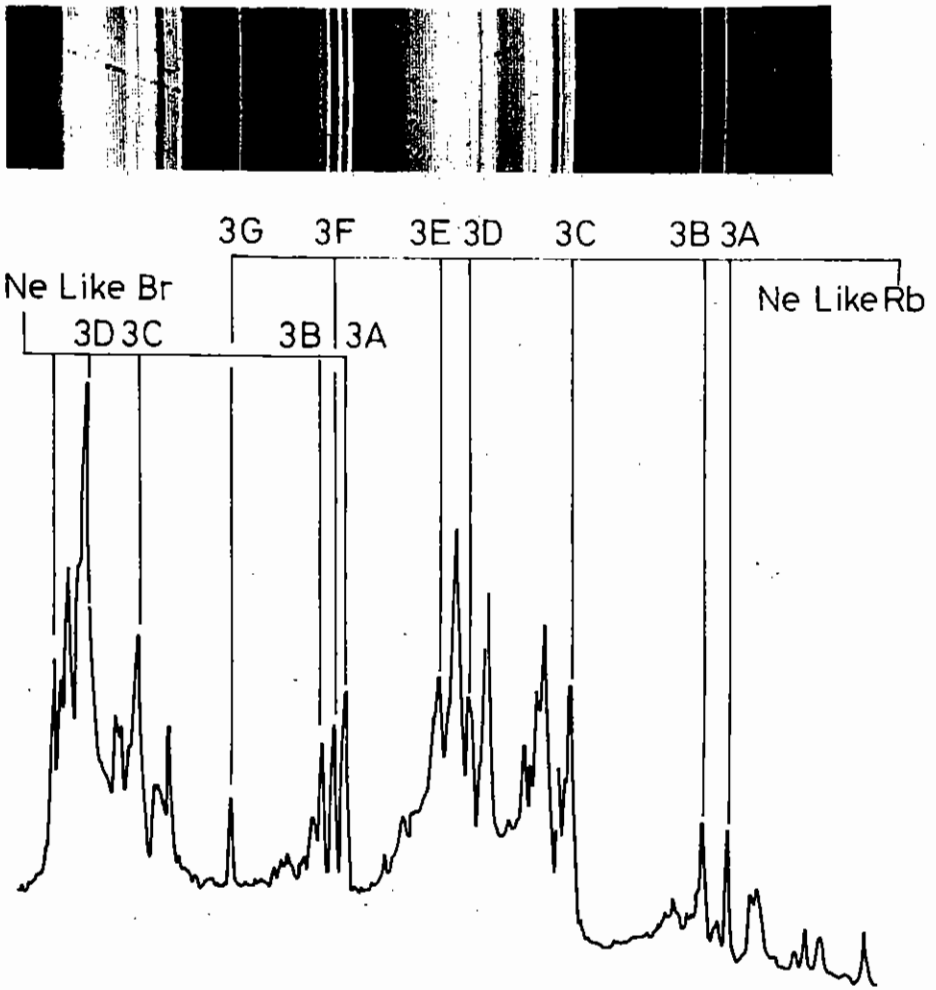

Fig A1.34 Time integrated X-ray emission from a RbBr plasma

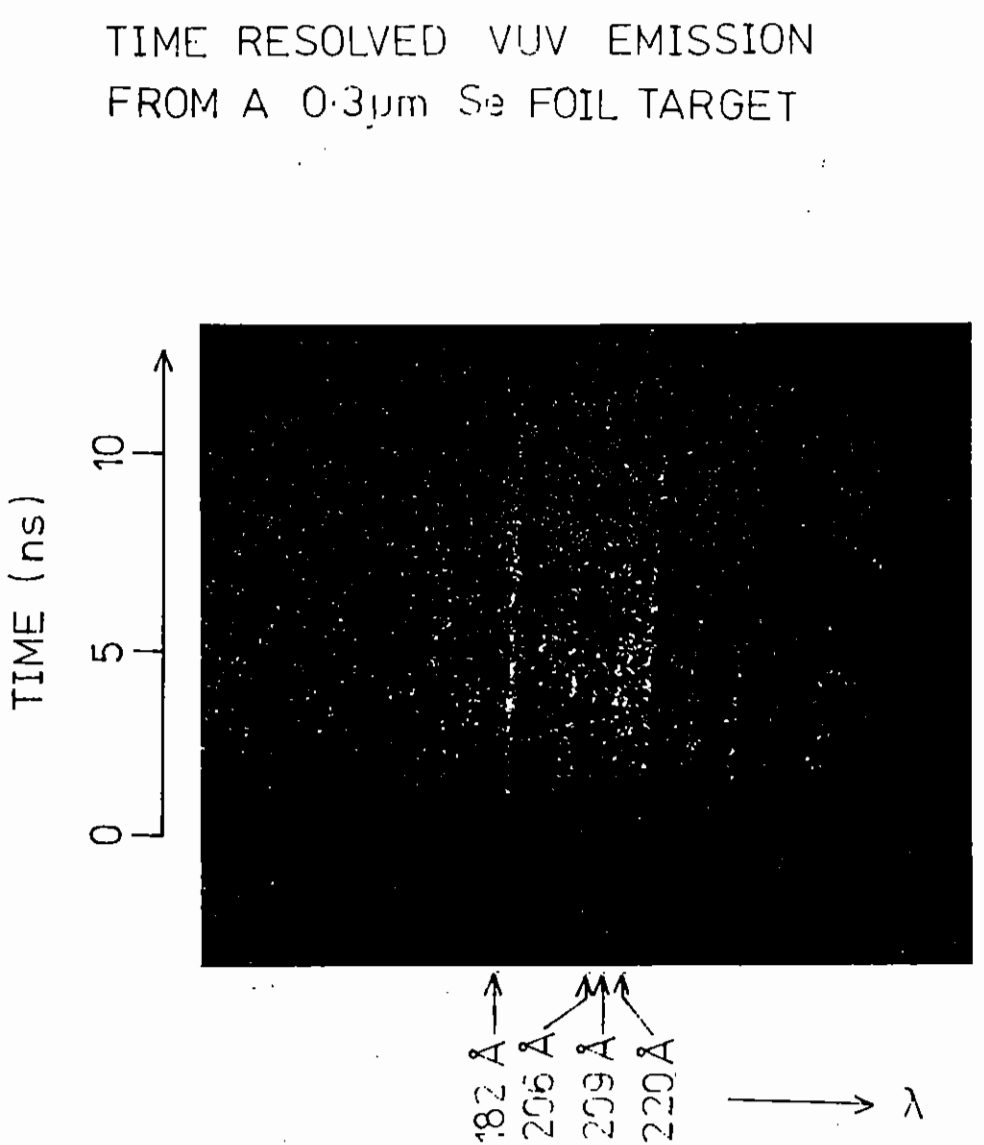

Fig A1.35 Time-resolved VUV emsission from a 0.3 μm Se foil target

A1.8 TIME RESOLVED X-RAY DIFFRACTION FROM LASER HEATED SILICON

D J Bradley, A J Rankin and J Wark (Imperial College) R W Eason (University of Essex), J Lunney (Dublin), U Zammit (Rome)

Time resolving the structural changes that occur in silicon during pulsed laser annealing is an area of current interest both from a theoretical and also experimental viewpoint. Previous work at the CLF[18,19] used a pump-and-probe technique in which the transient thermal strain induced by a 1ns, ≤1Jcm^{-2} annealing beam at λ = 0.53μm, was probed by X-ray diffraction measurements at progressively increasing time delays after the annealing pulse. The results obtained during this initial experiment were used to calculate the corresponding rocking curves (reflectivity as a function of angle around the original unperturbed Bragg angle). The one problem encountered in this first experimental run however, was the spatial uniformity of the annealing beam. Two schemes had been tried to improve the beam homogeneity. The most successful involved specular reflection at glancing angle from a plasma. While the uniformity was better than using the raw input beam from the VULCAN laser, shot-to-shot reproductivity was poor and the actual annealing energy could not be measured accurately on a particular shot.

Since these first results, progress has been made on two fronts. Firstly the experiment has been repeated with improved diagnostics, and a temporally and spatially smoothed annealing beam of known energy density used. Secondly the original data has been used as a comparison for a computer code which calculates the crystal rocking curves for a particular guessed strain-depth profile. The code iterates the guessed profile to achieve agreement between calculated and experimental curves to within some limit of acceptability.

The improved experimental arrangement used in the most recent run is shown in figure A1.36. The X-ray source was line emission from chlorine He-like ions at λ = 0.444nm. A He-Ne laser acted on a probe for time dependent optical reflectivity measurements of the silicon sample surface. An optical streak camera was used to monitor the temporal profile of the 14-16 individual beams derived from two input 108mm diameter VULCAN beams. This proved very useful as those beams whose individual contributions to the overall integrated annealing pulse was less than some acceptable value could be identified on each

shot, and appropriate corrections made. An energy calorimeter was placed at an equivalent target plane to provide a calibrated energy density measurement on each shot. The spatial intensity smoothing scheme used is shown schematically in figure A1.37.

Results were obtained for a range of time delays in the region of 0-250ns. A typical result is shown in figure A1.38 in which the right hand half of the spectrum is derived from the heated part of the crystal, and the left hand side is a witness spectrum of unheated silicon. As can be seen, the spatial uniformity of the spectrum from the heated region appears very good. A quantitative analysis of these improved spectra is underway. An iterative fitting routine is being used to derive the strain-depth profile as discussed below.

Theory and data reduction

The theoretical basis for understanding the diffraction from strained crystals has been given by Burgeat and Tauping[20] and by Takagi[21]. The Burgeat and Tauping formalism for dynamical diffraction has been used by Klar and Rusticelli to study the diffraction from curved crystals[22]. The theory essentially consists of solving Maxwell's equations to first order within a medium of complex and periodic wave refractive index (ie. the crystal) for radiation incident at varying angles around the Bragg angle. Strain-depth profiles are introduced via a depth dependent Bragg angle. The theory has been extensively used in the study of dopant induced stain[23], thermal annealing [24,25] and mechanical strain [22].

The form of theory presented by Klar and Rusticelli is useful for the present study. Klar and Rusticelli write two coupled differential equations for the real and imaginary parts of the depth dependent scattering amplitude, X_1 and X_2.

$$\frac{dX_1}{dA} = k(X_1^2 - X_2^2 + 1) + 2X_2(X_1 - y) - 2gX_1 \qquad (1)$$

$$\frac{dX_2}{dA} = -(X_1^2 X_2^2 + 1) + 2X_1(X_2 k + y) - 2gX_2 \qquad (2)$$

where A is the reduced depth given by

$$A = r_e f(\Psi)\lambda t / V_c \sin(\theta_b) \qquad (3)$$

where t is the depth with respect to the crystal surface, λ the X-ray wavelength, V_c the unit cell volume, r_e the classical electron radius, θ_b the Bragg angle and $f(\Psi)$ the complex X-ray structure factor as a funtion of scattering angle

$$f(\Psi) = f'(\Psi) + if''(\Psi) \qquad (4)$$

k and g are given

$$k = f''(\Psi)/f'(\Psi) \text{ and } g = -f''(0)/f'(\Psi) \qquad (5)$$

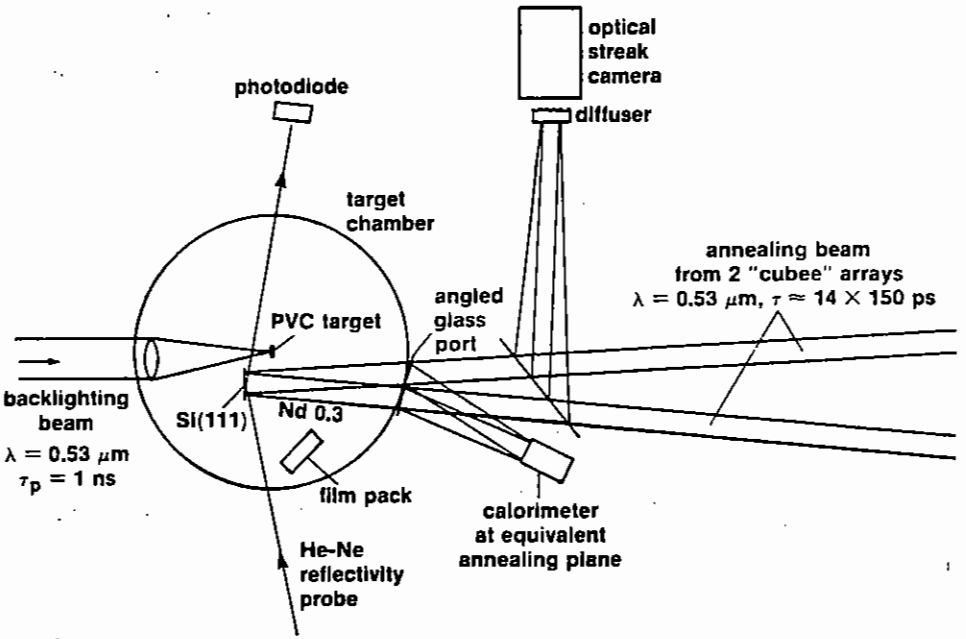

Fig A1.36 Experimental arrangement used in TAE target chamber.

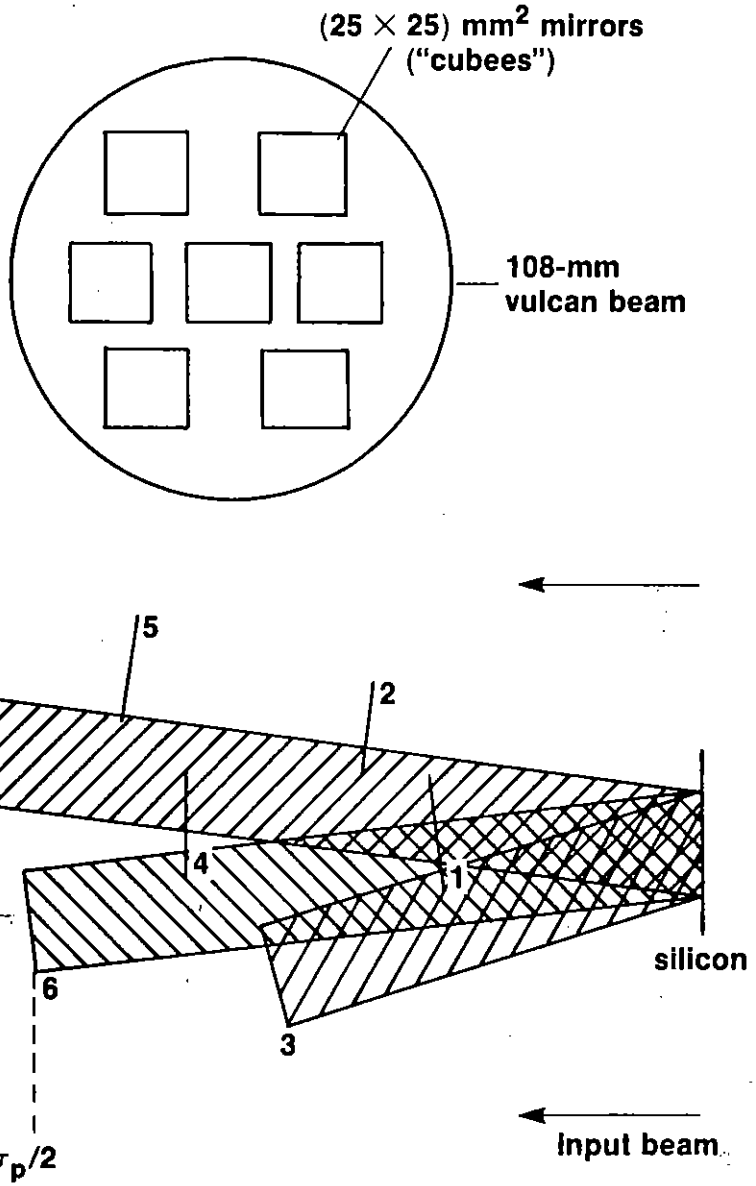

Fig A1.37 Spatial intensity smoothing scheme using multiple re-directable mirrorlets ("Cubees").

and the deviation from the Bragg condition is specified by the parameter y which, under the conditions of a depth dependent strain distribution ε(A), is given by

$$y = \frac{\pi V_c \sin(2\theta_b)}{\lambda^2 r_e f'(\Psi)} [\Delta\theta + \varepsilon(A) \tan\theta_b] - \frac{f'(0)}{f'(\Psi)} \qquad (6)$$

The crystal reflectivity, R, as a function of angle around the Bragg angle is found by solving the above equations with appropriate boundary conditions and noting that

$$R = |X(0)|^2 \qquad (7)$$

where

$$X(A) = X_1(A) + iX_2(A) \qquad (8)$$

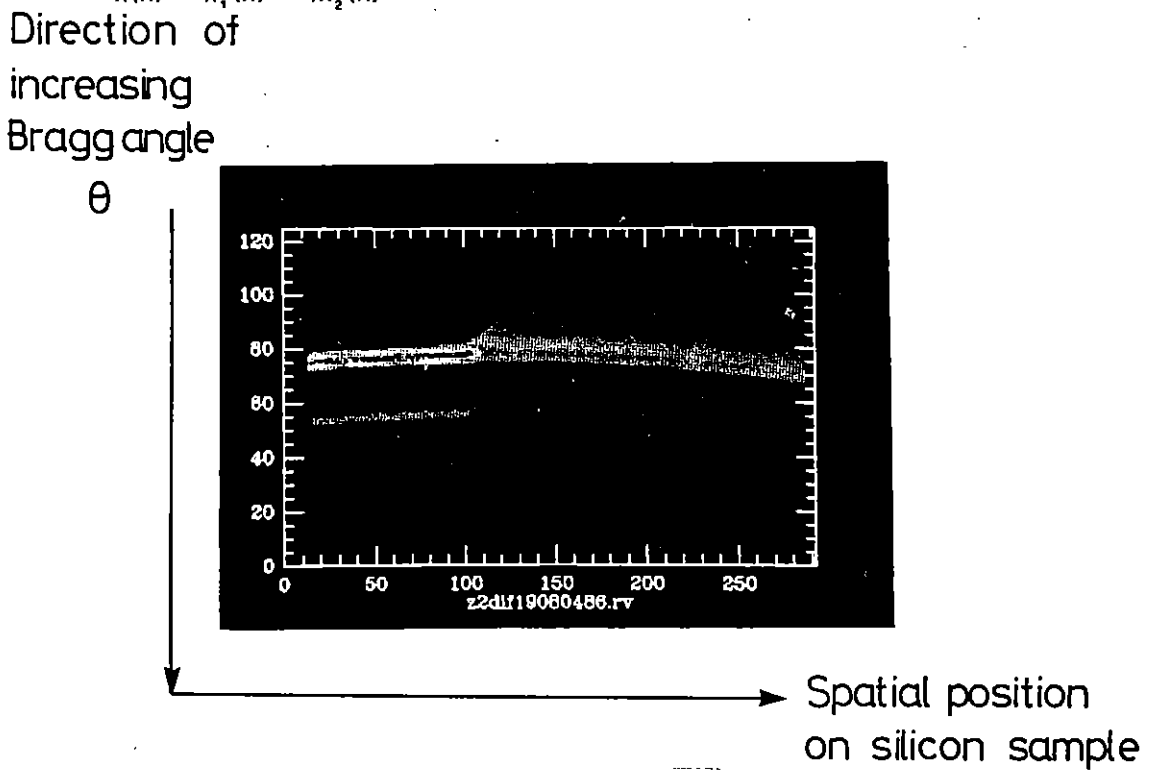

Fig A1.38 Typical enhanced 2-d microdensitometer trace of a shot from transiently heated silicon. Time delay between annealing and X-ray pulse is 10ns. Annealing beam energy density = 680mJ cm⁻².

The expressions given above apply only to the perpendicularly polarized X-ray component. The parallel component can be considered by replacing f(Ψ) with cos(Ψ)f(Ψ).

A computer code has been written that solves the above equations. The accuracy of the routine has been checked by calculating the rocking curves for cases where there are analytic solutions (i.e., crystals with no strain).

The above equations solve Maxwell's equations to first order within a medium of complex and periodic refactive index (i.e., the crystal). The strain is introduced via a depth dependent Bragg angle. For each shot, a monotonic strain-depth profile is guessed and the rocking curve calculated. This calculated rocking curve is then compared to that obtained experimentally, and the guessed strain altered accordingly. Thus the iterations proceed until the experimental and calculated rocking curves agree within some predetermined limits at this point the strain propfile used in the calulations is taken to be the actual profile within the crystal. The temperature-depth profile is obtained from the strain profile using temperature dependent coefficients of expansion, and allowing for the one dimensional nature of the expansion. Using the data shown in figure A1.39, temperature-depth profiles have been derived for results from the first experimental run [18,19], and these are shown in figure A1.40.

A comparison between experimental and calulated profiles is extremely good. Such close agreement implies that a high level of confidence can be attached to the derived profiles, and that further quantitative studies are possible of other dynamical systems, such as shocked materials, and plastic deformation.

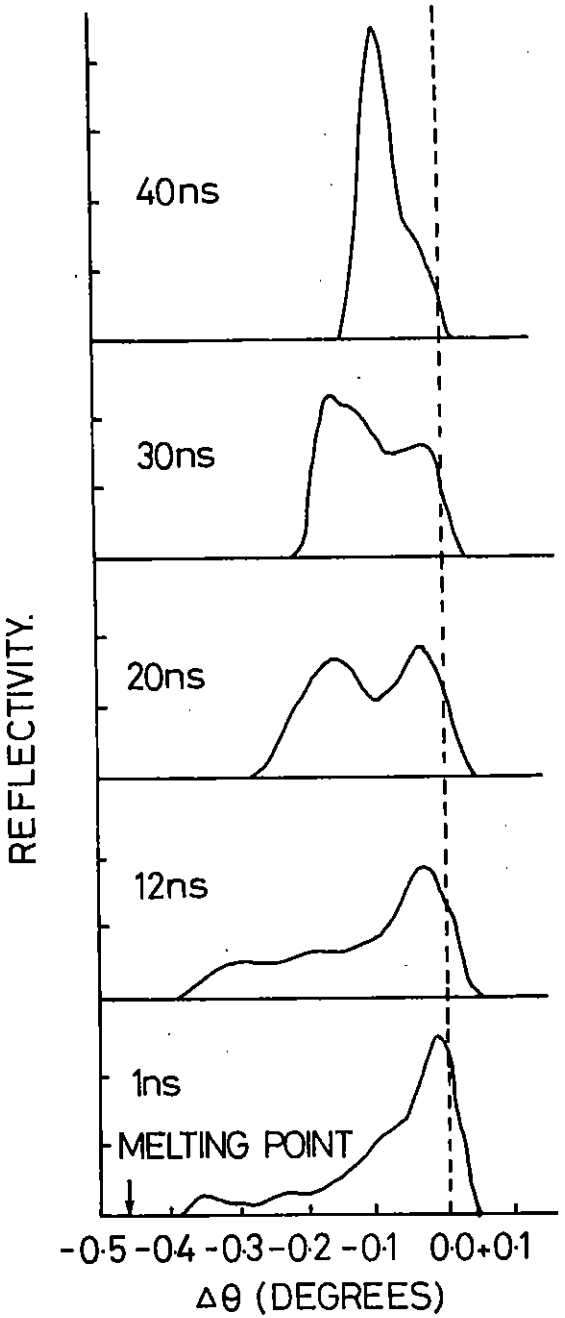

Fig A1.39 Rocking curves for heated silicon crystals at various time delays.

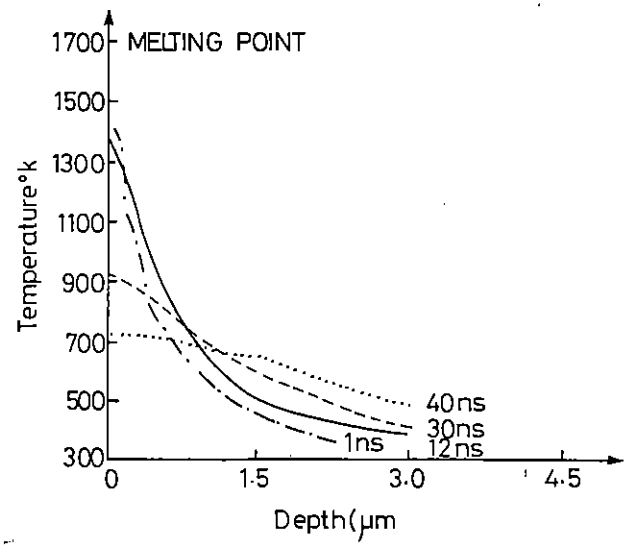

Fig A1.40 Calculated temperature-depth profiles obtained from curves in Fig A1.38, using iterative fitting routine.

A1.9 SOFT X-RAY CONTACT MICROSCOPY

A D Stead, T W Ford (Royal Holloway and Bedford New College)
R Rosser, A Ridgeley (RAL)
C Hills (Kings College)

The principles of X-ray contact microscopy were described as early as 1913 by Goby but both the sources of the X-rays and the contact medium within which the image is recorded are very different to those envisaged 70 years ago. The current resurgence of interest in contact microscopy is due mainly to the increased availability of sources of soft X-rays, in particular laser-produced plasma sources and synchrotron radiation sources, and to the availability of photosensitive resist materials. The use of soft X-rays was first reported by Ralph Feder (1977); soft X-rays have a better penetration and cause less damage to biological specimens than electrons whilst giving potentially much better resolution than visible light. By the careful choice of target materials (or accurate setting of a grazing mirror in the case of synchrotron radiation) it is possible to select the so-called "water-window" (2.3 - 4.4 nm), this is particularly suited to the imaging of biological material since it ensures good contrast between carbon- and oxygen-containing consituents of the cell. The use of soft X-ray contact microscopy therefore allows biological specimens to be imaged with a resolution considerably better than that possible with the light microscope (LM). The resolution, however, is not as good as that obtained with the transmission electron microscope (TEM), but the technique has the advantage that, unlike TEM, wet specimens can be imaged; thus the introduction of the artefacts, so often a problem with conventional TEM preparation, can be avoided.

The imaging process is remarkably simple, but the interpretation of the final images requires a thorough understanding of the way in which that image has been produced (Cheng et al., 1986). The specimen is placed in direct contact with the photosensitive recording medium and then exposed to the soft X-rays. The specimen is then removed and the resist usually developed in a mixture of 4-methylpentan-2-one (MIBK) diluted with propan-2-ol (IPA), producing a relief pattern which corresponds to the integrated mass absorption coefficient of the specimen. This can then be viewed by either interference light microscopy or, after sputter coating, by scanning electron microscopy (SEM).

In order to image wet biological specimens it is necessary to use the minimal possible exposure time to reduce the risk of radiation damage and furthermore the specimen must be physically isolated from the vacuum. The latter requirement can be met by mounting the specimen behind a thin (100nm) 1mm² Si_3N_4 window - itself about 70-80% transparent to soft X-rays. The window also protects the specimen and the resist from the longer ultra violet wavelengths and from the debris that is ablated from the target by the laser beam (Eason et al., 1986). In this latest series of experiments the resist material overlaying the Si_3N_4 window was removed to leave a grid-like pattern on the window, the dimensions of the wells created being about 30 x 30u by 1u deep. These wells helped to hold the cells in position and the bars prevented excessive pressure being put on the cells when the cell holder was tightened. The selection of the X-ray wavelengths is accomplished by careful choice of the target materials when laser-produced plasmas are to be used as a source of X-rays, for example, mylar, gold, brass and graphite have all been used successfully (Michette et al., 1986), in these experiments mylar

coated with 25nm of gold was used initially and later gold foil.

The use of VULCAN, and previously SPRITE (Stead and Michette, 1986), at RAL has produced sufficient yields of soft X-rays in a sufficiently short pulse to ensure that no damage could occur to the specimen during the image recording process. The use of laesr-produced plasmas has therefore enabled live-cell imaging to be performed using PMMA-MAA as the resist material and mylar as the target material.

The plant material used has included a variety of filamentous algae (Zygonema, Spirogyra, and Anabaena), and unicellular algae (Trebouxia, Cyanidium, Chlamydomonas and Dunaliella) and the epidermal hairs of Tradescantia. In addition to these specimens collaborative work with Professor Duckett (Queen Mary College) involved the imaging of Sphagnum protonema and onion epidermal cells, whist Dr. Susan Isaacs (Liverpool University) imaged the zoospores of Phytophora. The images obtained have been compared, where possible, to those obtained using LM (either transmitted white light or Nomarski interference microscopy) or TEM of material prepared by conventional aldehyde fixation followed by post-fixation with osmium tetroxide, dehydration in alcohol or acetone, cutting thin sections from the resin-embedded material and post-staining sections with uranyl acetate and lead citrate to enhance contrast.

In addition to the imaging of live specimens a number of the algal cells were imaged after being prepared for conventional TEM, that is to say after either fixation in glutaraldehyde alone or in glutaraldehyde followed by osmium tetroxide. In this way it was hoped to show the effects, if any, of these fixatives on the ultrastructure of living biological material.

Throughout a number of experiments were performed to ensure that the specimens remained hydrated at least until the exposure was made; in other words, to test that the Si_3N_4 window remained intact despite the pressure difference across it. As an alternative strategy the X-rays were relayed via a toroidal mirror to a position remote from the target so that the Si_3N_4 window would not be destroyed by materials ablated from the target and thus the specimens should still be wet when removed from the chamber. Both of these experiments were successful thereby showing that any images obtained would indeed be of the hydrated living cells.

Methodology

Biological material is particularly sensitive to dehydration which causes distortion of the cellular components and hence difficulties in the correct interpretation of the images obtained. Once cells have been mounted in the specimen holder, even though the internal pressure remains at atmospheric, the time delay before exposure to X-rays must be reduced to an absolute minimum. The new design of the cell holder has greatly facilitated rapid sample loading and the ability to control the pressure with which the resist and specimen are pushed together is also a great improvement over previous designs. However, the uncertainty of the exact timing of laser shots creates additional variables in the eventual interpretation of the resist images.

Although eventually successful the imaging of hydrated biological material at RAL has not been without its difficulties. In the latest series of experiments in particular the long delay, due to lack of any technical assistance, in developing the resists after exposure has resulted in the loss of much valuable information because it is now apparent that the chemical bonds that are broken upon exposure to the X-rays, and thereby made susceptible to subsequent chemical development, reform after a few weeks. This has meant that many of the resists could not be developed to the optimum depth for viewing by SEM, and thus for many specimens the photoresists have only been examined by LM. This reforming of the chemical bonds has also made the accurate prediction of development times from the known X-ray dose rather difficult, however, we have now established that ideally the depth of development should be in excess of 600nm or about half the nominal depth of the resist (1.1u). In some of the resist used recently the depth of resist coating was considerably less than the nominal quoted thickness and this too has made development of the resist unusually difficult.

In attempts to improve the development of resists a number of alternative developers have been tried. In previous experiments MIBK

diluted with varying proportions of IPA has enabled development times to be in the order of 5 - 7 minutes. If development times exceed this then the remaining resist material may swell and this results in a loss of detail; with shorter times it becomes difficult to assess the correct development time. In some cases resists from these particular experiments needed up to 40 minutes in 50% MIBK to reveal any detail (Fig A1.41a) and even then the development depth was less than 50nm, making examination by SEM very difficult (Fig A1.41b).
The use of 100% MIBK reduced development times only marginally and therefore butanone or ethyl acetate were tried as alternative developers, where appropriate these were again diluted with IPA. In order to assess the depth of development relative to the remaining thickness of resist a small scratch was made at the edge of each resist before development commenced and the depth of this scratch was assumed to reflect the remaining depth of the resist material (PMMA-MAA).

Biological Results

Resists developed so far have shown successful imaging of wet cells of the filamentous cyanobacterium Anabaena, the eukaryotic unicellular algae Cyanidium and Chlamydomonas (the latter being a motile alga prossessing two flagella), motile zoospores of the fungus Phytophora and from flowering plants onion epidermal cells and Tradescantia leaf hairs (Fig A1.41a-g). Photomicrographs taken by interference light microscopy of these resists show cell outlines with little ultrastructural information, however, in the case of the motile zoospores and the motile Chlamydomonas the flagella are visible (Fig A1.41a-b) and the two distinct cell types of Anabaena can clearly be distinguished (Fig A1.41d). The continuity between these two cell types is apparent in these living specimens but the connection between vegetative cells is clearly greater than that between vegetative cells and heterocysts; this probably explains why in critical point dried material examined previously the heterocysts appeared to be free cells.

Similar light microscopy of critical point dried material imaged by soft X-ray contact microscopy using the Daresbury synchrotron also showed little detail of internal structure, which was only revealed after the resists had been sputter coated and examined under the SEM. Some of the resist images of wet cells reported here have been examined by SEM, but due to the problems alluded to previously, insufficient depth of development has made viewing particularly difficult (Fig 1e). Given suitably developed resist, however, it should be perfectly feasible to produce good SEM images of the resists which will reveal the internal cell detail of living hydrated biological material.

The successful use of a toroidal mirror (reported in A1.10 by Hills et al.) is a major step forward and is further proof that given suitable operating conditions lower amounts of energy will be sufficient for the successful imaging of hydrated biological material. In the current series of experiments, however, critical point dried material was used, similar to that used in previous SXCM experiments using synchrotron radiation at Daresbury. The images obtained (Fig A1.41g) show comparable detail when viewed under the light microscope to similar images obtained using synchrotron radiation (Fig A1.41h). The major potential advantage of laser-produced plasmas as a source of soft X-rays, as opposed to the currently available UK synchrotron radiation source remains however, the much shorter exposure times (nsecs compared to secs) which ensure that no structural damage will occur to the delicate hydrated biological specimens during exposure to the X-rays.

Conclusions and Future Developments

1. The use of laser-produced plasmas is quite clearly already a successful means of studying the ultrastructure of hydrated cells, but to date only the high cost central research facility lasers can be used, future work must identify the lower limits of laser energy needed and from there a routine experimental facility can be designed, built and marketed. To further reduce the size, and cost, of the lasers needed, parallel research must develop more sensitive resist of materials. To improve the resolution thinner resists which can be viewed under the TEM are being evalutated;
alternatively it may be possible to produce carbon replicas of the resists, which themselves can be examined under the TEM.

Fig A1.41 Figures a-d and f-h are light micrographs taken with incident interference illumination, they are all x390. Figure e is a scanning electron micrograph and is x6650, all are images of the resist after chemical development with MIBK/IPA.

a) Image of the motile green alga Chlamydomonas. The particularly rounded appearance is probably due to excessive pressure being applied to the cell holder, the flagalla, arrowed, are about 250 nm in diameter.

b) Image of a motile zoospore (arrowed) of the fungus Phytophora, the flagellum (f) is just visible.

c) Fresh, unfixed filament of the blue-green alga Anabaena.

d) Anabaena that had been fixed in glutaraldehyde and osmium tetroxide as for conventional transmission electron microscopy. Note the two cell types, the larger heterocysts (H) and the more frequent vegetative cells (V). Despite similar exposure and development the cells are more prominent in this image (cf c) as the presence of heavy metal (osmium) absorbs the X-rays. In this case the Si_3N_4 window used had no bars of resist material remaining on it.

e) An image of a single vegetative cell of Anabaena as seem bu scanning electron microscopy. After sputter coating the resist with Au:Pa the depth of the image is so diminished that little detail is visible.

f) Images of fresh Cyanidium - a non-motile unicellular red alga.

g) Images of critically point dried Trebouxia cells, in this image the cell holder was placed in the 'toroidal' position. The detail seen in these cells is identical to that seen with similar material imaged by using synchrotron radiation (cf h). The cell wall can be identified (arrowed) from the internal cell components.

h) Criticial point dried Trebouxia cells imaged at Daresbury using synchrotron radiation. The detail visible by light microscopy is similar to that seen with laser produced plasmas (cf g) but examination by SEM has revealed greater detail.

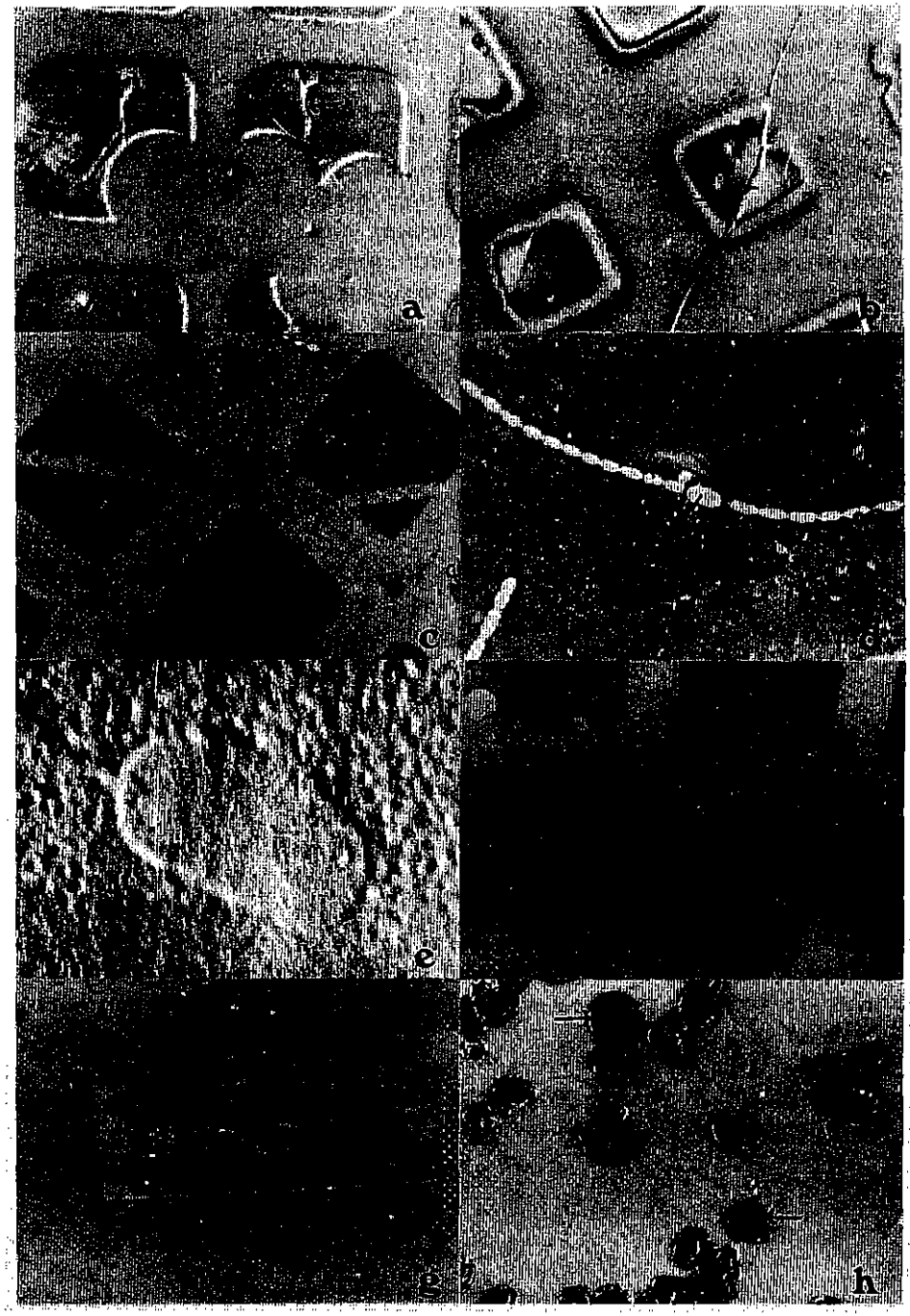

2. Soft X-ray contact mircroscopy is still obviously in its infancy, however, the technique is successful using laser-produced plasmas as the source of X-rays. The results obtained demonstrate the potential of the technique for studying the ultrastructure of hydrated biological material and it will now possible to use this technique, for example, in the study of the structure of cytoplasm and the changes that occur in the cytoskeleton of the cell during development - neither of which can be studied satisfactorily by other means.

3. Further development and refinement of the technique should enable routine imaging of biological material to be performed at RAL under conditions which are more suited to the particular needs of Biologists.

A1.10 IMAGING WITH SOFT X-RAYS RELAYED BY A TOROIDAL MIRROR FROM A LASER-PLASMA SOURCE

C P B Hills (King's College), R J Rosser, A Ridgeley (RAL), T W Ford, A D Stead (Royal Holloway and Bedford College)

In recent years soft X-ray contact microscopy has been performed by exposing an X-ray sensitive resist to X-rays coming directly from the laser-plasma sources(32). This can lead to damage to the silicon nitride (Si_3N_4) window used to maintain the biological specimen in a hydrated state and at atmospheric pressure whilst allowing the transmission of soft x-rays. Breakage of this window means that the condition of the specimen at the time of exposure is uncertain. Such window damage is due in part to the impact of debris from the laser-plasma source, so that elimination of the debris is necessary for obtaining images of verifiably hydrated specimens. One method for eliminating or reducing debris, is the use of toroidal mirror optics to relay soft X-rays from the source to the specimen(33), this technique also has the added advantage of collecting the X-rays over a large solid angle and focussing them onto the specimen. The experiments performed at the CLF were concerned with contact microscopy of biological material using a laser-plasma source viewed both directly and indirectly to eliminate the debris.

Indirect exposure of the resist was achieved by means of a grazing incidence concave toroidal mirror which imaged the laser-plasma source at a point 375mm from its pole, and on its Rowland circle at the conjugate focus 375mm on the other side, but for the purposes of this experiment the specimen chamber was positioned 2000mm from its pole, so that the X-rays were defocused and the whole Si_3N_4 window was illuminated. Thus it was possible to make a number of exposures with the same Si_3N_4 window, and to check on the state of the specimen after the exposure. The soft x-rays used were generated from a plasma produced by focussing 0.53μm radiation energy between 20J and 100J to a spot 300μm in diameter on a gold target, thus providing a continuum source of X-rays with which to expose the photoresist. Two types of resist were used PMMA-MA, a positive resist and Kodak X-ray Microresist which is a negative resist, although the negative resist was only used to image grid bars to ascertain its applicability to microlithography.

Work on contact microscopy using X-rays directly from the source was also carried out, continuing and improving upon previous work(34). One such improvement was the use of a circular mount which allowed 6 specimen holders to be exposed at any one time also allowing X-rays to be collected by the toroidal mirror, thus increasing the productivity of the technique; this allowed a greater range of specimens to be imaged including lead contaminated earthworms, zoospores of Phytophora, Sphagnum moss, Chloroplasts, Critical Point Dried Trebouxia, Anabaena, Chlamydomonas, fresh Cyanidium, fresh Dunaliella fresh Spirogyra cells and Fungal spores. Examples of the images obtained can be seen in Fig A1.41.

A1.11 X-RAY IMAGING OF BIOLOGICAL MATERIAL

K S Richards (Keele), A D Rush (RAL), D T Clarke, W J Myring (Daresbury)

Using Vulcan, attempts to contact image the following biological materials were made: "dry" ultrasections of heavy metal contaminated earthworm tissue; ultrasections of this tissue presented in a "wet" state; unicellular algae ("wet"); isolated chloroplasts ("wet"); fungal hyphae ("wet"). When the X-ray sensitive resists, after development, were examined by SEM, the results were variable. The algal and chloroplast attempts were not successful, possibly due to imperfect speciment preparation. However, the resists appeared to have properties different from those used during a previous trial using Sprite. Although the development time, judged subjectively using interference microscopy, seemed adequate, it turned out to be insufficient when the resists were examined by SEM and detail in a large number of the resists could not be resolved. Nevertheless, some encouraging images were produced of the earthworm and fungal material.

Figure A1.42a is an image of ultrasectioned, lead-polluted earthworm chloragogenous tissue and the granule (G) are clearly visible. However, contamination of the resist by 'dirt' from the target (asterisk) is problem. The images of earthworm tissue presented in the "wet" state were less satisfactory.

Figure A1.42b is an image of fungus Neurospora in the "wet" state and its septate nature (S) is apparent, as are longitudinal strands of cytoplasm (arrowheads). Target 'dirt' is also present. The strands are reminiscent of those of foxglove hair cells demonstrated by Stead & Michette in the last RAL Report (RAL-86-046 A4.2.3).

Clearly, further studies are necessary in order to standardize and then evaluate the technique of contact imaging using laser sources.

A1.12 X-RAY SOURCE BRIGHTNESS MEASUREMENTS

A J Cole, M H Key (RAL)

As an adjunct to the high power operations tests described in Section C1.2, it was decided to use the high energy "hot" beam for a simple target interaction experiment. The purpose was to measure the absolute brightness of a "typical" X-ray source, generated with a single beam of VULCAN, with the energy that will become available in the near future.

Approximately 200 J of green laser energy was available in a 900 psec pulse. This was focussed, using an F/2.5 aspheric lens, to a spot size of 200 μm on flat targets with dimensions of 2 mm x 2 mm. This gives an incident irradiance of $\approx 7.10^{14}$ Wcm^{-2}. Two target materials were used, Titanium and Calcium, the latter in the form of a 5 μm thick evaporated layer of Calcium Fluoride. These elements were chosen as their bright resonance lines are in the 3.5-5.0 Kev energy range. This is low enough to permit a reasonable conversion efficiency, yet high enough to penetrate significant thicknesses (≈ 100 μm) of organic type material. This would be of interest for low-angle X-ray diffraction measurements of biological structures, for example.

The targets were viewed with a standard minispectrometer at an angle of 35° to the input beam axis, with the target normal angled to bisect these two axes. A 4 Å Germanium crystal was used to produce the spectra which were recorded on Kodak DEF X-ray film.

Tracings of typical spectra are shown in Figure A1.43. The Ti spectrum shown is deliberately overexposed for the strong He_α line in order to show the weaker K_α, Ly_α and higher order He like lines. From well exposed spectra, such as that shown for Ca, the integrated brightness of the strong He_α line and its satellites has been determined, using published film response data(35). For Ca (Z=20 this quantity is 5.10^{11} photons per Joule of incident laser energy, and for Ti (Z=22) it is 2.10^{11}/J. These values are for symmetric radiation into 4π steradians.

These X-ray conversion efficiencies are lower than would be expected from previously reported measurements[36],[37]. Figure A1.44 shows the RAL results together with those of LLNL[37]. As can be seen, the RAL efficiencies are lower by approximately a factor of 10. The scaling with nuclear charge Z, however, is the same for both data sets in the limited range of target Z covered in the RAL results. This is probably explained by the uncertainty in the integrated reflectivity of the Ge crystal used in the RAL experiments causing an error in the deduced absolute brightness.

An interesting feature of the RAL spectra is the presence, at a measurable level, of the Ly_α hydrogenic line. This radiation is also seen in the Rochester LLE data[36], but not in the LLNL data at this irradiance and target Z. The authors in (37) suggest that he hydrogenic lines come from "hot spots" in the focal spot of the laser causing local increases in the plasma temperature. For the RAL data, the spectra were obtained using the "cleanest" laser beam ever used in target experiments so significant large scale beam breakup would not be expected. Plasma instabilities can cause hot spots in focussed laser beams but these should have occurred in the LLNL experiments as well as those at LLE and RAL.

In conclusion, high brightness, quasi-monochromatic X-ray sources have been produced with a single upgraded beam of the VULCAN laser. The measured X-ray conversion efficiencies agree, within experimental uncertainties, with previously reported values.

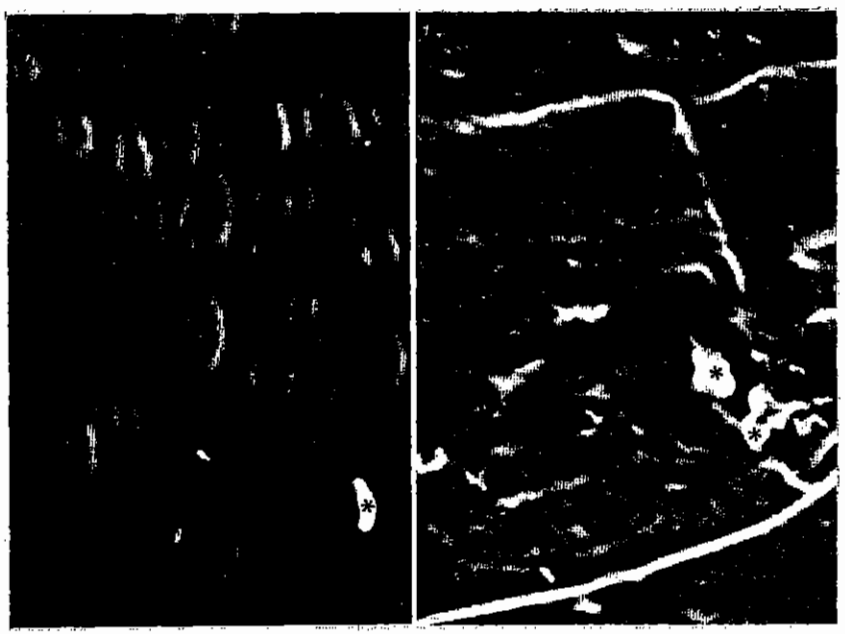

Fig A1.42 A. Sectional earthworm chloragogenous tissue.
B. Septate fungal hypha.

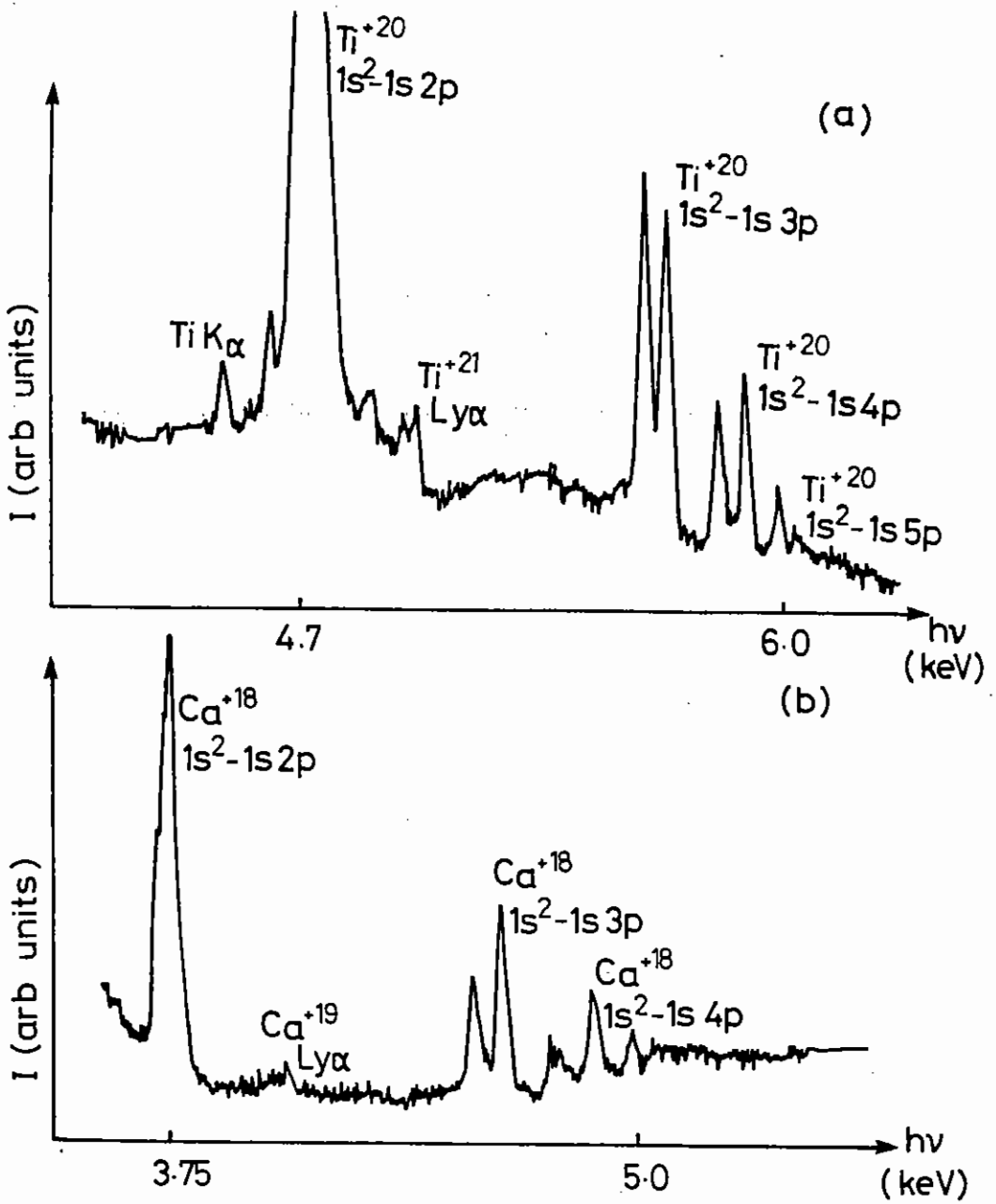

Fig A1.43 (a) Ti target irradiated with 160 J, filtering was 125 μm Be + 125 μm Mylar

(b) Ca target irradiated with 220 J, filtering was 125 μm Be + 250 μm Mylar

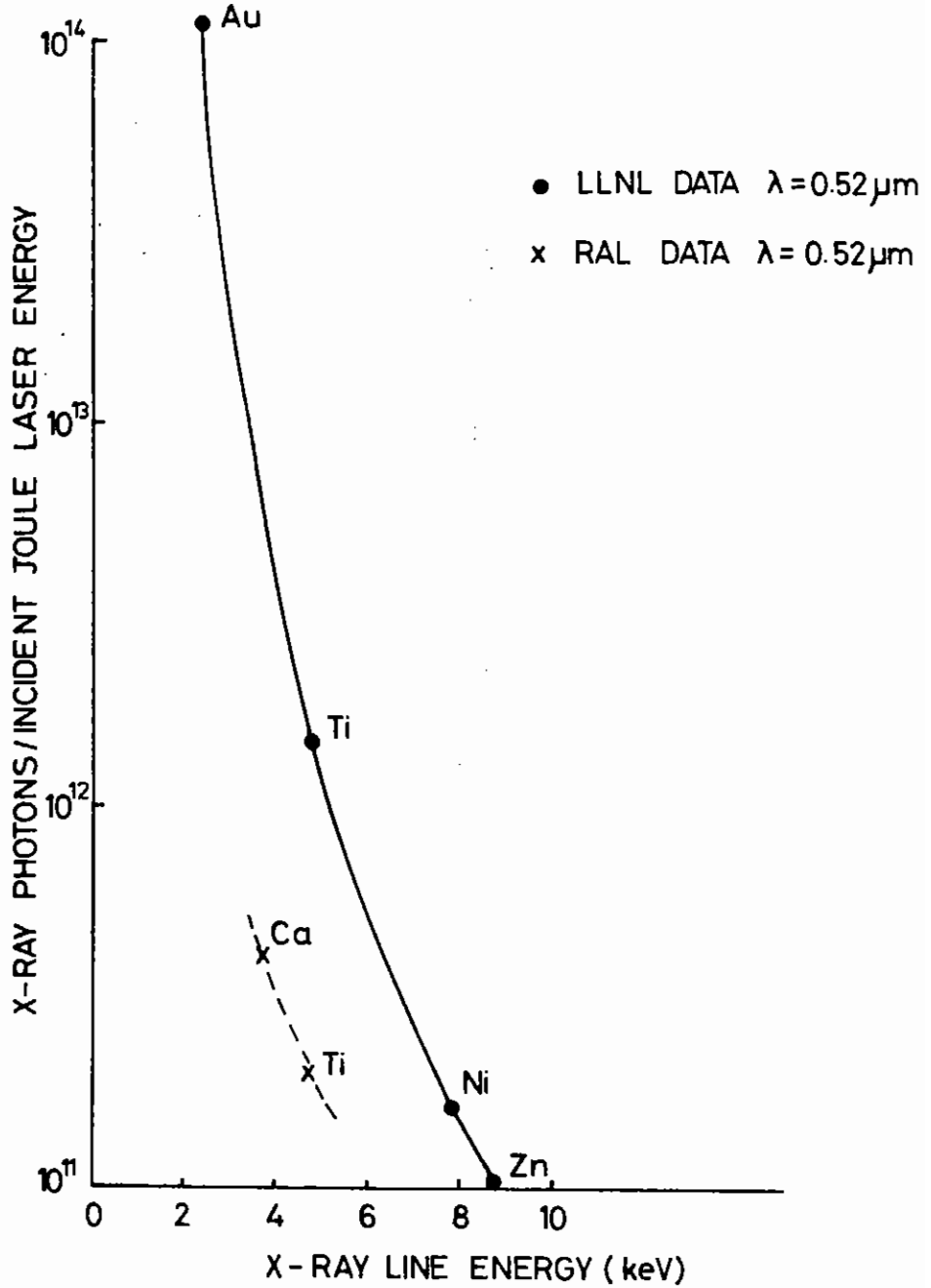

Fig A1.44 X-ray conversion efficiency as a function of target Z, the LLNL data is from Ref 37.

References:

A1.1 M H Key, Nature 316, 314 (1985).

A1.2 D L Matthews at al, Phys Rev Lett 54, 110 (1985).

A1.3 S Suckewer, C H Skinner, M Milchberg, C Keane, D Voorhees, Phys Rev Lett 55, 1753 (1985).

A1.4 G Jamelot, A Klisnick, R Carillon, M Guennou, A Sureau, P Jaeglé, J Phys B 18, 4647 (1985).

A1.5 J F Seely, C M Brown, U Feldman, M Richardson, B Yaakobi, W E Behring, Opt Comm 54, 289 (1985).

A1.6 G J Pert, J Phys B 9, 3301 (1976) and 12, 2067 (1979). M H Key, C L S Lewis, M J Lamb, Opt Comm 28, 331 (1979).

A1.7 R J Dewhurst, D Jacoby, G J Pert, S A Ramsden, Phys Rev Lett 37, 1265 (1976).

A1.8 D Jacoby, G J Pert, S A Ramsden, L D Shorrock, G J Tallents, Opt Comm 37, 193 (1981).

A1.9 I N Ross et al, Appl Optics (in press).

A1.10 G P Kiehn, O Willi, A R Damerell, M H Key, Appl Optis 26, 425 (1987).

A1.11 M H Key and G J Pert, Annual report to the Laser Facility Committee, RAL-86-046, A5.38 (1986).

A1.12 G P Kiehn et al, Annual Report to the Laser Facility Committee (1987 - to be published).

A1.13 V V Sobolev, 'Theoretical Astrophysics', Ed V A Ambartsumyan (London Pergamon), Chap 29, 475 (1958).

A1.14 P Jaeglé, A Carillon, G Jamelot, H Guennou, A Sureau, Europhysics Lett 1(II), 555 (1986).

A1.15 D L Matthews et al, Phys Rev Lett 54, 110 (1985); B MacGowan, Proc of SPIE Annual Meeting, San Diego (1986).

A1.16 G Kiehn et al, Appl Optics 26, 425 (1987).

A1.17 R London and M Rosen, Phys Fluids (preprint).

A1.18 Section A4 Annual Report to the Laser Facility Committee, RAL 84-049 (1984).

A1.19 J Lunney, J D Hares, P Dobson, S D Tabatabaei, R W Eason, Opt Comm 58, 269 (1986).

A1.20 J Burgest and D Taupin, Acta Cryst A24, 99 (1968).

A1.21 S Takagi, J Phys Soc Japan 26, 1239 (1969).

A1.22 B Klar and F Rusticelli, Nuovo Cimento 13B, 249 (1973).

A1.23 A Fukuhara and Y Takano, Acta Cryst, A33, 137 (1977).

A1.24 B C Larson, C W White and T S Noggle, Phys Rev Lett 48, 337 (1982).

A1.25 B C Larson, C W White, T S Noggle, J P Barhorst and D M Mills, Appl Phys Lett 42 (3).

A1.26 P C Cheng, R Feder, D M Shinozaki, K H Tan, R W Eason, A Michette, R Rosser, Nucl Inst and Methods in Phys Res A 246, 668 (1986).

A1.27 R W Eason, P C Cheng, R Feder, A Michette, R Rosser, F O'Neill, Y Owadano, P T Rumsby, M J Shaw and I C E Turcu, Optics Acta 33, 501 (1986).

A1.28 R Feder, E Spiller, A N Topalain, A N Broers, W Gudat, B J Panessa, Z A Zadunaiky and J Sedat, Science 197 259 (1977).

A1.29 P Goby, C R Acad Sci 156, 686, 1913.

A1.30 A Michette, P C Cheng, R W Eason, R Feder, F O'Neill, Y Owadano, R Rosser, P T Rumsby, M J Shaw, J Phys D: Appl Phys 19, 363 (1986).

A1.31 A D Stead and A Michette, Annual Report to the LFC A4.2.3 RAL 86-046 (1986).

A1.32 R J Rosser, K G Baldwin, R Feder, D Bassett, A J Cole, R W Eason, J Microscopy 138, 311 (1985).

A1.33 R J Rosser, R Feder, A Ng, F Adams, M Caldarolo, P Celliers, P C Cheng, L Da Silva, D Parfeniuk, R J Speer, J Microscopy 144, RP5 (1986).

A1.34 Annual Report to the Laser Facility Committee, Rutherford Appleton Laboratory Report No RAL-986-046 (1986).

A1.35 B L Henke, J Y Uejio, G F Stone, C H Dittmore and F G Fujiwara, J Opt Soc 3, 1540 (1986).

A1.36 B Yaakobi et al, Opt Comm 38, 196 (1981).

A1.37 D L Matthews et al, J Appl Phys 54, 4260 (1983).

Editor: A J Cole

A 2 . 1 GENERATION OF UNIFORM PLASMAS FOR BEAT WAVE EXPERIMENTS

A E Dangor, A K L Dymoke-Bradshaw, A Dyson, T Garvey, I Mitchell,
Blackett Laboratory, Imperial College, London

A J Cole, C N Danson, C B Edwards, R G Evans,
Rutherford Appleton Laboratory, Chilton, Didcot, Oxon OX11 0QX

A2.1.1 Introduction

The laser plasma "beat wave" mechanism for the generation of ultra-high electric fields requires plasmas of several metres length with density uniformity to about 1%. Multiphoton ionisation of molecular hydrogen gas at a pressure of a few torr provides a scaleable mechanism for generating these plasmas. We describe measurements of electron density, temperature and uniformity of plasmas generated by a frequency doubled Neodymium glass laser, at an irradiance of about 10^{14} Wcm^{-2}. The plasma density corresponds to 100% ionisation and is measured to be uniform to within the measurement errors over a length of 8 mm.

In essence the beat wave scheme requires that two parallel laser beams of slightly different frequencies ω_1 and ω_2 are focussed into a plasma whose resonant frequency $\omega_p = \omega_1 - \omega_2$. A longitudinal electrostatic (Langmuir) wave is driven resonantly and under suitable conditions may achieve an amplitude of tens or hundreds of Gev/metre. Since this is a resonant process of moderately high "Q" the plasma density is required to be accurate to about 1% or better over the entire length of the accelerator, perhaps as much as 100 metre. In order to avoid excessive collisional damping of the Langmuir wave the plasma temperature should be greater than about 20eV, while to minimise the trapping of background plasma electrons and the energy inefficiencies the temperature should not be too much higher than this minimum. To produce useful accelerating fields[A2.1], plasma densities of 10^{16} - 10^{18} cm^{-3} are envisaged, while in order to drive the beat wave on a fast time scale (i.e., less than the ion plasma period) and avoid plasma instabilities[A2.2], laser intensities greater than 10^{14} Wcm^{-2} are necessary.

Preliminary experiments in this field[A2.3][A2.4] have used DC arc discharges, Z or theta pinches, or air breakdown plasmas. These plasmas are recognised as having inadequate homogeneity and reproducibility for potential accelerator applications. Here we report on a technique for the production of exceptionally uniform plasmas with the appropriate density and temperature by multiphoton ionisation of molecular hydrogen. The technique is scaleable to plasmas of arbitrary size and automatically provides the required plasma conditions wherever the laser intensity is large enough to drive the beat wave. The energy used to produce the multiphoton ionisation is less than 1% of the energy needed to drive the beat wave.

A2.1.2 Multiphoton Ionisation and Gas Breakdown

Since the early days of Q-switched lasers a large body of experimental data has accumulated on the related subjects of multiphoton ionisation (essentially a single atom/molecule interacting with the high intensity light wave) and laser induced gas breakdown (the collisional avalanche following absorption of laser energy in a gas). The distinction between the two processes is one of time scale, if the laser pulse is long compared with the collision time then breakdown effects will predominate, while in the opposite limit true multiphoton ionisation will be seen. Reviews of gas breakdown physics[A2.5] and of multiphoton ionisation[A2.6] give appropriate bibliographies in these fields. For laser pulse durations of order 10^{-9} sec and gas pressures of about 1 torr the collision time approximately equals the laser pulse duration. Little work has been performed in this range but the work of Dewhurst, Pert, and Ramsden[A2.7], and of Krasyuk et al[A2.8] is noteworthy. Multiphoton ionisation in molecular hydrogen has been studied using 20nsec pulses from a ruby laser (λ=694.3nm) by Voronov et al[A2.9].

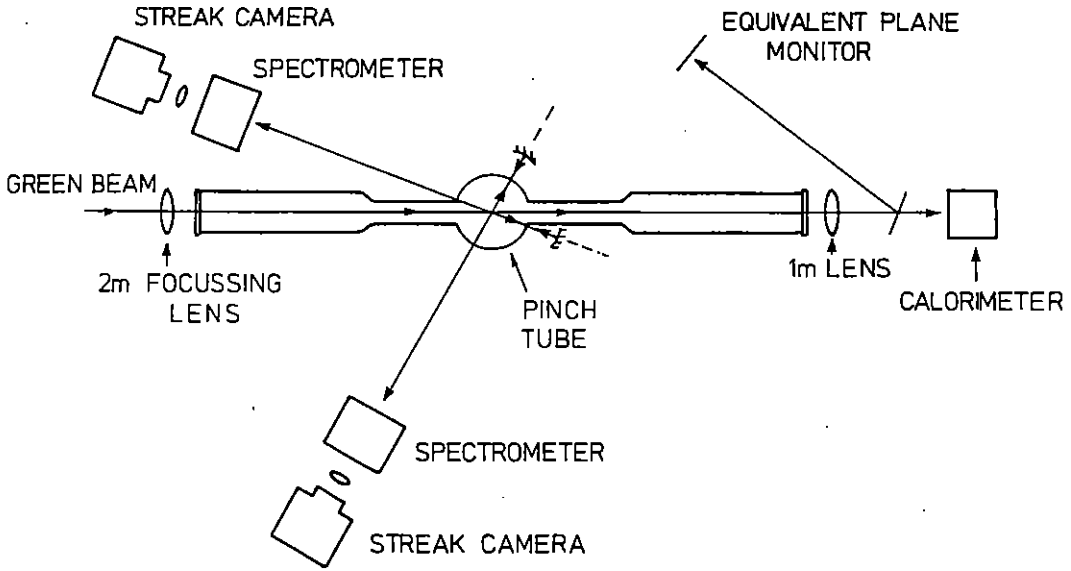

Fig A2.1 Schematic arrangement of the experiment

In subsequent discussion of our work we describe it as multiphoton ionisation since we believe this to be the dominant ionisation process even though it is followed by some collisional heating. This will be discussed more fully in the conclusions section.

A2.1.3 Experimental Arrangement

The 1.054μm light from the VULCAN laser was frequency doubled in a KDP crystal and focussed using either 1 metre or 2 metre focal length lenses of 10cm aperture into a glass vacuum vessel containing hydrogen gas at a pressure of 0.5-4 torr (actually a Z-pinch, but the pinch discharge was not fired). The laser energy was typically 10 Joules in 100 psec or 20 Joules in 1 nsec. The size of the focal spot was measured with an equivalent focal plane camera to be about 400 μm with the 2 metre focussing lens and 200 μm with the 1 metre focussing lens used for the long pulse measurements. Focussed irradiances were about $10^{14}Wcm^{-2}$.

The green light acted as a Thomson scattering probe beam and the scattered light was collected at four different angles (20, 60, 120, and 160 degrees) and hence four different values of the scattering parameter $\alpha = 1 / K\lambda_D$. Light from diametrically opposed channels was fed into the same spectrometer by means of a concave spherical mirror as shown (Fig A2.1), light emerging from the spectrometers was fed into two optical streak cameras whose time dispersion separated the direct and reflected light components. The streak camera output was recorded on HP5 photographic film and a calibration wedge was recorded individually for each data shot. The overall layout of the scattering and other diagnostics is shown in Fig A2.1. The spectral and temporal resolutions were respectively about 5A and 100psec.

A2.1.4 Experimental Results

The results of this experiment consist of four simultaneous time resolved Thomson scattered light spectra. The 20 degree scattering channel is predominantly sensitive to electron density and gives the electron density by direct measurement of the frequency separation of the plasma satellites. The 160 degree channel is mostly sensitive to electron temperature but in the other two channels the shape of the scattered light spectrum is dictated by both parameters and a fitting procedure is required. (Fig A2.2) shows the 20 degree (high α) scattering signal with a 1nsec laser pulse. It is clear from this data that there is little change in density or temperature during the 1nsec laser pulse and the same was true for all our measurements. The duration of the scattered light signal indicates that the plasma is formed very early in the laser pulse, but there is no absolute time reference.

The photographic data is corrected for film response, spectrometer and streak camera spectral sensitivity and finally fitted in a least squares sense to theoretical Thomson scattering profiles for a thermal plasma. Electron density and temperature are the fitting parameters and the absolute system sensitivity is uncalibrated. Examples of this fitting procedure are shown (in fig A2.3) for a scattering angle of 120 degrees. In all of the data obtained, the four scattering angles can always be fitted by a single density and temperature and there is no evidence of plasma turbulence or of non-Maxwellian distributions.

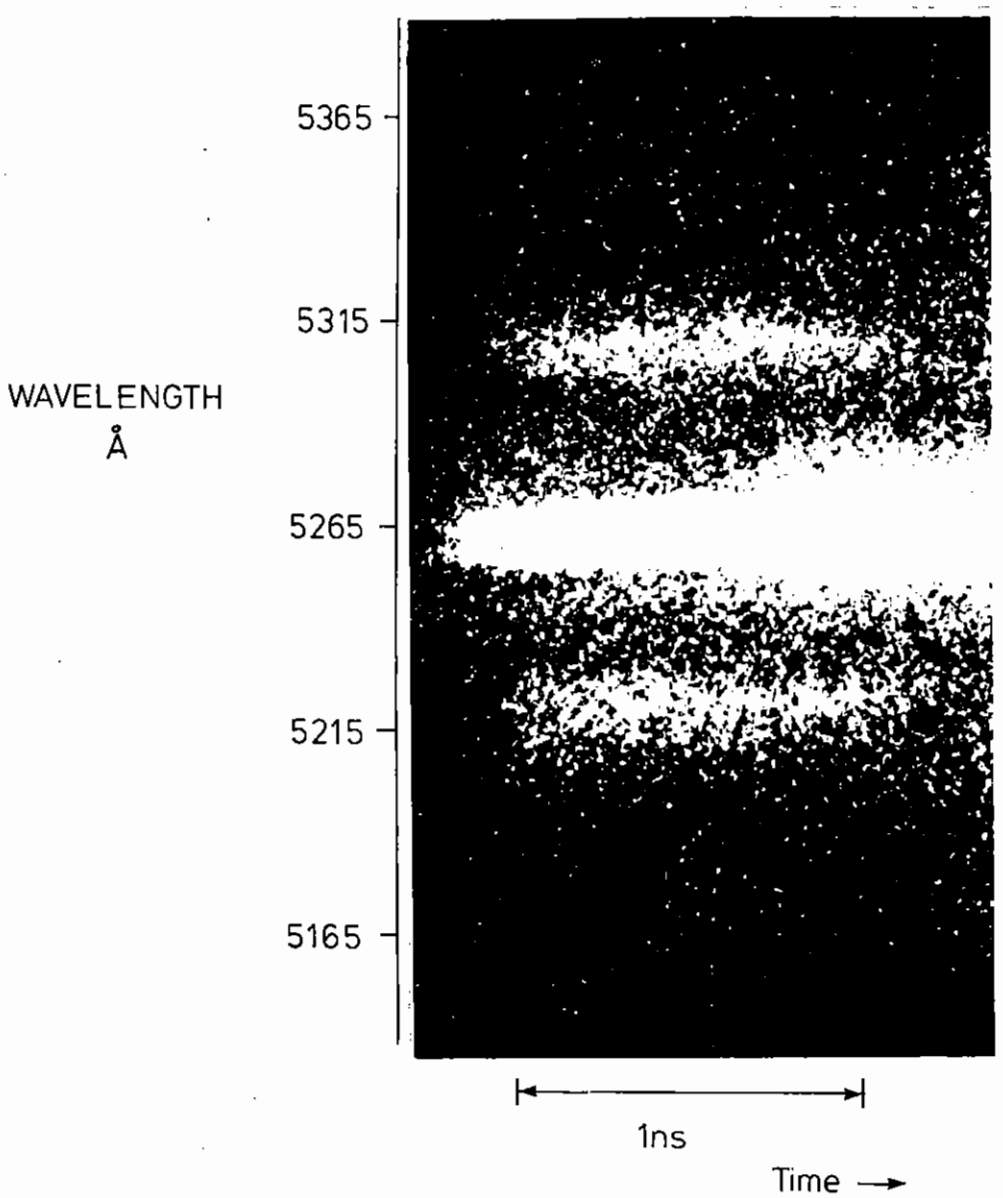

Fig A2.2 Thomson scattering at 20 degrees, 1 nsec laser pulse.

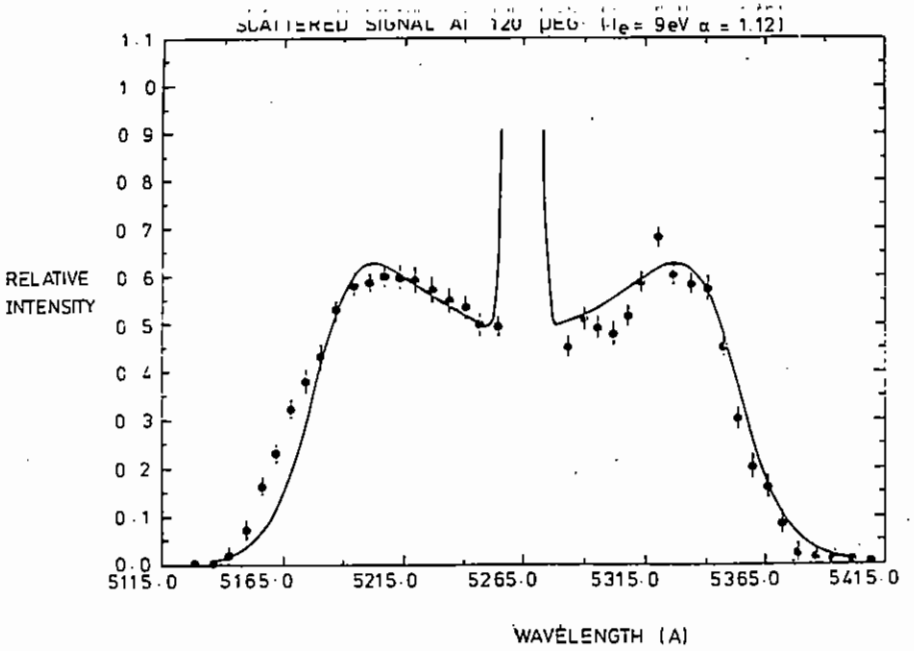

Fig A2.3 Computer generated best fit to the 120 degree scattering.

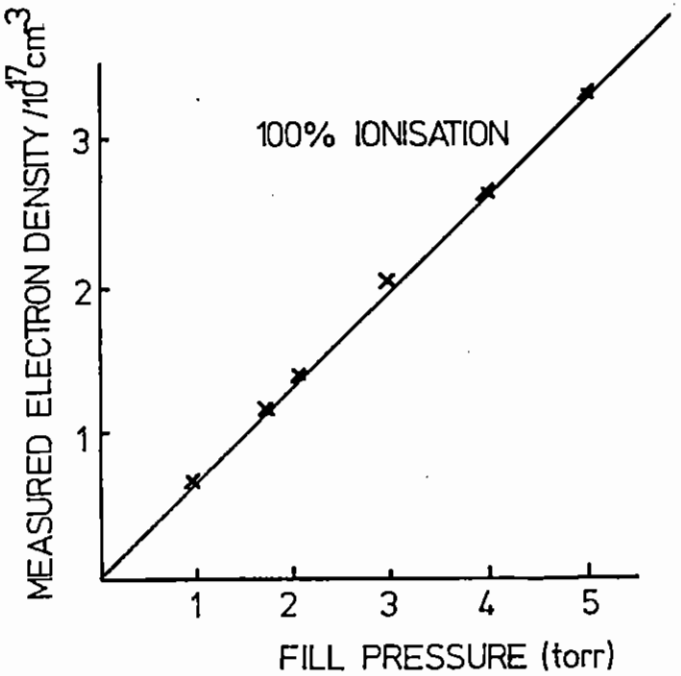

Fig A2.4 Electron density as a function of Fill Pressure.

For all the data, the electron density did not vary with the laser irradiance. Attempts to operate at lower irradiances and measure an ionisation threshold were limited only by the lack of scattered light. The measured electron density as a function of gas fill pressure is shown (in fig A2.4). The electron density is proportional to the fill pressure, and corresponds to 100% ionisation to within the measurement error.

Fig A2.5 shows the results of defocussing the input lens by +4, -4mm axially, while keeping the scattering volume fixed in space. This has the effect of measuring the electron density variations along the axis of the main focussing lens. The densitometer scans show that there is no measurable variation of ω_p at the 2% level, corresponding to a 4% uncertainty in n_e.

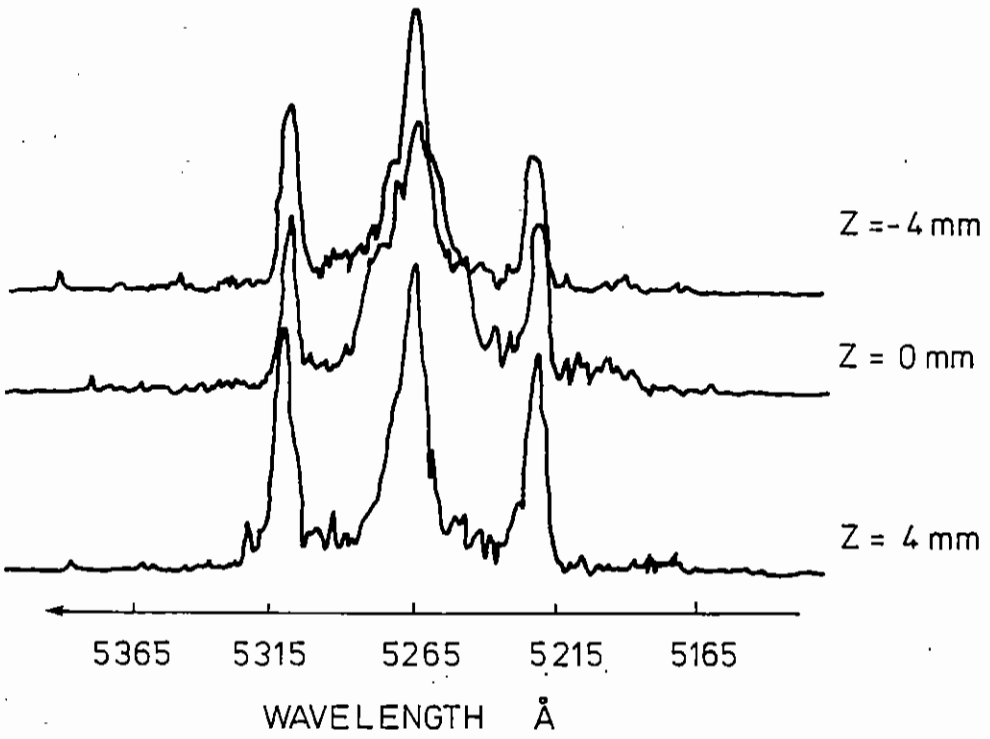

Fig A2.5 20 degree scattering signals from three axial positions.

The electron temperature is measured to be about 8 - 10eV for all the data independent of the laser irradiance. There is some suggestion that higher gas fill pressures correspond to higher temperatures.

A2.1.5 Discussion

We have modelled the plasma heating with a simple one dimensional (cylindrically symmetric) computer code, modelling absorption, thermal conduction, ion-electron equilibration, and hydrodynamic expansion. The laser is incident along the axis and has a Gaussian radial intensity profile. The model assumes at t=0 that the plasma is ionised, at a temperature of 1eV or less. The classical absorption cross section is modified to allow for the reduction in collision frequency[A2.10][A2.11] when the electron oscillating velocity in the light wave $v_{osc} = eE/m\omega$ exceeds the thermal speed $v_e = (k_B T_e/m)^{\frac{1}{2}}$.

$$\nu_{eff} = \nu_{class} \frac{v_e^3}{(v_o^2 + v_e^2)^{3/2}}$$

and the electron thermal conductivity is limited by the electron "free streaming" limit:

$$Q = \left(\frac{1}{Q_{class}} + \frac{1}{Q_{fs}} \right)^{-1}$$

The free streaming flux is defined as:

$$Q_{fs} = f\, n_e\, k_B\, T_e\, v_e$$

where k_B is Boltzmann's constant and f is an adjustable constant

which normally is 0.1 for best agreement with more rigorous calculations based on the Fokker-Planck equation[A2.12].

The model gives very good agreement with the measured temperatures using the standard value of flux limit and the modified inverse bremsstrahlung cross section. Ignoring the free streaming limit causes the electron temperature in the model to be too low, while ignoring the strong field bremsstrahlung correction causes the model to give too high a temperature. If both the free streaming limit and the strong field corrections are omitted then the model predicts too great a sensitivity to changing laser irradiance. This can be regarded as tentative evidence for the correctness of the strong field bremsstrahlung model.

The model does not include the effects of 'above threshold' ionisation[A2.13][A2.14] which creates the initial electrons with energies of a few electron volts. The computer model can be artificially started with an arbitrary initial electron temperature, but because of the strongly velocity dependent absorption the final temperature (i.e., after 100-200psec) is hardly altered. Our measurements of electron temperature can therefore say nothing about the velocity of the electrons immediately following multiphoton ionisation.

Since the electron density following 100% ionisation is only 10^{-4} of the critical density, the refractive index of the plasma is very close to unity. This means that there is virtually no self-focussing of the laser light which propagates almost under free-space conditions. The uniformity of the plasma created by multiphoton ionisation is then limited only by the uniformity of the initial gas fill pressure and by hydrodynamic motion following the laser heating. At a temperature of 10eV, and assuming a beam waist of 400μm, the acoustic transit time is about 4nsec. The results of the computer model indicate that even this is an overestimate of the plasma motion since the strong field bremsstrahlung results in a very flat temperature profile extending out beyond the beam radius. In the computer model the electron density changes by less than 10^{-4} in a 1nsec laser pulse.

A2.1.6 Conclusions

We have studied the laser ionisation of molecular hydrogen, using Thomson scattering techniques to measure the time and space resolved density and temperature. Our results show that the gas is fully ionised within a time which is very short compared with the laser pulse duration and is ionised over a length of at least 1 cm using 2 metre focussing optics. The uniformity of the plasma is very high and appears to be more than adequate for performing future beat wave experiments. The measured temperature is less than is needed to avoid collisional damping of the plasma beat wave, but this is offset by the reduced collision frequency caused by the large oscillatory velocity of the electrons in the electric field of the laser.

A2.2 HEAT FLOW INSTABILITIES IN SPHERICAL TARGETS

D Bassett, O Willi (Imperial College)

The occurrence of filamenting structures and strong magnetic fields in the underdense corona of an ablative plasma have been explained by a variety of different instability mechanisms. Experimental evidence has been unable, to date, to provide the necessary information to easily ascertain single shot growth rates.

Large diameter glass microballoons (of the order of 250 μm), coated with 500 nm of gold were irradiated with the 12 1.053 μm long pulse laser beams in TAW. Defocus conditions of D/R = 10 were used which gave good uniformity and an intensity on target of about $5 \times 10^{13} W/cm^2$ for the pulse length of 1.8 ns FWHM. The use of such a long pulse length was to negate any transient temporal intensity fluctuations due to its fast rise time. The large defocus, combined with the low intensities removed any large scale density fluctuations and restricted the formation of hot electrons.

The major diagnostic in this experiment was a four frame optical probe arranged to give Schlieren images of the expanding corona at different times during the same shot.

The probe beam (Fig A2.6) generated by back Raman shifting the frequency doubled synchronous short pulse, operated at a wavelength of 522 nm and a pulse length of 15 ps. This very short pulse was very useful in obtaining well defined images of the corona.

The short pulse probe is subsequently split into four discreet components via a silvered four facet prism. Each of these beams were then delayed with respect to each other and directed past the target. The imaging system, consisting of a x 5 microscope objective and a 500 mm relay lens gave an overall magnification of x 18. The four frames were then spatially separated. Each of the frames was separated by 50 ps, and a Schlieren stop of 200 μm width was placed at the focal point of the relay lens (Fig A2.7). This method of dark ground shadowgraphy is very useful in distinguishing large density gradients in the coronal plasma. Examples of the results obtained are shown in Figs A2.8 and A2.9.

The experimental observations imply that within 125 ps of the laser pulse finishing, the conditions for the smooth spherical expansion of the underdense plasma are altered dramatically. Fine scale jets of the order of 5-10 μm wide become visible, with a nodal structure perpendicular to the expanding plasma. The jets completely surround the microballoon and do not appear to convect outwards any significant distance in the next 1 ns. The interesting factor appears to be the fact that there is no traceable small scale correlation between any of the frames. Except for the periodicity of the jets, one must assume that either the transmission angle of the four beams causes the variation in image characteristics, or rather that the overall stability of the density fluctuations is low compared with the interframe time of 50 ps. What can certainly be deduced from the photographs is that the unstable structure grows initially faster than that 50 ps time scale. The limitations to the experiment, however, are such that the maximum density probed was relatively low due to the effectively large f-number of the collecting optics. These results, if only a tentative first glimpse at the formation of the thermal instability in expanding plasmas indicate certainly that further work with a larger aperture optical system, with the possibility of multi-frame holography, combined with a shorter frame time should yield the information needed to explain these effects.

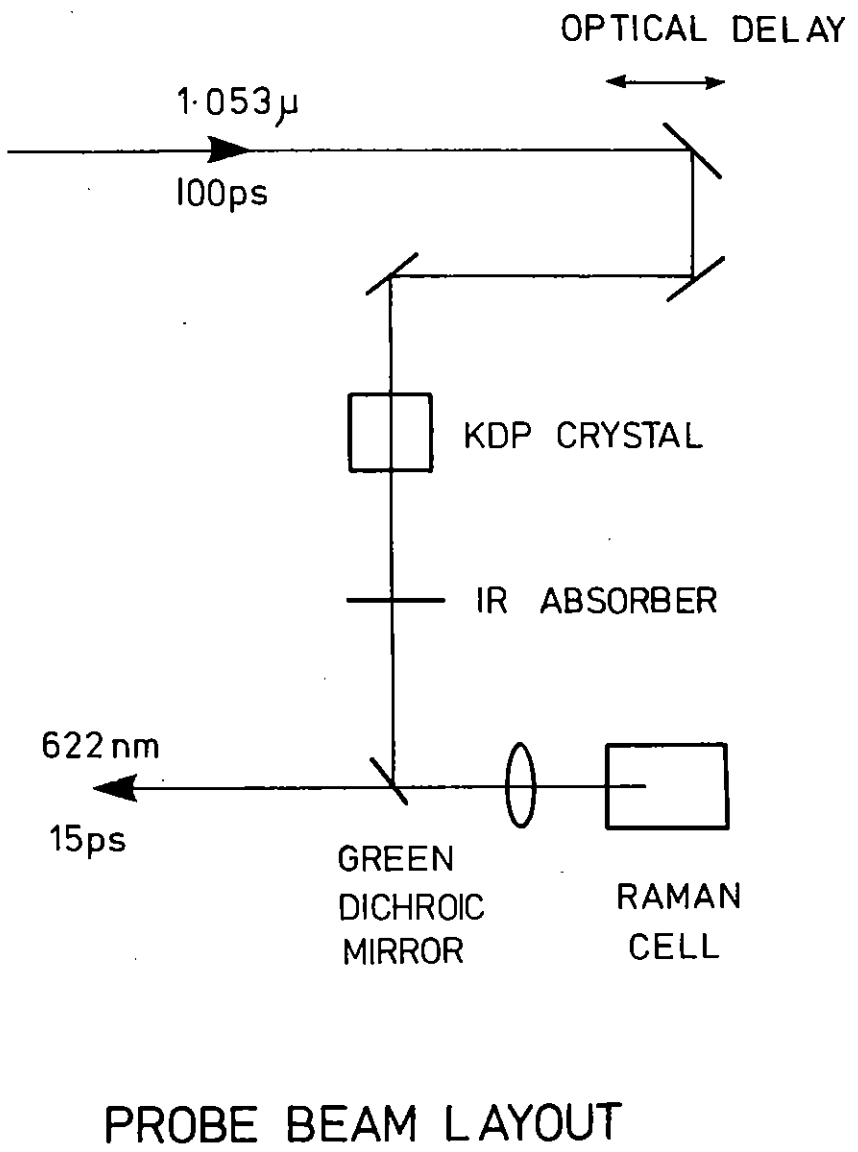

Fig A2.6 Method of generation of 622nm, 15ps optical probe beam.

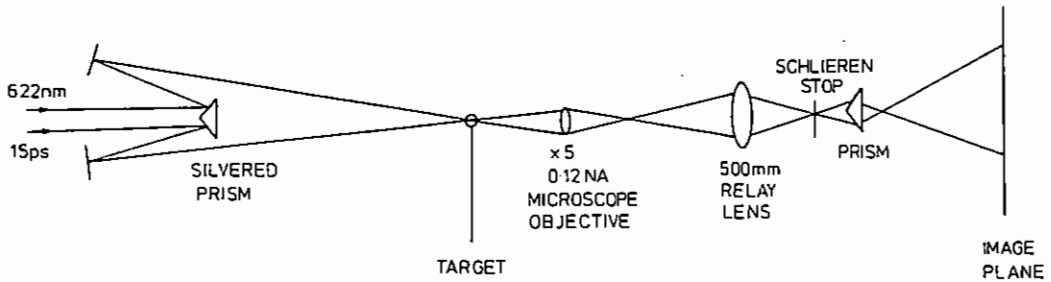

SCHLIEREN FRAMING CAMERA
(TWO BEAMS SHOWN)

Fig A2.7 Optical set-up of the multiframe schlieren imaging system.

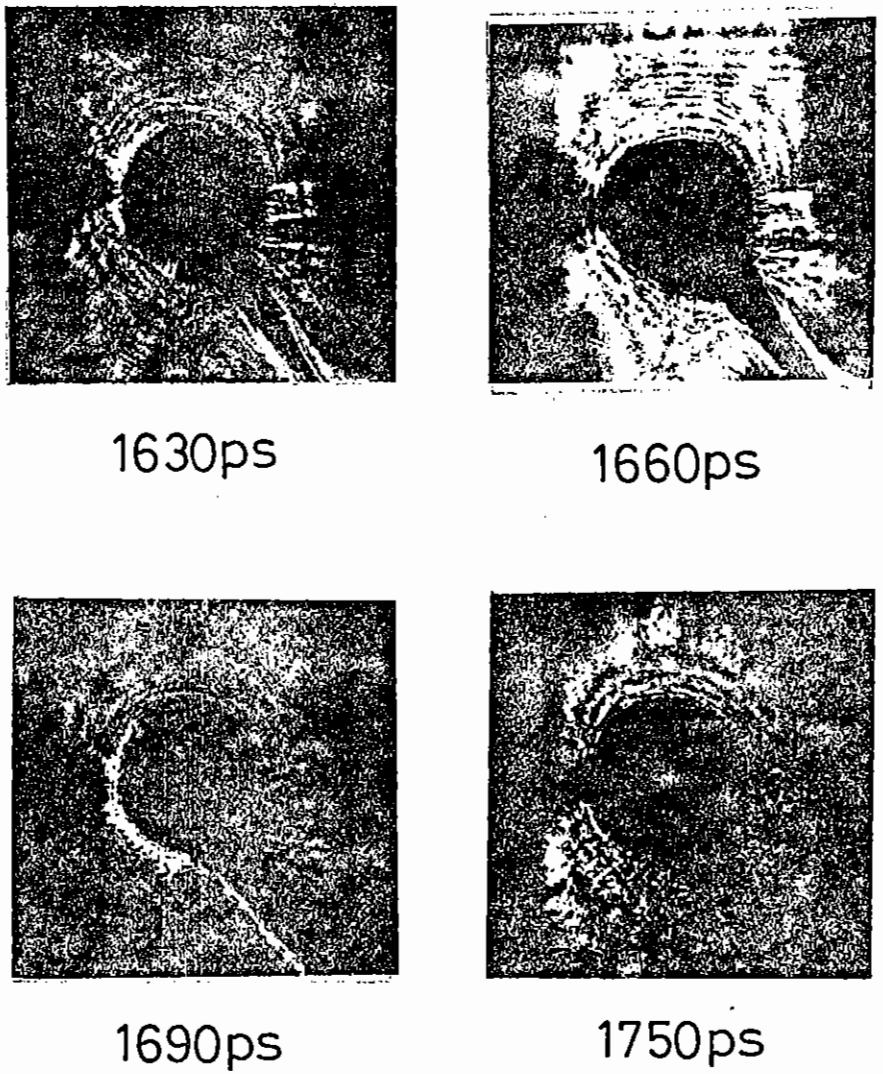

Fig A2.8 Four Schlieren images, taken on a single shot, during laser irradiation.

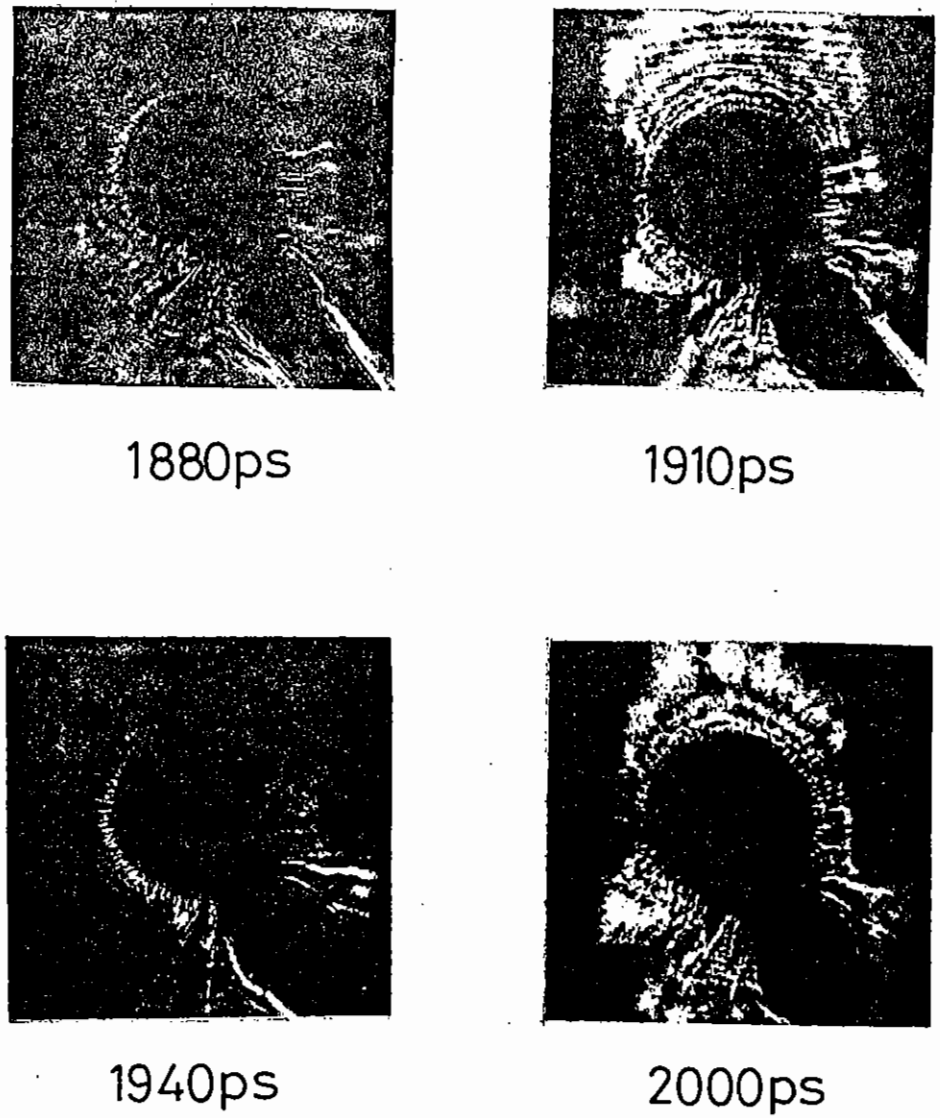

Fig A2.9 Four Schlieren images, taken on a single shot, after laser irradiation.

A2.3 OPTICAL REFLECTOMETRY OF ABLATING TARGETS

A.R. Bell and P. Choi (Imperial College), A.J. Cole (RAL)

The success of laser-driven implosions is largely determined by the degree of spherical symmetry. Asymmetry can be the result of non-uniform laser illumination, Rayleigh-Taylor instability or ablation instabilities. Asymmetry is important if it affects super-critical densities, and the dominant scalelength for shell disruption is thought to be the shell thickness (≤10 micron). Consequently, there is a requirement for a diagnostic which detects structure on a scale less than 10 micron in the super-critical plasma. Optical probing in transmission is limited to low density because of refraction, and X-ray imaging has difficulty providing the required resolution. An alternative diagnostic is optical reflectometry. A short pulse, short wavelength probe beam is directed onto the target. It is reflected from its critical surface, and the target imaged to find the area at which reflection occurs. The probe critical surface acts as a mirror. If the mirror is smooth the spherical probe light will only be reflected into the imaging optics from a small area determined by specular reflection, and the image will show a small spot of reflected probe light on the target. If the mirror is distorted as a result of asymmetry, probe light will be reflected into the imaging optics from widely-spaced parts of the target giving a disordered appearance to the image.

The feasibility of this technique was investigated in the last two days of a transmission probing experiment (Bassett & Willi, see section A2.2) using a 2nd harmonic probe, Raman shifted to 622 nm, with 12 driving beams at irradiances around 10^{14} W cm. Carbon targets (low Z) and 1 micron driving beams were used to reduce the collisionality of the plasma and hence inverse bremsstrahlung absorption of the probe beam. The main difficulty was in detecting the reflected probe beam above the self-emission of the target. If the intensity of the probe beam was reduced substantially, reflections were not detected, but with the probe at full intensity clear reflections were seen. On the occasion of the experiment only relatively broad band (100Å) filters were available to reject background self-emission. Use of narrow band filters (10Å) and simple steps taken to increase the probe intensity on target should bring the reflected signal well above the noise level.

Figure A2.10 shows the imaged reflection on one of a total of four successful shots. The reflection is the small soft-edged bright area toward the lower left of the 250 micron diameter target. The size of the bright region (approx. 7 micron across) is close to that expected for reflection from a perfectly spherical mirror, and suggests that departures in the mirror from tangential are at most only a few degrees. Hence the prelimary indications are that this kind of target is highly regular above critical density. The target was solid carbon, and therefore not susceptible to the Rayleigh-Taylor instability. It would be interesting to apply this technique to Rayleigh-Taylor unstable shell targets.

A2.4 SPACE RESOLVED MEASUREMENTS OF ABLATION UNIFORMITY

D Brown, E R Wooding, P Norreys (Royal Holloway and Bedford New College), A J Cole, M H Key (RAL)

A2.4.1 Introduction

We have previously developed an X-ray pinhole camera combined with a multilayer X-ray mirror to produce monochromatic images[A2.15]. The images produced had good spatial resolution (≤ 20 μm), high brightness and greatly improved contrast between the X-ray emitter (in this case Au M-band) and the background emission from the plastic. Combining the monochromatic X-ray pinhole camera with an X-ray streak camera, allows a direct observation of the spatial uniformity in the burn through to a buried marker layer as a function of time. If this is combined with a timing fiducial, either using a second target or by a UV fiducial, the spatial uniformity of the mass ablation rate, and therefore the ablation pressure, can be measured as a function of irradiance, focussing conditions and incident laser wavelength.

A2.4.2 Diagnostics

Both high power laser systems available at RAL, SPRITE and VULCAN, were used to provide intense laser radiation at 0.249 μm and 0.53 μm

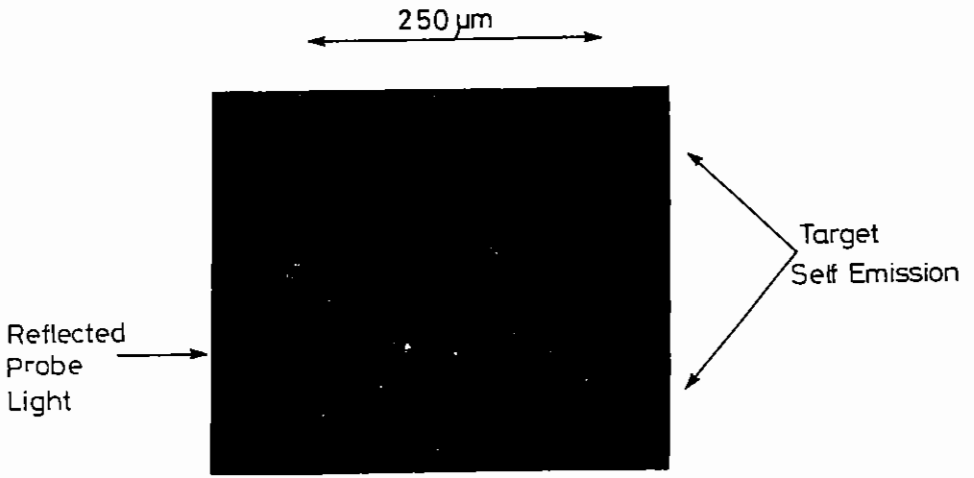

Fig A2.10 Target image showing reflected probe light and target self-emission.

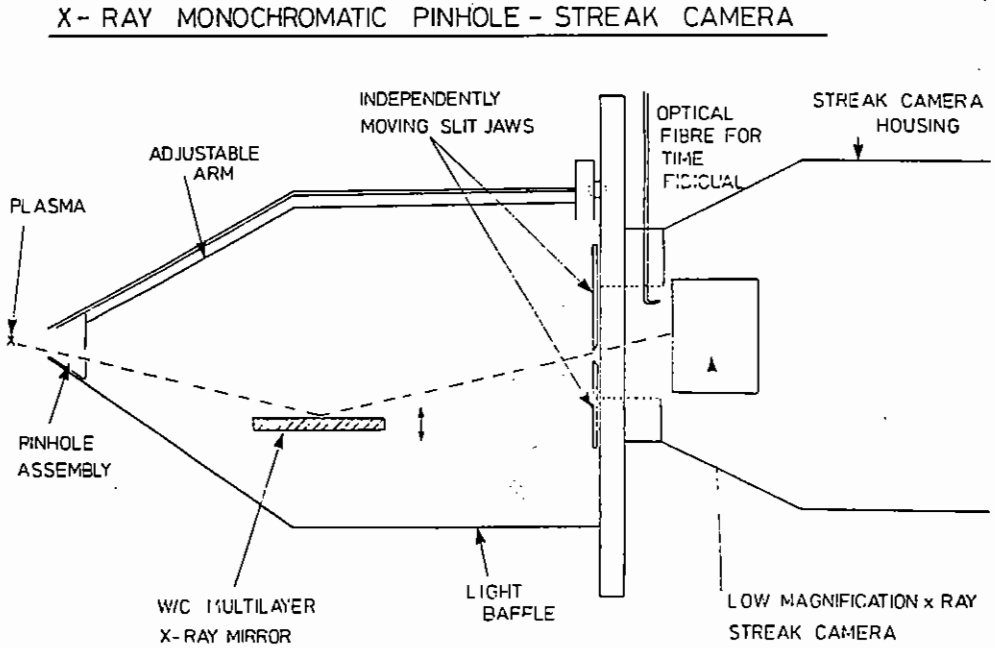

Fig A2.11 A time-resolving, monochromatic X-ray imaging device.

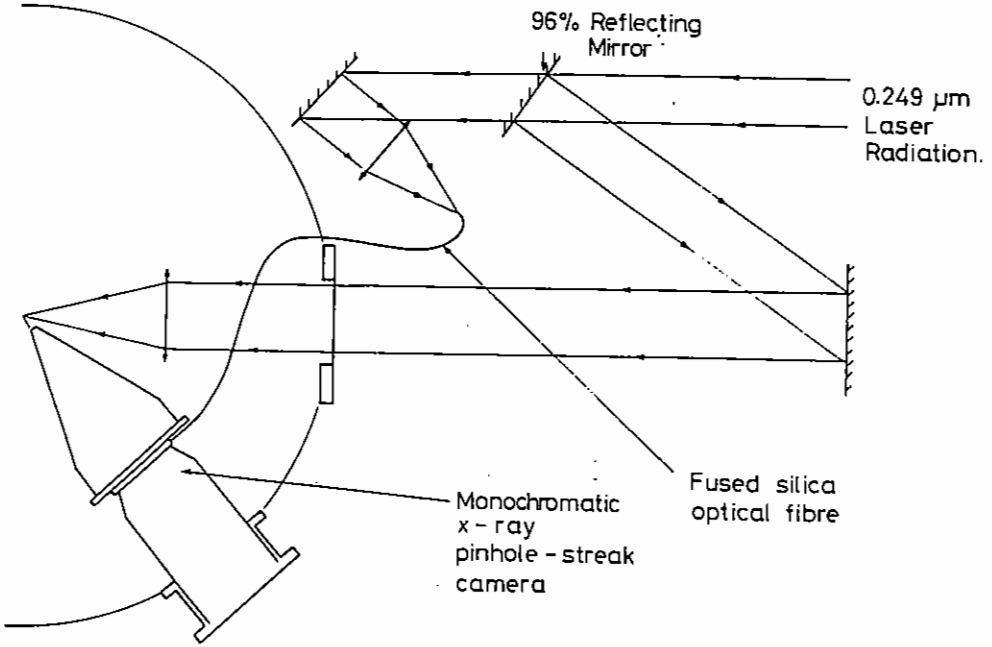

Fig A2.12 Experimental arrangement in the SPRITE target area.

TARGETS

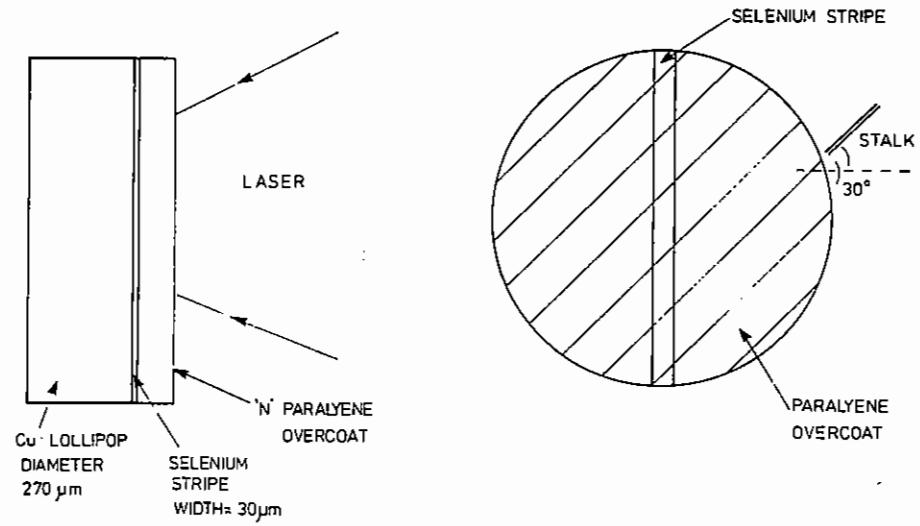

Fig A2.13 Flat lollipop targets used in the SPRITE run.

respectively. The diagnostics in both cases consisted of the monochromatic X-ray pinhole streak camera and an active pinhole camera.

The monochromatic X-ray pinhole streak camera (which is described in detail in Section C5.1 of this report) is shown in Figure A2.11. The mirror used was a W/C multilayered structure of 2d = 43.2Å. The pinholes were 20 μm in diameter and the total magnification of the camera was set at x 15. This gives a spatial resolution of 21.3 μm.

A2.4.3 Experimental Arrangement - SPRITE

The arrangement of the target area is shown in Figure A2.12. An optical fidicual monitor (described in Section C5.2) was set up to mark the beginning of the laser pulse.

The SPRITE laser provided a 15 ns, 30J pulse. This gave an irradiance of 2.5 x 10^{13} Wcm^{-2} for a focal spot of 100 μm. The targets, illustrated in Figure A2.13, consisted of flat copper lollipop targets overcoated with a selenium stripe (width 30 μm) and then with N paralyene. The stripe was used instead of closing the slit jaws on the streak camera. The wavelength was set at 7.8Å to give a monochromatic image in intense SeXXV L shell resonance line emission.

A2.4.4 Experimental Results - SPRITE

Figure A2.14 shows the first test result with the new system from the SPRITE data. The earliest burn through occurs after 2.5 nsec and the latest after 5nsec indicating spatial non-uniformity in the mass ablation rate with a 3:1 range from 3.0x10^5 to 1x10^5 $gcm^{-2}sec^{-1}$. Further analysis of the data is continuing.

A2.4.5 Experimental Arrangement - VULCAN TAW

Figure A2.15 illustrates the arrangement of the diagnostics in the TAW chamber. A secondary target without ablater layer was used to provide a timing fiducial. The main targets were solid plastic

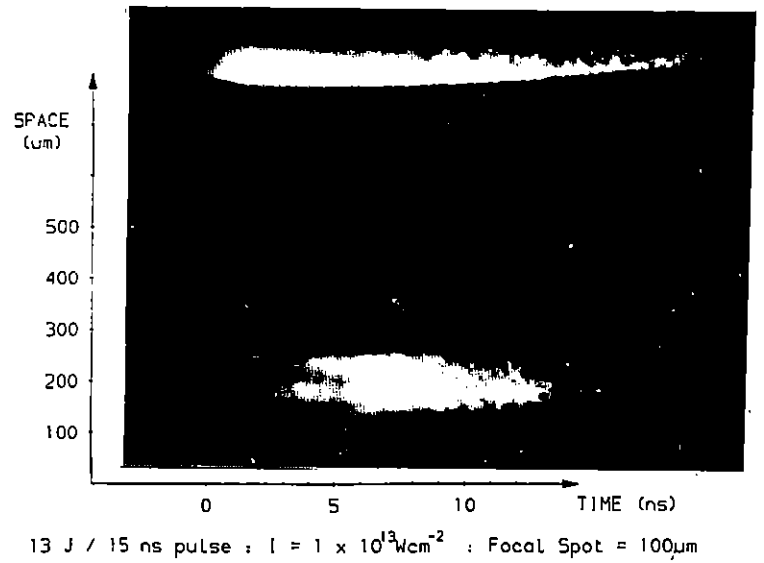

Fig A2.14 Typical data from targets irradiated at 0.249μm. The absorbed irradiance was 1x10¹³ Wcm⁻² and the plastic ablator thickness was 5.5μm.

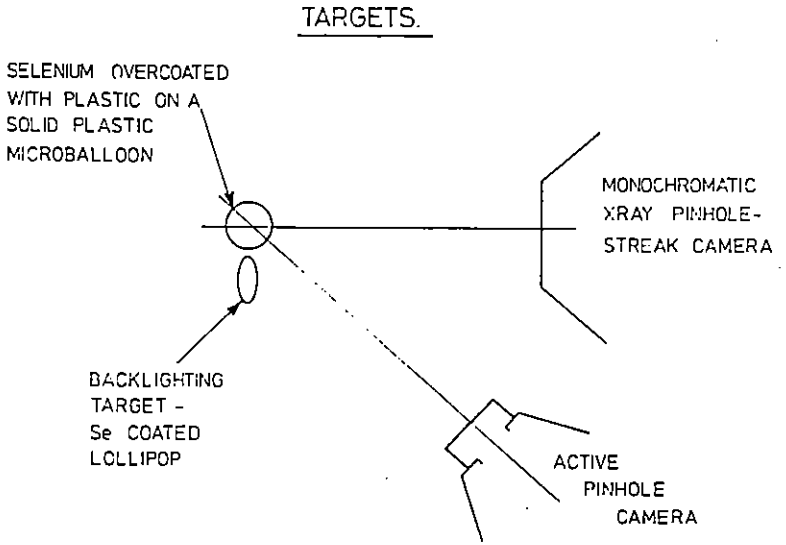

Fig A2.15 The arrangement of diagnostics in the TAW chamber.

microballoons, of diameter 300 μm, overcoated on one side with selenium and then with N paralyene of thickness 1 μm. The pulse length was 800 psec and the incident irradiance was between 1 and 2 x 10^{14} Wcm^{-2}. The X-ray wavelength was set at 7.8Å as before and the streak speed was 107 ps/mm on the film.

A2.4.6 Experimental results - VULCAN

The uniformity of the mass ablation rate due to beam overlapping on spherical target has been of considerable interest in implosion experiments[A2.16]. By systematically varying the focussing parameter D/R (D is the distance from the centre of the balloon to the focus and R is the radius of the balloon), the non-uniformities due to beam overlap can be varied and observed.

Figures A2.16, A2.17 and A2.18 show space and time resolved images of the burn through to the selenium layer.

It is seen that the non-uniformity diminishes rapidly with D/R in the range of 5 to 20. Each result was found to be reproducable. Figure A2.19 shows a diagram of the maximum and minimum mass ablation rate plotted against D/R.

Smaller targets (of diameter 150 μm) were irradiated with fixed D/R = 10 and variable irradiance. When the mass ablation rate $\dot{m}$ is plotted against the absorbed irradiance I_a, the scaling of $\dot{m}$ was found to be similar to previous results deduced from time resolved X-ray spectroscopy[A2.17]. When the larger targets were irradiated, there was a greater range between maxima and minima (see Figure A2.20) and the minima fell below spectroscopic data. The average mass ablation rates for large targets is about 30% lower than the X-ray results suggesting that the 30% difference between ion emission data and time resolved X-ray spectroscopy was due to beam overlap non-uniformities.

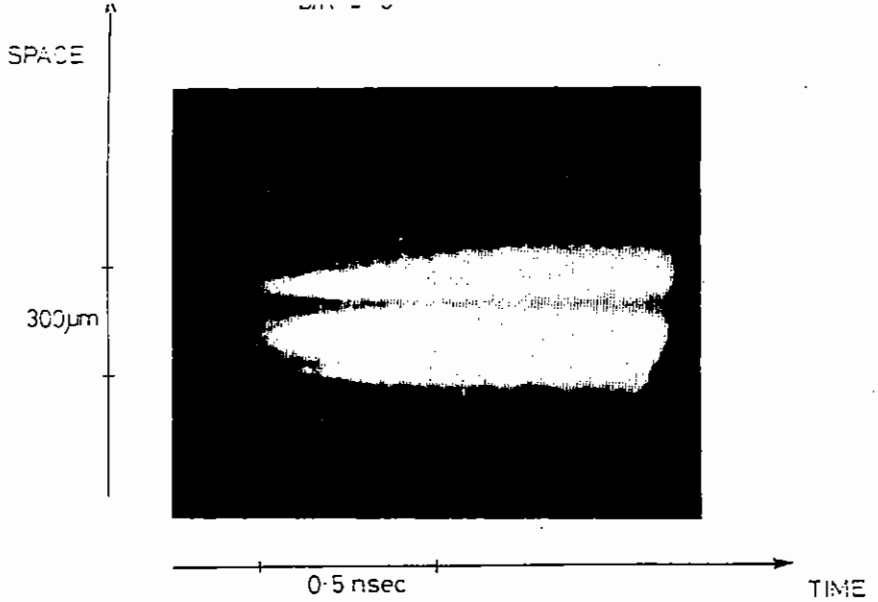

Fig A2.16 Space and time resolved image of ablation uniformity for D/R = 5.

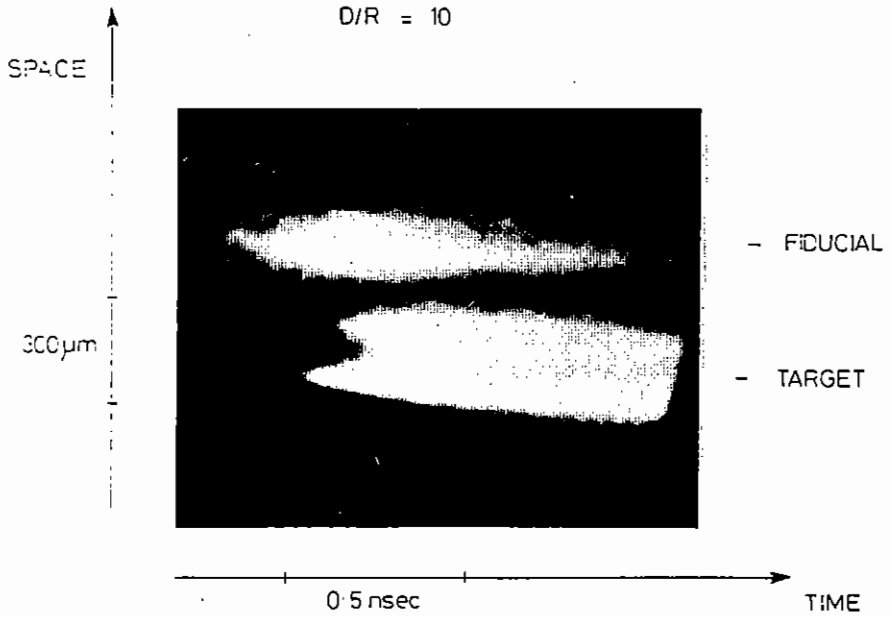

Fig A2.17 Space and time resolved image of ablation uniformity for D/R = 10.

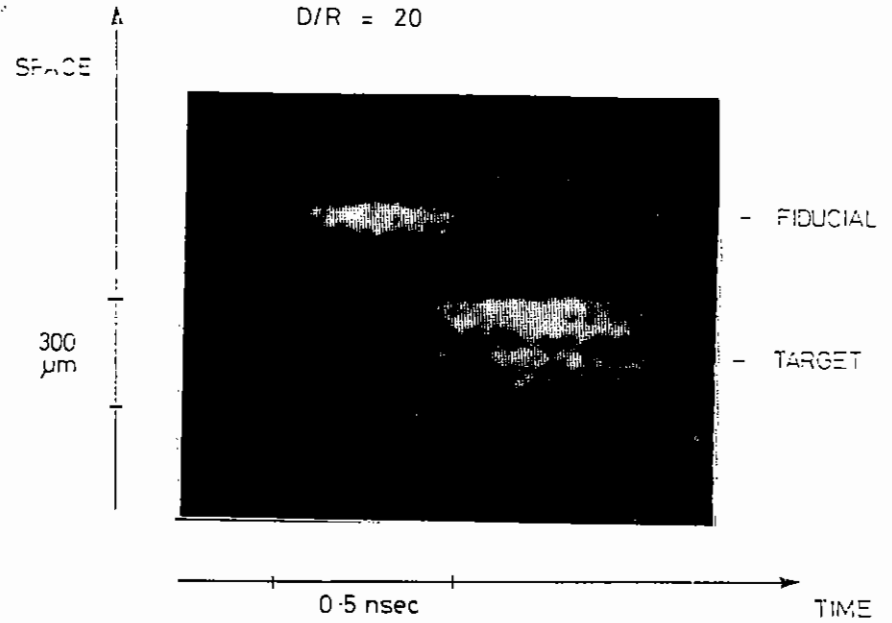

Fig A2.18 Space and time resolved image of ablation uniformity for D/R = 20.

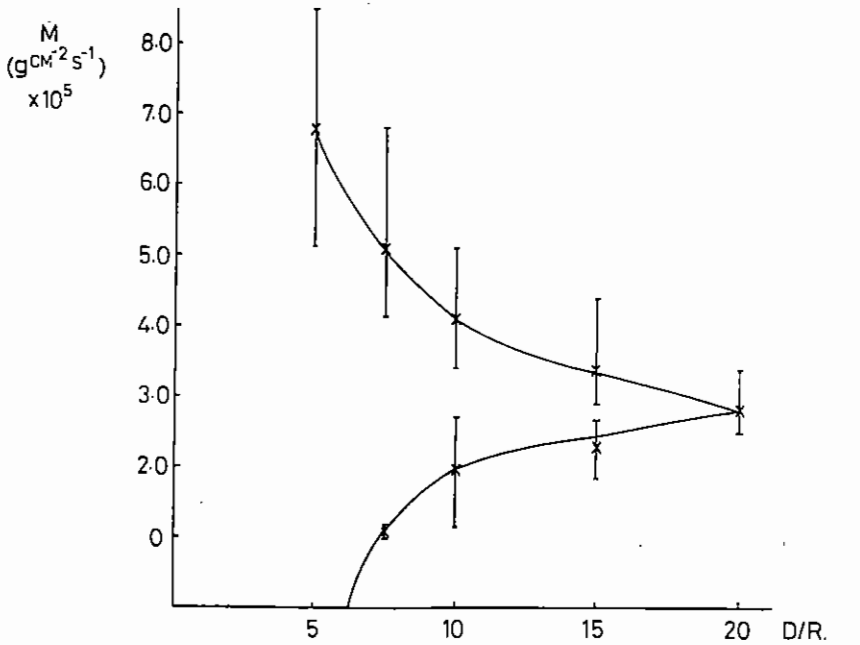

Fig A2.19 Maximum and minimum mass ablation rates plotted against D/R.

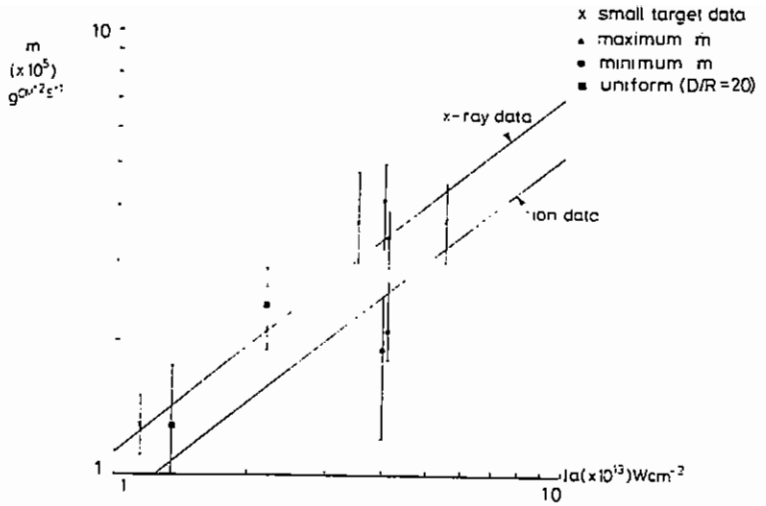

Fig A2.20 *Mass ablation rate $\dot{M}$ is plotted against absorbed irradiance I_a. The ion and X-ray lines are from ref (A2.17).*

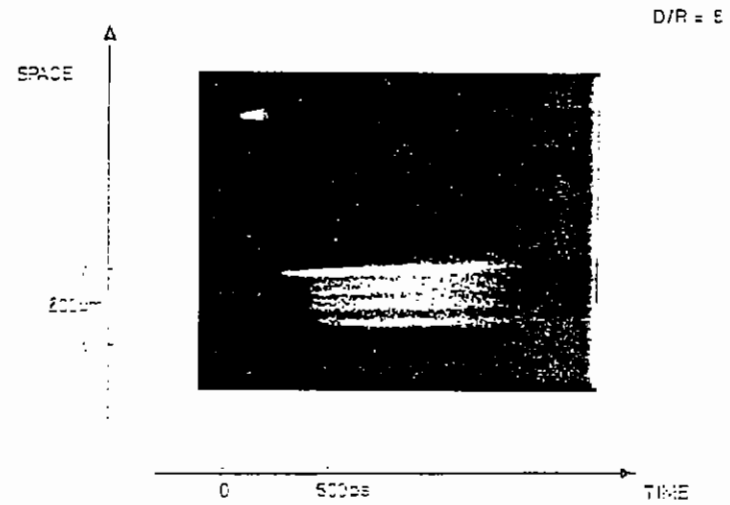

Fig A2.21 *Space and time resolved image for D/R = 8 irradiation conditions at higher irradiance (~1.10¹⁴ Wcm⁻²). The fudicial marker was produced with a fibre-optically coupled 4th harmonic pulse.*

A2.4.7 Conclusion

The error bars in Figures A2.19 and A2.20 can be reduced by employing a UV optical fiducial and by using thicker plastic overcoats. Increasing the magnification allows the diameter of the balloons to be reduced and the range of the absorbed irradiance increased. These improvements have been implemented in the most recent experiment in TAW, and an example of the better quality new data is shown in Figure A2.21.

A2.5 INTERACTION STUDIES IN LONG SCALE LENGTH PLASMAS

D Bassett, N Islava and O Willi (Imperial College)

A Giulietti (Pisa)

A2.5.1 Stimulated Raman Scattering, Two Plasmon Decay, Stimulated Brillouin Scattering and Laser Beam Filamentation

Preliminary experiments have been carried out to investigate various instabilities in large, hot, dense, preformed plasmas. The understanding of these processes in laser produced plasmas is crucial due to the detrimental effects of fast electron production and generation of non-uniformities. These instabilities are strongly dependent on the density scale length and consequently become more important in large millimetre sized plasmas.

(a) Stimulated Raman Scattering and Two Plasmon Decay

A large homogeneous plasma 1 mm in length and about 200 μm in width was produced using the line focus arrangement. Two pairs of two opposing green laser beams were focussed onto a thin foil target by the off axis lens-mirror configuration. The size of the line focus was 1 mm by 200 μm. All four laser beams were superimposed to give an irradiance of 1×10^{14} W cm^{-2} in a 70 ps pulse. The targets consisted of a 1000Å thick formvar substrate overcoated with either an Al stripe 200 μm in width and 350 nm in thickness or an Au stripe 200 μm in width and 50 nm in thickness.

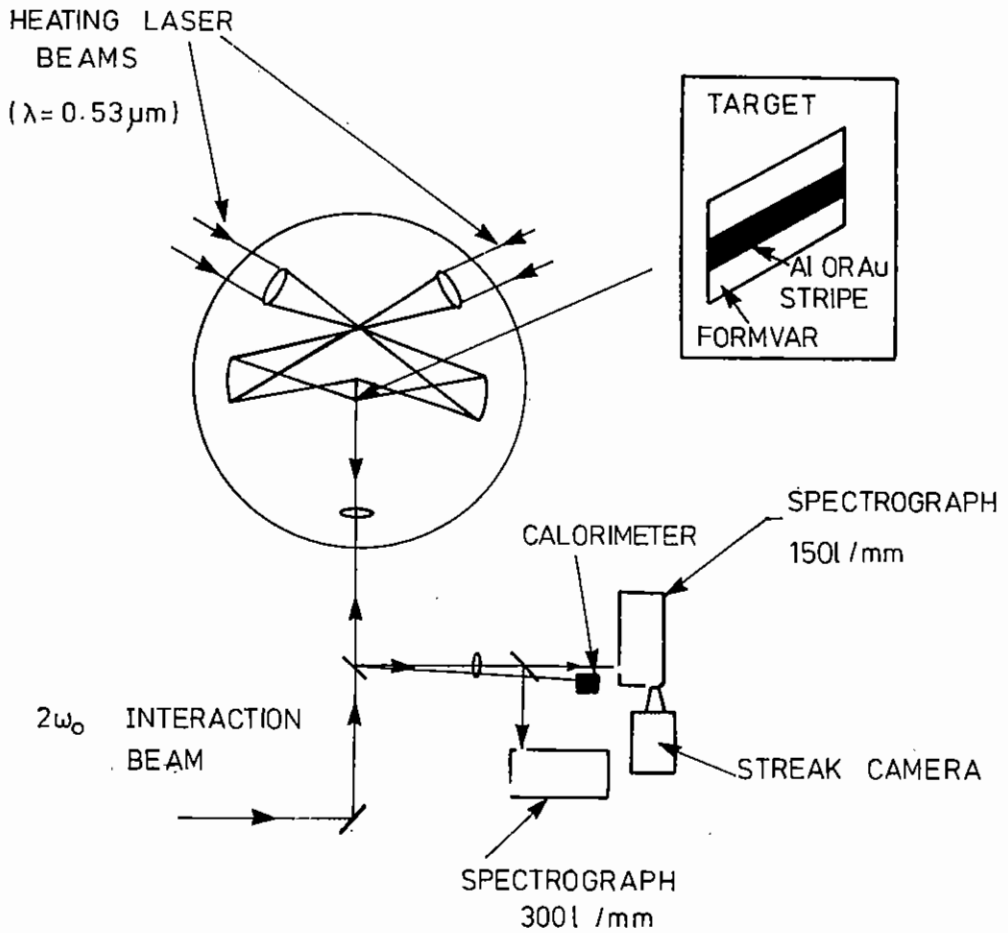

Fig A2.22 Schematic of experimental arrangement for SRS and TPD observations.

A green high power interaction beam was focussed axially into the preformed plasma with an f/2.5 lens. The pulse length was about 800 ps. The Raman signal scattered back from the plasma was collected by the focussing lens and imaged onto the slit of two spectrographs. The output of one of the spectrographs was coupled to an S20 streak camera. The experimental arrangement is shown in Fig A2.22.

The density and temperature of the preformed plasma was changed by varying the time separation of the heating laser beams forming the plasma and the interaction beam.

Fig A2.23 shows a series of microdensitometer traces of several time integrated stimulated Raman Scattering (SRS) spectra obtained on Au targets. The time delay of the interaction beam relative to the heating beams was varied between 2.2 and 4.2 ns. The intensity of the interaction beam was about 8×10^{14} W cm. As can be seen in Fig A2.23 when the separation between the heating and interaction pulse was increased the Raman signal was emitted in a narrower spectral band. The fall-off of the emission at shorter wavelength, was however, similar in all the cases.

When the separation of the two pulses was reduced to 1.2 ns (i.e., in this case the density of the plasma is higher when the interaction beam interacts with the plasma). 3/2 and 1/2 W_0 harmonic emission were observed instead of the SRS signal indicating the presence of the two plasmon decay (TPD). A microdensitometer trace is shown in Fig A2.24.

In addition to the time integrated data, time resolved SRS spectra were recorded. Fig A2.25 shows a spectrum taken on an Aℓ target. The irradiance of the interaction beam was 7×10^{14} Wcm^{-2}. The separation of two pulses was 3.2 ns. As can be seen the SRS signal is emitted in a narrow band which shifts to the blue later in the laser pulse when the plasma expands.

(b) Stimulated Brillouin Scattering

Backscattered Stimulated Brillouin Scattering (SBS) was investigated under similar experimental conditions as SRS and TPD. Again time integrated and time resolved spectra were recorded.

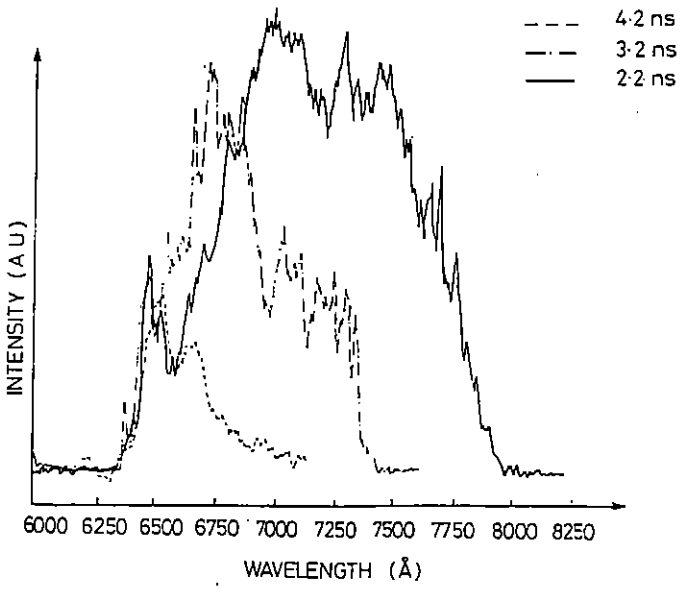

Fig A2.23 Microdensitometer traces of time integrated Raman spectra.

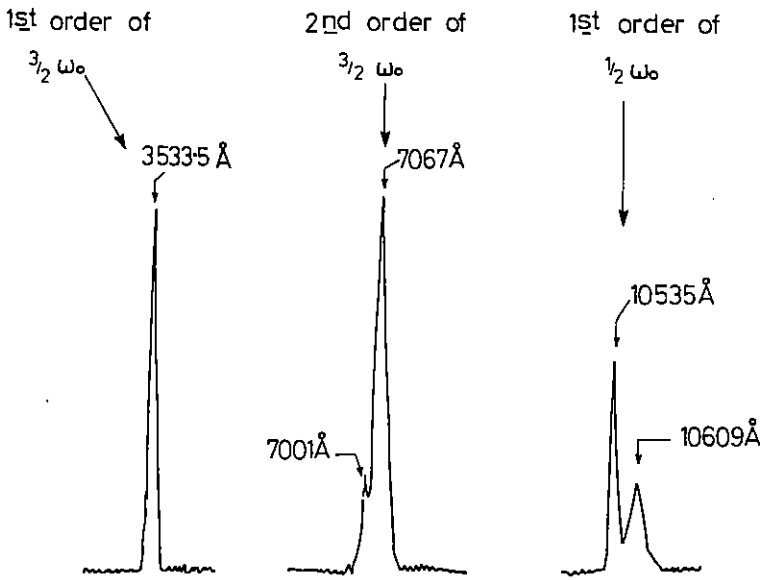

Fig A2.24 Traces of 3/2 and 1/2 W_0 harmonic emission.

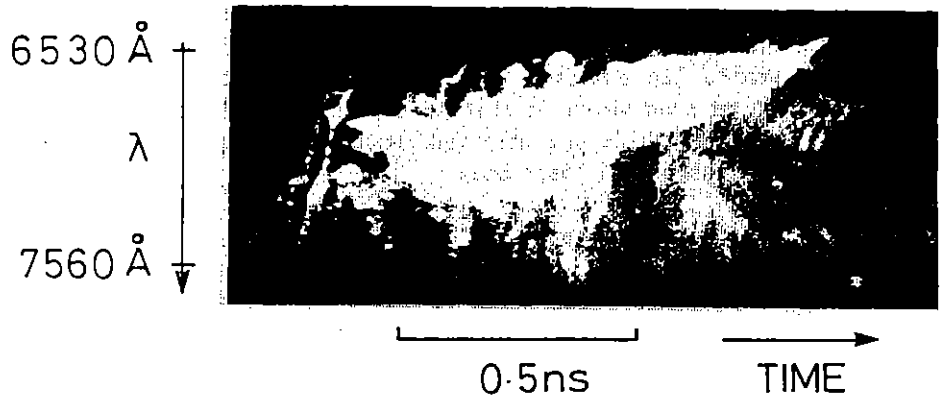

Fig A2.25 Streak record showing SRS spectrum.

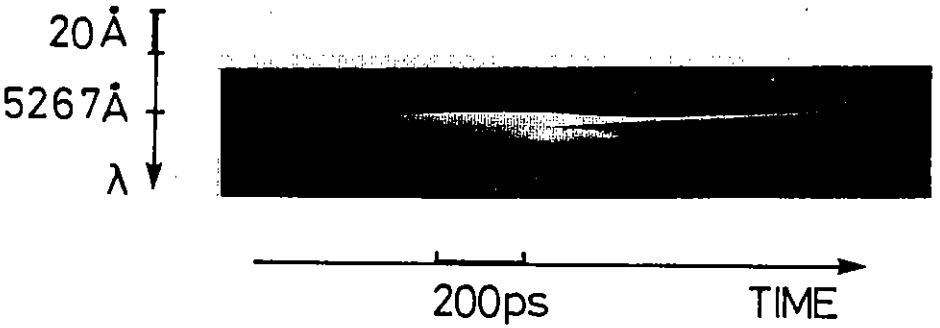

Fig A2.26 Streak record showing SBS spectrum.

Fig A2.26 shows a streak record of a SBS spectrum which was taken on an Al target. The separation of the heating and interaction pulse was 3.2 ns. The irradiance of the interaction beam was 3×10^{14} Wcm^{-2}. In addition to a reference line at 5267Å, the SBS spectrum can be seen which is shifted to the red. Short bursts with a longer spectral shift are observed which may originate from high intensity regions of the laser beam.

(c) Laser beam filamentation

Simultaneously to SBS, laser beam filamentation has been studied in large plasmas. Transverse to the plasma column, interferograms were recorded by using an optical probe beam (λ = 0.62 µm, duration ∿15 ps).

Fig A2.27 shows an interferogram taken at the peak of the interaction beam. The interaction pulse was delayed by 2.8 ns in respect to the heating pulse.

A small channel can be seen in the background plasma indicating that the whole laser beam was self-focussed. A detailed analysis is presently in progress.

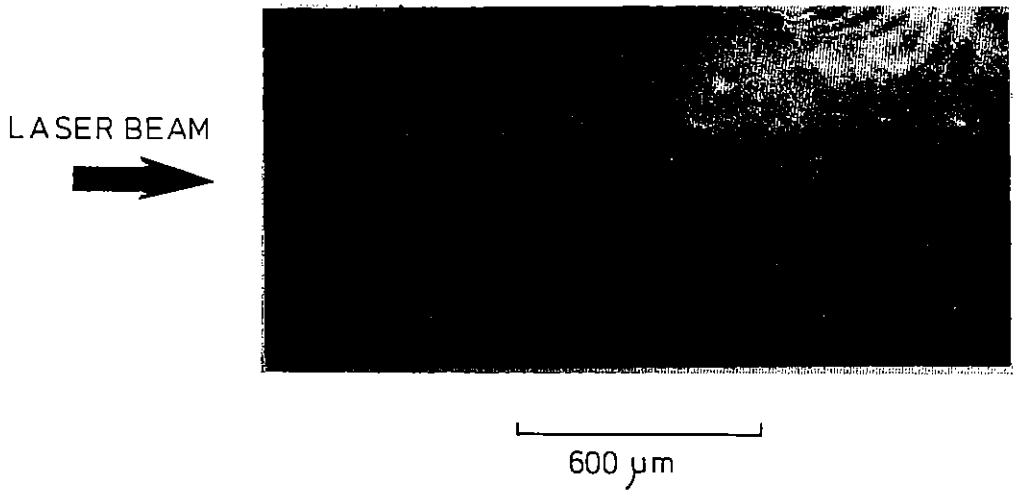

Fig A2.27 Interferogram showing a small channel which indicates whole beam self-focussing.

A2.5.2 The Rayleigh-Bénard Instability in Laser Produced Plasmas

D Bassett, O Willi (Imperial College) G Pert (Hull University),
R G Evans (RAL)

The ability to generate large aspect ratio plasmas (length >> height) has come about as a consequence of recent interest in the production of X-ray lasers. With this in mind an insight into the fluid dynamics of associated schemes becomes essential, especially when the target design prevents an expected cylindrical expansion of the regions where lasing may occur. This has proved the case for thin foil targets as will be explained, due to the interaction of the expanding stripe with the Formvar substrate. However, it is this region which proves interesting with respect to large scalelength instabilities.

The experiment primarily concerned itself with the irradiation of Aluminium stripes of a size 25μm x 173nm which were coated onto a substrate of 1000Å thick Formvar. The line focus arrangement in TAE operating with four symmetric beams exploded these stripes with energies of up to 40J in 70ps at 0.53μ along a length of 1.5mm.

The main diagnostic was the multiframe probe, previously described. Five low power 15ps pulses of wavelengths 622nm, separated in time recorded the plasma state both by interferometry and taking Schlieren photographs. The probe was directed across the axis of the stripe, a further two frames were directed axially to give some indication of the lateral expansion.

The results which ensued were not, however, as expected. The axial images did not show the cylindrical expansion which was predicted but rather implied that the plasma was forming a cold plasma above and below the heated aluminium. The predominantly carbon plasma travels faster since the velocity is inversely proportional to mass/area. The aluminium, now constricted pushes out becoming underdense to the 622nm probe within 150ps. However, what is interesting is the interaction region between the aluminium and plastic, which is viewed by the probe system. The inner material although of a lower density still remains hot, and is accelerating into the surrounding dense fluid. Such a system is possibly Rayleigh-Bènard instable, provided $-|\nabla T| > |\nabla \rho|$, see Figure A2.28.

A typical sequence of results can be seen in fig (A2.29). The first image, taken with a 500μm Schlieren stop appears 2.43ns after the target was illuminated with an intensity of 3×10^{14} Wcm^{-2}. The central underdense region appears reasonably turbulent with perhaps some background order which is only visible by comparison with the other three images. 110ps later a greater amount of uniformity is achieved until at 2.69ps the appearance of six square cells becomes obvious. The double image in the final two photographs is on account of the Nomarski type interferometry attempted in these frames. Consequently the images are just shadowgrams. The final frame, another 275ps later and the 50μm square cells are fully formed.

The ordering of the dense and underdense materials into such shapes can only be via some convective instability, since free flow should just encourage greater irregularity. The appearance of these large scale cells is also typical of a Rayleigh-Bènard type instability. However, conclusive proof would rely on an accurate temperature measurement across the active region combined with some method of measuring any vorticity if it occured within each cell.

It is hoped that future work will answer some of the questions and perhaps solve the driving mechanisms.

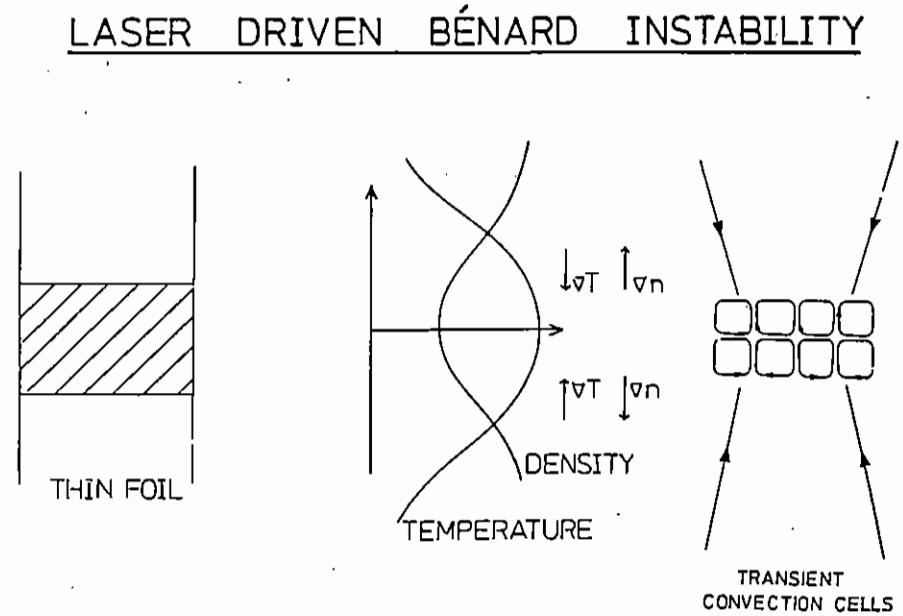

Fig A2.28 Schematic diagram of a Rayleigh-Bénard unstable system.

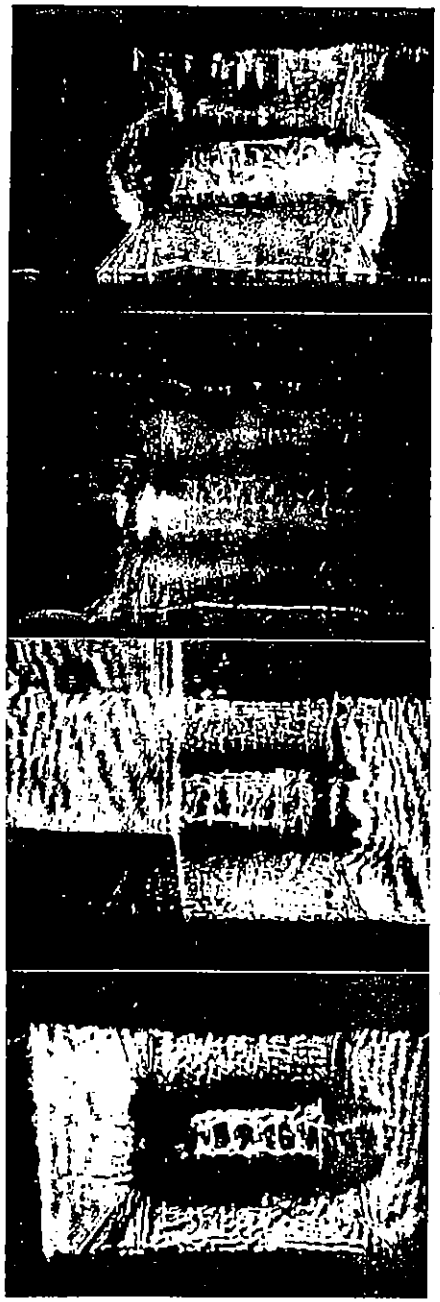

Fig A2.29 Optical shadowgrams showing the development of a possible convective instability.

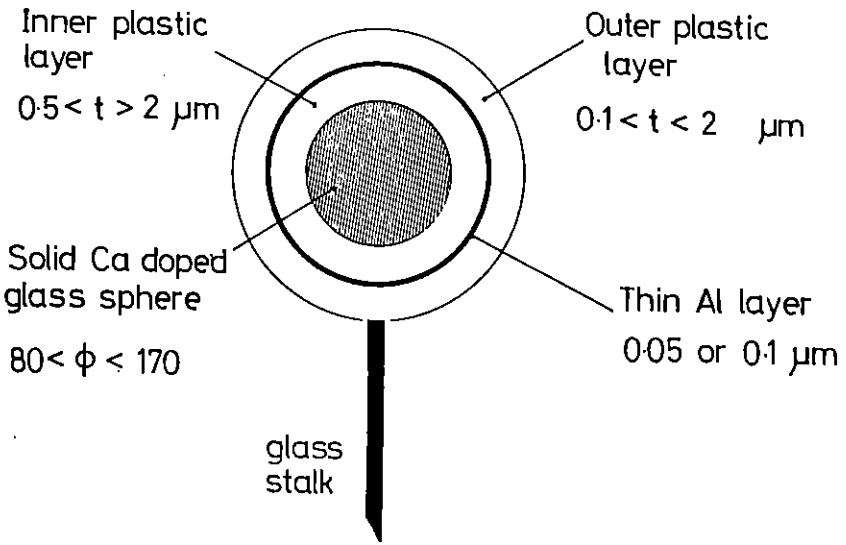

Fig A2.30 Typical target design for mass ablation rate measurements.

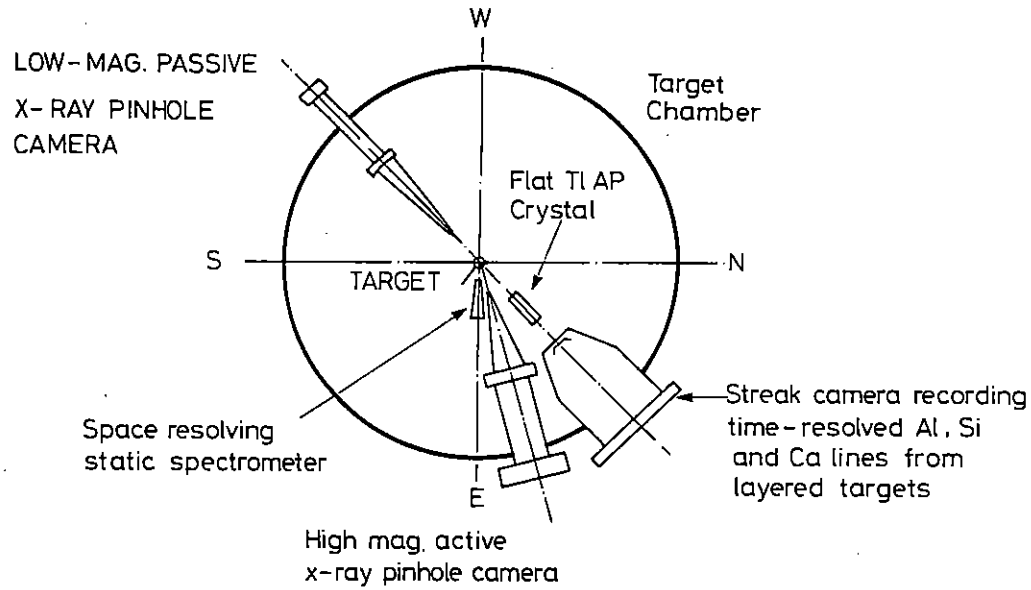

Fig A2.31 Schematic of experimental arrangement.

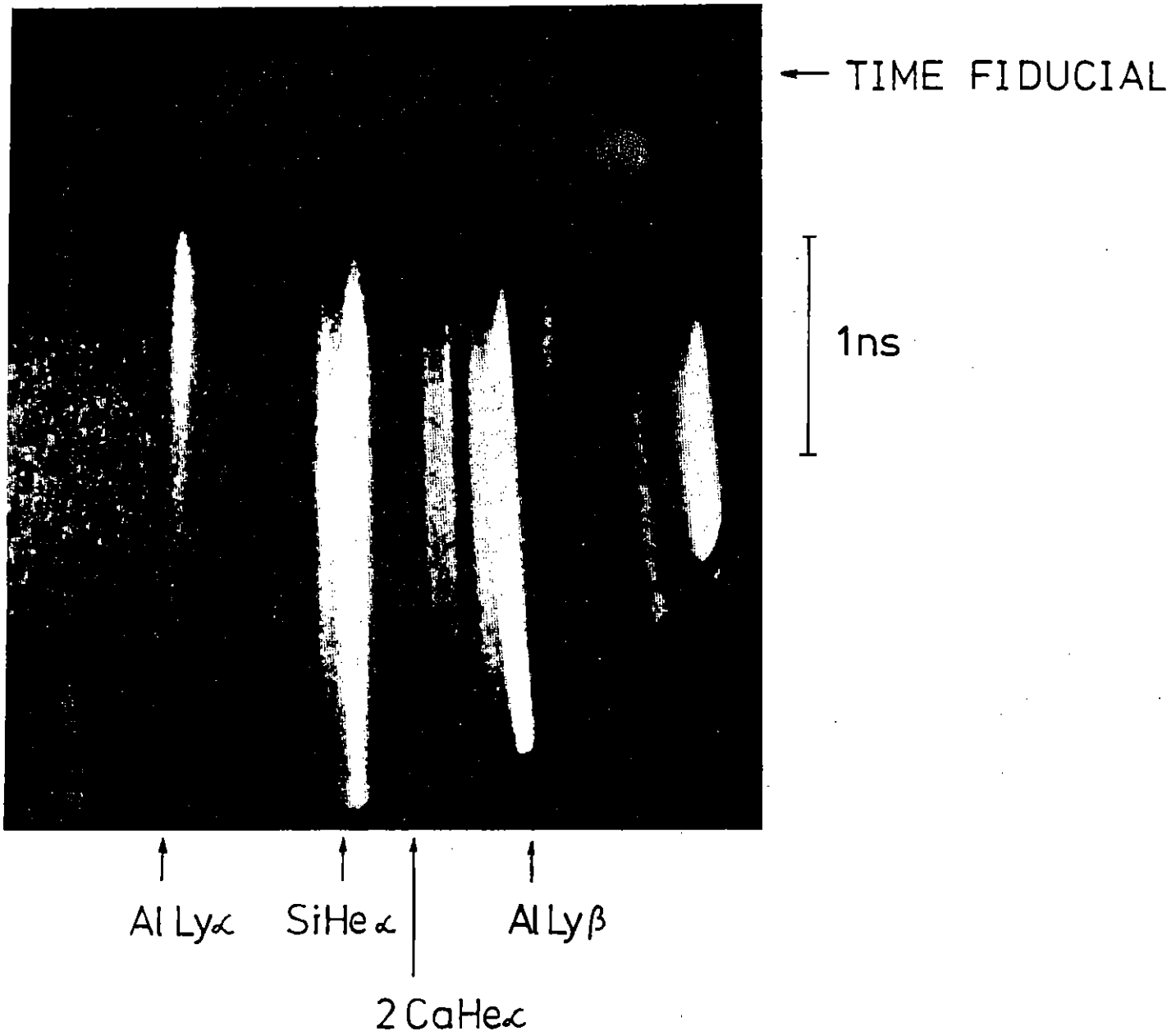

Fig A2.32 Streak record taken on a multilayered target giving the burn-through time.

A2.6 MASS ABLATION RATE MEASUREMENTS

S D Tabatabaei, O Willi (Imperial College)
C Chanais-Popovics (Palaiseau France)
P Apte (RAL)

In laser produced plasmas, the laser energy is absorbed below and up to critical density. In laser fusion targets, this energy must be transported beyond the absorption layer via electron thermal conduction towards colder, higher density regions of the target to heat up material and cause ablation which, in turn generates an inward pressure to compress the fusion fuel. If the thermal transport is inhibited, the consequences will be a weaker ablation and therefore, a weaker implosion. Detailed investigations have been carried out to measure the mass ablation rate on spherical targets which are uniformly illuminated with 12 green laser beams. The laser beams were focussed onto the target with f/2.5 lenses. The laser pulse had an approximately gaussian temporal profile with 0.8ns full width at half maximum. Targets used consisted of solid silicon spheres (80 to 150 μm in diameter) doped with calcium and overcoated with various layers of CH_2 (0.5 to 2μm), Aℓ (0.05 to 0.1μm) and CH_2 (0.1 to 2μm) (see Fig A2.30).

The primary diagnostic was a time resolved crystal spectrograph where a TLAP crystal was coupled to an X-ray streak camera. In addition, X-ray pinhole cameras, calorimeters, X-ray diodes and a time integrated X-ray crystal spectrograph were used.

A schematic of the experimental arrangement is shown in Fig A2.31. A separate laser beam with a short duration (100ps) was used to produce an X-ray time fiducial which references the X-ray spectra to the temporal profile of the incident laser pulse.

Fig A2.32 shows a streak record taken on target which had the following layers (diameter ∿155μm, CH_2 in 0.8μm, Aℓ = 0.05μm, CH_2 out = 1.3μm) and was irradiated at an intensity of 2 x 10^{14} Wcm^{-2}. X-ray transitions from the the Aℓ layer and glass core can clearly be seen. The time delay between these transitions can readily be obtained and is plotted in Fig A2.33. Zero corresponds to the peak of the incident laser pulse. The time separation between the Si Lyα and Ca He_α is small indicating that the heat front is steep.

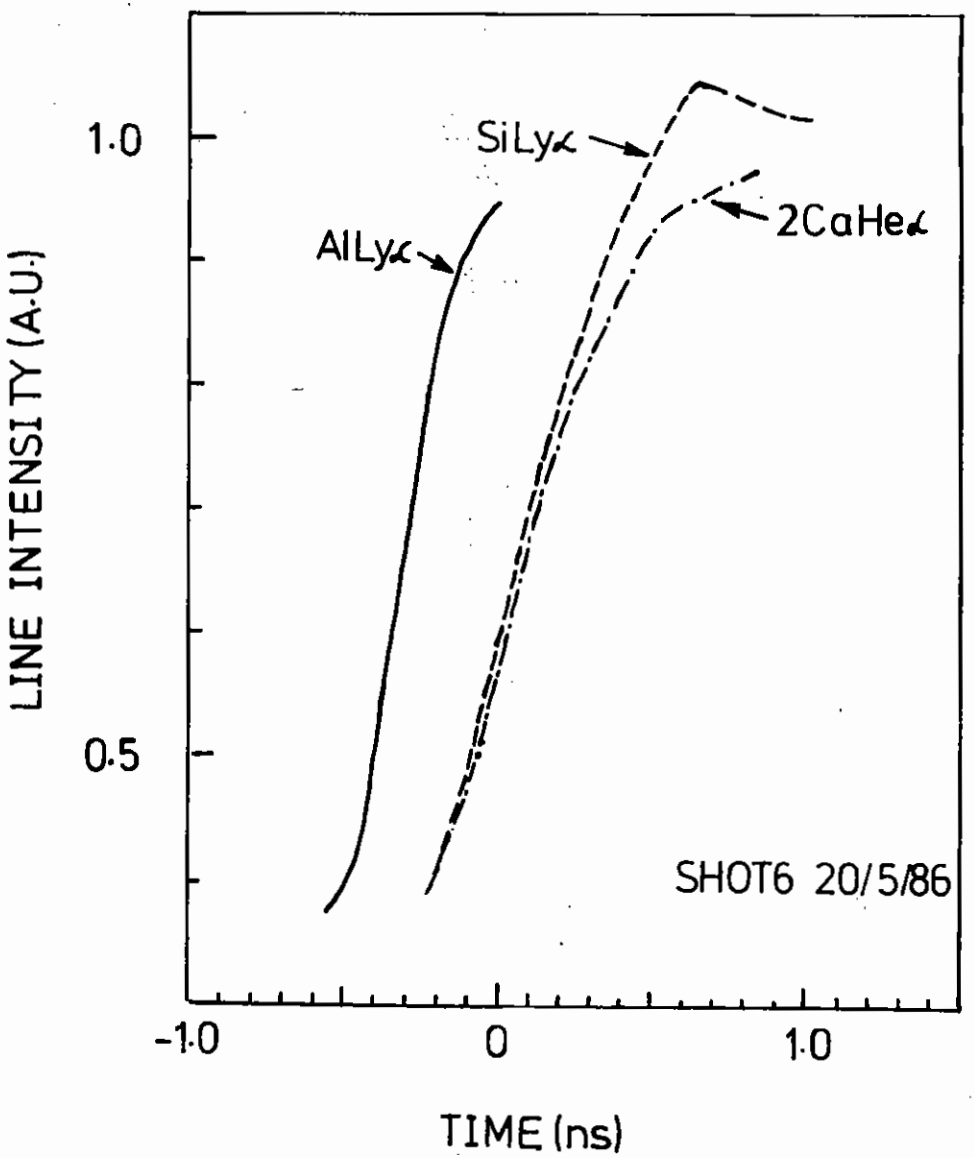

Fig A2.33 Microdensitometer traces showing the time delay between the Aℓ and Si transitions.

From a series of similar shots at various irradiances the mass ablation rate as a function of irradiance has been obtained. This is plotted as a function of absorbed irradiance in Fig A2.34, together with measurements taken on a previous experiment where similar targets were irradiated with six infrared laser beams.

A2.7 SHORT PULSE TRANSPORT STUDIES

S D Tabatabaei, D Riley, O Willi (Imperial College)
C Chanais-Popovics (Palaiseau France)

A series of experiments have been carried out where thermal transport was investigated using laser pulses which have a fast rise time and a short pulse duration. This avoids an interference of the hydrodynamic effects on thermal transport. In addition, the heat front scale length can be measured since the electron mean free path is larger than the layer thickness of the targets.

Targets used were solid glass balloons overcoated with layers of KCℓ (0.1μm) or CH_2 (0.1 to 0.3μm), Aℓ (0.05μm) and an outer layer of CH_2 (0.1 to 0.5μm). The targets were uniformity irradiated with 12 green (λ=0.53μm) laser beams. The pulse duration was 70 ps. A separate synchronised laser pulse was used to generate a short X-ray pulse for an absolute time fiducial by irradiating a saran target. The primary diagnostics was a time resolved X-ray crystal spectrograph. A flat TLAP crystal was coupled to an X-ray streak camera. The temporal and spectural resolution was 20ps and 100mÅ respectively.

Fig A2.35 shows a streak record taken on a target which was irradiated at an intensity of 3×10^{14} Wcm^{-2}. The target diameter was 150μm overcoated with layers of KCℓ (0.1μm), Aℓ (0.05μm) and CH_2 (0.2μm).

No potassium, Chlorine nor Silicon transitions are seen. The turn-on of H-like transitions of aluminium is delayed by about 35ps relative to the turn-on of the He-like transitions. When the laser irradiance was increased to about 9×10^{14} Wcm^{-2}, a fast turn-on of Aℓ, K, CL and Si transitions is observed. A streak record taken on a similar target as in Fig A2.35 is shown in Fig A2.36. Again the H-like lines of aluminium are delayed by about 35ps in respect to the He-like transitions. K He_α is delayed by about 50 ps relative to Aℓ He_α. This data is presently being analysed.

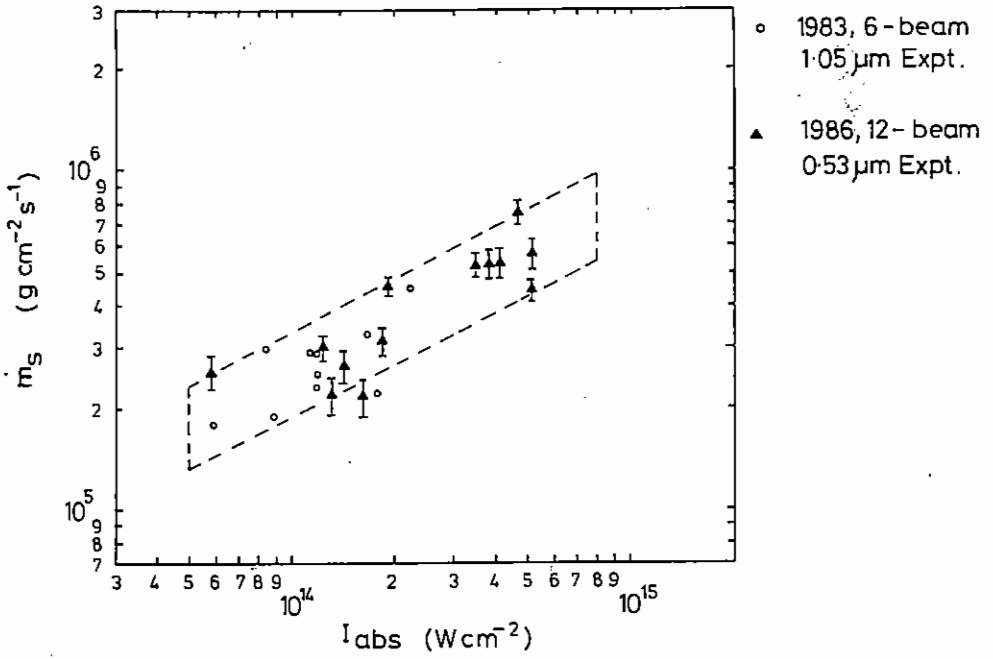

Fig A2.34 Measured mass ablation rates recorded on spherical targets which were irradiated with green laser light.

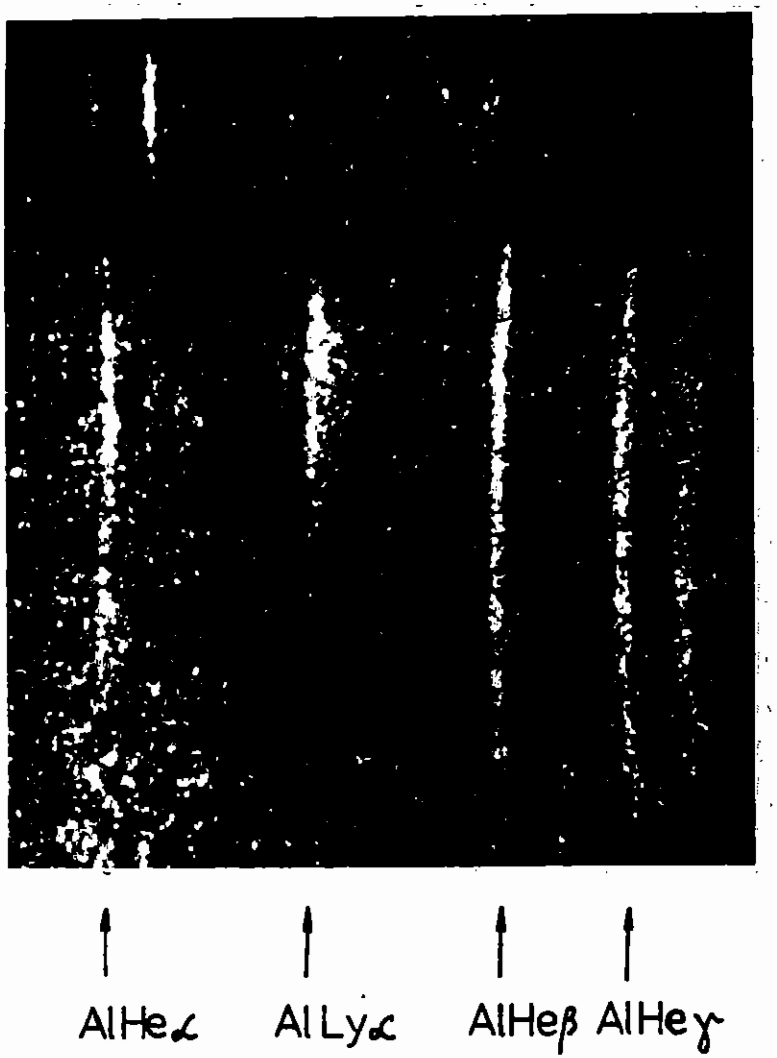

Fig A2.35 *Streak record taken on a uniformly irradiated multilayered spherical target showing no potassium, Chlorine nor Silicon lines.*

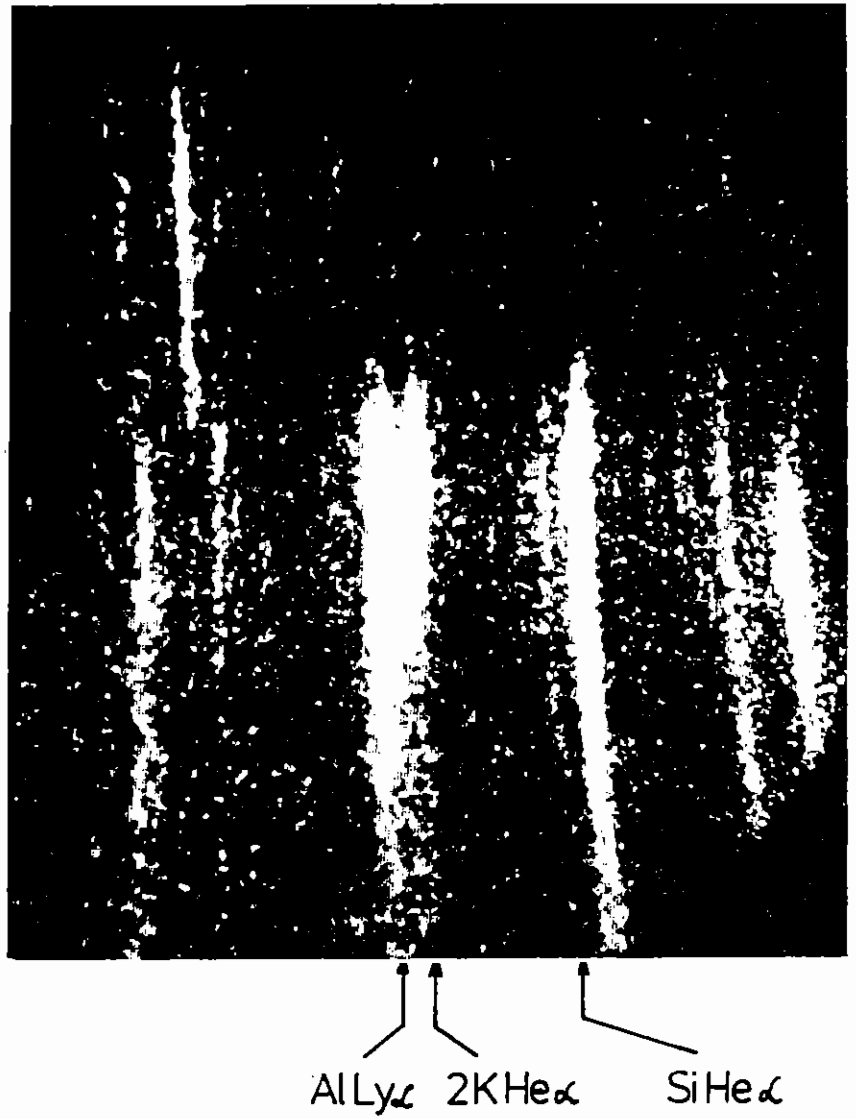

Fig A2.36 *Streak record taken on multilayered targets showing burn-through to the glass core.*

A2.8 DENSITY AND TEMPERATURE MEASUREMENTS

D Riley, D Tabatabaei, O Willi (Imperial College)
C Chenais-Popovics (Ecole Polytechnique Palaiseau France)
A Hauer (Los Alamos)
P Apte, A Cole and S Rose (RAL)

It is vital for a detailed understanding of electron thermal transport in laser produced plasmas to measure, in addition to the mass ablation rates, the density and temperature profiles in the region between the absorption and ablation layers. Using time resolved spectroscopy, these parameters were measured on spherical targets under similar conditions as the observations described in A2.6.

Targets consisted of solid plastic spheres (~150 μm in diameter) with an Aℓ tracer dot (75μm in diameter, 0.1 μm in thickness) which was buried below an overcoating of CH_2 (0.2 to 2.0μm). The solid balls prevented the target from imploding. The targets were illuminated uniformly with 12 green laser beams (λ=0.53μm). Again as in the mass ablation rate measurements, the pulse length was 0.8 ns (FWHM).

Extensive diagnostics were used to study the plasma corona. Time resolved streak profiles of Aℓ $H_e\gamma$ were recorded using a novel experimental arrangement where a toroidally focussing PET crystal was coupled to an X-ray streak camera. A schematic is shown in Fig A2.37. The spectral and temporal resolution was about 2 mÅ and 50ps, respectively. These observations resulted in density measurements. The temperature was obtained from time resolved line ratio measurements. X-ray line emission from the Aℓ tracer dot was dispersed by a TLAP crystal onto the slit of a second X-ray streak camera. The spatial movement of the tracer dot was observed with a space resolving X-ray crystal spectrograph. In addition, X-ray pinhole cameras, plasma calorimeters and XRD's were used. Again as described in A2.6 a separate laser beam was used to generate a time fiducial.

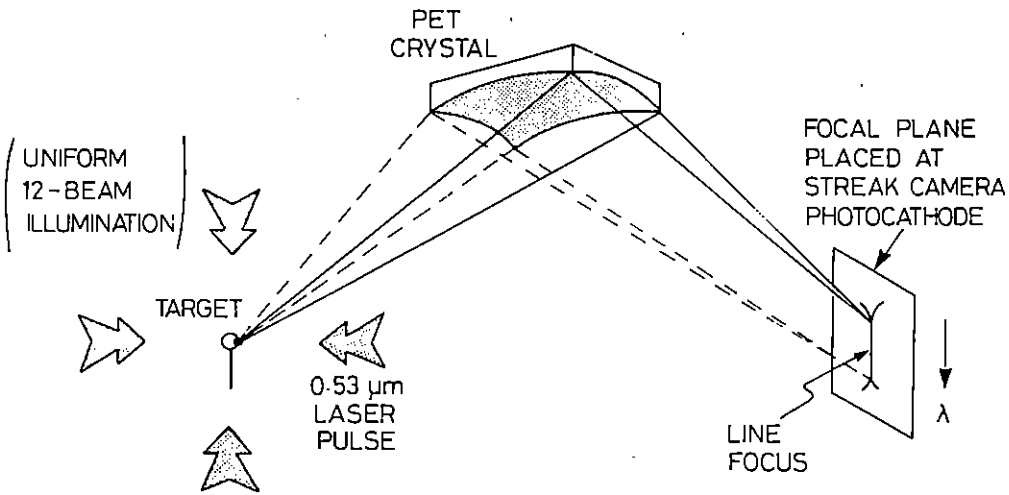

Fig A2.37 Schematic of the time resolved X-ray spectrograph using a toriodally focussing PET crystal.

Fig A2.38 X-ray pinhole camera image.

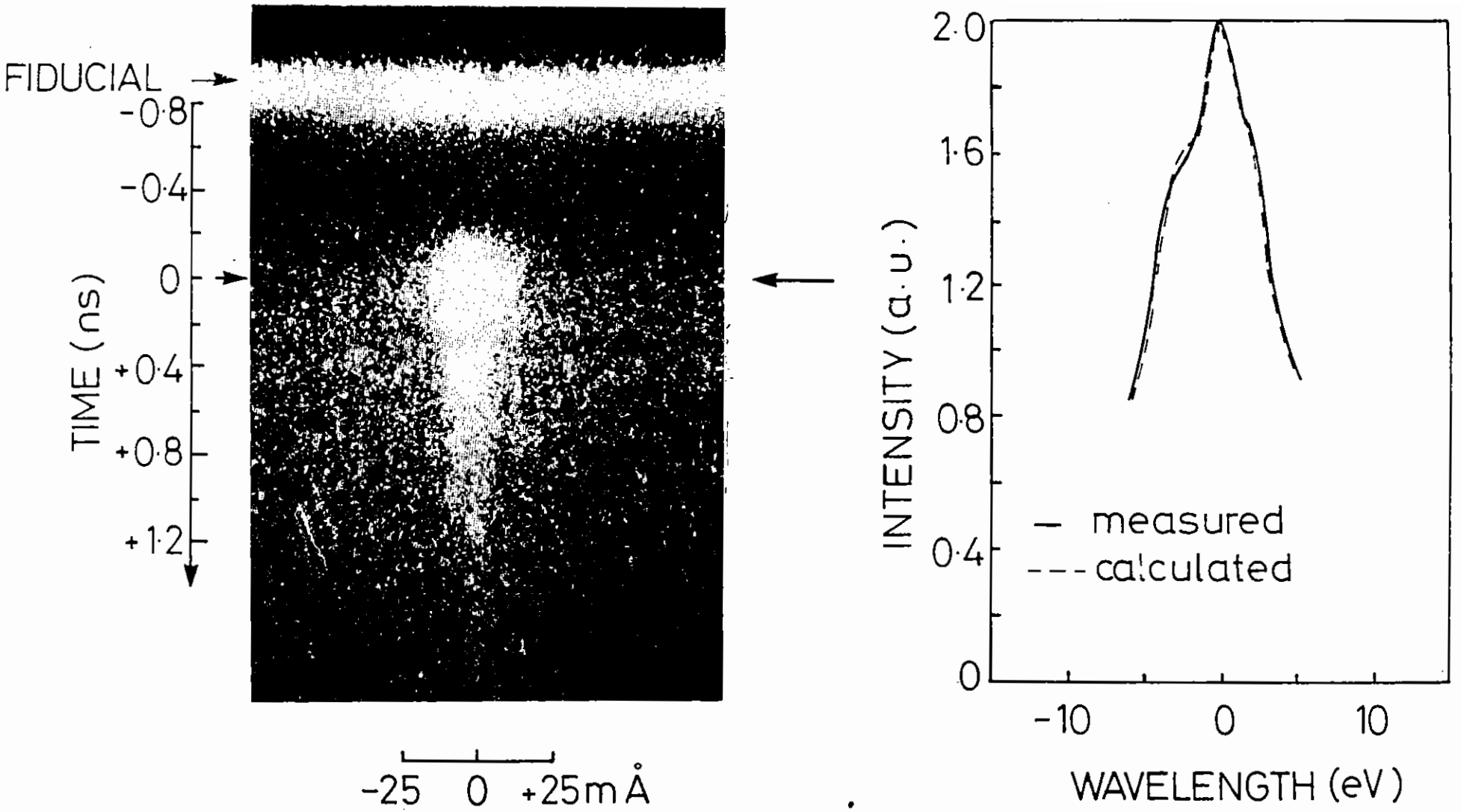

Fig A2.39 *Stark profile of Al He_γ recorded on a spherical target which was irradiated with 12 green laser beams. Also plotted is the measured profile at the peak of the laser pulse and is fitted with the codes RATION and SPECTRA.*

SHOT 7 28/5/86

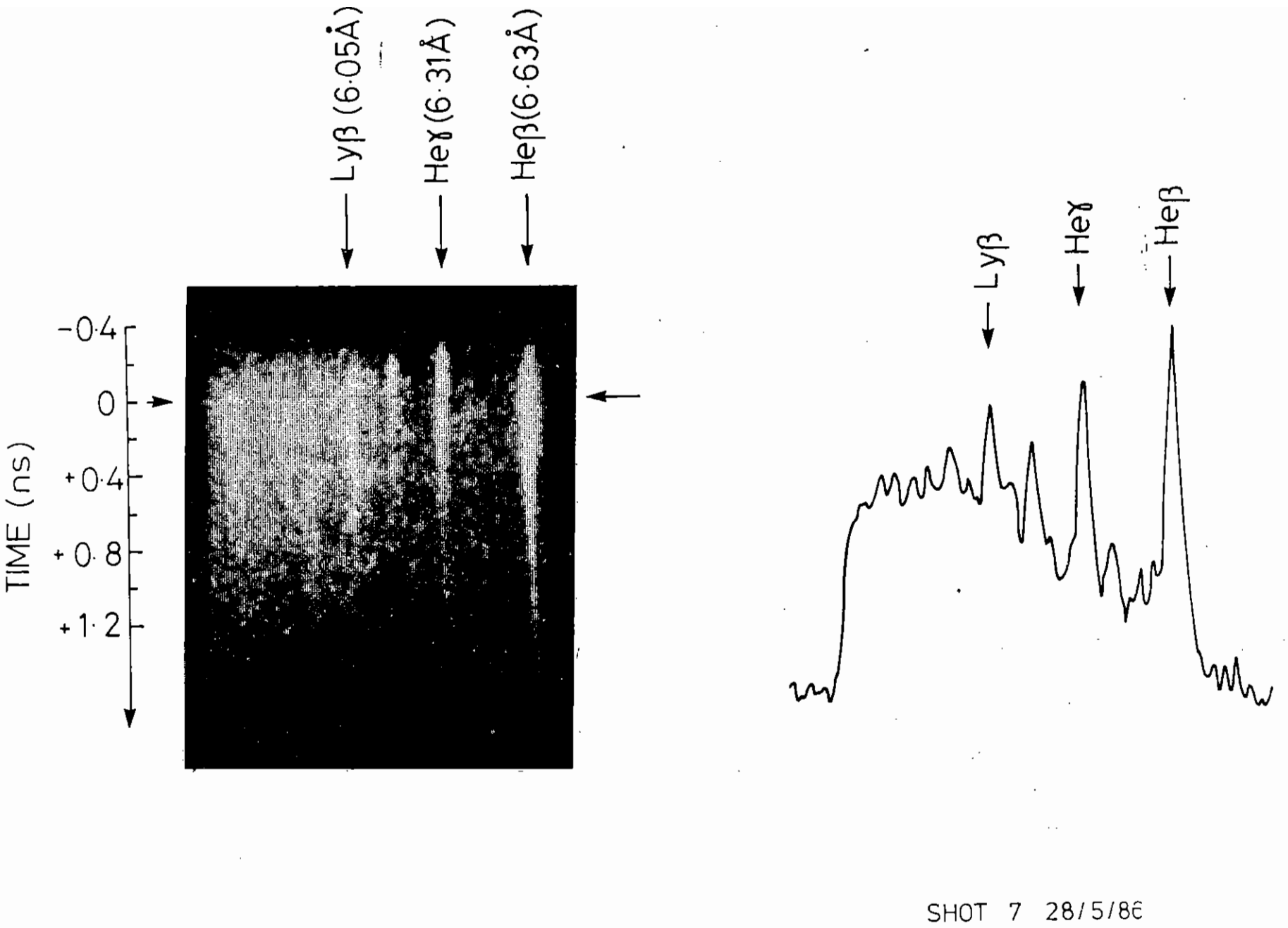

Fig A2.40 Streak record for line ratio measurements.

Fig A2.38 shows a typical X-ray pinhole camera image. The dot emission superimposed on the plastic emission can clearly be observed.

A stark profile of Aℓ $H_e\gamma$ recorded on a target with a 0.84μm outer plastic layer which was irradiated at an intensity of 3×10^{14} Wcm^{-2} is shown in Fig A2.39. The absorbed laser energy was about 59%. Also shown in Fig A2.39 a microdensitometer trace plotted at the peak of the incident laser pulse. The measured profile is fitted with code predictions (RATION and SPECTRA). The best fit is obtained for a density of 4×10^{21} cm^{-3}. The measured stark width of 40mÅ dominates instrumental, source, Doppler and opacity broadening of about 2mÅ. The density evolution versus time is presently being analysed.

Simultaneously to the stark profiles, a line emission spectrum was recorded. Fig A2.40 shows a streak record obtained on the same target as described above. A microdensitometer trace is also given in Fig A2.40. From the line ratio of H/He like transition the temperature can be obtained. The experimental spectrum is fitted with SPECTRA resulting in temperature profiles. This work is presently in progress.

Fig A2.41 shows the spatial emission of AℓHe_γ as obtained by the time integrated spectrograph. The spectrograph was located at 90° to the expanding dot. The peak emission occurs about 25μm from the initial target surface.

These observations are presently being compared to theoretical modelling.

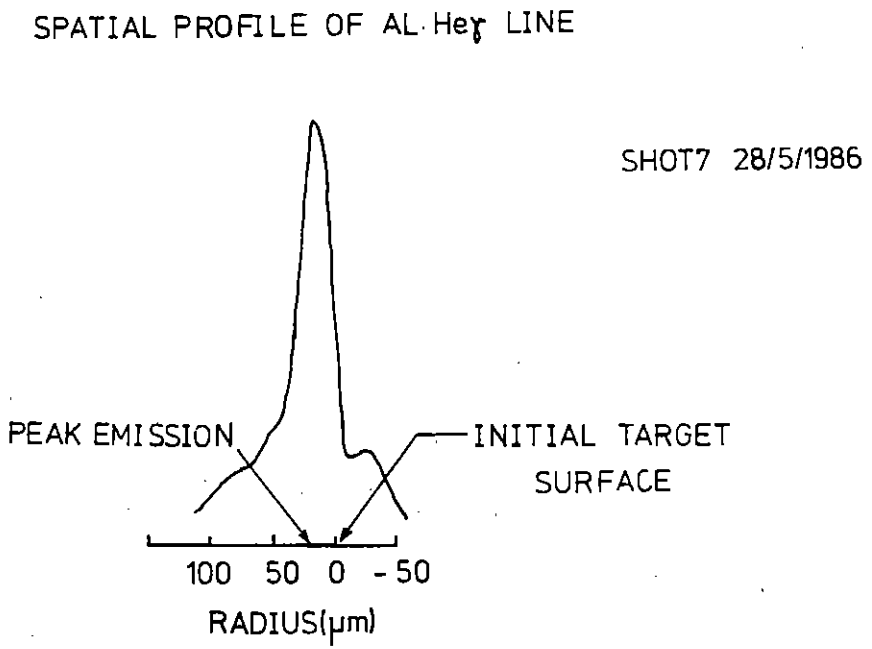

Fig A2.41 Spatial profile of AℓHe_γ transitions.

References:

A2.1 Lawson J D
Rutherford Appleton Laboratory Report
RAL-83-057 (1983)

A2.2 Bingham R, Mori W, Dawson J M
'Laser Acceleration of Particles' (Malibu 1985)
AIP Conference Proceedings No 130, p 138

A2.3 Clayton C E, Joshi C, Darrow C, Umstadter D,
Phys Rev Lett 54, 21, 2343 (1985)

A2.4 Ebrahim N A, Martin F, Brodeur P, Heighway E A, Matte J P,
Pepin H, Lavigne P
Proceedings 1986 Linear Accelerator Conf Stanford Ca

A2.5 Grey Morgan C,
Rep Prog Physics 38, 621 (1975)

A2.6 Chin S L, Lambropoulos P ed
'Multiphoton Ionisation of Atoms'
Academic Press 1984

A2.7 Dewhurst R J, Pert G J, Ramsden S A,
J Phys B (Atom Molec Phys) 7, 2281 (1974)

A2.8 Krasyuk P N, Pashinin P P, Prokhorov A M
Soviet Physics JETP 31, 860, (1970)

A2.9 Voronov G S, Delone G A, Delone N B, Kudrevatova O V
Soviet Physics JETP Lett 2, 8, 237 (1965)

A2.10 Pert G J
Journal of Physics A 5, 506 (1972)

A2.11 Rand S
Phys Rev B136, 231 (1964)

A2.12 Bell A R, Evans R G, Nicholas D J,
Phys Rev Lett 46, 243, (1981)

A2.13 Lompre L A, L'Huillier A, Mainfray G, Manus C,
Journal Opt Soc America B 2, 12, 1906 (1985)

A2.14 Kruit P, Kimman J, Muller H G, van der Wiel M J,
Phys Rev A 28, 1, 248 (1983)

A2.15 Ann Rep LFC. RAL 86-046, C.5.4 (a). (1986)
Opt Comm. 1987 (in press)

A2.16 L L E Review. DOE/DP40200-38.
Oct-Dec, 1, 1986

A2.17 Goldsack T J, et al.
Opt. Comm. 42, (1) 55 (1982)

Editor: A Ridgeley

A3.1 ION CORRELATION EXPERIMENTS IN HIGH DENSITY PLASMAS

T A Hall, R W Eason, A Djaoni, C Jackson, B Shiwai (Essex University)
S J Rose, A J Cole and P Apte (RAL)

Experiment

The preliminary experiments carried out last year (A3.1) were continued in order to provide a series of backlighting probe times for a range of target irradiances. The experimental arrangement is essentially the same as the previous year except that greater care was taken to set the spectrograph angle so that the backlighter-target-spectrograph axis corresponded to about 10eV above the aluminium K-edge. This ensured that all the X-ray wavelengths of interest passed through a shocked region of target.

In addition to the main diagnostic a pinhole camera observed the backlighting emission and the active pinhole camera observed the main target X-ray emission. The backlighting targets were 200μm diameter uranium spheres; these could be illuminated by 1,2,3 or 4, 100 psec green beams of the VULCAN laser to produce the short X-ray pulse. The pinhole camera photos of the X-ray emission from the backlighting targets showed some structure with multibeam illumination. This was assumed to be the result of pointing errors. The X-ray emission profile of the main target was, however, much more uniform over most of the 500 μm focal spot.

The crystal spectrograph was the same (TlAP) as for the previous experiment and attempts to coat the beryllium window with 10-15 μm of silicon was unsuccessful. Consequently the second order reflections from the TlAP remained a problem. As before, the second order was measured by filtering out the first order over part of the entrance aperture with 150 μm beryllium foil. Greater care was taken over wavelength calibration by using a thin silicon K edge filter. An aluminium emission spectrum was also recorded alongside the EXAFS spectrum by taking a second shot on each exposure of an aluminium target placed a few millimetres from the original backlighter target position.

We successfully acquired spectra on a total of shots at various irradiances and delay times of the backlighter probe. The most complete set of data was obtained for the irradiance range 4.5×10^{12} to $5.5 \times 10^{12} Wcm^{2}$ on target. Microdensitometer tracings of these spectra are shown in figure A3.1.

Data analysis

Since the aluminium K-edge will move under shock compression, this cannot be used as an absolute wavelength fiduciary. For the EXAFS measurements, however, this is of little consequence since the EXAFS spectrum is always relative to the edge. Nevertheless, an absolute spectral calibration is obtained from the silicon edge filter. Accurate dispersion was obtained from the first order aluminium spectra alongside the EXAFS spectra. The aluminium spectra could not be used as an absolute wavelength calibration since the spectrum's position relies on the precise placing of the aluminium target. Since this needed to be placed a few millimetres away from the original position of the backlighting target it was decided that this technique could not be relied upon. In practice most shots showed a placement accuracy better than expected.

The spectra shown in figure A3.2 were traced using wide slits on the microdensitometer: this reduced the grain noise of the film but did not remove defects in the image which mainly arose from crystal imperfections (TlAP crystals particularly seem to show variations in reflectivity, usually over small well defined areas). We have tried several numerical techniques to remove these marks but we have found that taking multiple densitometer scans and neglecting the regions where the marks exist by visual inspection gives the best results. The second order spectrum is then numerically subtracted from the combined spectrum by an iterative process which takes account of the different film sensitivities of DEF film to the first and second order spectral regions. As a part of this process the absorption coefficient is calculated.

The resulting spectra show usually at least two absorption bands near to the K-edge. As we move further from the edge however the noise introduced by the second order subtraction increases and less

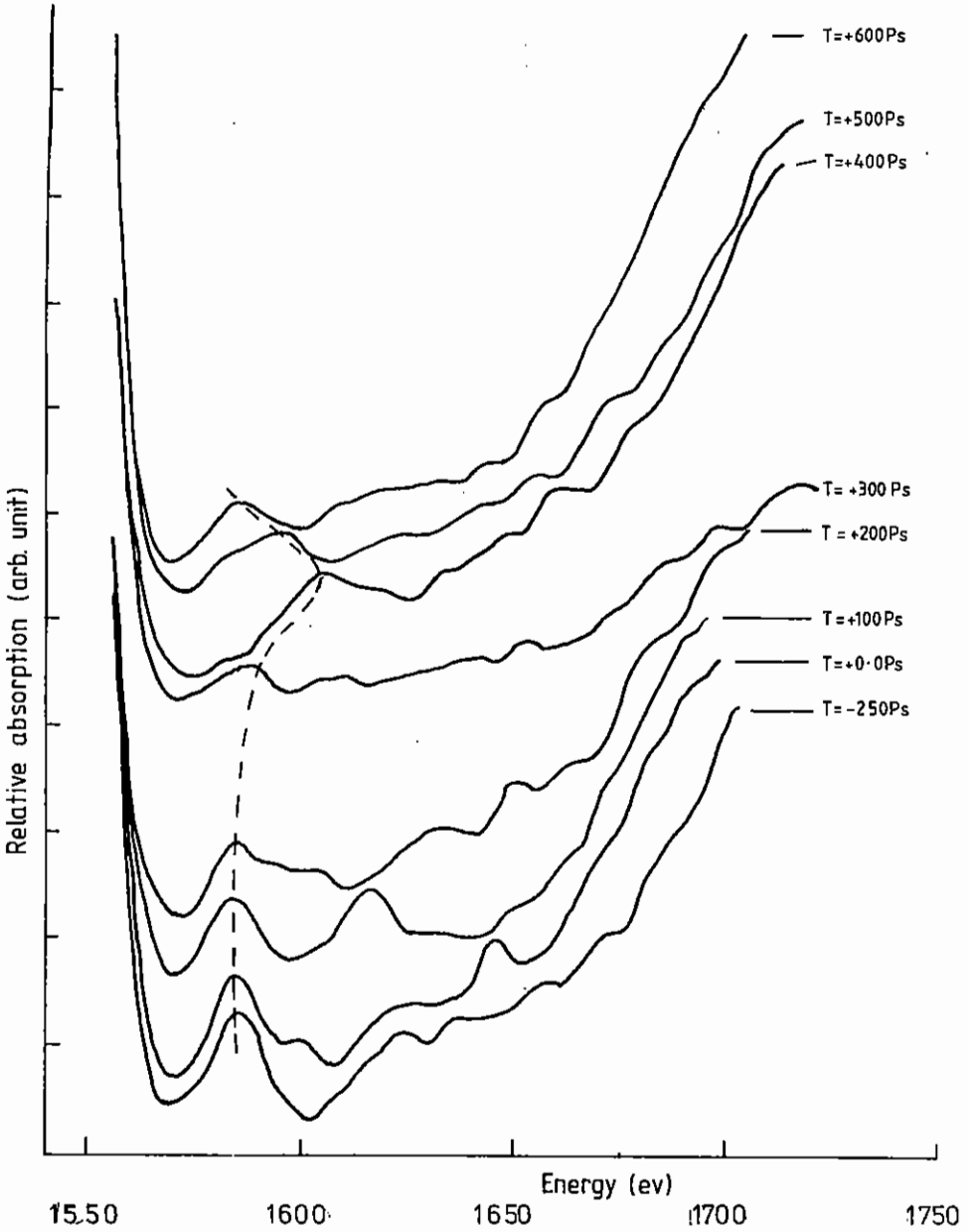

A3.1 Experimental EXAFS data as traced from microdensitometer scans for times between -250 ps and +600 ps.

reliance can be placed on the results. We have attempted to use the EXAFS analysis programmes at the Daresbury Laboratory to analyse this data. This technique, however, has not proved very successful, mainly because the programmes give a high weighting to spectral regions distant from the edge. In our case this means that the programmes give a high weighting to the noise, with the consequent unsatisfactory results. This problem can be partially overcome by "windowing" the data to contain spectral regions, but now the results depend to some extent on the window positions; again, an unsatisfactory situation. The best techniques that we have found uses EXAFS spectra calculations of cold compressed aluminium (A3.2). We have used results of one component plasma Monte Carlo calculations (A3.3) for the ion pair correlation function to determine the form of a Debye-Waller term to be included in this EXAFS data. This calculation is not self consistent but the results do show the general features of the experimental data. The first two absorption bands are not seriously affected by finite temperatures and are still given approximately by the formula (A3.2)

$$X = (E - E_F)\, S^2$$

where E is the energy position of the peak, X is a constant dependent upon which peak is considered and S is the Wigner-Sietz radius

ie $\frac{4}{3}\pi S^3 = V$, the volume occupied by one atom or ion.

Over the compression range of interest this formula differs by less than $\pm$ 5% from the code calculations of Albers et al.

The experimental points for the compression are plotted on figure A3.2 together with predictions of the MEDUSA for the compression. The experimental points have been shifted forward in time by 60 psec to give a better correspondence with the code. The justification for this is that the actual shape of the laser pulse will vary, particularly at early times, from the Gaussian shape assumed in the code calculations. The large error bars arise because of the uncertainty in the band positions.

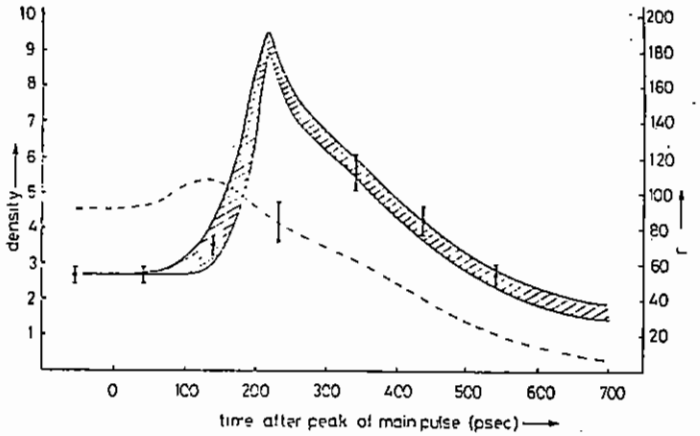

A3.2 Calculated points for aluminium density as a function of relative delay. Hatched region indicates MEDUSA simulation and broken line shows calculated value of Γ.

At present we are not able to give a very definite value for the ion coupling parameter, Γ, except to say that it must be greater than 10 for us to observe the depth of modulation of the spectra that we do. Other factors such as time smear, spatial and temporal inhomogeneities will also reduce the observed depth of modulation. We have not yet attempted to deconvolve these factors but rather crude estimates would suggest that the experimental point at +500psec would not have a Γ of greater than ∿ 30. At later times no EXAFS spectrum is observed suggesting the Γ ≤ 10. From the density and this value of Γ we can estimate the value of the ionisation, Z^*. This must lie somewhere in the range 2-3. The Thomas-Fermi equation of state calculations in the MEDUSA code suggest that at this time Z^* ≈ 5. The reason for this discrepancy is not understood.

The broken curve in Figure A3.2 shows the value of Γ calculated from the Thomas-Fermi when the ionisation has been reduced to correspond to the experimental values. This now gives an unrealistically low value for Γ at room temperature where Γ should be in the order of 150.

A3.2 X-RAY EMISSION MEASUREMENTS FROM HIGH ASPECT RATIO IMPLODING SHELLS

M J Lamb, C L S Lewis, E Robertson, J Corbett, P McCavana (Queen's University, Belfast)
P Norreys (Royal Holloway and Bedford New College)
C Popovics (Ecole Polytechnique, France)
A Rodin (Lebedev Institute, USSR)
B Fraenkel (Racal Institute, Jerusalem)

Introduction

We have previously reported x-ray radiographic studies of the 12-beam implosion of polymer shell targets having aspect ratio in the range 7 - 20 (A3.4, A3.5). On a number of shots, particularly at higher aspect ratio, strong X-ray self emission was observed from the implosion core. The core feature sometimes appeared elongated or even consisted of two distinct features, and was not always geometrically centred. The origin of this self emission was somewhat uncertain. One suggestion was that it might be due to the coalescence of inwardly directed jets of shell material. In this case it would be expected that the emission would occur before peak compression. It was also suggested that high Z impurities in the shell could be the source of the bright emission. However, the previously recorded X-ray emission spectra could not be interpreted unambiguously owing to the presence of bright emission from the supporting glue. The aim of the present experiment was to identify the origin of the core emission and to investigate the effect of increasing the target aspect ration on the implosion dynamics.

Experimental

Empty CH polymer shell targets having aspect ratio in the range r/dr = 10-16 were driven ablatively by 12 beams (0.53 micron, 0.8 ns FWHM) at absorbed irradiance levels of $\sim 10^{14} W/cm^{-2}$. The X-ray emission was recorded on a range of diagnostics comprised of:

- .active and passive pinhole cameras
- .two orthogonally oriented space-resolving crystal spectrometers
- .two time-resolving spectrometers looking at 0.6 keV and 2keV radiation respectively.

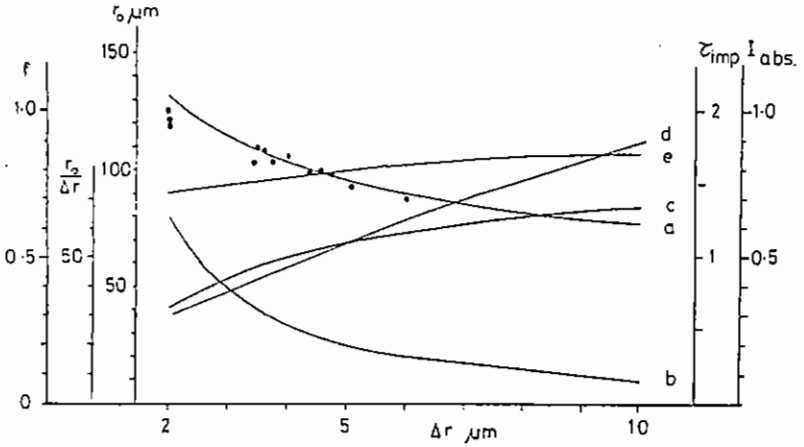

Fig A3.3 (a) r^3dr = constant normalised to r = 75 microns, dr = 10 microns, 0 actual targets (b) r/dr (c) f, th fraction of the shell wall remaining prior to void closure (d) I (ab), the absorbed irradiance in units of $10^{14} W/cm^2$; simulations have E(abs) = 65J and a 1.0 ns pulse (e) the implosion time is ns.

An X-ray timing fiducial was obtained by irradiation of a tungsten wire target with a 100ps laser pulse timed to arrive ∿1ns ahead of the main drive beams.

The polymer shell targets used were chosen as follows. Based on a crude analytic scaling argument it can be shown that if r^3dr is kept constant then targets of any aspect ratio r/dr will implode in approximately the same time for a fixed absorbed laser energy and a fixed pulse length. Targets designs were scaled from the low aspect ratio targets used previously (r ∿ 75 microns, dr ∿ 10 microns) with the knowledge that peak compression was on the falling edge of a 0.8 ns FWHM, 0.53 micron pulse and an absorbed energy of ~ 80 J.

Figure A3.3 shows the r^3dr line used, the actual targets shot and the results of Medusa simulations run over the r, dr parameter range. The implosion time, the fraction of the initial shell wall ablated and the absorbed irradiance are all slowly varying functions over the aspect ratio range from 10 to 60. A five-fold increase in compressed shell material temperature is indicated over the range.

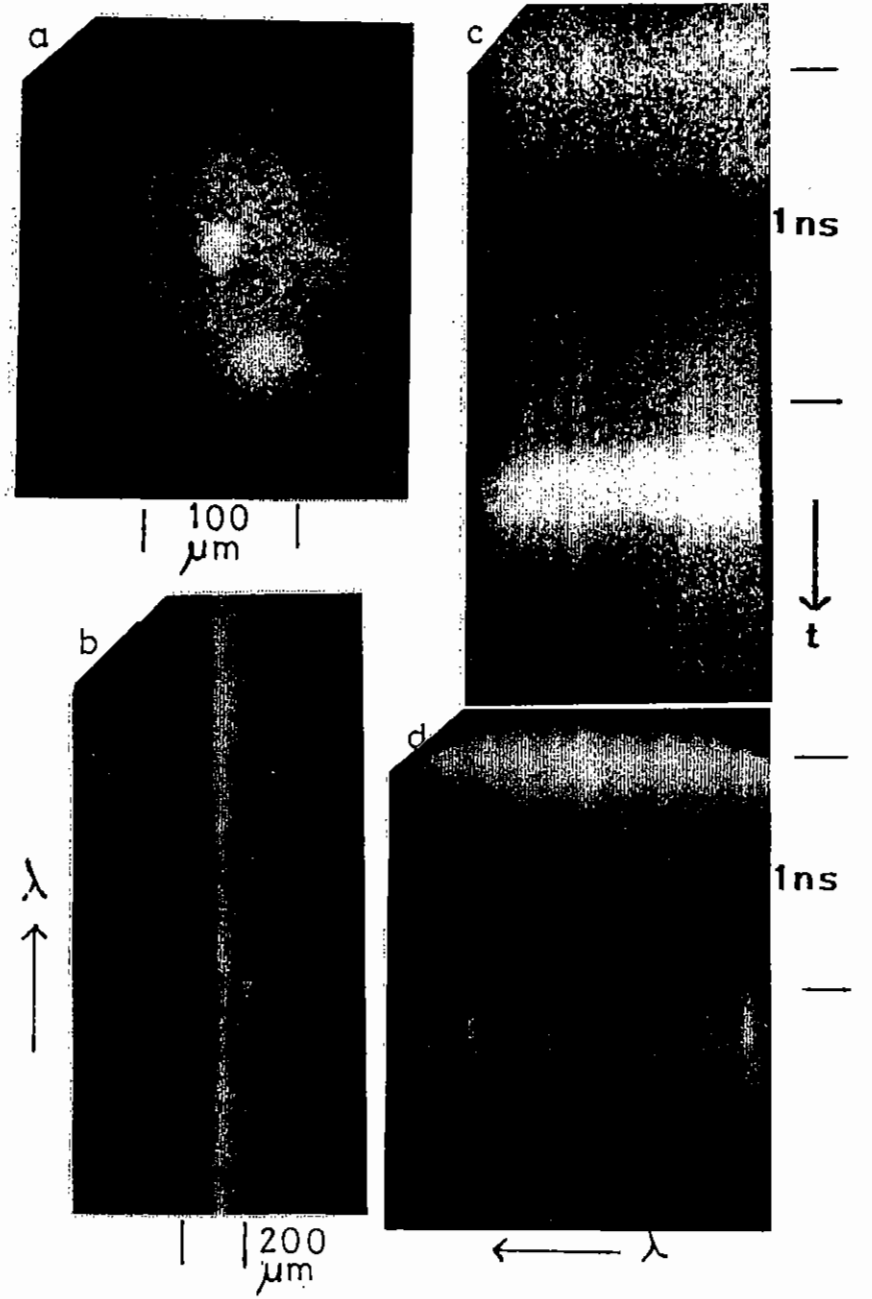

Fig A3.4 (a) Pinhole camera picuture showing core and coronal emission (b space resolved core emission at ∿1 keV (c) 0.6 keV streak showing pulsing in the core emission. The spectral lines are sulphur originating in the target support glue.

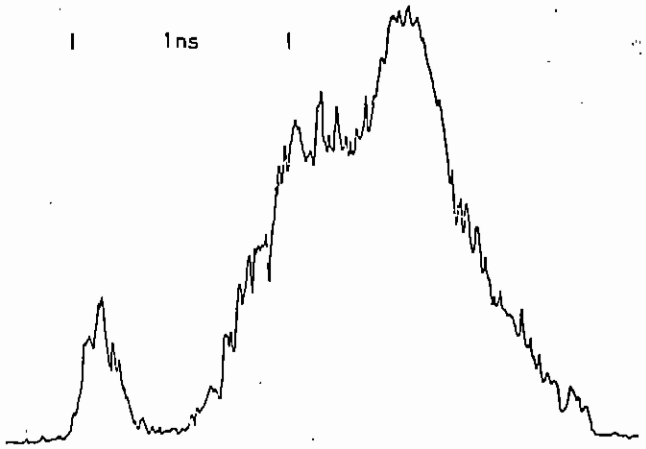

A3.5 Densitometer trace of 0.6 keV streak showing fiducial, coronal and core emission.

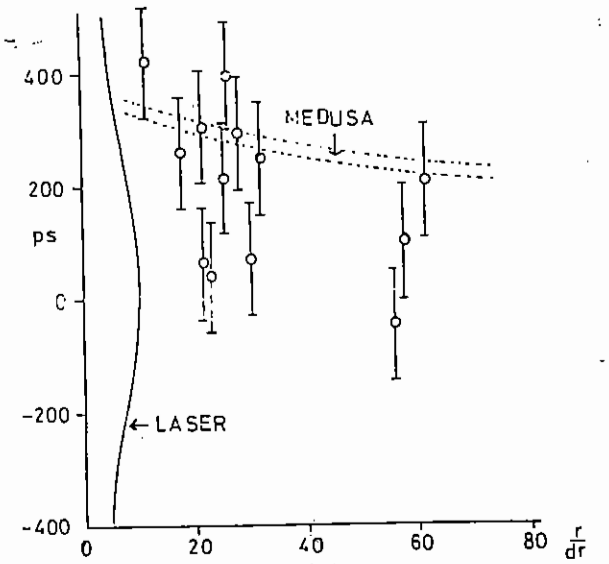

A3.6 Implosion times relative to the peak of the drive pulse as a function of aspect ratio. The simulation corresponds to 20% coupling of 400J incident energy in a 0.8ns FWHM pulse which was typical for the focussing conditions used.

Results and Discussion

The pinhole camera images (see e.g., Figure A3.4a) showed bright core emission with scale lengths < 20 microns, a ring of weak self emission from the shell, and bright emission from the target support glue.

The orthogonally oriented space-resolving spectrometers allowed us to unambiguously identify the X-ray emission from the various parts of the target. Strong K-shell lines from sulphur and chlorine were found to be due only to the glue which attached the target to the supporting stalk. The wall and core emission was found to be carbon continuum and there was no evidence of any line emission due to high Z impurities in the shell. A space resolved spectrum showing dominant core emission of carbon recombination radiation in the region of 1.5nm is illustrated in Figure A3.4b. Measurement of the continuum slope allows the core temperature to be estimated (T > 200 eV).

Streak records from the time resolving spectrometers are shown in Figure A3.4c and d. One spectrometer (c) was set to record a narrow spectral region at 2.0 nm and therefore once again shows carbon recombination radiation. A typical densitometer trace is illustrated in Figure A3.5 and shows the timing fiducial from the tungsten reference target followed by emission from the target shell enhanced at peak compression by a short burst of emission from the core. This represents the first direct measurement of implosion time in 12-beam ablative compression experiments. The 2 keV streak camera (Figure A3.4d) showed sulphur line emission coincident with the main laser pulses (as expected since they originate in the glue) and in shots corresponding to bright core emission (high aspect ratio) also showed the delayed carbon continuum from the core.

Figure A3.6 shows the measured implosion times with respect to the pulse peak with shots normalised to an absorbed energy of 80 J. Corrections involved are smaller than intrinsic error bars in all cases. Also plotted are the implosion times predicted by MEDUSA simulations. The effect of radiative preheat was included but found to make little difference to the time of peak compression. The implosion time discrepancies observed in comparison to simulation are

of the order of +/-200 ps over the entire aspect ratio range indicating that higher aspect ratio targets perform just as well as low aspect ratio targets within the limits of shot-to-shot perturbations introduced by illumination uniformity, alignment, and target quality.

On some higher aspect ratio targets, which otherwise imploded on the correct time scale, multiple emitting cores were observed in pinhole pictures and double pulsing in the core emission ws observed in the high energy channel. Similar targets radiographed at early times in the implosion showed signs of shell break-up yet yielded bright well defined cores on time integrated pinhole pictures. The phenomena involved in this behaviour are not fully understood.

An attempt ws made to observe compression of a Freon fill gas but this was frustrated due to bright chlorine emission from the ablation front due to Freon contamination in the shell.

During this run some trials were made of two new techniques for monochromatic X-ray imaging. These were imaging using reflection from spherically bent crystals (see section C5.4) and using double diffraction in crystals (see sections C5.2, C5.3). Some preliminary images were obtained.

Figure 3.7(a) shows a densitometer trace of space-resolved 0.85 nm emission from an imploded polymer shell recorded using a 300 mm radius of curvature quartz crystal (2d = 0.8509 nm) with a magnification of 5. Core emission on a scale of 15 microns can be seen. A double diffraction instrument using beryl crystals set to record radiation around 0.88 nm did not produce images from pure polymer targets. However, an image was recorded from a polymer target which was coated internally with bismuth. A densitometer trace of this is illustrated in Figure A3.8b and shows spatially-resolved bismuth M-band emission (around 0.44 nm) from the walls of the target recorded in second order. It is envisaged that such monochromatic imaging techniques will have an important role in future experiments.

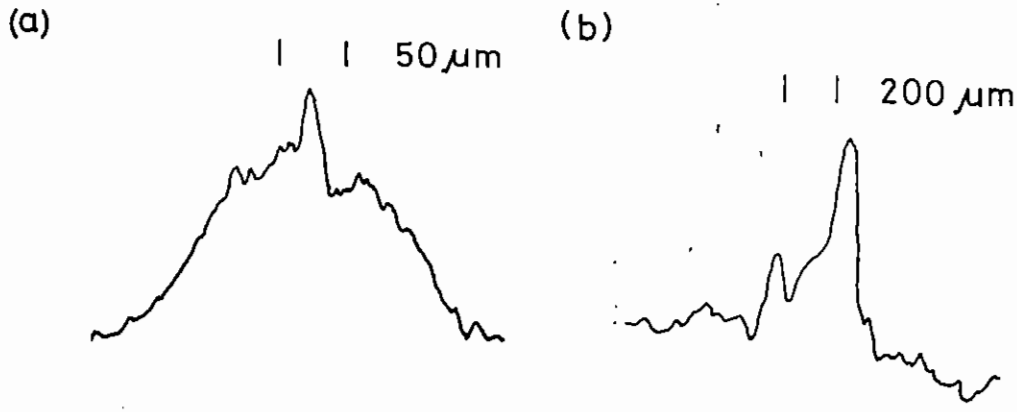

A3.7 Densitometer traces of monochromatic X-ray images recorded using (a) a spherical grating crystal mirror and (b) the double diffraction beryl crystal.

A3.3 ABSORPTION SPECTROSCOPY IN IMPLOSION EXPERIMENTS

C Chenais-Popovics (Ecole Polytechnique), P Norreys (Royal Holloway and Bedford New College), M Lamb, C L S Lewis, E Robertson, J Corbett, P McCavana (Queens University Belfast), M H Key, S J Rose (RAL)

Introduction

The quantitive diagnosis of shell conditions (that is temperature and $\rho\Delta R$) for hot ablative implosions using X-ray absorption spectroscopy has been demonstrated for 10.6 μm laser irradiation[A3.6]. A recent attempt[A3.7] to reproduce these results for 0.53 μm radiation showed that the absorbing layer had to be very thin and also had to be positioned less than 1 μm from the inner surface of the shell. We report here an experiment where these conditions were met and show the advantages of using absorption spectroscopy as a diagnostic for determining the $\rho\Delta R$ of the shell.

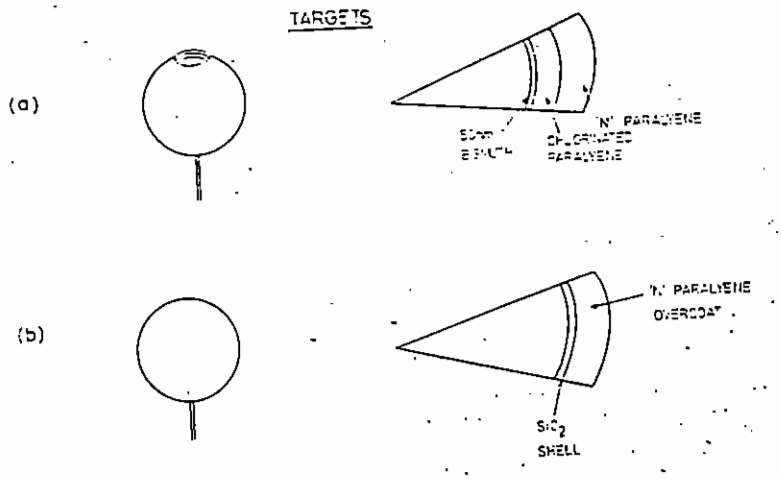

A3.8 Target designs for absorption spectroscopy.

(a) Manufacture balloon with bismuth as the inner shell

(b) Glass targets overcoated with N paralyne

Density and temperature diagnostic

If an intermediate Z ion is hot enough to be ionised between the flourine-like and Helium-like ion stages (100-300eV), each ion stage absorbs on a Kα line which lies on the red side of the Heα line of the absorber. The ρΔR of the absorbing layer can be determined from the equation[A3.6].

$$\rho\Delta R = \frac{M_i}{\sigma_o \alpha} \int \ln \left(\frac{I_o}{I_\nu}\right) d\nu$$

where I_o is the incident intensity, I_ν the attenuated intensity, M_i is the ionic mass and α is the fraction of all ions of each ionisation state which are in the ground state. α is usually very close to one. Also

$$\sigma_o = \left(\frac{\pi e^2}{mc}\right) f$$

where f is the absorption oscillator strength.

The integral above is simply the area enclosed within the absorption feature (provided the film density is proportional to ln(I)). If the absorption oscillator strengths are known, ρΔR can be determined.

The ionic composition can be deduced from the relative strengths of the absorption lines. A model describing the ionisation of the material can lead to a temperature determination. A shifted K-edge has been observed previously with glass targets[A3.8] and this allows determination of density.

Experimental Set-up

The 12 beam target chamber of VULCAN was used for the experiment. The pulse length was 800 ps FWHM and the focussing parameter d/R was set at +10. The absorbed laser intensity was in the range of 1-2 x 10^{14} Wcm^{-2}.

Two types of targets were used for the experiment. One type is illustrated in Figure A3.8(a) and shows a manufactured microballoon of 150μm typical diameter.Here a polymer balloon is overcoated with bismuth, 'D' (chlorinated) and then 'N' paralyene. A small laser is used to punch a hole (∿ 30 μm) through the overcoats. The balloon is subsequently placed in a solvent that dissolves the original balloon, leaving the bismuth as the inner layer of the manufactured balloon. The bismuth will be heated during the peak of the implosion, emitting M-band X-rays at 4.5Å to backlight the absorption features of the chlorinated layer. The other type of target was a glass shell overcoated with various thicknesses of 'N' paralyene. It is illustrated in Figure A3.8(b).

Two pinhole cameras, one active and one passive were placed orthoganally in the chamber to observe different viewing axes. A space resolving, time integrated mini crystal spectrometer was set up to observe the region around 4.5Å for the Bismuth-chlorine targets

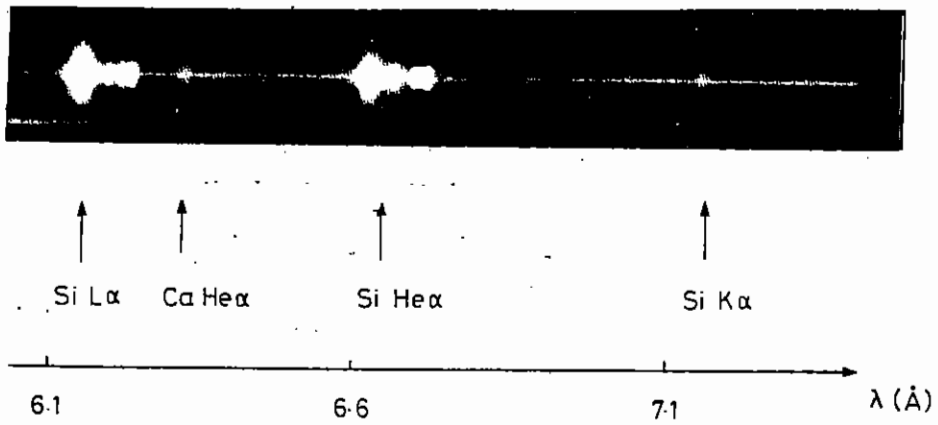

A3.9 (a) Space resolved spectrum of an imploding microballoon.

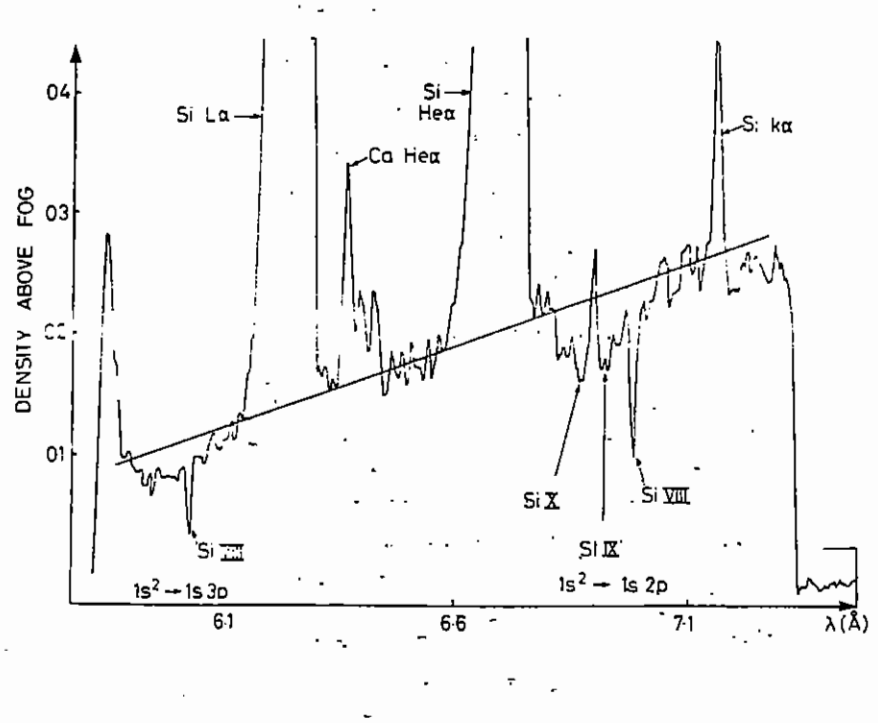

A3.9 (b) Densitometer tracing through the bright core region.

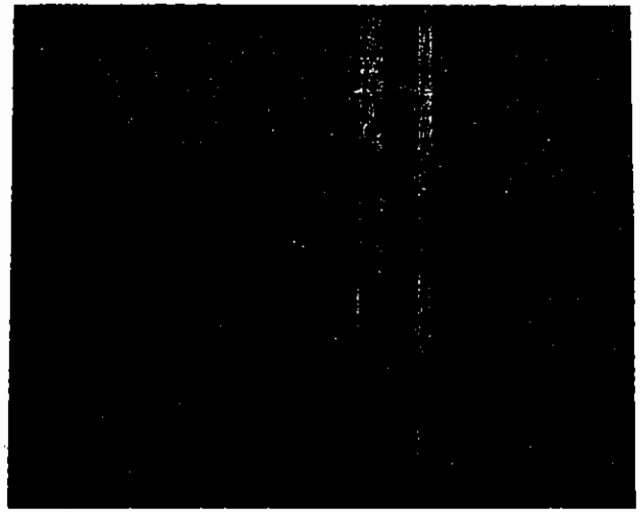

A3.9 (c) Pinhole picture of imploded balloon.

and subsequently at 6.8Å for the glass targets. The spatial resolution was 25μm. A time resolving spectrometer consisting of a flat PET crystal in front of an X-ray streak camera was used to record spectra at 4.5Å. The crystal was later changed to ADP for 6.8Å. Spectral resolution was around 3 mÅ on both spectrometers.

Experimental Results

When a spherical glass shell target is irradiated with high intensity laser light material is rapidly ablated from the surface creating an ablation pressure of several megabars for intensities of the order of 10^{14} W cm^{-2}. The ablation pressure drives a shock wave through the glass and also accelerates the shell. The shock wave converges and compresses either gas filling the shell or low density material ejected from the inner surface of the shell. A small central volume is heated to a temperature of several million K at a relatively low density (≤1g cm^{-3}). When the reflected shock waves meets the incoming shell deceleration begins, rapidly increasing the density x radius ρΔr of the shell. The high temperatures produced in the core mean that large amounts of X-rays are emitted from this region and can be detected after transmission through the imploding shell. The emitted spectrum is therefore the spectrum of the hot source modified

by absorption features due to the shell mixed with emission from the ablation plasma outside the shell.

Fig 3.9(a) shows a spectrum for an imploded glass microballon. (shot 11 28/8/86) that is spectrally resolved in one dimension and spatially resolved in the other. As spatial resolution is one dimensional, each point in this dimension represents the total emission along a chord from the target. Hence the bright feature in the centre of the picture shows the emission from the core plus a smaller contribution from the ablation plasma. It is noticeable the the core emission has a strong absorbtion feature on the long wavelength side of the Si Heα line.

Fig A3.9(b) is a microdensitometer tracing of the space resolved spectrum for a similar shot (shot 8 28/8/86) traced through the core emission. The microdensitometer slit was set at 45μm x 45μm.
The tracing shows a very sharp absorption feature associated with the $1s^2 \rightarrow 1s2p$ transition for the Si VIII ion, which is also repeated in the $1s^2 \rightarrow 1s3p$ transition for the same ion. Figure A3.9 (c) is a pinhole picture of this implosion and shows a bright imploding core.

The time resolving spectrometer could not resolve the absorption features because the spectrometer recorded both the emission from the core and the emission from the surface of the balloon. As the core is relatively small compared to the surface plasma the emission from this region was indistinguishable in the volume intergrated spectrum.

Figure A3.10(a) shows a time resolved spectrum of a Bismuth-chlorine microballoon. The bright emission lines are the resonance, intercombination and dielectronic satellites of Helium like chlorine ions. Noticeable absorption features can be seen in the microdensitometer tracing of Figure A3.10(b). The large absorption feature of C-like ion indicates the temperature of the shell at peak implosion was 200eV[A3.8]. The absorption features last for 300 ps. However the active pinhole picture A3.10(c) shows no implosion core and that the target did not implode symmetrically. Most other bismuth-chlorine targets showed no absorption features. Of those that did, great difficulty ensued in matching the unattenuated bismuth emission with the observed absorption features. However, as can be seen in Table (1), two bismuth-chlorine targets were analysed and showed a low $\rho\Delta R$ (1×10^{-3} gcm^{-2}), which also suggests that the implosion was not symmetric. We conclude that these targets are not satisfactory for an accurate determination of the shell $\rho\Delta R$.

Discussion

On figure A3.11 $\rho\Delta R$ is plotted against initial $\rho\Delta R$ (dots). The results obtained are very similar to those measured by alpha particle emission (crosses)[A3.9]. Error in the measurement is estimated to be 20%. This could be reduced by a comparison of the $\rho\Delta R$ obtained from the $1s^2 \rightarrow 1s2p$ and the $1s^2 \rightarrow 1s3p$ transitions. To do this, oscillator strengths need to be calculated for the $1s^2 \rightarrow 1s3p$ transitions. An ionisation model is being developed to give the temperature of the glass shell at peak implosion. Both calculations will be completed in the near future.

In conclusion, the diagnostic of $\rho\Delta R$ and temperature by absorption spectroscopy is achievable in compression experiments with 0.53μm laser irradiation, although the shell thickness is critical having to be thin enough for the target to implode and thick enough for the absorbing layer to absorb. Future measurements using this technique could include density as well by observing the shifted K-edge.

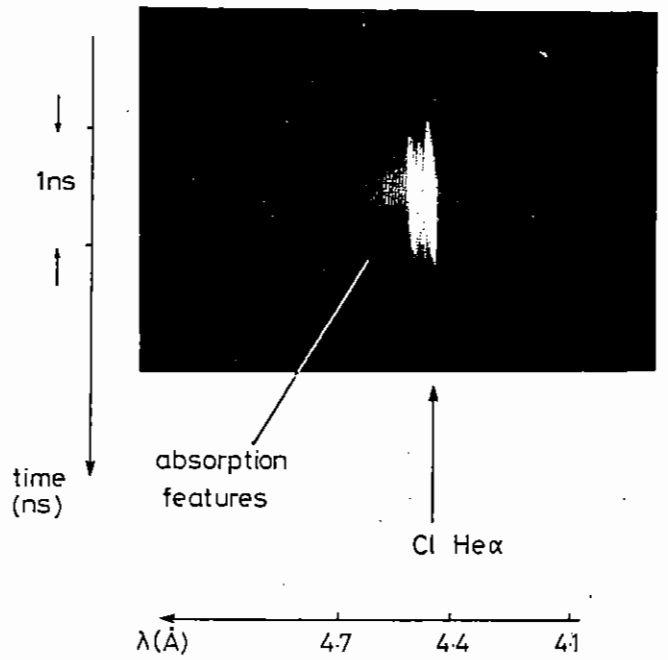

A3.10 (a) Time resolved spectrum of an imploding bismuth microballoon.

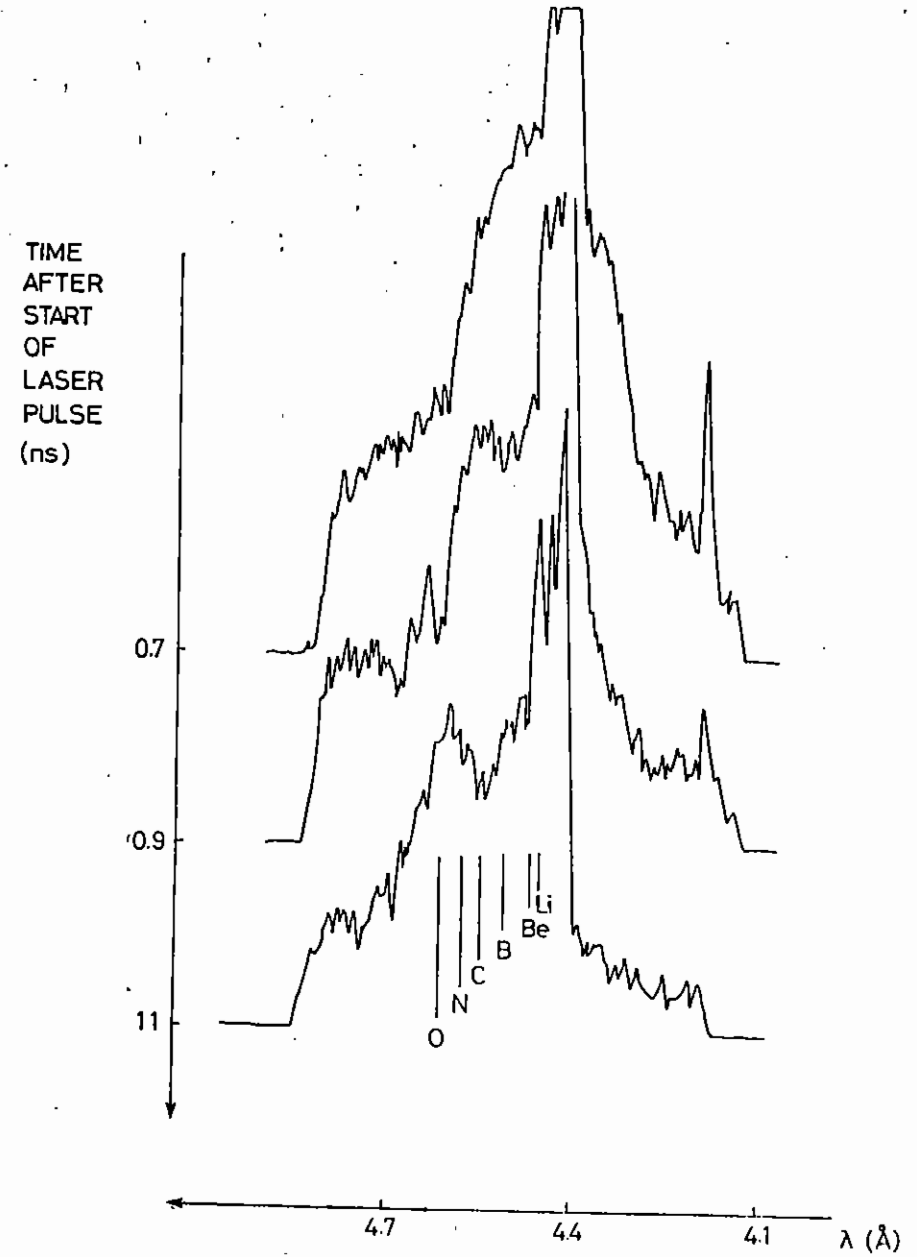

Fig A3.10 (b) Densitometer tracing through the spectrum of at various times. The onset of the absorption features starts at 700ps.

Fig A3.10 (c) Pinhole picture of imploded Bi shell.

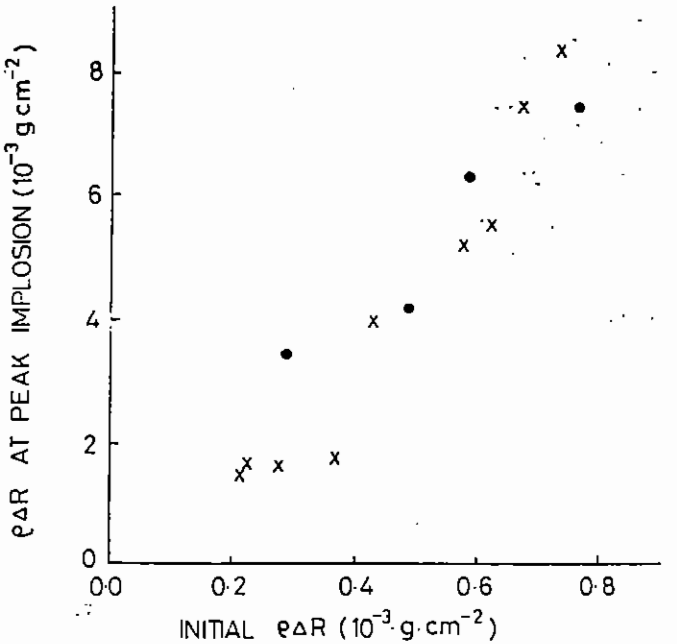

A3.11 Plot of PΔR versus PΔR initial for absorption spectroscopy; X for alpha particle emission.

TABLE 1

SHOT NR		D/R	I_a Wcm^{-2}	$\bar{E}$ (J)	GLASS THICKNESS (μm)	TARGET BISMUTH THICKNESS (nm)	DESCRIPTION D PARALYENE THICKNESS (μm)	N PARALYENE THICKNESS (μm)	INITIAL ρΔR	FINAL ρΔR
1	21/8/86	10	1.0×10^{14}	30±5 J	-	50	1.2	3.7	5.4×10^{-4}	1.1×10^{-3}
2	21/8/86	10	1.7×10^{14}	33±5.5	-	50	1.2	3.7	5.4×10^{-4}	1.0×10^{-3}
2	28/8/86	10	1.3×10^{14}	34±5.7	1.06	-	-	5.0	7.86×10^{-4}	7.3×10^{-3}
8	28/8/86	10	1.0×10^{14}	30±5 J	1.09	-	-	2.0	4.9×10^{-4}	4.2×10^{-3}
11	28/8/86	10	1.44×10^{14}	37±5 J	2.2	-	-	0.0	5.9×10^{-4}	6×10^{-3}
5	29/8/86	10	1.5×10^{14}	40±8 J	1.06	-	-	0.1	2.96×10^{-4}	3.4×10^{-3}

Editor: S J Rose

A4.1 STIMULATED RAMAN SCATTERING IN THE PRESENCE OF FILAMENTATION

H C Barr, T J M Boyd and G A Coutts (University College of North Wales, Bangor)

Last year we reported on how stimulated Raman scattering (SRS) growth rates were influenced by the presence of a sinusoidal density modulation (wave number 2K, amplitude $\delta n = \epsilon n_o$) transverse to the laser propagation direction which we used to represent a filament. We have extended those results to consider how more intense filaments (deeper density channels) modify SRS growth rates and spectra. The reaction of SRS on filamentation is not addressed here.

Localization of the SRS resonance is the first effect that occurs as the filament amplitude increases from zero ($\epsilon > 6K^2\lambda_D^2$) through the response of the plasma wave to the inhomogeneity in density; this is accompanied by a rapid reduction in growth as the bandwidth associated with the density variation dominates that associated with the growth ($\epsilon\omega_p \rightarrow \gamma_o$). Growth is strongly localized at density maxima or minima. Thereafter growth reduces more slowly (as $(\gamma_o/\epsilon\omega_p)^{1/3}$). When the density in the channel is low enough, Landau damping further strongly reduces growth at the density minimum. The focussing of the light waves (both laser and scattered) within the density channel strongly localizes SRS to the density minimum and can reverse the above decreases in growth until the filament is deep enough that Landau damping becomes strong and which ultimately wins over light wave focussing. This is illustrated in Figs A4.1 and A4.2.

In deep filaments, wave fronts are no longer planar: waves propagate as in a waveguide. Waveguide corrections to the dispersion relations together with phase matching can give rise to a more limited bandwith for SRS emission. To see this, consider our sinusoidal slab channel (approximately parabolic at the density maximum) and neglect plasma temperature. The light wave dispersion relation is

$$\omega^2 = \omega_p^2 + k^2c^2 + \omega_p c/L \qquad (1)$$

where L is the scale length across the filament. Phase matching then implies a scattered wave cut off frequency

$$\omega_s \simeq \frac{\omega_o}{2}\,\frac{1 + c/L\omega_o}{1 + c/2L\omega_o} \quad L\omega_o \qquad (2)$$

which exceeds $\omega_o/2$. If such filaments can focus down to a skin depth $L \sim c/\omega_o$ then $\omega_s \gtrsim 2\omega_o/3$ whence a gap would be apparent between $2\omega_o/3$ and $\omega_o/2$ (at which emission from the $2\omega_p$ instability would be indirectly generated). The same argument for a self-trapped cylindrical Gaussian filament of radius a has, instead of (1),

$$\omega^2 = \omega_p^2 + k^2c^2 + 4c^2/a^2 \qquad (3)$$

which yields a scattered wave cut-off frequency at

$$\omega_s = \frac{\omega_o}{2}\left(1 + \frac{4c^2}{\omega^2 a^2}\right) \qquad (4)$$

Using the minimum radius for a self-trapped filament of $a = (2e)^{1/2}\, c/\omega_{pmax}$, where ω_{pmax} corresponds to the density n_{max} outside the filament, gives

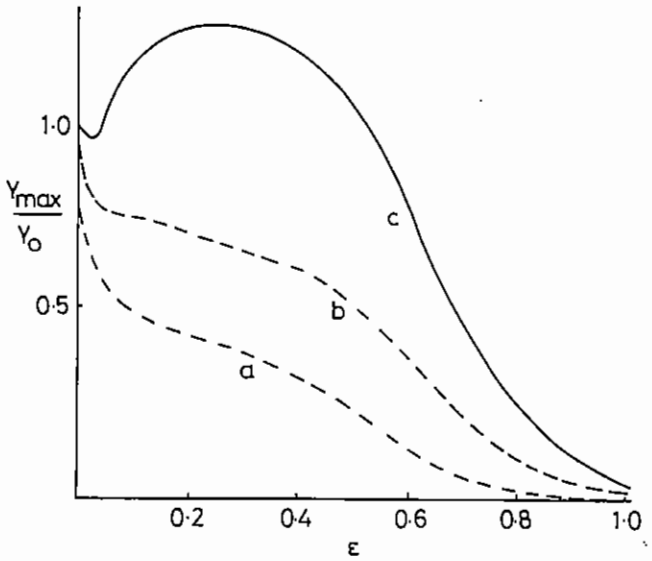

Fig A4.1 *Maximum SRS growth rates relative to their homogeneous plasma value versus filament depth for a mean density $\eta_o = 0.1\ \eta_c$, at a temperature of 0.63 KeV and $v_o = 0.01\ c$. Curve (a) shows the effect of the inhomogeneity on the plasma wave only, (b) includes scattered wave focussing and (c) includes also laser light focussing.*

$$\omega_s = \frac{\omega_o}{2}\left(1 + \frac{2}{e}\,\frac{n_{max}}{n_c}\right) \qquad (5)$$

If $n_{max} \sim n_c/2$ say, then $\omega_s \lesssim 2\omega_o/3$.

Inhomogeneities along the filament (due for example to filaments having singular or repeated foci) further complicate results: thresholds are sensitive to the local topology within filaments.

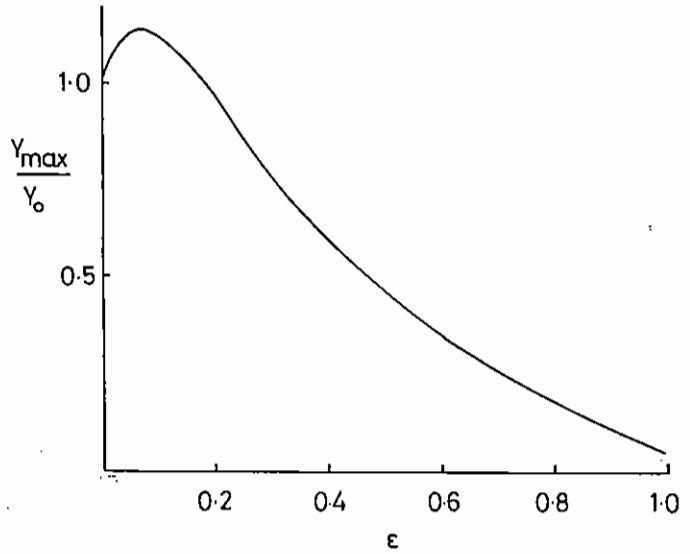

Fig A4.2 As for case (c) of Fig A4.1 but with a temperature of 2.5 KeV.

A4.2 THE CONTRIBUTION OF LIGHT FILAMENTATION IN LASER BEAMS TO ILLUMINATION NON-UNIFORMITY AT CRITICAL DENSITY

D J Nicholas (RAL) and S G Sajjadi (Lanchester Polytechnic)

The effects of plasma motion on filamentation, under the influence of both the pondermotive force and thermal gradients due to spatial variation in energy deposition, is studied. In the present model the filament is described in terms of an EM wave with a comlex amplitude. The initial distribution is Gaussian in both space and time. The time-dependent wave equation is adopted in the paraxial approximation (A4.1).

A two-fluid model is assumed for the plasma which is considered to be composed of ions, charge + Ze, mass M and of electrons, charge − e and mass m. The neutral plasma density condition is $N_e = ZN_i$ where N_e and N_i are the average electron and ion densities. Defining the rate of momentum change for the plasma (A4.2) as

$$\rho \frac{du}{dt} = N_e m \frac{dV_e}{dt} + N_i M \frac{dV_i}{dt} \qquad (1)$$

where V_e and V_i are the electron and the ion speeds, respectively.

The momentum equation will thus take the form

$$\rho \frac{du}{dt} \simeq \frac{1}{2}(\epsilon' - \epsilon_o)\,\nabla \langle E^2 \rangle - \nabla P_p \qquad (2)$$

where P_p is the total pressure for both the electrons and the ions.

The energy conservation equations for the electrons and the ions are

$$\rho C_{v\alpha} \frac{\partial T_\alpha}{\partial t} + \nabla \xi_\alpha u + \rho \nabla.u + \nabla q = \dot{E}(r,t) \pm K_\alpha \qquad \alpha = e,\ i \qquad (3)$$

where K is the rate of energy exchange between electrons and ions, q is the thermal energy flux, and a flux-limit of between 0.03 and 0.1 of the free-streaming limit (A4.3) is applied. ξ is the internal specific energy and $C_v = \rho^{-1}\frac{\partial \xi}{\partial t}$ the specific heat. The rate of heating due to the laserbeam, represented by $\dot{E}(r,t)$ is due to inverse-bremsstrahlung absorption so that the dispersion relation takes the form

$$\epsilon' = 1 - \left[\frac{\omega_p^2}{\omega_o^2 + \nu^2}\right] - \frac{i\nu}{\omega_o}\left[\frac{\omega_p^2}{\omega_o^2 + \nu^2}\right] \quad (4)$$

where ϵ' is the complex permitivity, ω_o is the laser light frequency, ω_p is the plasma frequency and ν is the electron-ion collision frequency, given respectively by

$$\omega_p^2 = \frac{e^2 N_e}{\epsilon_o m}\left[1 + \frac{Zm}{M}\right] \quad (5)$$

and

$$\nu = \frac{4.2 \times 10^{-5}\, ZN_e}{T_e^{3/2}} \quad (6)$$

where T_e is expressed in keV.

The phase shift $\partial\Phi$ in the laser light due to a density dependent refractive index can be written as

$$\delta\Phi = \frac{2\pi e^2}{m\omega_o c}\left(1 - \frac{4\pi e^2 N_e}{m\omega_o^2}\right)^{-1/2} \delta N_e \quad (7)$$

However, additional phase-shifts arise from this treatment. In the expression for the electrical current density J there is an additional term due to the local contribution to the plasma motion caused by the laser beam: a longitudinal component of the current $J_z \propto E^2$ and a transverse component $J_r \propto -2iFE^2 \nabla_r\Phi$ where F is the Fresnel number ($= \pi r_p/\lambda L$), λ the laser light wavelength, L the local density scale length ($= n^{-1}\nabla n$) and r_p the initial Gaussian radius of the beam. This latter component is associated with intensity dependent radial variations of phase. When $\frac{\partial\Phi}{\partial r} > 0$, self-induced focussing dominates and diffraction spread and locally, the beam converges.

This model has been used to study a number of problems associated with the wavelength of light filamentation. As a comparative example, the growth of a single filament, at a laser wavelength of 1054 nm is followed in a low Z plasma (Z = 10) at electron temperature T_e = 500eV. The filament is described initially by means of a Gaussian distribution in space and time with r_p = 6.0 μm, τ_p = 75 ps and $I_o = 2.7 \times 10^{14}$ W/cm^2. An initial electron density $N_e^p = 0.25N_c$ is taken, v_{osc} ($= eE_o/m\omega_o$) = 0.01 c and an arbitrary initial phase angle. Figure A4.3 shows the normalised intensity

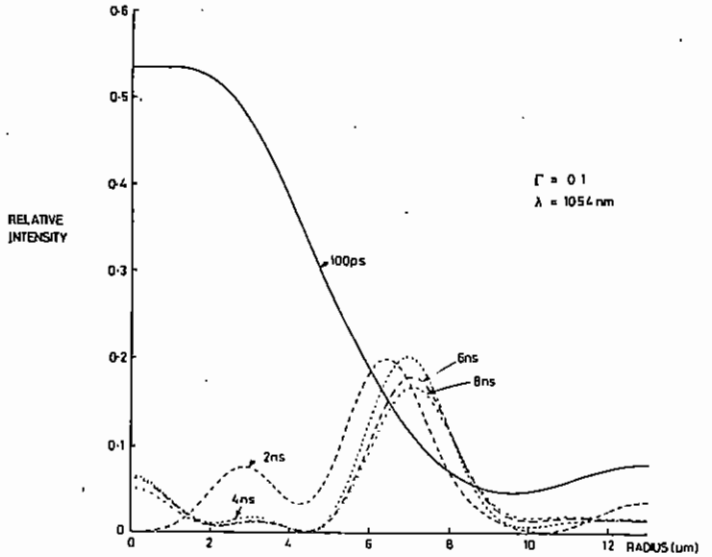

Fig A4.3 *Radial intensity profiles across the filament at λ = 1054 nm. Five profiles are shown at various time intervals. Note the bunching of the profiles at later times indicating pulse compression.*

distribution across the filament at critical density for five successive time intervals during the filamentary pulse. Oscillations in intensity appear across the beam which is increasingly defocused with time. The oscillating break-up of the beam into smaller filamentary structures occurs and peaks near the centre. This is a highly localised effect depending critically on the relative magnitudes of the net focusing and diffracting terms. The light is diffracted both inwards and outwards and can locally enhance the filamentary region. In this simulation the beam reaches the first focus at an axial distance z = 67 μm. After passing through the focus it diverges and then reconverges again in a succession of tighter focii. The pattern gradually increases in intensity and moves away from the axis in time. This successive focii has been observed previously (A4.4) and displayed graphically in recent numerical simulations (A4.4; A4.6; A4.7; A4.8). Other filamentary structures develop in time and as the simulation is followed beyond the first focus, these 'beat' with each other in increasing complexity.

A detailed study of the time dependent energy flow near the focal region shows that just prior to the focus, the local group velocity $\frac{\partial w}{\partial k}$ exceeds the phase velocity of the beam, temporal distortion of the pulse occurs and what amount to an optical shock is formed. In fact a succession of these shock waves are formed and propagate coherently. These have a significant effect on the stability of an imploding microballoon should they occur near the ablation region. An estimate of the pulse distortion can be obtained by comparing the interval between successive radial beam profiles shown in figure A4.3. It is interesting to note, that although a complex structure in the filaments is formed near the critical density, the maximum intensity at the focus is less than that of the initial peak intensity. In this simulation the maximum peak intensity at the focus is $5.4 \times 10^{13} W/cm^2$. This is due to the collisional absorption, which increases with the increase in density and decrease in average ionisation rate, at long wavelengths and high temperatures.

The second simulation described is carried out at the third harmonic wavelength blue light λ = 351 nm. Again the starting intensity I_0 = $2.7 \times 10^{14} W/cm^2$ and an initial Gaussian filament profile in both space and time (r_p = 6.0 μm, τ_p = 75 ps) is taken. Figure A4.4 shows the radial intensity profile near the critical density at z = 150 μm. As with previous simulations there are small scale length, high intensity stuctures, but in addition the whole beam waist has also narrowed down to ≈ 1 μm at the focus; in other words there is whole beam self-focusing. The previous simulation with green light appears to indicate this trend, but it shows up quite clearly with the blue light. The plasma, at this wavelength is highly collisional, small-scale structures in the filaments are smoothed out and thermal self-focusing dominates.

Thus, whilst at λ = 1054 nm there are filaments, they contain only a little of the total energy of the filament. At λ = 351 nm however, the intensity is increased and whole beam self-focusing dominates the filamentation process.

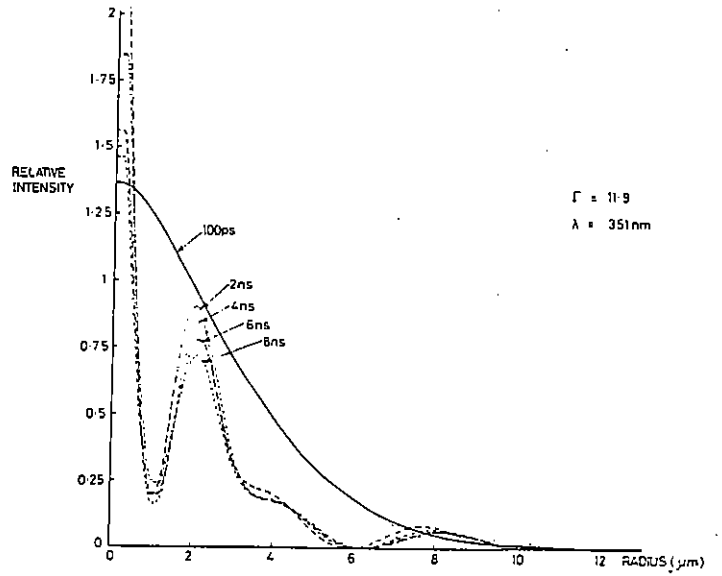

Fig A4.4 *Radial intensity profiles for blue light at λ = 351 nm. The radial width of hte filament has decreased to ≈ 1μm denoting whole beam self-focussing. There is also a marked absence of high spatial frequencies due to collisional smoothing.*

A4.3 NOISE IN PLASMA LENSES FOR HIGH ENERGY PARTICLE BEAMS

R G Evans (RAL)

It has recently been suggested that the final focussing system for a high energy linear collider might consist of a plasma supporting a large amplitude, but spatially limited, wave with the property of focussing charged particles simultaneously in both transverse planes. Such a wave could be induced either by a precursor bunch of particles or by the beating of two electromagnetic waves. In a plasma of density 10^{17} cm^{-3} the maximum 'wave breaking' electric field is about $3 \times 10^{8} Vm^{-1}$, equivalent in focussing effect to a quadrupole field gradient of 2×10^{6} Tesla $metre^{-1}$.

Since the plasma consists of a finite number of particles with random thermal motions there will be some noise associated with thermal excitation of plasma waves which will degrade the ultimate performance of such a lens system. There will in practice also be unwanted wave motions induced by the free energy source that drives the focussing wave, but this note calculates only the background level associated with thermal motion.

Suppose a plasma of particle density n and temperature T is contained in a cubical box of side L subject to periodic boundary conditions. The normal modes of the box are travelling waves having the spatial dependence $\exp(i\underline{k}.\underline{r})$ where $\underline{k} = (i,j,k)2\pi/L$ and i,j,k are integers. In the continuum limit the mode density in $\underline{k}$-space is

$$n_k \, dk = 4\pi \, k^2 \, dk \quad \left(\frac{L}{2\pi}\right)^3$$

We assume that each mode is excited with a thermal energy of $\frac{1}{2}k_B T$ where k_B is Boltzmann's constant. If E is the RMS electric field associated with each mode then we have

$$\frac{E^2}{4\pi} . \, L^3 = \tfrac{1}{2} k_B T$$

and

$$(E^2)_k \, dk = \frac{1}{\pi} k_B T \, k^2 \, dk$$

is the spectral energy density of the thermal fluctuations.

Conventionally the plasma wave spectrum is considered only to exist up to the Debye cut-off given by $k_D = 2\pi/\lambda_D$ where λ_D is the Debye length for the specified density and temperature.

Integrating the electric field energy up to this cut off gives the standard result that the ratio of electric energy to kinetic energy is of the order of the inverse of the number of electrons in a Debye sphere.

Consider an electron of energy $\gamma m_e c^2$, velocity = c, moving in the z direction through the above plasma for a length Δ. Consider the motion in the y-plane only and neglect the x motion, then

$$\gamma m_e \dot{y} = \sum_k e E_y e^{i(k_y y + k_z z + \Phi_k)}$$

After a path length Δ the deflection angle θ is given by

$$\theta = \frac{e}{\gamma m_e c^2} \sum_k E_y \int_{-\Delta/2}^{+\Delta/2} e^{i(k_y y + k_z z + \phi_k)} \, dz$$

where ϕ_k is the phase of the kth mode. This becomes

$$\theta = \frac{e}{\gamma m_e c^2} \sum_k E_y \, \frac{e^{i(k_y y + \phi_k)}}{i k_z} \, [2i \sin k_z \Delta/2]$$

The phases are eliminated using the random phase appoximation to give

$$\langle \theta^2 \rangle = \frac{e^2}{\gamma^2 m_e^2 c^4} \sum_k E_{yk}^2 \, \frac{4 \sin \, k_z^2 \Delta/2}{k_z^2} \, e$$

If $k_z \Delta/2 >> 1$ then the $\sin^2$ factor oscillates rapidly over the summation and averages to 1/2. The summation does not then depend on Δ and may be thought of as 'end effects'. The important contribution to the integral comes from modes for which $|k_z|\Delta/2 \leq \pi/2$ and the sine term can be approximated by $k_z \Delta/2$. We then obtain

$$\langle \theta \rangle^2 = \frac{e^2}{\gamma^2 m_e^2 c^4} \sum_{|k_z| \leq \pi/\Delta} E^2 \, \Delta^2$$

The number of modes satisfying this constraint is the volume of a disk in k-space of radius k_D and thickness $2\pi/\Delta$. We also use the fact that the rms y-field is half of that calculated earlier since the field is nearly perpendicular to the z-axis, and has only x and y components.

$$\langle\theta\rangle^2 = \frac{e^2}{\gamma^2 m_e{}^2 c^4} \quad \frac{1}{4} \quad k_D^2 \quad k_B T \, \Delta$$

We eliminate the temperature T by using the rms electron velocity $v_e=(k_B T/m_e)^{\frac{1}{2}}$ and remembering that the Debye length $\lambda_D=v_e/\omega_p$. Also substituting $\omega_p{}^2=4\pi ne^2/m_e$ we finally obtain

$$\langle\theta^2\rangle = \frac{4\pi^2}{\gamma^2} \quad r_c{}^2 \quad (n \, \Delta)$$

where r_c is the classical electron radius $r_c = e^2/mc^2$

The wave breaking electric field in the plasma is given by $eE=m_e c\omega_p$ and the actual field is some fraction $(\delta n/n)$ of this depending on the fractional density fluctuation in the plasma wave. The focussing strength depends on the rate of change of $\underline{E}$ with radius and this is maximised by making the radius of the plasma wave about equal to the wavelength. Much narrower waves effectively 'short out' the field lines and give no further increase in focussing strength. For a wave with phase velocity c the typical transverse dimension for strongest focussing effect is c/ω_p. We assume that the radial electric field increases linearly with radius off axis and attains the value

$$eE_{max} = \left(\frac{\delta n}{n}\right) m \, c \, \omega_p$$

at a radius of $r = c/\omega_p$

The angular deflection of an electron of energy $\gamma m_e c^2$ at radius c/ω_p is then given by

$$\delta\theta = \frac{e}{\gamma m_e c^2} \quad E \, \Delta \quad = \quad \frac{\Delta \, \omega_p}{\gamma \, c} \quad (\delta n/n)$$

and the focal length F is given by

$$F = \frac{\gamma}{(\delta n/n)} \quad \frac{1}{\Delta} \quad \left(\frac{c}{\omega_p}\right)^2$$

Using these expressions for the Focal length of the plasma lens and the RMS angular spread induced by the plasma thermal fluctuations we obtain the final results, expressible in one or two equivalent forms:

$$(r^2)^{\frac{1}{2}} = \frac{c}{\omega_p} \quad \frac{1}{2(\delta n/n)} \quad (n \, \Delta \, \frac{c^2}{\omega_p{}^2})^{\frac{1}{2}}$$

or $(r^2) = \frac{\pi}{\gamma(\delta n/n)} \quad r_c \, F$

Either of these results can be used equivalently depending which of the parameters is of most interest. The first form is very fascinating since the term under the square root sign is simply the total number of electrons in the lens. The spot size is related to the collisionless skin depth c/ω_p by the Poisson fluctuation of N independent events. Note also that neither expression contains the plasma temperature T.

It appears from these equations that for the parameters of interest for a collider at a few TeV centre of mass energy the intrinsic thermal noise of a plasma lens is not a serious limitation. The degree to which a practical lens would suffer from aberrations or from excess 'noise' due to plasma instabilities is a question which is still under investigation.

The quality of the focussing lens produced by a plasma beat wave depends also on the geometrical aberrations of the lens. The transverse electric field is produced by a two dimensional charge distribution set up by the ponderomotive force of the laser beams and to order $(\delta n/n)^2$ this may be assumed to be the solution of Poisson's equation for the instantaneous charge distribution.

The mathematically correct way to solve the Poisson equation for an axisymmetric system is to expand in terms of Bessel functions but for a solution close to the axis the same result can be obtained very quickly using a series expansion in the radius r. We assume that the charge density ρ and the potential ϕ may be written as:

$$\rho = (\rho_0 + \rho_2 r^2 + \rho_4 r^4 \ldots\ldots) \quad \cos kz$$

and

$$\phi = (\phi_0 + \phi_2 r^2 + \phi_4 r^4 \ldots\ldots) \quad \cos kz$$

Where k is the longitudinal wavenumber of the beat wave.

In cylindrical geometry, equating the coefficients of r^n in Poisson's equation gives:

$$4\phi_2 - k^2 \, \phi_0 = 4\pi\rho_0$$

$$16\phi_4 - k^2 \, \phi_2 = 4\pi\rho_2$$

$$36\phi_6 - k^2 \phi_4 = 4\pi\rho_6$$

etc.

The series solution is terminated by forcing (say) $\phi_8=0$ to give:

$$\phi_6 = - \frac{4\pi}{k^2}\rho_6$$

$$\phi_4 = - \frac{4\pi}{k^2}\rho_4 - \frac{36}{k^2} \cdot \frac{4\pi}{k^2} \rho 6$$

$$\phi_2 = - \frac{4\pi}{k^2}\rho_2 - \frac{16}{k^2} \cdot \frac{4\pi}{k^2}\rho_4 - \frac{16}{k^2} \cdot \frac{36}{k^2} \frac{4\pi}{k^2} \rho 6$$

$$\phi_0 = - \frac{4\pi}{k^2}\rho_0 - \frac{4}{k^2} \cdot \frac{4\pi}{k^2}\rho_2 - \frac{4}{k^2} \cdot \frac{16}{k^2} \frac{4\pi}{k^2}\rho_4 \ldots\ldots$$

The axial and radial electric fields are then given by:

$$E_z = - \frac{\partial\phi}{\partial z} = k \sin kz \, (\phi_0 + \phi_2 r^2 + \phi_4 r^4 \ldots\ldots)$$

and

$$E_r = - \frac{\partial\phi}{\partial r} = \cos kz \, (2\phi_2 r + 4\phi_4 r^3 + 6\phi_6 r^5 \ldots\ldots)$$

The 'spherical aberration' to lowest order in radius is then simply

$$\Delta = \frac{2\phi_4 r^2}{\phi_r} = \frac{2 r^2 \rho_4}{\rho_2}$$

With classical 'Gaussian' diffraction limited laser beams, the intensity in the far field is also a Gaussian in radius, and if we assume also that the charge density g is a Gaussian:

$$\rho = \rho_0 \exp (- \frac{r^2}{\sigma^2})$$

then by Taylor expanding the Gaussian we find that the spherical aberration is

$$\Delta = \frac{r^2}{\sigma^2}$$

The allowable spherical aberration in a thin lens is simply the ratio of the spot size to the beam size at the lens.

The above equation for Δ does not set a lower limit on the radius of the plasma lens since the radial focussing field decreases as the laser beam radius is increased. For a given set of lens and laser parameters the spherical aberration determines the maximum radius of the particle beam.

A4.4 A TWO DIMENSIONAL FLUID MODEL OF THE PLASMA BEAT-WAVE ACCELERATOR

P Gibbon and A R Bell (Imperial College)

There has been much interest of late in the concept of laser-driven particle acceleration schemes. One such scheme, the plasma 'Beat Wave' Accelerator (BWA) (A4.9) offers the possibility of a very high accelerating field of the order 10 GV m^{-1}, which is 100 - 1000 times that of a conventional synchrotron. Theoretical work on the BWA has been concerned with both 'wave dynamics' and 'particle dynamics'. The former is based on the growth of a large amplitude electrostatic field in the plasma (A4.10). Considerations of the latter aspect include the acceleration of injected particles by the electrostatic field to the high energies required for modern particle physics experiments (A4.11).

An understanding of the laser-plasma wave interactions is essential if we are to be confident that the above-mentioned plasma wave is of sufficiently high quality to accelerate a beam of particles. For example, particle simulations by Joshi et al (A4.12) have shown filamentation of the laser pumps, causing transverse break-up of the plasma wave, with adverse effects on an injected particle beam.

When two collinear laser beams are sent into a plasma, they excite a longitudinal electric field (plasma wave). This grows until it reaches a saturation level determined by one or more of several effects, some of which are listed below:

i) Pulse length
ii) Relativistic detuning
iii) Collisional damping
iv) Beat-plasma frequency mismatch: $\omega_o - \omega_1 = \omega_p + \delta$

These effects have been studied extensively in 1D fluid models (A4.10, A4.13 and A4.14). Another important aspect of the 'wave dynamics' of the BWA is the Raman Cascade which results from the scattering of the two laser pumps $(\omega_o, \underline{k}_o)$ and $(\omega_1, \underline{k}_1)$ into other electromagnetic modes $(\omega_m, \underline{k}_m)$.

$$\omega_m \rightarrow \omega_p + \omega_{m-1}$$

$$\omega_m + \omega_p \rightarrow \omega_{m+1}$$

Exact analytical solutions for this process under certain conditions have been found by Karttunen (A4.14).

In this report we outline a 2D fluid model of the plasmon/em cascade system. This model will allow us to study several features which cannot be included in a 1D prescription:

i) 2D structure of the plasma wave amplitude.
ii) Inclusion of radial field in the plasma wave equation.
iii) Diffraction and self-focussing of e.m. waves.
iv) Growth of em sidebands with non-collinear $\underline{k}$-vectors.

Some numerical results concerning i) and ii) above will be presented; the effect of iii) and iv) on the plasmon and the implications for pump depletion are currently being investigated.

Starting from the cold, collisionless Lorentz-Maxwell equations for a relativistic electron fluid, with fixed ions, we find after some manipulation:

$$\frac{\partial^2 \underline{E}}{\partial t^2} + \frac{\omega_p^2}{\gamma}\left[\underline{E} - \frac{(\underline{v}.\underline{E})\underline{v}}{c^2}\right] + c^2 \nabla \Lambda (\nabla \Lambda \underline{E}) = -\frac{\omega_p^2}{\gamma}\,\underline{v} \Lambda (\nabla \Lambda \underline{A}) - \frac{e n_o}{\epsilon_o}(\underline{v}.\nabla)\underline{v} + \frac{e}{\epsilon_o}\frac{\partial}{\partial t}(n\underline{v}) \qquad (1)$$

where the quantities $\underline{E}$, $\underline{v}$, n_o and $\underline{A}$ have their usual meaning, and $n = n_e - n_o$ is the perturbed electron density. Splitting the fields and fluid velocities into 'fast' and 'slow' components representing the em and 'background' electron fluid timescales respectively, we may then average over the fast time-scale $\tau_o = 2\pi/\omega_o$ (noting that $\omega_o >> \omega_p$) to obtain separate equations for the plasma and e.m. waves:

$$\left[\frac{d^2}{dt^2} + \frac{\omega_p^2}{\gamma^3}\right]\underline{E}_p = -\frac{e\omega_p^2}{2m} < \nabla(\underline{A}^2) >_{\tau_o}$$

$$\left[\frac{\partial^2}{\partial t^2} - c^2\nabla^2 + \frac{\omega_p^2}{\gamma}\left\{1 - \left|\frac{e\underline{A}}{mc}\right|^2\right\}\right]\underline{A} = \frac{e^2}{m\epsilon_o} n\underline{A} \qquad (2)$$

We now let each field be the product of a slowly varying envelope times a rapidly varying phase, so that;

$$\underline{E}_p = \frac{1}{2} (\underline{E}\, e^{i\psi} + \underline{E}^*\, e^{-i\psi})$$

$$A = \frac{1}{2} \sum_m (A_m e^{i\psi_m} + A_m^* e^{-i\psi_m}) \qquad (3)$$

where we have split the em vector into its cascade modes m. The laser pumps are represented by m = 0 and m = 1. We choose the phases ψ and ψ_m such that we may solve the equations numerically in a 'window' following the front of the laser pulse. This offers considerable computational advantage over an earlier 1D numerical model (A4.13). Substitution of equations (3) into (2), using the matching condition $\omega_o - \omega_1 = \omega_p + \delta$, and neglecting harmonic terms, gives the normalised envelope equations:

$$\left[\frac{\partial}{\partial z} - i\delta + \frac{3i}{16} |\underline{E}|^2\right] \underline{E} = \frac{1}{4} \sum_m [\nabla + i\underline{\Delta}]\, a_m a_{m-1}^* \qquad (4a)$$

$$\left[\frac{\partial}{\partial t} - \frac{i}{2\omega_m} \left[\frac{\partial^2}{\partial x^2} + \frac{\partial^2}{\partial z^2}\right]\right] a_m = \frac{1}{\omega_m} [g^* a_{m+1} - g\, a_{m-1}] \qquad (4b)$$

where:

$$\delta \equiv \frac{\omega_p^2 - \Delta\omega^2}{2\Delta\omega^2}$$

$$g = \frac{1}{4} (E_z - i\nabla.\underline{E})$$

In the plasma wave equation $\partial E/\partial t$ because comparison with $\partial E/\partial z$ reveals $\partial_t E/\partial_z E \approx \lambda_0/L$, where λ_0 is the laser wavelength; L is the scalelength of the pulse profile, typically $10^3\, \lambda_0$ for experimental parameters (A4.15).

We have also neglected any slow $\underline{B}$-fields which might arise in the plasma by setting $\nabla \wedge \underline{E}_p = 0$. This assumption is subsequently contradicted in solving equations (4) by allowing $\underline{E}_p$ to have both longitudinal and transverse parts, and by setting $\nabla = (\partial_x, 0, \partial_z)$. However, to include the $\underline{B}$-field we require a full quasi-linear treatment taking into account harmonic terms which were neglected in

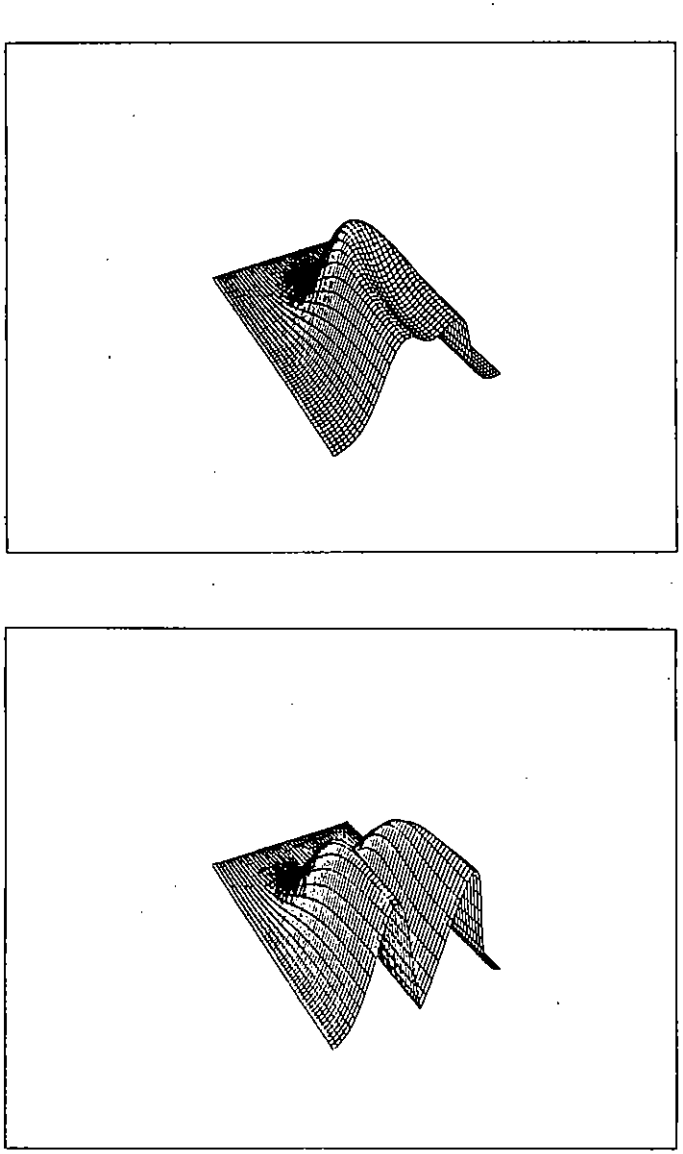

Fig A4.5 *(a) Longitudinal field E_z and (b) radial field E_x as a function of x andz for pulse intensity I_o = 2x10¹⁴Wcm⁻², spot size $X_{fwhm} = 20c/\omega_p$, pulse length T_{fwhm} = 200 ps. The grid is $9000c/\omega_p$ long and $60c/\omega_p$ (400 μm) wide. Maximum field values are: E_z(max) = 0.09, E_x (max) = 0.009.*

deriving equations (4). E_x is included to investigate its effect on the saturation of E_z via the $|E|^2$ term in Equation (4a). We expect E_x to become important when the transverse scalength $L_x \approx c/\omega_p$, so that the source terms in (4a) are of the same order.

The following plots are obtained from the numerical solution of Equation (4a) and show the plasma electric fields after a single timestep, ie: we regard the em pumps as constant, neglecting cascading, and integrate $E_z$and E_x over the space mesh. In these examples, the laser parameters used were close to those to be used in the proposed IC/RAL Beat-Wave experiment (Section A2.1). The pump wavelengths are 1.064μm and 1.053μm; the plasma frequency and beat frequency (assuming perfect matching) $\omega_p = \Delta\omega = 1.85 \times 10^{13}\ s^{-1}$. All figures shown are symmetric about the x=0 axis; the laser pulse propagates in the z-direction.

Figure A4.5(a) shows the topography of the longitudinal field E_z for a 200ps gaussian pulse with intensity $2 \times 10^{14} Wcm^{-2}$. The ratio of the pulse length (T_{fwhm}) to the Rosenbluth-Liu saturation time (τ_{rl}) is 0.65 in the case. In Figure A4.6 the ratio is 1.6, which results in the more pronounced structure observed. The latter is due entirely to the variation in the relativistic saturation time τ_{rl} and amplitude E_{sat} across the width of the pulse. In Figure A4.6(b), the radial field $E_x$also exhibits modulations in the z-direction (not present in Figure A4.5(b), owing to the higher laser intensity off axis (as well as on axis).

The inclusion of E_x did not significantly affect E_z in these examples, even though the ratio E_z:E_x was approximately 1:0.3 in Figure 2. However, it can be shown that reducing the spot size even further, so that $E_z/E_x \approx 1$, qualitatively alters the growth and saturation of E_z. To investigate this regime properly, we should include plasma harmonics and B-field (Section A4.5).

A4.5 ELECTRON NON-LINEARITIES IN LANGMUIR WAVES WITH APPLICATION TO BEAT-WAVE EXPERIMENTS

A R Bell and P Gibbon (Imperial College)

Much attention has been paid to Langmuir wave non-linearities produced by ion motion as expressed in the Zhakarov equations (reviewed by Goldman, A4.16). It has been known for some time that two- and three-dimensional Langmuir waves also exhibit electron

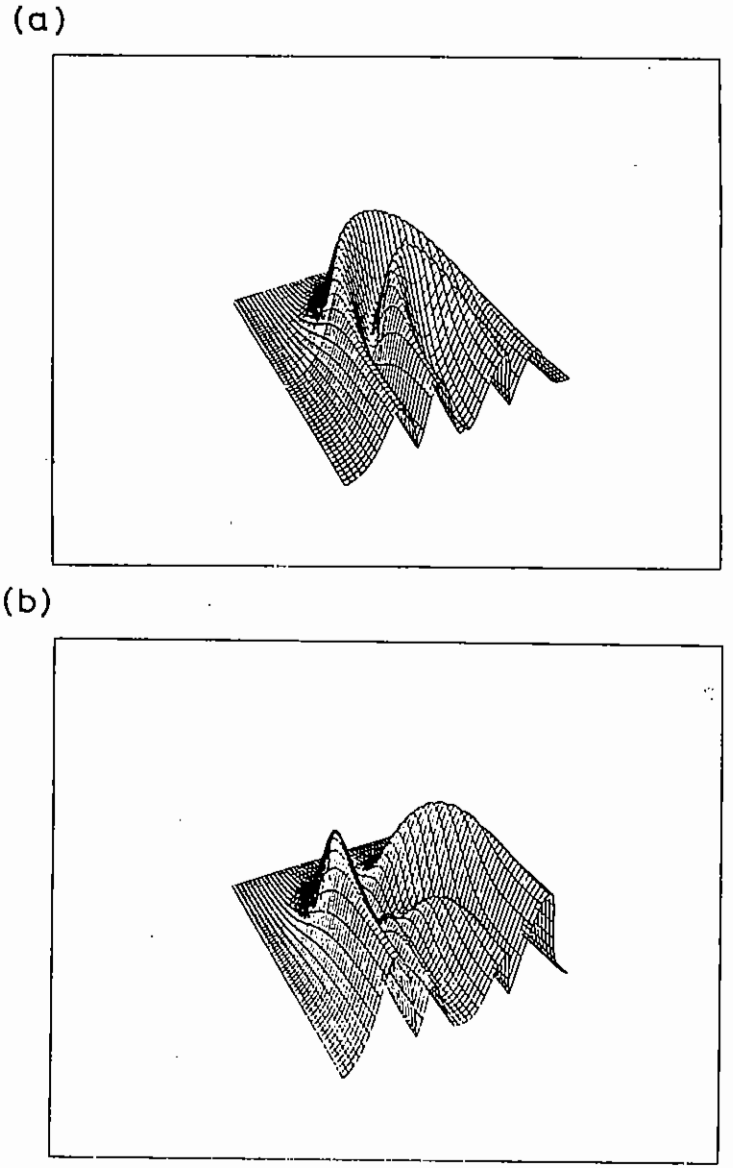

Fig A4.6 *(a) Longitudinal field and (b) radial field for $I_o = 8x10^{14}Wcm^{-2}$, $X_{fwhm} = 10c/\omega_p$, $T_{fwhm} = 200$ ps. The total laser energy is the same as in Fig A4.5; the grid size $9000c/\omega_p$ x $30c/\omega_p$. Maximum field values: $E_z(max) = 0.13$, $E_x(max) = 0.035$.*

non-linearities (A4.17, A4.18 and A4.19). Beat-wave experiments present a new environment in which electron non-linearities may be important. Indeed, the non-linearity usually considered in this context is that due to the relativistic mass increase of oscillating electrons. Ion motion is less important due to the relatively slow inertial ion response. Previously, the non-linear equations have been developed in Fourier space (with the exception of Dawson, A4.18), and have neglected the magnetic field. We present a formulation in configuration space which includes magnetic field. We find that the additional magnetic terms are usually comparable in magnitude with or exceed the electrostatic terms. When the scalelength for transverse structure on the Langmuir wave is the collisionless skin depth, the magnetic non-linearity is also comparable with the relativistic non-linearity and must not be ignored. We assume the cold plasma and quasi-linear approximations.

We adopt units in which c=1, e=1, m=1, and the fixed background ion density is $n_0 = 1$. The starting equations are then

$$\nabla \times B = nv + E \qquad \nabla \times E = -\dot{B}$$
$$\nabla . B = 0 \qquad \nabla . E = n-1$$
$$\dot{p} + v.\nabla p = E + v \times B \qquad p = v(1-v^2)^{-1/2}$$

where v(x) is the velocity of electrons instantaneously at x, and p(x) is the corresponding momentum. Our aim is to derive a Langmuir wave equation which is correct to third order in amplitude. We therefore manipulate these equations, neglecting all terms of 4th order and above, and arrive at two simultaneous equations.

$$\ddot{u} + u = (u.\nabla - u\nabla .)u - (u.\nabla - u\nabla .)(s.\nabla)\dot{u} + \nabla \times B + s.\nabla(\nabla \times B) + \frac{\partial}{\partial t}(u \times B) - \frac{\partial^2}{\partial t^2}(u^2 u/2)$$

$$\nabla \times (\nabla \times B) + \dot{B} + B = \nabla \times (u\nabla .\dot{u})$$

s(x,t) is the vector displacement of an electron originally at position x, and $u = \partial s/\partial t$ is the electron velocity.

Using the standard techniques of quasi-linear analysis, we expand u and B as a sum of harmonics

$$u = \sum_{-\infty}^{\infty} u_m \exp(imt) \qquad B = \sum_{-\infty}^{\infty} B_m \exp(imt)$$

where $u_{-m} = u_m^*$ and $B_{-m} = B_m^*$

and u and B are slowly varying in time. After further algebraic manipulation, we get

$$2i\nabla .\dot{u}_1 = S_E + S_B + S_R$$

where

$$S_E = \sum_{p,q,r=+1} \delta_{1-p-q-r} \nabla .(\tfrac{p}{2-r}(u_r.\nabla - u_r\nabla .)(u_p.\nabla - u_p\nabla .)u_q) + r u_r.\nabla u_p.\nabla u_q - r u_r(\nabla u_p : \nabla u_q))$$

$$S_B = i\nabla .(2u_{-1}.\nabla(\nabla \times B_2)/3 + u_{-1} \times B_2 + u_1 \times B_0)$$

$$S_R = \sum_{p,q,r=+1} \delta_{1-p-q-r} \nabla .((u_p.u_q)u_r)/2$$

and S_E, S_B and S_R are the electrostatic, magnetic and relativistic non-linearities respectively.

The equations determining the 2nd order magnetic field are

$$\nabla \times (\nabla \times B_2) - 3B_2 = i\nabla \times (u_1\nabla .u_1)$$

$$\nabla \times (\nabla \times B_0) + B_0 = i\nabla \times (u_{-1}\nabla .u_1 - u_1\nabla .u_{-1})$$

It is clear from these equations that the electrostatic and magnetic non-linearities disappear in one dimension leaving the linear equation valid to 3rd order (and in fact to all orders) apart from the relativistic non-linearity.

We now consider the case of a laterally modulated plane wave

$$u_1 = \nabla(W_1(x)e^{ikz})$$

with a magnetic field in the y-direction only

$$B_m = b_m e^{imkz}$$

This example can be used to examine a plane wave of limited width, and therefore resembles a beat-wave generated Langmuir wave where the Langmuir wave is approximately a cylindrically bounded plane wave ie it can be thought of as a plane wave travelling in the z-direction

with a phase velocity close to the speed of light but occupying the region of space defined by $x^2+y^2 \leq r_o^2$, where r_o^2 is the radius of the laser beams. The modulation in the z-direction usually has a length-scale much greater than r_o. u_1 is written as the gradient of a potential to ensure that it is purely longitudinal to first order.

In this case,

$$2i \frac{\partial}{\partial t} (W_1''-K^2W_1) = S_E + S_B + S_R$$

where

$$S_E = k^2(3W_{-1}W_1'W_1''' + 3W_1W_1'W_{-1}''' - W_1W_{-1}'W_1''' + 4W_1'W_{-1}'W_1'' + 2W_1'^2W_{-1}'' + 4W_1W_1''W_{-1}'' - 3W_{-1}W_1''^2)/3$$

$$S_B = k(2W_{-1}'b_2''/3 + (4W_{-1}'' + 4k^2W_{-1} - 3W_{-1})b_2'/3 + (8k^2/3 - 2)W_{-1}'b_2 + W_1b_0')$$

$$S_R = -3k^4W_1^2W_{-1}/2 + k^2(W_1''W_{-1} + W_1''W_{-1}^2/2 - W_1'W_1' + 3W_{-1}'^2/2) + 3(W_1'^2W_{-1})''/2$$

$$(4k^2-3)b_2 - b_2'' = k(W_1W_1''' - W_1'W_1'')$$

$$b_0-b_0'' = k(2k^2W_1W_{-1} - W_{-1}W_1'' - W_1W_{-1}'')'$$

and

$$b' = \frac{\partial b}{\partial x} \quad \text{and} \quad W' = \frac{\partial W}{\partial x}$$

b_o and $b_2\exp(2ikz)$ are the y-components of B_0 and B_2 respectively. b_o decays evanescently to large and small x (ie outside the wave column) because the oscillation frequency is below the plasma frequency. Electromagnetic waves emitted at $2\omega_p$ are allowed to propagate, but, unless $k^2<3/4$, the source term has a spatial frequency which is too large to match to a solution of the e.m. dispersion relation, and b_2 also decays evanescently.

In the case of a beat-wave generated Langmuir wave, the phase velocity is close to the speed of light, and hence we take k=1 since in our units

$c/\omega_p=1$.

The relativistic term dominates for $L \geq 1$ ($L=W_1/W_1'$), but when $L \sim 1$, the terms are of equal magnitude. We investigate the regime $L \sim 1$ by considering the magnitude of the terms for a Gaussian wave profile.

$$W_1 = A \exp(-x^2/2D^2)$$

Figure A4.7 is a plot of $\Delta n/n$, b_o, b_2, S_R, S_E and S_B as functions of distance x from the wave centre when D=1, ie the radius of the beam is one collisionless skin-depth. $\Delta n/n$ is the magnitude of the fractional density fluctuation. The magnetic field is in units of $m\omega_p/e$. It can be seen that the magnetic non-linearity is larger than the relativistic non-linearity and must be included in any non-linear analysis of waves with this transverse extent. Even waves which are wider than this will have strong magnetic non-linearities if they have sub-structure, eg caused by laser beam hot-spots, on the scale of a collisionless skin-depth.

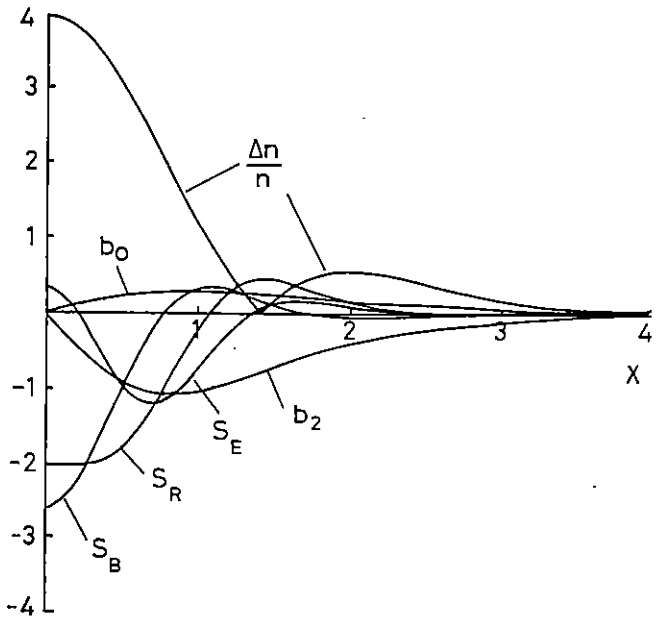

Fig A4.7 *Transverse spatial profiles of wave amplitude, magnetic field, and non-linear terms. a) $(\Delta n/n)/A$, b) b_o/A^2, c) b_2/A^2, d) S_R/A^3, e) S_E/A^3, f) S_B/A^3.*

A4.6 "SPARK", A TIME DEPENDENT FOKKER-PLANCK CODE

E M Epperlein and A R Bell (Imperial College)

It has long been realized that the accurate modelling of electron transport in laser fusion plasmas requires the solution of the electron Fokker-Planck equation. This requirement becomes particularly stringent when, as a result of non-uniformity in the laser illumination, the transport is two dimensional. To this date there exists several computer codes which solve the Fokker-Planck equation in 1-D. None of them, however, are easily convertible to 2-D.

We set out to construct a 2-D Fokker-Planck code in November 86 by initially formulating an efficient 1-D code. This has now been successfully accomplished with the code SPARK(= SPeedy and Reliable Kinetics). The following important features have been included during its construction:

1) Particle and energy conservation
2) Stability
3) Accuracy
4) Reliability
5) Speed

The first criterion has been achieved by appropriately differencing the kinetic equation in conservative form and using "Chang - Cooper" interpolation for the distribution (as described in detail by Langdon, A4.20). Stability has been achieved by integrating the kinetic equations using the standard A.D.I. method (A4.21). Accuracy to second order in the time step has been used as far as possible, with the exception of certain non-linear terms like the electric field and Rosenbluth potentials. Reliability in the coding was chosen at the expense of some loss in computational speed.

The code can reproduce the results obtained by the Kho et al in 1986, (A.22) as shown in Fig A4.8. Here we used only 30 velocity groups (rather than 80) and the running time of the present unoptimised version of SPARK is approx 5 CPU sec for every picosecond

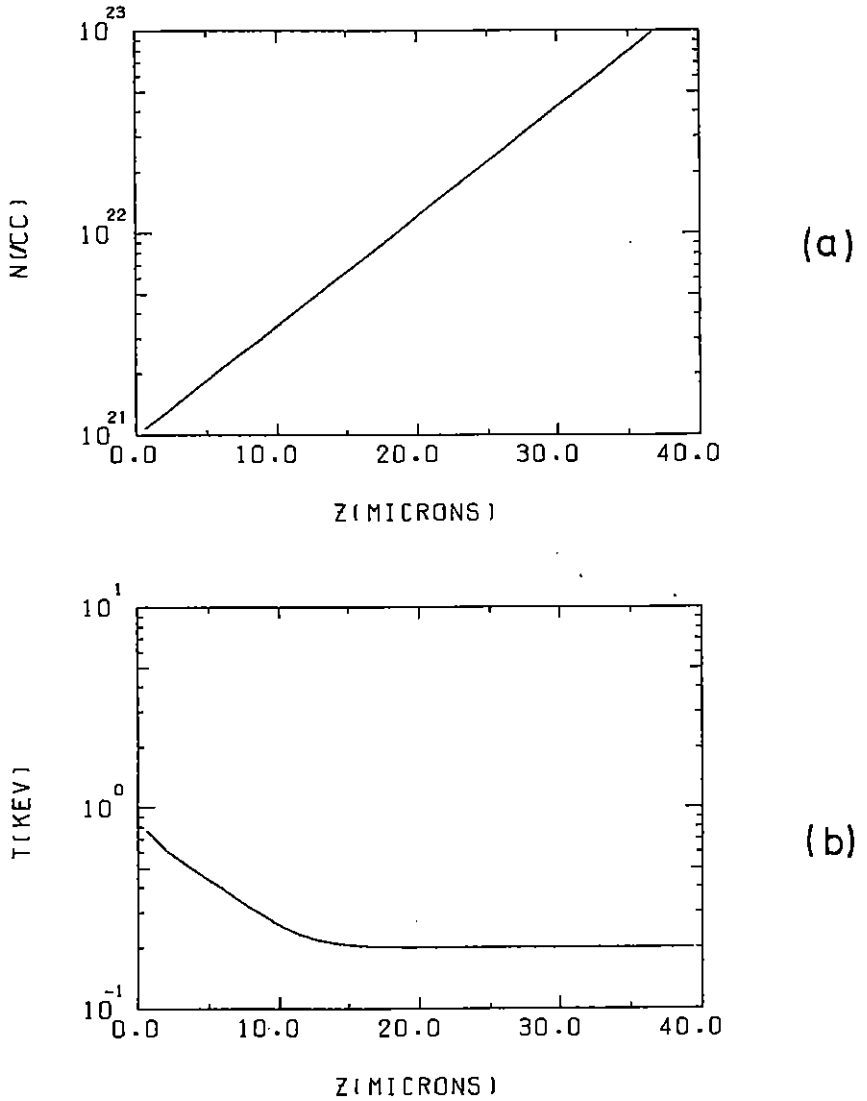

Fig A4.8 Profiles of a) density, b) temperature, c) heat flow/free streaming, d) E-field, e) fo, f) fo/$f_{maxwellian}$ and g) f_2/fo.

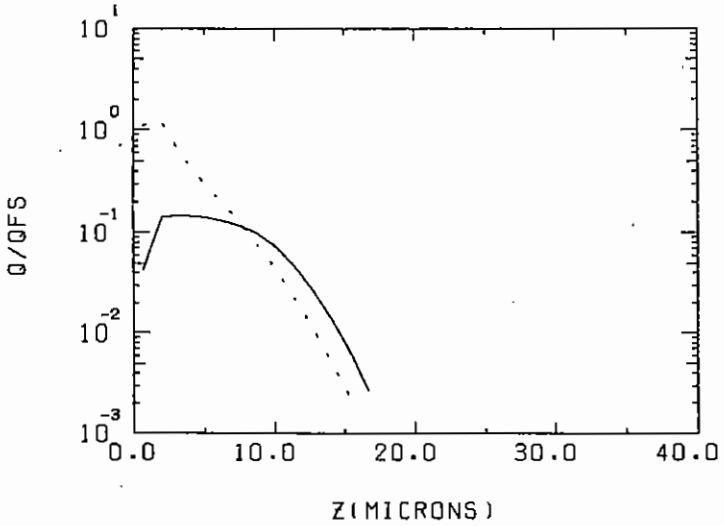

(c)

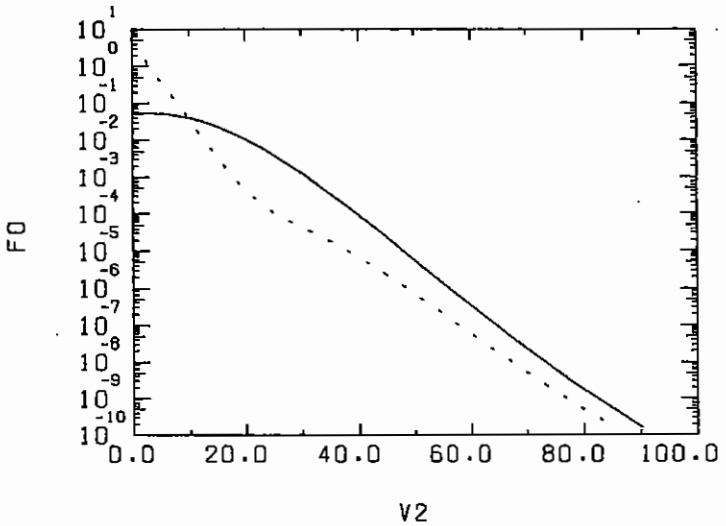

(e)

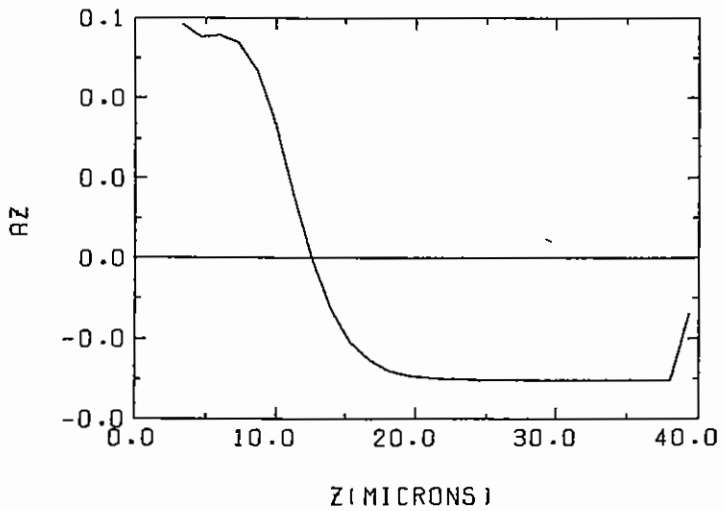

(d)

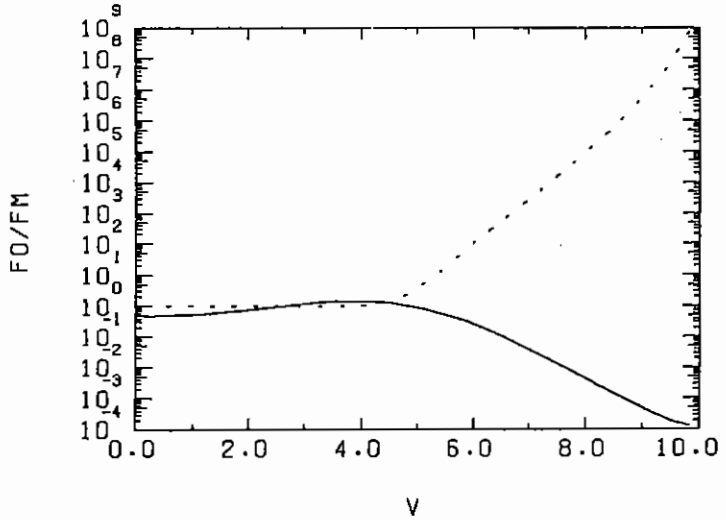

(f)

Fig A4.8 Profiles of a) density, b) temperature, c) heat flow/free streaming, d) E-field, e) fo, f) fo/$f_{maxwellian}$ and g) f_z/fo.

of simulation on the CRAY 1-S. The present time-step constraint is mainly due to the electric field calculation, and improvements should be fairly straight forward.

The following extensions to SPARK are currently being considered.

1) Inclusion of momentum exchange between electrons.
2) Allowance for the hydrodynamic response of the plasma.
3) Deposition of the laser energy self consistently in the corona.
4) Addition of an extra spatial dimension (with B-fields included).

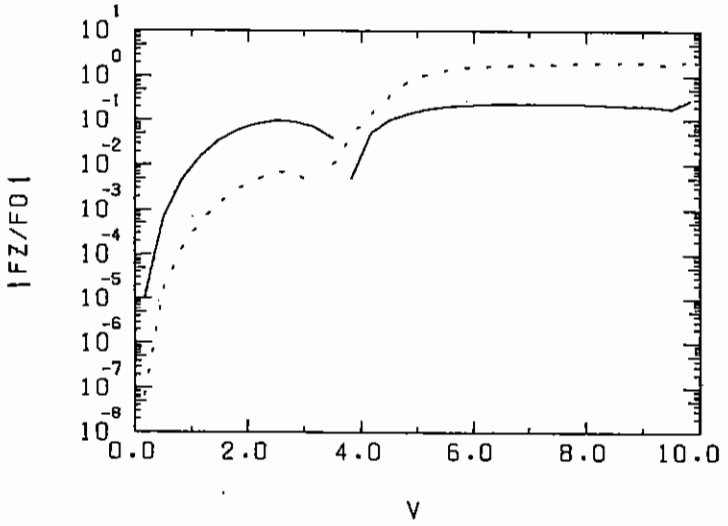

(g)

Fig A4.8 Profiles of a) density, b) temperature, c) heat flow/free streaming, d) E-field, e) fo, f) fo/$f_{maxwellian}$ and g) f_z/fo.

A4.7 HEAT TRANSPORT CALCULATIONS WITH A FOKKER-PLANCK CODE

S Jorna and L Wood (St Andrews University)

As a result of our studies on non-classical heat conduction we now have a Fokker-Planck code which is independent of those based on the Lawrence Livermore Laboratory code hierachy. The code has been formulated in spherical geometry (at present with azimuthal symmetry) and treats velocity anisotropy by calculating the Rosenbluth potential from the anisotropic, most recently calculated, single-particle distribution function. That retaining the full anisotropy in calculating the potential is important is illustrated by two examples. In the first example, we study the randomisation of a bi-Maxwellian plasma in which the time temperatures are initially greatly different. In the second, we study the problem of heat transport in a diode in which the hot boundary is treated by a bi-Maxwellian distribution.

The isotropisation of initially highly anisotropic velocity distributions has recently been examined analytically by Schamel, Duchs and Stringer (A4.23). They conclude that the rate of isotropisation of a bi-Maxwellian distribution (normalized to unity)

$$f(\mu,v,t) = \pi^{-\frac{3}{2}} (2\langle\mu^2v^2\rangle)^{-\frac{1}{2}} \langle(1-\mu^2)v^2\rangle^{-1} \exp[-\mu^2v^2/2\langle\mu^2r^2\rangle - (1-\mu^2)v^2/\langle(1-\mu^2)v^2\rangle], \quad (1)$$

depends on whether the ratio, ϵ say, of the perpendicular temperature ($T_\perp$) to the parallel temperature ($T_{\parallel}$) is initially much larger or much smaller than unity. Their assumption that the distribution function is throughout the isotropisation process a bi-Maxwellian would seem to be unreasonably restrictive. To study this process without making this assumption, we have developed a Fokker-Planck code in which the Rosenbluth potentials are calculated exactly from the anisotropic distribution function.

In spherical coordinates, the Fokker-Planck equation takes the form (we assume azimuthal symmetry)

$$\frac{\partial f}{\partial t} + \frac{v\mu}{r^2}\frac{\partial}{\partial r}(r^2 f) + \frac{v}{r}\frac{\partial}{\partial \mu}[(1-\mu^2)f] + \frac{eE_r}{m}\left[\frac{(1-\mu^2)}{v}\frac{\partial f}{\partial \mu} + \mu\frac{\partial f}{\partial v}\right] = \frac{1}{\Gamma}\left(\frac{\partial f}{\partial t}\right)_c \qquad (2)$$

where the single particle distribution function f depends on v, the total velocity, μ the cosine of the angle between $\bar{v}$ and the radial vector, $\bar{r}$, the radial distance r, and E_r is the radial component of the electric field.

The collision term for like-particle interactions is as defined by Rosenbluth, MacDonald and Judd (A4.24):

$$\begin{aligned}\frac{1}{\Gamma}\left(\frac{\partial f}{\partial t}\right)_c &= -v^{-2}\left(\frac{\partial}{\partial v}\right)\left(f\frac{\partial h}{\partial v}\right) - v^{-2}\left(\frac{\partial}{\partial \mu}\right)\left[f\,(1-\mu^2)\frac{\partial h}{\partial \mu}\right] \\ &+ (2v^2)^{-1}\left(\frac{\partial^2}{\partial v^2}\right)\left(f\,v^2\frac{\partial^2 g}{\partial v^2}\right) \\ &+ (2v^2)^{-1}\left(\frac{\partial^2}{\partial \mu^2}\right)\left\{f_a\left[v^{-2}(1-\mu^2)^2\frac{\partial^2 g}{\partial \mu^2} + v^{-1}(1-\mu^2)\frac{\partial g}{\partial v} - v^{-2}\mu(1-\mu^2)\frac{\partial g}{\partial \mu}\right]\right\} \\ &+ v^{-2}\left(\frac{\partial^2}{\partial \mu \partial v}\right)\left\{f\,(1-\mu^2)\left[\frac{\partial^2 g}{\partial \mu \partial v} - v^{-1}\frac{\partial g}{\partial \mu}\right]\right\} \\ &+ (2v^2)^{-1}\left(\frac{\partial}{\partial v}\right)\left\{f_a\left[-v^{-1}(1-\mu^2)\frac{\partial^2 g}{\partial \mu^2} - 2\frac{\partial g}{\partial v} + 2\mu v^{-1}\frac{\partial g}{\partial \mu}\right]\right\} \\ &+ (2v^2)^{-1}\left(\frac{\partial}{\partial \mu}\right)\left\{f\left[v^{-2}\mu(1-\mu^2)\frac{\partial^2 g}{\partial \mu^2} + 2\mu v^{-1}\frac{\partial g}{\partial v} + 2v^{-1}(1-\mu^2)\frac{\partial^2 g}{\partial \mu \partial v} - 2v^{-2}\frac{\partial g}{\partial \mu}\right]\right\}, \end{aligned} \qquad (3)$$

with $\Gamma = (4\pi e^4/m^2)\ln\Lambda$, and Λ the ratio of the Debye length to the classical distance of closest approach of the scattered particles. The potentials h and g are defined by

$$h(\bar{v}) = 2\int f(\bar{v}')|\bar{v} - \bar{v}'|^{-1} d\bar{v}, \qquad (4)$$

$$g(\bar{v}) = \int d(\bar{v}')|\bar{v} - \bar{v}'|\, d\bar{v}\,. \qquad (5)$$

For the case of azimuthal symmetry here considered the ϕ- integration can be performed to yield the two-dimensional integrals

$$h(v,\mu) = 2\int_0^\infty v'^2 dv' \int_1^1 f(v',\mu')\Lambda(v',\mu';v,\mu)\, d\mu', \qquad (6)$$

$$g(v,\mu) = \int_0^\infty v'^2 dv' \int_1^1 f(v',\mu')\, Q\,(v',\mu';\, v,\mu)\, d\mu', \qquad (7)$$

where the functions Λ and Q are defined in terms of the complete elliptic integrals K and E (note the misprint in Eq (33) of Rosenbluth et al (A4.24)):

(loc cit.))→

$$\Lambda = \frac{4}{P(v,v',\mu,\mu')}\, K\left\{\left[\frac{Q(v,v';\mu,\mu')}{P(v,v';\mu,\mu')}\right]^{1/2}\right\}, \qquad (8)$$

$$Q = 4P(v,v';\mu,\mu')\, E\left\{\left[\frac{Q(v,v',\mu,\mu')}{P(v,v';\mu,\mu')}\right]^{1/2}\right\}, \qquad (9)$$

where to save writing we have introduced the further abbreviations

$$P(v,v';\mu,\mu') = (v^2 + v'^2 - 2vv'(\mu\mu' - [(1-\mu^2)(1-\mu'^2)]^{1/2}))^{1/2}, \qquad (10)$$

and

$$Q(v,v';\mu,\mu') = 4vv'\,[(1-\mu^2)(1-\mu'^2)]^{1/2} \qquad (11)$$

If the Rosenbluth potentials are assumed to be isotropic h and g have no μ-dependence and the collision term reduces to three terms associated with friction, diffusion and scattering.

There is no radial dependence in this problem and Eq (2) is solved by the method of fractional steps (A4.25) in μ and v. Second-order accuracy is obtained by mixing explicit and implicit components in equal proportions. The boundary condition in μ is $\partial f/\partial\mu = 0$ at $\mu=0$. The boundary conditions in v are $\partial f/\partial v = 0$ at $v = 0$ and f decays to zero at the cut-off velocity, taken to be six times the thermal velocity. The code preserves a Maxwellian distribution; with radial dependence included and without collisions it calculates the Landau damping decrement with an accuracy of better than 1%, and with collisions included it agrees to better than 1% with the calculations of Dolinsky (A4.26) for the relaxation of a Gaussian hump on a Maxwellian.

If we now suppose that initially the distribution is given by the bi-Maxwellian, Eq (1), with

$$\epsilon \equiv T_\perp/T_\parallel \equiv \langle(1-\mu^2)v^2\rangle \,/\, 2\langle\mu^2 v^2\rangle = 10 \qquad (12)$$

the isotropisation follows curve c in Figure A4.9. Curve a is obtained by employing an angular average for f in calculating h and g from Eqs (6) and (7). The co-ordinate is the time scaled by the self-collision time $t_o = 3.325 \times 10^{-16} T^{3/2}/_{\ln\Lambda}$, where $T = \frac{1}{3}(T_{||} + 2T_{\perp})$ expressed in eV.

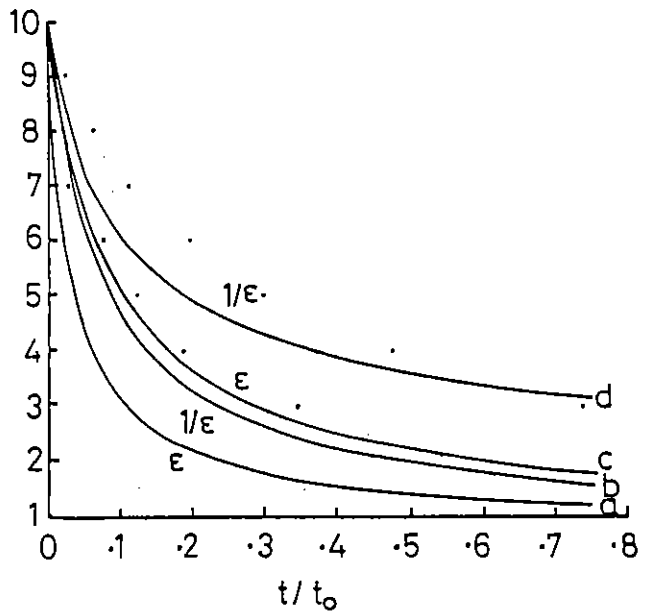

Fig A4.9 *Isotropisation of initial bi-Maxwellian distribution for $\epsilon \equiv 1\perp/T|| = 10$ at $t = 0$ (curves a,c) and for $\epsilon = 0.1$ at $t = 0$ (curves b,d).*

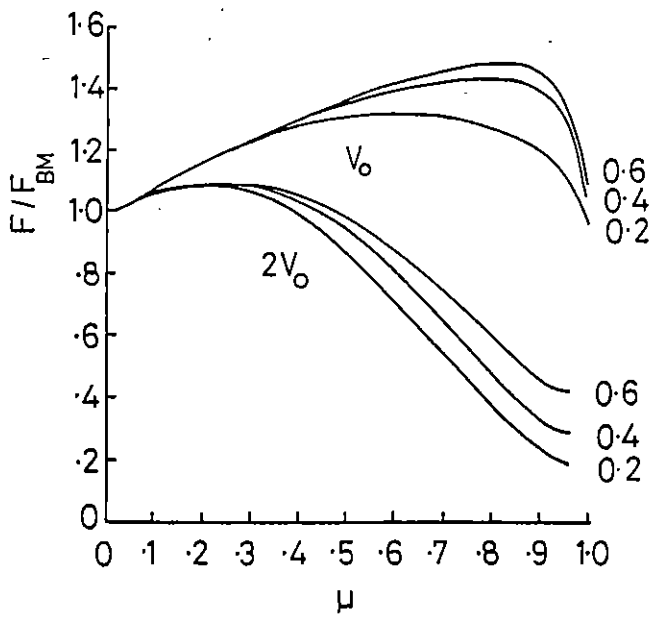

Fig A4.10 *Ratio of the calculated distribution function f to the bi-Maxwellian (with T⊥ and T|| calculated from f) as a function of μ for $\epsilon = 10$ at $t = 0$. Ratios are given at the thermal velocity (V_o) and $2V_o$ at times $0.2t_o$, $0.4t_o$, and $0.6t_o$.*

It is clear that the rate of isotropisation is in both cases faster than that for small temperature differences (measured by t_o). The dots are the analytic results obtained by Schamel, Duchs, and Stringer (A4.23), and the agreement is reasonably good. Thus, for ϵ initially much larger than unity, the bi-Maxwellian assumption leads to a fairly accurate estimate. In fact, as Figure A4.10 shows f does not depart greatly from a bi-Maxwellian form throughout the isotropisation, except at very high velocities.

The situation is quite different for $\epsilon \lesssim 1$ as shown by curves b and d in Figure A4.9. The isotropisation is now slower than that for small temperature differences and the agreement with the analytic results (upper series of dots) at early times is no longer good: the distribution function differs significantly from the corresponding bi- Maxwellian (same $T_\perp$ and $T_\parallel$) as indicated in Figure A4.11. The qualitative difference between the code in which an angular average was used for f (Curve b in Fig A4.9) and the code without this approximation (Curve d) is as for $\epsilon \gg 1$, with the former showing the faster rate of isotropisation.

Because of the two degrees of freedom in the perpendicular direction and the single degree of freedom in the parallel direction, it is not surprising that the flat (oblate) distribution isotropises faster than the elongated (prolate) distribution. The good agreement for $\epsilon \gg 1$ with the analytic results and the lack of it for $\epsilon \ll 1$ can be traced to the fact that for $\epsilon \gg 1$ the distribution function is peaked around $\mu=0$ where the correct boundary condition, $\partial f/\partial\mu = 0$, is also satisfied by a bi-Maxwellian, while for $\epsilon \ll 1$ the peak of the distribution function is at $\mu = \pm 1$ and an inaccurate boundary condition at these points, such as the assumption that f is a bi-Maxwellian there, should result in the inaccuracy demonstrated in this paper. Thus, for beam-like distributions the bi-Maxwellian assumption appears to be invalid.

In laser fusion plasmas where because of the absorption process (eg resonant absorption) or because of instabilities (eg Weibel instability) the distribution function is initially highly anisotropic it may well be important not to make the usual linearising assumptions in calculating the Rosenbluth potentials:

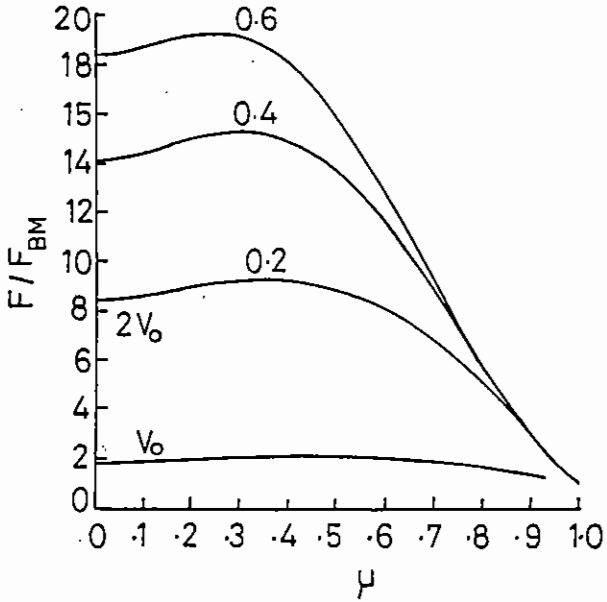

Fig A4.11 As for Fig 4.9 but with ϵ = 0.1 initially. The curves for V_o at successive times are not resolved on this scale.

accurate knowledge of the electron distribution function would for instance be needed to interpret laser-plasma X-ray spectra. The non-linear nature of the collision term should also be taken into account in the assessment of neutral beam heating and current-drive in magnetic confinement experiments.

In some cases the plasma is heated by charged particles whose distribution function is not isotropic. Examples are heating by resonant absorption in laser-heated plasmas and neutral beam heating and current-drive in magnetic confinement experiments. In these cases it should be especially important to take account of the anisotropy of the distribution function in calculating the Rosenbluth potentials and we expect a significant difference between the heat fluxes calculated from the Anisotropic and Isotropic Codes. It has, for instance, been shown by Schamel, Duchs and Stringer (A4.23) and by Jorna and Wood (A4.27) that the rate of isotropisation in a plasma described by a strongly anisotropic distribution functions depends on the degree of anisotropy and on the shape of the velocity distribution, for instance; whether it is oblate or prolate.

To study the effect of temperature anisotropy, suppose that in a diode with spherical boundaries (r_2 = 120μm, $r_2 - r_1$ = 12μm) the outer boundary is heated from 1 keV to 2 keV in 0.3 t_0 but the distribution is given by the bi-Maxwellian (t is the electron self-collision time) described previously.

The temperature components are chosen such that their ratio $T_{||}/T_{\perp}$ at r_2 is initially 2. The background plasma is initially described by a Maxwellian at 1 keV and to avoid high-frequency transients the anisotropy is introduced over a time 0.1 t_0.

The inner boundary is initially at the ambient temperature of T_0 = 1 keV, and the net zero current condition is as given in the previous section, but with a bi-Maxwellian injected at r_2. To bring out the significance of the anisotropy we have calculated the heat fluxes and temperatures with the Anisotropic and Isotropic Codes. Figure A4.12 shows the propagation of the heat flux into the plasma at different times. At the latest time recorded there (0.35 t_0) the steady-state has essentially been reached. The heat flux calculated with the Isotropic Code differs little from that of Figure A4.12 for a Maxwellian distribution at r_2. It is clear from Figure A4.13, which shows the spatial variation of the ratio of the heat fluxes obtained with the two codes, that angular averaging in calculating the potentials underestimates the heat flux by almost a factor of two. More severe initial anisotropy increases this inaccuracy further still. The spatial variation of temperature differs less: the collisional process of heating tends to smooth out the anisotropy. In Figure A4.14 we have plotted the dependence of the heat flux on the mean-free path (scaled by the scale height of the temperature). Results are for 0.2 t_0 and 0.35 t_0 (dots connected by line). The upper straight line represents the free-streaming limit, and the lower line is the heat flux for two counterstreaming half-Maxwellians, with a temperature ratio $T_{||}/T_{\perp}$ = 2. The dots represent equally spaced points in r from r, where λ/L has its largest value, to r_1. The heat flux is not a local quantity nor a unique function of λ/L. Indeed, at early times the heat flux is quadruple-valued for $0.02t_0 \leq \lambda/L \leq 0.035t_0$. Near the hot boundary the particles are essentially free-streaming, moving towards the upper limit as the system isotropises. The Spitzer-Harm approximation is no longer good which indicates the need for including the angular dependence of f in the Rosenbluth potentials in describing plasmas with large velocity anisotropies.

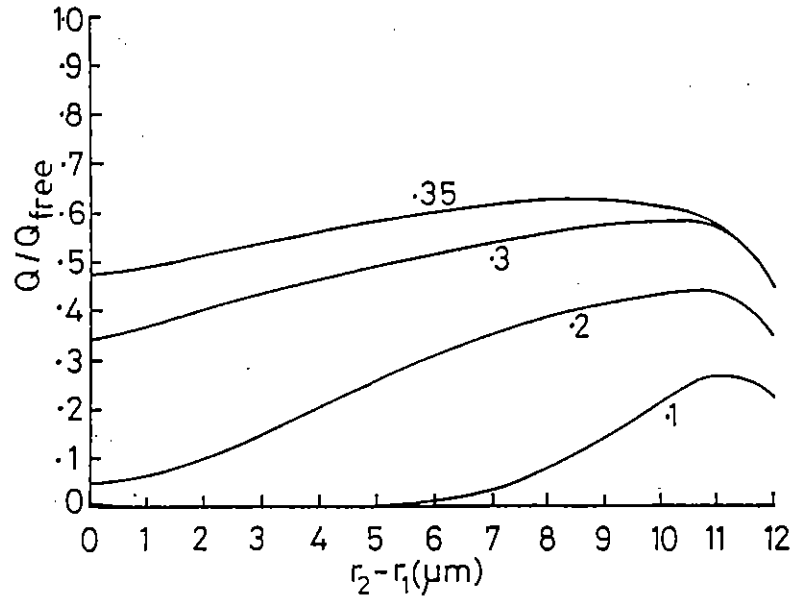

Fig A4.12 *Heat flux vs. distance at times 0.1 t_0 - 0.35 t_0 for a heated bi-Maxwellian distribution of initial temperature ratio T||/T⊥ = 2.*

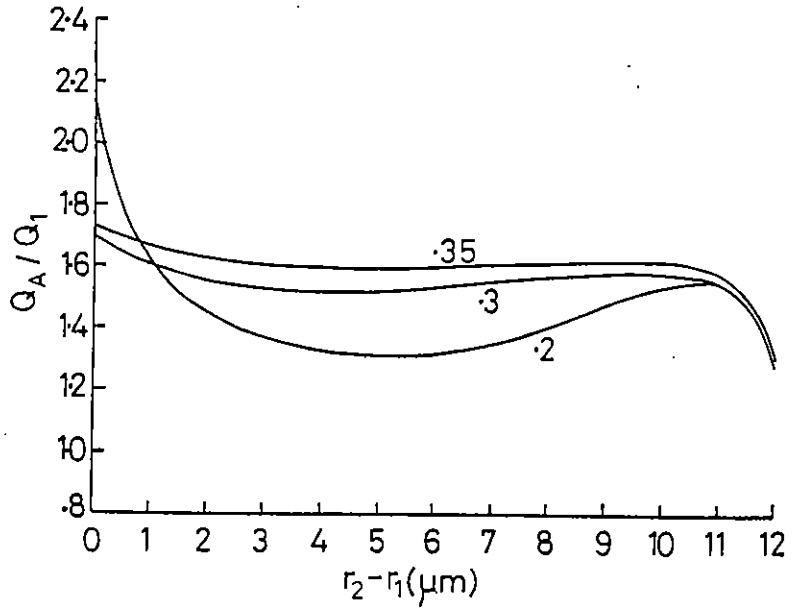

Fig A4.13 *Ratio of heat fluxes calculated from the Anisotropic and Isotropic Codes at times 0.2 t_0 - 0.35 t_0.*

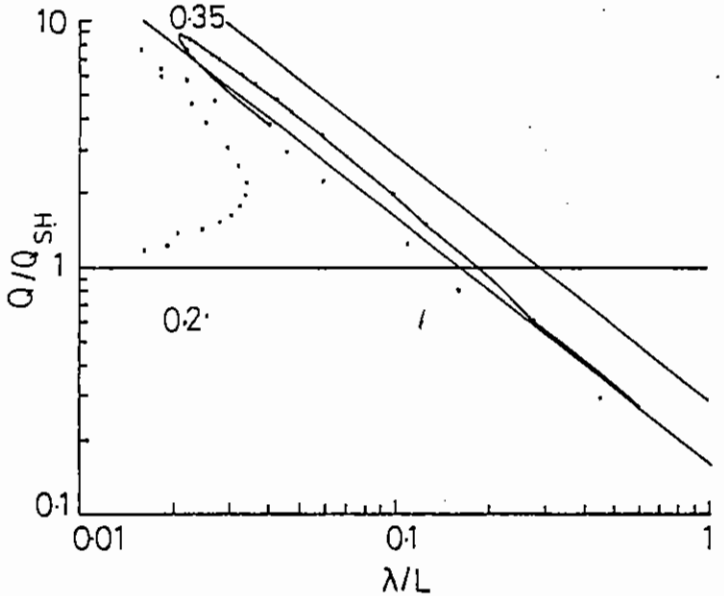

Fig A4.14 Heat flux as a function of mean free path. The lower straight line is for two counter-streaming half-Maxwellians with a temperature ratio of 2. The upper line is the free-streaming limit. Times are scaled by t_0. Dots represent the values at equal spatial intervals from r_2 (larger λ/L) to r_1.

A4.8 ATOMIC DATA FOR MODELLING SOFT X-RAY LASERS

K A Berrington, G P Gupta, A E Kingston and P G Burke (Department of Applied Mathematics and Theoretical Physics, The Queen's University of Belfast)

In the last few years there has been a great deal of experimental work on the development of a soft X-ray laser. Most of the proposed schemes have relied on high power visible lasers to provide the high energy density needed to produce population inversion against the short radiative lifetimes. Experiments at the Lawrence Livermore National Laboratory have demonstrated gain in experiments which produced and excited neon-like selenium in a laser produced plasma about 1 cm long. They obtained gain length products of around 6 on $2p^5 3p - 2p^5 3s$ transitions at about 206Å. Gain has also been observed in the isoelectronic transitions in yttrium.

The main features of the inversion process for Se XXV are shown in Figure A4.15. There are strong optically allowed transitions from

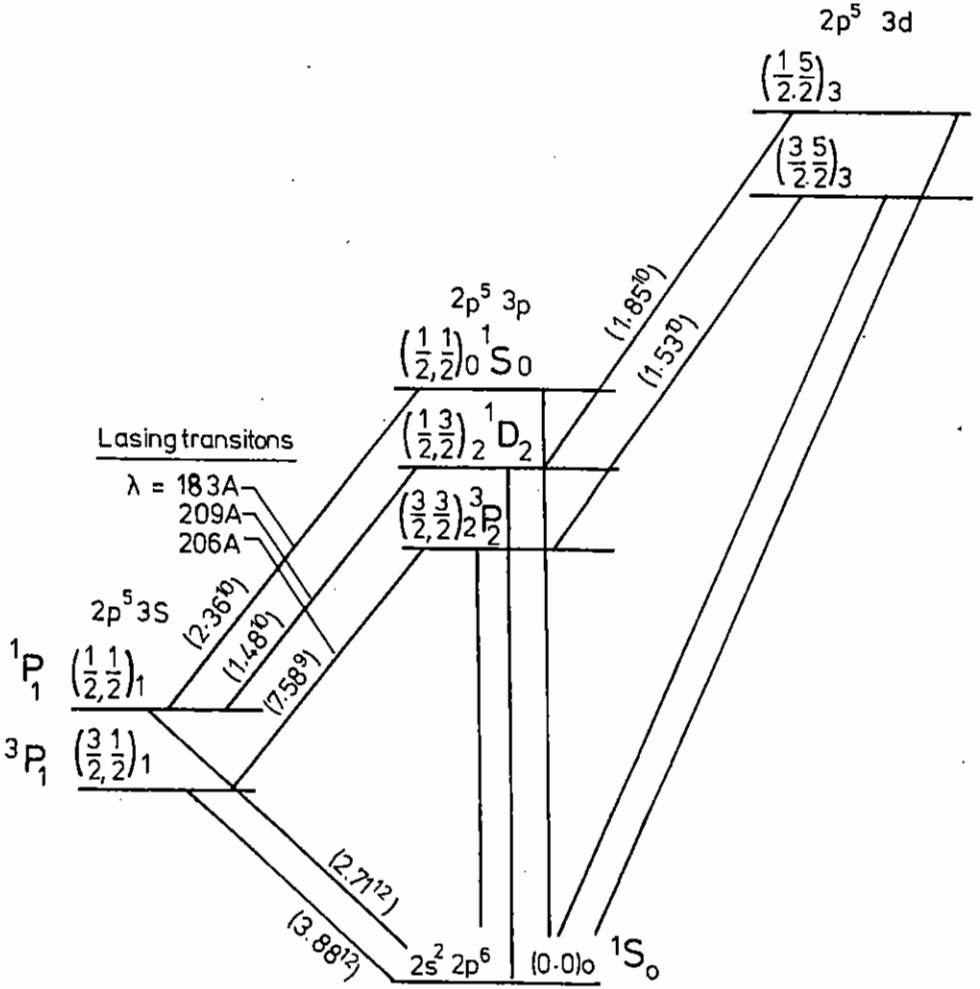

Fig A4.15 Energy levels of Se XXV. The numbers in () are theoretical A-values.

the ground $2p^6$ state to the $2p^53s$ states but the transitions from the ground $2p^53p$ to the ground state are very weak. The $2p^53p$ states are populated by electron excitation from the ground state and radiate to the $2p^53s$ states. Sophisticated theoretical models suggest that the lines at 183, 209 and 206Å should have approximately the same intensities but the Livermore experiments show that the 183 line is almost an order of magnitude weaker than the other lines. To reduce uncertainties which may arise from using inaccurate atomic data in the modelling of the system we have started a series of calculations on the energy levels, A-values and electron excitation rates of neon-like ions.

In the calculation of energy levels and A-values we were primarily concerned with the first twenty-seven levels of Ne-like selenium i.e., the levels with $1s^22s^22p^6$, $1s^22s^22p^53s$, 3p, 3d configurations. Our calculated energy levels and A-values have been discussed in detail in the 1986 Annual Report to the Laser Facility Committee. In these calculations we have used the Hartree-Fock 1s, 2s and 2p orbitals and have used the CIV3 code (A4.28 and A4.29) to obtain 3s,3p and 3d orbitals. Our calculated wavelengths were in reasonably good agreement with observations. For example with a very large configuration interaction (CI) wavefunction we were able to calculate the wavelengths of the 206 and 209Å transitions to better than 1% and even the difficult 183Å line is only in error by 1%. Using these wavefunctions we also are able to calculate the Einstein A-values for the transitions in neon-like selenium and we found that there was reasonably good agreement between the present calculations and the earlier calculations for A-values. In these atomic structure calculations relativistic effects were included in the Breit-Pauli approximation (A4.29).

In the calculation of electron excitation rates in neon-like selenium we considered all $(2p^6)$, $(2p^5)3s$, $(2p^5)3p$, $(2p^5)3d$ states i.e., the twenty-seven levels $(2p^6)\ {}^1S^e$; $(2p^5)3s$, ${}^3P^o$ ${}^1P^o$; $(2p^5)3p\ {}^3S^e_1$, ${}^1S^e\ {}^3P^e_{0,1,2}\ {}^1P^e_1\ {}^3D^e_{1,2,3}\ {}^1D^e_2$; $(2p^5)3d\ {}^3P^o_{0,1,2}\ {}^1P^o_1\ {}^3D^o_{1,2,3}\ {}^1D^o_2$, ${}^3S^o_0\ {}^3F^o_{2,3,4}$, ${}^3F^o_{0,1,2}\ {}^1F^o_3$. From our structure calculations it is clear that it is important to take account of relativistic effects when considering a heavy highly charged system such as neon-like excitation. In the simpler calculation we used the R-matrix method (A4.30) in LS coupling for the fifteen ${}^{S}L^{\pi}$ states and then transferred to jj-coupling using JAJOM (A4.31) with term coupling coefficients. The more complex calculation uses the Breit-Pauli approximation to produce relativistic target wave functions, and then carried out the R-matrix collision calculation in the Breit-Pauli approximation (A4.32) for the twenty-seven J levels. This calculation became very large: there are up to 109 coupled channels for a given total J symmetry.

Work has been completed on the L-S R-matrix calculation, and work on the more difficult Breit-Pauli R-matrix calculation is well underway. Our calculated cross sections differ significantly from earlier distorted wave calculations since below the excitation thresholds we obtain complicated resonance structures for many transitions. However, above the highest threshold considered there are no resonance effects and in general our cross sections are in good agreement with earlier calculations. Because of the complicated resonance structure it is difficult to compare our cross sections directly with earlier results at lower energies. A better comparison is obtained by considering the thermally-averaged effective collision strengths; in Table 4.1 we compare our L-S coupling results with earlier calculations. At low temperatures where resonance effects are important our results tend to disagree but at higher temperatures they tend to agree with earlier results.

In order to obtain an indication of how our new A-values and electron excitation rates effect the level population of Se XXV we used our A-values and our electron excitation rates from the L-S R-matrix calculation.

The effect of the $1s^22s^22p^6$ 3s, 3p and 3d configurations was taken into account by using the energies and A-values calculated at Livermore (A4.33). For these ten levels only excitation from the

ground state was considered. These values were chosen from the paper of Reed et al (A4.34). We have also considered the effect of the $1s^2 2s^2 2p^6 4s$, 4p, 4d states. The energies of these 26 levels were taken from the paper of Zhang et al (A4.35). The effective collision strength and A-values of n=4 levels were obtained from the values of n=3 levels assuming that the cross sections are proportional to the cubic power of the ratio of their principal quantum numbers. The choice of these extra energy levels, effective collision strength and A-values may provide a rough estimate of their contribution on the level population. With these 63 levels we solved the 63 simultaneous equations to obtain the equilibrium population. In Figure 2 we compare the variation of two of the levels at T_e=1000eV for a range of electron densities. The relative populations were normalised to that the sum of the level populations is unity.

Since the 183Å line originates from state 15, $2p^5 3p\ ^1S_0$, and the 209Å line originates from state 14, $2p^5\ 3p\ ^5D_2$, it is seen that lowest ratio of the population of the upper state to the lower one is 1 to 5 i.e., their statistical weight. The higher electron excitation rates found in our work make the level population ratios tend to their statistical weights at lower electron densities.

Work is continuing with the XUV laser study group to extend our model to include recombination and ionization effects.

A4.9 THEORETICAL MODELLING OF RECOMBINATION LASER SYSTEMS

G J Pert, M J Henshaw (Hull University) and S J Rose (RAL)

1. Detailed Models (Hull)

The development of the theory of carbon fibre recombination lasers and their derivatives was accomplished using a series of hydrodynamic and ionisation codes. Each of these allowed an accurate and efficient representation within the limitations of its model. A description of the complete system was obtained by matching the physical development between code and the other. This approach proved extremely powerful in developing the underlying scaling

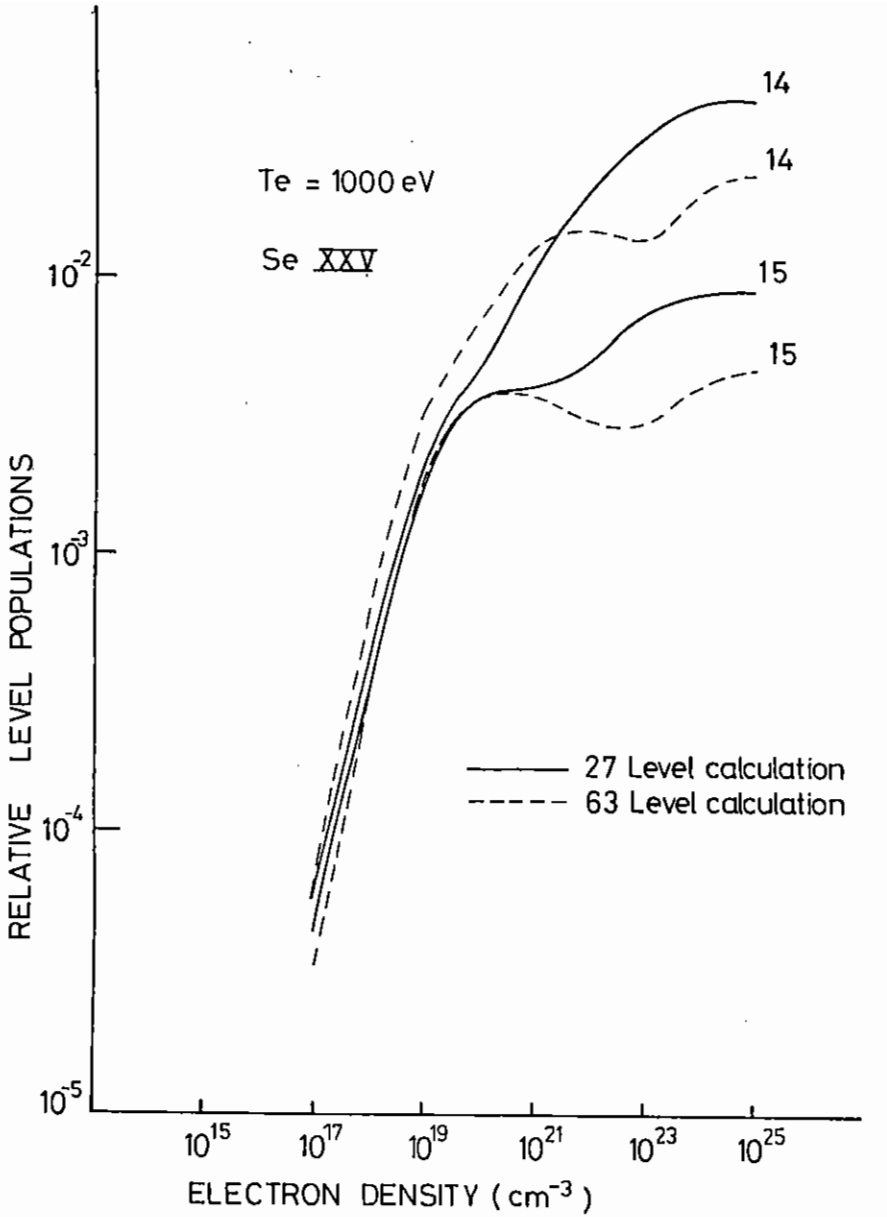

Fig A4.16 Relative populations of $(2p^5)3p\ ^1S_0^e$ (level 15) and $(2p^5)3p\ ^1D_2^e$ (level 14) of neon-like selenium at Te = 1000 eV. The sum of the populations is normalised to unity.

relations and checking the sensitivity of the design to experimental imperfections. It was, however, incapable of providing a detailed picture of the complete spatial and temporal history of the lasant, necessary for an accurate comparison with experiment.

The complete modelling of the expansion and recombination of the plasma formed by laser heating of the fibre requires simultaneous treatment at a self-consistent level of both hydrodynamics and ionisation. This is most simply achieved within a one-dimensional approximation using a Lagrangian fluid description: a level which two-dimensional hydrodynamic simulation had shown to be adequate. The von Neumann-Richtmyer code, LAGR, was adapted to include the ionisation physics subroutines from GAIN. The code therefore provides a fully consistent description of ionisation, hydrodynamics, thermal conduction, ion/electron equilibration and laser heating (with refraction) of a cylindrical target. Designated ionisation stages may be treated by a full collisional-radiative analysis to calculate populations in individual energy states and hence gain. Radiative trapping is treated by an escape factor approximation, with broadening by motional and thermal Doppler and ionic and electron Stark terms. Radiative energy loss from both lines and recombination is included together with reheat from direct three body recombination.

The importance of the motion Doppler effect in determining the escape factor at late times, and its spatial variation gives rise to problems of major uncertainty. At the times of major importance it is determined essentially by two quantities, a non-local velocity gradient and density over distances of the order of the photon mean free path. A good estimate of the velocity gradient is obtained from the equivalent self-similar expansion. The density on the other hand must include reabsorption effects from upstream as well as loss downstream: a good estimate is therefore the local density. The equivalent self-similar flow was calculated simultaneously with the cells using the predetermined ablated mass and actual absorbed energy.

The plasma lasant in the fibre systems is formed from only a thin surface layer of the cylinder. If a general zoning scheme is adopted this usually leads to a relatively coarse mesh over the ablating plasma, which is unsatisfactory for accurate simulation. The code therefore includes a preparatory stage in which an estimate of the ablated mass is calculated on a relatively coarse mesh by running the code until ablation is complete. The code is then re-initialised with the majority of the cells (constant mass) being used to describe the ablated plasma, and only a few the inner core. The penalty, in time, for this preparation is generally small.

2. Average-Atom Model (RAL)

A second, completely different approach to the calculation of the atomic physics of the recombination system has been undertaken at RAL. The hydrodynamics code MEDUSA has been adapted to include a time-dependent screened-hydrogenic average-atom model of the atomic physics. This model is based, in part, on the XSN package currently used in the LLNL code LASNEX. However, in order to study recombination schemes where the effect of line radiation transport is crucial, a different radiation transport model is used. The effect of Doppler decoupling on resonance line trapping is included using the same escape factor approach as in the Hull code. An ideal gas equation of state for electrons and ions is assumed where the degree of ionization is taken from the atomic physics calculation, although unlike the Hull code the excitation, de-excitation, ionization and recombination energies are not included in the hydrodynamics. The calculations are performed in one-dimensional cylindrical geometry with many finely-spaced Lagrangian cells in the outer part of the fibre. A comparison between the radial temperature, density and gain profiles from MEDUSA (RAL) and LAGR/GAIN (Hull) show good agreement. Using the radial gain profiles from MEDUSA a calculation of the time variation of the intensity in the C VI H_α line has been obtained by solution of the axial two-level radiation transport equation. From the computed H_α intensities for two experimental fibre lengths (ℓ_1 = 0.8 mm and ℓ_2 = 0.22 mm) the value of the gain α is deduced by solution of the equation

$$\frac{I(\ell_1)}{I(\ell_2)} = \frac{1-e^{\alpha\ell_1}}{1-e^{\alpha\ell_2}} \qquad (1)$$

in the same way as is performed experimentally. The time variation of α is shown in figure A4.17, together with the experimental results. Because of an experimental time-smearing of ∿400 psec due to the slit width in the spectrometer, the theoretical intensities, calculated with a 400 psec top-hat convolution function, have also been computed and the time-variation of α deduced from solution of equation (1) with these modified intensities is also shown in figure A4.17. The calculated values of gain are too large at early times, yet at the time of peak gain in the experiment (∿1nsec) the calculated value of gain has dropped below the experimental value. We are investigating the reasons for these differences.

A4.10 ISOELECTRONIC SCALING OF PLASMA XUV LASERS

M H Key

Recent success in producing very large single transit amplifications in XUV lasers based on laser-produced plasmas as the amplifying media (A4.36 and A4.37) has prompted intense interest in reducing the operating wavelength by isoelectronic scaling, that is the use of ions having the same number of electrons and therefore similar atomic physics, but a larger positive charge on the nucleus, giving transitions of shorter wavelength.

The major initial successes were with Se XXV(A4.36) at 206/208Å, C VI at 182Å (A4.37) and Aℓ XI at 105Å (A4.38). The first of these used collisional excitation of 3p-3s transitions in Neon-like ions and the latter two used pumping by transient recombination cascade of 3 to 2 transitions in hydrogenic ions and 5f-3d transitions in Li-like ions respectively. The Neon-like scheme has since operated at wavelengths down to 106Å in Mo XXXIII (A4.39), and in our own work the hydrogenic scheme was demonstrated in F IX at 81Å (see Secton C1 ibid). There is also considerable current interest in the scaling behaviour of the Li-like scheme (A4.40) and in further scaling in the hydrogenic scheme (A4.41) but no significant experimental results as yet.

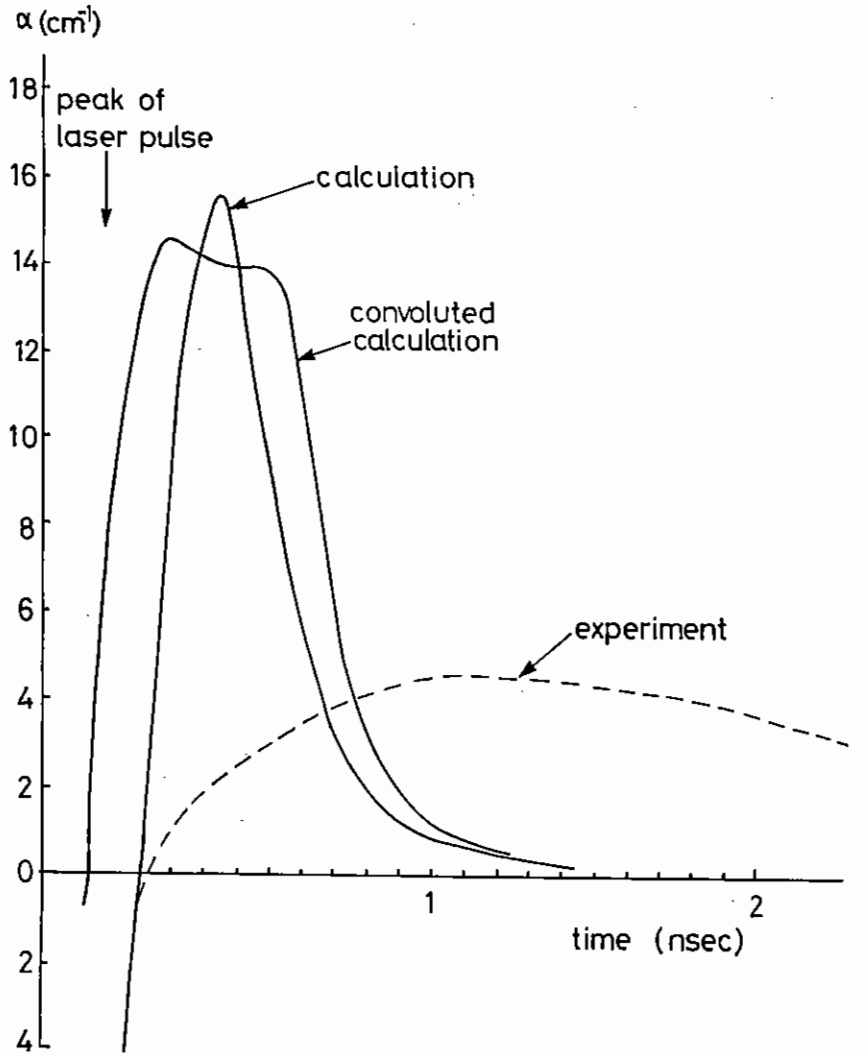

Fig A4.17 Theoretical and experimental time dependance of the gain on H_α taken from two fibre lengths (8.0 and 2.2 mm) with 2.5 J/cm absorbed energy.

A major near term objective is to reach wavelengths in the 'water window' range of 44-23Å where important applications in probing living biological material are possible. Some simple physical reasoning is helpful in assessing the feasibility of this objective and in identifying the problems.

There are well known 'ideal' scaling relationships pertaining to adiabatic expansion and cooling an initially fully ionised plasma of hydrogenic ions and free electrons to produce population inversion.

The transition wavelength scales, with atomic number Z, as Z^{-2} with values shown in Table 4.2 for elements of interest. The element of lowest Z giving a 3-2 transition wavelength in the water window is Aℓ with Z = 13.

The initial temperature (kT) of the plasma must be sufficient to give ionisation to bare nuclei. The ionisation fraction n^Z/n^{Z-1} is proportional to the ratio of collisional ionisation and radiative recombination rates and from their temperature and density dependence we have

$$\frac{n^{Z+}}{n^{Z-1}} \sim Z^{-2}(kT/Z^2)\ \exp\ (-E_H(Z^2/kT))$$

To a first approximation it follows that $kT/Z^2 \sim$ const and more accurately that the ratio kT/Z^2 must increase slightly with Z because of the stronger Z dependence of radiative recombination relative to collisional ionisation.

Transitions to lower energy between bound state of the hydrogenic ion separated by ΔE occur either by radiation with a rate $A \sim \Delta E^2 \sim Z^4$ or in collisions with a rate scaling as $n_e\ (kT)^{-\frac{1}{2}}\Delta E^{-1} \sim Z^{-3}$. A constant ratio of radiative to collisional rate is therefore obtained if n_e the electron number density, scales as Z^7. The laser mechanism relies on production of maximum inversion density when LTE (collision dominated) conditions prevail for levels above n = 3, and n = 2 is depopulated mainly by radiative decay. This condition is reached at a density n_f scaling as Z^7. Therefore the ideal initial density n_0 also scales as Z^7 allowing a constant volumetric expansion ratio and cooling factor in the adiabatic expansion.

The population of the n = 3 level for maximum inversion is close to that for LTE which from Saha's equation scales as

$$n(3) \sim (kT)^{-3/2} n_e\ n_i\ \exp\ ((E_H/9)(Z^2/kT))$$

where $E_H/9$ is the ionisation energy of the n = 3 level of hydrogen and n_i is the density of hydrogenic ions. With the previous assumptions $n(3) \sim Z^{10}$. The laser linewidth is predominantly Doppler broadened giving $\Delta\nu \sim \nu(kT)^{\frac{1}{2}} \sim Z^3$ so that the gain coefficient for constant fractional population inversion has the scaling $G \sim n(3)\ \Delta\nu \sim Z^7$. Since radiative relaxation rates scale as Z^4, choice of an adiabatic expansion time with the same Z^4 scaling preserves the ratio of hydrodynamic and atomic timescales thus $r \sim Z^{-3}$ is required because expansion velocity $v \sim (kT)^{\frac{1}{2}} \sim Z$ giving $t \sim Z^{-4}$. The plasma mass $M \sim Z$ in this model. The need for sufficient collisions to produce equilibrium ionisation gives a requirement for a minimum $(n_e t)$ which is then over fulfilled with $n_e t \sim Z^3$.

There is also a crucial requirement that resonance radiation should not be reabsorbed, which places a constraint on the optical opacity, $\tau \sim n(1)\ r\ \Delta\nu^{-1} \sim Z^{0.5}$ which is almost satisfied in this ideal model.

Clearly in the ideal model the gain increases rapidly with Z^7 and isoelectronic scaling to short wavelengths is strongly favoured. The difficulty which arises in practice is that the initial conditions of plasma temperature and density cannot be chosen at will, but are constrained by the process of laser heating of a solid target (also called laser ablation). Table 4.2 summarises the scaling relationships of the ideal model and contrasts them with the constraints of a model in which laser ablation produces the plasma.

In practice we are concerned with laser irradiation of a solid cylindrical target (fibre) and the process of plasma production can be approximately described as laser ablation in which plasma is formed and flows away from the solid at a steady rate. There has been extensive study of the process in the context of the physics of laser fusion (A4.42). The most appropriate model for the present application is that which requires collisional (inverse Bremsstrahlung) absorption to absorb the laser energy at sub critical density. This gives a self regulating behaviour with $T \sim I^{4/9}(z\ell)^{2/9}$ where ℓ the scalelength of the plasma is determined by the solid target radius which we can take to be constant at this point. Thus $I \sim Z^4$ gives $T \sim Z^2$, establishing the required increase of laser intensity. The electron density n_e at which the peak temperature is

produced is the density to which the laser light penetrates and the model shows that $n_o \sim I^{1\cdot3}(z\ell)^{1\cdot3} \sim Z$.

The major problem is immediately apparent. The temperature can follow the ideal scaling by variation of the irradiance but the density cannot. We have $n_o \sim Z$ instead of the ideal requirement $n_o \sim Z^7$.

The consequences of this constraint can easily be evaluated. The ideal electron density for gain remains as before $n_f \sim Z^7$ but the volumetric expansion ratio and associated adiabatic cooling between n_o and n_f decrease with Z so that instead of the ideal $T_f \sim Z^2$ we have $T_f \sim Z^6$. It follows from the previous discussion of Saha's equation that in this case $n(3) \sim Z^4$ and therefore that the gain $G \sim Z^{-\frac{1}{2}}$.

Instead of strongly increasing gain there is a weak decrease with $Z^{-\frac{1}{2}}$.

The ablated mass scales as Z if the laser pulse length is $t_\ell \sim Z^{-1}$ and the hydrodynamic expansion timescale $t \sim v/r \sim Z^{-1}$ for constant target radius. The number of collisions scales as $n_o t \sim Z^0$ so the system is exactly able to obtain initial ionisation. The opacity $\tau \sim Z^{-1.5}$ indicating that there is a less severe constraint from opacity with increasing Z.

Figure A4.18 presents graphically the conclusions of the previous discussion and is made quantitative by scaling from optimised conditions (A4.43)calculated in detail for C VI. The encouraging aspect of the results is that the laser power and absorbed irradiance required for laser action in the water window are attainable with present day high power laser facilities.

The main difficulty is the convergence of the initial and final densities at $Z \geq 13$ precluding direct access to laser action in the water window by simple ablative heating and adiabatic cooling.

The cooling process must reduce the temperature enough to give a significant sudden increase in the population of n(3) relative to n(1). Significant implies a factor of 3 or more which from Saha's equation implies a minimum expansion ratio of about 10 times. This suggests that the mechanism will operate according to the scaling described here up to about F IX but not much beyond and that alternative approaches are necessary to reach Aℓ XIII. This

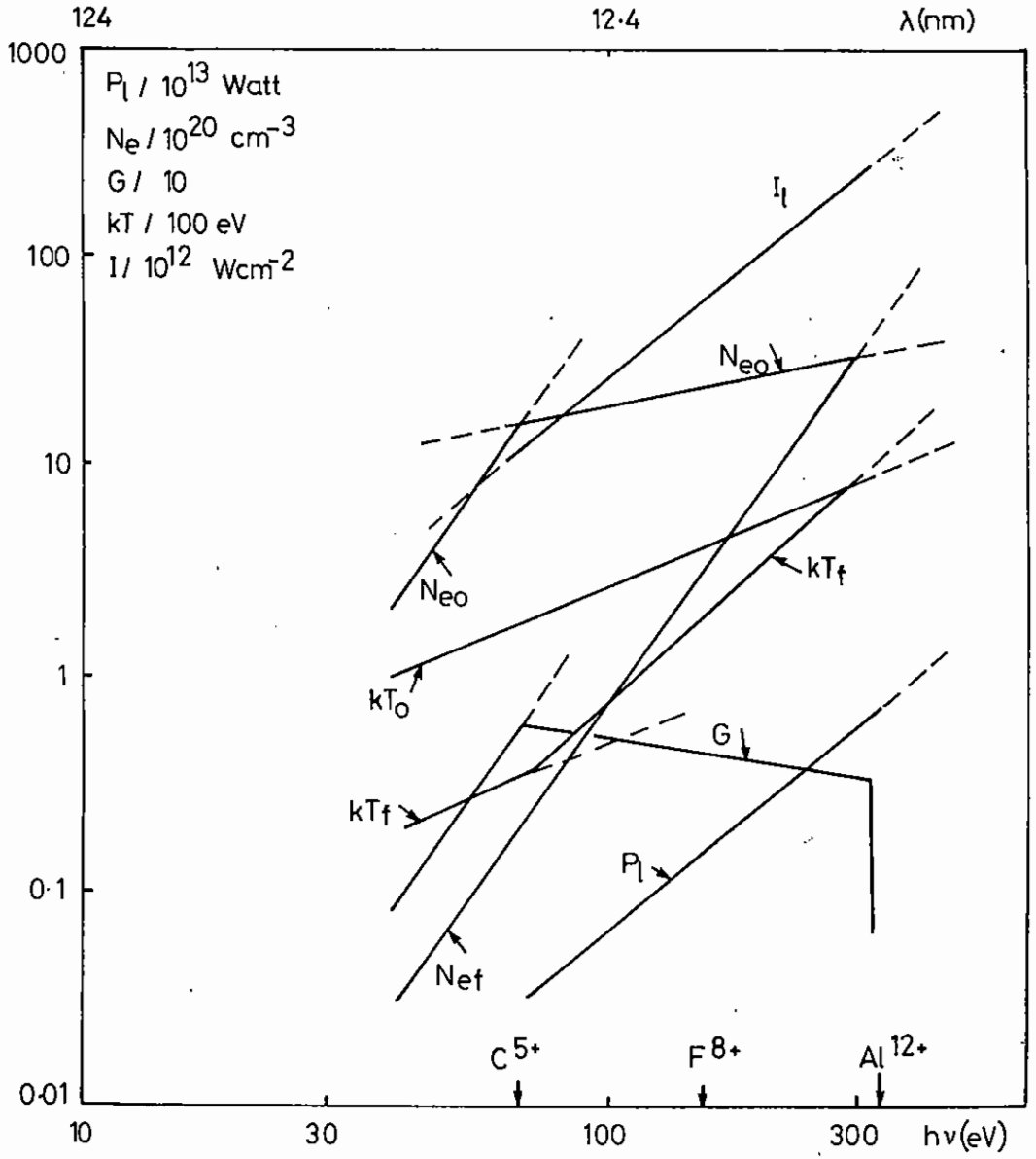

Fig A4.18 P_l: the laser power required for saturated laser action, N_{eo}: the required initial density of the plasma, N_{ef}: the required density after expansion and adiabatic cooling, kT_o: the required initial temperature, kT_f: the required final temperature, I_l: the required laser intensity on target. G: the laser gain coefficient.

conclusion is substantiated by numerical simulations and these plus further details of experiments with F IX are given in section C1. Radiation cooling is an alternative possibility together with creation of plasma at a higher initial density by a different heating process and both these are currently being studied.

$\lambda \sim Z^{-2}$	C	N	O	F	Ne	Na	Mg	Al	
	182	134	102	81	66	54	46	39	Å
Ionise $n^Z/n^{Z-1} \sim Z^{-2}$ (kT/Z^2) $\exp(-Z^2E_H/kT)$ $\therefore kT \sim Z^2$									
Ideal								Laser ablation front $I \sim Z^4$	
Radiative Rates $\sim \Delta E^2 \sim z^4$								Collision Rates $n_e(kT)^{-\frac{1}{2}}\Delta E^{-1} \sim z^{-3}$	
$N_{eo} \sim Z^7$								$N_{eo} \sim Z$ (1B model)	
$N_{ef} \sim Z^7$								$N_{ef} \sim Z^7$	
Upper level $n_u \sim T^{-3/2} n_e n_i \exp(E_I/kT)$									
$n_4 \sim Z^{10}$								$n_4 \sim Z^4$	
$G \sim Z^7$								$G \sim Z^{-\frac{1}{2}}$	
$t \sim Z^{-4}$								$t \sim Z^{-1}$ (ablation layer)	
$M \sim Z$								$M \sim Z$	
$r_o \sim r_f \sim Z^{-3}$								$r_o \sim Z^0$, $r_f \sim Z^{-3}$	
$N_o t \sim Z^3$								$N_o t \sim Z^0$	
Opacity $\tau \sim n_i r_f \lambda (M/T)^{\frac{1}{2}}$ – assuming const recomb fraction									
$\tau \sim Z^{0.5}$								$\tau \sim Z^{-1.5}$	

TABLE A4.2 Z-scaling in H-like recombination

Transitions from ground state to		Te = 500 eV Present L-S R-matrix	Reed et al' HCDW*	Reed et al' DSW‡	Te = 1000 eV Present L-S R-matrix	Reed et al' HCDW*	Reed et al' DSW‡
$1s^22s^22p^5$	$(3S)^3P^o_2$	5.19(-13)	1.46(-13)	1.46(-13)	9.56(-13)	3.71(-13)	3.68(-13)
	$(3S)^3P^o_1$	8.21(-13)	2.62(-13)	2.32(-13)	1.70(-12)	9.73(-13)	8.53(-13)
	$(3S)^3P^o_0$	1.04(-13)	2.60(-14)	2.60(-14)	1.92(-13)	7.00(-14)	6.90(-14)
	$(3S)^1P^o_1$	1.10(-12)	1.80(-13)	1.70(-13)	2.30(-12)	6.62(-13)	6.19(-13)
$1s^22s^22p^5$	$(3P)^3S^e_1$	3.23(-13)	2.83(-13)	2.71(-13)	7.81(-13)	7.49(-13)	7.09(-13)
	$(3P)^3D^e_2$	4.04(-13)	3.70(-13)	3.14(-13)	1.11(-12)	1.13(-12)	9.55(-13)
	$(3P)^3D^e_3$	4.88(-13)	3.62(-13)	3.49(-13)	1.17(-12)	9.53(-13)	9.16(-13)
	$(3P)^1P^e_1$	3.14(-13)	1.59(-13)	1.62(-13)	6.80(-13)	4.21(-13)	4.26(-13)
	$(3P)^3P^e_2$	3.43(-13)	2.91(-13)	2.66(-13)	9.59(-13)	9.17(-13)	8.39(-13)
	$(3P)^3P^e_1$	1.09(-12)	1.00(-12)	8.07(-13)	3.63(-12)	3.29(-12)	2.65(-12)
	$(3P)^3D^o_1$	2.40(-13)	1.37(-13)	1.28(-13)	5.38(-13)	3.73(-13)	3.47(-13)
	$(3P)^3P^e_1$	2.37(-13)	1.53(-13)	1.44(-13)	5.57(-13)	4.25(-13)	3.98(-13)
	$(3P)^1D^e_2$	4.12(-13)	3.02(-13)	2.88(-13)	1.13(-12)	9.77(13)	9.39(-13)
	$(3P)^1S^e_0$	4.25(-12)	3.40(-12)	3.11(-12)	1.28(-11)	1.17(-11)	1.06(-11)
$1s^22s^22p^5$	$(3D)^3P^e_0$	1.54(-13)	1.70(-13)	1.56(-13)	4.16(-13)	4.91(-13)	4.28(-13)
	$(3D)^3P^o_1$	4.37(-13)	4.24(-13)	3.87(-13)	1.21(-12)	1.20(-12)	1.09(-12)
	$(3D)^3F^o_3$	3.94(-13)	3.85(-13)	3.51(-13)	1.17(-12)	1.19(-12)	1.62(-12)
	$(3D)^3F^o_4$	5.32(-13)	6.19(-13)	6.24(-13)	1.42(-12)	1.70(-12)	1.10(-12)
	$(3D)^3P^o_2$	5.09(-13)	5.97(-13)	6.49(-13)	1.36(-12)	1.66(-12)	1.66(-12)
	$(3D)^1D^o_2$	2.31(-13)	3.38(-13)	4.46(-13)	6.03(-13)	7.65(-13)	7.03(-13)
	$(3D)^3D^o_3$	2.76(-13)	2.72(-13)	2.52(-13)	8.40(-13)	8.67(-13)	8.11(-13)
	$(3D)^3D^o_1$	4.92(-12)	5.22(-12)	4.65(-12)	1.98(-11)	2.00(-11)	1.78(-11)
	$(3D)^3F^o_2$	2.68(-13)	3.47(-13)	3.91(-13)	7.08(-13)	8.45(-13)	8.54(-13)
	$(3D)^3D^o_2$	3.88(-13)	4.05(-13)	4.64(-13)	1.04(-12)	1.17(-12)	1.16(-12)
	$(3D)^1F^o_3$	3.54(-13)	-	-	1.07(-12)	-	-
	$(3D)^1P^o_1$	7.71(-12)	-	-	3.07(-11)	-	-

‡ L-S distorted wave * Relativistic distorted wave

TABLE A4.1 Excitation rates (in units of cm^3s^{-1}) for Se XXV

Editors: A) M J Shaw
B) J E Boon

A5.1.1 SPRITE OPERATIONS

M J Shaw RAL

This year has seen the end of Sprite as a long-pulse injection-locked oscillator and its rebirth as the final amplifier of a multiplexed MOPA (Master Oscillator/ Power Amplifier) system.

In its traditional oscillator mode Sprite was used for an intensive period of target shooting between 21 April and 23 July 1986. During this period a total of 739 laser shots were delivered to the Sprite target area, the vast majority with energy between 100 and 120 J in a 50ns pulse. For most of these shots the laser resonator was configured as an off-axis unstable resonator and a fairly high energy (≈100 mJ) broad-band injection pulse was used. The injection timing was adjusted to give the fastest risetime, highest energy pulse on target. In this mode the Sprite laser is really operating as a regenerative amplifier and slight misalignment of the injection beam gives rise to a temporal variation at the focal spot as discussed below in section A5.1.4.

During this period the Sprite system performed with commendable reliability and in particular the new output water lines have performed very well with no indication of breakdown in this section of the pulsed power system. Also the extended period of operation without letting the laser up to air has improved the fluorine passivation of the system and well over 100 shots between laser fills can be obtained without significant degradation in laser energy. The new command trigger system has also functioned well, the only problem being RFI from the Marx trigger modules. This has been overcome by rehousing the thyratron units in RFI shielded enclosures and using a new fibre optic link to trigger the thyratrons.

Between August and October 1986 the Sprite system was converted to its new MOPA mode of operation. The details of the modifications to the oscillator and to the Goblin optical system are described below in section A5.1.2. The new system is considerably more complex than the old and this point is illustrated in Fig.A5.1 which shows a block diagram of the Sprite laser configured as an injection-locked

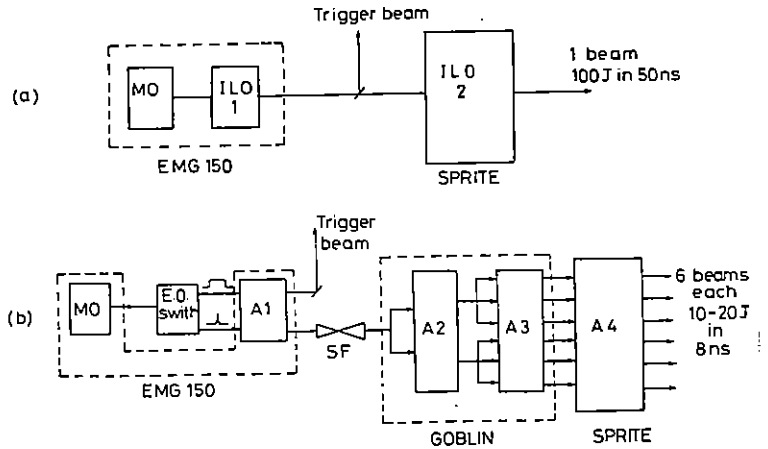

A5.1 The Sprite System as a) an injection-locked oscillator and b) as a six-beam multiplexed MOPA. MO = Master Oscillator, ILO = injection-locked oscillator, A1 - A4 = amplifiers, SF = Spatial Filter.

oscillator and as a multiplexed MOPA. Some of the aspects of the performance of the system are discussed in section C2.1.

Of the six beams amplified in Sprite, only one has been used in the target area. Using this single beam, 341 shots were delivered to the target area between 4 November 1986 and 22 February 1987. The laser energy and pulse length have been rather erratic over this period largely due to ASE and pulse tail amplification, however, the "best" shots had energies of around 20J in a pulse duration of 8 ns with a rise time of 1 ns or better.

The operation of the new system has not been without its teething troubles. In particular the foil lifetime of Goblin, which appears to be a few hundred shots, gives some cause for concern and a major redesign of the Goblin diode to attempt to achieve greater foil life is being considered. On the otherhand, the large number of mirrors in the multiplexer room appear to stay in alignment rather well and constant attention is not required.

A5.1.2 SPRITE MULTIPLEXER DEVELOPMENT

C Hooker (RAL)

Introduction

Preliminary experiments on short-pulse multiplexing were begun early in 1986 using Goblin as its own preamplifier, taking advantage of the long gain lifetime of 110ns to double-pass the cell twice. The success of this technique led to its adoption for the final multiplexer design, which was commissioned in the autumn of 1986.

We decided that the output stage of the multiplexed system should have six beams, double-passing Sprite at a separation of 10ns. Such a pulse train would completely fill the 50ns gain envelope, allowing all the available energy to be extracted. This decision dictated the major design features of the earlier parts of the system, which are discussed in the following sections.

Short pulse generator and preamplifier

The main requirement for the short-pulse generator was that the pulse length should be less than 10ns, to ensure that no overlap of pulses occurred in the amplifiers. Previous work (Ann Rep 1986 Section C2.2.2) had shown the possibility of switching pulses of this length from the output of a Lambda Physik EMG150, but to obtain greater flexibility for extraction experiments we felt a still shorter pulse was desirable.

The eventual layout of the short-pulse generator is shown in Fig A5.2. The oscillator section of the EMG150 is run as an unstable resonator, giving an output of about 200mJ in 25ns at 249nm, in a beam approximately 2cm high by 1cm wide.

The lower half of the beam is clipped off by P1 on the switchout table, and follows an H-shaped path to P3. The remainder is sent to the electro-optic switchout section, which consists of two quartz Wollaston prisms, W1 and W2, and a Pockels cell, PC. The first

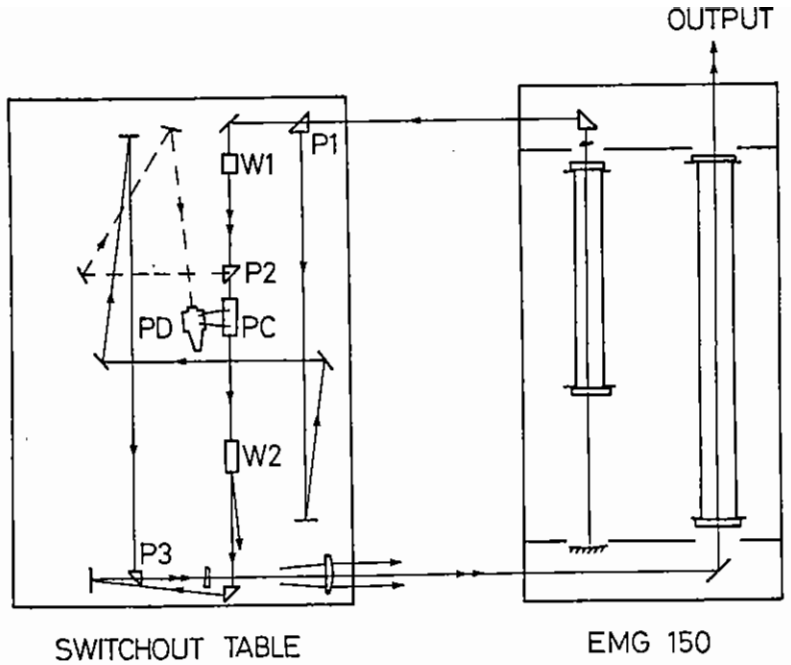

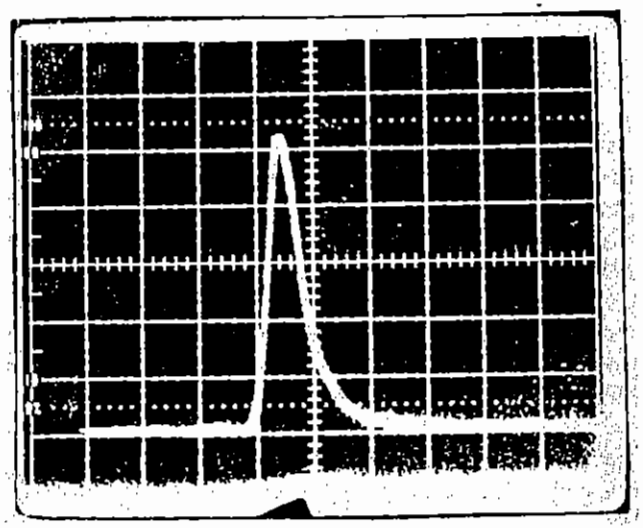

A5.2 a) The Sprite short-pulse switch-out system. P1 - P3 = prisms, W1 - W2 = Quartz Wollaston Prisms, PD = Photodiode, PC = Pockel's Cell.

b) Amplified output pulse.

Wollaston produces two beams of orthogonal polarisations, which diverge until they are spatially separated at prism P2. The lower beam is deflected by the prism, while the upper, which is horizontally polarised, traverses the Pockels cell and the second Wollaston. The second Wollaston is aligned to transmit only the vertical polarisation to the rest of the system. If the Pockels cell is not energised, therefore, no light can pass the switchout.

The vertically-polarised beam collected by P2 is sent via a pair of mirrors onto the window of a vacuum photodiode PD, connected to the Pockels cell. When not illuminated, the diode holds off the full-wave switching voltage of the Pockels cell, about 4.8kV. The illuminating beam is intense enough to drive the diode to saturation, causing the full voltage to be switched across the cell in a time determined by the rise-time of the optical pulse: about 6ns. During that switching time, the voltage across the cell passes through the half-wave voltage, at which value the polarisation of the transmitted light is rotated by 90 degrees, becoming vertical, and thus being transmitted by the second Wollaston prism. Once the voltage on the cell reaches the full-wave voltage, the rotation of polarisation is 180 degrees, and the transmitted light is again horizontally polarised. The output from the second Wollaston prism into the rest of the system thus consists of a pulse whose full width is equal to the rise-time of the diode triggering pulse. This output is sent, via a Galilean beam-expander, into the amplifier section of the EMG150.

In practice, the electrical mismatch between the photodiode and the Pockels cell causes some voltage ringing, which produces a series of weak post-pulses following the main pulse. The main pulse saturates the amplifier strongly: the relative amplitude of the post pulses is thus increased, reaching roughly 50 per cent of the main pulse. To overcome this problem, the portion of the oscillator beam split off by P1 is used as a quenching pulse. It is injected by prism P3 into the same beam expander as the switched-out pulse, but at a slight angle to it, and delayed by a few nanoseconds. The quenching pulse is roughly 100 times more intense than the other, and saturates the amplifier very heavily, thus suppressing the amplification of the post-pulses. The delay is adjusted, by varying the optical path of the quench beam, to the point where the short pulse is slightly reduced in amplitude at the amplifier output.

Once the two beams have separated spatially, the quench beam is redirected and used as a trigger beam for the spark gaps in the Sprite water capacitor and the Goblin pulse-forming line. The switched-out beam is spatially filtered and relayed to the multiplex room, where the pulse energy is typically 30mJ and the pulse length 4ns FWHM.

Goblin Multiplexer

In order to use the full gain lifetime of Goblin by double-passing twice, it was necessary to redesign the optical layout of the multiplexer. The original design used positive lenses to first focus the beams, then expand them to the 6cm diameter of the Goblin cell. The beams were reconverged by the concave back mirror and recollimated by indentical positive lenses. The optical path required for this focusing system made it impossible to return the beams for a second double-pass within the gain lifetime. Accordingly, a system using negative lenses was chosen, which shortened the overall system by 50 per cent, since the lenses were 5 metres from the back mirror instead of 10 metres. However, the angular spread of the beams around the axis of the cell could not be increased, so the new layout forced the lenses to be half as far apart as before, and the same constraint applied to the mirrors that would send the beams back to Goblin. With six beams undergoing two double-passes, twenty-four beam paths were needed, with twelve intermediate mirrors and mounts placed so that all the paths were unobstructed. This proved to be impossible in the reduced space.

The solution that was eventually reached is shown in Figure A5.3. The beam from the switchout is split into two beams, A and B, which are double-passed with a relative delay of 30ns. Each amplified beam is split into three, with 10ns between the components. The resulting beams 1-6 are amplified in a second double-pass of Goblin. Fig A5.3(a) shows typical beam paths for the first (upper) and second (lower) double passes; Fig A5.3(b) shows the timing of all the beams relative to the gain profile in Goblin. The reduced number of mirrors fits readily in the available space. In the final version,

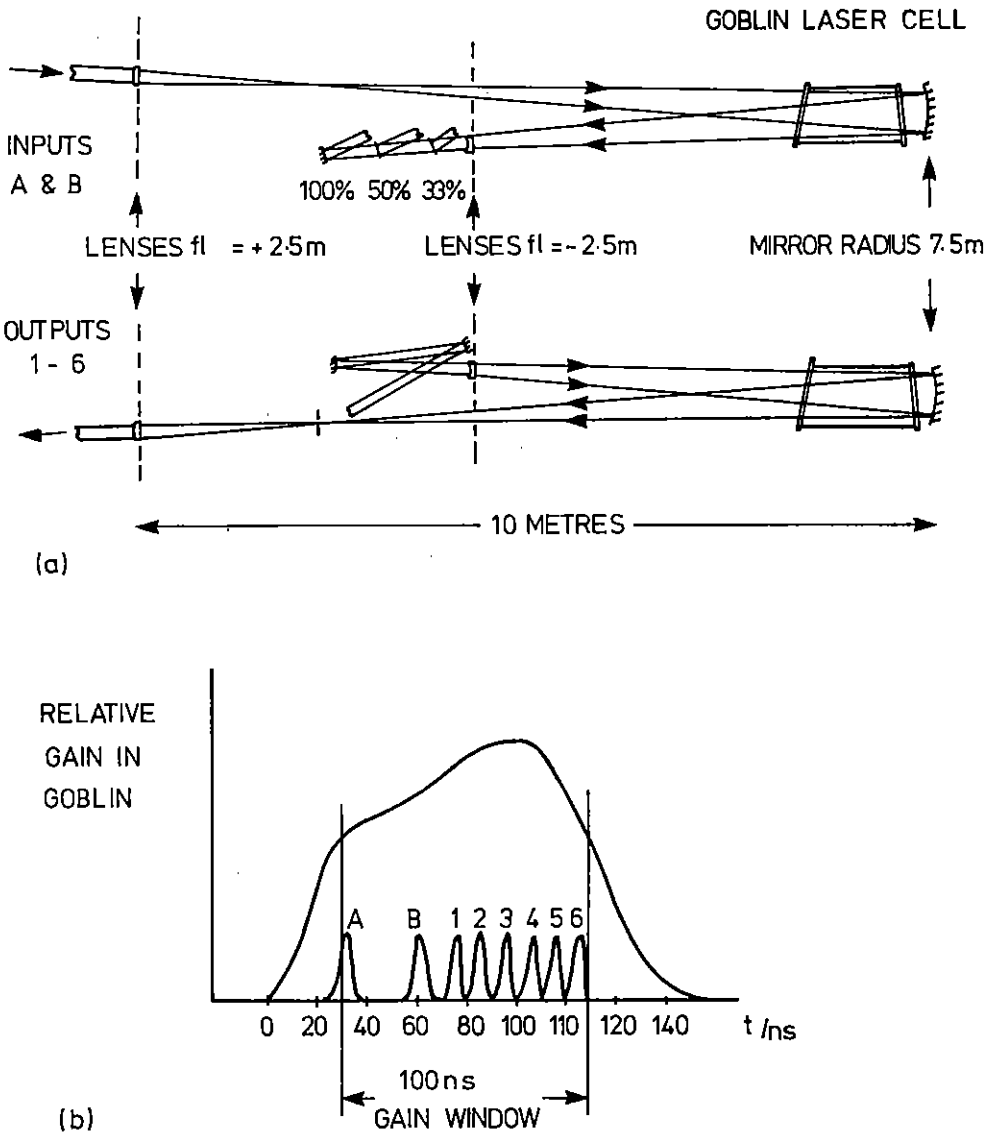

A5.3 Beam splitting and amplification in the Goblin amplifier.

as shown, the positive lenses are retained for the inputs and the final outputs: this allows the possibility of spatial filtering to improve the beam quality and reduce ASE.

Sprite Multiplexer

The Sprite multiplexer is the part of the system least changed from the original design. Each beam makes one double-pass, so two of the eight beam paths are not used, but the optics are unchanged. The 2cm beams from Goblin are expanded by negative input lenses to fill the 25cm aperture of Sprite, then reconverged by the 17m radius back mirror. The output lenses are in the same plane as the input lenses, but have an aperture of 10cm, the output beam diameter being 8cm at that plane. This fourfold expansion is introduced by the multiplexer optics, and ensures that the power density is kept below the damage threshold for the coated mirrors downstream.

The output from Sprite is a train of six pulses separated by 10ns in time and travelling on separate beam paths. The final stage of the multiplexer is an array of mirrors in the multiplex room which removes the relative delays and synchronises the beams at the shutter leading to the target area.

A5.1.3 SPRITE TARGET OPERATIONS

F O'Neill and I C E Turcu

Until September 1986 Sprite target area was operated in the mode presented in last year's Annual Report (A6.1.3). In most experiments the beam was directed in the target chamber along the EW direction and focused by an F:10 aspheric fused silica lens. Alternatively for X-ray laser related spectroscopic measurements involving the high resolution GML5 spectrometer (see section A1.7) the beam was directed through the Upper North port using 45° incidence dielectric mirrors. This set up was also designed to provide a line focus by slightly bending the thin mirrors in conjunction with the F:2:5 aspheric doublet and a quartz plate but was not yet used as such. Due to the poor luminosity of the GML5 runs of 5 shots were fired at 5-10 min intervals which is remarkable for high power lasers. Beginning with October 1986 one of the six short pulse (5-15ns) multiplexed beams of Sprite was used in the target area. The 80mm diameter beam was focused with the F:2.5 aspheric doublet especially ghosted for λ = 249nm. The spatial profile of the beam was monitored by an equivalent focal plane system. The fraction of KrF laser beam transmitted through the second turning mirror was reflected by a flat mirror through an NO_2 cell onto an aspheric fused silica 1.25m focal length lens. The focus was produced on a thin glass plate in front of a CCD camera. The image is then stored on discs and analysed by an Apple computer. Figure A5.4 shows a microdensitometer trace of the beam profile at the focal plane. A FWHM of 23.5µm was measured after taking the ratio of the focal length of the lens used in the target chamber (f = 23cm) to that used for diagnostic (f = 125cm).

The time dependence of the pulse is monitored with a fast photodiode and could be changed from a fast (∿ nanosecond) rise-time but longer pulse (Fig A5.5a) to a shorter pulse (FWHM ∿ 6ns, Fig A5.5b) using saturable absorbers. The peak power in the beam was the same ∿ 2GW and the fast rise-time mode of operation was used in the majority of shots.

The irradiance on target is routinely varied with calibrated NO_2 cells of which two have been built to an improved design.

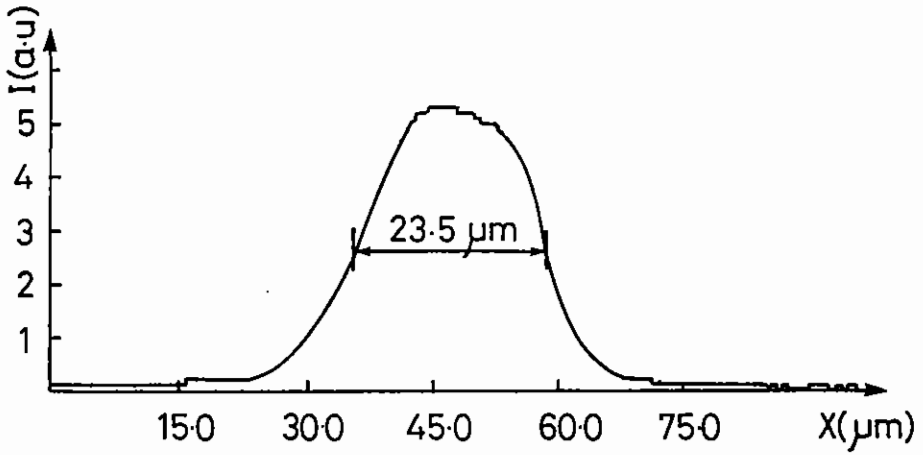

A5.4 Microdensitometer trace across the focal spot of a multiplexed Sprite beam. Lens focal length = 23cm.

The main KrF beam parameters available on target from one of six multiplexed beams are summarised below:

Wavelength	249nm
Energy on target	20-30J
Pulse duration	6-15ns
Minimum rise time	∿1ns
Spot size	25µm
Peak intensity on target	4 x 10^{14}W/cm²
Shot rate	average 10 shots/day

The target alignment was improved by setting up two projection telescopes. The KrF oscillator beam following identically the path of the Sprite beam but having only ∿ 1mJ in the Target Area - is used for focusing the lens by observing obscuration behind the West port on a fluorescer (eg white paper).

The target insertion was improved by using an airlock - redundant from Vulcan TAW - which cuts down the changeover time to a few minutes allowing good use to be made of the relatively high repetition rate of the Sprite laser.

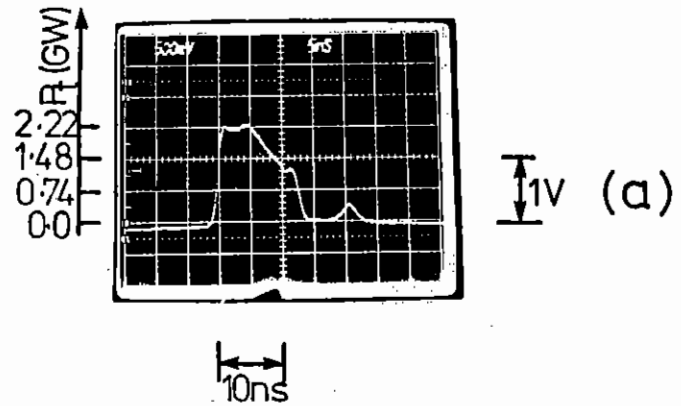

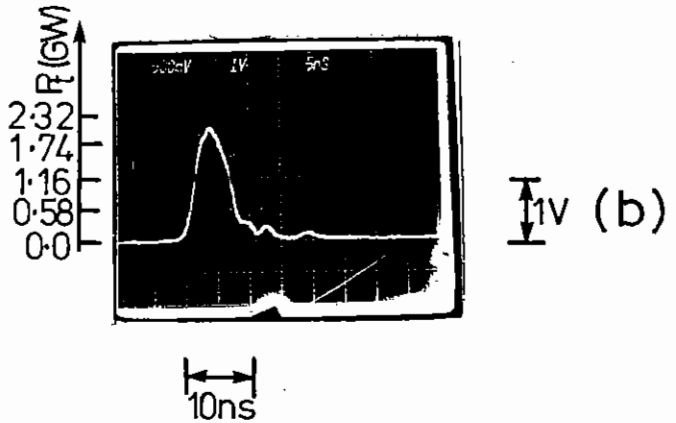

Fig A5.5 Temporal profiles of the multiplexed Sprite beam used in the target area. Upper trace (a) as normally used, lower trace (b) short pulse obtained by introducing saturable absorbers in oscillator beam.

A triggering signal for X-ray streak cameras was derived from a fast photodiode illuminated with a fraction of another multiplexed beam derived before amplification in Sprite. This provided a fixed delay (the multiplexed beams have only optical delay) as well as the possibility of checking the timing of the streak camera trigger pulse with respect to the laser pulse by using only the oscillator pulse running at 1Hz.

A time fiducial for X-ray streak cameras was implemented. The KrF laser beam transmitted through the first high reflectivity turning mirror was reflected to introduce the appropriate optical delay - and focused by a 1.25m focal length lens onto a fused silica optical fibre which guided the light to the X-ray streak camera photocathode (for a complete system description see Section C4.2).

The overall performance of the target area represents a considerable improvement over last year and user experiments utilizing this facility are described in section A1 and A2.

A5.1.4 TIME RESOLVED OBSERVATION OF THE SPRITE BEAM FOCUS

T Tomie (Electrotechnical Lab., Japan)
E Turcu, S Hicks, M Shaw (RAL)

Many plasma experiments have now been performed using Sprite. To understand experimental data correctly, the characteristics of the laser beam must be well known. In an injection type laser, the quality of the output beam may vary during the pulse.

The time resolved focussed pattern was observed as shown in Fig.A5.6. A photodiode observed the pulse through a slit and the slit position was scanned at the focal plane of the beam. At the same time, the focussed pattern of the whole beam was observed by a TV system described in 1986 annual report (sect C2.3).

The beam was focussed by an aspheric lens of 1m focal length which is equivalent to the one used for plasma experiments. The beam was attenuated by an NO_2 absorption cell. A narrow-band filter was used

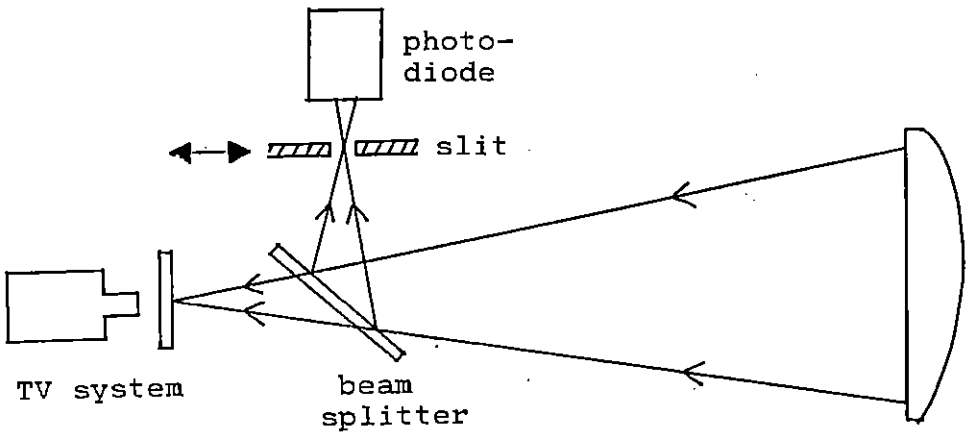

A5.6 Set-up for observing the Sprite beam focus.

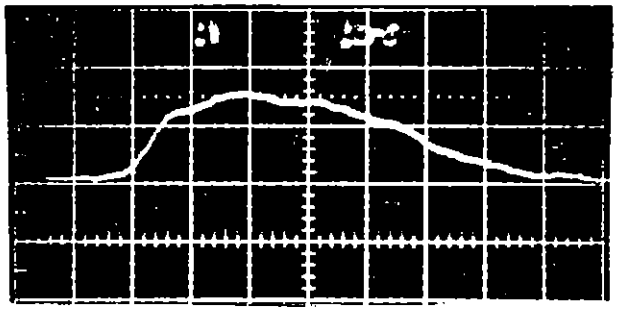

Fig A5.7 Temporal profile for the whole beam.

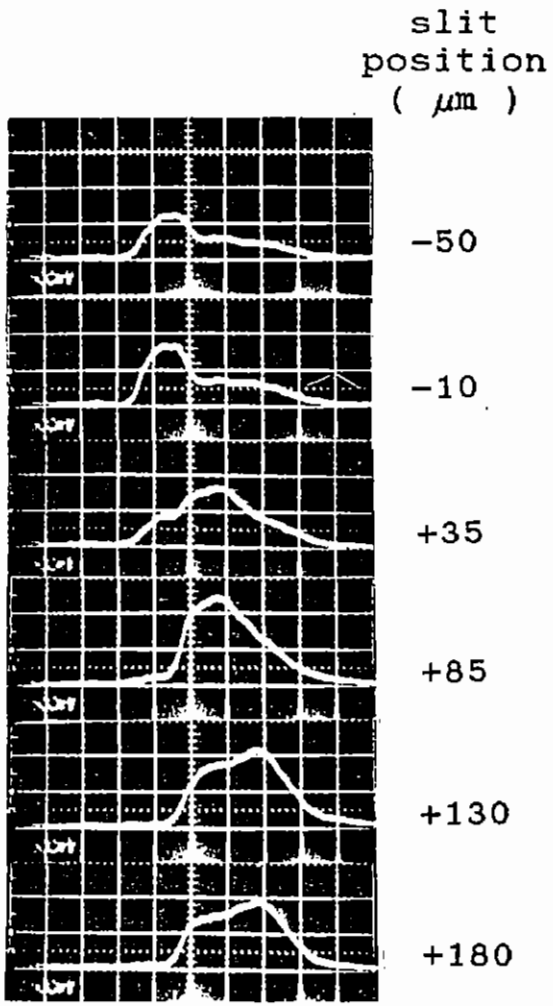

A5.8 *Change in temporal profile viewed through the slit as the slit is scanned across the beam.*

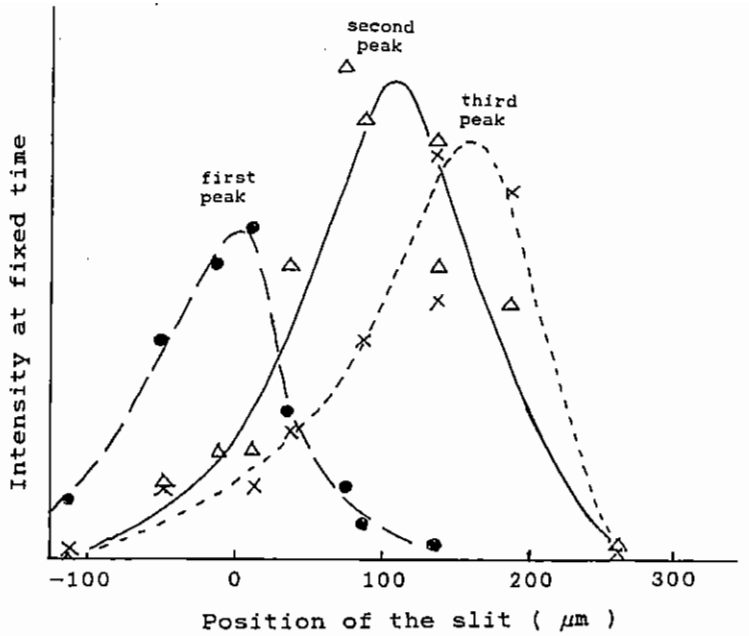

A5.9 *Spatial variation of the three peaks at 3 fixed times during the pulse.*

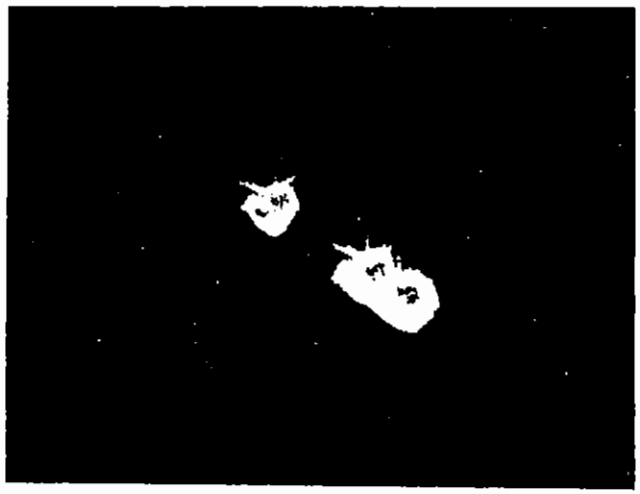

A5.10 *Time integrated focus pattern observed by the TV system. Each spot had a different temporal shape and the beam moved from left to right.*

in front of the photodiode and the slit-photodiode set-up was covered from the scattered light in the room.

Figure A5.7 shows the temporal shape of the whole beam observed by a photodiode before the slit. The pulse width was 50 ns and laser energy was 100 J.

Figure A5.8 shows the temporal shapes of the pulse observed through the slit at various positions. There appears to be three peaks, the separation being 14 ns. The intensity, temporal shape and focussed pattern of the whole beam did not change during the slit scan. The intensities of the three peaks had different spatial distributions as shown in Fig A5.9. Three corresponding beams can be seen also in the time integrated focussed pattern observed by the TV system as shown in Fig A5.10. Each beam had a focussed diameter of 50μm.

The separation of 14 ns between pulses shown in Fig A5.8 corresponds to the round-trip time in the Sprite unstable resonator. Therefore, we can say that the observed pulses were the amplified injected pulse of 10 ns width which appeared successively after each round-trip. The moving focussed position was caused by mis-alignment of the injected pulse. The mis-alignment is improved by 1/M after each round trip and the beam direction converges to the resonator direction. M is the beam expansion factor of the unstable resonator. This rapid improvement of mis-alignment is clearly seen in Fig.A5.10 in which the beam moved from left to right.

The above experimental results show that we have to be very careful in understanding experimental data when we use an injection-locked laser. Firstly, it may be difficult to estimate the focussed diameter from time integrated observations which are commonly used. Secondly, the beam is essentially a train of pulses and non-linear phenomena can have sharp pulsations. This characteristic of the beam is easily overlooked when the pulse temporal shape is observed in the case where ASE smears out the pulsed structure of the beam.

A5.2 VULCAN

A5.2.1 INTRODUCTION AND OPERATIONAL STATISTICS

P T Rumsby (RAL)

This year has seen intensive use of all VULCAN'S facilities with major experimental runs in both multibeam target areas TAW and TAE and in the single beam area TA2. In particular the novel line focus optics available in TAE have been used very successfully for extended experimental runs on XUV laser work. To enhance the facilities available for experiments, cluster beam optics were installed in TAE towards the end of the year with the result that all 6 beams available can now be overlayed on a single focal spot for high irradiance experiments. Further expansion of experimental facilities were made at the end of the year by upgrading the single beam target area TA2 to full 6 beam and backlighting capability. Both these topics are detailed below. The 3 multibeam target areas on VULCAN are now operated in an efficient and effective way with experiments being performed in some while others are being modified and prepared for later experiments.

Operation of the glass laser for the scheduled experiments has been considerably more intensive than previous years with a total of over 5000 shots fired for all purposes during the year. 2013 main high power shots were fired into target areas with the division between TAE, TAW and TA2 being 745, 923 and 345. Failure rate due to laser system faults has remained at about the 3% level.

The usual operational pattern of 3 or 4 week experimental runs followed by 1 week laser maintenance periods has been maintained. For 37 weeks out of the year the laser has been available for experimental use leading to 74 target area experimental weeks.

Several improvements have been made to VULCAN during the year the most notable being a major improvement in beam fill factor due to the introduction of scatter plate apodizers. In addition major improvements to optics and disc amplifier maintenance routines have been achieved with the commissioning of a new clean room. Both of these developments are discussed below.

A5.2.2 APODISER DEVELOPMENT

N Rizvi, D Rodkiss, C Danson RAL

Apodisation is used in the rod amplifier chains of VULCAN both to minimise diffraction effects caused by the amplifier housings and to obtain a more uniform beam profile so as to utilise the stored gain in the amplifiers more effectively. Until Autumn 1986, copper sulphate-filled quartz apodisers had been used in the system but solid-state, sand-blasted apodisers have now been developed and installed. Unlike the $CuSO_4$ apodisers, these new apodisers are relatively inexpensive and quick to manufacture and once installed in the system, they do not require adjustments on a daily basis.

To produce these apodisers, an automatic turntable rig installed in the chamber of a commercial sandblaster unit was used to produce an annular pattern of radially-varying density profile onto BK-7 glass substrates (see Figure A5.11). The parameters which affect the profile are: height of nozzle above substrate; angle of nozzle; pressure at which grit exits the nozzle; flow rate of the grit; grit size; amount of grit deposited onto the substrate. Of these factors, it was found that the most critical in determining the profile were the height and angle of the nozzle and the amount of grit deposited.

The energy in the wings of the laser pulse is scattered by the sandblasted region of the apodiser, and since the phase is also scrambled, diffraction effects are avoided. The amount of scattered light is dependent on the density of grit deposited. The beam profile is affected by the contour and size of the apodising region. Obviously, a sharp contour (ie one having a large density variation with radial distance) acts like a hard aperture and produces diffraction rings. Figure A5.12 compares the transmission profiles of four apodisers and shows how adjustments in height from which they were produced leads to varying roll-offs. Changing the height provided the most effective and predictable method for changing the roll-off.

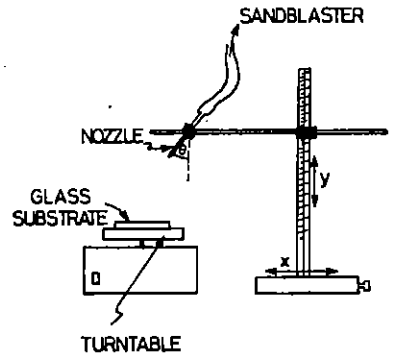

Fig A5.11 Arrangement inside sandblasting unit.

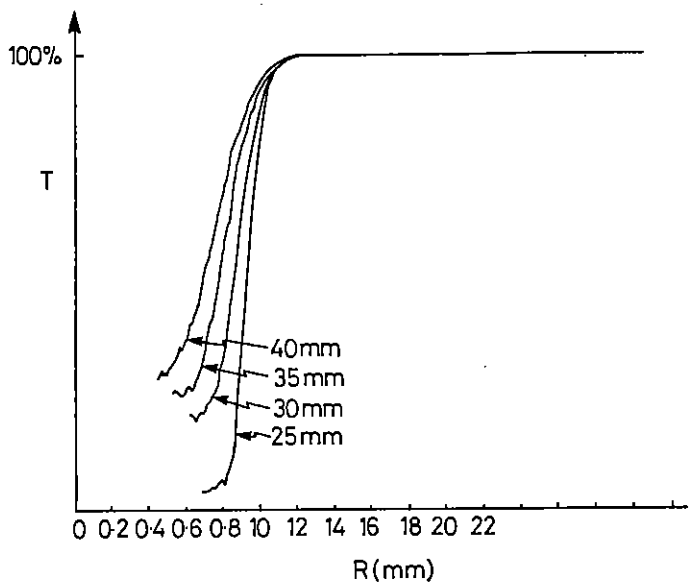

Fig A5.12 Transmission profiles of solid-state apodisers showing variation in roll off with height of nozzle above substrate.

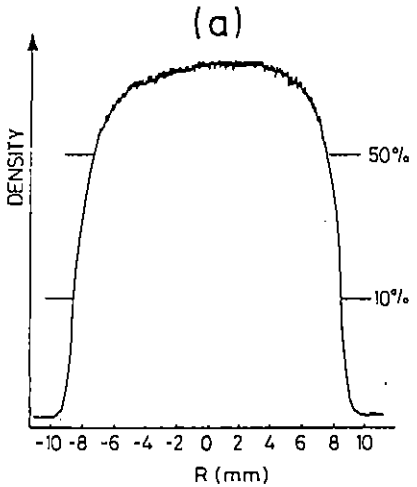

Fig A5.13(a)

Microdensitometer trace of long pulse in near field of apodiser.

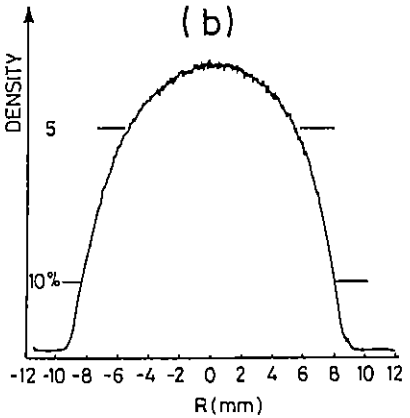

Fig A5.13(b)

Microdensitometer trace of short pulse in near field of apodiser.

Densitometer traces of the long and short pulse beams taken in the near-field of the apodisers are shown in Figure A5.13. Figure A5.14 shows densitometer traces of the beams at the output of the rod amplifier chains. Both beams exhibit better uniformity than that obtained with the old apodisers and there has also been a significant increase in the beam fill factor. The long pulse beam, which has displayed the most marked improvement, has a fill factor of ≥ 0.8 and a peak-to-valley modulation of 17%. Although both beams are slightly smaller in diameter than before, the enhanced fill factor has meant that a bigger diameter green beam is produced by the frequency doubling crystals.

A5.2.3 COMPUTER CONTROL AND DATA ACQUISITION

C J Reason, D A Pepler (RAL)

The GEC 4080 computer and its associated Camac equipment has continued to run reliably during the year despite being now over ten years old. The system has changed very little during the year except

Fig A5.14(a)

Microdensitometer trace of short pulse at output of rod amplifier chain.

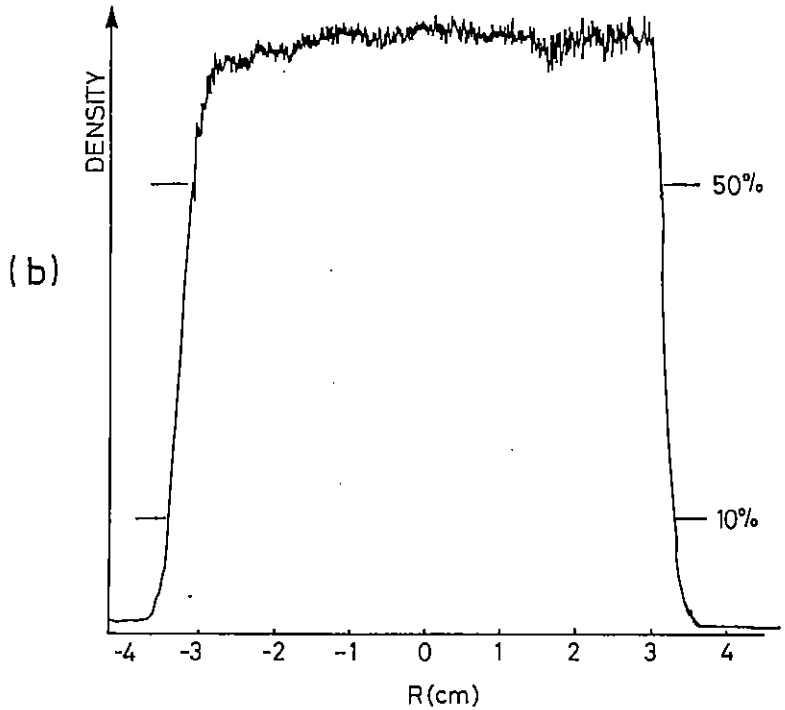

Fig A5.14(b)

Microdensitometer trace of long pulse at output of rod amplifier chain.

that one of the crates on the parallel branch has been moved nearer the 4080. Within the next few weeks the two crates in the laser area which are, at present, on the parallel branch will be converted to the serial fibre optic branch giving added isolation from electrical noise pickup and flexibility to their geographical location.

Much of the information that the laser operator requires about the laser is provided on a colour layout diagram representing the current state of the laser. It shows the state of the various mirrors and shutters, whether various items of equipment are switched on and the actual beam paths for the short and long pulses and the YLF alignment laser.

The equipment has been upgraded with a new Sigmex display capable of storing four 768 x 512 images with 256 colours in each, switching any one onto the screen. It is driven down a RS232C interface but running at twice the speed (i.e., 9.6 Kbaud), of the original display. It is controlled by a separate process in the computer, running asynchronously to the main laser control program but communicating with it via inter-process messages to obtain data and synchronisation when necessary. As several diagrams are stored in the display at once, the computer can switch between the layout diagram and the charging diagram in one frame time. The operator also has control of the laser while the diagram is being updated.

The layout display now provides a more complete representation of the laser and because the new process has been written to be table driven (i.e., the information about the laser is held in a data table and not in the code) it has proved much faster to update the display to allow for changes to the laser. There is also the possibility to make further changes interactively. The two free pages in the display are available to provide more information for the operator (e.g., interlock information).

A5.2.4 NEW CLEAN ROOM COMPLEX

D Rodkiss, J Boon E Madraszek, R Wellstood (RAL)

Due to continuous Vulcan Glass Laser enhancement programmes which have increased the number of 108 mm disc amplifiers from 2 in 1977 to the present total of 12, this year has seen the construction within part of the new Laser Facility north extension of a much larger and more effectively designed Clean Room Complex.

The primary aim in the construction of this new area is to enable the vital maintenance procedures carried out presently on the 108 mm disc amplifiers, and in the future, 108 mm and 150mm Box amplifiers, to be more effective, efficient and of a higher standard that previously possible within the existing Clean Room layout.

It will be seen from the floor layout diagram fig A5.15, that the new Clean Room Class 10,000 area now has direct access to the Main Laser Hall. This is a major step forward in amplifier servicing as the original Clean Room was remote from the Main Laser Hall and all serviced amplifiers had to be transported from the Clean Room through the main building corridor before being installed in the Vulcan Laser system. The new access available enables a much more efficient and clean transfer of serviced amplifiers to take place.

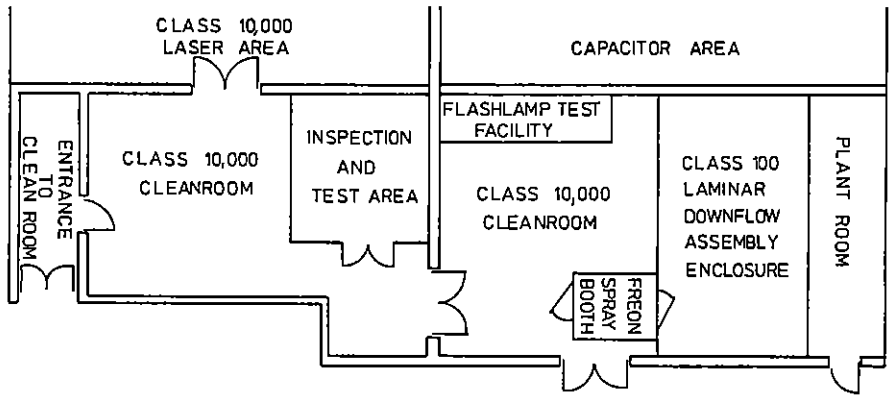

Fig A5.15 Floor layout of new clean room complex.

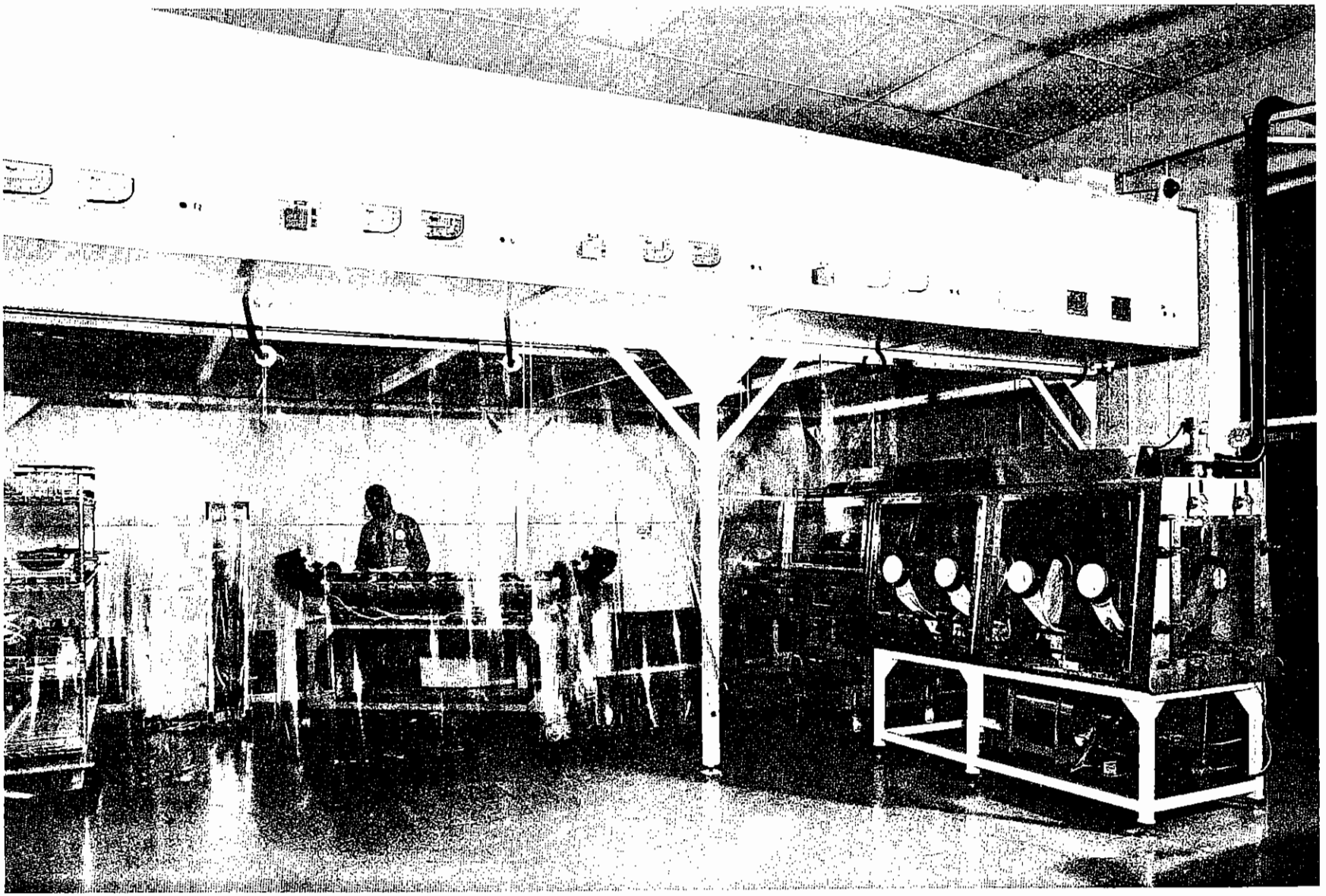

Fig A5.16 View in new Clean Room showing the class 100 laminar downflow assembly area and the high pressure freon spray cleaning booth.

The overall layout of the complex also places the most critical area, the Class 100 Laminar Downflow Assembly Enclosure at a position which will be least affected by the presence of contamination caused by personnel movement.

A further improvement in the Clean Room Complex is an area which is both light proof and air turbulence free, where the large number of sensitive laser components essential to run a High Power Glass Laser system can be inspected, tested and stored under enviromentally ideal conditions. An important modification has also been made to the operation of the High Pressure Freon Spray Booth by purchasing a purpose built distillation plant which is self contained and fully automated. Research has shown that considerable savings in the running costs of the Freon Spray system will be achieved through the more efficient distillation process.

The whole Clean Room complex is air contamination, pressure, temperature and humidity controlled to fine limits and all the plant associated with air handling is contained in a plant room which is accessible from the outside of the building thereby reducing the need for intrusion into the Clean room by maintenance staff.

Also included in the Class 10,000 area is the High Voltage Flashlamp Test Facility. This new layout gives the Clean Room Complex the capability to store, inspect, test, clean and assemble under the correct conditions all the optical components necessary to run a High Glass Laser System.

Fig A5.16 shows a view of part of the new Clean Room showing the Class 100 Laminar Downflow assembly area and the High Pressure Freon spray cleaning booth.

A5.2.5(a) TARGET AREA WEST

A J Cole

Target Area West has operated for a total of 32 weeks during the reporting period.

The area has operated with a range of beam configurations varying from full twelve beam symmetric irradiation with backlighting, to cluster type geometries, as described in last years report. All experiments were performed with 0.52μm radiation, with the exception of a five week run using 1.05μm light to investigate heat flow instabilities. The wavelength change overs were completed with the minimum loss of running time from the experiments.

Target Area West was also used to investigate the propogation of large fill-factor, high power beams, both in terms of the performance of the optical components, and target interactions. (See sections C1.2 and A1.10).

A5.2.5(b) TARGET AREA EAST

M Grande

General

With the exception of one three week period TAE has run scheduled experiments continuously throughout the duration of this report. While the majority of these experiments were performed using the X-ray line focus (see e.g., A1.1, A1.2, A1.3), a number of other configurations were used, emphasising the great flexibility of the TAE experimental environment. Besides repeating the optically complex laser annealing experiment (A1.8) and the absorbtion spectroscopy experiment A1.5), two significant innovations were made, which again extend the target area's operating potential.

Six Beam Cluster Configuration

At the beginning of February 1987 installation and comissioning of a major new facility configuration was begun in target area East. This was the implementation of the six beam cluster configuration originally proposed in the 1985 annual report (A6.5.2). Fig A5.17

shows the implementation adopted. By arranging beams on the space frame as shown in Fig A5.18 it is possible to avoid problems of clipping with a 108mm diameter beam. Beams are focussed onto target via f10 aspheric singlet lenses arranged around a 16° half angle cone.

Targets are aligned to ∿ 5 μm via two telescope systems relayed to a viewing screen above the operations console giving a magnification of 220. Beam alignment is by observing the Foucault shadow through the outgoing ports. A backlighting beam can be implemented either via an f2-5 lens on axis or, as shown in Fig A5.17 via an f10 lens on one of the output ports.

One important application of the cluster technique is to produce shaped pulses by varying the relative timings of the main beams in the switchyard under microprocessor control as described in the 1986 annual report (A6.2.5).

The first shot with this arrangement was fired onto a planar target on 5 February 1987.

Variable Line Focus Length

In two separate experiments, the original line focus configuration has been modified in order to increase the range of experimental parameters accessible. The method used is described in the 1985 Annual Report, section A6.6.1. By increasing the angle the incident beam makes with the spherical mirror normal, the spherically aberated line focus thus produced is lengthened; this increases the possible gain attainable in single pass ASE X-ray laser schemes, but of course correspondingly reduces the incident energy per unit length. Line focus lengths of up to nearly five times the original length have been used; a length shortened by a factor 4 has also been used in order to provide a high intensity per unit length for the long scale-length plasma experiment (A1.6). Fig A5.19 shows the distribution of energy along the line focus for three different line focus lengths.

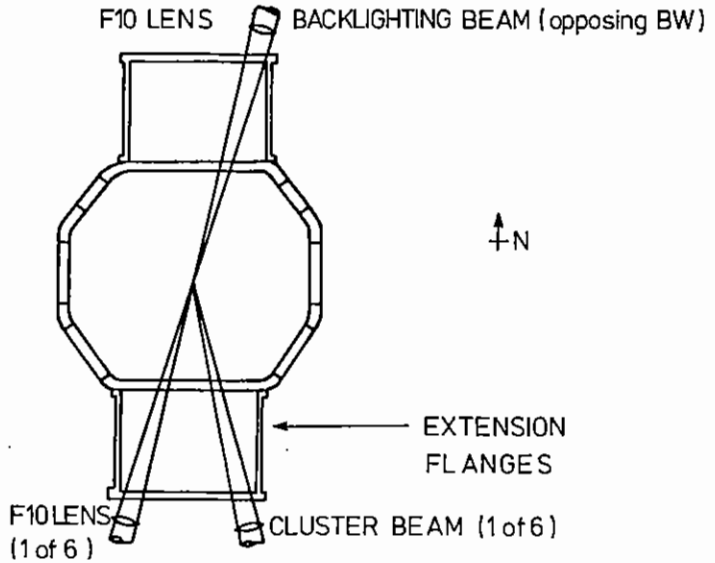

Fig A5.17 Arrangement of six beam cluster in Target Area East.

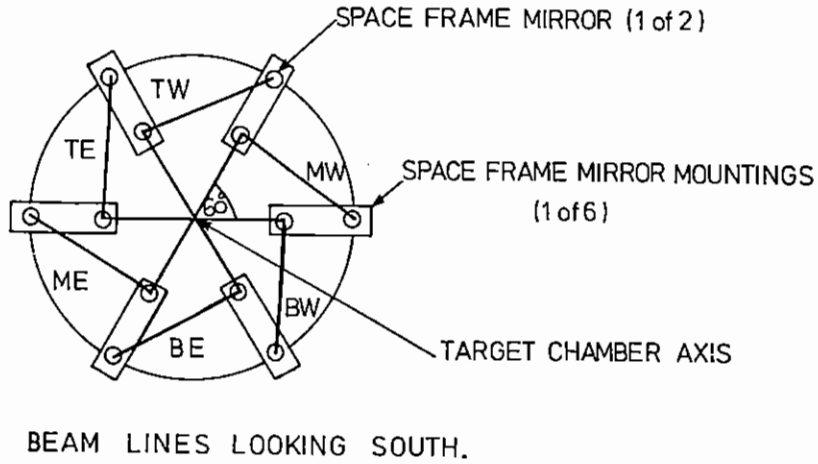

Fig A5.18 Arrangement of beams and mirrors on the space frame to avoid beam clipping.

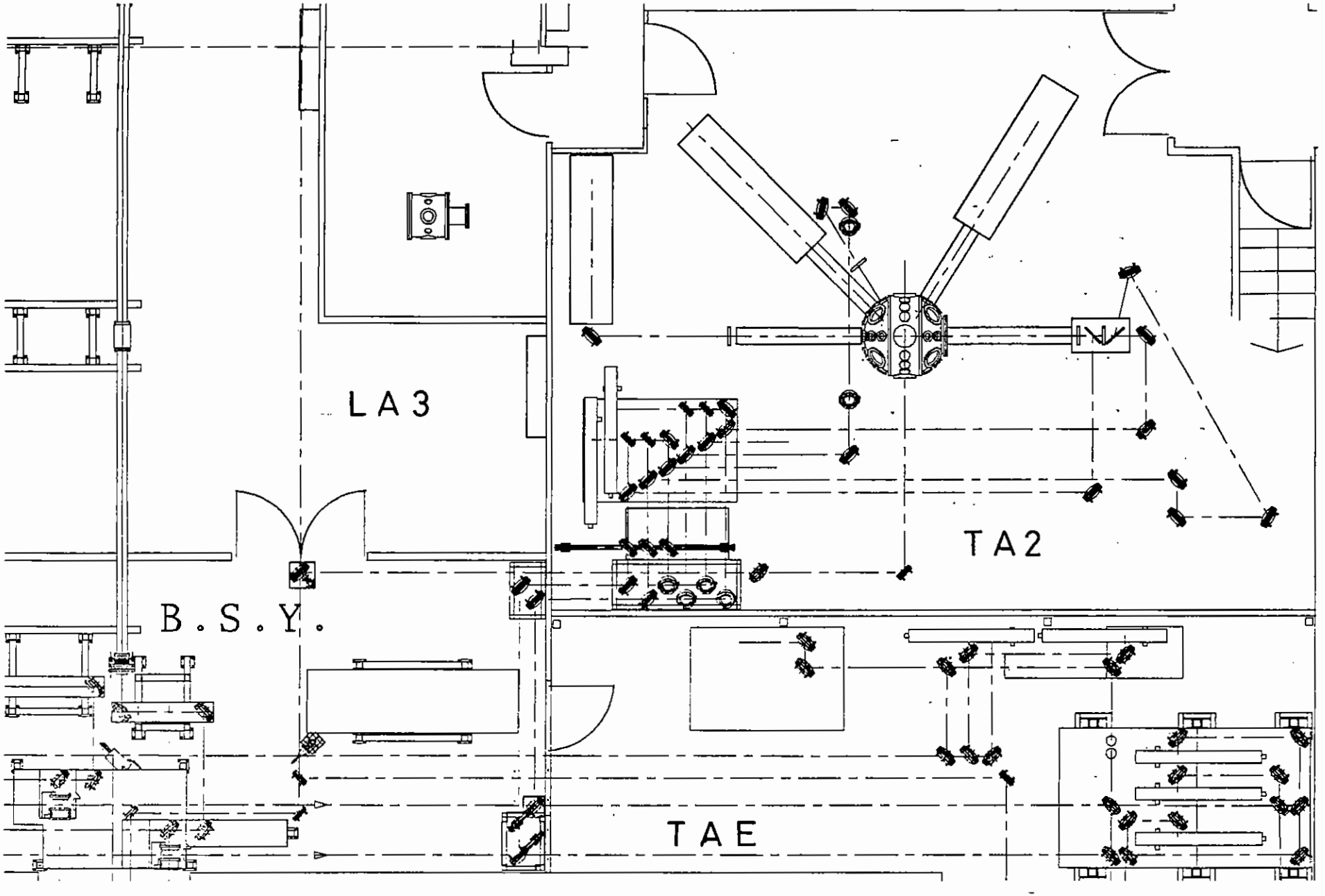

Fig A5.20 New beam layout to TA2 via the beam switchyard area. The target chamber is shown in its new position with a schematic representation of the Beat-Wave experiment attachments.

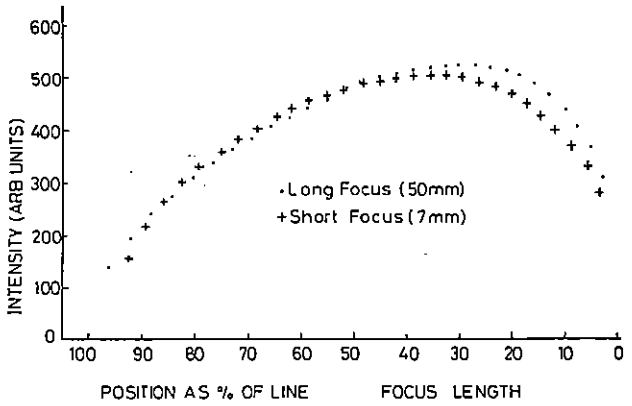

Fig A5.19 Distribution of energy along the line focus for different line focus lengths.

A5.2.5(c) TARGET AREA 2

A J Cole, S Hancock

During the reporting period, TA2 was recommisioned as a scheduled area for high power laser experiments. Several experiments have since been performed using either one or two beams. These beams were transported to the area via the existing beam-pipe system installed when TA2 was first constructed (see Annual Report 1979).

In order to increase the range of experiments which can be performed in TA2, it was decided to reconfigure the way in which the beams are injected to the area. The switchyard area (see 1986 Annual Report section A6.19) at the end of the glass laser has been extended to enable the main six beam array plus backlighting beam and probe beam to be directed into TA2. The beam paths are shown in Fig A5.20. In addition, as one can be seen in the diagram, the target chamber has been moved to a more central position in the area floor space.

It is not envisaged that any one experiment would use all the available seven beams but more than two beams is now possible. In addition, if the parallel operating target area does not require a full complement of beams then it is now possible to split the beams between the two areas in such a way as to minimise the number of switching operations between successive laser shots.

An additional advantage to TA2, is that the beams are image-relayed and spatially filtered by the output vacuum spatial filters (see 1985 Annual Report section A6.26) of the VULCAN system. The beam quality is therefore expected to show some improvement over that seen previously.

This upgrade work is being carried out during February and March 1987. The first experiment to use the new facilities will be the Laser-Beat-Wave investigation, which will use four of the main beams and the small aperture probe beam. This is typical of the kind of experiment which it is hoped will make good use of the new TA2 facilities.

A5.2.5(d) CHANGES TO THE TARGET AREA CONTROL COMPUTERS

C J Reason, D A Pepler

The hardware in TAE and TAW was controlled by DEC Falcon (11/21) computers housed in CAMAC modules. The computers used a suite of six CAMAC modules to drive a number of multiplexed cards, housed in a Eurocrate system controlling motors, shutters, filter wheels and TV systems. Through these the operator uses a joystick, switches and a keyboard to adjust the mirrors and lense to align the system.

As the requirement of the target areas became more complex the addressable space of the falcons became full and as more CAMAC modules were added to the crate the power supply tended to overload. It was therefore proposed to replace the falcons with a compatable computer system. This should have a larger addressing space and be housed outside the CAMAC crate with a separate interface thus reducing the current drain on the CAMAC power supply. The computer chosen was a DEC 11/23 board level computer with a multifunction board containing memory and two serial lines housed in a Hytec 1101 8 slot box and interfaced into CAMAC via a Hytec 1151 interface.

The code running in the computer is written in the DEC language Micropower Pascal and the same code runs on both processors with only the systems configuration file changed to describe the new system. The new system gets its increased addressing space from the use of addressing registers giving an address range of 4 Mbytes although any one static process can only address 64 Kbytes.

The new system has been installed but some problems have been encountered with the use of the addressing registers by the manufacturers software (now fixed by DEC) and the increase of speed of the new processor. These have largely been overcome and the system is now running with approximately the same reliability as before. There is also the potential for further upgrades in the software.

As part of this exercise the processor in the development system has been upgraded from a 11/23 to a 11/73. This was entirely transparent and gained an increase in speed of a factor of 2 to 3 in program build time.

A5.3 TARGET PREPARATION

C Brown, B Child, D Hall, N Prior, P Rumsby, S Whittaker (RAL)

The year has been a busy one for the target preparation group as on several occasions 3 target areas have been operating simultaneously creating an unusually heavy demand for targets.

In addition many novel target fabrication techniques have been developed during the year to deal with the new requirements of the experimental programme which has called for targets of significant increase in complexity. The XUV and X-ray laser programme has required the development of a variety of techniques to handle and coat carbon fibres. Using thermal evaporating and sputtering techniques fibres have been coated with a wide range of fluorine containing compounds for hydrogen-like recombination schemes and with aluminium and titantium for Lithium-like schemes. For double pass laser schemes involving mirrors fibres up to 20mm long have been mounted in the centre to allow access to both ends. Fig A5.21 shows section of such a 7µm diameter fibre which is 20mm long overall and has had 70µm diameter microspheres mounted on each end as alignment aids. Fibres up to 150mm long have been selected, measured and satisfactorily mounted for experiments.

Experiments investigating filamentation in large scale length plasmas have user line focus irradiation of two types of target to produce a long preformed plasma. For one scheme polymer cylinders 1mm long, 125µ diameter and 1 µm thick have been made by parylene c ating onto polystyrene fibres or copper wires. After cutting to length the mandrel is dissolved out to leave a free standing hollow cylinder. The other approach involves coating an aluminium stripe of 50µ width and 0.5 µm thickness onto a thin (100mm) Formvar substrate and subsequently cutting the substrate and stripe to a length of 1mm.

Novel shell targets containing bismuth as an inner layer have been fabricated for pusher absorption spectroscopy experiments. Such targets are made by coating sequentially onto a polystyrene shell layers of bismuth followed by parylene C followed by parylene N as

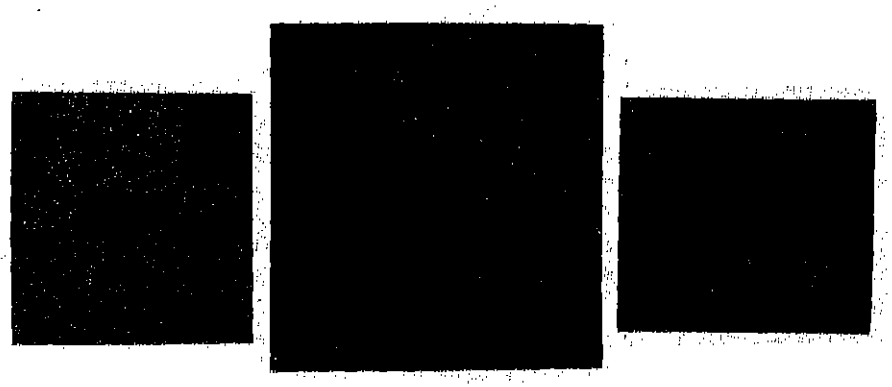

Fig A5.21 A 7µm diameter carbon fibre 20mm long with 70µm diameter microspheres mounted each end.

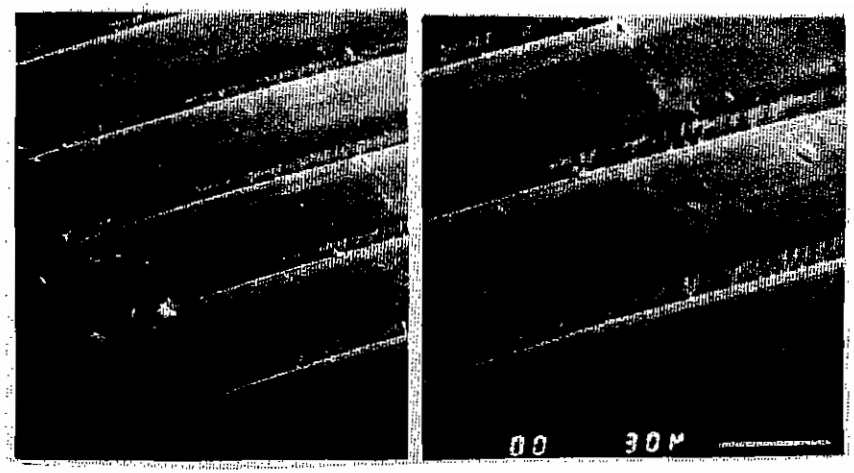

Fig A5.22 Rear surface of a plastic staircase target.

the pusher. After laser drilling a 10µm hole the polystyrene mandrel is dissolved out leaving an empty shell. Shells with thin inner layers of bismuth, and copper have been fabricated by this process.

A major part of the experimental programme in the last year has been devoted to studying the coallescing of shocks of increasing strength launched sequentially into targets. Foil targets with a multiplicity of steps on the rear surface have been fabricated for this purpose from plastic and aluminium. Fig A5.22 shows a photograph of the rear surface of such a plastic staircase target which has been made by UV laser photoablation techniques. Each of the 6 steps are 5µm high and 50µm wide with the thinest part of the target only 8µm. Using laser machining methods it is possible to vary the step width and depth over a wide range from micron to millimetre dimensions.

B1 CHEMISTRY

Editors: S Tavender
A Langley

Section B INTRODUCTION

The Laser Support Facility which came into being in May 1985 operates a Laser Loan Pool and three laboratories at RAL (Dye, Excimer and Picosecond Laser Laboratories) to support academic research in all fields covered by the Science Board of the SERC. The remarkable breadth of the research programme that results can be seen from the scientific contributions to sections B1, B2 and B3 which range from multiphoton physics to in-vivo molecular biology by way of several fields of physics, biology and organic and inorganic chemistry. There are thirty contributions, an increase of twenty five per cent over last year due to strong growth in the Loan Pool and Picosecond programmes. They come from twenty one institutions spread from Belfast and Dundee to Essex and Southampton.

This research is backed up by an active research and development programme within the facility which is described in sections B4, C3 and C4.2 and is presently concentrated on picosecond techniques.

B1.1 SERRS OF MODIFIED ELECTRODES

R E Hester and H R Virdee
Chemistry Department, University of York

Recent advances in the techniques of Raman spectroscopy have resulted in major improvements in sensitivity. One important area of application for the new methods is the study, in situ, of electrode surfaces.

Reactions at metal and semiconductor electrode surfaces typically involve low concentrations of solution or surface-bound species which are confined to the thin film zone at the interface. Probing the structures and dynamics of such thin films places stringent demands on analytical techniques. Although laser Raman spectroscopy readily provides the spacial resolution required and yields data which relate directly to the structures and nature of chemical bonding in electrode surface species, it is necessary to employ additional enhancement techniques in order to achieve the required sensitivity. Typically, solution concentrations in excess of millimolar are needed for normal spontaneous Raman spectroscopic studies but this sensitivity limit has been extended to the sub-micromolar range by the use of resonance Raman enhancement techniques or surface enhancement techniques. We have shown that combination of the two - surface enhanced resonance Raman spectroscopy (SERRS) - can yield good quality vibrational spectra from species in the sub-nanomolar concentration range.

In order to obtain strong resonance enhancement of Raman band intensities the species of interest must have an intense optical absorption at the laser wavelength used for excitation of the spectra. Surface enhancements of a worthwhile magnitude have been demonstrated for only a small range of metals, notably silver, gold, and copper. These represent rather severe constraints on the applicability of SERRS to the study of electrode surfaces. A major aim of our work at the LSF has been to lift these constraints and thereby to open up this novel form of sensitized vibrational spectroscopy to a much wider range of electrode materials and adsorbate species. The key ingredient in this programme then is the availability of laser sources for Raman excitation which are tunable through the ultraviolet region. In addition to the intrinsic advantages of fourth-power frequency dependence and a good detector sensitivity in the UV region as compared with the red end of the visible range (where most of the previous work has been conducted), many more molecules give strong absorptions (and have resonance enhancement) in the uv and it was hoped that surface enhancement mechanisms would be discovered in a wide range of materials in this wavelength region.

To date it has to be reported that these expectations have been only partly realised. Our work during this past year has concentrated on the study of modified electrodes. In particular, we have prepared a variety of different metal electrodes overcoated with thin films (electro-deposited from aqueous solution) of thionine and of polypyrrole. Both of these systems can be induced to undergo oxidation state changes in situ by polarization of the electrodes and there is much interest in the surface structures and electron transport mechanisms of the thin surface films. Complementary RRS and SERRS studies in our York laboratory have yielded extensive data relating to structure and mechanism in these systems during this

period but the uv excitation studies have been less productive so far. Strong uv absorption bands for both the thionine and the polypyrrole systems were expected, on account of their different electronic origins from the visible absorptions, to yield complementary vibrational mode enhancements and thus to add significantly to our understanding of them. However, in the limited periods of access which we have had to the LSF uv lasers, we have encountered a series of problems which, so far, have prevented achievement of our objectives for this project. Notable among these are the - not entirely unexpected - problems of sample fluorescence interferences and of sample decomposition at the electrode surface. Previous related studies had led us to the reasonable expectation that both of these problems would be less severe than has in fact proved to be the case. Our experimental systems have had to be extensively modified to cope with the technical problems and the work has some way to go yet before it can drawn to a conclusion.

B1.2 RESONANCE RAMAN SPECTROSCOPY OF PROTEIN SECONDARY STRUCTURES

R E Hester, J de Groot, B Stewart, H R Virdee, and J C Austin
Chemistry Department, University of York

The primary structure of a protein molecule is determined by the nature and sequence of the amino-acid (AA) residues of which it is composed. Proteins are mostly linear chain polymers with a great deal of flexibility and the way in which the individual AA residues arrange themselves in relation to one another determines the secondary structure. The three major classes of such secondary structure are α-helices, β-sheets and disordered or random coil arrangements. These may be further sub-divided and there also are important connecting structures such as the β-turn. Intra-chain hydrogen bonding is an important determinant of protein secondary structure, but other types of interaction also are influential. The arrangement of helices, sheet structures, etc, in relation to one another constitutes the protein tertiary structure. Some proteins further aggregate in natural conditions to form dimers, tetramers, hexamers, etc (eg haemoglobin is tetrameric), thus generating a quaternary structure.

It is at the level of the interactions which determine the protein secondary structure that much biological activity and control appears to reside and there is correspondingly great interest in developing spectroscopic methods which are capable of probing this structure and responding to changes induced by protein denaturation and other less drastic structural modifications. X-ray crystallography has so far been the primary tool in determining protein structure but it is clear that the requirement for a well ordered crystalline sample constitutes a severe constraint on this method in the context of real biological systems. For dilute aqueous solutions circular dichroism (CD) or optical rotatory dispersion (ORD) can yield global information on protein conformation but lack the ability to probe specific structural features.

There has been an enormous growth in activity, world-wide, in recent years in the use of Raman spectroscopy for the study of proteins and other biomolecular systems (nucleic acids, membranes, hormones, etc). The reasons for this activity are not hard to find; the Raman method does yield specific structural information (eg on disulphide links, tyrosine, tryptophan, phenylalanine, and histidine residues), it is sensitive to overall conformational features (through amide I and III band shapes and intensities), and it is applicable equally to crystalline, amorphous solid, aqueous solution, and membrane-bound protein systems.

In our York laboratories we have been using resonance-enhanced Raman spectroscopy to study haem proteins with excitation in the visible region of the spectrum. These experiments have yielded much interesting new data, particularly on haemoglobins, which related specifically to the active site and the way in which this responds through oxidation and spin-state changes, to ligation changes at the iron centre. Our aim in using the LSF lasers in this programme has been to generate complementary information on the structure of the protein part of these molecules by excitation of their resonance Raman spectra in the short-wave ultraviolet region. The aromatic amino-acid residues absorb in the wavelength region 200-260 nm and the peptide link which is a repeating unit in the protein polymer backbone absorbs in the 180-200 nm region. Thus by uv wavelength-selective resonance excitation of protein Raman spectra we have been attempting to probe secondary structure and

microenvironment of aromatic amino-acid residues.

Most of our time at the LSF has been spent in system development and working with model systems. We have greatly improved the performance of the Spex Triplemate triple spectrometer in the short-wave uv region and have worked on a variety of different laser systems (ArF 193 nm, KrF 248 nm, with and without stimulated Raman shifting, frequency multiplied dye, etc). But the present sensitivity of the whole system at short ultraviolet wavelengths remains inadequate for routine protein resonance Raman spectroscopy. Further enhancements in the technical specification are required and we have identified the way forward in this area, which remains important.

B1.3 TIME-RESOLVED RESONANCE RAMAN SPECTROSCOPY OF ELECTRONICALLY EXCITED STATES

D Phillips, I McCubbin, A Parker, J N Moore (The Royal Institution) and R E Hester (University of York)

Time-resolved resonance Raman (TR^3) spectroscopy of a variety of molecular systems has been carried out using techniques described in earlier reports.

1. Anthraquinone derivatives

Interpretation of the copious results obtained on a series of so-called 'strong' and 'weak' photosensitisers based upon sulphonated anthraquinones has been completed, and most of the results now published (Ref B1.1-B1.8). Results on the 'weak' sensitisers (see figure B1.1) are typified by the TR^3 spectra of anthraquinone 1,5 disulphonate (1) shown in Figure B1.2, with the time dependence of the spectra given in Figure B1.3. The transient was ascribed to the $^3\pi\pi^*$ state of the sensitiser. In the case of the other 'weak' sensitiser, AQ1B2MS, (II), no transient Raman spectra were observed, probably because of the short triplet lifetime of this molecule.

2. Duroquinone

Benzoquinone and its derivatives have been the subject of many photochemical and pulse radiolysis investigations seeking to establish the reactivity and decay characteristics of their excited states and semiquinone forms. Such derivatives include duroquinone, plastoquinone and uniquinone, whose roles as reversible biological electron carriers make them of particular interest. Whilst such studies have been able to provide kinetic and broad spectral information, until recently little was known about the structural changes inherent in the transitions from ground to excited states or neutral to semi-reduce forms. TR^3 spectroscopy has the potential of providing valuable information in this regard, and we report here the results of preliminary experiments on this system (Ref B1.9). The structure of duroquinone is shown in Figure B1.4.

Following excitation of DQ by 248 nm radiation, rapid relaxation to

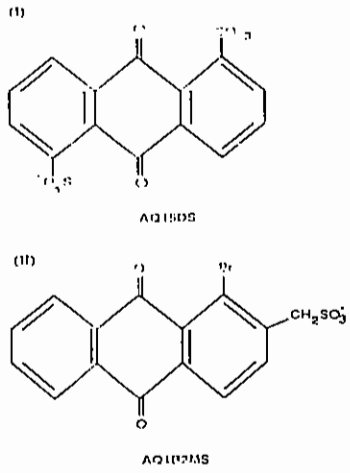

Fig B1.1 Structure of the weak sensitisers.

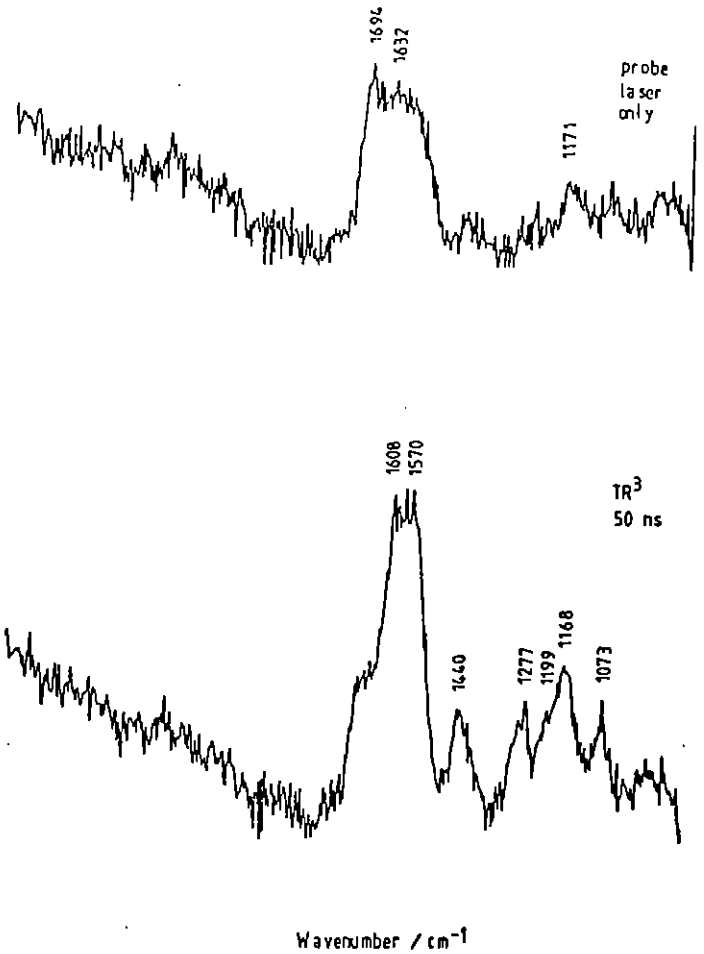

Fig B1.2 Raman spectra observed for AQ1,5DS (5 x 10^{-3} M) in aqueous solution using a probe laser wavelength 425 nm. Pump laser 357 nm.

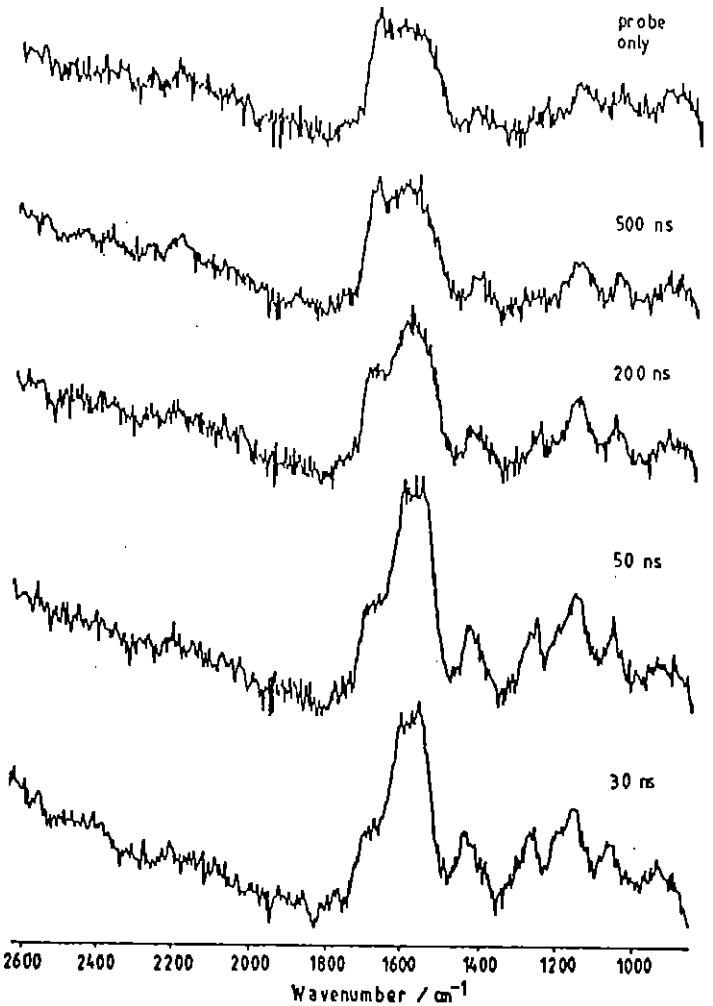

Fig B1.3 Time-dependence of the TR^3 spectrum observed on photolysis of AQ1,5DS (5 x 10^{-3}) in aqueous solution. Pump laser 351 nm; probe laser 425 nm.

S_1 is followed by intersystem crossing to the triple state (the quantum yield, ϕ_T, for this process being unity). Flash photolysis absorption spectra (see Figure B1.4) show that a resonance enhancement of the triplet state Raman scattering may be expected to occur using a probe wavelength of 500 nm. Figure B1.5 shows spectra obtained in the present work from a 5 x 10^{-3} M solution of DQ in ethanol with 50 ns delay between the pump (248 nm) and probe (500 nm) pulses.

Comparison with the ground-state Raman spectrum of DQ revealed the presence of a new band at 1562 cm^{-1}. Previous results for the analagous triplet benzoquinone reveal some ambiguity of vibrational mode assignments due to Fermi resonance coupling of the symmetric C = O and C = C (Wilson 8a) modes, the extent of which evidently varies with solvent and between the solution and solid state phases. The assignments given in Table B1.1 are indicated by H/D isotope

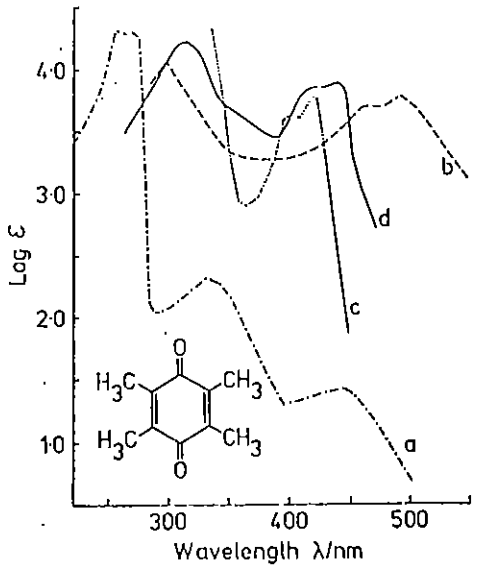

Fig B1.4 Duroquinone absorption spectra for (a) the ground singlet state (S_0 in n-hexdane, (b) the excited triplet state (T_1), (c) the semiquinone neutral radical (DCH), and (d) the semiquinone radical anion (DQ).

shift data. If we associate the 1562 cm^{-1} band with the C = C stretching mode we must conclude that there is substantial π^* antibonding electron density in the ring as well as on the carbonyl groups in the DQ excited triplet state.

TABLE B1.1 Vibrational Band Wavenumbers/cm^{-1} and Band Assignments for Duroquinone and Benzoquinone

Species	DQ	BQ	Assignments
Ground state	1662	1674	ν_s(C=C)(8a)
S_0	1638	1660	ν_s(C=O) Fermi resonance double
Triplet state	1562	1554	ν_s(C=C)(8a)
T_1	-	1496	ν_s(C=O)
Semiquinone	1646	1622	ν_s(C=C)(8a)
Radican anion Q^-	1464	1438	ν_s(C=O)

By varying the delay between the laser pulses, the time dependence of the formation and decay of this transient can be studied. This gives an apparent and approximate pseudo-first-order decay rate constant of 8.1 x 10^6 s^{-1}, this value being in reasonable accord with the literature value for the triplet state decay of duroquinone in 1 millimolar solutions. This provides some support for the assignment of this transient feature to a triplet state vibration although the variation absorption attentuation of the Raman band intensities limits the reliability of these uncorrected intensity data rather severely for the determination of rate constants.

Changing the probe wavelength to 440 nm should lead to resonance enhancement of the Raman scattering from the DQ semiquinone radical (Figure B1.4). Since triplet state DQ is thought to be capable of hydrogen abstraction in alcohol solvents, we would expect to observe bands characteristic of the neutral radical in the Raman spectrum, as well as the triplet band, which may still be enhanced, albeit at reduced intensity. Figure B1.6 shows the spectra obtained with 440 nm excitation at various delay times after pumping at 248 nm. Two new features are observed in these spectra, at 1645 cm^{-1} and at 1510 cm^{-1}. The band at 1562 is still observed, but is greatly reduced in intensity compared with the band given by 500 nm probe excitation.

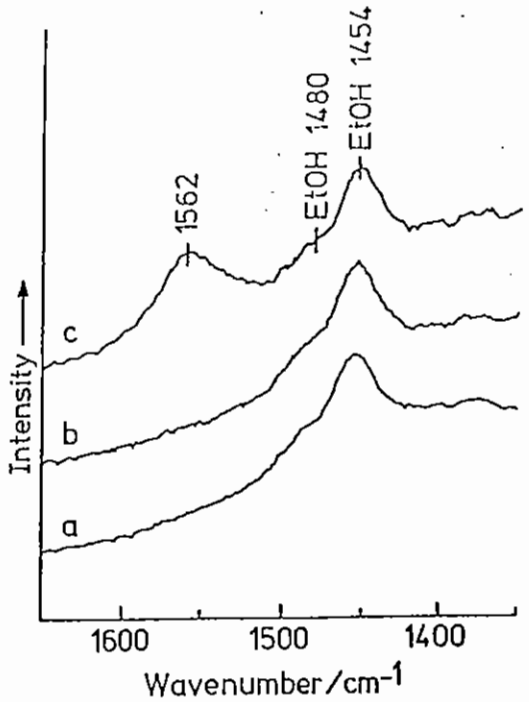

Fig B1.5 Raman spectra of (a) ethanol, EtOH, (b) 5 x 10^{-3} M DQ in EtOH, 500 nm probe laser only, (c) as (b) but with 248 nm pump, 50 ns delay, then 500 nm probe.

Again by comparison with assignments previously made for the neutral (ie protonated) benzoquinone radical we attribute the 1645 cm^{-1} RR band to the C = C (8a) stretching and 1510 cm^{-1} to the C = O stretching mode. The double bond character of the quinone carbonyl in this free radical DQH species evidently is much reduced from that in the DQ ground state parent, indicative of extensive delocalisation of the odd electron from the C-OH end of the molecule. We do not observe a band attributable to the C-OH vibration, presumably because this bond is no longer a part of the π-electron systems and thus its resonance enhancement in the Raman spectrum is lost.

A change of solvent to EtOH/H_2O (50/50 v/v) was found to decrease the relative intensity of the 1498 cm^{-1} band. Since the pKa of DQH in water is 5.1, it is to be expected that it will partially dissociate in the EtOH/H_2O solvent to form the DQ radical anion.

Figure B1.7 shows the spectra excited by a probe beam of wavelength 440 nm focussed into a solution of DQ in 50/50 v/v EtOH/H_2O containing 4 x 10^{-2}M $NaNO_2$ as a reducing agent. A drastic increase in the intensity of one band is observed (slightly shifted to 1646 cm^{-1}) as compared with the spectrum from pure EtOH solution, and only a small contribution, at short time delays, from the band previously assigned to the triplet state (1565 cm^{-1}). One other transient band is observed at 1464 cm^{-1} (see Figure B1.7), although this is partially obscured by overlap with a solvent EtOH band. We can therefore conclude that, due to the addition of excess NO_2^-, the triplet state of DQ is reduced to the semiquinone radical anion, DQ^-, in this experiment. No other bands due to DQ^3 were detected, as in the previous mixed solvent experiment in the absence of NO_2^-, again implying that any other bands are intrinsically weak due to their relatively low RR enhancements. From comparison with the other data given in Table B1.1, we can conclude that the odd electron in DQ^- is heavily localised on the two C = O groups, in contrast with $DQ(T_1)$ wherein substantial delocalisation of the π^* electron over the ring orbitals was indicated.

The build up of a steady state concentration of DQ^2 can be inferred from the fact that a signal is obtained from the scattering of the

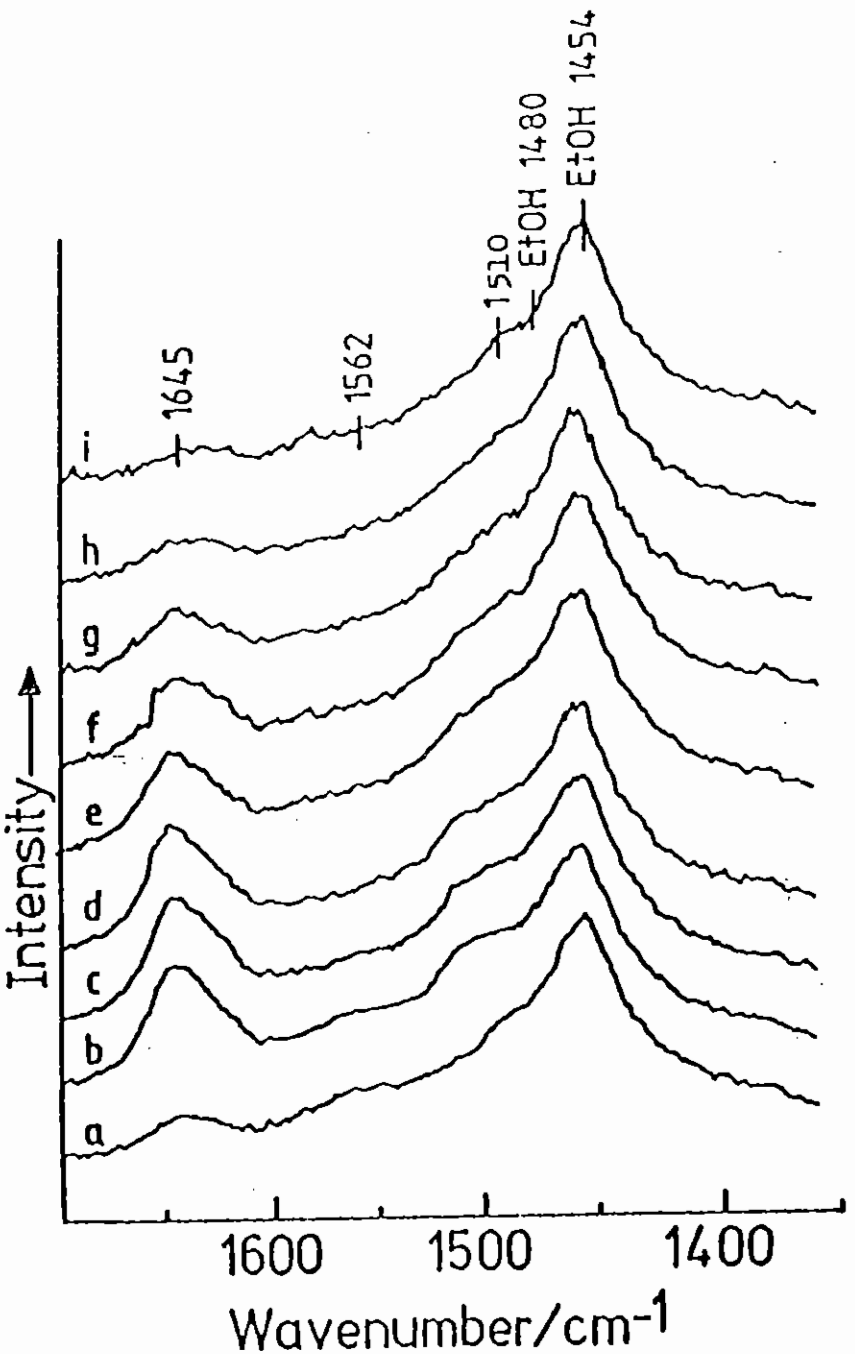

Fig B1.6 Pump (248 nm)-then-probe (440 nm) TR^3 spectra of 5 x 10^{-1} M DQ in EtOH with delay times of (a) 50ns, (b) 100ns, (c) 150ns, (d) 200ns, (e) 300ns, (f) 500ns, (g) 1 µs, (h) 2 µs, (i) 4 µs.

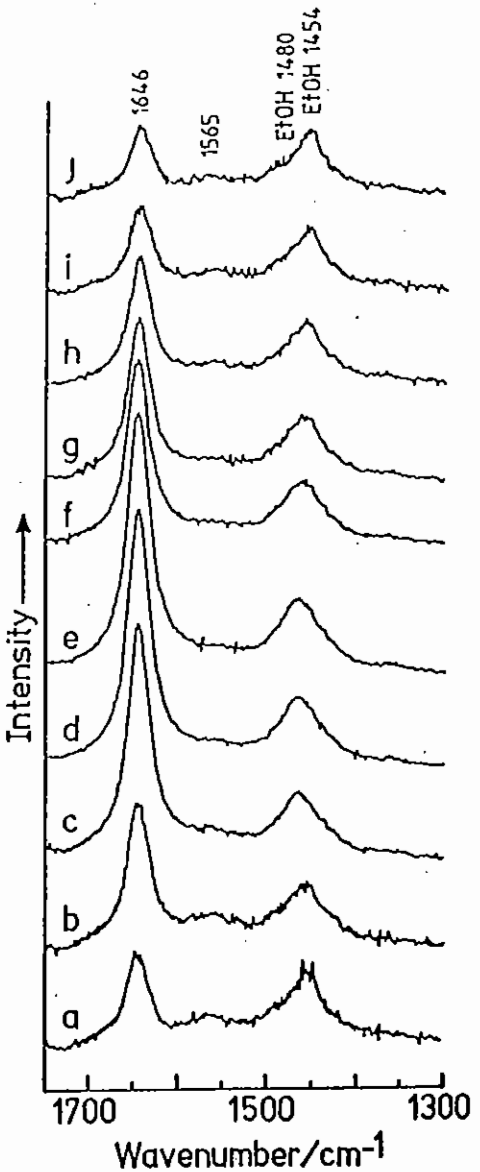

Fig B1.7 Pump (248 nm)-then-probe (440 nm) TR^3 spectra of 5 x 10^{-3} M DQ with 4 x 10^{-2} M $NaNo_2$ in $EtOH/H_2O$) (50/50 v/v) with delay times of (a) 0, (b) 25 ns, (c) 50 ns, (d) 100 ns, (e) 200 ns, (f) 3.5 µs, (g) 10 µs, (h) 20 µs, (i) 100 µs, (j) probe laser only.

laser alone (Figure B1.5) after previous irradiation of the solution

The DQ- formed in these experiments appears rapidly in conjunction w the virtual disappearance of triplet state scattering, even at zero time delay between pump and probe pulses (pulse width ca 5 ns) the DQ- then decays over a period of several microseconds.

B1.4 TR³ SPECTROSCOPY OF METAL CARBENE COMPLEXES

J J McGarvey, S E J Bell and K C Gordon
Dept of Chemistry, Queen's University of Belfast

The programme at the LSF on the resonance Raman (RR) spectroscopy of four-coordinate copper (I) complexes was concluded during the early part of the year; one paper has been published (B1.10) and others are in course of preparation. Work on these complexes will be continuing at QUB using the OMA III system installed there at the end of 1986.

Since the 1986 Annual Report, in the course of two visits to the Facility we have extended our single-colour resonance Raman investigations of photogenerated transients in the metallacarbene complex, $(CO)_5W{=}C(OMe)Ph$. To provide further evidence for the structure (involving a $-W-\overset{H}{-}-C$ interaction) proposed in the last report for the 10μs transient formed by photo-induced CO loss we have varied the Raman excitation wavelength, studied the deuterated ($-OCD_3$) complex and also carried out two-laser, time-resolved Raman experiments.

Experimental

Ground state RR spectra were generated using UV (363.8nm) and visible (488nm, 514.5nm) outputs from the Innova Ar+ laser. Figure B1.8 is a schematic diagram of the set-up for time-resolved studies of transient species using either the pulsed dye laser alone (as pump and probe), or as probe in conjunction with the EMG150 excimer (broadband output) pump laser. All solutions were degassed by argon purging and flowed through quartz capillaries. Both Spectroscopy Instruments (OSMA) and EG&G (OMA) diode array detectors were used to record Raman spectra, as indicated on the appropriate figure captions.

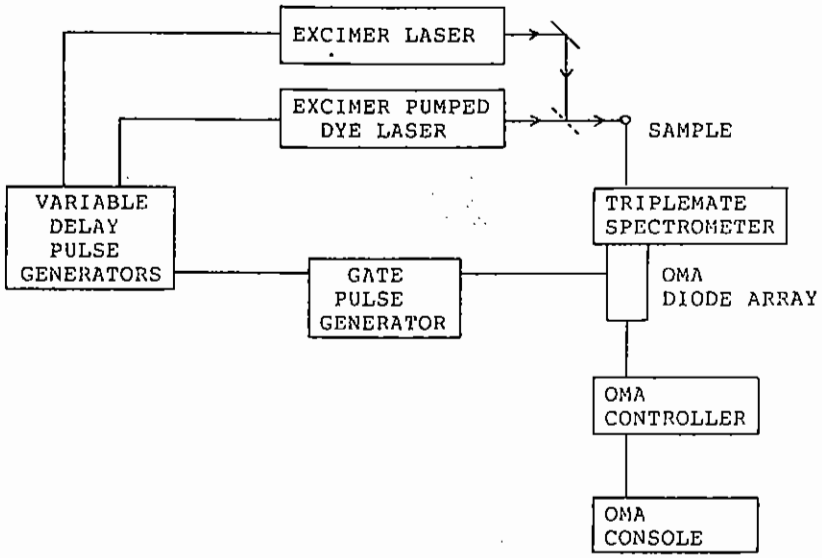

Fig B1.8 A block diagram of the experimental layout used for two-laser, time-resolved resonance Raman studies.

Results and discussion

The resonance Raman spectrum of the deuterated Fischer complex generated by pulsed laser excitation at 370nm is shown in Figure B1.9. Vibrational features attributable to both ground state and transient species are evident and the spectrum bears a strong resemblance to previously reported spectra (B1.11) of the normal Fischer complex. Although a strong solvent band at 1026cm^{-1} masks part of the low frequency region of the spectrum, it is nevertheless clear that most of the features visible are shifted only slightly (<10cm^{-1}) from their respective positions in the spectrum of undeuterated Fischer. The one exception is the band at 1156cm^{-1} which appeared at 1105cm^{-1} in the transient spectrum of the undeuterated complex and was the only feature in that spectrum with no obvious ground state counterpart. The marked frequency shift which occurs on deuteration suggests that the 1105cm^{-1} band is intimately associated with the methyl group of the transient species.

However, the direction of the shift, to higher rather than lower frequencies, shows that it cannot be attributable to a "normal" vibrational mode of a terminal CH_3 group but instead may be due to an unusual deformation mode of CH_3 such as could arise from the proposed $--W-\overset{H}{-}-C=$ ("agostic") interaction referred to above.

Figure B1.10 shows a selection of spectra from a series of two-laser, time-resolved Raman experiments on the Fischer complex. In these experiments the dye laser probe wavelength chosen was 405nm since this was considered to be sufficiently remote from the photoactive ligand-field absorption bands of the complex to prevent sample photolysis by the probe pulse. However, Figure B1.11 shows spectra recorded using the 405nm output from the dye laser alone. These show that as the focus of the laser beam is tightened, a pronounced increase occurs in the intensity of transient vibrational features with respect to ground state bands, showing that 405nm radiation does indeed photolyse the sample. The problem was minimized in the two-laser experiments by using a well-defocussed probe beam and the lowest dye pulse energy possible, consistent with detectable Raman scattering. [Moving to longer probe wavelengths would have been a much less satisfactory alternative due to the marked fall-off in transient absorption intensity and hence in resonance enhancement.] While the signal-to-noise ratio of the two-laser spectra in Figure B1.10 is lower than in single laser experiments, it is quite clear that the same transient features appear in the 150ns time delay spectrum as were observed in single laser experiments. These features decay over a period of microseconds and there is a corresponding growth in the features associated with the unphotolysed complex. The spectra in Figures B1.10 and B1.11 thus show that the same transient species which is formed within the duration of the laser pulse decays over several microseconds back to the parent Fischer complex and so may be reasonably identified with the transient species observed in independent laser flash photolysis (transient absorbance difference) studies at QUB. To our knowledge, the spectra in Figure B1.10 provide the first reported examples of time-resolved resonance Raman scattering from organometallic transient species. A preliminary account of the conclusions from the single-laser work has recently been published (B1.12). The two-laser studies were reported at the 1986 (September) Fast Reactions in

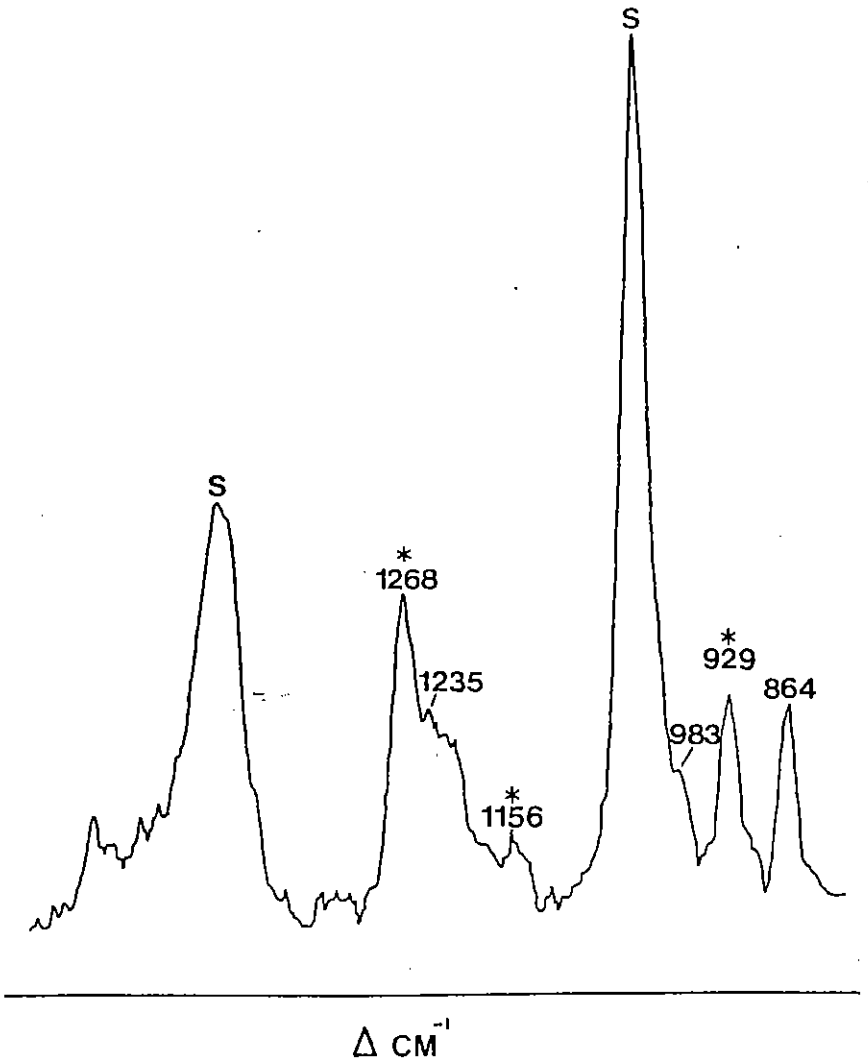

Fig B1.9 *Resonance Raman spectrum of a deuterated analogue [$(CO)_5W = C(OCD_3)$ (Ph)], of the Fischer complex. (Solution ca. 10^{-3} mol dm^{-3} in $CDCl_3$; pulsed dye laser excitation at 370 nm, 2mJ per pulse; 50 seconds total signal accumulation time on OSMA detector. Excited state features are denoted by *. S = Solvent bands.*

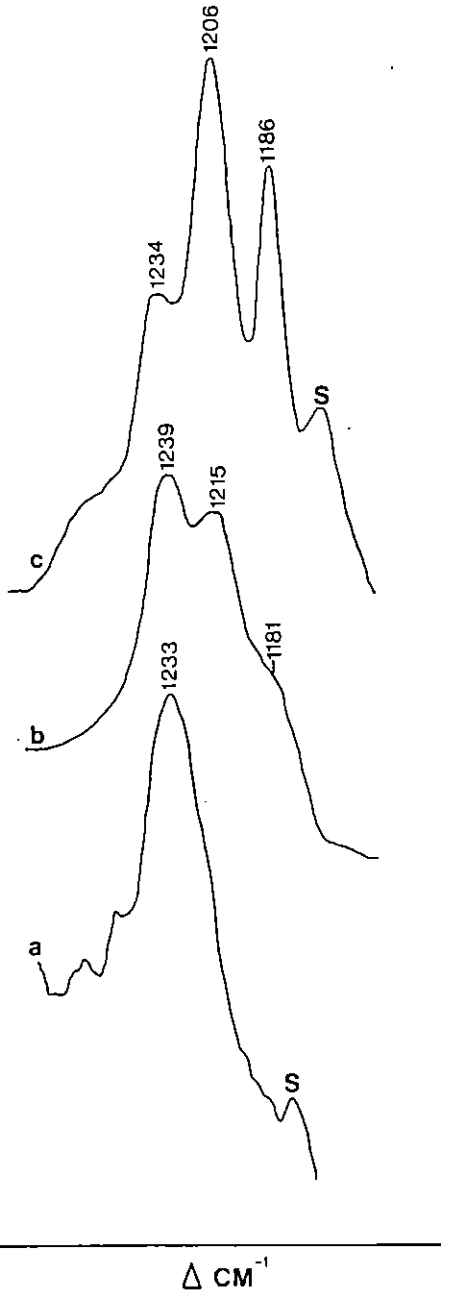

Fig B1.12 *Resonance Raman spectra of the Fischer complex recorded at three different excitation wavelengths: (a) 363.8nm, CW, Ar^+; (b) 405nm, pulsed dye excitation [an excited state feature at 1270 cm^{-1} has been removed for clarity]; 488.0nm, CW, Ar^+.*

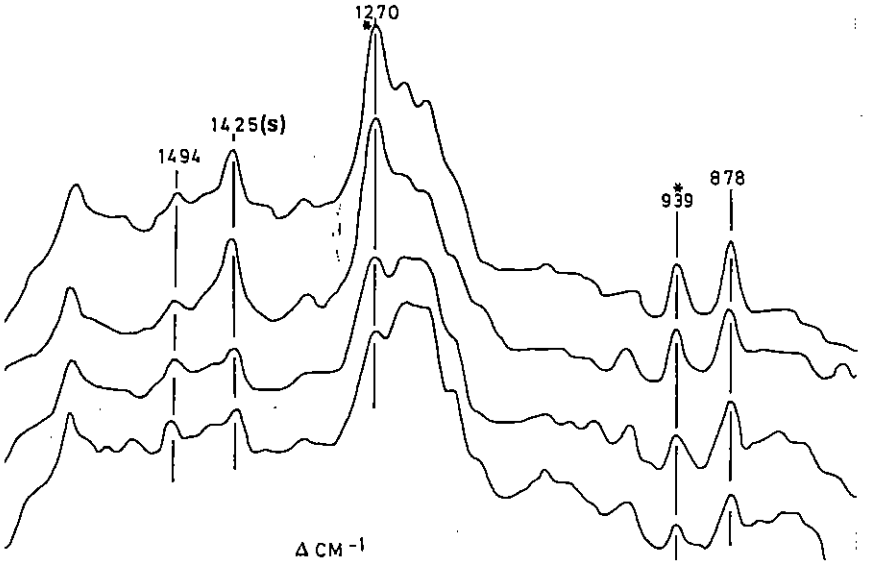

Fig B1.11 *Influence of increasing excitation laser beam focus (reading from bottom spectrum) on resonance Raman scattering from the Fischer complex. (ca. 10^{-3} mol dm^{-3} solution in CH_2Cl_2); Pulsed dye excitation at 405nm, 0.5m per pulse.*

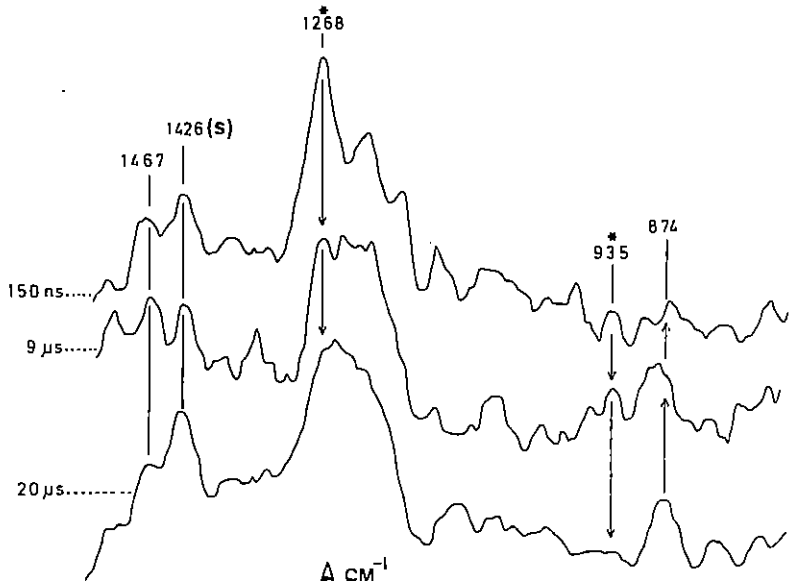

Fig B1.10 *Time-resolved resonance Raman spectra of the Fischer complex. Excimer pump laser, 2mJ, 10 Hz at 351nm; dye laser probe, 0.5mJ, 10 H_z at 405nm. Probe beam well-defocussed to minimize secondary pumping. Pump - probe time delays are as shown on spectra.*

Solution Meeting, Gargnano, Italy (B1.13) and a full paper is now being prepared for publication.

We have also begun a more detailed investigation of resonance Raman scattering in the Fischer and related complexes as a function of laser excitation wavelength. Raman spectra of unphotolysed Fischer at three different probe wavelengths are shown in Figure B1.12.

Clearly, several new features at ca.1200cm^{-1} increase in intensity on going to longer wavelengths. Analysis of these results (including the construction of corresponding Raman excitation profiles) is still at a preliminary stage but it appears that they may provide new information concerning the conformations adopted by these interesting and catalytically important species in solution. We plan to continue this line of investigation and also to explore the use of the resonance Raman method as a structural probe of photogenerated transients in other metal carbonyl systems.

B1.5 RESONANCE RAMAN SPECTROSCOPY OF SOLIDS

T J Dines (Dundee University)

An attempt was made to obtain resonance Raman spectra of the $[CrO_4]^{2-}$ ion in the solid state using dye laser excitation in the range 25,000-30,000 cm^{-1} (ca. 330-400 nm). This experiment is part of a long-term project concerned with the measurement of RR excitation profiles (plots of Raman band intensities versus laser excitation wavenumber) of inorganic solids. Theoretical analysis of excitation profiles that display vibronic fine structure enables the determination of excited-state molecular geometries with greater precision than is usually obtained by Franck-Condon analysis of absorption spectra.

The measurement of detailed excitation profiles requires tunable dye laser excitation in order to obtain data points at intervals of 100 cm^{-1} or less. Whilst much has been achieved in the last 10-20 years using cw dye lasers in the visible region, there is a clear need to extend this work into the u.v., so that a broader range of molecules can be studied. Some previous experiments, using the u.v. lines of an argon ion laser, have demonstrated that $[CrO_4]^{2-}$ (K^2 or Cs^+ salt dispersed in an alkali halide disc) is an ideal prototype because it displays strong, well-resolved RR spectra and does not appear to undergo photo-decomposition.

Initial experiments at RAL were carried out during Division Head's week using the FL2002 dye laser in conjunction with the Monospek spectrometer and OSMA detector. The optical alignment of this system was first established by measurement of Raman scattering from liquid samples (CCl_4 and cyclohexane). Spectra could be obtained although the stray light rejection of the single monochromator was very poor. The solid samples produced a much higher level of Rayleigh scattering and it was not possible to detect any Raman signal within 1000 cm^{-1} of the exciting line (even by using a laser filter between the sample and spectrometer). It was concluded that the stray light rejection of the single monochromator was insufficient for RR experiments on solids. During the last two days of the experiment the Triplemate became available. Using this spectrometer the Rayleigh background was reduced to an acceptable level and some Raman scattering could be observed. However, even with the laser pulse energy considerably reduced, there was evidence of sample damage, such that it was not possible to obtain reliable RR intensity measurements. These trial experiments indicate that it will be necessary to use a dye laser operating with a much faster repetition rate and lower pulse energy. In conjunction with the triple monochromator this should produce the desired results.

B1.6 REACTION DYNAMICS OF REACTIONS BETWEEN TWO FREE RADICALS

A M L Irvine, B J Orr, I W M Smith and R P Tuckett
(Dept of Chemistry, University of Birmingham)

We are studying the energy disposal into the products of exothermic reactions between two free radicals. Such measurements can indicate the role played in the dynamics by the formation of transient collision complexes. In particular, we are studying the energy disposal in radical-radical reactions which produce nitric oxide as one of their products. The following reactions are being studied:

		ΔH° (kJ mole^{-1})	
$H + NO_2 \rightarrow OH + NO$		−124	(1)
$O + NO_2 \rightarrow O_2 + NO$		−193	(2)
$N + OH \rightarrow H + NO$		−204	(3)

The NO $X^2\Pi(v,J)$ internal state distribution is probed by single photon laser-induced fluorescent to the $A^2\Sigma^+$ state at 226 nm. The (0,0) band is obtained by Raman shifting the output of an excimer-pumped dye laser at 360 nm through a high pressure cell of hydrogen, and using the 4th Anti-Stokes line to drive the A-X transition. Due to the non-linear effect of Raman shifting, pulse-to-pulse stability of AS4 can be as high as ±40%. The Stanford Research System 2 channel gated integrator (on loan from the RAL Loan Pool) is used to ratio fluorescence from the pm tube to laser pulse intensity shot-by-shot, and the integrated and smoothed output is then recorded. The apparatus is now under micro-computer control from a BBC Master. The computer drives the dye laser and collects fluorescence intensity from the pm tube with each shot ratioed to the laser pulse intensity. The spectra are stored on disc, and are then transferred to the University Mainframe Computer for plotting and analysis.

We have now studied reaction (1) in some detail, and preliminary results were presented at the 9th International Conference on Gas Kinetics in Bordeaux in July 1986. Both OH and NO products have been probed by LIF, and the results can be summarised as follows. The NO is produced vibrationally and rotationally cold. The lack of vibrational excitation in the NO is surprising, since this suggests that the NO is a 'spectator' to the reaction and that the dynamics are dominated by a 'direct' mechanism. In other words, as far as the NO is concerned, the HONO* complex plays no part in the dynamics. The OH product, however, is produced vibrationally and rotationally hot, with unequal Λ-doublet population of rotational levels of OH $X^2\Pi$. This last point can be explained if some of the reaction goes via the HONO* $^1A_1$ ground state potential energy surface. The degree of rotational excitation of OH is greater than would be expected for a statistical redistribution of the available energy.

B1.7 INFRARED DIODE LASER SPECTROSCOPY OF TRANSIENT MOLECULES PRODUCED BY LASER PHOTOLYSIS

P Davies (University of Cambridge)

Although the original application sought to generate relatively long lived and spectroscopically well studied radicals such as SO and PH it became clear that these could only be generated with 193 nm excimer radiation. However, there seemed a good possibility of generating chlorine atoms (with the appropriate substrate) using the quadrupled Nd:YAG. Krasnoperov et al (ref B1.14) have achieved this using S_2Cl_2 as starting material, the liberated chlorine atoms reacting with SiH_4. Chlorine atoms are good candidates for tunable diode laser detection as they have a fine structure transition $^3P_{3/2} - {}^3P_{1/2}$ at 880 cm^{-1} which has already been detected in cw experiments (ref B1-15). Although we have not so far detected these species with our diode laser in the laser photolysis experiment there is little doubt that the S_2Cl_2 decomposes and forms particulate deposits, possibly sulphur. The multiple pass arrangement shown in the figure in the application could not be used because of a shortage of appropriate optics. In particular the parallel plate multiple reflection mirrors for confining the photolysis pulses inside the white cell were inadequate. Another problem uncovered concerned the effect of intense reflected visible/uv beams on the detection of the sensing infrared diode beam. In future experiments we shall adopt the capillary photolysis cell arrangement developed by Beckworth et al. (ref B1.16) at McMaster University with subsequent separation of the two laser beams with a grating prior to detection.

Although this preliminary experiment met with limited success we are keen to continue with these experiments and strongly advocate obtaining a fluoride excimer laser which can be dedicated to photolysis experiments.

B1.8 PHOTO-INDUCED ELECTRON TRANSFER IN PYROMELLITIMIDE-BRIDGED PORPHYRINS

R J Harrison, B Pearce, G S Beddard*
(Department of Chemistry, University of Manchester)

J A Cowan, J K M Sanders
(University Chemical Laboratory, Cambridge)

The kinetics of intramolecular photoinduced electron transfer in a series of pyromellitimide-bridged porphyrins (H_2/Mg/Zn BPC_n, n=2,3,5 [ref B1.17]) have been studied in both absorption and emission using the picosecond laser spectrometer in Manchester [ref B1.18, B1.19, B1.20] in conjunction with a streak camera from the laser loan pool. In the compounds used the pyromellitimide group is covalently bound by two alkyl chains and sits atop the porphyrin ring and at a separation and orientation determined by the length of the chain, fig B1.13. On excitation of the porphyrin an electron is transferred from the porphyrin (P) e_g orbital into the LUMO orbital on the pyromellitimide (A). Subsequently the electron can be transferred back to the a_{1u} or a_{2u} orbital in the porphyrin, reforming the ground state:

$$P{-}{-}A \xrightarrow{h\nu} P^* {-}{-}A \xrightarrow{k(sep)} P^+ {-}{-}\bar{A} \xrightarrow{k(rec)} P{-}{-}A$$

The dependence of both charge separation and recombination rates on connecting chain length, metallation state, coordination state, conformation, solvent and temperature have been systematically studied and found to be broadly in agreement with theoretical predictions [3,4]. In particular the inverted region, where rates fall even though the exoergicity is increasing, is clearly observed [B1.19, B1.20].

Using the streak camera the initial fast (10^{11} s^{-1}) charge separation event was followed from the porphyrin fluorescence emission and confirmed our picosecond absorption measurements in each compound and solvent used. Furthermore, the fluorescence was non-exponential with a part of the emission having a noticeably longer lifetime, fig

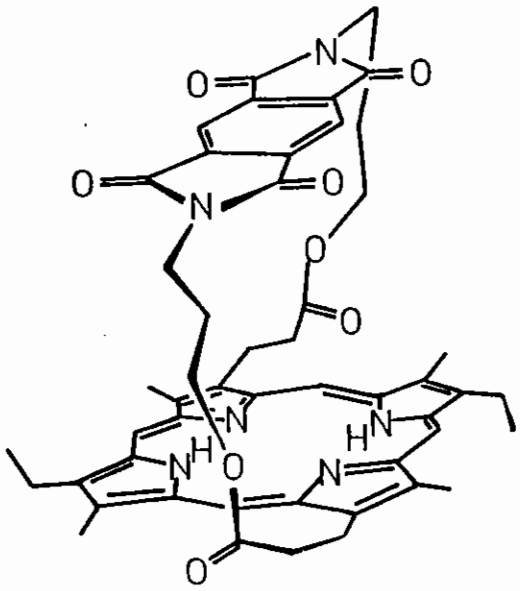

Fig B1.13 Structure of BPC_3

B1.14. This long decay is assigned to that fraction of the molecules having unfavourable orientations and separations for electron transfer between the porphyrin and porphyromellitimide acceptor [fig B1.20].

With BPC_3 the measured fluorescence lifetimes were 16 ps in toluene, 10 ps in chloroform and 8 ps in dichloromethane. The shorter values are slit width limited by the streak camera and appear longer than those measured in absorption. The fluorescence lifetimes were also measured at several temperatures in toluene DMF and EPA solvents. In each solvent an increase in lifetime is observed as the temperature falls, the effect being most marked in toluene, which is the least polar and also has the highest activation barrier. A fall-off in rate begins at 150 K and becomes effectively constant below 100 K with a value of 4.2×10^8 s^{-1} in toluene and 1.0×10^9 s^{-1} in EPA and

1.5 x 10^9 s^{-1} in DMF. This deviation from typical Arrhenius behaviour is characteristic of nuclear tunnelling becoming important at lower temperatures. Activation energies have been calculated from the higher portions of the data and give values of 0.095 eV in toluene and 0.066 eV in EPA, these values reflect the role of the solvent in governing the rate of electron transfer. A detailed account of this work will be published elsewhere [B1.20].

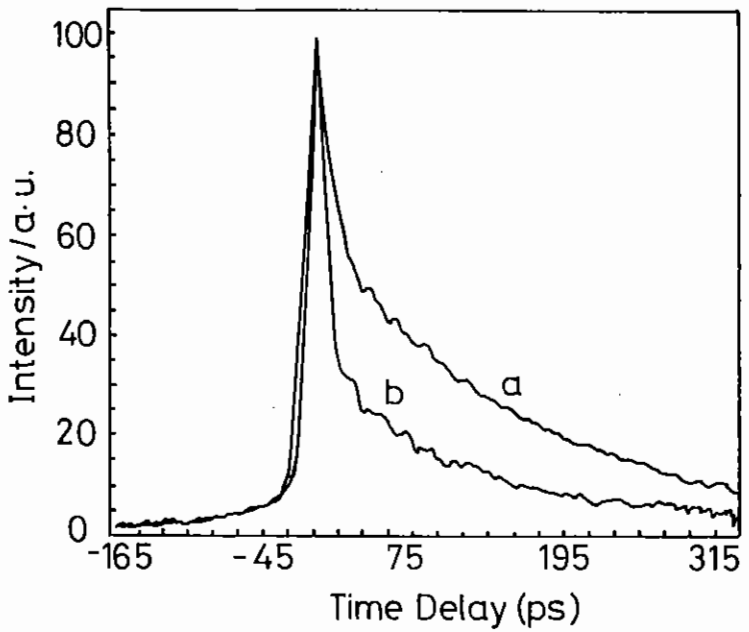

Fi

Fig B1.14 Non-exponential fluorescence decay profiles of BPC_3 measured by streak camera (a) in toluene (b) in dichloromethane both observed 625 nm and excited at 570 nm.

B1.9 LASER-INDUCED FLUORESCENCE MEASUREMENTS ON THE KINETICS OF REACTIONS OF THE OH,OD AND CH_3O RADICALS

J Brunning, D W Derbyshire and I W M Smith
University of Birmingham

Introduction

There have been many direct, spectroscopic studies of the reactions of the OH radical, but far fewer kinetic investigations of reactions of OD and of CH_3O. Using pulsed photolysis to generate radicals, their rate of removal can be observed by measuring the intensity of fluorescence induced by a pulsed tunable laser fired at variable time delays after the photolysis pulse. With OH and OD radicals, LIF signals can be observed when the laser is tuned to lines in either the (0,0) or (1,1) band, providing information about the independent kinetic behaviour of the radicals in the v=0 and v=1 levels (ref B1.21). Comparison of the rate constants for hydrogenated and deuterated species and for excited and unexcited radicals can provide important information about the detailed reaction mechanism which removes the radicals.

Methoxy radicals, like hydroxyl radicals, play an important part in atmospheric chemistry especially in the oxidation of methane, initiated by $OH + CH_4 \rightarrow CH_3 + H_2O$. Despite this the kinetic data base for reactions of CH_3O remains quite limited. A long term aim of our work is to add to this data base by measuring rate constants for a number of key reactions of CH_3O radicals. In the loan period we made our first measurements of this kind.

Experimental

The fourth harmonic of the JK Lasers Nd:YAG laser from the Laser Loan Pool was used to generate OH, OD or CH_3O radicals by photolysis of HNO_3, DNO_3 or CH_3ONO:

$$HNO_3,\ DNO_3 + h\nu(\lambda = 266\ nm) \rightarrow OH,\ OD + NO_2$$
$$CH_3ONO + h\nu(\lambda = 266\ nm) \rightarrow CH_3O + NO$$

At 266 nm, the laser produced ca 10-15 mJ/pulse which, after beam steering, gave typically 5 mJ/pulse in the reaction cell.

This photolysis laser was coupled with a frequency-doubled, flashlamp-pumped, dye laser (Chromatix, CMX-4) in our experiments. In work on OH and OD, the dye laser was tuned to a line in the (0,0) band of the A-X system. At the relatively long photolysis wavelength provided by the Nd:YAG laser, no LIF signals from OH(v=1) or OD(v=1) could be detected. The CH_3O concentrations were monitored by exciting single photon laser induced fluorescence at 297.5 nm (the 3,0 band of the A-X system). Emission was observed at longer wavelengths with careful optical filtering to minimise background from scattered laser radiation.

The experiments ran under the control of a microcomputer which accumulated the LIF signals after they had been digitised in a gated integrator. Variable time delays between the two laser pulses were provided by a commercial delay generator (Racal-Dana, GP 1500).

Results

In the first series of experiments, rate constants were determined for the reactions of OH and OD with CO at room temperature and 20 Torr total pressure:

$k(OH + CO) = 1.66 \times 10^{-13}$ cm^3 molecule^{-1}s^{-1}
$k(OD + CO) = 4.9 \times 10^{-14}$ cm^3 molecule^{-1}s^{-1}

The kinetics of OH + CO were studied largely to test the system. The value of the rate constant which we obtained is in good agreement with the recommended value (ref B1.22) which is, in turn, based on several thorough, direct studies. The kinetics of OD + CO have been studied less but our data are in agreement with other values (ref B1.23, B1.24).

In the second series of experiments, we concentrated on the reaction:

$$CH_3O + NO_2 \ (+M) \rightarrow CH_3ONO_2 \ (+M)$$

At room temperature and in 25 Torr of argon, we found a second-order rate constant of 7.2×10^{-12} cm^3 molecule^{-1}s^{-1}.

The only published values of rate constants for this association reaction were obtained at total pressures below 10 Torr (ref B1.25), but our high pressure value falls on a sensible extrapolation of the lower pressure results. We intend to extend our experimental investigation of this reaction before carrying out calculations based on unimolecular rate theories.

A preliminary attempt to measure the rate at which CH_3O radicals react with SO_2 was thwarted by the strong phosphorescence which the dye laser produces from SO_2. We hope to extend our measurements on the kinetics of reactions of CH_3O radicals in future experiments.

Discussion

The rate constants for reaction of OH and OD with CO, together with those for loss (reaction plus relaxation) of OH(v=1) and OD(v=1) with CO obtained in earlier studies, allow us to construct quite a detailed picture of this reactive system. It appears that initially OH, OD adds to CO and that the adduct so formed can then either redissociate to OH + CO or fragment to H + CO_2 (or at higher total pressure be collisionally stabilised). The rate constants for loss of vibrationally excited radicals probably correspond to the rate constants for formation of the radicals. The relatively large kinetic isotope effect observed is probably a reflection of the difference in zero-point energies in the two transition states (leading to OH + CO and to H + CO_2) in the hydrogenated and deuterated systems. Transition state calculations designed to explain the observed rate constants are being made.

The association of CH_3O with NO_2 is analogous to the well-studied reaction of OH with NO_2. However, the greater number of atoms means that the former reaction approaches its high pressure limiting rate at a smaller, more easily accessible, total pressure. A comparison of the fall-off behaviour of these two reactions will be made once the kinetic data sets are complete.

B1.10 TWO-PHOTON EXCITATION SPECTROSCOPY OF Mn^{2+}

R G Denning, J R G Thorne and I D Morrison (Department of Inorganic Chemistry, University of Oxford)

Recent interest in two-photon absorption (TPA) spectroscopy of inorganic chromophores has concentrated on centrosymmetric systems where the parity selection rules of two-photon spectroscopy complement those for single photon transitions [ref B1.26, B1.27]. We have shown that in a molecule lacking a centre of inversion we may still observe totally different selection rules for the two spectroscopies.

The absorption spectrum of tetrahedral Mn^{2+} compounds corresponds to spin forbidden electronic transitions from the ground $^6A_1$ state to the excited quartet manifold. The intensity of these is borrowed from the allowed $^6T_2$-$^6A_1$ transition via the spin-orbit interaction. Such a mechanism can give rise to intensity in all excited states except $^4A_2$ [ref B1.28, B1.29]. Using the Datachrome YAG pumped dye laser with Raman shifting as a source of radiation in the 700-1000 nm range, we excited transitions from 350-500 nm by simultaneous TPA, in single crystals of Cs_3MnX_5 and $(NR_4)_2MnX_4$ (X=Cl,Br,I:R=Me,Et) at 4 Kelvin, and directly accessed the previously unobserved $^4A_1$ state. Total luminescence was monitored at 550 nm. Figure B1.15 shows absorption and two photon luminescence excitation spectra for Cs_3MnBr_5 in the region of ^4E,$^4A_1$. We relate the energy difference between the two states (degenerate in a crystal field model) to the covalency parameters for the series of compounds.

We have observed also the two-photon luminescence excitation spectrum of $(CH_3)_4NMnCl_3$, TMMC. The absorption spectrum of this compound is dominated by magnon-assisted transitions [ref B1.30]. By the same mechanism as above, the $^4A_1$ origin band, obscured in single photon spectroscopy, is revealed in TPA.

In the course of our studies of the two-photon luminescence excitation spectrum of tetrahedrally coordinated Mn2+ in Cs_3MnBr_5, we observe intense green Mn^{2+} emission when the exciting pulsed red laser beam was tuned between 7200 A and 6700 A. We attribute this to an unusual energy transfer up-conversion taking place as follows:

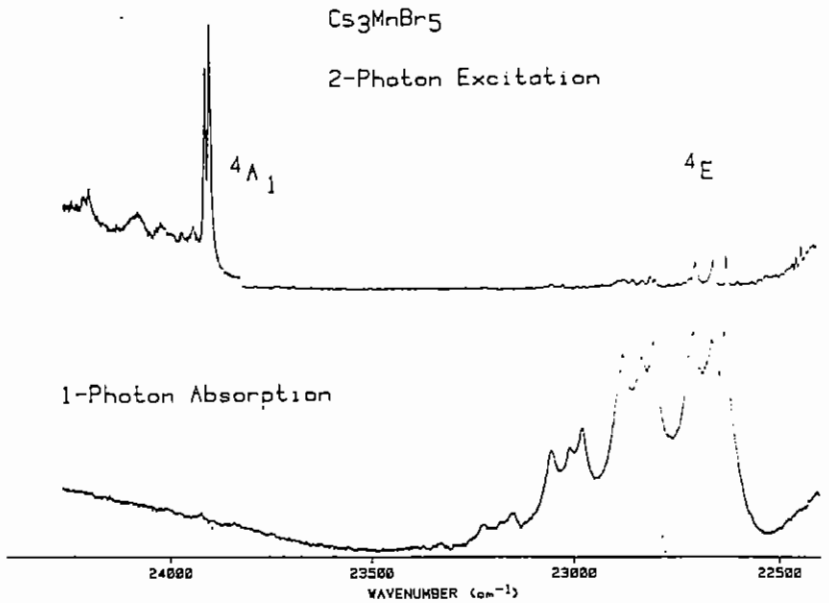

Fig B1.15 Absorption and two photon luminescence excitation spectra for Cs_3MnBr_5.

i) A small amount of Co^{2+} impurity (≤ 0.1% Co/Mn) is excited to the $^4T_1(P)$ state. This state has recently been observed to have a lifetime of 250 ns when doped in $LiGa_5O_8$ [ref B1.31]. Excited state absorption leading to hole burning has been performed in this material [ref B1.32].

ii) A second photon is absorbed which creates a Mn-Co pair state at 3550 A. Neither pure Cs_3MnBr_5 nor the cobalt analogue has an excited state at this energy and this band was previously unassigned[ref B1.33]. A similar pair transition is observed for Cu-Mn in $KZnF_3$ [ref B1.34].

iii) Non radiative decay of this state populates the luminescent $^4T_1$ lowest excited state of Mn^{2+} at 5000 A.

Artificial doping of Co^{2+} into the compound at a level of up to 0.5% indeed shows the 3550 A absorption intensity to be linearly dependent upon [Co^{2+}]. The lifetime of the emission excited at 3550 A is independent of [Co^{2+}] dopant at low temperature. The cobalt does not provide a non-radiative trap.

Acknowledgements

We should like to thank Dr A Langley for his considerable technical expertise with the loan laser.

B1.11 LASER INDUCED DESORPTION OF PHYSIOSORBED MOLECULES FROM SURFACES

C J S M Simpson (Oxford University)

During this period the results from our first investigations have been published (ref B1.35).

Most of this period has been devoted to improving the apparatus now that the preliminary experiments have been performed. In order to reduce the likelihood of adsorption on the helium cooled probe as well as the crystal, the crystal mount has been gold plated as adsorption takes places less strongly on gold than on the crystals used. In addition, a doser system has been developed so that the test gas can be directed only onto the crystal. This has involved the development of miniature ultra high vacuum valves which enable a volume of 0.25 cm^3 to be enclosed and titrated onto the crystal rather than the volume of 70 cm^3 using commercial U.H.V. valves.

Improving the signal to noise

The signal to noise was excellent for the desorption of multilayers, but poorer for monolayers. To improve this we have (1) improved the ultrahigh vacuum by installing a pumped liquid N_2 cryopump (2) improved the collection by the quadrupole mass spectrometer by mounting it inside the chamber close to the crystal.

These changes have greatly improved the performance of the apparatus, and further experiments on laser desorption of atoms and molecules are in progress. The fact that molecules are desorbed intact following laser heating rather than as fragments has considerable bearing on the study of catalytic reactions.

B1.12 PICOSECOND FLASH PHOTOLYSIS OF DIFFUSELY SCATTERING MEDIA

G P Kelly, P A Leicester, FR Wilkinson
Loughborough University of Technology, Loughborough, Leicester.

A R Anstee, J R M Barr, A J Langley
Rutherford Appleton Laboratory.

We have reported previously the development of diffuse reflectance laser flash photolysis and the successful extension of this technique into the picosecond time domain using the picosecond laser facility at RAL (ref B1.36,37). We discuss here the implementation of further developments which have been carried out over the past year. These include the extension of the wavelength range by means of continuum generation, full automation of the data collection procedure, and refinement of data analysis to account for luminescent properties of some materials. Discussion of these changes is made with particular reference to recent results obtained with crystalline 2-pyrazolines.

Experimental

Picosecond laser pulses, after 3 stage dye amplification at 10 Hz to 500μJ are frequency doubled, the residual fundamental (probe) light and frequency doubled (pump) light are dispersed by a prism. The probe light is focussed into a 4cm pathlength cell containing water. The resultant picosecond continuum (ref B1.37) is recollimated and directed onto the computer controlled variable optical delay line from whence it is directed onto the sample. The pump light is directed through a frequency programmable chopper operating at 35 Hz and synchronised with the dye amplifier. This removes alternate pump shots. The pump beam is then directed onto the sample as collinear with the probe beam as possible. Small fractions of the pump and of the probe beams are deflected using beam splitters and their intensities monitored as references.

Detection is carried out with the aid of Hamamatsu photodiodes and necessary circuitry (ref B1.38). Neutral density filters are placed in the pump reference beam as necessary. The probe reference, and probe light diffusely reflected off the sample, are collected by means of two fibre optics and directed into the input slit of a monochromator. The two beams are then detected by two photodiodes positioned intimately against the exit monochromator slit. The monochromator enables the probe wavelength of interest to be selected, within the confines of the spectral distribution produced by the probe fundamental in the continuum generation cell. The probe reference is passed through the same monochromator so that the beams remain faithful to each other; experience has shown that no optical or electronic cross-talk occurs between two signals. The geometrical relationship of all the optical components is shown in fig B1.16. The signals from the three detectors are fed to 3 separate gated integrator and box car averagers (Model 250, Stanford Research Systems) which are triggered at 10 Hz synchronised with the laser amplifier. The signals are integrated over their duration and recovered as an analogue signal and read by an A/D converter/computer interface (Model 245, Stanford Research Systems) which stores and transfers digitised signals to the IBM computer. The IBM computer controls the SR245 unit, the stepping motor which drives the optical delay, and mechanical shutters to block off the laser beams. A typical data collection sequence would be as follows: the computer sets the optical delay to a preprogrammed position; if emission is to be measured, the pump shutter is opened. A sequence of 200 shots is recorded and the data stored in the SR245 unit's memory. The shutter is closed and the data are transfered to the computer and stored on disk. Both shutters are then opened and a second sequence of 200 shots is collected, transferred and stored. The shutters are closed and the variable delay moves to the next programmed position. Both sequences are sorted by the computer into pump on and pump off sets. Hence the first sequence gives the background signals (no light on detectors) and if measured, the emission from the sample with corresponding pump reference signals. The latter data are fitted by a leastsquares polynominal curve fitting routine to enable a value for the emission intensity, E to be interpolated for any known pump intensity, P.

$$E(P) = \sum_{i=1}^{n+1} C_i\, p_i \qquad (1)$$

where C_i is the i^{th} coefficient of the calculated polynomial of order n. The second sequence gives sample detector intensitites, D, and the probe reference intensities, N, with both pump on and pump off. A straight line fit is performed on the pump off data to give the relationship between D_{off} and N.

$$D_{off} = \alpha N + \beta \qquad (2)$$

The quantity we are looking for is the relative change in reflectance which is equal to the relative change in the sample detector signals, D.

$$\frac{\Delta R}{R} = \frac{\Delta D}{D} = \frac{D_{off} - D_{on}}{D_{off}} \qquad (3) \text{ for pump intensity P.}$$

If emission is to be accounted for this must be calculated using (1) and the pump intensity P. D_{off} must be calculated using (2) taking the value for N corresponding to D_{on}.

$$\text{Hence } \frac{\Delta R}{R} = \frac{\alpha N + \beta - (D_{on} - E(P) - Pg)}{\alpha N + \beta - Dg} \qquad (4)$$

where Pg and Dg are the background signals for the pump reference detector and sample detector respectively. When the relative change

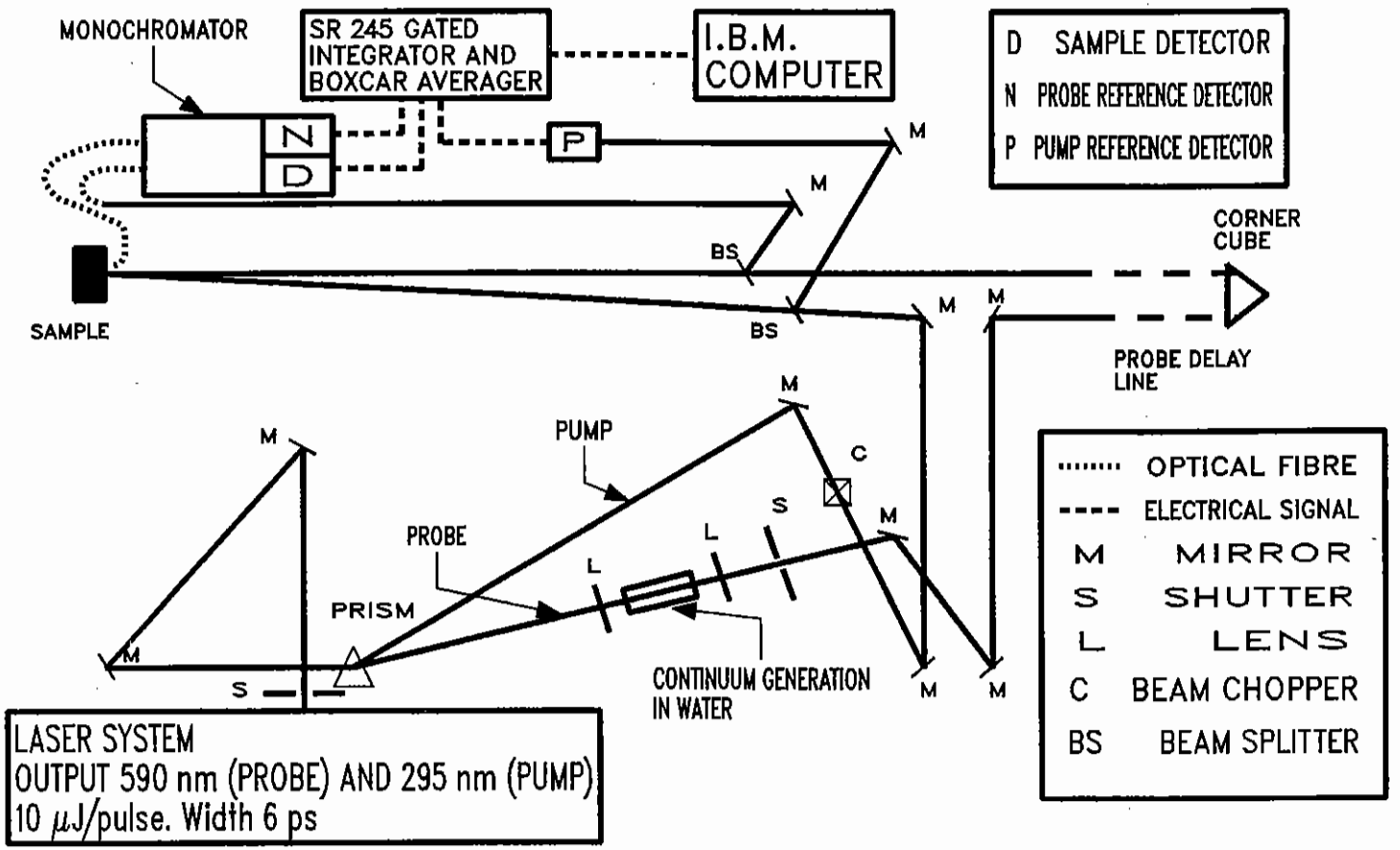

Fig B1.16

Fig B1.16 Schematic diagram of optics and detection system used in picosecond diffuse reflectance laser flash photolysis.

in reflectance is proportional to pump energy the value obtained using (4) is normalised to P and all the values are averaged. A nonlinear dependence between ΔR/R and P has also been observed and in this case a polynominal fit is calculated for ΔR/R upon P and a typical value for P chosen to yield the actual absorption change and the same value of P is used for a set of probe delays.

Results

Since our last report on the developments of the technique we have recorded data for a number of samples, mainly pyrazolines within polymer films and as microcrystals. Figure B1.17 shows a transient decay obtained with microcrystalline 1,5 diphenyl-3-styryl-2-Pyrazoline which shows considerable scatter and is displaced from zero. When excited at 295 nm this pyrazoline shows a strong fluorescence, shown in figure B1.18 as a function of pump energy; the non-linear dependence indicates that at these energies saturation is

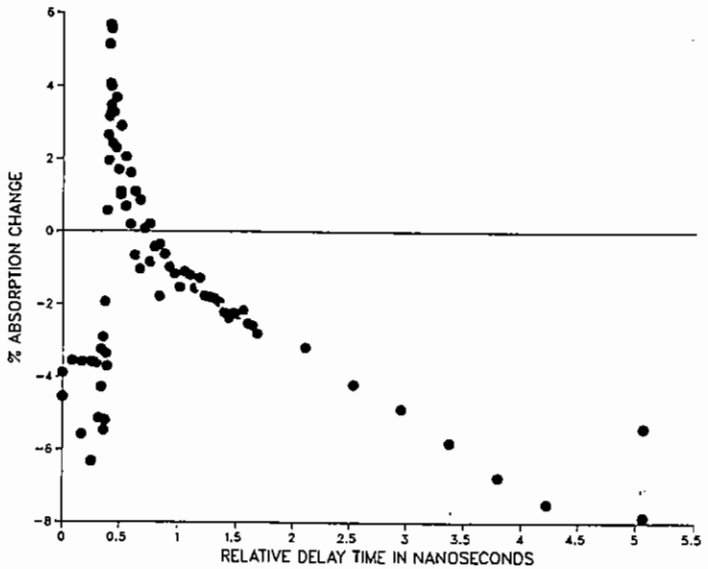

Fig B1.17 Transient absorption decay for microcrystalline 1,5-diphenyl-3-styryl-2-pyrazoline (no emission correction).

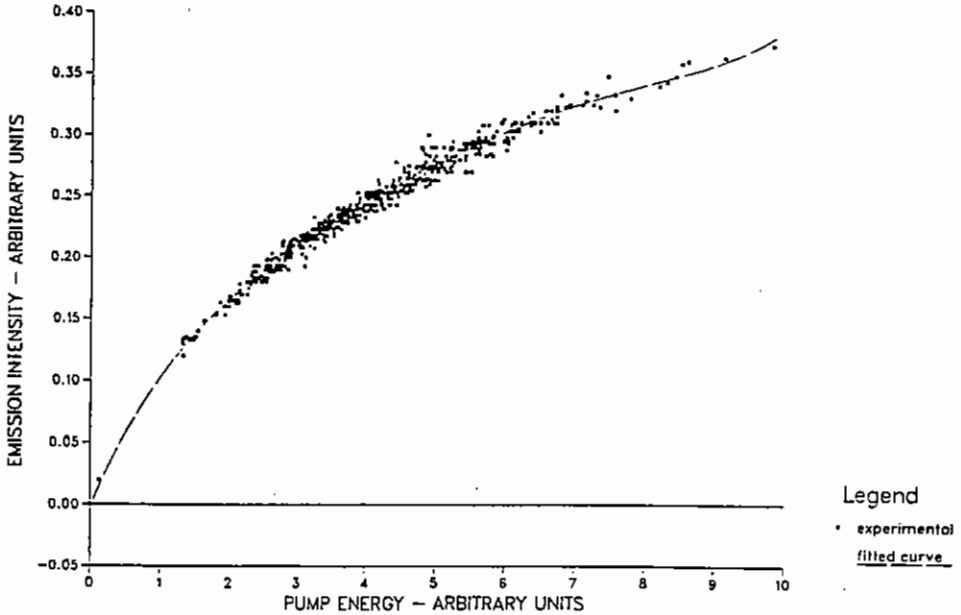

Fig B1.18 Emission intensity versus pump energy for microcrystalline 1,5-diphenyl-3-styrly-2-pyrazoline.

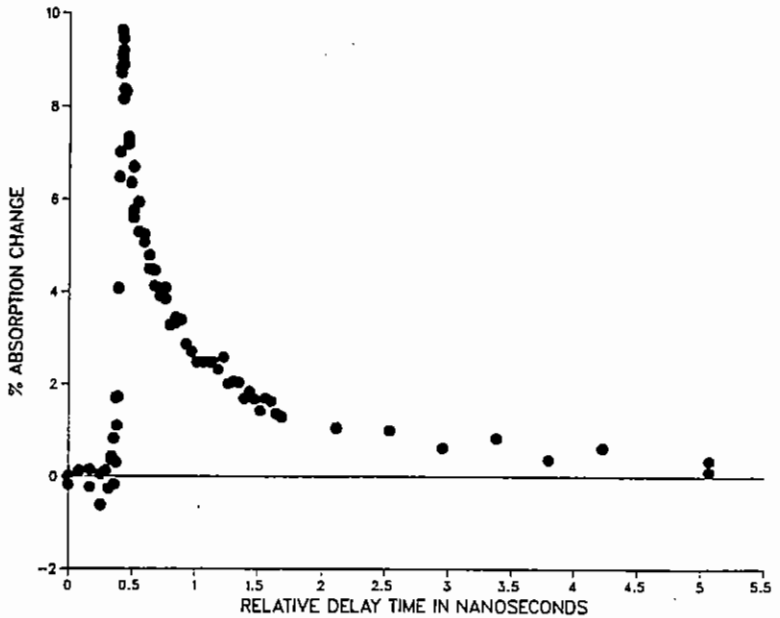

Fig B1.19 Transient absorption decay for microcrystalline 1,5-diphenyl-3-styryl-2-pyrazoline (emission corrected).

occuring. By correcting the transient absorption for emission on a shot to shot basis, the scatter is much reduced and where the probe interrogates the sample before excitation by the pump the signal approaches zero as expected. The emission corrected transient decay is shown in Figure B1.19. The probe wavelength was 590nm.

Data have also been taken using the continuum as probe with dispersion of the diffusely reflected light as described above. Clear signals have been seen and the data are in course of analysis.

Conclusion and Further Work

We are making good progess towards our goal to be able to measure the growth and decay of photoinduced transients within opaque heterogeneous systems. When we have improved our ability to record time-resolved spectra we shall continue by studying proton, energy and electron transfer reactions occuring at surfaces of catalytic interest and within semiconductor suspensions in the presence of electron donors and acceptors.

B1.13 PICOSECOND OBSERVATION OF FLUORESCENCE FROM ALL TRANS DIPHENYL POLYENES

J R M Barr, A J Langley, W T Toner (RAL)
A J Ferguson, T F Palmer (Nottingham)

Introduction

The luminescence properties of the linear all-trans diphenyl polyenes Ph-$(CH=CH)_n$-Ph which are widely used as fluorescence probes in biological systems and are related to vitamin A and the visual pigments, have been extensively studied for many years (ref B1.39-41) It has now been established that while absorption in the near ultra violet or visible regions for these compounds arises due to a strongly allowed $^1A_g \rightarrow {}^1B_u^*$ transition, there are excited states of A_g symmetry in close proximity and under certain conditions at lower energy than the $^1B_u^*$ state (ref B1.42). A model has been proposed which purports to relate the anomalous fluorescence of many polyenes (including all trans 1,6-diphenyl-1,3,5 hexatriene (DPH), all trans 1,8-diphenyl-1,3,5,7-octatetraene (DPO) and trans retinol) to a single nominally forbidden $S_1(^1A_g^*) \rightarrow S_0(^1A_g)$ transition induced by borrowing intensity through coupling to the strongly allowed $S_2(^1B_u^*) \rightarrow S_0(^1A_g)$ radiative transition(B1.43, B1.44). Recently it has been shown (B1.45, B1.46) that for DPH and several simple derivatives emission occurs from both the $S_1(^1A_g^*)$ and $S_2(^1B_u^*)$ excited states and thermal repopulation of $S_2$from S_1 can proceed at a rate which is comparable to radiative or non-radiative decay from S_1. Transient behaviour has been observed recently in the picosecond time resolved $S_1 \rightarrow S_n$ absorption spectra of all trans 1,4-diphenyl-1,3-butadience (DPB) (B1.47) and S_n-S_0 fluorescence spectra of DPH and DPO(B1.48). For these reasons picosecond time resolved fluorescence studies of several diphenylpolyenes have been initiated using the RAL picosecond laser system.

Experimental

A schematic diagram of the experimental configuration is shown in Figure B1.20. The RAL picosecond laser system comprising the synchronously pumped Spectra Physics 375 dye laser and frequency doubled Spectra Physics CW modelocked YAG model 3460 laser, was used to generate red light (80mW at 82 MHz, 3ps) which was frequency doubled using a KDP crystal. The resulting ultra violet (typically 320 nm) radiation was separated from the dye fundamental using a

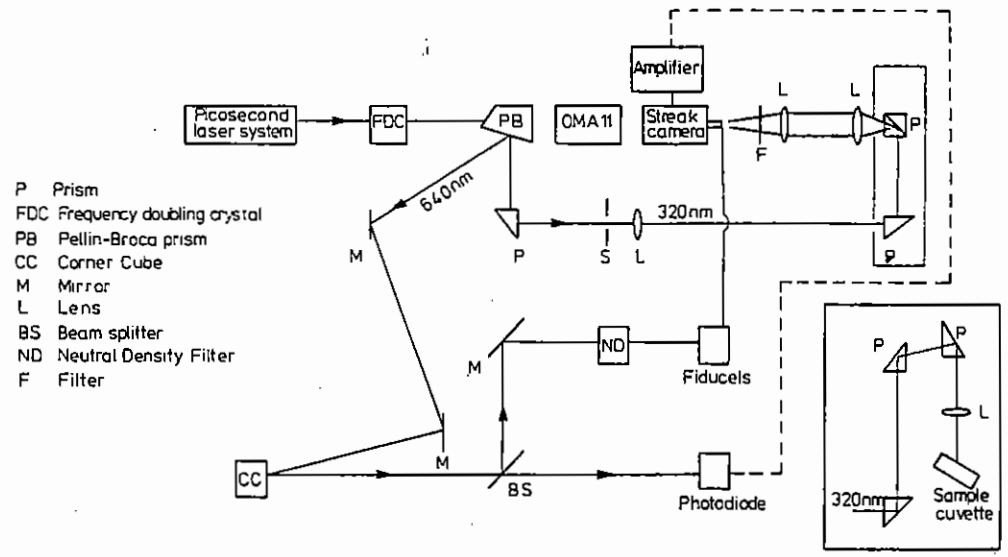

B1.20 Experimental configuration for time resolved fluorescence measurements.

Pellin-Broca dispersing prism, spatially filtered and passed on to the sample cuvette. Focussing of the uv radiation into the sample cuvette containing a solution of diphenyl hexatriene created a visible sharp dagger of the characteristic blue fluorescence which was collected and focussed on to the entrance slit of the Delli Delta (Dellistrique D/S3) streak camera. The residual red light from the dye fundamental radiation was reflected into a corner cube prism and track assembly and further reflected through a beam splitter onto a photodiode. The signal from the photodiode was used to trigger the streak camera in synchroscan as input to the rf amplifier of the sweep generator and optical delays were adjusted by movement of the corner cube and photodiode positions so that the fluorescence was recorded during the nearly linear part of the rf sine wave. Light from the beam splitter was focussed onto fiducials consisting of a series of optical fibres of differing lengths which terminated at a second entrance slit of the streak camera and acted as markers in time. The signal from the streak camera was monitored by an OMA II Intensified Diode Array system which digitised and allowed manipulation of data for background correction and channel intensity variations. An initial time calibration was carried out in a preliminary series of experiments in which red light was reflected onto the entrance slit of the streak camera and the position of the laser pulse was monitored as the corner cube assembly was moved through known distances.

Materials

1,4 di-2-(5-phenyloxazolyl) benzene (POPOP), all trans 1,6-diphenyl-1,3,5-hexatriene (DPH) and all trans 1,8-diphenyl-1,3,5,7-octotetraene (DPO) were scintillation grade materials and were used without further treatment. all trans isomers of 1,6-di(4'-fluorophenyl)-1,3,5-hexatriene (FDPH) and 1,6-di-(2'4'dimethoxyphenyl)-1,3,5-hexatriene (DMEODPH) were prepared using the Wittig reaction and purified as described previously (ref B1.45). Solvents used were spectroscopic grade materials treated and purified as described previously (ref B1.41). All solutions were bubbled with nitrogen gas prior to measurement.

Results and Discussion

A calibration for the streak camera time base was obtained by adjusting the corner cube prism location and monitoring scattered radiation from the fundamental dye laser pulse on the channels of the OMA II. Figure B1.21 shows that there was a linear relationship leading to a time interval calibration of 4.9 ps/channel, between the position of the corner cube and the channel number in which the maximum intensity for the scattered laser light was located. Exposure to scattered picosecond laser light (2.2 ps pulse width) using the instrument in the synchro-scan mode, showed that the instrumental response function had broadened the pulse consistently to an 11 channel width (FWHM 54 ps) (Figure B1.22). The time dependent decay of fluorescence from POPOP in cyclohexane solvent (which is widely used as a fluorescence standard τ_F = 1.13 ns (ref B1.49) was measured in order to characterise and check the detection system (Figure B1.23). Analysis gave a moderate fit to a single exponential with a fluorescence decay time of 1.31 ns but beyond about channel 400 the data showed a definite tail.

The time dependent profiles of fluorescence from solutions of the diphenyl polyenes DPH and FDPH in toluene and DPO in cyclohexane are recorded respectively in figures B1.24-26 for (a) total fluorescence and fluorescence passing through broad band pass filters (50 nm FWHM) with maximum transmissions at (b) 400 nm (Chelsea-Oriel 5752) and (c) 450 nm (Chelsea-Oriel 5754). The fluorescence profiles for DPH and FDPH were not affected by the presence of the filters and were consistent with the relatively long decay times previously measured for these compounds in toluene by nanosecond single photon counting (ref B1.41, B1.46). The spike on the time dependent profile for filtered fluorescence from DPO (figure B1.26b) was pulse duration limited, unaffected by the further introduction of plate glass and Chance OX7 filters and can be due to neither scattered radiation of red light from the fundamental nor uv from frequency doubled light of the dye laser. Since the camera streaks twice during each laser pulse, a wrap around effect occurs leading to distortion of the fluorescence time profiles. This distortion becomes especially significant at long fluorescence decay times and attempts to take

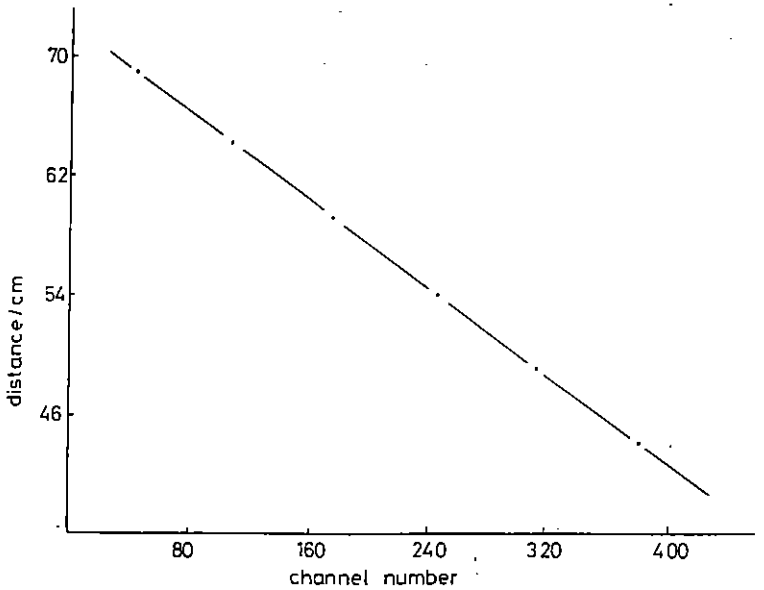

B1.21 Calibration of streak camera time base

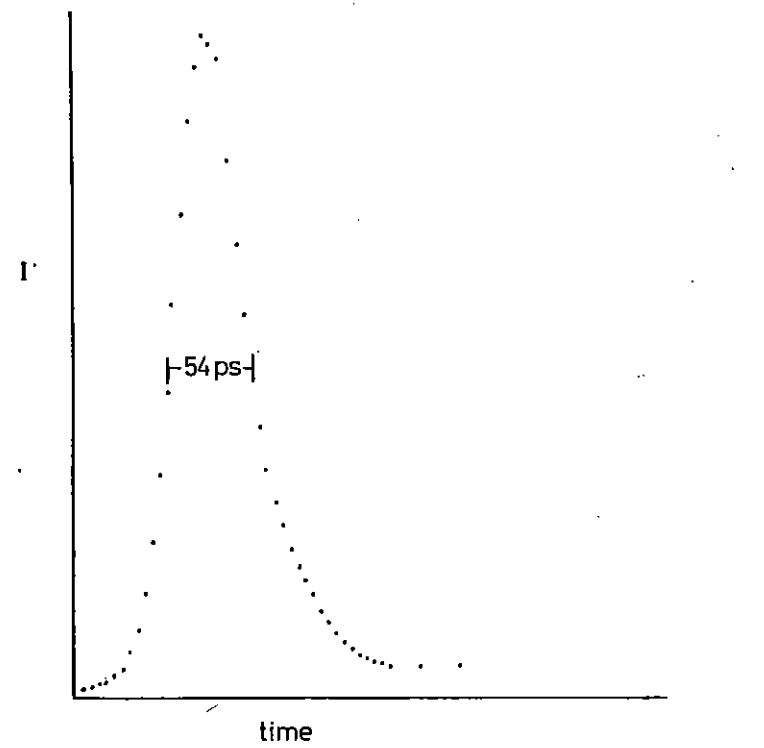

B1.22 Temporal resolution of streak camera - OMA 11 system.

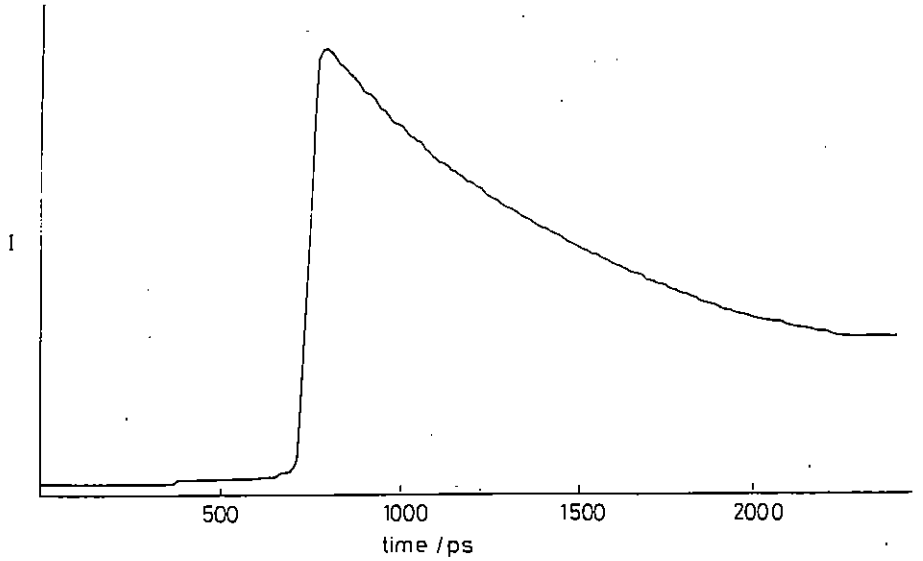

B1.23 Time dependent fluorescence decay of 1,4-Di-2-(5-phenyloxazolyl) benzene (POPOP) in cyclohexane solvent.

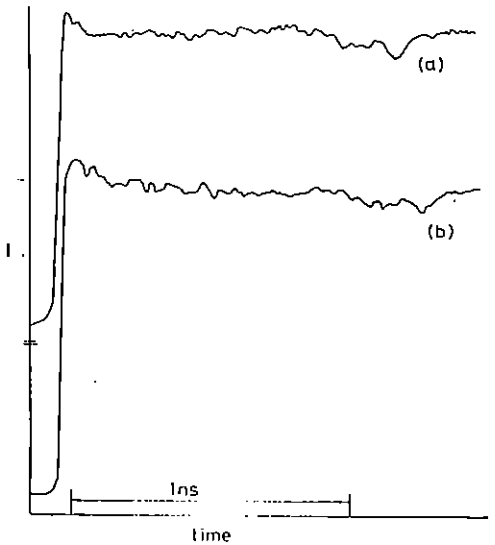

B1.24 Time dependence of fluorescence from DPH in toluene
(a) emission passing through broad band pass filter (λ_{max}=400 nm)
(b) emission passing through broad band pass filter (λ_{max}=450 nm)

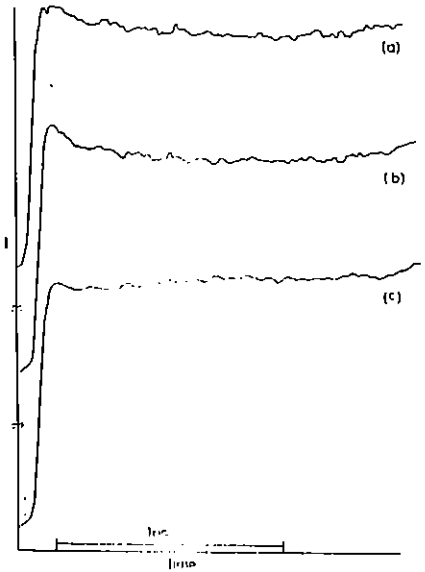

Fig B1.25 Time dependence of fluorescence for FDPH in toluene
(a) unfiltered emission
(b) broad band pass filter (λ_{max}=400 nm)
(c) broad band pass filter (λ_{max}=450 nm)

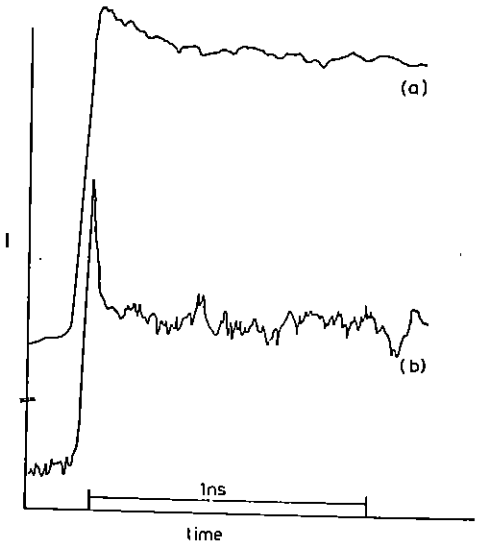

B1.26 Time dependence of fluorescence from DPO in cyclohexane
(a) unfiltered emission
(b) broad band pass filter (λ_{max}=450 nm)

account of this factor are in progress. The time dependence of the decay of fluorescence from DMEODPH in toluene was also measured (figure B1.27). The fluorescence profiles were not affected by the presence of filters and the data gave a reasonable fit to a single exponential decay with a fluorescence lifetime of 2.2 ns. There is considerable interest in the use of DPH and DPH derivatives as fluorescence probes in biological systems. For these reasons a brief study was made of the time resolved fluorescence emission anisotropy of DMEODPH in toluene by determining the time dependences of parallel and perpendicular polarised fluorescence emission using flat plate polarisers (Polacoat 105). At long times after excitation the curves for $I_{||}(t)$ and $I_{\perp}(t)$ become nearly identical and a normalisation factor of 0.97 was applied to the $I_{\perp}(t)$ curve to achieve tail matching and eliminate the emission correction factor (G). Figures B1.28, B1.29 show that the emission anisotropy (r_t) decayed exponentially between the values 0.2 and 0.01.

The results of this study were obtained over a period of two weeks and are of a preliminary nature. Analysis of data is continuing but useful conclusions can be made.

For the polyenes in question the lowest excited state(s) is nominally of A_g symmetry (ref B1.42). The time evolution of the fluorescence from DPO in cyclohexane isolated through a filter with maximum transmission at 450 nm (figure B1.26b) is virtually identical to the time resolved fluorescence emission at 452 nm reported by Felder et al.(ref B1.48) for DPO in hexane, using third harmonic excitation radiation from a mode-locked Nd YAG laser incorporating an injection mode-locked regenerative amplifier and fluorescence detection by frequency conversion gating techniques. The pulse-duration limited feature was attributed to prompt fluorescence from the $S_2(^1B_u^*)$ excited state with an intrinsic time constant calculated to be 4×10^{-13}s. The long time component of about 50% of the initial intensity persists for several nanoseconds and is consistent with emission from the S_1 excited state (A_g^*) the spectrum of which overlaps the $S_2 \rightarrow S_0$ emission envelope.

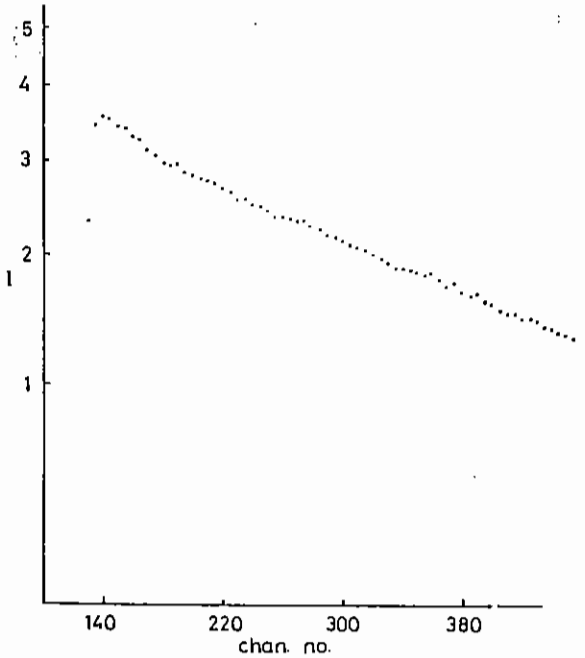

Fig B1.27 Time dependent fluorescence decay of DMEODPH in toluene

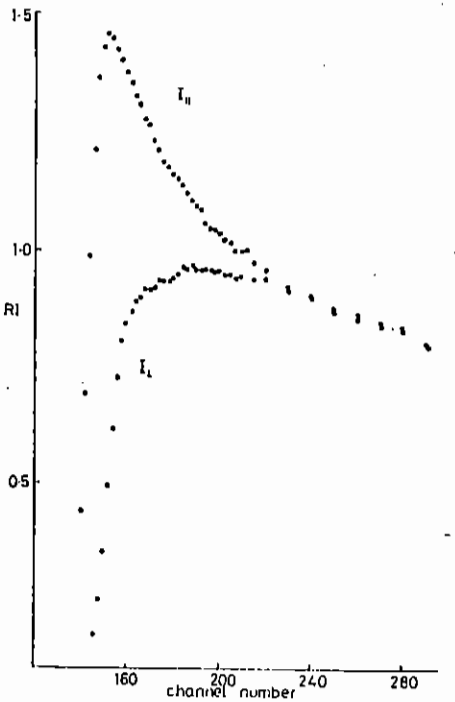

Fig B1.28 Time dependence of polarised fluorescence from DMEODPH in tolune.

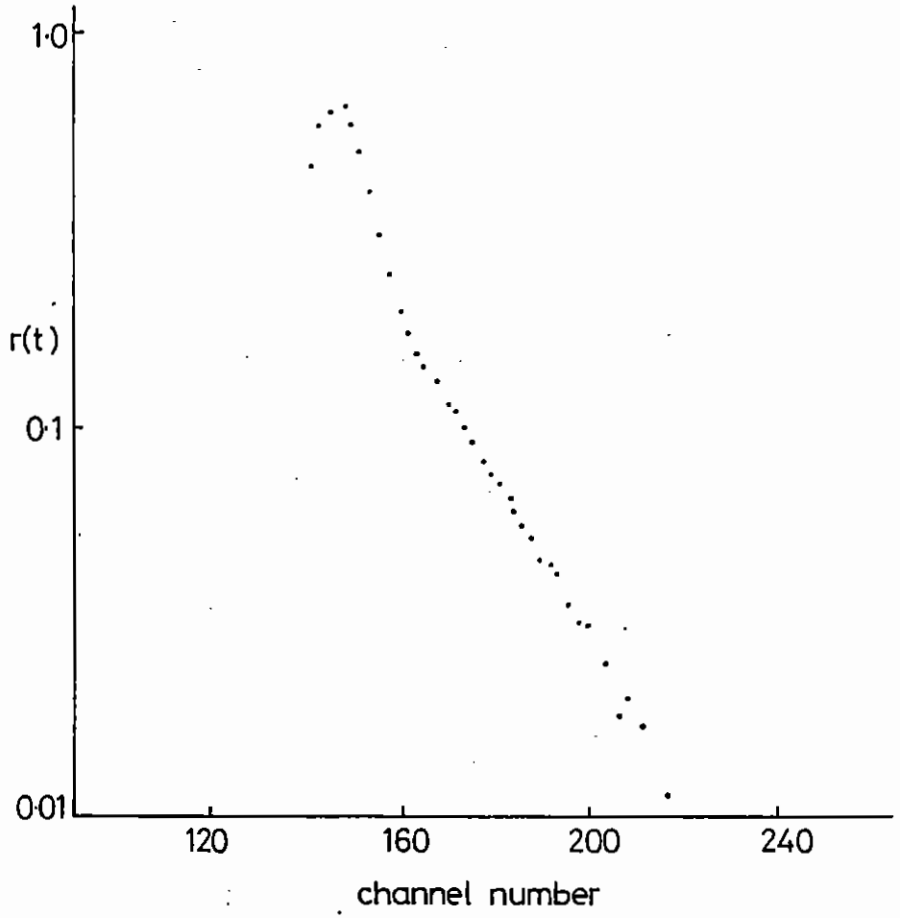

Fig B1.29 Time dependence of rotational anisotropy, r(t).

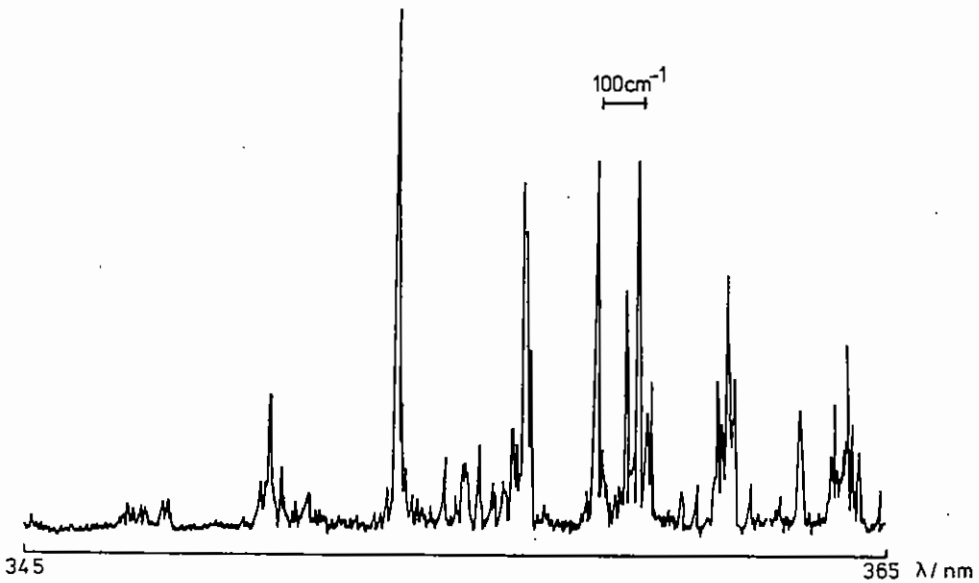

Fig B1.30 LIF spectrum from nozzle at approximately 700°C (Total scan 1588cm⁻¹)

The absence of significant pulse-duration limited features in the time resolved fluorescence spectra for the diphenyl hexatrienes is most interesting. For DPH, FDPH, and DMEOPH it has been shown that emission occurs from both the $^1A_g^*(S_1)$ and $^1B_u^*(S_2)$ excited states at room temperature in aromatic solvents (ref B1.45,46). The failure to observe prompt fluorescence from the initially populated S_2 excited state shows that $S_2 \rightarrow S_1$ internal conversion for these compounds is extremely rapid (sub-picosecond) in solution and is consistent with the proposal that thermal repopulation of S_2 from S_1 can proceed at a rate which is comparable to radiative and non radiative decay from S_1. The shortening of the fluorescence decay time for DMEOPH compared to DPH and FDPH reflects the decrease in the S_2-S_1 energy gap for this compound and is consistent with previous measurements using nanosecond single photon counting (ref B1.41,46). For DPH the absorption and emission transition dipoles lie parallel to the long molecular axis which is the symmetry axis (ref B1.50). If this is also the case with DMEODPH the appropriate expression for emission anisotropy, r(t) reduces to a single exponential term:

$$r(t) = \frac{2}{5} \exp(-6D_{\perp}t)$$

where $D_{\perp}$ is the rotational diffusion coefficient for the long molecular axis about a perpendicular axis(B1.50). Assumption of a prolate ellipsoid model for the rotational diffusion of DMEODPH in which the ellipsoid ratio, a/b= 6 and using Perrins' equation

$$D = \frac{3\,k\,T}{16\,\pi\,\eta\,a}\,(2\,\ln\frac{2a}{b} - 1)$$

where η is the solvent viscosity, would lead to an estimate of 20Å for the length of the DMEODPH molecule along the long molecular axis.

B1.14 LASER INDUCED FLUORESCENCE IN MOLECULAR BEAMS OF FIRST ROW TRANSITION ELEMENT CHLORIDES

I R Beattie, T R Gilson, K R Milligan (Southampton),
and J M Brown (Oxford)

Many first row transition element chlorides can be vaporised to give a few torr pressure at temperatures below 1,000°C. These molecules are seeded into a high pressure (several atmospheres) of an inert gas, followed by expansion through a jet into a rapidly pumped vacuum system. In this way the rotational energy and (to some extent) the vibrational energy is converted into translational energy. This isentropic expansion results in rotationally cold molecules (a few K). The jet is crossed by a narrow band tunable dye laser. Ideally this would be a cw laser with a line width of less than 0.001 cm^{-1}. However, in the preliminary experiments it was necessary to cover a wide frequency range. The relatively (0.04 cm^{-1}) narrow band pulsed dye laser at RAL is particularly suitable for such trial experiments.

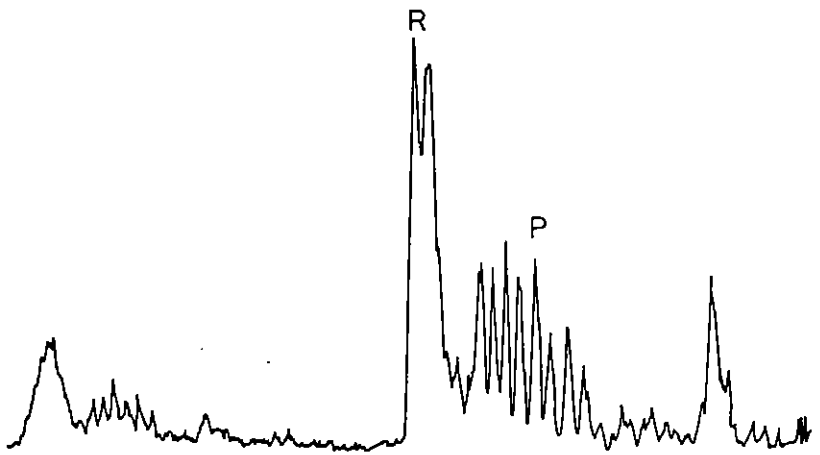

Fig B1.31 High resolution spectrum from high temperature nozzle (Total scan ca 10cm^{-1}).

High quality spectra were obtained. Figure B1.30 shows a broad scan from 345 nm to 365 nm, while figure B1.31 shows a section of the spectrum around 366.5 nm, under high resolution. These results are extremely encouraging as they suggest we may for the first time be able to get rotationally resolved information on the ground and excited states of a range of otherwise inaccessible molecules. In this way it should be possible to resolve the long standing controversies on the ground state geometries of these species. Further, the data will also yield information on the excited states and their geometries. This should lead to an enhanced understanding of the nature of the bonding in transition element halides.

An inevitable difficulty in working at high temperatures is that reaction occurs with the apparatus. Further, the fluorescing species may not be the primary component of the beam. From dispersed fluorescence studies carried out at Oxford using argon uv laser lines to excite the fluorescence, we observe main progressions showing a 360 cm^{-1} frequnecy separation. We believe these to be associated with twice the bending frequency of $FeCl_2$. The bend in this case is not totally symmetric so progressions in ν_2 itself are not expected.

We are at present working on the analysis of the spectra and on a beam source involving inert materials such as sapphire or silica. We are also hoping to obtain a frequency doubler for our dye laser so that we may carry out high resolution studies on these bands obtained at RAL.

B1.15 DYNAMICS OF TRANSITION METAL ATOM REACTIONS

M R Levy, Department of Chemical and Life Sciences,
Newcastle-upon-tyne Polytechnic

Introduction

In reaction dynamics, very little attention has been given to the study of transition metal atom reactions, owing largely to the refractory nature of the metals. Yet these reactions are of considerable interest, since many reactant and product electronic states, at the transition between Russell-Saunders and spin-orbit coupling schemes, are available at relatively low excitation energies. It is therefore desirable to be able to prepare beams containing both ground and excited metal atoms, and to monitor the different reactivity of the species present. In these "trial" experiments, a start has been made on such studies, using the JK 2000 Nd:YAG loan laser to generate a pulsed atomic beam with a range of translational energies. By means of this technique, chemiluminescence has been observed from the reaction of Fe, Mn and W atoms with N_2O and O_2. In two cases (Fe, Mn + O_2), product electronic excitation from ground state atoms is highly endothermic.

Experimental

Figure B1.32 shows the typical experimental arrangement. The apparatus consists of two linked, but separately pumped, chambers, in

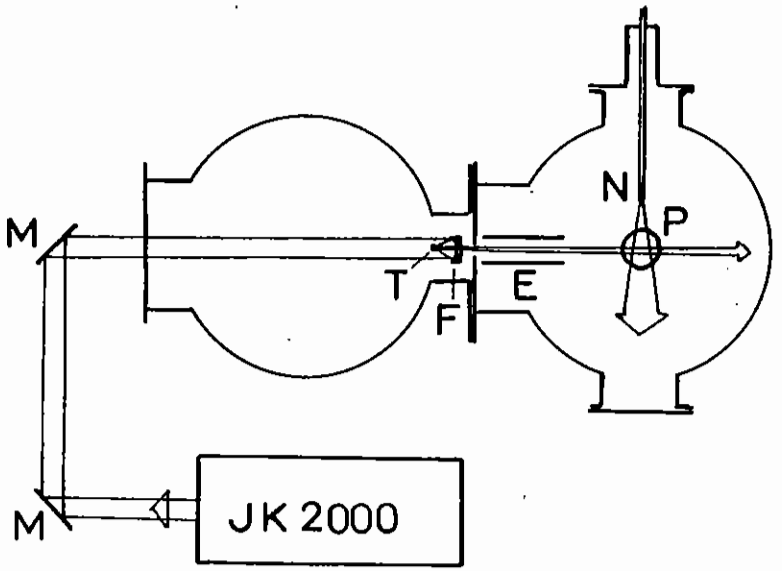

Fig B1.32 Schematic of experimental arrangement. M = mirror, T = target, F = focussing mirror, E = dc electric field plates, N= uncollimated nozzle beam, P = collection optics and photomultiplier.

the first of which the metal atom beam is produced by laser vaporisation of a metal target. This is either: (i) a ≈ 1μm metal film (Al, In or Sn) deposited on a microscope slide, and irradiated through the glass by the focussed laser beam; or (ii) a solid metal target (Fe, Mn or W), 1-2 mm wide, onto which the laser beam is focussed back by a 25 mm focal length concave mirror with a 2-3 mm hole in the centre. In both cases the target can be translated vertically from outside of the vacuum system. The pulsed beam, consisting of atoms and ions, passes via a collimating aperture into the scattering chamber, where the ions are deflected away by a dc electric field. At the centre of the scattering chamber, the remaining atoms intersect an uncollimated nozzle beam of N_2O or O_2, and the resulting chemiluminescence is imaged by an f/1 telescope onto a R928 photomultiplier. The signal is amplified without significant loss of time resolution and displayed on an oscilloscope.

Atomic Beam Characterisation

Both laser vaporisation configurations are know to yield atomic beams with a wide range of translational energies (ref B1.51, B1.52), but only the former has previously been applied to the study of chemiluminescent reactions. Therefore considerable effort was devoted to comparing the techniques, including measuring, by means of an ionisation gauge detector, the atomic flight time to the centre of the scattering chamber. It had been hoped that the same metals could be employed in the two cases, but in the event of the plant for depositing films of refractory metals was not available during the loan period.

Vaporisation of thin films was easily achieved at a single shot, using the Q-switched laser output at 532 nm (≈150 mJ per ≈10 ns pulse, focussed to ≈1 mm dia). This did have the disadvantage, however, that the target had to be moved for each laser pulse. For Al, the ion gauge indicated pulses with peak velocity ≈1600 ms^{-1}, and peak atomic number density at least 10^{12} cm^{-3}. Previous workers (ref B1.51) used much higher fluences, producing beams of somewhat higher number density and peak velocity. For Sn and In, number densities here were smaller than for Al, presumably because the metal films were thinner.

Solid targets could in principle be irradiated for a number of shots without having to be moved; but no distinct atom signal was detected by the ion gauge when the Q-switched 532 nm laser beam was employed. In addition, visual examination of the targets indicated little damage. Vaporisation was achieved with the fixed-Q output at 1064 nm, and Fe atom pulses were detected, but this was not a satisfactory approach since the long time period of the laser pulse made the atomic flight time very uncertain. Application of the Q-switched output at 1064 nm (≈750 mJ $pulse^{-1}$) was at first impossible owing to rapid damage to the mirrors used to steer and focus the laser. This problem was eventually solved by coating all laboratory mirrors, including the convave mirror inside the vacuum, with a ≈1 μm gold film. Using this arrangement, vaporisation of the target was readily achieved, although the rapid erosion meant that it had to be translated frequently for reproducible pulses to be maintained.
In fact, atom signals could still not be detected by the ion gauge, although a very large ion signal was found when the dc field was switched off. However, the vaporisation process produces atoms and ions in a range of electronic states, and metastable emission was detected by the photomultiplier (fig B1.33). For Fe and W, the species responsible for that emission were not identified unambiguously, as a monochromator was not available; but, for Mn, cut-on filters, together with the duration of the emission, identified it as from the ^6P state. The time of arrival of the metastable atoms was strongly dependent on the laser fluence, but typical optimised peak velocities were ≈10 kms^{-1}, corresponding to an effective flux of emitters ≈10^{10} s^{-1}. However, owing to the long and different radiative lifetimes of the different ^6P sub-levels, and the low probability of emission on passing the photomultiplier, the true peak flux of ^6P atoms is estimated to have been ≈10^{12} s^{-1}. Clearly a number of other metastable states, and the ground state, would also have been populated, so the overall flux of atoms must have been much higher still. The lack of detection with the ion gauge suggests that the atoms were constrained very close to the beam axis, a result which was expected from the original work with this technique (ref B1.52).

Chemiluminescence Detection

A search was made for chemiluminescence from the reaction of all 6 metals with N_2O. However, none was detected for the vaporised thin films, despite the ion gauge detection of the atomic beam in those cases. Previous work, using the same technique, did claim emission from In and Sn + N_2O (ref B1.53); but the different laser focussing used there may have resulted in a higher population of metastable atoms. Published beam work on Al + N_2O indicates that any emission should be weak (ref B1.54).

Fe and Mn + N_2O have also been attempted previously by evaporation of thin films (ref B1.53), but in that case emission was found from Fe only. In the present work, all 3 of Fe, Mn and W gave emission with N_2O: the relative signal intensities are given in Table B1.2. As reported already, a monochromator was not available; but the use of cut-on filters allowed the emitters to be clearly identified as excited metal monoxide, MO*. Although the dependence of signal on crossed-beam intensity could not be determined unambiguously, it seems highly likely that the chemiluminescent species were primary reaction products, since the signal could be detected easily even with N_2O background pressures in the scattering chamber as low as ≈5 x 10^{-4} Pa. In the Mn case, the metastable emission decreased as the chemiluminescence increased, implying that Mn*(^{6}P) + N_2O may favour MnO*($A^2\Sigma^+$) production.

Table B1.2: Relative Signal Magnitudes at Peak

	N_2O	O_2
Fe	1.2	.08
Mn	.5	5.0
W	1.0	.7

The high beam translational energies also allowed the study of substantially endothermic reactions. Chemiluminescence was detected from Fe, Mn + O_2, respectively 299, 351 kJ mol^{-1} endothermic from ground state atoms, as well as from W + O^2, only 45 kJ mol^{-1} endothermic (see Table B1.2 for relative intensities). None of these reactions had previously been investigated. Fig B1.33 shows a typical time-resolved trace for Mn + O_2, compared with the Mn metastable signal. In this case, the emission was further to the red than for Mn + N_2, reflecting the expected lower vibrational excitation; and this made it difficult to determine whether the ^{6}P emission was quenched. However, the duration of the signal indicates that a part of it, at least, originated from excited Mn* atoms. Similar results were obtained for Fe + O_2; but, for W + O_2, it was not possible to determine whether ground or excited atoms were responsible for the chemiluminescence, as the threshold is so low.

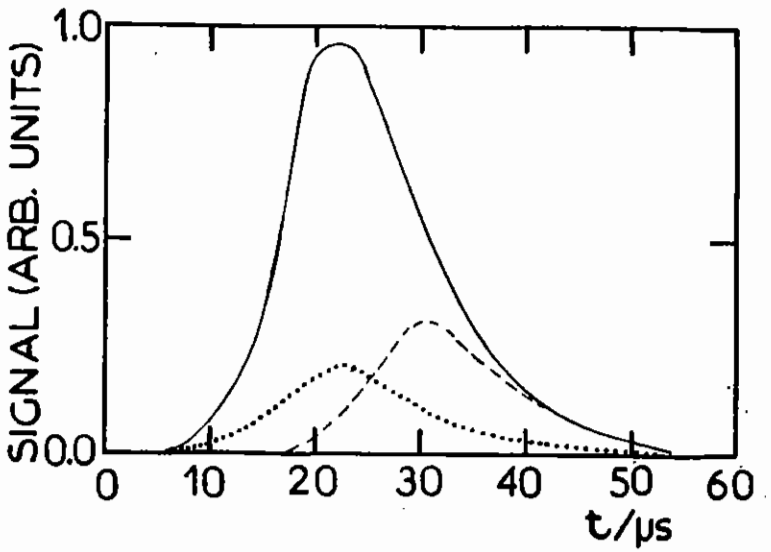

Fig B1.33 Typical time-resolved light traces due to: Mn(^{6}P) metastable emission at =540 nm (.....); total emission (MnO* + O_2 (_____); emission ≥ 590 nm in Mn + O_2 (-----). The atomic beam flight distance to the detection region was 262 mm.*

Conclusions

As pointed out above, these experiments were of a "trial" nature. A considerable number of questions therefore remain to be answered. For example; the distribution of states in the atomic beam; the relative contributions of the different states to the observed chemiluminescence; the vibrational exitation of the luminescing product molecules. However, the feasibility of this technique for studying transition metal atom reactions has clearly been demonstrated.

B1.16 EXCITED STATE PHOTOELECTRON SPECTROSCOPY OF RADICALS

J M Dyke, A Morris, M Feher and A Ellis, Southampton University

Laser multiphoton ionization of a molecule should be enhanced at a laser frequency at which the photon energy (mhν) is in exact resonance with one of its specific excited states. Indeed, such enhancement has been widely observed in various ion-current spectra (ref B1.55). The multiphoton (MPI) ion-current spectrum in general consists of many peaks, which correspond to m-photon allowed excited states. From such spectra one can obtain information about resonant intermediate excited states, but no information is obtained about final states of the ion. In comparison MPI photoelectron spectra contain information about the energy levels and populations of ionic states which are produced from selected excited state. This report is an account of work done in developing a MPI ion-current and photoelectron spectrometer during a two-month loan period of a Quantel Datachrome 5000 laser.

Before the laser was installed a combined MPI time-of-flight electron spectrometer/total ion spectrometer had been constructed from borrowed equipment. Installation of the laser meant that both parts of this instrument could be tested and improvements made. The apparatus layout is shown in fig B1.34. Multiphoton ionization total ion spectra of nitric oxide were obtained within 1-2 weeks of the laser being installed and these were at least as good in terms of sensitivity and resolution, as previously published literature spectra. However, problems were experienced in obtaining reproducible time-of-flight photoelectron spectra of nitric oxide at

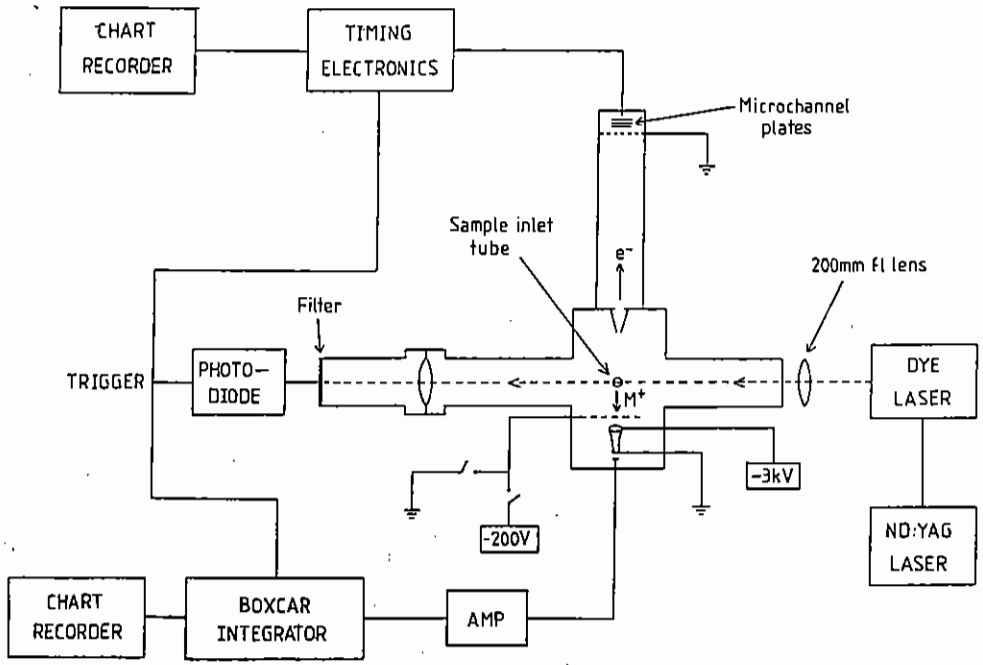

Fig B1.34 Block diagram of MPI/MPI PES apparatus.

low output power from the dye laser (< 0.4 mJ pulse^{-1}). The output power was improved to 1.6 m J pulse^{-1} and this, as well as more accurate alignment of the beam, allowed photoelectron spectra of nitric oxide to be recorded at fixed laser wavelengths with no accelerating voltage. Figs B1.35, B1.36. These spectra showed that the electron energy analyser was working well and a number of improvements were made in the ionization region to allow improved resolution spectra to be obtained. A detailed MPI ion-current spectrum of $O_2(a^1\Delta g)$ has also been obtained and this is currently being analysed to yield spectoscopic constants of a previous unobserved excited state of oxygen. Unfortunately, time did not permit any attempts to obtain the corresponding MPI photoelectron spectra.

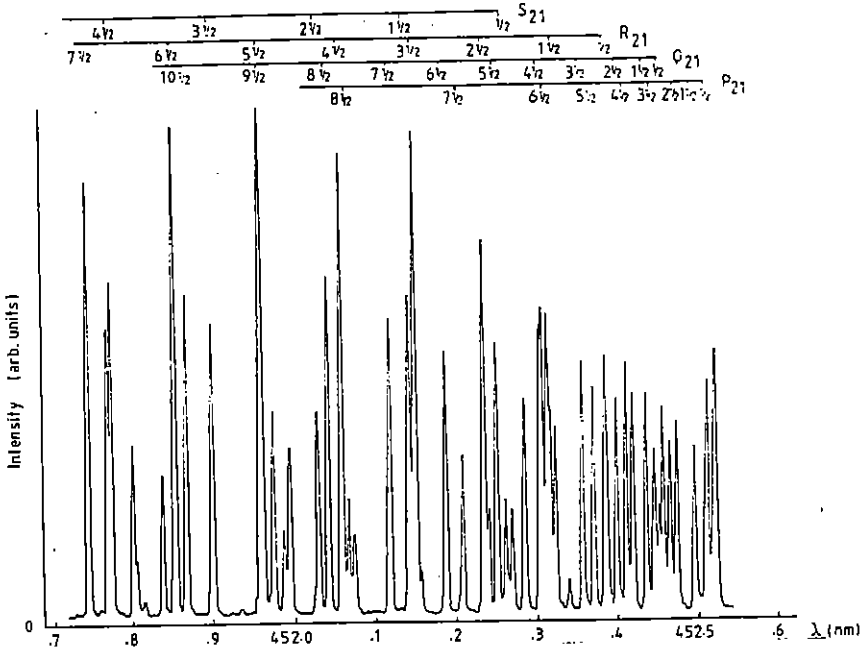

Fig B1.35 Section of the MPI spectrum of NO ($A^2\Sigma^+$, $v'=0 \leftarrow X^2\Pi, v''=0$).

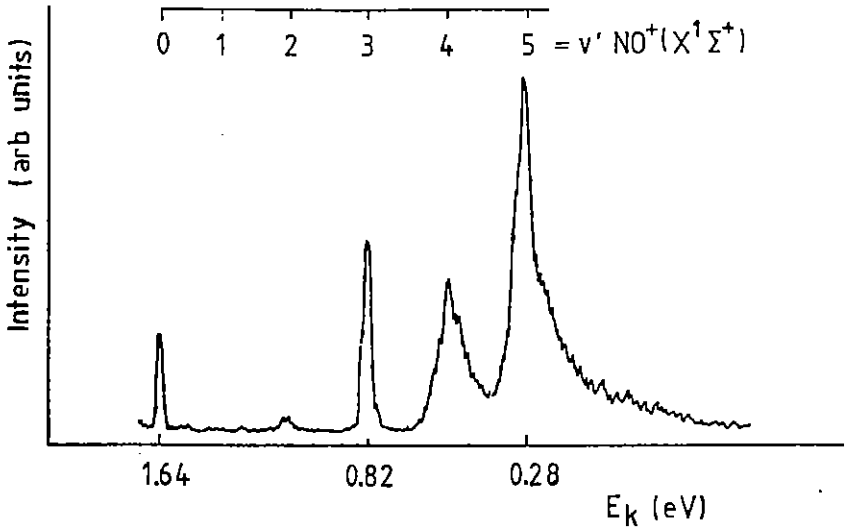

Fig B1.36 MPI photoelectron spectrum of NO at 454.370 nm.

B1.17 TWO-PHOTON VUV LASER-INDUCED-FLUORESCENCE DETECTION OF $I^*(^2P_{1/2})$ AND $I(^2P_{3/2})$ FROM ALKYL IODIDE PHOTODISSOCIATION AT 248 nm

F G Godwin, P A Gorry, P M Hughes, D Raybone, T M Watkinson and J C Whitehead, Dept. of Chemistry, University of Manchester, Manchester

Introduction

The investigation of the photodissociation of alkyl, and substituted alkyl iodies in the A band has played a substantial part in our general understanding of photodissociation processes and photofragmentation dynamics(ref B1.56). This is not suprising since the alkyl iodides offer, within a simple framework, a unique

opportunity for the systematic variation of several of the key factors that affect photodissociation dynamics such as radical size, substitution and structure.

The A band arises from an $\sigma^*\leftarrow n$ transition localised on the C-I bond with the transition dipole moment parallel to the C-I axis (the $^3Q_0\leftarrow N$ transition). Dissociation is very rapid (1-3 x 10^{-13} s) with the energy disposal indicating an impulsive mechanism. The $^3Q_0$ state correlates with $I^*(^2P_{1/2})$ and ground state $I(^2P_{3/2})$ is produced by curve crossing to the $^1Q_1$ state [ref B1.57-61]. Thus an important quantity in understanding the photofagmentation processes is the I^* quantum yield Φ^*. Several different techniques have been applied to the measurement of I/I^* ratios including translational photofragment experiments (ref B1.57-61), VUV absorption (B1.62), IR emission (B1.63,64), optoacoustic spectroscopy (B1.65), laser gain measurements (B1.66) and diode laser IR absorption (B1.67). Most of these techniques suffer from experimental defects such as overlapping spectra, strong absorption of the probe light by the parent iodides, long radiative lifetimes or difficult analysis procedures. A particulary powerful and direct technique pioneered by Brewer et al is that of atomic two-photon VUV laser-induced fluorescence (B1.68). This report describes the use of this technique to determine the I^* quantum yields for several substituted and cyclic alkyl iodides.

Experimental

The experimental arrangement is shown in figure B1.37. A purified sample of alkyl iodide is maintained at a constant temperature and enters the flow cell via a needle valve providing a low pressure (30-40 mTorr) of the gas. The alkyl iodide is photodissociated by the collimated 248 nm output of an excimer laser (EMG 103, at 12 Hz, 50 mJ/cm²). After a delay of 100-200 ns the iodine atoms are detected using the frequency-doubled focussed output (0.5 mJ/pulse) of the loaned excimer-pumped dye laser (EMG 101/FL 2002) operating on

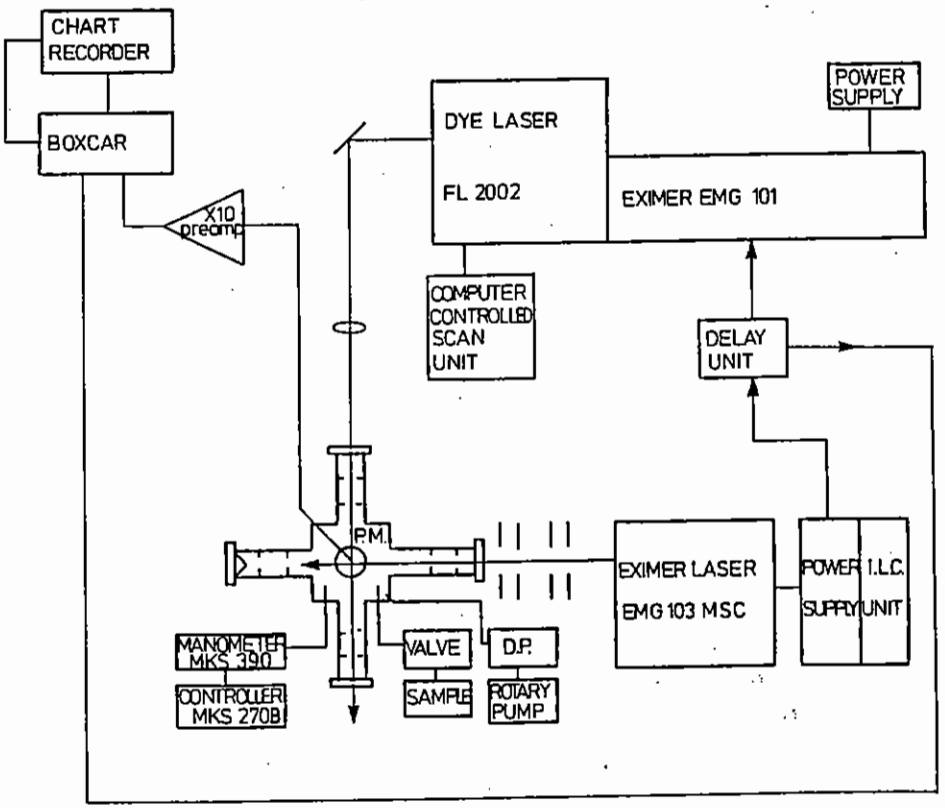

Fig B1.37 Experimental Layout

Rhodamine B (Rh-610). This laser scans over a pair of two-photon absorption lines ($^2D_{5/2} \leftarrow {}^2P_{3/2}$ for I and $^2D_{3/2} \leftarrow {}^2P_{3/2}$ for I^*) at 304.7 and 306.7 nm respectively. The exited atomic states fluoresce twice emitting first an IR photon and then a VUV photon in the range 158-206nm. The VUV fluoresence is then detected using a solar blind photomultiplier (EMI 9431B, 50Ω load resistor) which efficiently discriminates against light from both the photolysis and probe lasers. The signal is then processed by a x10 preamplifier (Ortec 9301) and boxcar integrator (Brookdeal 9425).

By scanning over the two absorption lines, two laser-induced fluorescence peaks are observed whose relative intensities depend on the quantum yield for I^* production ($\Phi^*=I^*/(I+I^*)$). The calculation of the quantum yield requires calibration of the system by use of a molecule of known quantum yield. This was chosen to be CH_3I whose quantum yield is now well established, $\Phi^*=0.73$ (B1.67). Care must be taken to ensure that the probe beam does contribute to the overall signal by acting as both photolysis and probe. This was achieved by attenuating the probe beam power to a level where there was no discernable signal on either the I or I^* peaks with the photolysis laser blocked. Typically the peaks were measured eight times, with four measurements of CH_3I either side of these to check calibration.

Typical data are shown in figure B1.38 for the photolysis of CH_3I and cyclo pentyl iodide. The Φ^* values obtained are given in table B1.3 and are shown in figure B1.39 (together with those obtained by other workers (B1.57-67)).

Discussion

The states involved in the photodissociation dynamics of the alkyl iodides in the A band were first described by Mulliken (B1.69) and are shown in figure B1.40. Two of the transitions ($^1Q_1 \leftarrow N$ and $^3Q_1 \leftarrow N$) are polarised perpendicularly to the C-I bond, whilst the third ($^3Q_0 \leftarrow N$) is parallel polarised. All of the translational photofragment experiments

Table B1.3 : I^* quantum yields

Molecule	Φ^* (248 nm)	
CH_3I	0.73	
C_2H_5I	0.62	(0.64)[a]
$t\text{-}C_4H_9I$	<0.1	(0.04)[a]
C_3F_7I	>0.95	
CF_3CH_2I	0.8	
CH_2ClCH_2I	0.7	
$C_3F_7CH_2I$	0.77	
cyclo C_5H_9I	0.35	
cyclo $C_6H_{11}I$	0.27	

[a] Φ^* quantum yield from Brewer et al (B1.68)

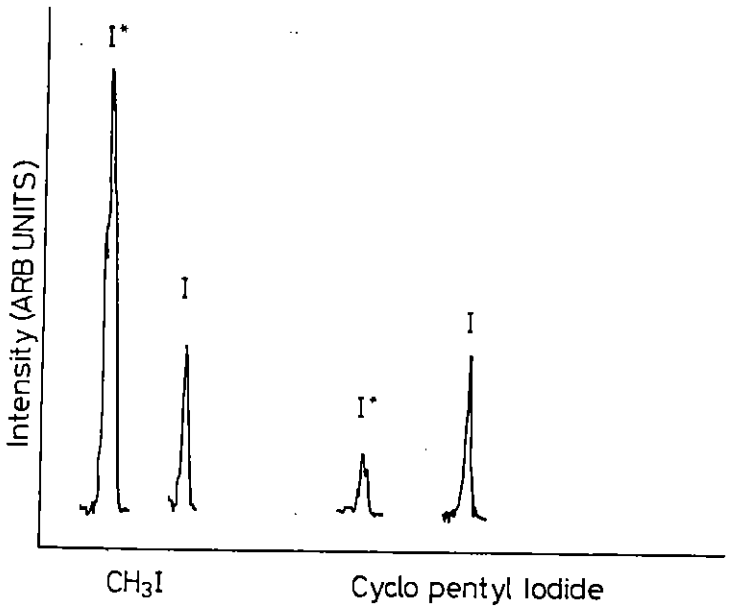

Fig B1.38 Typical two-photon atomic LIF signals. Results are shown for the calibrant, CH_3I, and cyclo iodopentane.

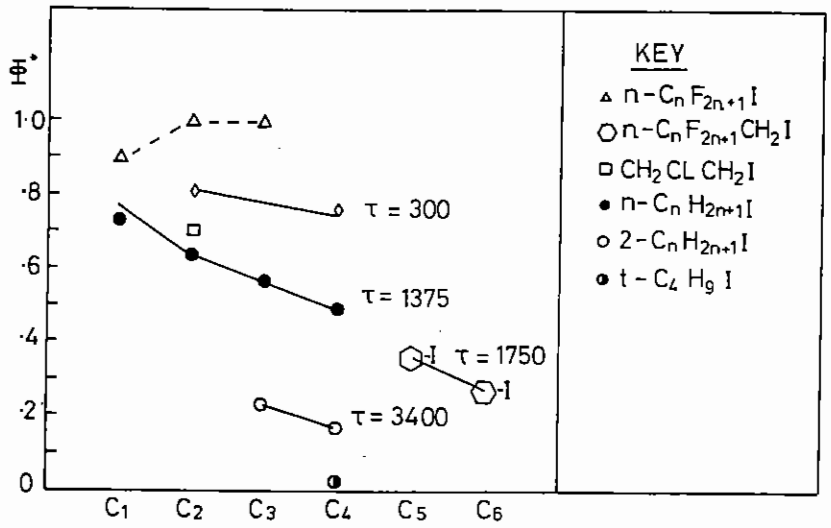

Fig B1.39 The quantum yield for I^* production from photodissociation at 248 nm as a function of radical size, structure and substitution. The horizontal axis shows the number of carbon atoms in the molecule. The solid lines are backfits from equation 3 with the ζ values indicated on the diagram.

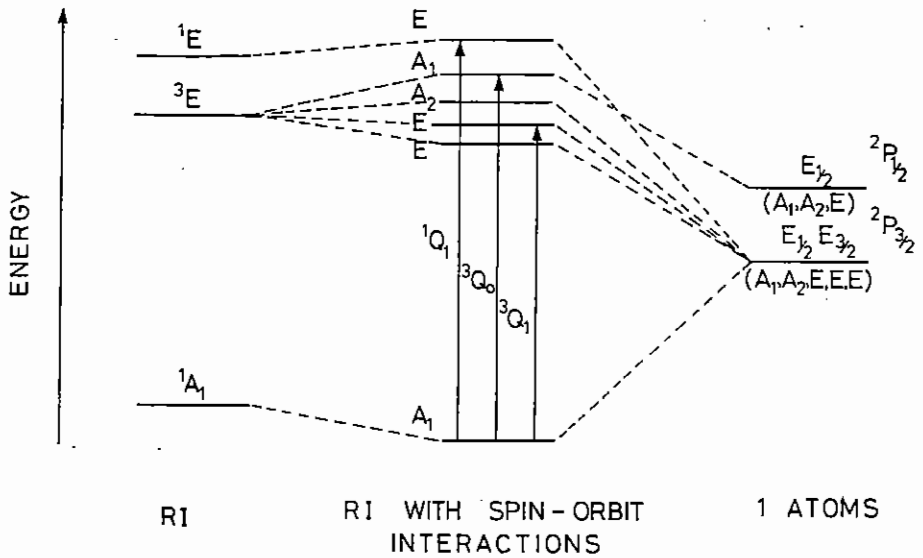

Fig B1.40 The correlation diagram for the σ^*←n transitions in the A band. The central levels are the full spin-orbit states with the symmetry labels appropriate to CH_3I. The transitions are labelled according to Mulliken's original prescription (B1.68).

to date (B1.57-B1.61) show that the overwhelming absorption at 248 nm is from the parallel $^3Q_0$←N transition which correlates with I^*. Any ground state atoms must then arise from a curve crossing to the $^1Q_1$ surface and, in this case, the quantum yield Φ^* is just the probability of not crossing to the $^1Q_1$ surface. The localised nature of the σ^* orbital strongly suggests that only changes to the α carbon (the one containing the I atom) would be expected to alter the $^1Q_1$ and $^3Q_0$ surfaces.

The translational photofragment experiments have also shown (B1.57, B1.59) that the energy disposal is best described by an impulsive mechanism in which the initial dissociation step involves only the C-I bond. The C atom then recoils into the rest of the radical and partitioning of energy between translation and internal excitation is decided by simple conservation of energy and momentum.

Godwin, Paterson and Gorry (B1.59) have recently proposed a model which combines the soft-radical impulse model (B1.57) for the energy disposal with a simple Landau-Zener description of the curve crossing probability. On this basis the I^* quantum yield is given by the probability of staying on the original curve:

$$\Phi^* = \exp\left(\frac{-2\pi V_{12}}{F_1\,|\Delta F|\,v}\right) = \exp\left(-\zeta/v\right) \qquad (1)$$

where V_{12} is the coupling term, ΔF is the difference in gradients at the crossing point, and v is the velocity through the crossing point. Considering the localised nature of the n and σ^* orbitals involved it seems likely that the V_{12} and ΔF terms should be similar for related iodo-alkanes. These terms can then be absorbed into a single parameter ζ which should characterise that related set of molecules. There remains the task of finding the velocity at the crossing point. To do this we calculate the translational energy disposal from the soft radical model (B1.57).

$$E_t = (\mu_a/\mu_f)\,E_{avl} \qquad (2)$$

where μ_a is the reduced mass of C and I, μ_f is the reduced mass of the radical and I, and $E_{avl} = h\nu - \Delta D_0^\circ$ is the available energy. In reality the crossing point lies at an unknown energy between the initial excitation value and the final asymtotic energy given by the impulsive model, however since this should be a constant within a related family of iodoalkanes, the proportionality constant is subsumed into ζ. We thus obtain an expression for Φ^*

$$\Phi^* = \exp - \left(\frac{\mu_f \zeta}{(2\mu_a E_{avl})^{\frac{1}{2}}}\right) \qquad (3)$$

The only information required by this model are the masses of R (the radical) and I, the total available energy, and an empirical parameter ζ - which is found using one molecule as a calibrant. It should then be possible to calculate the Φ^* values for all other molecules in the family.

The solid lines in Figure B1.39 are calculated from equation 3 with the ζ values indicated on the diagram, and a constant E_{avl}=255 kJ mol^{-1} in all cases. The diagram shows several different families of alkyl iodides which clearly reveal both dynamic and electronic contributions to the Φ^* values. If we consider a vertical column such as the 'ethyl' iodides (C_2 on the diagram) we can see a consistant reduction in curve crossing probability (increasing Φ^*) with substitution of electronegative atoms at the β, and then α, carbons. Since the energy disposed into translation decreases with the heavier radicals this trend is in the opposite direction to that predicted on a dynamical basis alone. There is thus a genuine change in the potential curves involved, although it is not possible to unravel effects due to changes in V_{12}, ΔF and the curve crossing postion. The electronic effect is further illustrated by the butyl iodides in which the change in radical structure from primary to secondary to tertiary (increasing electron donation to the α carbon) is accompanied by a steady decrease in the Φ^* values.

The dynamical effect is responsible for the trend in Φ^* within a given family. Unfortunately, so far, many of the 'families' only contain two compounds but in all cases the ζ value calculated from the first member correctly predicts the Φ^* value of the second one. Within the n-iodoalkanes the anomolous cases of Ch_3I and CF_3I are understandable given that these have different structures at the α carbon (three hydogens as opposed to two hydrogens and one carbon), they thus really constitute a separate class. We thus have a situation in which the Φ^* values are governed by electronic considerations across families (vertically) but by dynamics within families (horizontally).

B1.18 Quantum State Selected Photodissociation of SO_2

J August, M Brouard, J P Simons (University of Nottingham)

The study of energy and angular momentum disposal among the primary fragments of molecular photodissociation provides an insight into the fragmentation dynamics. Studies conducted close to threshold are of particular interest, especially when the parent molecule is fluorescent, so that spectroscopic probing can be focussed on both the fragments and the dissociating molecule. The sulphur dioxide molecule provides a 'well-tuned' system where such a dual approach can be attempted since it presents a sharp predissociation threshold in the $\tilde{C}^1B_2$ electronic state at ~218 nm. Its absorption spectrum is rotationally structured at $\lambda \geq 218$ nm, and the $SO_2(\tilde{C} \rightarrow \tilde{X})$ fluorescence has a natural lifetime ~40 ns. Structure is still preserved at wavelengths below threshold, but the predissociation reduces the fluorescence lifetime to $\leq$ 2 ns. The retention of rotational (and vibrational) structure offers the possibility of probing the

rovibronic quantum state dependence of predissociation rates, provided (a) the structure is sufficiently 'de-congested' (b) the fluorescence decay can be monitored, (c) the primary fragments $SO(X^3\Sigma^-)$ can be detected via laser induced fluorescence techniques, and (d) narrow line tunable laser radiation is available at $\lambda \sim 218$ nm. Decongestion can be achieved by jet-cooling in a supersonic expansion system; laser radiation at ~ 218 nm is not too readily obtained but as an alternative the SO_2 molecule can easily be excited via two photon absorption using intense dye laser radiation at 430 nm. This can be generated using excimer laser pumping (ns system) or ion-laser pumping coupled with Nd/YAG amplification (ps system), both of which are available on loan, or centrally at the LSF. State resolved detection of SO(X) can be achieved via L.I.F. on the $SO(X \rightarrow A^3\Pi)$ system at $\lambda \sim 260$ nm, though the sensitivity is relatively low and interference from the fluorescence of SO_2 has to be accommodated.

This report describes some preliminary experiments exploring the feasibility of both ns and ps studies.

Experimental

(i) 'Nanosecond' Experiments

Tunable, 420 to 450 nm radiation from the loaned JK 2000 Nd/YAG-pumped dye laser (10 Hz, 3-4 mJ pulse^{-1} at 440 nm) was focussed with a 30 cm focal length lens into a reaction vessel which could be operated either as a static (thermal) cell at pressures of 1 to 10 Torr or in conjunction with a pulsed supersonic jet expansion. The axis of the pulsed nozzle (Newport Corporation BV 100, typical backing pressue of 1 atm He seeded with 5-10% of SO_2, orifice diameter 0.5 mm) was orthogonal to both the laser propagation and fluorescence detection axes. Total molecular fluorescence from ~ 220 to 400 nm was detected with an EMI 9813 photomultiplier via three layers of OX7 black glass filter and recorded on a boxcar averager (PAR model 165). Time-resolved decay profiles were recorded on a transient digitiser (Biomation, 6500) and stored on a microcomputer.

(ii) 'Picosecond' Experiments

The above cell in static mode of operation (10-100 Torr SO_2) was used at the LSF for experiments employing the picosecond laser radiation source. Light at ~ 430 nm (20 μJ pulse^{-1} at 10 Hz) was focussed into the cell with a 10 cm focal length lens and the fluorescence was detected at right angles to the laser axis (with appropriate filtering) by a streak camera and optical multichannel analyser. Residual radiation at ~ 700 nm (after mixing with the YAG fundamental at 1064 nm) was used to trigger the streak camera.

Results and Discussion

(i) 'Nanosecond' Experiments

The two photon total molecular fluorescence excitation spectrum (FES) of SO_2 has been recorded under thermal and jet-cooled conditions at wavelengths from ~ 420 to 450 nm, i.e., at energies below and, for the first time, above the predissociation threshold (see figures B1.41 and B1.42). The thermal two photon spectra, which agree well with earlier work of Vasudev and McClain (B1.70), show clearly the severe rotational congestion which is significantly relieved on

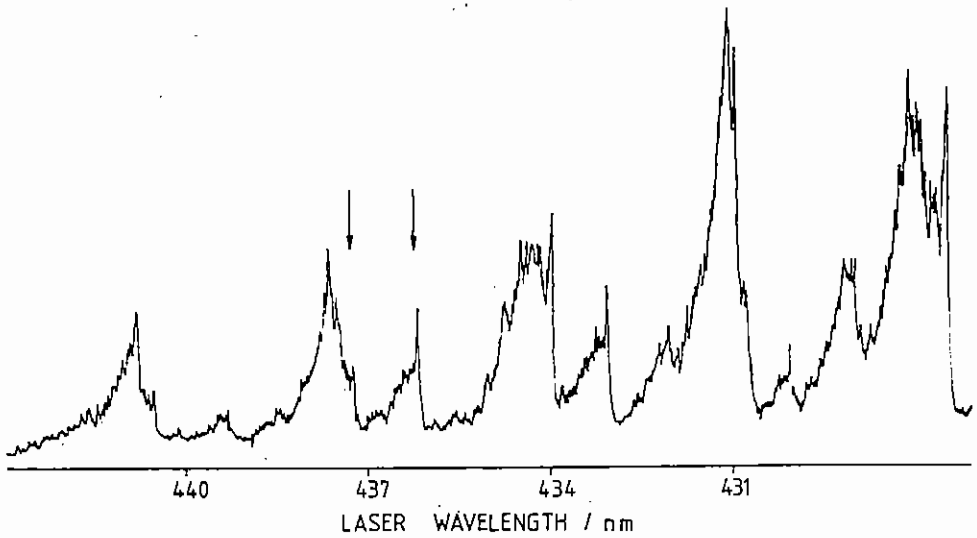

Fig B1.41 Thermal two photon fluorescence excitation spectra of SO_2 (9 Torr). Spectra are not corrected for fall-off in dye laser power.

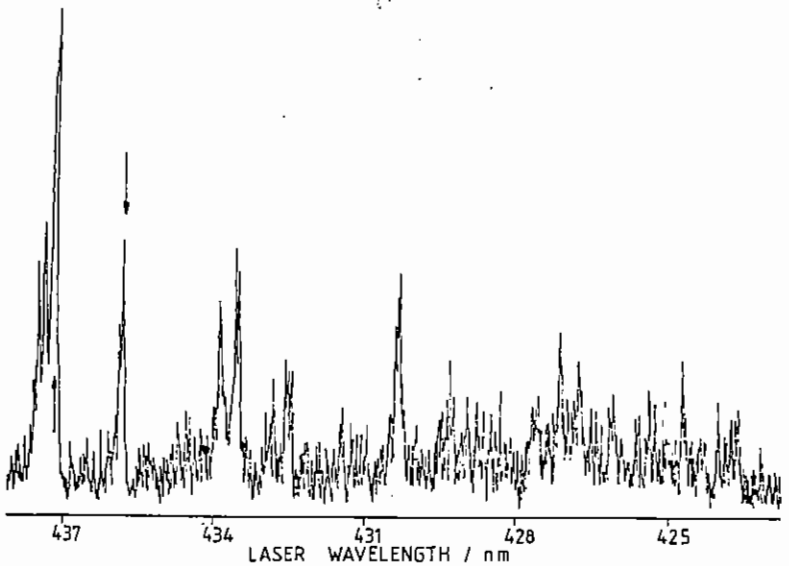

Fig B1.42 Jet-cooled two photon fluorescence excitation spectra of SO_2. Arrows indicate the two peaks whose lifetimes were measured, as discussed in the text.

jet-cooling (figure B1.42). Unfortunately the rotational structure was unresolvable with the JK laser system employed but an approximate temperature reduction was estimated from two photon L.I.F. experiments on jet-cooled NO (1% in He at 1 atm backing pressure) at ~430 nm; they indicated a rotational temperature of ∿ 3K. The vibrational features in the jet-cooled SO_2 FES spectra can be readily identified with assigned features in the thermal spectrum (fig B1.41, B1.42) but there are differences (as yet tentative) in the relative intensities of some of these features close to threshold. Predissociation is believed to occur predominantly via coupling of levels with $v_3'=0$ (v_3' is the $\tilde{C}(^1B_2)$ state antisymmetric stretching mode) to continuum levels in the S02 ground state (ref B1.70, B1.71). This evidence is supported by the observation that in the region close to threshold our jet-cooled FES spectra appear to be dominated by transitions to levels with v3 = 0, which do not couple strongly with the ground state continuum and thus have the largest fluorescence quantum yield. (The (v_1', v_2', v_3') labelling is only a crude representation of the vibrational states at these energies due to large anharmonic coupling between the v_1' and v_3' modes.) The thermal FES at energies below and slightly above the threshold and at pressures of > 1 Torr are partially vibrationally relaxed (fig B1.41) and hence the relative intensities of transitions to levels with $v_3'=0$ are larger compared with those in the jet-cooled FES.

There is, at present, some uncertainty regarding the predissociation threshold in SO_2, although more recent work, and thermodynamic data, suggest a value of between 46000 cm-1 and 45400 cm-1 (ref B1.70, B1.71). Using the JK 2000 laser system we have performed preliminary lifetime measurements of a number of vibrational levels close to the predissociation limit. Whilst these measurements were limited to lifetimes of > 10 ns it was possible to observe a sharp reduction in lifetime between features in the jet-cooled two photon FES at ~437.3 and ∿435.9 nm from ∿40 ns down to < 15 ns respectively. The above implies that the predissociation threshold should lie at energies between ~45880 and 45740 cm^{-1}, in broad agreement with the earlier work (this, it should be noted, corresponds to a wavelength range just accessible to tunable frequency doubled radiation at λ > 217.2 nm).

First attempts to monitor the SO photofragments by L.I.F. at ~260 nm proved unsuccessful. This was partly due to strong background SO_2 fluorescence excited at this wavelength, which is not easily filtered or gated out, but was also hampered by the low power (and low resolution) of the JK 2000 dye laser system. However, the feasibility of performing these pump-probe experiments using an excimer-pumped-dye laser either by two photon excitation at 430 nm or using tunable frequency doubled radiation at λ > 217.2 nm (see above) is currently under investigation.

(ii) Picosecond experiments

Although the LSF was successful in providing picosecond laser radiation at ∿430 nm in principle of sufficient energy, we were

unable to observe the molecular fluorescence from thermal SO_2 in the limited time available (one week). The main problems arose from the poor collection and detection efficiency and high temporal jitter (approximately ±1 ns) of the streak camera. It is felt, however, that many of these problems can be surmounted by employing a fast photon counting apparatus.

Whether the technique could be improved sufficiently to observe signals from jet-cooled SO_2, using 2-hν excitation, remains to be seen. It may well have to await the availability of tunable picosecond radiation at ∿(217-218) nm.

Acknowledgments

We are most grateful to the LSF support staff for their help, particularly at RAL.

B1.19 LASER PHOTOCHEMISTRY AND SPECTROSCOPY OF MOLECULES CONTAINING NO

J A Dyet, M R S McCoustra and J Pfab
(Department of Chemistry, Heriot-Watt University)

This report covers work carried out with the EMG101/FL2002 dye laser of the LSF loan pool during a three month loan period.

Introduction

In these experiments, we aim to characterise the internal energy and quantum state distribution of the nascent NO from the photodissociation of a range of nitroso-compounds. In the C-nitroso compounds, we are primarily concerned with slow predissociation on the nanosecond timescale following single-photon absorption in the 560 to 720 nm region. Their structured electronic absorption spectra in this region are due to a $^1A''-^1A'$ (n, π^*) transition. From dispersed and fluorescence excitation spectra of the jet-cooled molecules, we wish to obtain information on the level structure and potential surfaces of both electronic states (Ref. B1.72). Time resolved fluorescence measurements will allow us to deduce the rates and mechanism of non-radiative processes preceding the disassociation step and will permit us to correlate the dynamics of vibronic states of these compounds with the final product state distribution of the nitric oxide photofragment. In the work reported here, we employed the loan laser system for the state-selective photodissociation of jet-cooled nitroso-compounds and our own laser for state-resolved probing of the NO photofragment by two-photon laser-induced fluorescence (TPLIF).

Experimental

As shown in Figure B1.43, the experiment utilised two synchronised pulsed dye lasers and an expansion chamber with associated gas handling equipment for supersonic jet-cooling of the sample vapour. For the pulsed supersonic expansion, a solenoid valve with 500 μm nozzle diameter was employed, with ca. 10% mixtures of the gaseous nitroso-compound in argon at stagnation pressures near 300 torr and pulse durations of about between 0.1 and 0.25 ms. The pulsed jet was crossed by the two collinearly aligned counter-propagating dye laser beams. Pulse powers of 0.5 to 1 mJ in the 675-720 nm region (Oxazin 170 in methanol, DCM in DMSO) were obtained from the loaned Lambda Physik EMG101/FL2002 laser system. Nascent NO was probed by two-photon LIF with a Lambda Physik EMG50E/FL2002 dye laser. The lasers and pulsed nozzle were synchronised by an analogue delay generator in combination with a crystal controlled master oscillator. Unless specified otherwise, a delay of 100 ± 20 ns was used between the dissociation and probe pulses. Details concerning the fluorescence collection and signal acquisition can be found elsewhere (Ref. B1.72-B1.75).

Results and Discussion

a) Chlorodifluoronitrosomethane ($CClF_2NO$)

The excitation spectrum of jet-cooled $CClF_2NO$ has now been analysed and is well understood. The evaluation of the photofragment spectra of nascent NO (Ref. B1.73) has been completed. Rotational and spin-orbit population distributions of the NO X(v"=0) fragment have

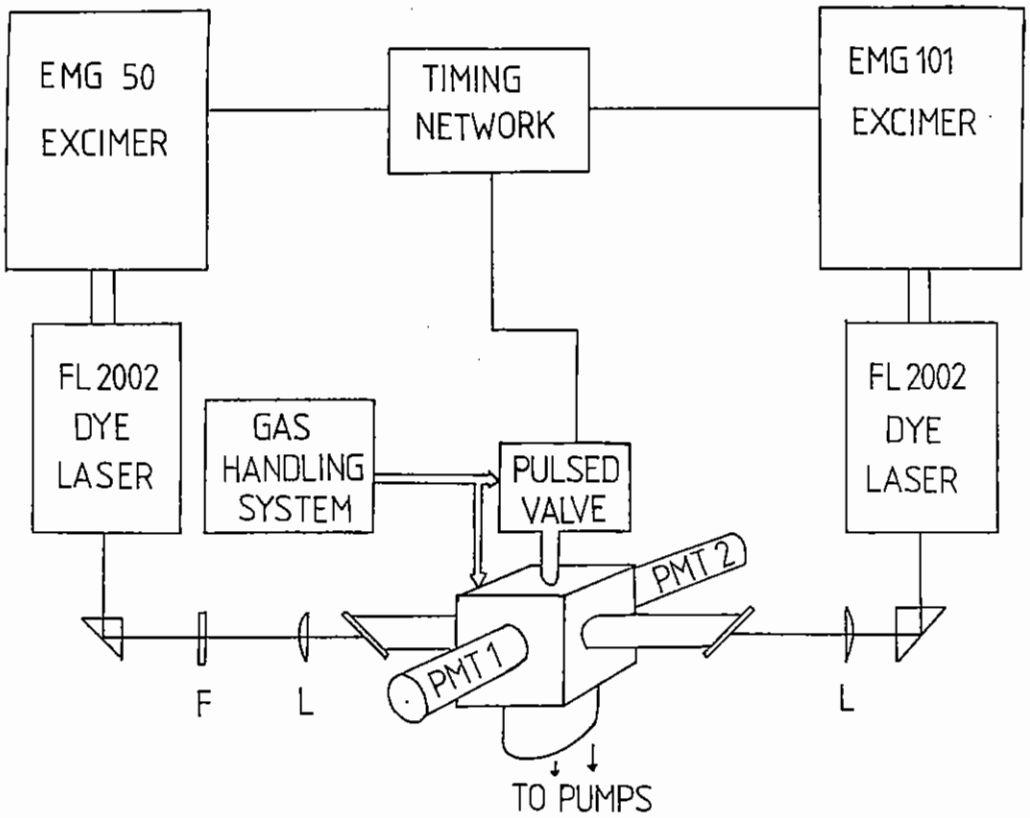

Fig B1.43 Arrangement used for pulsed dissociation-probe experiments of jet-cooled C-nitroso compounds.

been obtained at fourteen isolated vibronic features of the jet-cooled parent. In all cases, the NO (v"=1) yield was too small for detection. As the excitation energy increases, the fraction of energy partitioned into rotation of NO increases, and the spin-orbit population ratios approach unity. Figure B1.44 presents results from the photolysis on the 12^1_0 vibronic feature near 699.5 nm as an example and provides a comparison of the observed and calculated a priori rotational distributions. Within the limits dictated by the poor sensitivity of the two-photon probe technique, the rotational population distribution of each spin-orbit state is statistical and no state-specific effects are apparent in the rotational energy disposal. The spin-orbit ratios, however, are markedly colder than the statistical ratios. A dissociation energy of 13500 ± 350 cm-1 (162 kJ mol-1) has been evaluated by comparing observed with calculated statistical rotational distributions. The energy disposal at 646.6 nm and the photofragment yield spectrum of the jet-cooled parent has been reported and discussed in detail (Ref. B1.75).

b) Dichlorofluoronitrosomethane (CCl_2FNO)

The electronic origin in the fluorescence excitation spectrum has been located at 688.58 nm. The spectrum is dominated by torsional and bending progressions as with $CClF_2NO$ indicating that changes in the dihedral and CNO bending coordinates dominate the (n, π^*) electronic transition in the visible. A detailed analysis is in progress. Photodissociation of the cold parent on nine assigned vibronic features between 674 and 650 nm provided TPLIF spectra of nascent NO (v"=0) over a considerable range of excess energies. Figure BI.45 presents one example from the photolysis in the intense but as yet unassigned vibronic band near 643.3 nm. Rotational population distributions of NO (v"=0) from photolysis on the 649.3 nm vibronic transition $\gamma^1_0 12^1_0$ are shown in figure B1.46. Mode γ is an a' skeletal bending mode while the twelfth normal mode is the lowest frequency torsional mode. It is not yet clear whether these rotational distributions show marked deviations from statistical behaviour.

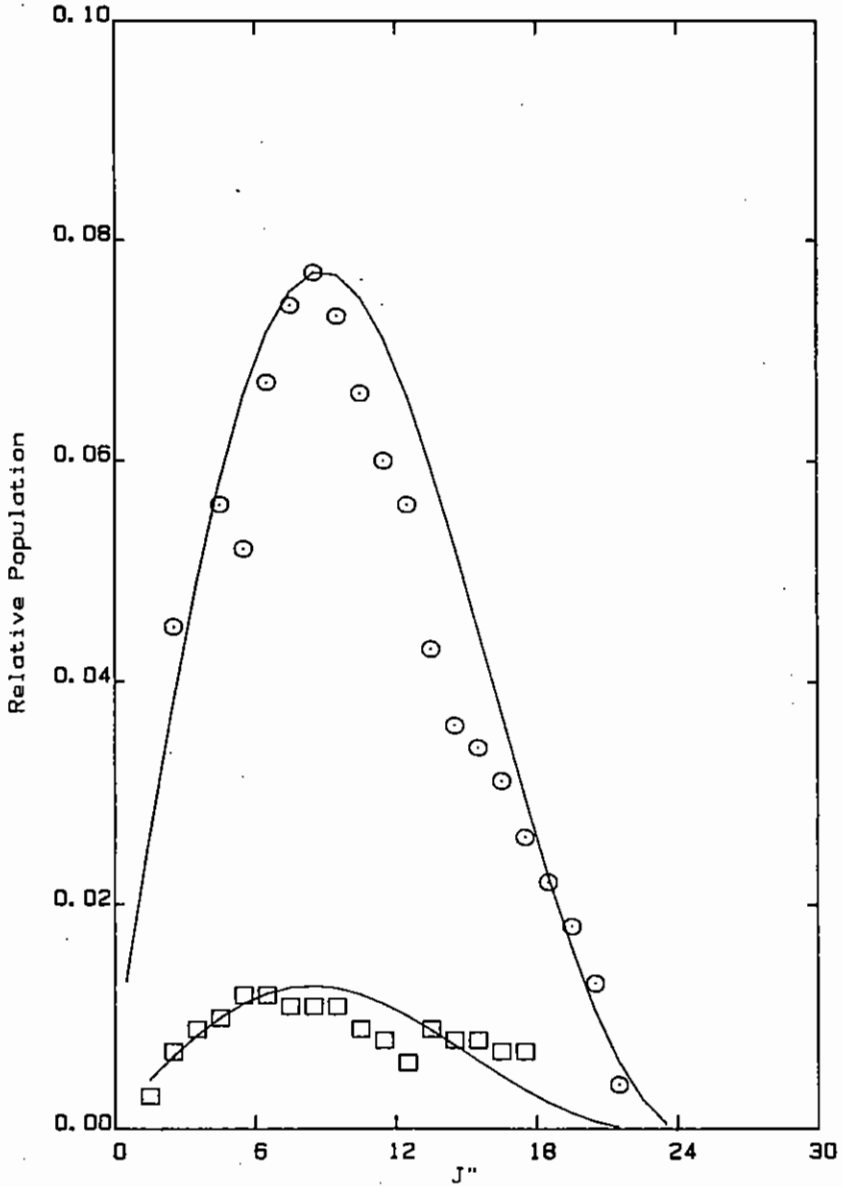

Fig B1.44 Rotational distributions of NO (v"=0) from the photolysis of jet-cooled $CClF_2NO$ on the 12^0_0 vibronic feature near 699.5 nm. (O) $^2\Pi_{1/2}$ and (□) $^2\Pi_{3/2}$ states of NO. (-) Calculated a priori distributions except for the spin-orbit ratio, which has been scaled to permit better comparison with experiment.

c) Trifluoronitrosomethane (CF_3NO) revisited

CF_3NO represents one of the first polyatomic molecules where vibrational state selection in the excitation step and detailed measurements of non-radiative transition and dissociation rates have been combined with mapping of nascent quantum state distributions of a photofragment (Ref. B1.76). We have recently re-examined and reassigned the fluorescence excitation spectrum of the jet-cooled parent (Ref. B1.72) and discovered that many $\tilde{A}$ state levels show biexponential fluorescence decay behaviour (Ref. B1.77). This prompted us to re-examine the dissociation dynamics. Figure B1.47 presents a comparison of earlier work (Ref. B1.76, upper spectrum) and our own work (lower spectrum) showing TPLIF scans of nascent NO (v"=0) from photodissociation following excitation of the v=6 torsional level of the parent $\tilde{A}$ state. With the significant improvement we achieved, we obtained reliable state-resolved population distributions. No significant deviation from statistical

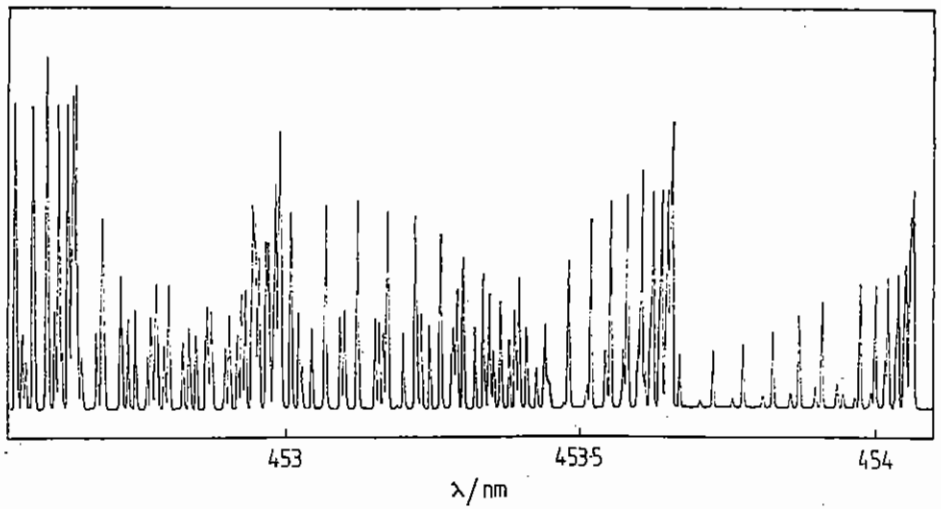

Fig B1.46 Two-photon LIF of the nascent NO (v"=0) photoproduct from the photolysis of jet-cooled CCl_2FNO on the 643.3 nm feature.

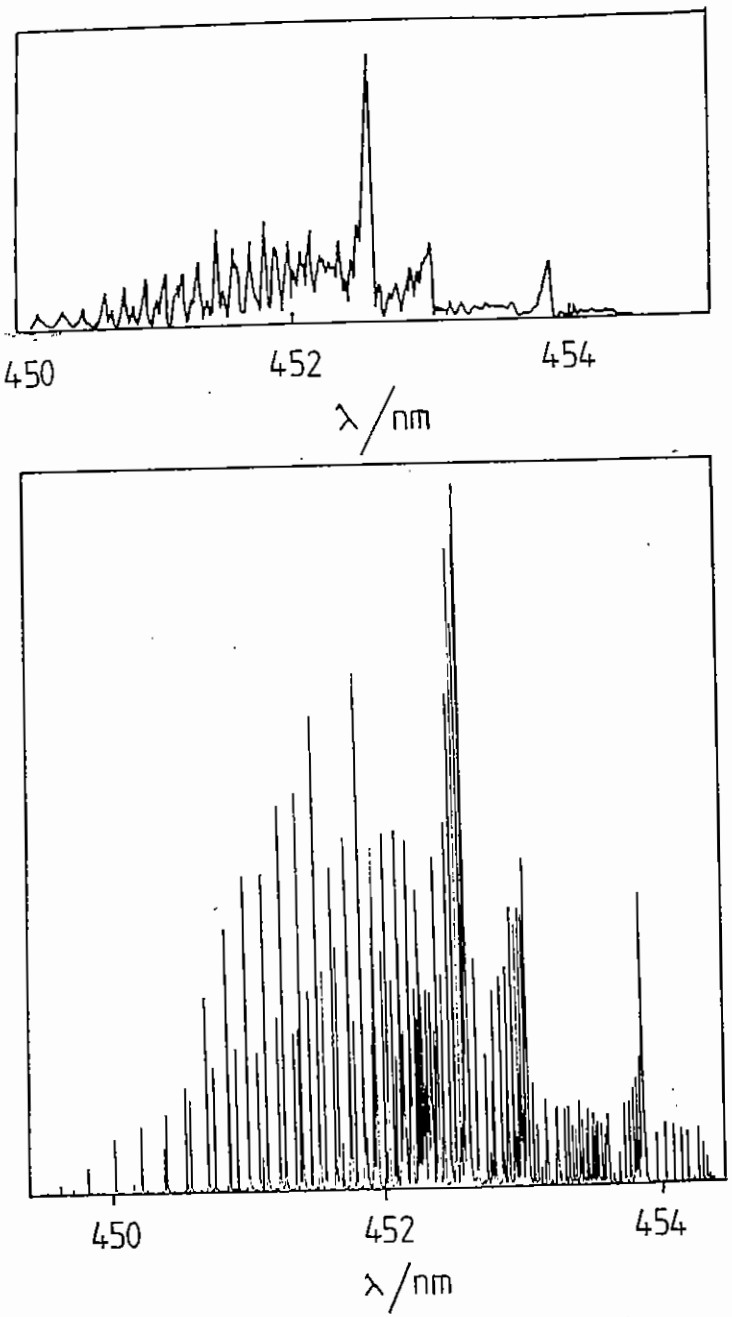

Fig B1.47 Comparison of NO (v"=0) two-photon LIF spectra obtained by photodissociation of jet-cooled CF_3NO following excitation of the 126§ vibronic feature. Upper trace - Ref B1.76, lower trace - this work.

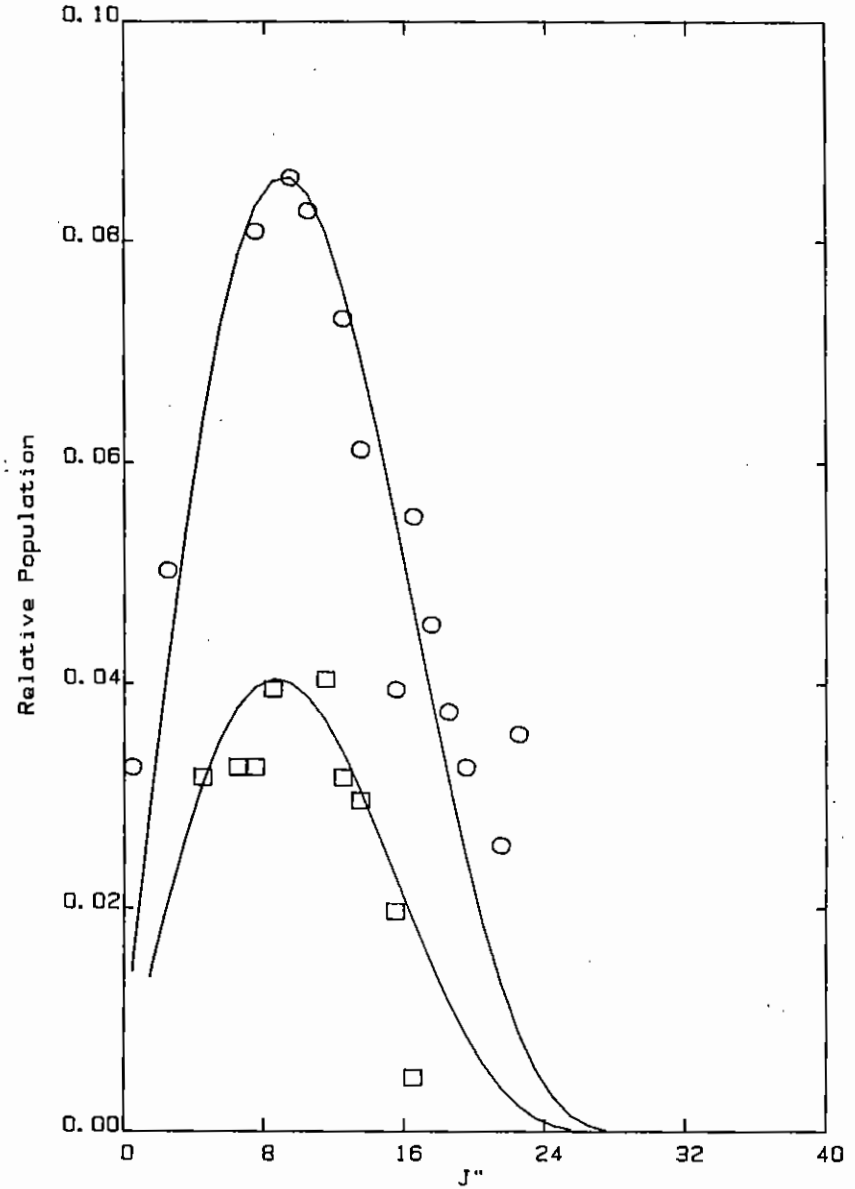

Fig B1.45 Rotational population distributions of NO (v"=0) from the photolysis of jet-cooled CCl_2FNO on the γ§12§ vibronic feature near 649.3 nm. Other details as in Fig B1.44.

significant deviation from statistical distributions could be identified for photodissociation in the well-structured region of the excitation spectrum. Excitation of features beyond the threshold where the fluorescence yield drops provides rotational distributions such as the example in Figure B1.48. The observed distributions are narrower than the a priori distributions and there is evidence of bimodal character at high J particularily for the $^2\Pi_{3/2}$ state. A more accurate value for the C-N bond dissociation energy (D_0=13970±40 cm^{-1}) was obtained spectroscopically from the observation of the highest rotational state of the NO fragment.

d) Alkyl Nitrites and Nitrosamines in the Near UV

The photodissociation dynamics of these compounds is already being studied in detail in the laboratories of Huber (Switzerland), Lahmani (France) and Rosenwaks (Israel). We have attempted to record NO yield spectra in the jet but contrary to our expectation no distinctive spectral features could be seen, and the NO yield spectra simply reflected the dye tuning curve of the dissociation laser.

Preliminary work on the near-UV photodissociation of jet-cooled N-nitroso-methylcyanamide ($CH_3N(CN)NO$) provided good TPLIF spectra of the NO fragment, and evidence for the production of CN at shorter wavelengths has also been obtained. We plan to study this molecule in detail in the future.

Conclusions

We are now beginning to learn from fluorescence decay measurements that the dissociation dynamics of C-nitroso compounds involves intersystem crossing to the lowest triplet state T_1 as well as internal conversion to the ground state. With the molecules we have studied thus far, the rotational state distributions of the NO fragment are statistical and non-statistical effects only become apparent at high excess energies. The time-resolved fluorescence technique is a more sensitive probe for mode-specific effects and the involvement of T_1 than the rotational distributions of the NO

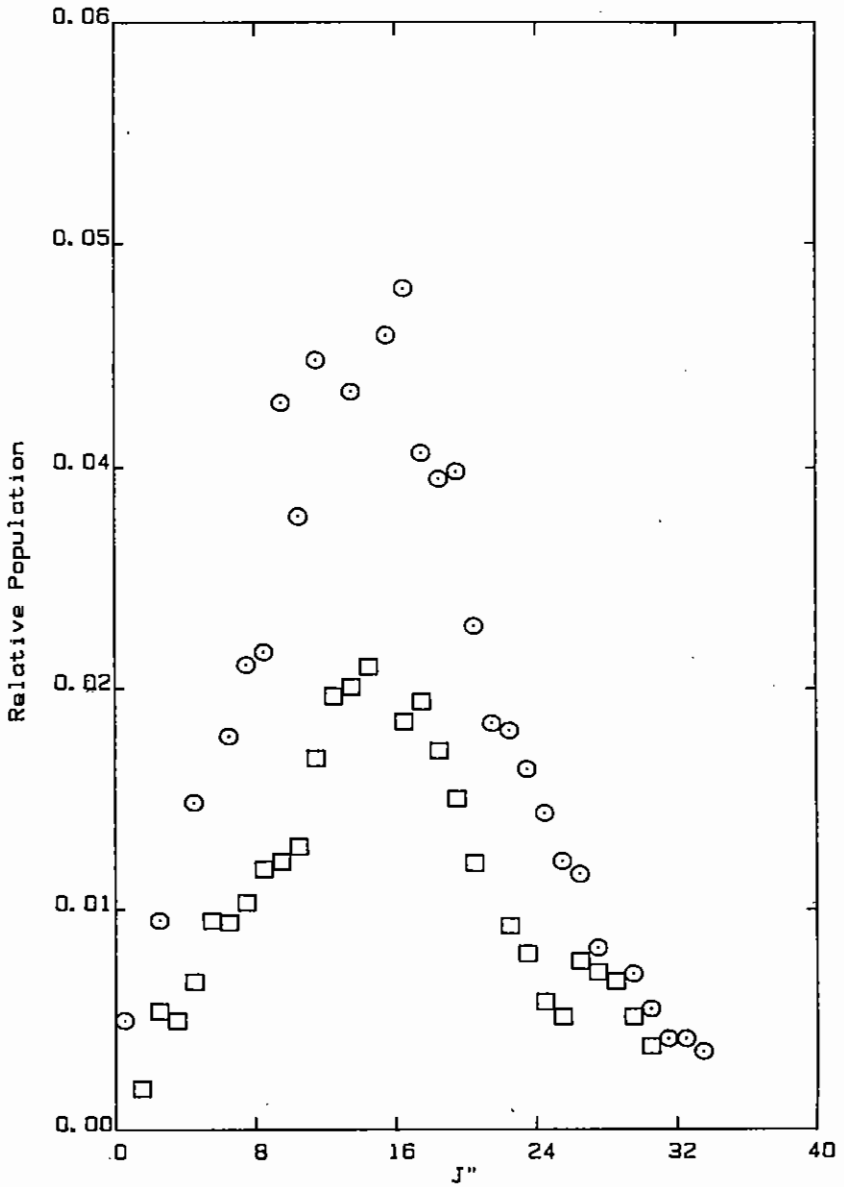

Fig B1.48 Rotational distribution of NO (v"=0) from the 676.4 nm photodissociation of jet-cooled CF_3NO. Other details as in Fig B1.44

photoproduct. The measurement of reliable and detailed state distributions in the jet is not trivial and requires careful experimentation and high sensitivity of the probe technique. With these molecules, accurate bond dissociation energies can be obtained by locating the highest rotational state of the NO. The full power of this technique will become apparent with the use of the more sensitive single-photon LIF technique.

B1.20 ANALYTICAL APPLICATIONS OF ULTRAVIOLET RESONANCE RAMAN SPECTROSCOPY

K P J Williams (British Petroleum Research Centre, Sunbury-on-Thames, Middlesex)

The industrial application of Raman spectroscopy has become more widespread over the past decade. The Raman spectroscopy group at the British Petroleum Research Centre has been one of the leaders in this field. Applications of the method have ranged from solving plant problems, through structural elucidation of, for example polymers, to device technology. For bulk samples in the main, we have used spontaneous Raman spectroscopy, however, when working at low concentration resonance Raman methods have been employed. The drawback with the latter method, using continuous wave lasers as the excitation source, is that it confines the range of systems that can be studied to those possessing a visible chromophore. Whilst systems such as polyenes can be studied readily many others, possessing UV electronic absorptions, have been difficult to investigate with our laser capability.

One of the main aims of the Raman group at BP is to investigate the potential for new methods in the general area of Raman spectroscopy. The application of ultraviolet laser excitation to resonance Raman spectroscopy for the analysis of samples present at low levels is one such area of interest. Whilst our laser capability was unable to provide a tunable ultraviolet laser output we were aware of the Laser Support Facility at the Rutherford Appleton Laboratories (RAL). An application for time on the Facility was made and over the period of a few weeks an assessment of the method has been made with some pleasing results.

In broad terms resonance Raman scattering occurs when the laser excitation wavelength is coincident with an allowed electronic transition. For molecules possessing aromatic moieties the electronic transitions tend to occur in the ultraviolet region of the spectrum. The molecules of general interest include polycyclic aromatics and chemical additives to both polymers and oils. The results obtained at the RAL will be confined to the former.

Polycyclic aromatics are found in many oil and coal fractions. The normal method of detection at trace levels is by high pressure liquid chromatography which provide a non specific analysis. Since resonance Raman spectra depend heavily on both the electronic absorption and the incident laser wavelength it seems likely that by a judicious choice of experimental conditions a more specific analysis can be provided. The example given in Figure B1.49 is of the resonance Raman spectra obtained from four polycyclic aromatics, (a) anthracene, (b) 9-methylanthracene, (c) 9,10-dimethylanthracene, (d) 9,10-diphenylanthracene. The spectrum recorded from the solvent is shown at the foot of each column, for reference. All of these data were obtained under similar conditions with the laser excitation wavelength set at 261 nm, a repetition rate of 70 Hz, a laser energy of ∿0.7 mJ/pulse and an accumulation time of ∿ 20 minutes. The concentration of the samples, in tetrahydrofuran, was ∿ 10^{-3}M. Data was easily obtainable from the 9-methylanthracene at a much lower concentration of ∿ 5 x 10^{-5}M. This lower concentration still provided a spectrum with a signal to noise ratio for the major bands of ∿ 10:1 which obviously indicates that the limit of detection can be yet lowered.

It is apparent from Figure B1.49 that the spectra recorded, from the four substituted anthracenes selected, that each spectrum is unique in terms of its appearance and band positions. At the prevailing concentration the solvent peaks are weak and as such do not greatly obscure the spectra. On this basis a mixture of the four components, given a suitable library of spectral data, should be quite amenable to analysis. An illustration of the importance of excitation wavelength with spectral intensity is given in Figure B1.50. Anthracene (∿ 10^{-3}M) excited at 261 nm provides a very intense resonance Raman spectrum which is rich in Raman bands. The same sample excited at 302 nm, on the other hand, produces only one

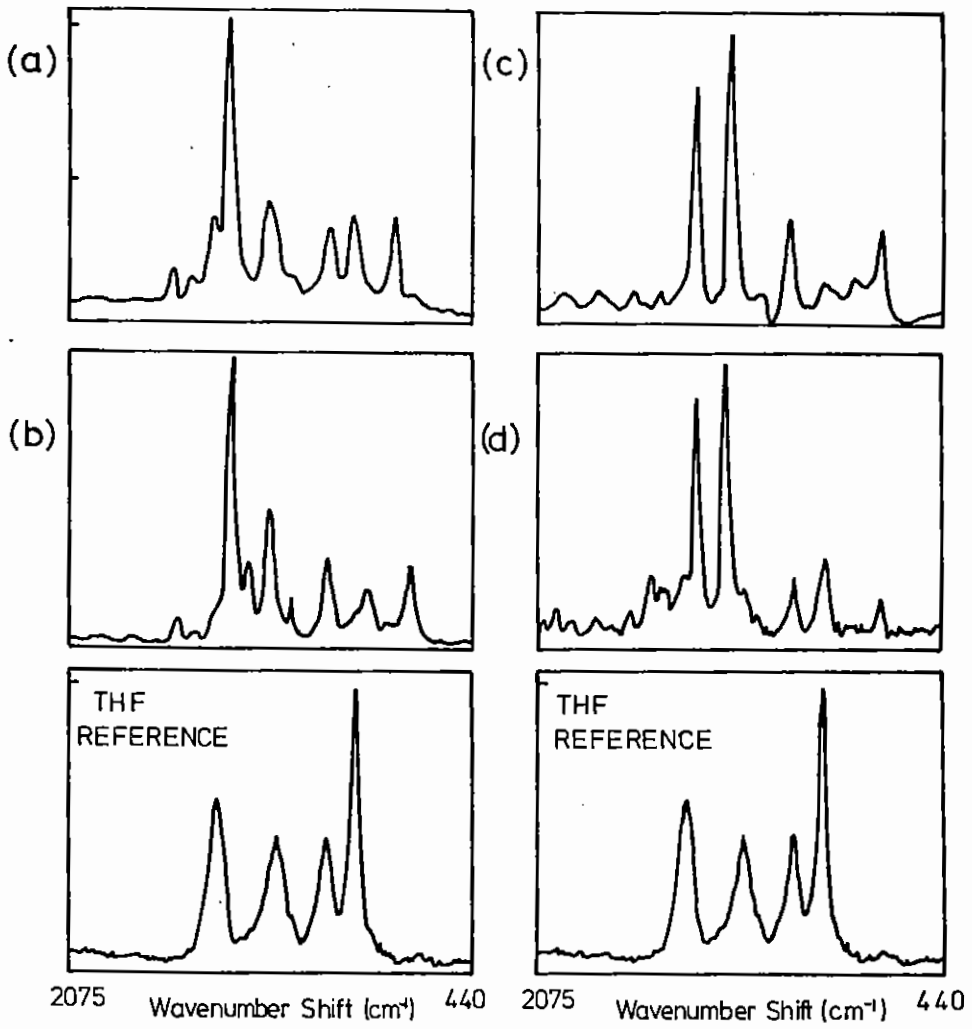

Fig B1.49 Resonance Raman spectra recorded from substituted anthracenes using λ 261 nm, 70 Hz, and 0.7 mJ per pulse. Accumulation time ∿20 minutes (a) anthracene, (b) 9-methylanthracene, (c) 9,10-dimethylanthracene and (d) 9,10-diphenylanthracene. The spectra of the solvent THF is shown under each column for reference purposes.

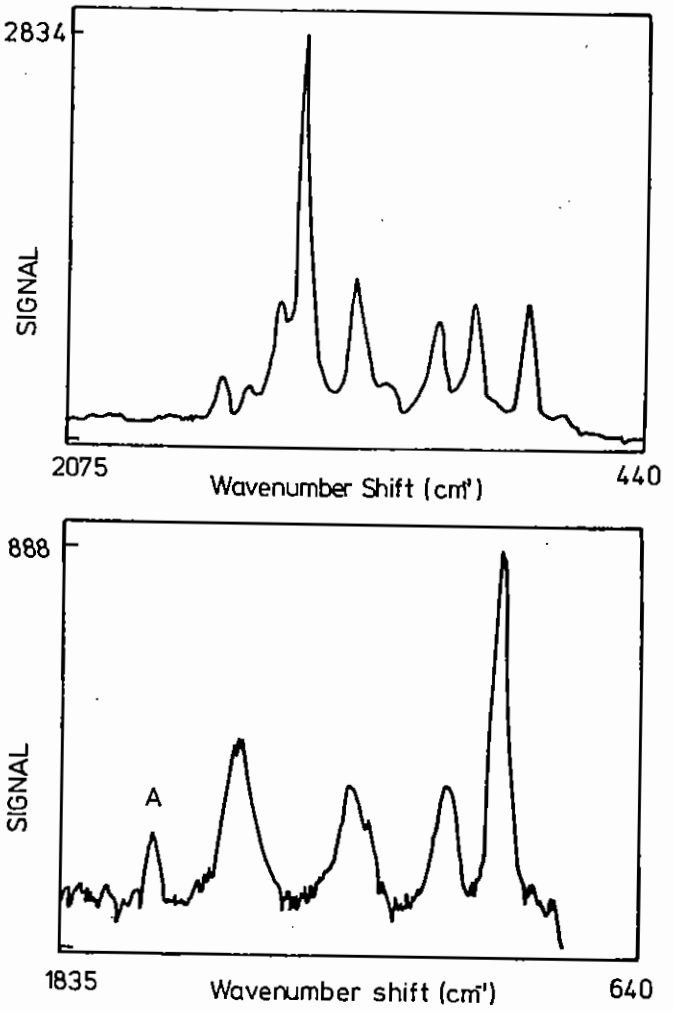

Fig B1.50 Resonance Raman spectra recorded from anthracene under similar conditions and sample concentration. (a) using 261.0 nm excitation, (b) 302 nm excitation.

readily discernable Raman band (marked A) which is far weaker than the major solvent (tetrahydrofuran) peaks. Clearly, a shift of 40 nm in laser excitation wavelength produces dramatic changes in the Raman spectrum. Although no experimental data from mixtures is available at this stage of our work it is thought that mixtures of similar molecules (possessing different ring substitutions) could be resolved into their individual components using this method.

Finally, our work in the Laser Support Facility at the RAL has provided a good background for us to assess the potential of the UV excited resonance Raman method. It has also given a grounding in the problems, which are far from trivial, of implementing the technique. Most importantly it has shown that after a few weeks of intensive effort that the type of systems of interest to British Petroleum are capable of providing good quality and potentially useful Raman data. We are grateful to the supporting staff within the LSF for their assistance.

Acknowledgement

Permission to publish this work has been given by British Petroleum plc.

References:

B1.1 J N Moore, G H Atkinson, D Phillips, P M Killough and R E Hester, Chem Phys Lett, 107, 381 (1984).

B1.2 Photochemistry of 9,10-anthraquinone-2,6 disulphonate, J N Moore, D Phillips, N Nakashima and K Yoshihara, J C S Faraday Trans 2, 82, 745 (1986).

B1.3 Time-resolved resonance Raman Spectroscopy applied to anthraquinone photochemistry, D Phillips and R E Hester, J C S Faraday Trans 2, 82, 1093 (1986).

B1.4 Photophysics and photochemistry of sulphonated derivatives of 9,10 anthraquinone 'strong' versus 'weak' sensitisers', J N Moore and D Phillips, J C S Faraday Trans 2, 83, (1987) in press.

B1.5 Raman Spectroscopic Studies of Transient Chemical Species, R E Hester in Time-Resolved Laser Raman Spectroscopy, Eds D Phillips and G H Atkinson, Harwood Academic Publishers, London, 5 (1987).

B1.6 Time-Resolved Resonance Raman Spectroscopy of Electronically Excited Species, J N Moore and D Phillips in Time-Resolved Laser Raman Spectroscopy, Eds D Phillips and G H Atkinson, Harwood Academic Publishers London, 23 (1987).

B1.7 Time-Resolved Resonance Raman Spectroscopy of Sulphonated Anthraquinone Derivatives, J N Moore, D Phillips, R E Hester, G H Atkinson and P M Killough in Time-Resolved Laser Raman Spectroscopy, Eds D Phillips and G H Atkinson, Harwood Academic Publishers London, 23 (1987).

B1.8 Resonance Raman Studies of Transient Intermediate in Photoreactions of Anthraquinone and Flavone Species, J N Moore, D Phillips, P M Killough and R E Hester in Time-Resolved Vibrational Spectroscopy, Eds A Laberau and M Stockburger, Springer-Verlag, Heidelberg, 136 (1985).

B1.9 Time-resolved Resonance Raman Spectroscopy of the Triplet State and Semi-reduced form of Duroquinone, I McCubbin, D Phillips and R E Hester, J C S Faraday Trans 2, 83, (1987) in press.

B1.10 J N Bechara, S E J Bell & J J McGarvey, (1986), Inorg. Chem., 25, 4325.

B1.11 Annual Report to the Laser Facility Committee, 1986, B1.3.

B1.12 J N Bechara, S E J Bell, J J McGarvey and JJ Rooney. J.Chem. Soc., Chem. Commun., (1986), 1785.

B1.13 J N Bechara, S E J Bell and J J McGarvey. Ricerca Scientifica ed Educazione Permanente, (1986), Suppl. 50, 83.

B1.14 L N Krasnoperov, E N Chesnokov and V N Panfilov, Chem Phys 89, 297 (1984).

B1.15 P B Davies and D K Russell, Chem Phys Lett 67, 440 (1979).

B1.16 P H Beckwith, C E Brown, D H Danagher, D R Smith and J Reid, Appl Optics (in press).

B1.17 J A Cowan & J K M Sanders; J Chem. Soc. Perkin (I), 2435, (1985).

B1.18 M P Irvine, R J Harrison, M A Strahand & G S Beddard; Ber. Bunsen. Phys. Chem. 89, 226 (1985).

B1.19 M P Irvine, R J Harrison, G S Beddard, P Leighton & J K M Sanders Chem. Phys. 104, 315, (1986).

B1.20 R J Harrison, B Pearce, G S Beddard, J A Cowan, J K M Sanders, submitted Chemical Physics 1987.

B1.21 I W M Smith and M D Williams, J Chem. Soc., Trans. 2, 82, 1043 (1986).

B1.22 D L Baulch, R A Cox, R F Hampson, J A Kerr, J Troe and R T Watson J.Phys. Chem. Ref. Data, 13, 1259 (1984).

B1.23 G Paraskevopoulos and R S Irwin, Chem. Phys. Letters, 93, 138 (1982).

B1.24 A R Ravishankara and G L Vaghjiani, private communication (1986).

B1.25 J A McCauley, S M Anderson, J B Jefferies and F Kaufman, Chem. Phys. Letters, 115, 180 (1985).

B1.26 T J Barker, R G Denning and J R G Thorne, Inorganic Chemistry, (in press)

B1.27 R -L Chien, J M Berg and D S McClure, J Chem Phys, 84, 4168 (1986).

B1.28 M Vala, J C Rivoal, J Badoz, Mol Phys, 30, 1325 (1975).

B1.29 J C Rivoal, B Briat, Mol Phys, 38, 1829 (1979)

B1.30 P Day and L Dubicki, J Chem Soc, Faraday Trans II 69 363 (1973)

B1.31 J F Donegan, F J Bergin, G F Imbusch and J P Remeika, J Lumin, 31,32 278 (1984).

B1.32 R M Macfarlane and J -C Vial, Phys Rev, B34, 1 (1986)

B1.33 M T Vala, C J Ballhausen, R Dingle and S L Holt, Mol Phys, 23 217 (1972)

B1.34 J Ferguson, H J Guggenheim and E R Krausz, J Phys C:Solid St Phys 4 1866 (1971).

B1.35 Chem Phys Lett 130, 175 (1986).

B1.36 F Wilkinson, C J Willsher, P A Leicester, J R M Barr and M J C Smith, J Chem Soc Chem Comm 1216 (1986).

B1.37 M J C Smith, Laser Support Facility Picosecoind Note 7 (1986).

B1.38 H J Polland and W Zinth, J Phys E 18, 399 (1985).

B1.39 B S Hudson and B E Kohler, Annu Rev Phys Chem 25, 437, (1974).

B1.40 J B Birks and D J Dyson, Proc Roy Soc. A275 135, (1963).

B1.41 E D Cehelnik, R B Cundall, J R Lockwood and T F Palmer, J Phys Chem. 79 1369, (1975)

B1.42 B S Hudson, B E Kohler and K Shulten, Excited states 6, 1. (1982)

B1.43 J B Birks, G N R Tripathi and M D Lumb, Chem Phys 33, 185, (1978)

B1.44 J R Andrews and B S Hudson, J.Chem Phys 68 4587, (1978)

B1.45 P C Alford and T F Palmer, J Chem Soc araday Trans. 79 433, 1708(E), (1983)

B1.46 P C Alford and T F Palmer, Chem Phys Letters 127 19, (1986)

B1.47 C Rulliere, A Declemy and Ph Kottis, Laser Chem. 5 185, (1985)

B1.48 T C Felder, K-J Choi and M R Topp, Chem Phys. 64 175, (1982)

B1.49 R A Lampert, L A Chewster, D Phillips, D V O'Connor, A J Roberts and S R Meech, Anal Chem. 55 244 (1983)

B1.50 E D Cehelnik, R B Cundall, J R Lockwood and T F Palmer, J Chem Soc Faraday Trans.II 70 244 (1974)

B1.51 J F Friichtenicht, Rev Sci Instrum 45 51 (1974)

B1.52 H Kang & JL Beauchamp, J Phys Chem 89 3364 (1985)

B1.53 J F Friichtenicht & S P Tang, Proceedings of the 2nd Summer Colloquium on Electronic Transition Lasers, P 36 (JI Steinfeld Ed, MIT Press, Cambridge, (1976).

B1.54 J L Gole and G J Green, cited in SB Oblath & JL Gole, Combu Flame 37, 293 (1980).

B1.55 K Kinura, Photoelectron Spectroscopy of Excited States in Photodissociation and Photoionisation, 1 (Wiley and Sons (1985).

B1.56 (a) J R Majer, and J P Simons, Adv Photochem, 2, 137 (1964),
(b) R C Mitchell and J P Simons, Faraday Discuss. Chem Soc, 44, 208 (1967),
(c) S R Leone, Advances in Chemical Physics, 50, 255, edited by K P Lawley (Wiley), (1982).

B1.57 S J Riley and K R Wilson, Faraday Discuss. Chem Soc, 53, 132. (1972).

B1.58 M D Barry and P A Gorry, Molec Phys, 52, 461 (1984).

B1.59 (a) C Paterson, F G Godwin and P A Gorry, Molec Phys. (in press)
(b) F G Godwin, C Paterson and P A Gorry, Molec Phys. (in press).

B1.60 (a) G N A van Veen, T Baller, A E de Vries and N J A van Veen, Chem Phys, 87, 405 (1984),
(b) G N A van Veen, T Baller, A E de Vries and M Shapiro, Chem Phys, 93, 277 (1985),

B1.61 (a) R K Sparks, K Shobatake, L R Carlson and Y T Lee, J Chem Phys, 75, 3838 (1981)
(b) T K Minton, P Felder, R J M Brudzynski and Y T Lee, J Chem Phys, 81, 1759 (1984),
(c) D Krajnovitch, L J Butler and Y T Lee, J Chem Phys, 81, 3031 (1984).

B1.62 (a) T Donohue and J R Weisenfeld, Chem Phys Lett, 33, 176 (1975),
(b) T Donohue and J R Weisenfeld, J Chem Phys, 63, 3130. (1975),
(c) T Donohue and J R Weisenfeld, J Phys Chem, 80, 437. (1976).

B1.63 W H Pence, S L Baughcum and S R Leone, J Phys Chem, 85, 3844. (1981).

B1.64 E Gerck, J Chem Phys, 79, 311 (1983).

B1.65 T F Hunter, S Lunt and K S Kristjansson, J Chem Soc, Faraday Trans. 2, 79, 303. (1983).

B1.66 R J Donvan, F G M Hathorn and Husain, Trans Faraday Soc 64, 3192. (1968).

B1.67 W P Hess, S J Kohler, H K Haugen and S R Leone, J Chem Phys, 84, 2143. (1986).

B1.68 P Brewer, P Das, G Ondrey and R Bersohn, J Chem Phys, 79, 720. (1983).

B1.69 (a) R S Mulliken, J Chem Phys, 3, 506. (1935),
(b) R S Mulliken, J Chem Phys, 8, 382. (1940).

B1.70 R Vasudev, W M McClain, J Mol Spect 89, 125 (1981)

B1.71 M Ivanco, J Hager, W Sharfin, S C Wallace, J Chem Phys, 6531 (1983)

B1.72 J A Dyet, M R S McCoustra and J Pfab, Chem Phys Lett, 1987, (in print).

B1.73 M R S McCoustra, J A Dyet and J Pfab, Ann Rep Laser Facility Committee, B1.48. (1986).

B1.74 M R S McCoustra and J Pfab, Chem Phys Lett, 1987, (in print).

B1.75 M R S McCoustra, J A Dyet and J Pfab, Chem Phys Lett, 1987, (in print).

B1.76 R W Jones, R D Bower and P L Houston, J Chem Phys, 76 3339 (1982)

B1.77 J A Dyet, M R S McCoustra and J Pfab, Faraday Discuss. Chem. Soc, 82 (1986) in print.

Editor: J Szechi

B2.1 THE KINETICS AND MECHANISM OF DNA REPAIR: LASER-INDUCED TRAPPING OF BREAKS IN DAMAGED MAMMALIAN DNA.

C W Wharton, Dept of Biochemistry, University of Birmingham

R A Meldrum, S Shall, Dept of Biological Sciences, University of Sussex

The consequences of damage to DNA by ultraviolet or ionising radiation were described in the 1986 Annual Report. The generally accepted scheme of repair of pyrimidine dimers which are formed as a result of uv-irradiation, is shown in Fig B2.1. Our proposed experimental procedure for the study of the early events in DNA repair is shown in Fig B2.2. While the 248 nm laser pulse causes DNA damage in the form of pyrimidine dimers, the 351 nm laser pulse is used to photoactivate the caged α^{32}P-labelled break trapping agent. The photoreleased trapping agent is α-^{32}P dideoxyadenosine triphosphate which acts as a chain terminator in repair DNA synthesis (see 1986 Report).

In this report we describe the progress that has been made towards realisation of the complete experimental scheme that is shown in Fig B2.2.

Laser and Sample presentation

The EMG 150 laser has been used to provide both 248 nm and 351 nm laser irradiation. The oscillator section filled with KrF has been used for damaging the DNA presented in the form of a cellular monolayer ($\sim 10^6$ cells) in a 3.5 cm diameter petre dish. 351 nm radiation has been obtained by filling the amplifier section with XeF. Beam shaping has been rendered relatively simple by fitting a plane mirror at the back of the amplifier which has eliminated the hole in the centre of the beam. The laser beams are simply expanded by using a diverging lens, constrained to a circle by using a diaphragm and turned onto the horizontal target by using appropriately coated mirrors. The energy seen at the target is approximately one third of the total beam energy; this rather low figure being the result of using an initially rectangular beam. Serious problems have been experienced with the stability of the XeF beam. The energy has been found to decrease to half its initial value within 15-30 min after filling the laser. The net result is that some 5-30 mJ of energy can be delivered to the target per pulse. Since we need 1J of 351 nm light in order to achieve optimum photoactivation of the trapping agent (see below) we have to use 30-40 pulses which takes 3-4 seconds to deliver. We hope to be able to achieve some improvement in the laser performance since we wish to be able to achieve photoactivation in less than one second.

It is not difficult to arrange for the 248 nm and 351 nm beams to impinge on a single target position. A sample changer is being constructed at RAL which will allow a number of samples to be irradiated automatically.

Synthesis and photolysis of caged compounds

In the 1986 report we described the synthesis and purification of caged α-^{32}P dideoxyadenosine triphosphate (c-ddATP). This was purified by adding cold carrier c-ddATP and was isolated as 96% caged material. An unfortunate consequence was that the cold material diluted the radioactivity to an extent that led to inconclusive ^{32}P-incorporation in DNA during repair; this despite a very low level of added cold material. It became apparent that it was necessary to prepare the reagent at an enrichment of 5000 Ci/mmole with no added carrier. This was attempted for our next session at RAL.

Tailing of peaks in HPLC elution

The yield of reagent was disappointingly low at 10% but more seriously, severe tailing of peaks occurred on HPLC analysis. The tailing was such that the caged reagent could not be separated from uncaged material. The final product, used for the experiments described below contained 18-35% uncaged material. Although experiments using this material were successful it became obvious that it was necessary to develop a method that would allow preparation of the reagent in much higher yield and most importantly at ca. 100% purity in terms of caging.

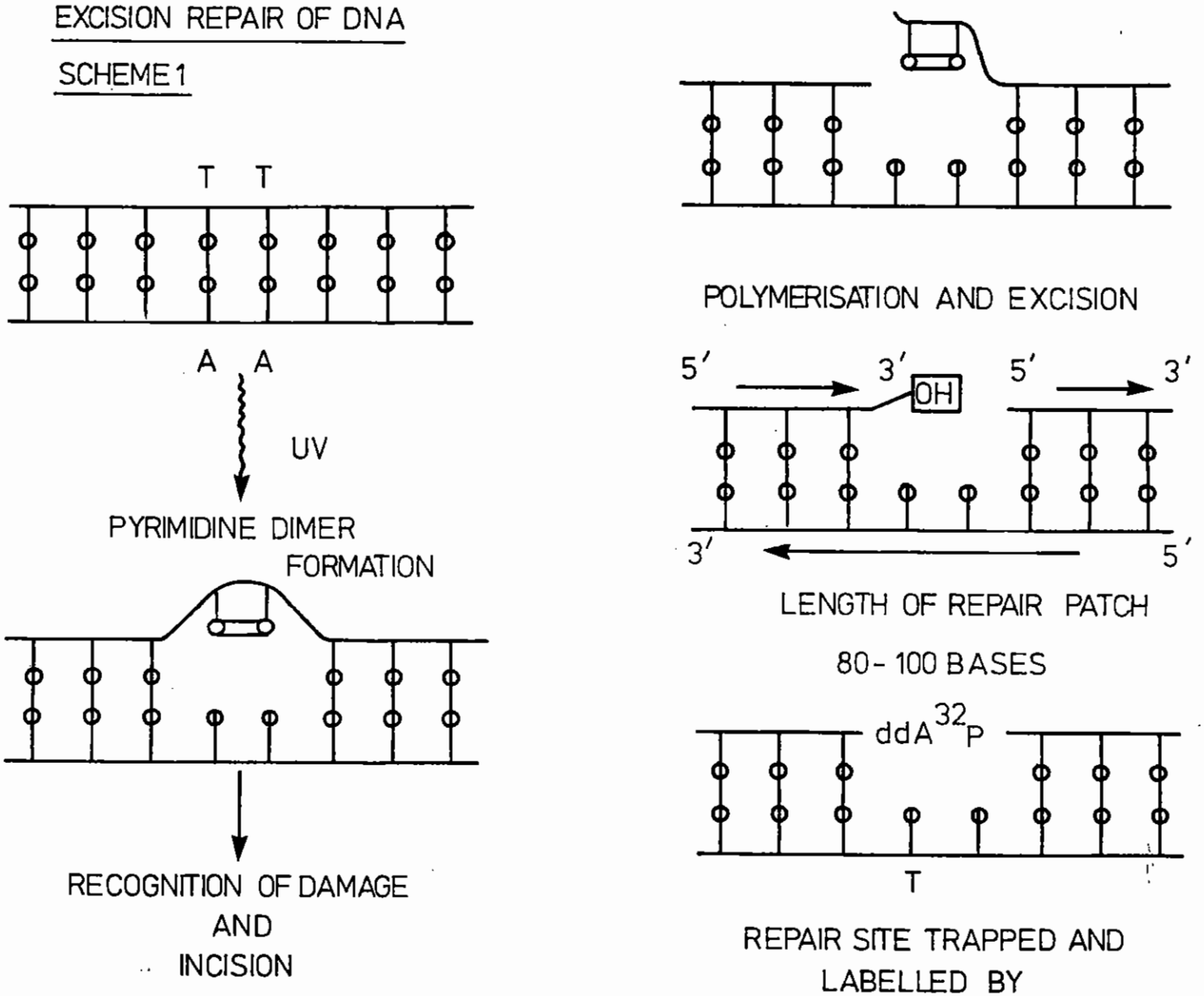

Fig B2.1 General experimental scheme for the study of the (rapid phase) kinetics of the repair of uv-induced pyrimidine dimers in mammalian DNA.

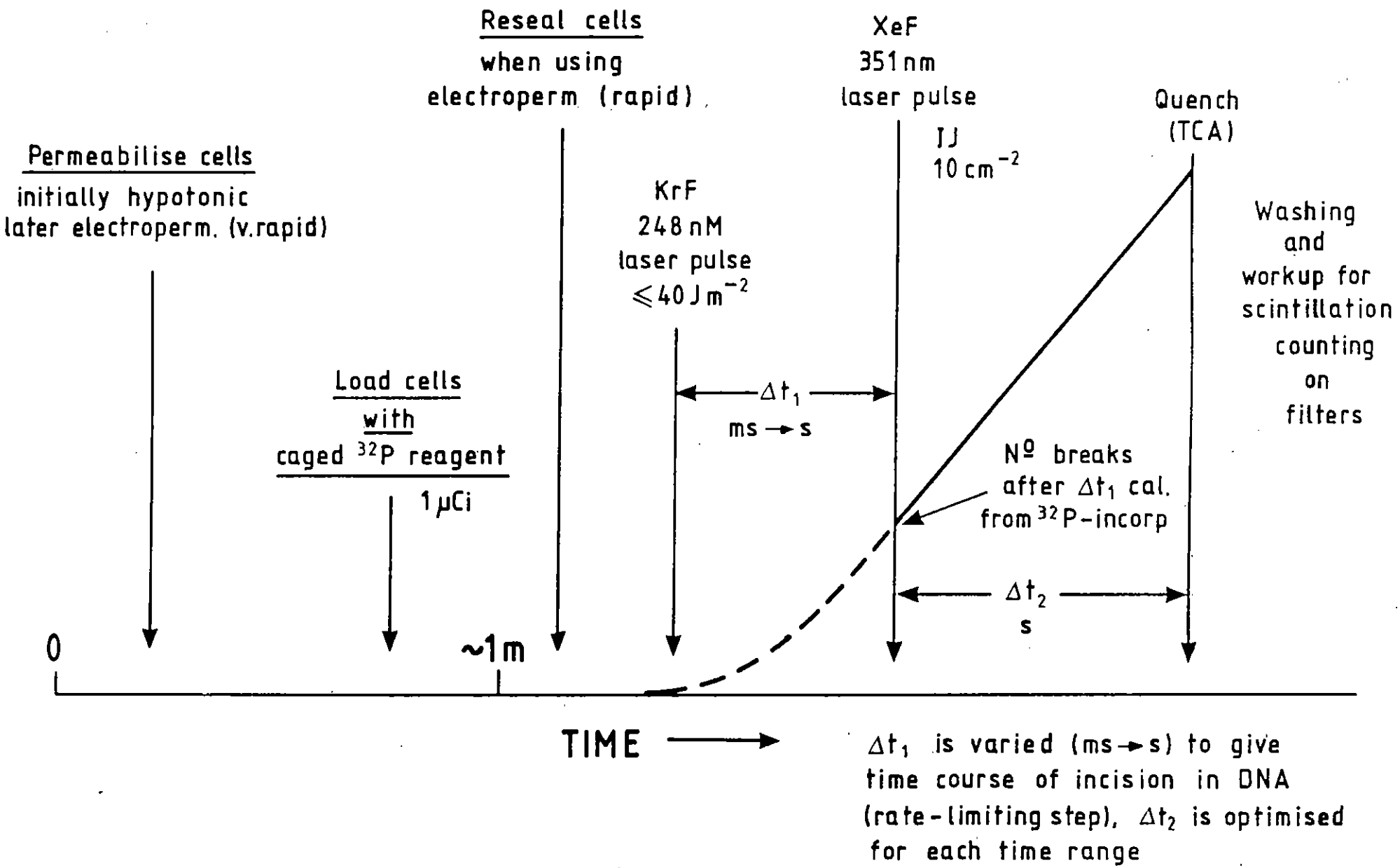

Fig B2.2 Complete experimental scheme.

Use of inorganic phosphate

It is believed that the severe tailing encountered during HPLC elution of radiolabelled material occurs because only picomolar quantities are present. Nonlinear behaviour results when such small amounts of material is used since non-specific absorbtive events assume importance. In an attempt to cure this problem inorganic phosphate was included in the caging reaction mixture. The reaction gave a 40% yield and the presence of caged phosphate in the reaction mixture (5mM) significantly improved the resolution that was obtained by using preparative HPLC. Caged material was obtained at 89% purity but it was contaminated by micromolar caged phosphate. This occurred since caged phosphate elutes just before c-ddATP and there was some overlap of the peaks. The resulting material when used in experiments with cells gave erratic results although high levels of ^{32}P-uptake were seen consequent upon 248 nm damage.

Use of ATP

The next strategy adopted was to use ATP as the buffer in the preparation of caged radiolabelled material. The ATP becomes caged during the reaction and elutes on HPLC between ddATP and c-ddATP, well before the latter. Thus c-ATP should easily be separable from c-ddATP. It was found that some 5% of the ATP hydrolyses during the 24 h reaction period, at pH 4. This leads to the formation of c-ADP which unfortunately elutes coincidentally with c-ddATP and so leads to contamination of the radiolabelled product.

Use of caged ATP

As a final strategy it was resolved to use caged ATP as the reaction buffer, i.e., to put caged ATP in at the start of the reaction. Most fortunately c-ATP has a pK_a value of 3.9 (see Fig B2.3) and so is an ideal buffer for the reaction. It remained to be established whether c-ATP was stable during the 24 h reaction period and if degradation, followed by recaging, could lead to c-ADP formation. c-ATP has been shown to form less than 0.1% c-ADP during a 24h period and so appears to be an ideal buffering material. It will be incorporated in all future reaction systems.

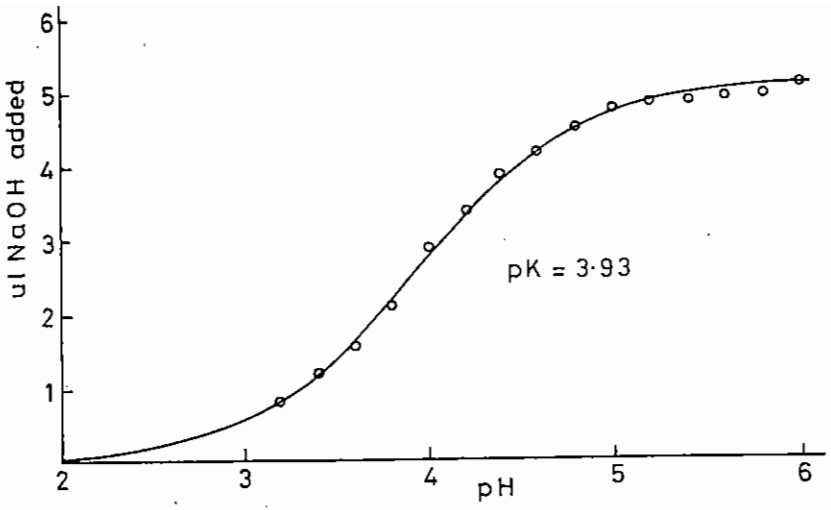

Fig B2.3 *The ph titration of caged adenosine triphosphate*

Caged-ATP was purified and desalted by using HPLC to 98% purity. A 1 ml solution containing 1:25 µmoles was made 0.1M in NaCl and titrated with 5 l aliquots of 50 mM NaOH. A blank titration curve of 0.1M NaCl, determined in the same way, was subtracted. The circles are experimental points, the solid line the best fit line.

Shaken not stirred

The reaction between nucleotide triphosphates (NTP) and the diazonium derivative of 2-nitrophenylethanol has, until recently, been conducted by vigorous stirring of equal volumes of water containing the NTP and chloroform in which the diazonium derivative ws dissolved. Yields (in micromole scale preparations) were ca. 70% and were variable owing to irreproducible stirring conditions. Yields consistently over 90% have been obtained by vigorous shaking of the reagents for 24 h.

Photolysis experiments

Although we had previously established that our caged compounds photolysed quantitatively, there remained some uncertainty regarding

the stoichiometry of the photorelease process. This has now been resolved by using 98% pure full authenticated (by HPLC) c-ATP as a standard of comparison with c-ddATP. The difference spectrum which develops at 310 nm on photoactivation of caged reagents has been used to compare c-ATP with c-ddATP, also free of ddATP contamination. The difference extinction coefficient $\Delta\varepsilon_{310}$ of each compound had been determined by exhaustive photolysis. The numerical values obtained were: 2695± 60 c-ATP and 2705 ± 40 c-ddATP. This proves that the stoichiometry of c-ddATP photorelease is identical to that of the well-studied c-ATP process.

Energy requirement for optimum photolysis

The equation:

$$\frac{Q(1 - T)I_o}{N_o} = \ln\left(\frac{N_o}{N_o - Np}\right)$$

where T = transmittance
Q = quantum yield of photoactivation
N_o = number of photoactivatable molecules
Np = number of photoactivated molecules
I_o = number of photons impinging

has been derived in order to permit calculation of the light energy required to give a certain fraction of photoactivation. For 10^6 cells in a 3.5 diameter dish ca. 34% of the surface is occupied by cells. The quantum yield has been determined to be 60% (see 1986 CLF Report). If 90% photoactivation is to be achieved and the number of caged molecules per cell is 5000 then 1.4×10^{18} photons are required which is equivalent to 0.82 J at 351 nm. Accordingly we have used 1J in order to ensure nearly quantitative photoactivation. The absorbance at 351 nm was measured using cold material and calculation gave a value of 4×10^{-8} for the fraction of light absorbed in an experiment using 10 µCi of α-^{32}P caged-ddATP.

Stability of caged compounds in cells

Py 3T3 cells have been incubated with caged α-^{32}P ddATP. The incubation medium was analysed over a period of time for caged and uncaged material. Fig B2.4 shows that very little decomposition occurs within 60 min although after 18 h extensive decomposition has occurred. This is an important finding since it means that a time gap between permeabilisation/loading of the cells with caged reagent and firing of the 248 nm laser will not lead to complications which result from reagent decomposition. It is notable that cellular phosphodiesterase enzymes are not able to rapidly degrade the caged molecule and this finding adds to the robustness of the method. Permeabilisation and/or lysis of the cells made no difference to the pattern observed in Fig B2.4. Dilution of the radioactive material also did not affect the pattern seen in Fig B2.4 despite causing lysis of the cells after 15 min.

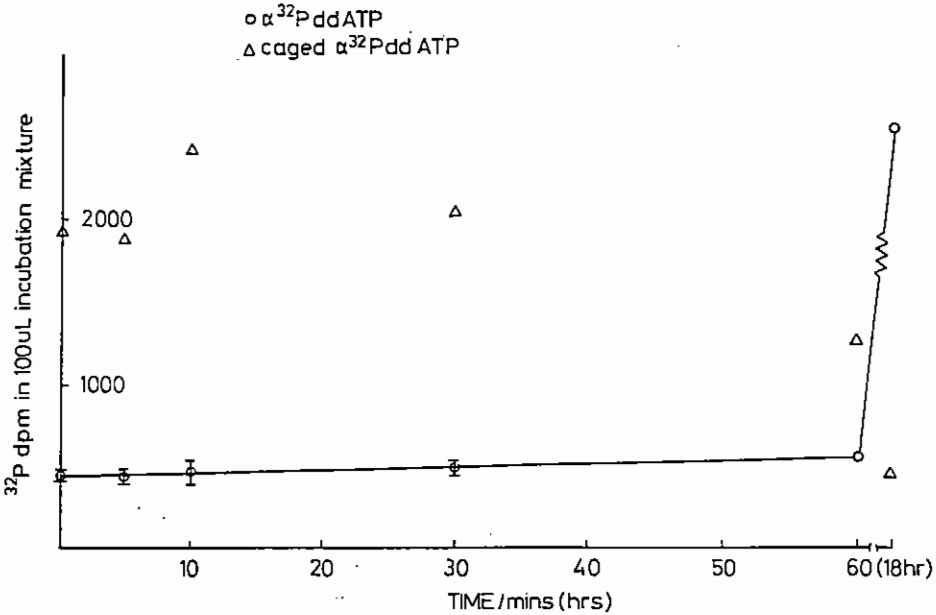

Fig B2.4 *Stability of caged dideoxyadenosine triphosphate in the presence of Py 3T3 cells.*

10^6 cells in 5 ml phosphate buffered saline were incubated for the times shown in the Fig. Samples were frozen and stored until analysed by HPLC. Elution with 25% MeOH: 10 mM phosphate pH 5.5 using a C-18 column allowed caged and uncaged materials to be measured quantitatively by integration of A_{260}. 83% of ^{32}P-labelled material was caged at time zero.

Validation of technique

Since writing the last report unequivocal results achieved in a crucial experiment finally confirmed that the technique was fully applicable to DNA repair studies in mammalian cells. This had been anticipated by results of previous experiments which had showed this by less direct means.

Py 3T3 transformed fibroblasts were loaded with caged ^{32}P-ddATP after permeabilising the cells with hypotonic solution. Cells were damaged by 248 nm UV irradiation before permeabilisation and loading with caged reagent. Fig B2.5 shows the results obtained when cells loaded with radiolabelled reagent were subjected to 248 nm and/or 351 nm irradiation. This result was obtained with reagent that was only 75% caged. Uptake of ^{32}P unirradiated permeabilised cells would be due to incorporation of the contaminating uncaged reagent by DNA replication synthesis. Uptake of the free agent was increased by about 40% in cells which had been damaged by 248 nm UV. When caged reagent was photoactivated by 351 nm irradiation, uptake due to DNA replication synthesis reached saturation level. This was 50% higher than the uptake in cells in which the 'caged' reagent was not photoactivated.

When repair synthesis was promoted by 248 nm UV irradiation and optimum uptake of ^{32}P-ddATP allowed by photoactivation of the caged compound by 351 nm irradiation, the ^{32}P incorporation increased four-fold over that of undamaged cells in which the caged reagent was not activated and three-fold over that of damaged cells with unactivated caged reagent. Since ca. 80% of caged compound was predicted (see above) to be released by the 1 Joule of 351 nm that was applied the three-fold enhancement of uptake approximately corresponds to the proportional increase of ^{32}P-ddATP made available by photoactivation.

The increase in uptake by DNA replication synthesis in undamaged cells with maximally activated reagent present, over undamaged cells with unactivated agent present, is not as proportionately great as the additional ^{32}P-ddATP made available for incorporation of photoactivation. It would seem, therefore, that uptake due to DNA

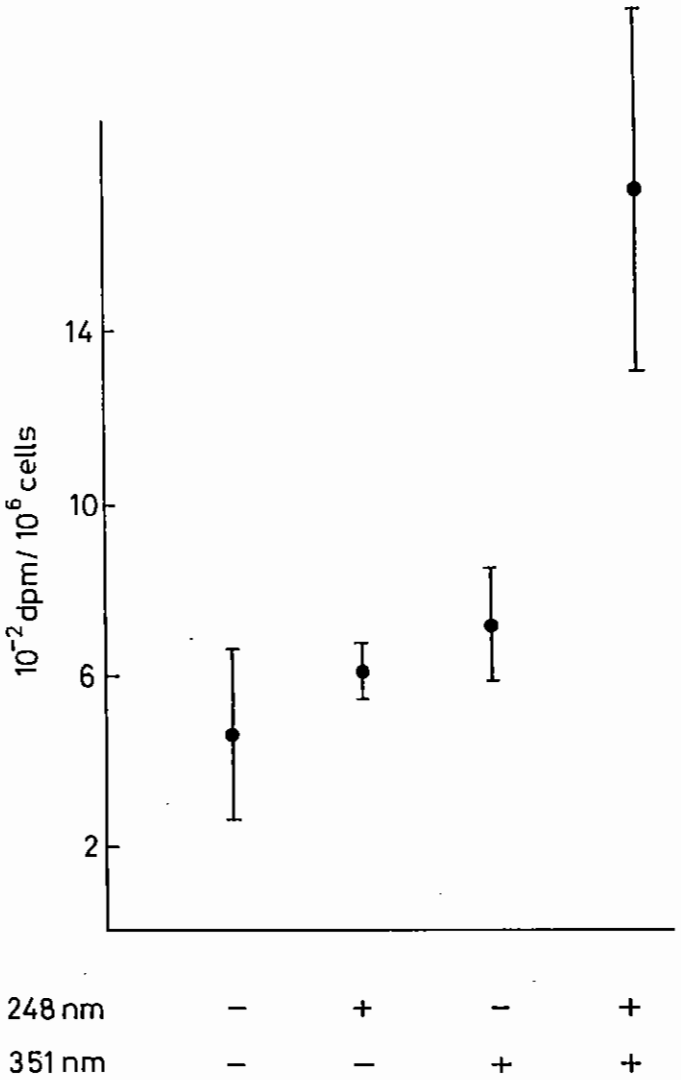

Fig B2.5 Incorporation of 351 nm-photoreleased α^{32}P dideoxyadenosine triphosphate into 248 nm-damaged DNA of mammalian cells. 10^6 cells in 3.5 cm dia. petri dishes were irradiated with 40 J M^{-2} 248 nm light. Cells were permeabilised, caged α-^{32}P-ddATP was added (0.4 μCi per dish) and the cells were irradiated with 1KJ/m^{-2} 351 nm radiation. After 15 min 1 ml TCA (10%) was added, the cells were removed from the dishes and collected on glass fibre filters. After thorough washing with TCA and ethanol, the filters were dried and scintillation counting was used to determine ^{32}P retained on the filters.

replication synthesis is saturated by added concentration of caged ^{32}P-ddATP (68 fmoles). However, when breaks are induced by 40 Jm^{-2} of 248 nm UV, the proportional increase in uptake approximately matches that of the reagent made available for incorporation by photoactivation. This suggests that at this level of damage, saturation of breaks present is not achieved by a concentration of ca. 58 fmole of ^{32}P-ddATP.

In an experiment performed on Py 3T3 cells in which DNA replication synthesis was arrested due to confluence of the cells a ten-fold enhancement of ^{32}P-ddATP uptake was seen consequent upon 248 nm irradiation. This indicates that when 100% caged material is photoactivated in cells in which DNA replication synthesis is minimal, at least a ten-fold enhancement of uptake should be observed upon stimulation of repair synthesis. An enhancement of at least ten-fold incorporation produced by stimulation of DNA repair synthesis will allow good resolution in kinetic studies.

Introduction of caged reagent into cells by permeabilisation

During our most recent session at RAL, aspects of our preliminary experiments which do not strictly conform to the procedures described in the general scheme (Fig B2.2) were examined. The results confirmed that practical concessions which were made in preliminary experiments, will not influence measurements obtained when the procedure is followed precisely.

It is required to make cells permeable to the caged dideoxynucleotide molecule since normally such a molecule cannot cross the cell membrane because of its negative charge.

Cells were permeabilised before and after damage so that the caged trapping reagent was present or absent during 248 nm damage. Incorporation did not differ in cells where the caged reagent was present during 248 nm damage from that in cells where it was absent during damage. The fact, therefore, that our results were obtained using the variation of 248 nm damage before addition of caged reaction in the preliminary experiments, does not influence our conclusion that, if the caged reagent is present during damage, as in Fig B2.2, it will yield appropriate results.

Up till now we have used hypotonic buffer to permeabilise cells to introduce the caged molecule, but when apparatus is built we intend to use electropermeabilisation. The time course of this is much more advantageous to our break trapping technique since permeabilisation may be achieved in milliseconds and resealing of cells is effective. A recent pulication describes electropermeabilisation as more consistently effective with different cell types (Ref B2.1). In our experiments hypotonic permeabilisation was very effecive on Py 3T3 transformed fibroblasts and HL60 leukaemia cells. It fully permeabilised these cells in less than ten minutes. However, hypotonic permeabilisation was less effective in AA8 and 3T3 non-transformed fibroblasts, a significant proportion of the cells remaining unpermeabilised after 20 minutes in the buffer. Resealing by addition of isotonic solution is not optimal in any cell type.

Although permeabilisation of AA8 cells was not as good as in Py 3T3 cells, results which were qualitatively similar to those obtained with Py 3T3 cells, were achieved when the main features of the break trapping method were tested on AA8 cells.

Saturation of DNA breaks by photo-activated caged dideoxynucleotide

Experiments on which different concentrations of caged reagent were added to the cells in permeabilisation solution produced results which gave a positive linear relation of uptake ^{32}P with increasing concentrations of caged reagent. However, since a plateau was not reached a saturating concentration in terms of break trapping appears not to occur in this concentration range when using hypotonic buffer permeabilisation. The saturating concentration of break trapping reagent will depend upon the diffusional access of the reagent to the cell DNA. This will have to be assessed for any permeabilisation method used.

The experiment was mimicked by adding one concentration of caged ^{32}P-ddATP to the cells in permeabilisation buffer, then applying different doses of 351 nm UV to release the ^{32}P-ddATP for incorporation into DNA. Since the photoactivation of the caged molecule is a first order process the proportion of agent released

for incorporation is directly related to the dose of 351 nm UV when applied at levels well below that for optimum photoactivation. As the dose of 351 nm UV was increased, the incorporation of ^{32}P increased, but a saturation plateau was not reached by this method either.

B2.2 INVESTIGATION OF FAST ABSORBANCE CHANGES IN PHOTOSYSTEM I

E H Evans, R Sparrow, L Tramontini and R G Brown (Lancashire Polytechnic, Preston, Lancs).

M J C Smith and W T Toner (RAL).

Introduction

Recently, attempts have been made to probe the energy transfer of Chlorophylla bound to Photosystem I (PSI) and to discriminate between absorbance changes due to chlorophyll in an excited state and those due to reversible oxidation of the reaction centre chlorophyll, P700. (Refs B2.2, B2.3). In the last Annual Report (Ref B2.4) we reported the development of a flash spectrometer which enabled us to measure a fast absorbance change at 705 nm in PSI preparations excited by a 5 ps laser pulse. The experiment was performed by using the pump-probe technique exciting the sample with the pump at 585 nm, and splitting the beam to provide a probe at 705nm by Raman shifting that part of the beam through ethanol. This technique limited our capacity to analyse the data by restricting the wavelength of the probe, so we have now eliminated the Raman Shifter and replaced it with a cell containing water, enabling the generation of a continuum which is subsequently monochromated by using interference filters.

Results and Conclusions

All experiments were performed using a PS1 preparation from the cyanobacterium Chlorogloea fritschii as previously described (Ref B2.4). Figure B2.6 shows the wavelength dependency of the transient absorbance change measured 8 ± 3 ps. after excitation, between 680 nm and 720 nm, measuring at 10 nm intervals and at 705 nm. It is clear that there are two maxima, at 690 nm and at 705 nm.
Figure B2.7 shows the time course of the absorption transients measured at 680 nm and 705 nm. The transient at 705 nm is similar to our earlier report, rising within 20 ps and decaying to 50% of the original extent at ∿ 40 ps. The absorption change at 680 nm, however, rises extremely quickly, over a timescale that we we have, as yet, been unable to resolve. This absorbance change at 680 nm is reversible within the timescale of the rise of the 705 nm transient. We have performed some preliminary measurements on the pump intensity dependence of these transients which suggests that the 705 nm transient saturates at lower intensity than that at 680 nm. These results would be consistent with the absorbance change at 680 nm arising from excitation of accessory chlorophylls which, subsequently, transfer energy to P700, to which we attribute the absorbance change at 705 nm. A similar interpretation has been made by Giorgi et al (Ref B2.3) of their data. Support for the assignment of a rapid (approx. 15 ps) energy transfer time between Chl* and P700 is gained by our measurement of the chlorophyll fluorescence decay time of these PS1 preparations, which, when fitted by these exponential components, has a fast decay component τ_1 = 16-33 ps (Ref B2.5).

We are continuing with our investigations of the pump dependency of the absorption changes over the wavelength range 680-720 nm. Some early data suggested that an additional component appeared at 700 nm at high pump intensities, and the interpretation above may be very oversimplistic.

B2.3 A PRELIMINARY INVESTIGATION OF POSSIBLE OPHTHALMOLOGICAL USES OF AN EXCIMER LASER

M N R Ashfold, S J Moss and J E A Hoare Nairne (University of Bristol)

Introduction

There is much current interest in the possible use of excimer lasers as a means of cutting and shaping corneal tissue [Refs B2.6, B2.7 and B2.8]. A number of recent studies have demonstrated the particular potential of the ArF laser output (λ = 193 nm) for this kind of

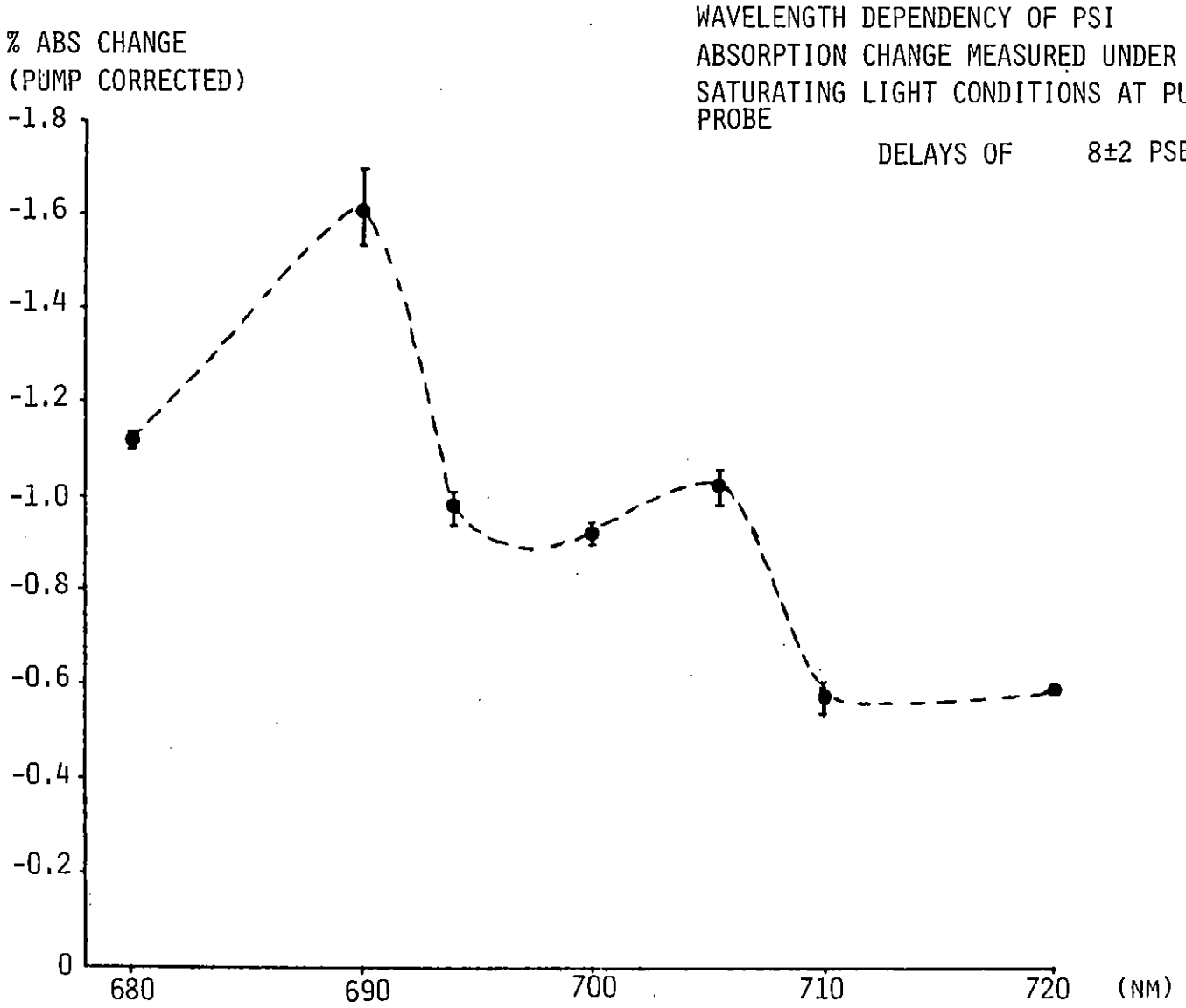

Fig B2.6 Wavelength dependancy of PS1 absorption change measured 8 ± 3 ps after excitation.
26 g cm³ Chl a in 0.06 M Tris HCl, 0.03 M EDTA pH 7.8.

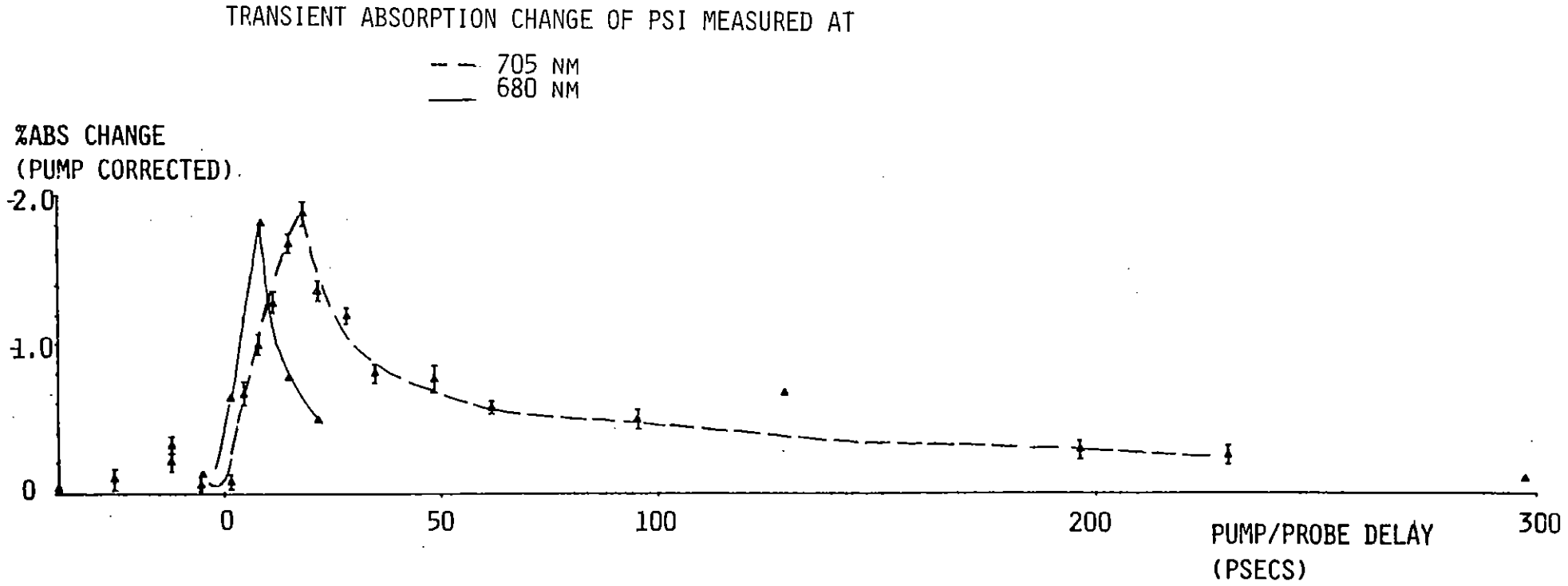

Fig B2.7 Transient absorption change of PS1 at 680 nm and 705 nm. Conditions as Fig.B2.6.

refractive modification. Photoablation appears to be the dominant tissue removal mechanism at this short excitation wavelength; investigations to date suggest that the effect is localised almost exclusively within the irradiated region, with very little thermal damage to adjacent structures. Hence the possible appeal to ophthalmologists.

Materials and Methods

The objective of these preliminary experiments (carried out during part of one Division Heads Week in July 1986) was to acquire some first hand knowledge of the process of corneal photoablation and any attendant difficulties. All experiments were conducted using fresh bovine cadaver eyes, and an EMG 150 laser (amplifier only, not line narrowed) operating on the ArF transition at a repetition rate of 5Hz. With a fresh gas fill this provided pulse energies ≤60 mJ. The output was arranged to be incident on the cornea after passage through either (i) a 8 mm x 1 mm vertical slot, (ii) an adjustable iris diaphragm or (iii) a cylindrical lens. The laser output was attenuated for the latter studies, in which the eye was positioned such that its front surface was at the laser focus (at which point the beam had imaged to a rectilinear stripe ∿15 mm x 1 mm. For each experimental arrangement the parameters investigated were (i) the number of laser pulses and (ii) the effect of pulse energy. A total of ∿50 series of exposures were made on 30 eyes.

Immediately after irradiation the corneal tissue was removed surgically and fixed in 2.5% glutaraldehyde. The specimens were then transported to the Bristol Eye Hospital for subsequent investigation by scanning electron microscopy (SEM). Further samples were placed in formalin for subsequent evaluation by light microscopy.

Results

Quantitative measurements were hindered by the large shot to shot variation in energy and beam quality of the laser output. Nevertheless the results of these preliminary studies provide support for previous finding (Ref B2.6) that:

(i) there is a threshold energy below which no detectable

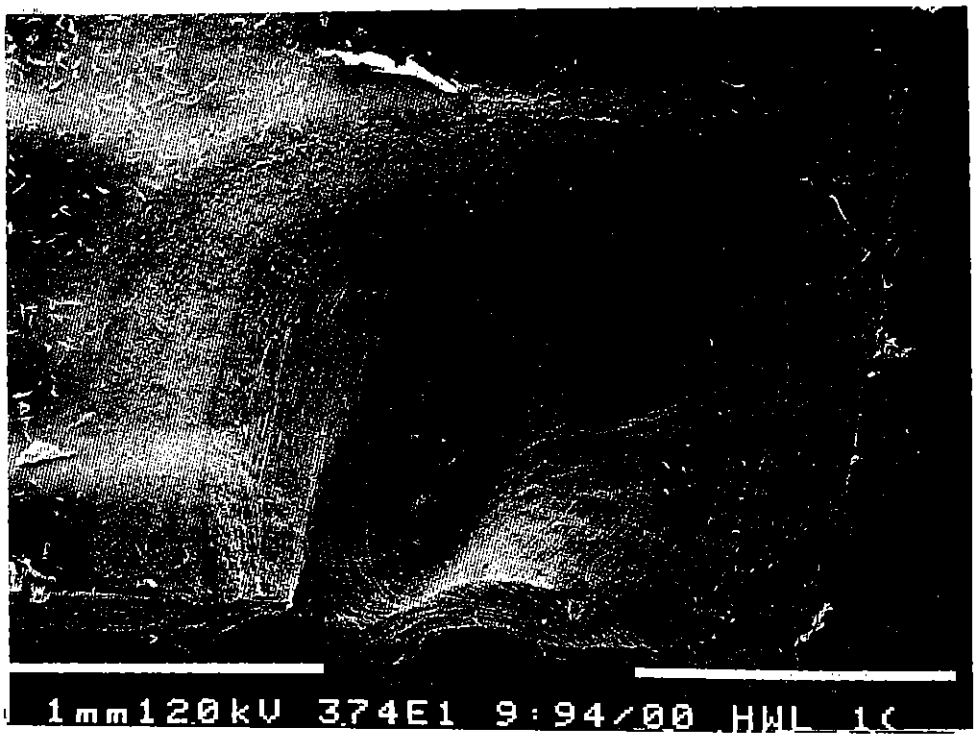

Fig B2.8 Bovine cornea viewed from epithelial surface after 3½ minutes exposure to unfocussed 193 nm radiation (5 Hz repetition frequency) using a progressively reducing iris diaphragm in the delivery system.

photoablation occurs. Without any means of varying the laser pulse duration it was not possible to establish whether laser fluence (J cm^{-2}) or intensity (W cm^{-2}) was more important in controlling this threshold.

(ii) above this threshold the depth of tissue removed scaled with the pulse energy and with the number of laser shots, and

(iii) with the slot mask and with the focussed beam the cut was always 'V shaped', i.e., deeper at the centre of the cornea (where the beam was perpendicular to the corneal plane) than at the periphery. The edges of the incision were clean and smooth but SEM showed the surrounding surface to be really quite irregular, presumably owing to the presence of particulate matter interfering with the beam. Diffraction effects were clearly evident with the mask experiments and a lesson from these studies is that, if a mask must be used, it should be placed as close as possible to the sample. Endothelial damage was evident when the photoablation depth approached Descemet's membrane.

Conclusions

193 nm radiation does photoablate corneal tissue, but its utilisation in surgical procedures will require a lot more research, especially with regard to an efficient and versatile design for the optical delivery system. DNA damage and potential mutagenesis are real worries when using such short wavelengths, and further study of the effects of uv radiation on corneal epithelium, stromal keratocytes and the endothelium will be needed if the excimer laser is to feature as a standard ophthalmological tool.

B2.4 PROTEIN FLUORESCENCE LIFETIME MEASUREMENTS USING THE STREAK CAMERA-OMA SYSTEM IN SYNCHROSCAN MODE

K J Willis and D Phillips (The Royal Institution, London)
P Bayley (National Institute for Medical Research, London)

1. Configuration

A schematic diagram of the apparatus is given in Figure B2.9. The

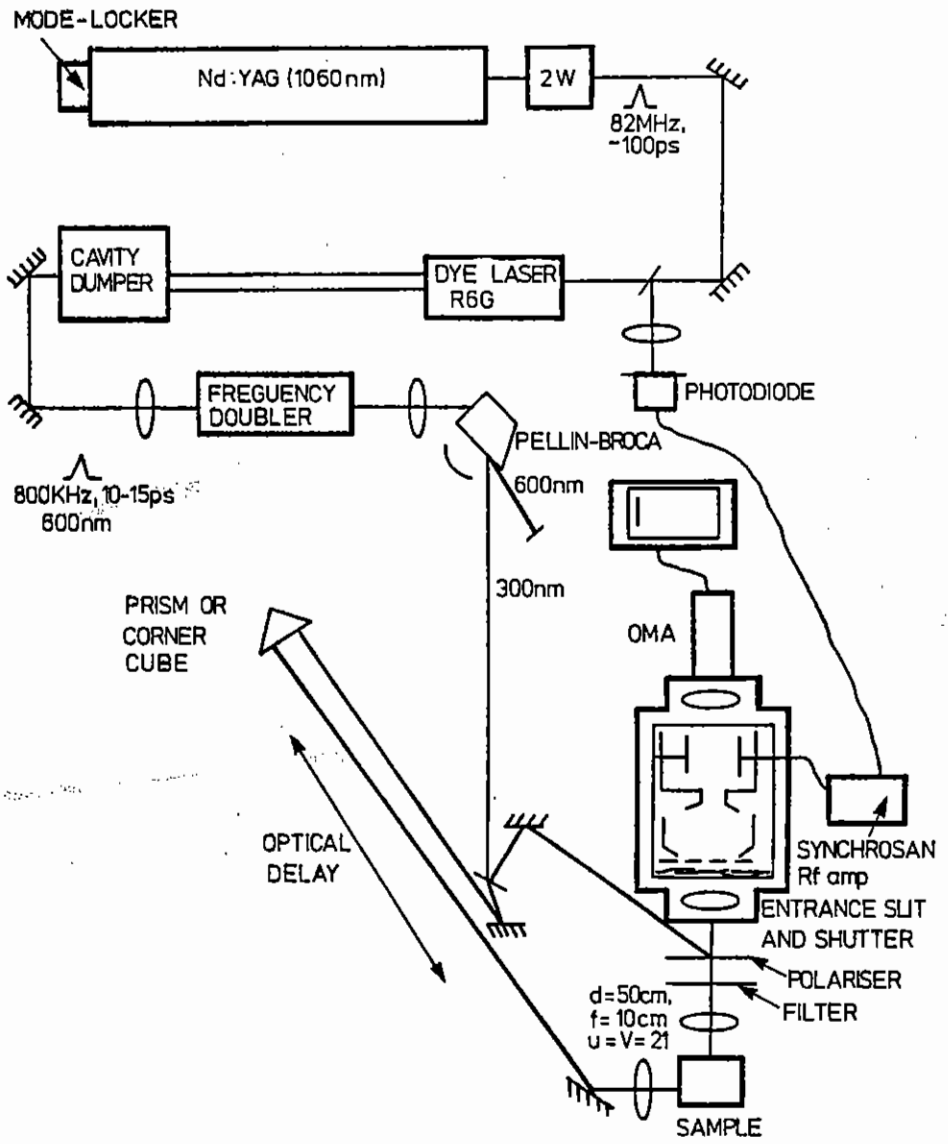

Fig B2.9 Experimental layout.

laser pulse train had a repetition frequency of 800 KHz with a pulse width of 10-15 ps tuned to 600 nm. This was frequency doubled to 300 nm and the UV or visible beams were selected by a pellin-broca prism and passed into the sample via an optical delay. Part of the selected beam bypassed the delay to provide a 'time marker'.

The streak camera was operated on the 'focus' setting (ie no DC plate deflection) with the intensifier and fibre optic coupler removed. The streak image was monitored using an optical multichannel analyser (OMA). Part of the 530 nm second harmonic beam from the Nd:YAG sampled by a vacuum photodiode served as a reference signal (100 - 150 mV) for the synchroscan Rf amp, the output from which (82 MHz, 4W) was applied to the streak plates via an LCR circuit.

2. Performance

With the synchroscan off, the narrowest practicable slit gave an image with a FWHM of 9 channels (scattered laser pulse, 600 nm, 10 ps). This increased to 13 channels when the synchroscan Rf was appled (Rf power at the maximum 4W limited by breakdown in the tube). This corresponds to a time resolution of $\sim$ 60ps, FWHM at 4.6 ps/ch (see later). The broadening due to synchroscan, presumably mainly electronics jitter is therefore $\sim (13^2-9^2)^{1/2} \times 4.6 = 43$ ps FWHM and is similar to that observed by others for operation of the camera in multiple shot mode (trigger jitter). However, if the optical or electronic delay is altered so that the laser pulse does not arrive at the mid-point of the voltage ramp the time resolution decreases ie the FWHM of the image increases. Since the voltage ramp is linear across the time window observable on the OMA (see below) the resolution loss is presumably due to deficiencies in the streak tube/detector coupling optics.

The instrument was calibrated by means of a variable optical delay. The controller was set to record a large number of scans and the optical delay was adjusted in known steps to move the position of the scattered laser pulse image across the screen, resulting in a comb like display (Fig B2.10).

The increase in optical path length (30 cm in air = 2.001 ns) was then plotted against the position of the laser pulse image (in

Fig B2.10

channels). A typical result at two synchroscan Rf powers is shown in Figure B2.11. At the maximum Rf power (4W) the linearity is good, corresponding typically to 4.6 ps/ch. This method of stepping (manually) an optical delay was slow but more effective than other time calibration methods attempted which were based on interferometers and etalons. It was found that there was a drift in the synchroscan ie the laser pulse image moved slowly across the screen in one direction at a rate of $\sim$ 1.3 channels per minute. This is a serious problem as it increases the time resolution and distorts the profile when long data collection times are required. The origin of this asynchrony between the laser pulse and voltage sweep was not established. The variations in the sensitivity of the detection system across the streak image was determined by allowing room light to enter the camera with the synchroscan on. This resulted in a reasonably flat trace and subsequent decays were divided by this profile. Clearly it would be desirable to develop an intensity calibrator at the sample emission wavelength.

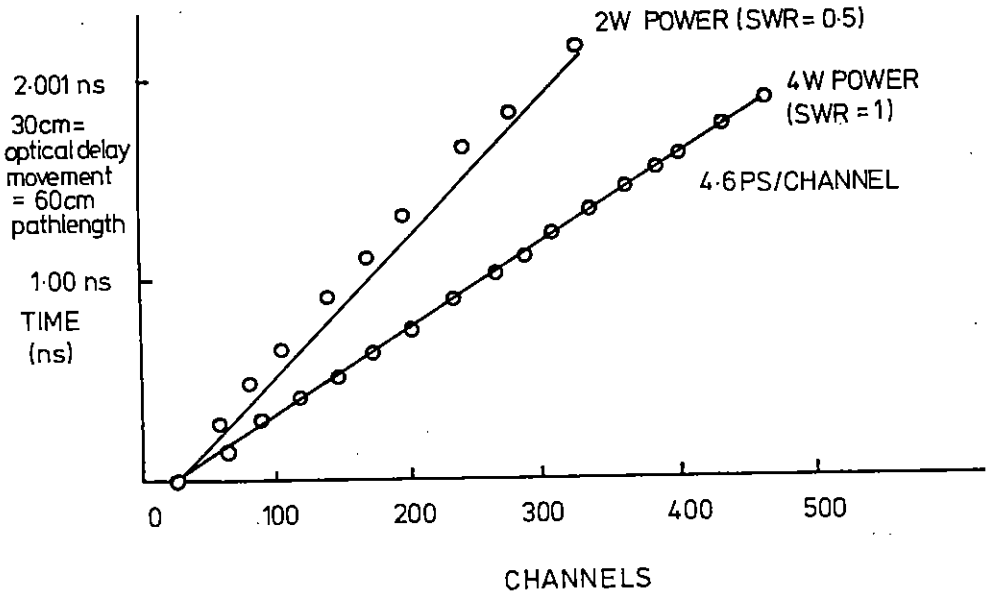

Fig B2.11 Time Calibration.

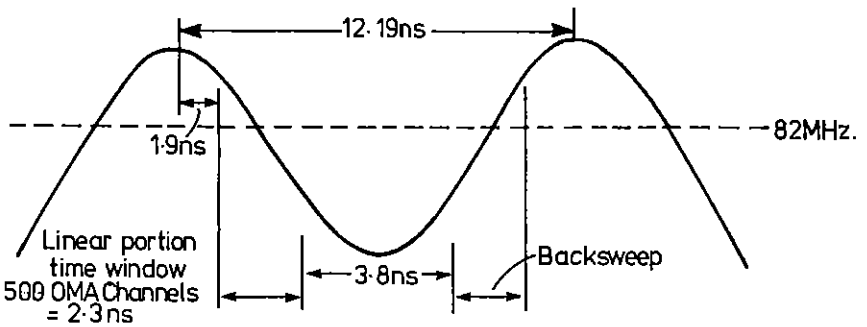

Fig B2.12 Time window.

3. Time Window

The 82 MHz sinusoidal voltage applied to the streak tube deflection plates limits the time window and produces fold back problems.

If the excitation pulse is timed to arrive at the start of the time window (ie the start of the approximately linear portion of the sinusoidal deflection voltage channel 1) any fluorescence intensity which has not decayed after ∿ 6.1 ns will be folded back onto the initial decay profile by the reverse sweep, distorting the decay profile. A compound with a fluorescence lifetime of 1.3 ns decays to 1% of its initial intensity in 6.1 ns. Most protein samples have fluorescence lifetime components ≥ 1.3 ns).

4. Detection Sensitivity

Without a monochromator, filters or polarisers between the sample and detector the fluorescence of the scintillant PPO (in cyclohexane, ex 300 nm, optical density 0.1, quantum yield ∿ 0.9) could be recorded with difficulty . With the protein lysozyme at 0.1 mg/ml it was virtually impossible.

A suitable image intensifier was not available for the streak camera at the time this work was done.

B2.5 UV-RESONANCE RAMAN SPECTROSCOPY OF GLYCERALDEHYDE-3-PHOSPHATE USING A DIODE ARRAY DETECTOR

R A Chittock and C W Wharton, Department of Biochemistry, University of Birmingham,
R E Hester, Department of Chemistry, University of York

Introduction

We have been studying the reaction mechanism of the enzyme glyceraldehyde-3-phosphate dehydrogenase (GAPDH), which catalyses the

conversion of glyceraldehyde-3-phosphate (GAP) to 1,3-diphosphoglycerate (DPG) in three stages. First the thiol group at the enzyme active site attacks the 2-carbon of GAP to form a hemi-thio acetal. This is oxidized in the second stage to a thioester with corresponding reduction from NAD to NADH. In the third stage, a nucleophile, such as phosphate attacks this thioester to liberate DPG and regenerate the active site thiol. If the reaction is performed at pH 6.0 in the absence of nucleophiles the reaction will stop after a single turnover, with the enzyme active site acylated by a thioester bond (Ref B2.9).

Model compounds of thioesters have an absorbance maximum in the region of 235nm. This work aims to obtain a resonance enhanced Raman signal from this thioester bond. From this deductions can be made regarding the thermodynamics of the reaction mechanism, in particular the degree of hydrogen bond interaction of the ester bond carbonyl oxygen with the enzyme. Such an interaction, enhanced in the transition state, is proposed to represent an important aspect of rate enhancement by the enzyme.

We have used several laser systems during the past year at the LSF. Most work has been performed using the Lambda Physik EMG 150 excimer laser with a KrF gas fill to produce line-narrowed 248nm laser light. We have also used frequency doubled and frequency mixed dye lasers in an attempt to excite nearer to the thioester peak absorbance.

Line-Narrowed Excimer Laser

Fig B2.14a shows a resonance Raman spectrum obtained from acyl GAPDH. This was formed by mixing enzyme + NAD with GAP in a continuous flow apparatus a few seconds before presentation to the laser. This apparatus was identical to that used to obtain a resonance Raman spectrum of acyl papain (Ref B2.10). The spectrum was recorded using the Spex Triple Mate spectrophotometer equipped with the optical simultaneous multichannel analysis (OSMA) diode array detector. All spectra shown are the smoothed sum of six 200 second accumulations.

The acyl GAPDH spectrum peaks at 1336cm^{-1} and 1484cm^{-1} arise from the adenine ring of NAD, which has a strong absorbance peak centred at

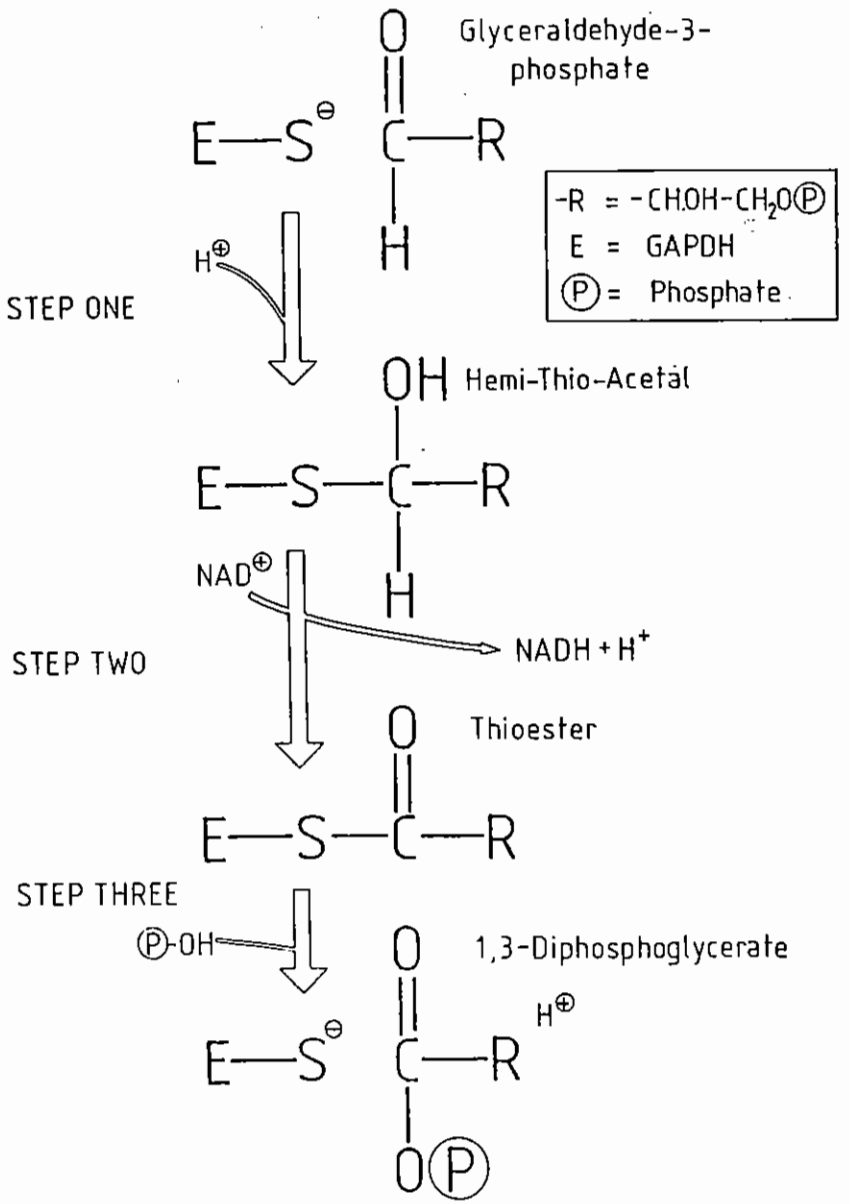

Fig B2.13 Simplified reaction mechanism of GAPDH. At pH6.0 in the absence of phosphate the reaction stops at the thioester stage. Since thiol esters absorb around 235 nm, and acyl enzyme band can be seen in the resonance Raman spectrum from 248 nm wavelength light.

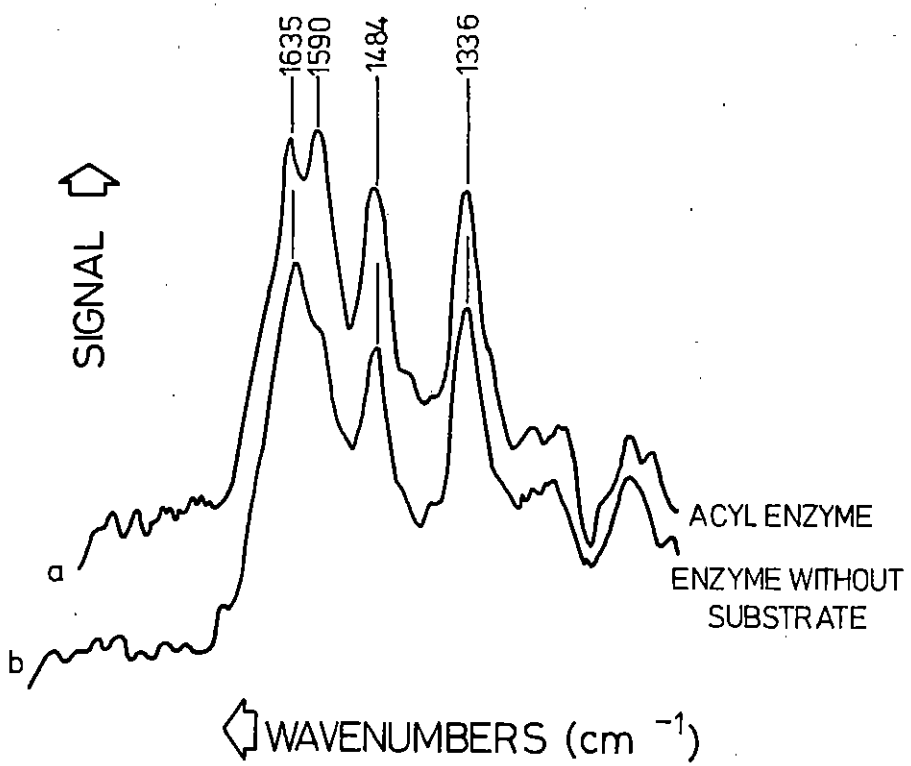

Fig B2.14 Resonance Raman spectrum of GAPDH (4mg/ml) + NAD (350 μm) at pH6.0, (a) with substrate, (b) without substrate. Bands at 1336 cm^{-1} and 1491 cm^{-1} arise from NAD. Band at 1635 cm^{-1} arises from the amide I band. Extra peak in (a) at 1590 cm^{-1} arises from the thioester band. Each spectrum is the total of 6 runs consisting of 5 sequential scans comprising 25 exposures of the diode array.

260nm. The peak at 1635cm^{-1} is the protein amide I band. The peak at 1590cm^{-1} does not appear in the spectrum of GAPDH + NAD in the absence of GAP (Fig B2.14b). This could arise from the acyl enzyme or the NADH formed in the single turnover of the reaction. The resonance Raman spectrum of NADH (Fig B2.15a) does have a feature at 1583cm^{-1} which might account for this extra peak. However this feature is also present in the resonance Raman spectrum of NAD (Fig B2.15b), present in excess in both enzyme preparations, and can be seen as a weak feature amidst the amide I band in the 'enzyme without substrate' spectrum. For these reasons we believe that the band at 1590 cm^{-1} arises from the thioester bond of the acyl enzyme. We hope to be able to confirm this with future experiments in the coming year.

We have previously located the acyl enzyme peak at 1633cm^{-1}, but this experiment was performed prior to the realignment of the Triple Mate and made use of the old OMA diode array detector so was consequently of inferior quality. We have found the appearance of a new peak at 1590cm^{-1} to be repeatable and so believe it to be the true result.

Resonance Raman spectra of model thioesters in free solution show a peak in the resonance Raman spectrum in the region of 1670cm^{-1}. Our observation of the acyl enzyme thioester at 1590cm^{-1} indicates an extremely large stabilization of the acyl enzyme intermediate, much greater than that observed in the thiol protease papain (Ref B2.10). This can be explained by the specific nature of GAPDH, which acts on a single set of substrates and can thus interact strongly and specifically with them to give maximum catalytic action. Papain works on a wide range of protein molecules, so its active site substrate interactions are weaker in order to accommodate a wider range of substrates.

GAPDH can be prepared with or without NAD bound. We have performed experiments to compare the resonance Raman spectra of the two forms using the EMG 150. We hope to be able to improve the quality of these spectra by using 260nm wavelength light from a frequency doubled excimer-pumped dye laser to excite nearer the peak absorbance of NAD.

Dye Lasers

We have made two attempts to obtain data using an exciting wavelength

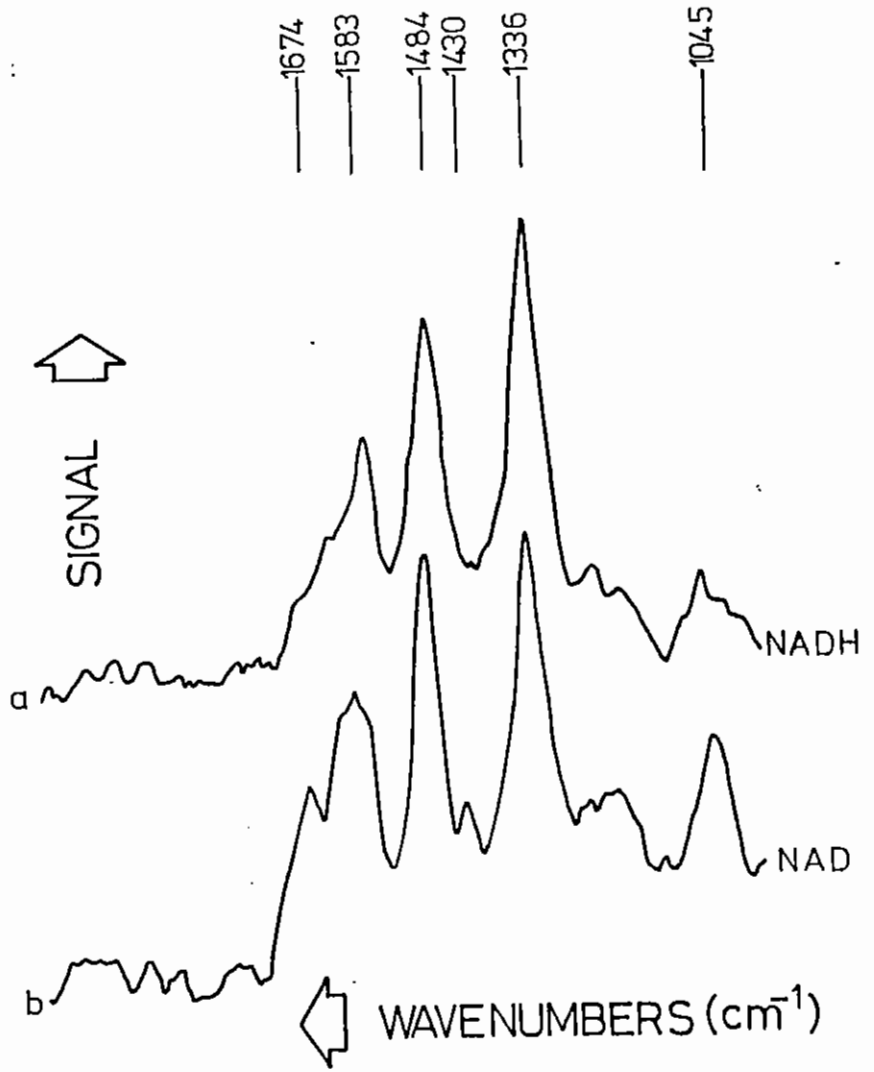

Fig B2.15 Resonance Raman spectra of (a) 350 μM NADH and (b) 350 μM NAD. Each spectrum is the total of 6 runs consisting of 5 sequential scans comprising 25 exposures of the diode array.

nearer the absorbance maximum of the thioester absorbance band.

The first system used was the JK/ Spectra Physics Wavelength Extender, which mixed the near IR fundamental from a Nd-YAG laser with the UV output from a frequency doubled YAG-pumped dye laser to generate light at 235 nm. Despite sterling efforts by the LSF staff this system would not provide more than 0.1mJ/pulse at this wavelength, insufficient for even an ethanol spectrum to be observed.

The second system tried was the HX460/ FL3002 excimer-pumped dye laser with a urea frequency doubling crystal, to produce light at 239nm. It was found that at the dye laser energies required to obtain useful energy at 239 nm the urea crystal sustained damage, and so was unsuited for this work.

At present we have yet to obtain a protein spectrum using light of a wavelength less than 248nm.

We have also used the excimer pumped dye laser to obtain resonance Raman spectra of NAD,NADH and ADP. This work has confirmed that the three main features of the NAD(H) spectrum arise from the adenine part of the molecule, since they are also present in ADP. We hope to be able to repeat this work using 260 nm wavelength light, which will give better resonance enhancement.

Conclusions

In summary it is clear from the foregoing that reasonable progress has been made during the past year. An important factor is the very significant improvements that have been achieved recently in all aspects of the performance of the Raman apparatus. We look forward to relatively routine acquisition of high quality resonance Raman spectra of the demanding systems we have chosen to study.

Editor: W T Toner

B3.1 LASER FREQUENCY UP-CONVERSION IN INVERTED HIGHLY VIBRATIONALLY EXCITED MOLECULAR SYSTEMS

H F J Cormican, D J Denvir, I Duncan, I T F Gillan, M J McAllister, W D McGrath and T Morrow (Queens University, Belfast)

Our earlier work which investigated the 193 nm laser photodissociation dynamics of NOCl and the subsequent redistribution of the nascent NO.$X^2\pi$ vibrational population was discussed in previous annual reports (Ref B3.1, B3.2). The latter demonstrated, that with a typical ArF laser output pulse energy of $\sim$ 100 mJ, vibrational inversion number densities in the higher vibrational levels v'' = 8-12 (with respect to v'' = 0,1) of up to 8 x 10^{15} molecules cm^{-3} in a volume of 0.07 cm^3 can be maintained for times > 20 ns after the photodissociation pulse. In order to obtain the maximum population inversion per rotational level the NOCl must be photodissociated in the presence of excess inert gas ($\sim$ 60:1) which rapidly (< 5 ns) thermalises the mixture rotationally and translationally to $\sim$ 700 K. Under such thermalised conditions the maximum population inversion density per rotational level will be $\sim$ 2 x 10^{15} molecules cm^{-3} in a 0.07 cm^3 volume.

The objective of this programme is to assess the potential of such inversions for generation of tunable VUV laser outputs either by direct optical pumping (on resonance) to higher excited (D,E etc) electronic states or via the stimulated anti-Stokes Raman process. Experiments carried out during the year investigated:-

(a) the general experimental conditions required to achieve observable optical gain on elect.-vib.-rot. transitions in NO and the influence of gas pressure (NO and inert gas) on such gains, and

(b) the laser potential of higher (D,E) electronic states of NO.

B3.1.1 Influence of Pressure on NO γ-System Laser

The optically pumped NO γ-system laser, shown schematically in Figure B3.1, provided a convenient model for investigating the general experimental conditions required to achieve observable optical gain on elect.-vib.-rot. transitions in NO and the influence of gas pressure (including collisional rotational redistribution processes) on such gains.

B3.1.2 Experimental

The computer controlled diagnostic system described previously (Ref B3.1, B3.2) was further developed (Figure B3.2) to enable direct recording of accurate high resolution absorption spectra. The $\sim$ 226 nm dye laser energies incident on and transmitted through a static fill gas cell were monitored by two pyroelectric detectors the outputs of which were fed, via a dual channel A/D converter, to the Apple microcomputer which integrated the areas under the pyroelectric signals. The microcomputer software provided for signal averaging over a number of dye laser pulses (generally 10) and also controlled the tuning steps and firing of the excimer/dye laser. After recording these pyroelectric detector signals as a function of incident dye laser wavelength over the required wavelength range (a maximum of 512 tuning steps of the dye laser) the computer software converted the two sets of data (ie, I_0 and I_t) into an absolute absorption spectrum. In order to provide high resolution absorption spectra the FL2002E excimer pumped dye laser was line-narrowed to $\Delta\upsilon \sim 0.04$ cm^{-1} (at the fundamental wavelength of $\sim$ 452 nm) using an intra-cavity etalon. The optically pumped NO γ-system laser outputs at 237 and 248 nm were recorded in a similar manner as shown in Figure B3.2.

B3.1.3 Results and Discussion

The integrated absorption cross-section of a single elect.-vib.-rot. line is related to the Einstein A coefficient by the expression (1)

$$\int \sigma_{\upsilon(abs)}\, d\upsilon = \frac{\lambda_0^2}{8\pi c}\, A_{v'v''}\, \frac{G'}{G''}\, \frac{S_{J'J''}}{2J''+1} \qquad (1)$$

where the integrated cross-section is in cm molecule^{-1} when $d\nu(cm^{-1})$, $c(cm\ sec^{-1})$ and $\lambda_o(cm)$.

The number of molecules N_J in the rotational level J of the $X^2\pi$ ground state is given by the Boltzmann expression (2)

$$\frac{N_J}{N_V} = \frac{(2J''+1)\ \exp-(hcE(J)/kt)}{Q} \qquad (2)$$

where Q is the rotational partition function.

Since the Einstein A coefficients, Honl-London factors $S_{J'J''}$ and molecular constants are well known for the X and A states of NO the integrated absorption cross-sections for single elect.-vib.-rot. transitions can be accurately calculated.

Using low incident (226 nm) dye laser energy densities of < 1μJ/mm^2 the absorption spectra of several No γ(0,0) rotational lines were recorded for NO pressures in the range 4-15 torr and for cell lengths of 1.2 cm and 4.4 cm. The experimentally determined integrated absorption cross-sections were all within ± 20% of the values calculated from expressions (1) and (2). On addition of 760 Torr of helium the NO Doppler linewidths ($\Delta\nu \sim 0.1\ cm^{-1}$) were pressure broadened to 0.45 ± 0.03 cm^{-1} leading to a corresponding factor of ∿ x 4 reduction in optical gains attainable.

The general conditions necessary to obtain observable optical gain on elect.-vib.-rot. transitions in NO, where only one rotational level is initially populated by a high power narrow band-width dye laser, were obtained by investigating in detail the operational characteristics of the optically pumped NO γ-system laser. The latter were obtained by optically pumping (see Figure B3.1) specific rotational lines in the No γ(0,0) transition at ∿ 226 nm, using a

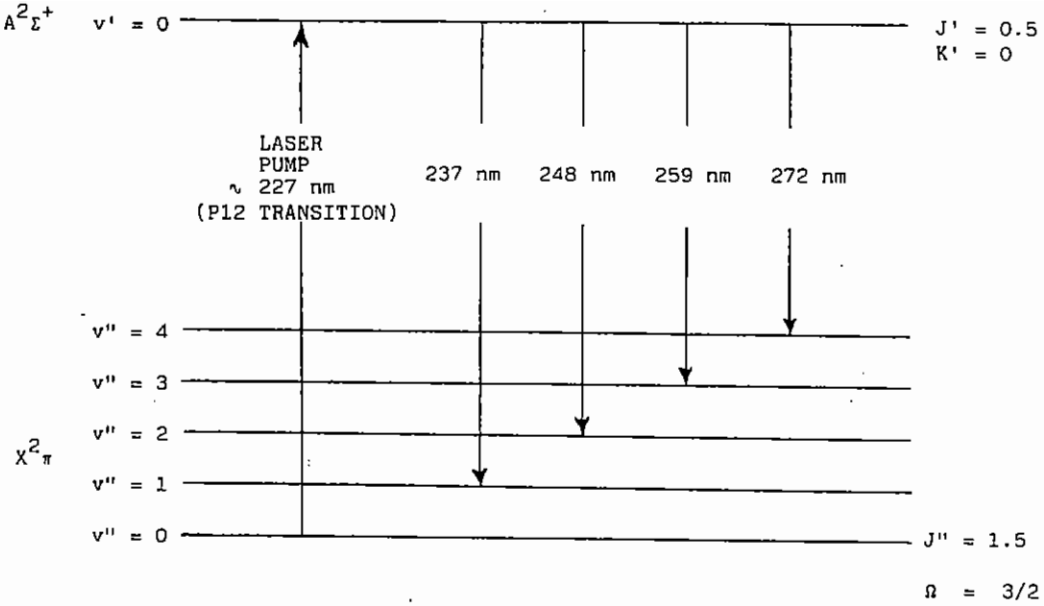

Fig B3.1 Optically pumped NO($A^2\Sigma^+ \rightarrow X^2\pi$) ultraviolet laser.

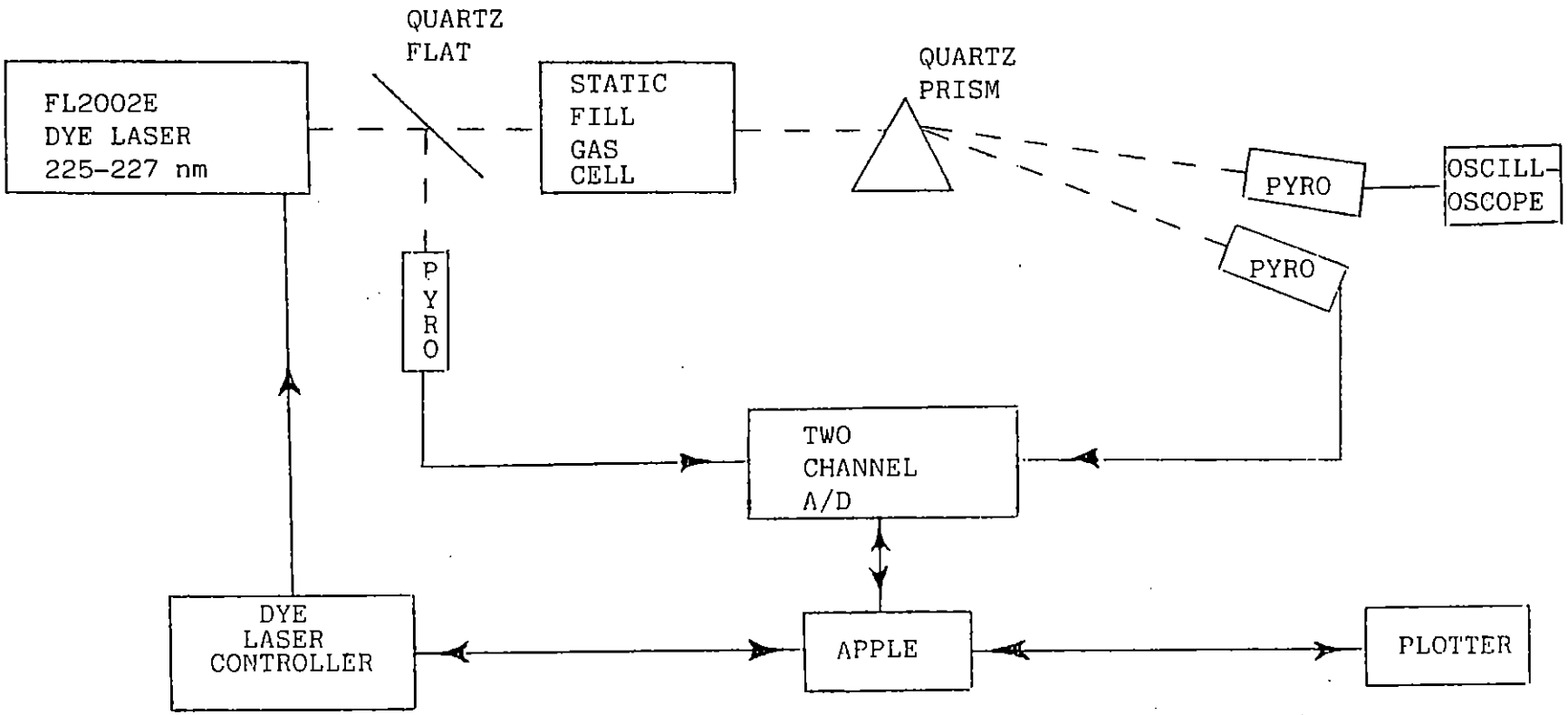

Fig B3.2 Experimental layout used to determine absolute absorption spectra and investigate NO γ - system laser.

narrow bandwidth dye laser, resulting in strong optical gain on corresponding rotational lines of the γ(0,1), (0,2), (0,3) and (0,4) transitions at 237, 248, 259 and 272 nm respectively. Optical gain had been observed previously on only two of these transitions viz γ(0,1) and (0,2) (Ref B3.3). Since the net absorption from the pump dye laser beam (and hence the inversion density created) and the optical gains on these down-converted laser transitions could be directly measured, this γ-system laser provided a convenient model for elucidation of the essential conditions necessary for observation of optical gain on up-converted systems. The influence of the cavity configuration, NO pressure and added buffer gas pressure on the down-converted laser outputs were investigated in detail. The main conclusions of this investigation were as follows:-

(i) In the pure NO system, easily observable optical gains on the γ-system lasers were obtained, using a basic cavity consisting of two aligned uncoated flats, for calculated single pass gains $G \geq \exp 5$. Such gains on the stronger ($\sigma_0 \sim 10^{-15}$ cm^2 molecule^{-1}) rotational lines of the γ(0,1) band at 237 nm were obtained, for an optical path length of 4.4 cm, at inversion densities per rotational level $\geq 1.4 \times 10^{15}$ molecules cm^{-3}.

(ii) The experimental configuration of Figure B3.2, which provides simultaneous measurements of the ∿ 226 nm dye laser energy absorbed into γ(0,1) and the laser output energy, was used to investigate the effect on laser gain of rotational redistribution at high gas (NO and inert gas) pressures. The % absorptions and ∿ 237 nm NO γ-system laser output energies obtained as a function of NO pressure are shown in Figures B3.3 and B3.4 respectively for a 226 nm pump laser energy of 80 μJ. The effects of added helium pressure, at a fixed NO pressure of 10 Torr, on the % absorption and 237 nm γ-system laser output were also investigated. With increasing added helium pressure the % absorption increased to ∿ 80%, for 135 Torr helium, whilst the 237 nm laser output showed a gradual decrease to lasing threshold at ∿ 135 Torr helium.

The absorption (bleaching) process was modelled theoretically using an iterative computer programme based on the simple scheme summarised in Figure B3.5. The stimulated emission cross-section σ_S at the ∿ 226 nm pump wavelength was estimated from expression 3 using the appropriate Honl-London factor $S_{J',J''}$ and other stimulated processes (i.e., γ-system

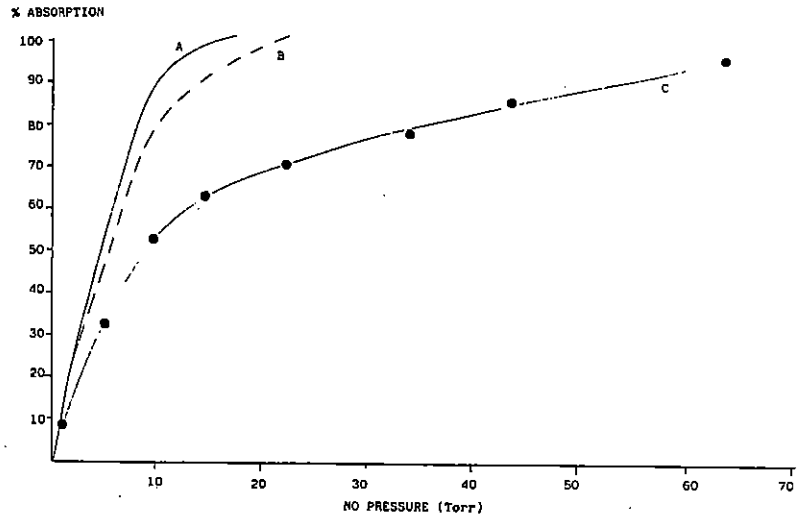

Fig B3.3 Percentage dye laser energy absorbed as a function of NO pressure (Torr). A - Theoretically predicted absorption from the model schematically outlined in Fig B3.5. B - The absorption derived from the model when rotational relaxing is ignored. C - Experimental results. The dye laser is tuned into resonance with the ($A^2\Sigma^+ \rightarrow X^2\pi_{3/2}$ $J'' = 1.5$) P12 absorption line and focussed by a 1 m lens at the centre of a 4 cm long quartz cell.

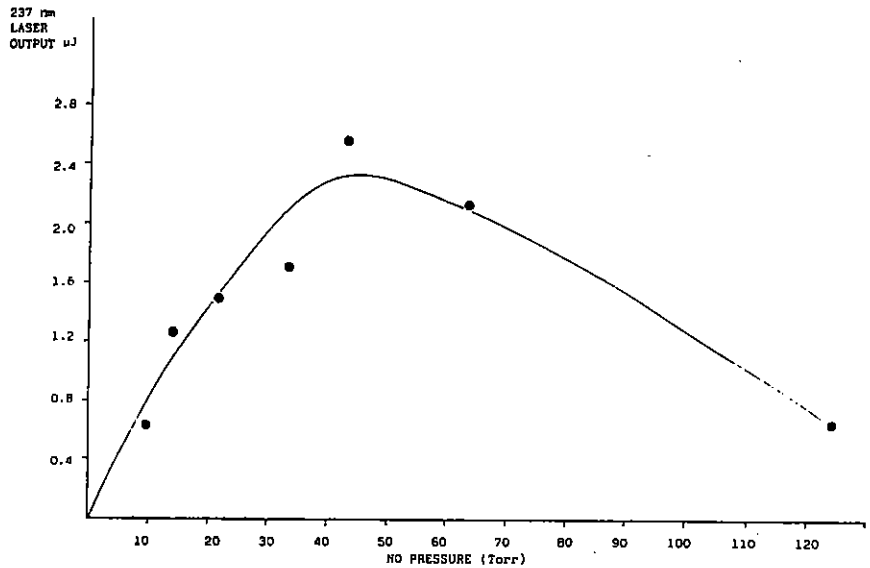

Fig B3.4 Graph of 238 nm $A^2t^+ - X^2\pi$ laser output energy μJ as a function of NO pressure (Torr). The dye laser is tuned into resonance with the ($A^2\Sigma^+ \rightarrow X^2\pi_{3/2}$ $J'' = 1.5$) P12 absorption line and focussed by a 1 m lens at the centre of a 4 cm long quartz cell.

lasers) were assumed to have a negligibly small effect on the rotational populations during the pump laser pulse duration

$$\sigma_{\upsilon}(\text{gain})d\upsilon = \frac{\lambda_o^2}{8\pi c} \cdot A_{v'v''} \cdot \frac{G'}{G''} \cdot \frac{S_{J'J''}}{2J'+1} \qquad (3)$$

The rates of repopulation of the lower rotational level and depopulation of the upper rotational level by collisional redistribution were estimated from the work of Sudbø and Loy (Ref B3.4) and Ebata et al (Ref B3.5).

The % absorptions predicted including (Curve A) and neglecting (Curve B) collisional redistribution of the rotational populations are also shown in Figure B3.3. The experimentally measured % absorptions show a marked deviation from the behaviour predicted using the model of Figure B3.5. The influence of rotational relaxation is in fact negligibly small in comparison to the major deviation of the experimental results from predicted behaviour. The anomalously high % transmissions of NO mixtures at high incident 226 nm power densities was a general phenomenon observed throughout this work and can be attributed to power broadening of the stimulated emission line width of the pumped rotational line due to the high power density of the ∿ 226 nm pump laser at the entrance end of the absorption cell. The latter process leads to progressive transfer of part (∿ 20%) of the incident narrow bandwidth ($\Delta\upsilon < 0.04$ cm^{-1}) pump radiation into broader ($\Delta\upsilon > 0.1$ cm^{-1}) bandwidth super-radiant laser which propagates through the cell co-linear with the narrow bandwidth pump laser. The reduced power densities incident further into the cell produces less power broadening of the pumped line and therefore only the centre frequencies ($\Delta\upsilon \approx 0.1$ cm^{-1}) of the super-fluorescent laser are re-absorbed. The slow increase in % absorption with NO pressure above 10 Torr is due to progressive suppression of the super-fluorescent broad band laser gain by increased absorption of an increased length of pressure broadened NO absorption. Although pressure broadening, which reduces the peak gain of the γ-system laser (by a factor of 1.4 for 100 Torr pure NO system and by a factor

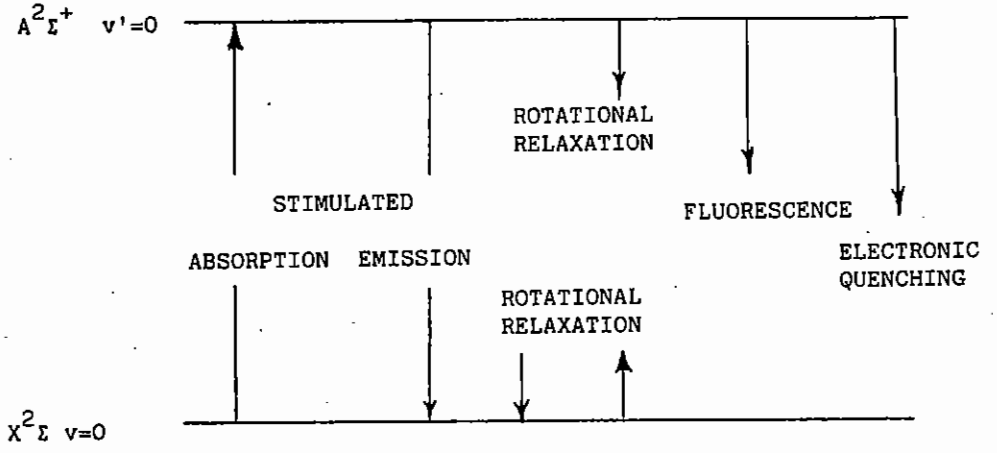

Fig B3.5 Theoretical model for $A^2\Sigma^+ \leftarrow X^2\pi$) Absorption

$X^2\pi$ ELECTRONIC GROUND STATE

(i) Rotational relaxation rate for $X^2\pi$ levels ∿ 2.83×10^{-10} cm^3 molecules^{-1} sec^{-1} (based on the results of ref B3.4 for $X^2\pi$ (v=2) level).

$A^2\Sigma^+$ RYDBERG STATE

(i) $A^2\Sigma^+$ (v' = 0) radiative lifetime ∿ 200 ns.

(ii) $A^2\Sigma^+$ (v' = 0) electronic and vibrational quenching rate ∿ 1.88×10^{-10} cm^3 molecules^{-1} sec^{-1}.

(iii) Rotational relaxation rate for $A^2\Sigma^+$ level $(1.8 \pm 0.5) \times 10^{-10}$ cm^3 molecules^{-1} sec^{-1}.

of 1.2 for the 10 Torr NO:100 Torr He mixture), makes a minor contribution to reduction in ∿ 237 nm laser output the dominant effect which terminates the laser action is the reduced lifetime of the upper lasing level at high pressures. Estimation of the upper level lifetime τ from expression (4)

$$1/\tau = 1/\tau_o + k_e[NO] + \Sigma k_q[Q] \ldots. \qquad (4)$$

Where τ_o is the radiative lifetime (∿ 200 ns), k_e the rate constant (Ref B3.6) for electronic self-quenching (1.88×10^{-10} cm^3 molecules^{-1} sec^{-1}) and k_q the rate constant (Ref B3.4 and B3.5) for rotational relaxation ($k_q(He) \approx k_q(NO) = 1.8 \pm 0.5 \times 10^{-10}$ cm^3 molecules^{-1} sec^{-1}), indicates that laser action terminates for $\tau < 1$ nsec.

B3.1.4 Laser Potential of the higher (D,E) excited states of NO

Direct optical pumping with a narrow bandwidth dye laser, at ∿ 226 nm, of specific single rotational lines in the $\gamma(0,0)$ system of NO is discussed in (a) above. For an incident dye laser pulse energy of 80 μJ this technique can provide, over a gain length of 4 cms, known high inversion densities (∿ 10^{17} molecules cm^{-3}) in selected rotational levels of the NO ($A.^2\Sigma$, v'=0) state, inverted with respect to corresponding rotational levels in the NO ($X.^2\pi$, v=1,2,3 etc.,) states. Such highly inverted single rotational levels, combined with the narrow linewidths and inherently simple kinetics of the low pressure pure NO system, provide convenient inverted intermediate states for initial investigation of laser frequency up-conversion schemes.

An experiment using direct optical pumping, with a second high power dye laser at ∿ 600 nnm, from such highly inverted A state rotational levels to the higher excited E electronic state was carried out in order to assess the VUV laser potential of the E → X transition. Laser potential of the higher excited (D,E) states of NO has been discussed previously by several workers (Ref B3.7).

B3.1.5 Experimental

The unique feature of the experimental set-up was the provision of two synchronised tunable narrow bandwidth dye laser outputs (i.e., ∿ 226 and ∿ 600 nm). This was achieved by sequentially pumping two FL3002 dye lasers using the same high power (Model Hx460) Lumonics excimer laser. The pump configuration used is shown in Figure B3.6. Rearrangement of the excimer pump steering optics of the first dye laser allowed the oscillator and pre-amplifier to be pumped by ∿ 20% of the excimer laser output (∿ 150-200 mJ) and provided an output, at ∿ 600 nm, of ∿ 200 μJ (without intra-cavity etalon) and ∿ 100 μJ (with intra-cavity etalon).

The remaining ∿ 80% of the excimer beam, transmitted by the first dye laser, pumped the second dye laser in its normal configuration. The second harmonic of the line-narrowed output (i.e., with intracavity etalon) from this laser provided ∿ 100 μJ at ∿ 266 nm. The dye lasers were synchronised in the cell interaction region by adjusting the lengths of the beam paths.

The spectral diagnostics used are shown in Figure B3.7. The two counter propagating laser beams were overlapped within the gas flow cell close to and parallel with the entrance slit of the spectrometer (Bausch and Lomb). The latter was flushed with helium and fitted with a sodium salicylate scintillator plate in order to extend the spectral response down to ∿ 160 nm. The resulting fluorescence spectra were imaged onto the intensified diode-array (OMA) system and laser induced fluorescence excitation spectra were recorded under computer control as described in detail previously (Ref B3.1,B3.2).

B3.1.6 Results and Discussion

Detailed investigation of the emission spectra, obtained on sequential two-photon (E←A←X) pumping of specific rotational levels in the E state over a range of experimental conditions, showed only the presence of strong D → X emission (along with the expected γ-emissions). No spectral features unambiguously assignable to E → X

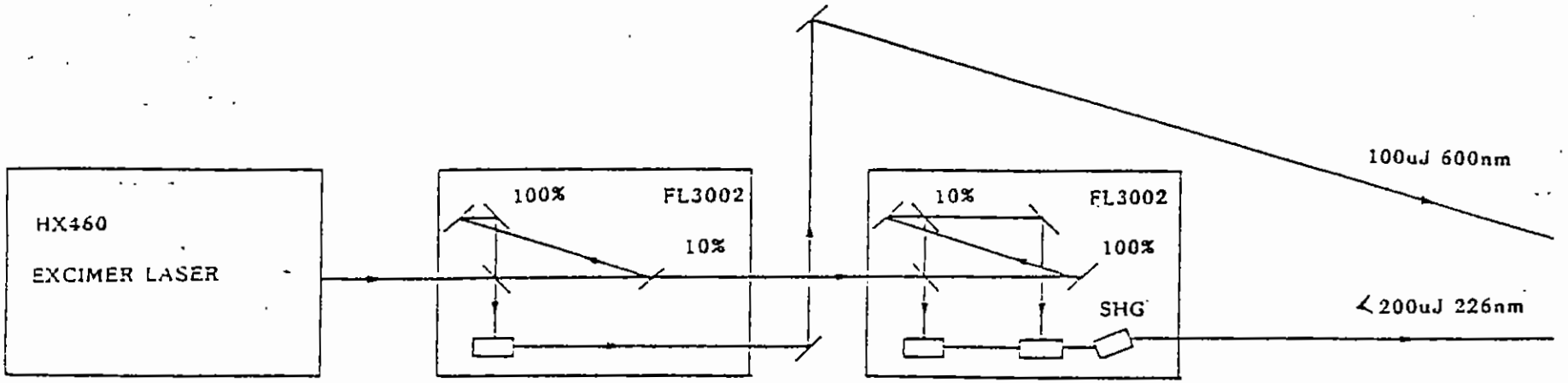

Fig B3.6 Layout of dye lasers to provide synchronous pulses. Note the rearrangement of beam splitting mirrors in the first dye laser.

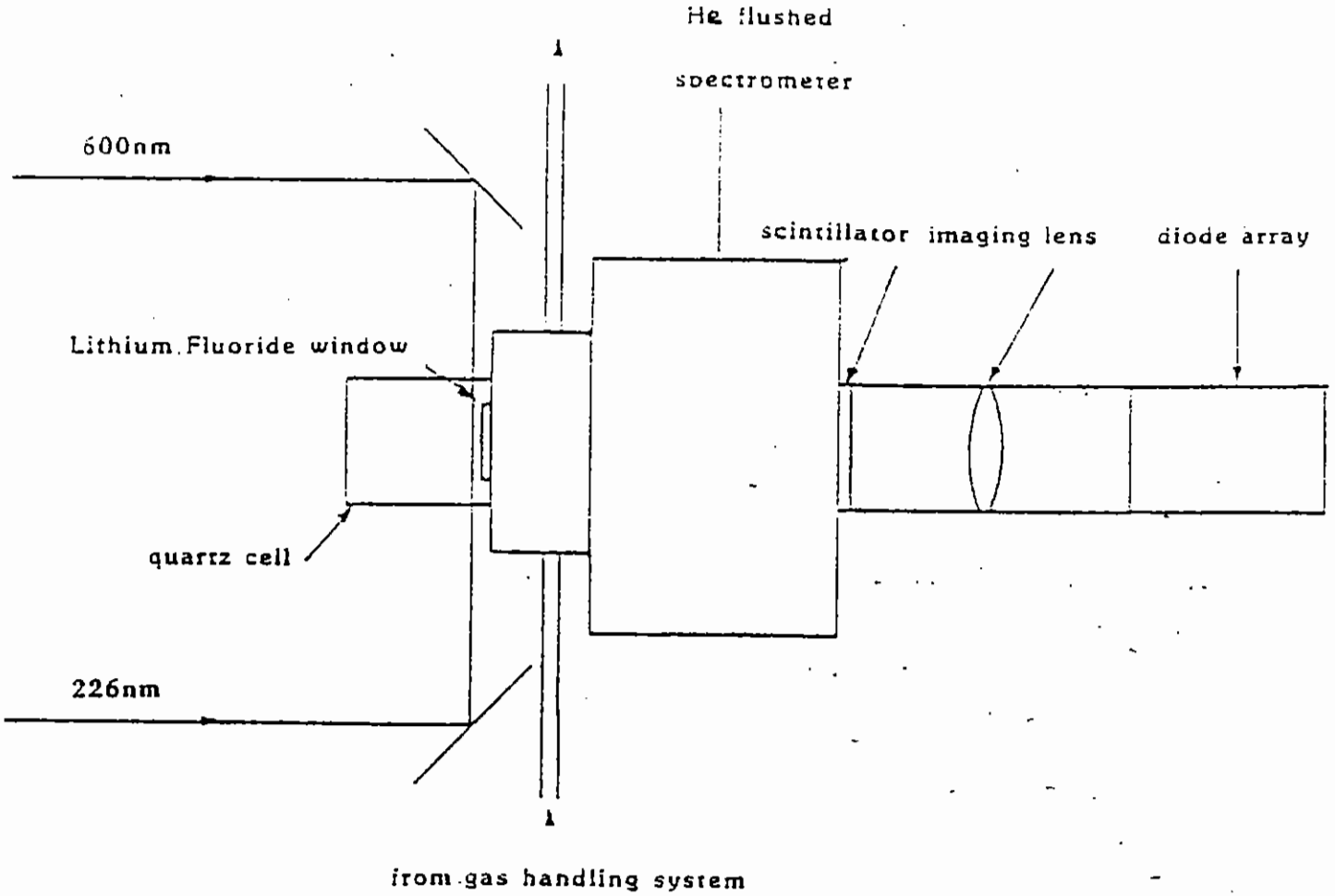

Fig B3.7 Experimental layout for VUV laser induced fluorescence.

emission were observed during this work, indicating a large E → D branching ratio and a small E → X branching ratio.

Attempts were made to confirm the latter conclusion by pumping on resonance with the RII line of the E(v=1, J=5/2) ← A (v=0, J=3/2) transition. For the latter E state strongly peaked Franck-Condon factors result in the dominance of E(v=1) → A(v=1) → X and E(v=1) → D(v=1) →A(v=1) → X cascade emissions which are easily resolved from the A(v=0) → X emissions in the same spectral region. The fluorescence spectra were recorded at low NO pressures (∿0.1 Torr) in order to avoid self-quenching but relatively high pump power densities (50 μJ at 226 nm and 50 μJ at 526 nm, both focussed within the gas cell by a 1 m lens) were requied to compensate for the weak absorption on the 526 nm transition. The integrated emission intensities in the different emission systems, after correction for detector response, yielded branching ratios for ED:EA:EX: of 0.75:0.20:<0.05 (the latter being determined by limits of detectability). In hindsight (see discussion below) it would seem likely that the latter branching ratios for E→D and E→A emissions may have been strongly enhanced by amplified spontaneous emission under our high power excitation conditions.

Laser induced fluorescence (D→X) excitation spectra (shown in Figure B3.8 and B3.9), recorded on scanning the dye laser over the E(v=0)←A(v=0) absorption, showed the presence of severe broadening effects on the E←A transition. The latter was investigated as a function of input power density (of the ∿ 600 nm laser) and NO pressure. In order to eliminate possible two photon mixing processes the ∿ 226 nm and ∿ 600 nm laser pulses were temporally separated by 12 ns during these experiments. The broadening increased linearly with increasing NO pressure (or A state rotational level number density) and showed an ∿ 1/6 power dependence on laser intensity. Although these effects require further study, it would seem likely that they are due to saturation power broadening, modified by the transient nature of the high power pump pulse.

Evaluation of the laser potential of the higher (D,E) states of NO in terms of the stimulated emission cross-sections, calculated from

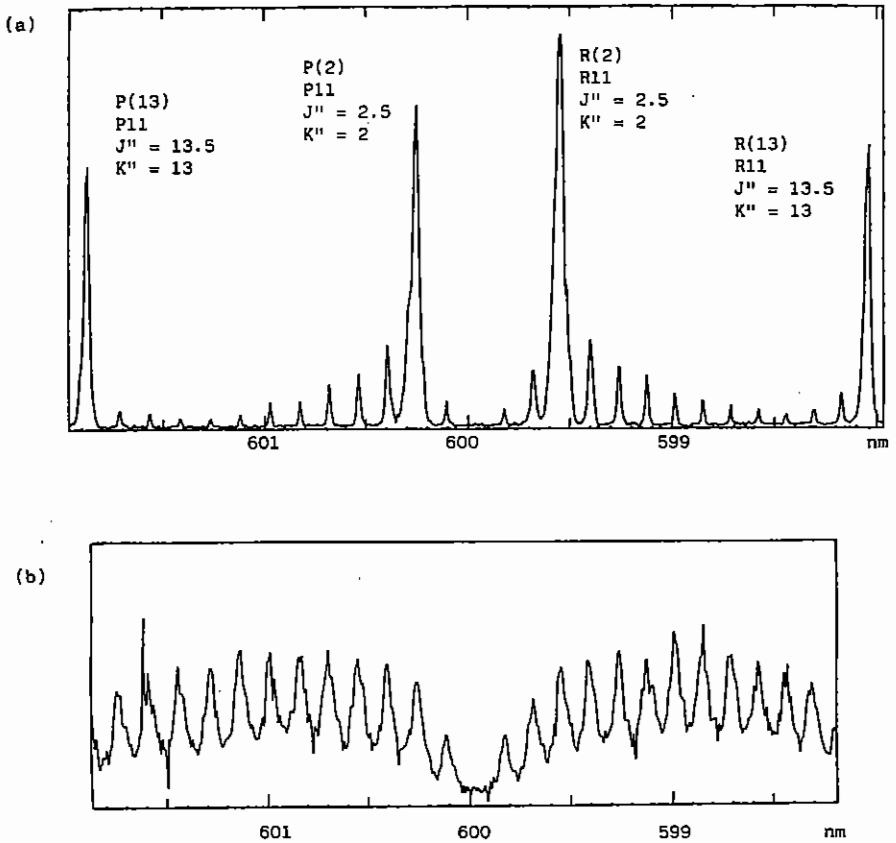

Fig B3.8 (a) LIF excitation (absorption) spectrum of the NO $E^2\Sigma^+ \leftarrow A^2\Sigma^+$ transition, recorded in pure NO at 4.8 Torr, when only two rotational levels of the $A^2\Sigma^+$ are initially populated by tuning a 100 μJ dye laser into resonance with two overlapping P11 transitions at 226.3 nm in the NO_γ (0,0) band. The laser induced fluorescence, excited by a second dye laser (0.5 mJ, ∿ 600 nm) which overlapped the first beam temporarily and spatially, was observed in the D → X transition at 193 - 208 nm. Note some rotational relaxation in the $A^2\Sigma^+$ state is observed even within the laser pulse duration of ∿ 10 ns.

(b) The corresponding LIF excitation (absorption) spectrum recorded in a mixture containing 3 Torr NO and 1 Atmosphere of Helium shown complete rotational equilibration of the $A^2\Sigma^+$ state within the laser pulse duration.

expression (3), for transitions to lower electronic states requires a knowledge of the absolute band (v',v") transition probabilities $A_{v'v"}$ The latter may be estimated from the upper state radiative lifetime . $\tau_e(v')$ provided the electronic branching ratios from the upper state and the appropriate Franck-Condon factors are available (Ref B3.8).

Individual $A_{v'v"}$ values may be estimated from the Franck-Condon $q_{v'v"}$ using the expression (5)

$$A_{v'v"}/A_{v'} = \frac{R_e^2\, q_{v'v"}\, \bar{\nu}^3\, G"}{\sum_{v"} R_e^2\, q_{v'v"}\, \bar{\nu}^3\, G"} \qquad (5)$$

where R_e is the electronic transition moment of the v'-v" transition with a mean band frequency $\bar{\nu}$ and G" is the number of orbitals in the lower state with which a given upper level combines. For a given band system occurring over a narrow frequency spread and where R_e is approximately constant (and equal to $\bar{R}_e$) expression (5) may be simplified to (6)

$$A_{v'v"}/A_{v'} = \frac{q_{v'v"}\, \bar{\nu}^3}{\sum_{v"} q_{v'v"}\, \bar{\nu}^3}$$

The $A_{v'}$ value for a given band system can be determined from the radiative lifetime $\tau_e(v')$ of the upper v' level and the branching ratio B(v') to the lower electronic state i.e., $A_{v'} = B(v')/\tau_e(v')$. The parameters which exhibit most uncertainty are the branching ratios B(v') for competing emissions for the D and E states to the available lower electronic states. The branching ratios for E→C (Ref B3.9) and D→C (Ref B3.10) emissions have been shown to be negligibly small.

In the case of the D state a detailed survey of literature values (Ref B3.9-12) indicates a reasonable consensus on values for the lifetime, branching ratios and oscillator strengths. Such relevant

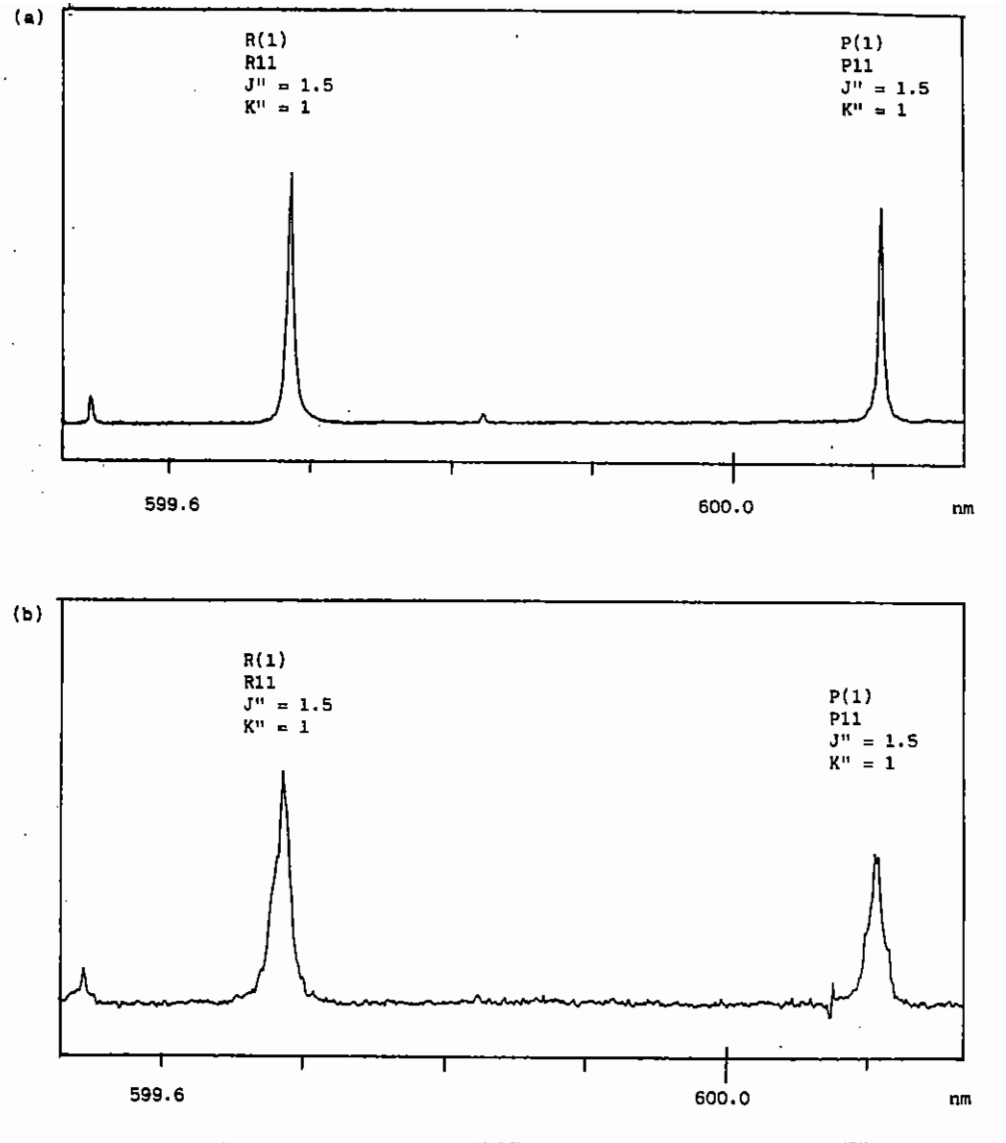

Fig B3.9 (a) LIF excitation spectrum of the NO $E^2\Sigma^+ \rightarrow A^2\Sigma^+$ transition recorded in 0.5 torr NO with 80 μJ 256 nm and 1.5 μJ 600 nm lasers.

(b) Corresponding LIF excitation spectra recorded with 0.2 torr NO with 80 μJ 226 nm and 150 μJ 600 nm lasers showing the effects of power broadening.

values (with associated uncertainty) are summarised below together with mean electronic transition moments $\bar{R}$ estimated from the expression (7) given by Hesser (Ref B3.8).

$$-A_{v'} = \frac{R_e^2\ G''}{4.94 \times 10^5} \sum_{v''} q_{v'v''}\ \bar{\nu}^3_{v'v''} \qquad (7)$$

$A(DX) = (4.4 \pm 0.3) \times 10^7\ s^{-1}$
$A(DA) = (1.5 \pm 0.6) \times 10^7\ s^{-1}$
$\tau_o(D) = 20\ (\pm 4)$ ns
$\bar{R}_e(DX) = 0.22 \pm 0.04$ a.u.
$\bar{R}_e(DA)/\bar{R}_e(DX) = 10.5\ (\pm 1.5)$

In the absence of any reliable literature values for the E state lifetime and branching ratios order of magnitude $A_{v'}$ values for E state transitions were estimated from (7). Since the E, D and A states have nearly identical r_e values and the $q(0,v'')$ values for E→D, E→A and D→A transitions are all strongly peaked for the (0,0) transitions then to a good approximation the sum in expression (7) may be replaced by $\bar{\nu}^3_{oo}$. Thus, using available spectroscopic data in expression (7) and assuming that to a first order approximation the mean electronic transition moments $\bar{R}_e$ for similarly disposed NO states are equal (i.e., $\bar{R}_e(ED) = \bar{R}_e(EA) = \bar{R}_e(DA) \approx 10.5\ \bar{R}_e(DX)$ and $\bar{R}_e(EX) \approx R_e(DX) = 0.22$ a.u.) yields the following rates for competing radiative emission from the E(v'=0) state:- $A(EX) = 7.4 \times 10^7\ s^{-1}$, $A(ED) = 9.4 \times 10^6\ s^{-1}$, $A(EA) = 9.9 \times 10^7\ s^{-1}$. The latter indicate a radiative lifetime $\tau_o(E)$ of ∿ 5.5 ns and branching ratios EX:ED:EA of 0.41:0.05:0.54.

The integrated stimulated emission cross-sections, calculated from expression (3) and the data discussed above, for the strongest single rotational lines in various emission bands arising from excitation of D and E states, are summarised in Table B3.1 along with corresponding Doppler half-widths and peak cross-sections σ_o at line centre. The stimulated cross-sections σ_o reported in Table B3.1 are based on Doppler linewidths and neglect the possible power broadening effects reported above. It should be noted that although the VUV D→X and E→X transitions have large stimulated cross-sections (a factor of ∿ 5 greater than the γ-system 237 nm laser) lasers on such transitions compete with strong E→A→X and E→D→A→X cascade lasers which have stimulated cross-sections a factor of ∿ 10^3 larger. The large D→A cross-section agrees with the observation of stimulated emission on this transition at NO pressures down to 20 m Torr by Scheingraber and Vidal (Ref B3.11) and the essentially quasi-CW D→A laser action observed on flash photodissociation of NO_2 (Ref B3.13). The large E→D and low E→X branching ratios observed under our high power excitation conditions could be attributed to stimulated enhancement of the E→D and E→A intensities.

TABLE B3.1

Emission System	Transition (v'v")	Approx Wavelength (nm)	Doppler halfwidth (cm^{-1})	$\int\sigma_s d\nu$ * (cm^2 molecule^{-1})	σ_o * (cm^2 molecule^{-1})
A → X	γ(0,1)	237	0.1	7.6×10^{-17}	7.1×10^{-16}
D → X	ε(0,1)	195	0.12	4.8×10^{-18}	3.8×10^{-16}
E → X	γ'(0,1)	169.5	0.14	6.2×10^{-16}	4.2×10^{-16}
E → D	(0,0)	1320	0.02	6.5×10^{-14}	3.1×10^{-12}
E → A	(0,0)	600	0.04	1.4×10^{-13}	3.3×10^{-12}
D → A	(0,0)	1090	0.02	7.05×10^{-14}	3.3×10^{-12}

* - stimulated emission cross-sections are quoted for the strongest single rotational lines in each band

B3.2 PICOSECOND PHOTOLUMINESCENCE IN AMORPHOUS SEMICONDUCTORS

Z Sobiesierski, R T Phillips (Dept of Physics, Exeter University)
W T Toner, J R M Barr and A J Langley (RAL)

B3.2.1 Introduction

In the past year our programme of experiments on photoluminescence in amorphous semiconductors has produced its first scientific results. The topic under study has been picosecond luminescence in red amorphous phosphorus, which has proved to show rather complicated features in its photoluminescence. Two emission bands have been identified in time-resolved studies (refs B3.14and B3.15): a low energy (LE) band which moves from about 1.35 eV to about 1.15 eV during the first 200 ns after pulsed (nanosecond) excitation, and a high energy (HE) band which remains near 1.4 eV at all times. The LE band dominates the radiative recombination for the first few hundred nanoseconds when the specimen is held at a temperature below about 130K; above this temperature the photoluminescence appears to be characteristic of the HE process at all times. We showed in an earlier paper (ref B3.15) that the mean energy of the LE band decreases when the energy of the exciting photons is reduced below about 2 eV. Fasol showed previously (ref B3.16) that the HE process has such a linear relationship between its mean energy and the energy of excitation. This form of behaviour has been found in other amorphous semiconductors, and has been particularly carefully studied in a-Si:H (ref B3.17). What is interesting about the observation of such an energy- dependence of both bands in a-P is that is suggests that the two emission processes share a common radiative centre - just as was originally inferred (under slightly different circumstances) from optically-detected magnetic resonance (ref B3.18). One candidate for this may be a carrier trapped in a band-tail state, such that for sufficiently high energies in the tail, energy loss by phonon emission leads to a temporal shift of the luminescence band. At low energies in the band-tail (within the "thermalisation gap"), radiative recombination precedes downward hopping, thus leading to a proportionality between the emission and excitation energies (refs B3.19 and B3.20). In the case of a-P the LE band shifts with time even in the regime in which the initial energy is proportional to excitation energy, which appears to eliminate the "thermalisation gap" approach to description of the recombination. Nonetheless the shift of the LE band can still be fitted by Kastner's estimate (ref B3.21) of the energy, E, of a carrier group thermalising in an exponential band tail characterised by an energy scale kT_0: $E \approx E_0 - 3kT_0 \ell n(\ell n \nu_0 t)$, where ν_0 is of order $10^{12} s^{-1}$. However, we have previously analysed the temporal shift in terms of a "Coulomb model" in which recombination is by radiative tunnelling between carriers trapped at oppositely charged intrinsic defects (ref B3.15). In this approach the tunnelling probability $\exp(-2R/R_0)$ (where R_0 is a localisation length) ensures that there is a correlation between the separation of carrier pairs, R, and the radiative time, and therefore a correlation between time and energy via the Coulomb term α 1/R. In our study of the LE process confined to the nanosecond time range it proved very difficult completely to eliminate thermalisation as an explanation for the band shift. However, the two models offer radically different predictions for behaviour at shorter times. The thermalisation model predicts a steady increase in the mean energy of luminescence as shorter times are probed, while the "Coulomb model" leads to a maximum energy characteristic of recombination of the closest pairs of defects. We attempt here to resolve the question of the recombination channel by studying the luminescence decays in the time range 10-1000 ps. This further enables us to study the effect of temperature on the luminescence, which produces the changeover from LE to HE recombination around 130 K. Picosecond time resolution allows direct observation of the rate of non-radiative recombination which we compare with similar observations on other materials.

B3.2.2 Experimental Technique

To achieve meaningful picosecond luminescence measurements on an amorphous semiconductor demands a different approach from that usually applied to crystalline materials. This is a result of the enormous range of radiative lifetimes found in the amorphous state - extending from nanoseconds through to a peak in the distribution of lifetimes at about 4 ms for a a-P. In order to maintain the specimen in a state relatively unchanged by the excitation, the experiment is best carried out with illumination of low intensity (to avoid

fatiguing) at low repetition rate (to avoid overlapping of emission from successive pulses). Our experimental arrangement used the picosecond tunable dye laser in the LSF and relied on the amplified pulses (∿ 100 μJ, 5 ps) to give sufficient luminescence to be detected (Figure B3.10). These amplified pulses, together with the 82 MHz pulse train, passed through an optical delay before reaching the specimen. About 5% of the beam was used to illuminate a vacuum photodiode which provided a low-jitter signal for the Dellistrique streak camera. A small part of the beam was diverted through the entrance slit of the streak camera to give a fiducial time marker. We cannot assess fully the effect of the weak quasi-cw illumination of the specimen arising from the unamplified pulse train, but the effects of overlapping of the pulses during the streak are several orders of magnitude below the lower detection limit of our apparatus. A much more serious problem is the presence of luminescence during the relatively slow fly-back of the deflection potential of the streak camera, which demands that a long blanking pulse be applied to the grid. The length of the blanking pulse was varied so that this problem was identified and eliminated. The streak camera output was passed through a two-stage image intensifier before being scanned by an optical multichannel analyser in the usual way. The response of the system to scattered laser light gives an indication of the time response of the system - typically the laser pulse gave a peak with FWHM ∿ 70 ps when integrating over the same number of pulses used to obtain experimental decay data.

Experimental conditions were chosen so as to provide a test of the recombination models. Excitation was at 1.968 eV- the peak of the luminescence excitation spectrum. The optical bandwidth of detection was limited to ∿ 1.45 eV at the low-energy end by the S25 photocathode response, and to 1.6, 1.73 or 1.85 eV at the high-energy end by appropriate "edge" filters (which also eliminated scattered laser light). The specimens were polished lumps of high purity red a-P obtained from MCP Electronic Materials Ltd, and were prepared by transformation of white P_4 at ∿ 280°C. These were held in helium exchange gas controlled at temperatures between 4 and 300 K. Experimental data have been corrected for non-linearity in the timebase and for lateral variation in sensitivity of the detection system.

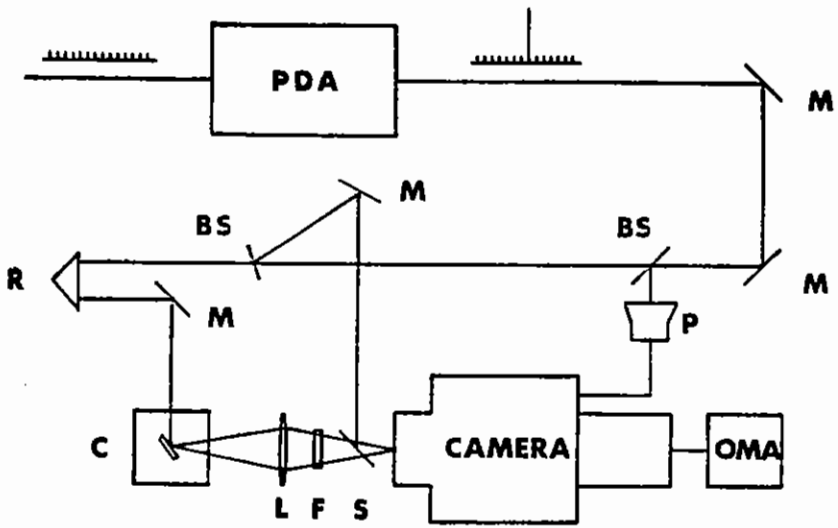

Fig B3.10 A schematic diagram of the apparatus. A mode-locked train of pulses from a standing-wave dye laser pass through a pulsed dye amplifier (PDA) to give amplified pulses superimposed on the mode-locked train. The beam is directed by several reflectors (reprsented here by M) to the sample via a retroreflector (R) arranged in order to give a variable delay. Parts of the beam are extracted with beam splitters (BS) to give a trigger signal from the photodiode P and also to give a fiducial marker. The sample is held in a cryostat C and luminescence is focussed with lens L on the slit of the streak camera. The energy window is selected by filter F and the luminescence and fiducial are superimposed at the streak camera by a glass slide S.

B3.2.3 Results and Discussion

Figure B3.11 shows a typical luminescence transient as recorded by the optical multichannel analyser. The non-linearity of the timebase results from variation of the streak rate across the field of the streak tube. The risetime of the signal is dominated by the characteristics of the detection system, and is consistent with a risetime for the luminescence of 50 ps or less (ref B3.22). Figure B3.12 displays data corrected for timebase non-linearity and detection sensitivity in the form ℓn (intensity) versus time, over that range of time for which a single exponential decay is observed. Data are plotted for the energy windows 1.45 - 1.85 eV and 1.45 - 1.73 eV. The initial decay rate $\nu(T)$ is the sum of the radiative and non-radiative components - the latter becoming dominant progressively as the temperature is increased. The logarithmic decay rate $\nu(T)$ is seen to be independent of the spectral window to a level of about 1%. If the luminescence is modelled by a Gaussian band shifting rigidly according to the thermalisation formula then the two spectral windows would be expected to lead to decay rates differing by 10-20% depending upon the detailed choice of parameters appropriate to a-P. We therefore infer from these data that thermalisation must be substantially less important in determining the position of the band than the simple model suggests. The "Coulomb model" relies on the existence of a Stokes shift to explain part of the energy difference between the excitation and emission spectra. Unfortunately our present limit on the experimental risetime - 50 ps- is insufficient to corroborate directly this interpretation, which implies a very rapid energy loss in a multi-phonon emission process.

Figure B3.13 shows the temperature dependence of the initial radiative rate for the wider energy window, together with a fit to the data of the form $\nu(T) = \nu_1 + \nu_0 \exp(T/T_0)$. This empirical rule has previously been found successful in describing the initial rate in a-Si:H (B3.3.10). In the case of a-P at 4 K $\nu_1 = 8.6 \times 10^8 s^{-1}$, $\nu_0 = 3.7 \times 10^8\ s^{-1}$ and $T_0 = 104$ K. Attempting a fit to an equation of the form $\nu(T) = \nu_2 + \nu_3 \exp(-E/KT)$ gives $\nu_2 = 1.4 \times 10^9\ s^{-1}$, $\nu_3 = 3.5 \times 10^{10}\ s^{-1}$ with E = 47 meV. Though these seem reasonable parameters we abandon this model because of the problems identified in its

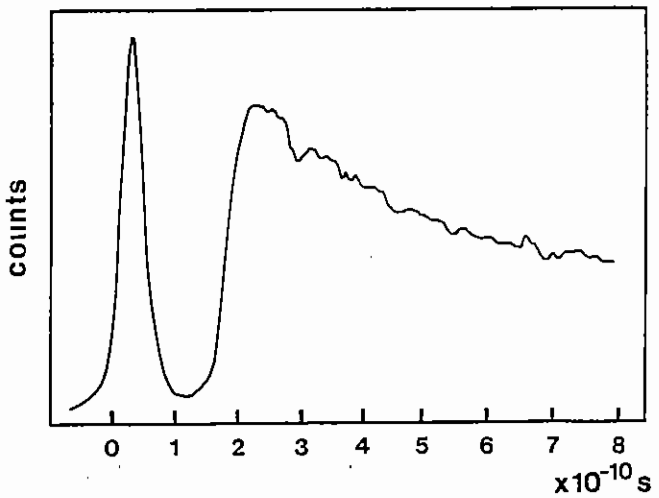

Fig B3.11 Photoluminescence signal obtained from a specimen held at 60 K. The raw data are plotted in the form of counts at the optical multichannel analyser and a time scale has been added which is corrected for nonlinearity of the streak ramp. The large initial peak is the fiducial marker whose width gives an indication of the time resolution.

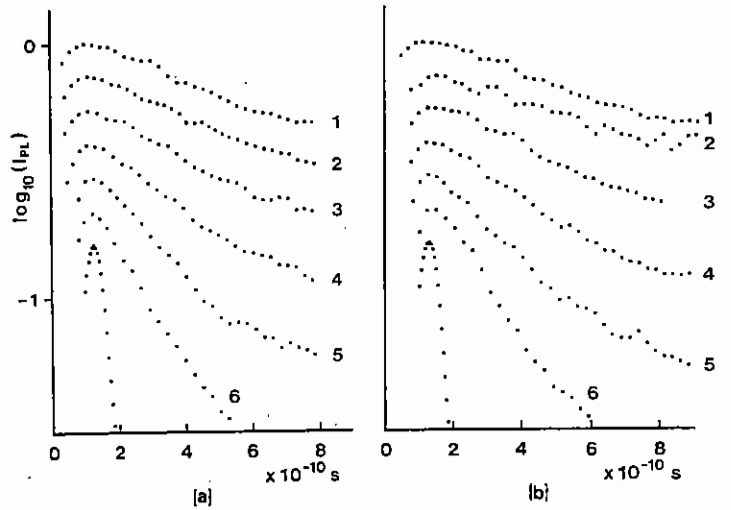

Fig B3.12 The logarithm of the luminescence intensity versus time for the ranges of photon energy 1.45 - 1.85 eV (a) an 1.45 - 1.73 eV (b) at temperatures (1) 4 K, (2) 50 K, (3) 100 K, (4) 150 K, (5) 200 K and (6) 250 K. The unlabelled data correspond to the trailing edge of a laser pulse measured under the same conditions.

application to silicon (ref B3.23). What is interesting about the data shown in Figure B3.13 is that by ∿ 130 K the non-radiative rate is only about 3.5 times that a K. Yet measurements of the PL spectrum in the nanosecond regime show that the nature of the radiative recombination alters radically as the specimen is warmed to 130 K, with the lower-energy transitions absent at higher temperatures. Furthermore, the decay in the nanosecond regime is characterised by a lifetime of the order of 10-100 ns. The picosecond and nanosecond data can be reconciled if the branching ratio at photoexcitation is temperature dependent. Thus at low temperatures electrons and holes trap close to one another and lead preferentially to LE recombination, whereas at higher temperatures one carrier traps rapidly and the other has increasing opportunity to hop away as the temperature is increased. This also fits the assignment of the LE process to recombination between carriers trapped at nearby charged defects and of the HE band to recombination involving one carrier trapped at one of the charged defects and the other in a band-tail state. The non-radiative quenching in the sub-nanosecond time range depletes subsets of both radiative populations but with almost complete depletion of the LE pairs by 130 K.

The requirement that one of the charged defects should rapidly trap an appropriate carrier seems likely to be met by the P_4^+ centre. This defect is extremely sensitive to its environment (ref B3.24) even to the extent, perhaps, of forming a broad band overlapping the conduction band tail. The proportionality between excitation and emission energies would be regarded, on this model, as a manifestation of the inhomogeneous broadening of the P_4^+ band. On the other hand, we require that the P_2^- defect should lie deeper in the gap and trap only a small proportion of the available holes.

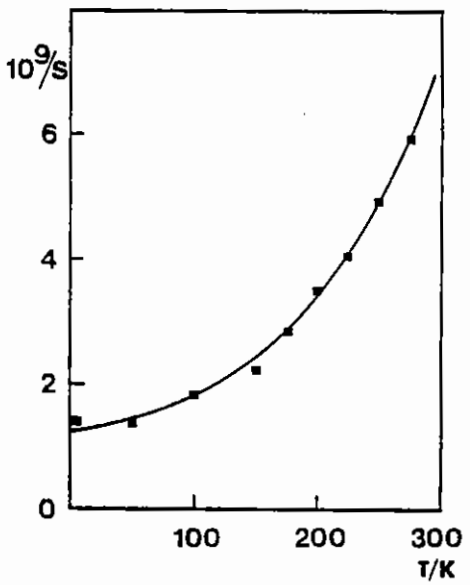

Fig B3.13 The initial decay rate ν of photoluminescence in the energy range 1.45 - 1.85 eV as a function of sample temperature, T. The solid line shows the empirical rule

$$\nu = 8.6 \times 10^8 + 3.7 \times 18^8 \exp(T/104\ K).$$

B3.2.4 Conclusions

This study of the luminescence decay in a-P from 50-600 ps appears to bear out our earlier suggestion that the low energy PL band is associated with recombination of carriers trapped at pairs of oppositely charged defects. The temperature dependence of the initial decay rate follows the empirical law $\nu(T) = \nu_1 + \nu_0 \exp(T/T_0)$ despite the fact that, in the nanosecond time regime, the recombination channel changes to a different mechanism above 130 K. Conventional explanations of recombination meet with difficulty in explaining these observations, so we propose that there is a temperature-dependent branching ratio between two main recombination channels, both of which involve carriers trapped in a broad and shallow P_4^+ band.

B3.3 FEMTOSECOND DYNAMICS OF MULTIELECTRON DISSOCIATIVE IONISATION USING A PICOSECOND LASER

L J Frasinski, K Codling and P Hatherly (University of Reading)
J Barr, I N Ross and W T Toner (RAL)

The multiple ionisation of molecular nitrogen has been studied using an intense picosecond laser (0.6ps: 3×10^{15} W/cm^2: wavelength 600nm). By measuring the energies of the various fragment atomic ions (N^+, N^{2+} and N^{3+}) using a time-of-flight mass spectrometer it has proved possible to investigate the dynamics of the multielectron dissociative ionisation process on a time-scale of about 30 fs. Data was also obtained on a wide variety of gases, including Xe, HI and I_2 and is under analysis.

We do not wish to emphasise the multiphoton aspect of the multiple ionisation processes observed (ref B3.25) but prefer to describe the laser in terms of a classical electromagnetic field. The mechanism involved is thought to be similar to that invoked in order to explain the field ionisation of Rydberg atoms (ref B3.26) but in this case the laser field is so intense that it produces a potential difference across the molecule comparable with the binding energy of the outer electrons in the ground state.

The idea behind the experiment is quite straightforward. A diatomic molecule is subjected to a large electric field created by a focused picosecond laser. As the molecule is ionised beyond the single-ion stage, the fragment atomic ions mutually repel in the Coulomb field and the resulting energetic ions are detected by a time-of-flight (TOF) mass spectrometer. If additional electrons are stripped away as the molecule dissociates, the ions are now subjected to an even larger Coulomb repulsion. They will gain more energy and this will be reflected in the TOF spectrum. Thus, the detailed dynamics of multielectron dissociative ionisation (MEDI) can be investigated on a time-scale of femtoseconds (the dissociation time-scale), even though the laser pulse itself is of picosecond duration.

The basic components of the experiment were the following. A dye laser was pumped by a mode-locked, frequency-doubled Nd-YAG laser, producing 2.5ps pulses (0.6ps pulses with a saturable absorber in the dye). These individual pulses were amplified in a dye amplifier driven by a Q-switched frequency-doubled Nd-YAG laser operating at 10Hz. The laser light was focused down to a diffraction-limited spot by a f/3 doublet lens corrected for spherical aberration, and housed within the experimental chamber (base pressure 2×10^{-6} Torr). An identical doublet lens at the output was used to monitor the laser characteristics. The energy reaching the focal region at a wavelength of 600nm using a pulse length (FWHM) of 0.6ps was 50μJ per pulse, with pulse-to-pulse variations of ±20%. Approximating the pulse shape to a sech^2 function and taking into account that 70% of the energy was contained within the Airy disc of measured diameter 4.4μ (theoretical maximum 84%) leads to a peak power density of 3×10^{15} W/cm^2.

The gas was introduced into the laser focus region using a simple gas jet giving a pressure in the focal region of approximately 10^{-5} Torr. The resulting photoions were subjected to a field in the region of 10kV m^{-1} and traversed a drift tube of length 50mm. The ions passed through two concave meshes with radii of curvature egual to their

distances from the interaction region and were finally detected by a pair of 35mm diameter microchannel plates. The ion signal was fed via a preamplifier to a Lecroy 9400 Transient Digitiser with a 100 MHz sampling frequency. Low noise spectra such as those shown in Figures B3.14 and B3.15 were obtained in less than 10 minutes using a 0.5ps laser pulse width. Space-charge problems were avoided by running the experiment at low pressures but detector ringing was a problem that could not easily be removed - see oscillations in Figure B3.15(b).

The spectra obtained when air was introduced into the laser-focus region are shown in Figures B3.14 and B3.15. The peaks from N_2^+ and O_2^+ thermal ions are somewhat sharper than expected, indicating a degree of directionality in the gas beam. The mass and energy resolution is high due to the small size of the focal point. Those ions which have kinetic energies above thermal can be grouped into two catagories. Those that initially ejected towards the detector have TOF's that decrease almost linearly with their initial velocity but those ejected away from the detector with the same velocity range arrive virtually simultaneously at the detector. This focusing effect can be seen for the N^{2+} ions of Figure B3.14(a) occuring at TOF's between 2 and 3μs. Ions with an energy release spread of 10-30eV have a range of TOF's of 0.3μs, whereas those ions moving away from the detector and with an identical energy release spread arrive within a time interval of less than 0.05μs. The kinetic energy release scales were obtained using computer simulation of the ion trajectories and confirm this focusing effect which produces the sharp peaks for energetic ions N^+, N^{2+} and N^{3+} seen in Figures B3.14 and B3.15.

Before discussing the dynamics of N_2 multiple ionisation, it is worth noting the structure below 1μs in Figure B3.14(a), associated with energetic protons from unidentified hydrocarbon impurities from the gas-handling system. The scale below the trace shows the kinetic energy release in eV for H^+ produced from a C-H bond. It is not yet clear what process is responsible for producing protons with such high kinetic energies.

Let us turn now to the main structures observed in Figures B3.14(a), B3.14(b) and B3.15(b), obtained with voltages of 50, 100 and 200V respectively across the 12mm interaction region. The kinetic energy releases of the various N^+, N^{2+} and N^{3+} ions (the energies quoted relate to the peaks in the kinetic energy distributions) lead us to suggest the following sequence of events:

$$N_2 \rightarrow N_2^+ \rightarrow N_2^{2+} \rightarrow N^+ + N^+ + 7eV$$

$$\downarrow$$

$$[N_2^{3+}] \rightarrow N^{2+} + N^+ + 14eV$$

$$\downarrow$$

$$[N_2^{4+}] \rightarrow N^{2+} + N^{2+} + 25eV$$

$$\downarrow$$

$$[N_2^{6+}] \rightarrow N^{3+} + N^{3+} + 38eV$$

In Figures B3.14(a) and B3.14(b) there are peaks at 14eV in both the $N^+$and N^{2+} energy spectra and so their behaviour is assumed to be correlated. There is no convincing evidence, however, for correlated N^{2+} and N^{3+} ions. This may be because N_2^{5+}dissociates completely to N_2^{6+}. There is a peak in the N^{3+} energy spectrum at 38eV but no such peak is evident in the N^+ or N^{2+} kinetic energy spectra. This suggests that these energetic N^{3+} ions are the result of a Coulomb repulsion process with N_2^{6+} as parent. The heights of the peaks

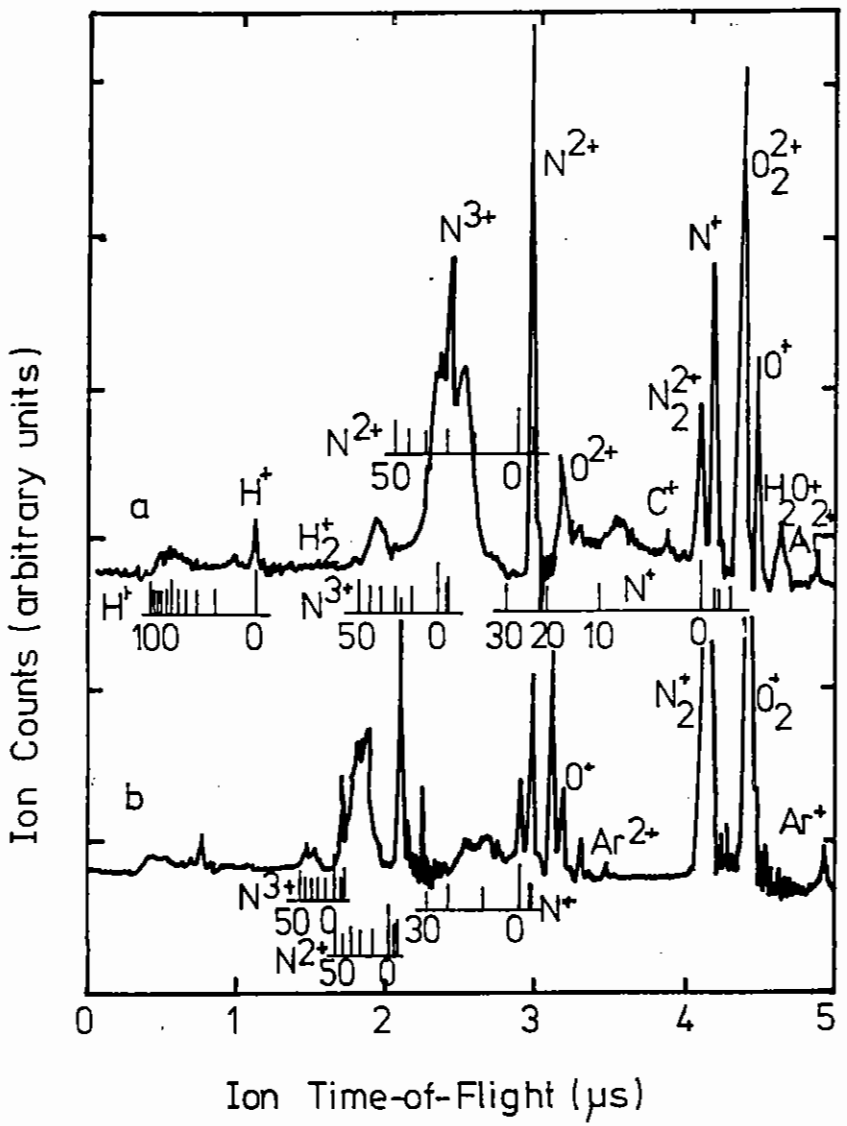

Fig B3.14 The time-of-flight spectrum of air, showing the various singly and multiply-charged atoms and molecules of nitrogen. The scales alongside are the kinetic energy releases in eV associated with the N^+, N^{2+} and N^{3+} ions. The structure associated with the energeitc protons is discussed briefly in the text.

(a) 50 volts
(b) 100 volts across the 12 mm interaction region.

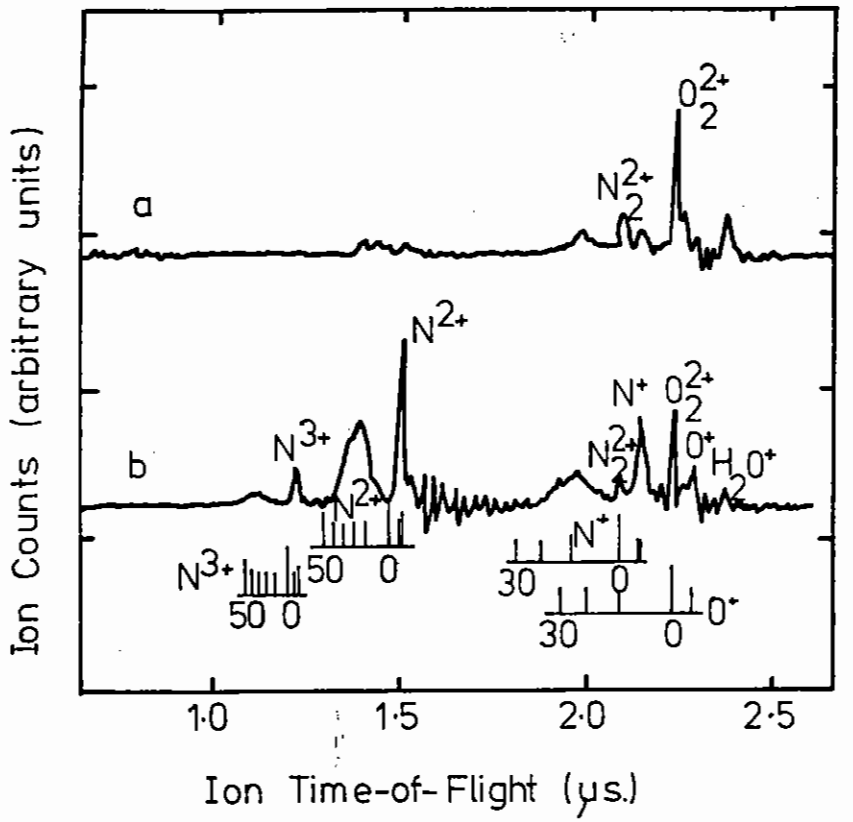

Fig B3.15 The time-of-flight spectrum of air with 200 volts across the 12mm interaction region. (a) E-vector of the linearly-polarised laser perpendicular to the axis of the drift tube, (b) E-vector along the drift tube axis. The small periodic flulctuations in signal reflect the digital sampling technique.

associated with the higher stages of ionisation were very dependent upon the laser peak power but their widths were not. The finite widths of these peaks in the kinetic energy distributions and their increase with ionisation stage may reflect a complex interplay between Franck-Condon overlaps, electron ionisation rates and oscillations of the laser field.

Although N_2^{2+} ions are known to be metastable (Ref B3.27), those N_2 ions involving higher stages of ionisation are presumably unstable. Certainly we see no evidence of such ions with thermal energies in Figures B3.14 and B3.15. It is therefore possible to make an estimate of the time-scale of the entire process $N_2^{2+} \rightarrow N_2^{6+}$. We take a simple model where the two positively charged ions repel each other with a pure Coulomb force and where the electron removal is instantaneous. Using the experimentally observed dissociation energies given above, the transitions $[N_2^{2+}] \rightarrow [N_2^{3+}] \rightarrow [N_2^{4+}] \rightarrow [N_2^{6+}]$ are found to occur at inter-ion separations (r) of 2.0Å, 2.5Å and 5.5Å respectively. The N_2^{2+} molecular ion starts to dissociate at 2.0Å and the time taken to increase r from 2.0 to 2.5Å and from 2.5 to 5.5Å is 10fs and 20fs respectively. The 9fs is a realistic estimate but the 8fs should be increased somewhat, because at small r-values and low ionisation stages the electron bonding is of the same order as the ion-ion repulsion.

In fact we know that the equilibrium internuclear separation of the metastable N_2^{2+} ion is 1.1Å rather than the 2Å value assumed in the model (ref B3.27). Taking this into account, we estimate that the $N_2^{2+} \rightarrow N_2^{6+}$ sequence takes about 20fs., which is only 10 periods of the incident laser field. This is about 5 times faster than the equivalent process observed in Xe using a 0.5ps, 193 nm laser (refs B3.28 and B3.29) (the $Xe^{2+} \rightarrow Xe^{6+}$ part of the multiple ionisation process is the fastest part of the entire $Xe \rightarrow Xe^{9+}$ process). The strong dependence of the amplitude of the N^{3+} peak on laser power leads us to believe that in this experiment the $N_2^{2+} \rightarrow N_2^{6+}$ process only occurs at the peak of the laser pulse and that the above increase in ionisation rate is to be associated with the rapid increase in potential difference across the molecule (caused by dissociation) rather than any time development of the envelope of the laser field.

While the behaviour of the heavy nuclei is quite well described by this simple model, that of the electrons is more problematical. The electron removal time may be comparable with the time-scale of the whole process and therefore the molecular ion stages are bracketed above. The initial picture of sequential multiple ionistion should perhaps be replaced by a complex multielectron dissociative ionisation (MEDI) process. The electron configuration of N_2 is KK $2\sigma_g^2\ 2\sigma_u^2\ 1\pi_u^4\ 3\sigma_g^2$. The N_2^{2+} ion results from the removal of the two outer electrons. The stage $N_2^{2+} \rightarrow N_2^{5+}$ corresponds to removal of the four $1\pi_u$ electrons. Neglecting the fine structure of the $1\pi_u^4$ subshell, then a single-electron picture would envisage the wavefunction of all four electrons evolving in the same way under the influence of the laser field. However, we can expect that electron correlations will modify this simple picture and the short time-scale of the MEDI process will add even more complexity. The whole process becomes diabatic and the Born-Oppenheimer approximation no longer applies. Clearly, the discussion of step-wise versus direct ionisation (refs B3.28 and B3.30) is not closed and a more advanced, time-dependent approach is required to clarify the situation and explain the present data in detail. Apparently, at the power levels employed here, the phenomenon is molecule-specific because a similar MEDI process is not observed in oxygen (see Figures B3.14 and B3.15) nor is it in hydrogen iodide (Ref B3.30). Experiments using H_2, HD and D_2 should throw considerable light on the situation, since the theoretical treatment will be much easier in this case.

The phenomenon depicted in Figures B3.15(a) and (b) is perfectly consistent with this classical field ionisation model. Figure B3.15(a) shows the TOF spectrum when the E-vector of the linearly polarised laser beam is perpendicular to the axis of the drift tube.

Figure B3.15(b) has the E-vector along the drift tube axis. The energetic ions are ejected preferentialy along the E-vector. That is, the molecules are ionised only when their axes are close to the direction of the E-vector. The explanation of this effect is simply that the potential difference created by the laser field is larger along the molecular axis than at right angles to it and thus the potential barrier is not so high.

B3.4 RESONANCE RAMAN SCATTERING IN GaAs-AlAs SUPERLATTICES

S R P Smith (Department of Physics, University of Essex)

The LL6 argon ion-pumped CW dye laser system has been used to investigate resonance Raman scattering in GaAs-AlAs superlattices. Preliminary investigations have concentrated on the GaAs LO-phonon region, where the optic phonon modes show several bands due to the confinement of the excitation to the GaAs layers. The excitation frequency is in effect determined by fitting an integral number m of optic phonon half-wavelengths into a GaAs layer. If m is odd, these modes are observable under non-resonant conditions because the scattering intensity is determined by the usual deformation potential type of interaction, whilst if m is even,, the scattering intensity comes from the Frohlich interaction and is only observable near to an electronic resonance. The resonance condition used is that in which the exciting laser frequency is close to the energy of the n=1 heavy hole exciton in GaAs (∿ 1.86 eV).

The Raman scattering experiments were performed in the back-scattering configuration with light incident upon the (001)-oriented face of GaAs-AlAs superlattices grown by molecular beam epitaxy at Philips Research Laboratories, Redhill. The sample temperatures were either 77 K or ∿ 10 K, and the scattered light was analysed using a computer-controlled Spex 1401 double monochromator with photon counting detection. The spectra were excited using around 500 mW from DCM dye, with about 4 W of Ar+ pump.

Figure B3.16 shows a typical spectrum obtained from sample D420, which contained 20 layers of GaAs-AlAs superlattice with $d_1=d_2=27.8$ A, followed by 40 layers of superlattice in which $d_1=55.6$ A, $d_2=27.8$ A (with the middle region of the GaAs layers doped n-type) on a GaAs substrate, the whole with a .1 μm capping layer of GaAs. The modes observable in the figure are: (A) the GaAs LO mainly from the capping layer; (B) and, (C) the resonantly-enhanced even-m confined modes of the superlattice structure; (D) leakage from the TO modes; and (E) is tentatively assigned as an electromagnetic interface mode. These modes and their assignments are similar to those observed by Sood et al. (Ref B3.31). They were excited at a laser frequency of 14 850 cm^{-1}, and the exciton peak occurred at 14 366 cm^{-1} at 10 K. The resonant enhancement has been studied as a function of the exciting laser frequency, and it is clear that the enhancement of the superlattice modes (B)-(E) is much more pronounced than that of the capping layer mode (A).

A principle part of this investigation is the study of plasmon excitations in superlattices, which are expected to be observable only under conditions of resonant enhancement. So far, these preliminary measurements have not shown any clearly defined plasmon features, but measurement on similar structures, both doped and undoped, is still being carried out. A detailed analysis of the intensity behaviour and frequencies of the measured phonon modes is in progress, from which information about the phonon structure and the light scattering mechanism can be obtained.

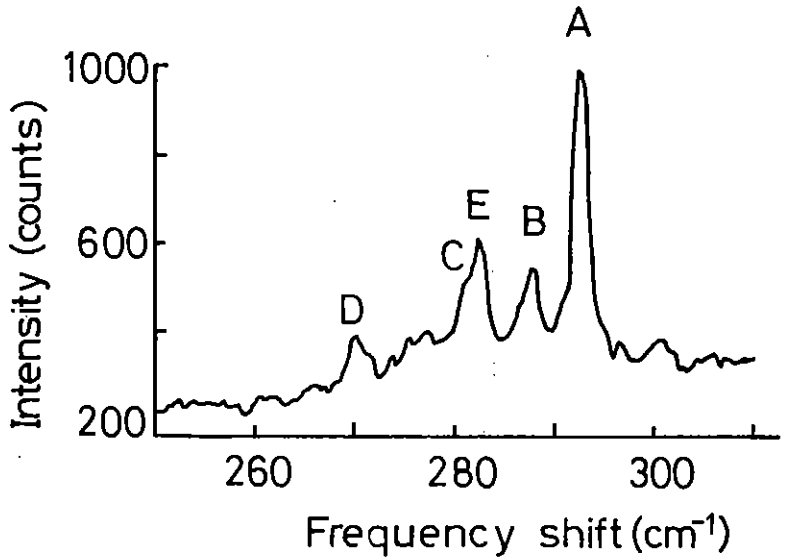

Fig B3.16 Spectrum of sample D420.

B3.5 PICOSECOND GAIN AND PROPAGATION MEASUREMENTS AT 249nm

I N Ross. W T Toner, J M Barr (RAL), Y P Kim (Imperial College)

The first experiment in a programme to look at picosecond dynamics at a wavelength of 249nm was carried out in the LSF with the following aims:

(i) to measure the energy extractable on a pulse of a few picoseconds duration from the EMG 150 laser

(ii) to estimate the difficulty of keeping the amplified spontaneous emission down to a reasonable level

(iii) to determine the extent to which the output beam departs from diffraction limit under optimum conditions

(iv) to estimate the threshold and magnitude of the spectral broadening generated when such a high power beam is focused into air

(v) to investigate several methods of measurement of the nonlinear refractive index (n_2) and possibly obtain an estimate of n_2 for fused silica

(vi) to measure the spectral changes in the nonlinear processes used to generate the input beam at 249nm.

Further, more quantitative experiments are planned to follow up this preliminary work.

Figure B3.17 shows a schematic of the experimental layout. The picosecond dye laser and amplifier generated pulses at 628nm, followed by the second harmonic and mixing crystals which generated 10-20μJ at 249nm (B3.32). These seed pulses were spatially filtered and amplified by the EMG150 using its gain sections as single pass amplifiers in series. The optics were designed to provide close to diffraction limited pulses at the input of the EMG150 and to provide good ASE isolation between the two sides of the EMG150.

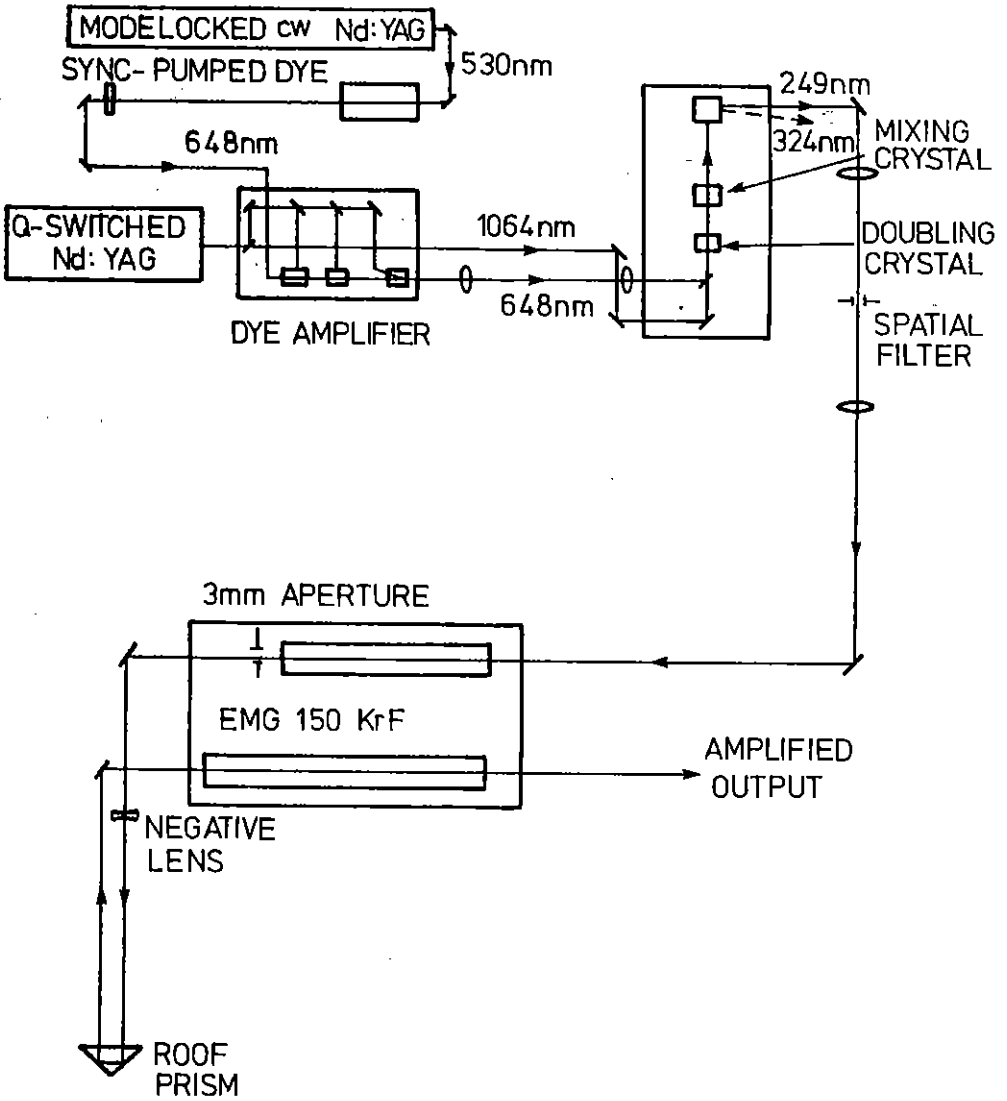

Fig B3.17

A cw power meter was used to measure the mean power output under 10Hz operation. Maximum pulse energies calculated from these measurements were 27mJ with typical shot to shot variations of up to 50%. Beam size was approx 30 x 15 mm giving an output intensity of 6mJ/cm^2. Figure B3.18a shows the near field spatial profile of the output beam showing good uniformity and demonstrating a high level of amplifier saturation.

The ASE from the first gain section amplified by the second was expected to be a problem but measurement of the output ASE energy showed it to be easily filtered down to the few percent level and indicated an increase of only 30% due to amplified ASE from the first gain section.

The far field spot size was estimated by measuring the pinhole size in the focal plane of a lens which transmitted 50% of the beam energy. This size was measured at 2.7 times the expected pinhole size for a diffraction limited beam, suggesting a peak focal intensity of 1/7 x diffraction limited intensity. For an estimate of the focal intensity achievable let us assume the use of an F/2 lens, and let the pulse duration be 5ps. Then:

Peak intensity $\approx 2 \times 10^{17}$W/cm^2

Fig B3.18b shows densitometer traces across the far-field intensity distribution for both the injected beam and the final amplified output beam. There can be seen to be some small imperfection on the input beam, which is correctable, and only a small degradation due to amplification, which may not be correctable.

Spectral measurements were made using a grating disperser (1800 l/mm working in 3rd order) and long focal length lens. Spectra were recorded with the beam focused in air and with the beam left unfocused, and compared. Figure B3.19 shows typical examples of each and includes the ASE spectrum in the background (showing input wavelength not quite perfectly matched to peak amplifier gain wavelength). The unfocused beam spectrum was typical of the input beam with a FWHM of 11cm^{-1} showing it to be not close to the transform limit and variable from shot to shot. The focused beam spectrum had a typical FWHM of 55cm^{-1} (similar to FWHM of ASE) and showing significant intensity over a bandwidth of 200cm^{-1}. Similar picosecond continua have been reported by (B3.33).

Other observed effects associated with this spectral broadening were an audible crack but with only the faintest of evidence of white light emission in the focal region and a blue fluorescence which extended by as much as 20cm on either side of the focus of a 2m lens.

Over the small parameter range tested the threshold of the effects was, as expected, only dependent upon the beam power. The threshold energy was measured at 0.8mJ giving a threshold power, assuming a 5ps pulse, of 160 MW. It is however expected that the beam will suffer less severe nonlinear effects at reduced power levels.

Measurement of n_2

Four methods of measurement of the nonlinear refractive index n_2 were assessed and compared. The test sample was a fused silica flat and in all measurements a comparison was made between the front and back reflections. The difference between these two reflections results only from the nonlinear effects in the silica which are characterised by the B-integral (B) where, for λ = 249nm:

$B = 0.1\ n_2\ II$

where II is the intensity length product in the silica and n_2 is in esu x 10^{13} for II in GW/cm. At 350nm and 1060nm, n_2 for silica has been measured to be 1.0×10^{-13} esu. (Ref B3.34).

a) Focal spot intensity

The focal spot intensity was assessed by measuring the energy transmitted by an aperture in the far field with a diameter equal to the 'diffraction limited' spot size. The fraction of energy passing through this aperture was the same for the front and back reflections and was not therefore sensitive to the nonlinear response of the silica plate. Shot to shot movements of the farfield distribution with amplitudes of about the diameter of the aperture and probably

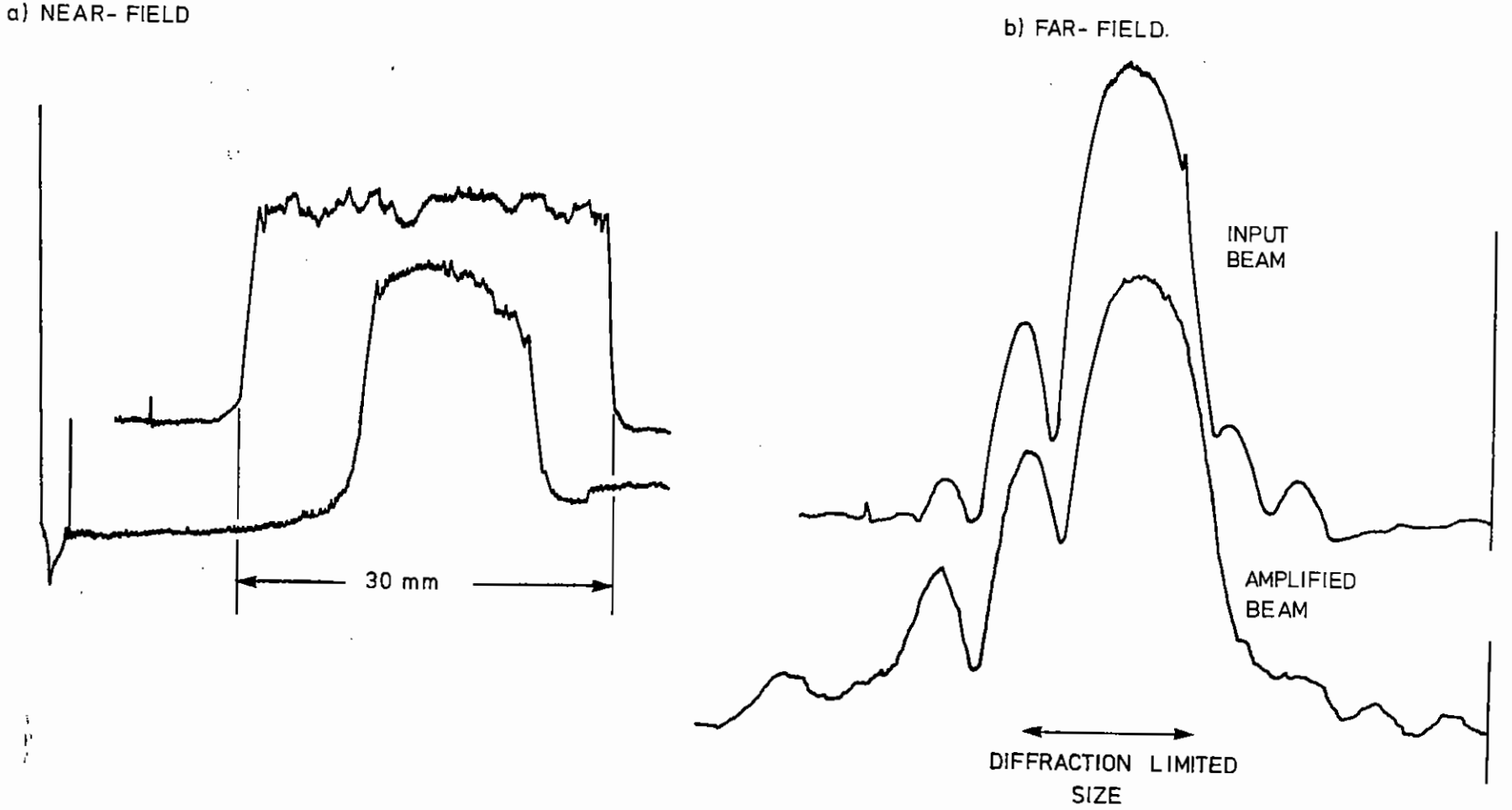
a) NEAR- FIELD
30 mm
b) FAR- FIELD.
INPUT
BEAM
AMPLIFIED
BEAM
DIFFRACTION LIMITED
SIZE

Fig B3.18

caused by room air effects are thought to have seriously affected the accuracy of the measurement.

b) Off-axis intensity enhancement in far field

One effect of n_2, and directly dependent upon the B-integral, is the enhancement of beam intensity fluctuations over a range of spatial frequencies. The maximum gain in modulation is given by $G_0 = \exp B$ for a spatial frequency given by $\omega_0 = 140\sqrt{(B/l)}$ at $\lambda = 249nm$.

Since a given spatial frequency in the near field corresponds to a given distance off-axis in the far field, it is expected that an enhancement of off-axis intensity will be observed over a range of off axis distances equivalent to the spatial frequency range around ω_0.

An aperture in the far field plane was used to select the spatial frequency range $50 \leq \omega \leq 100cm^{-1}$ over which there was expected to be considerable enhancement. An enhancement by a factor 1.7 was measured. However due to the low magnitude of the signal and the presence of noise from scattered light it was concluded that this was not a promising method for a quantitative measurement of n_2.

c) Enhancement of spatial frequencies in the near field

From the previous section we note that the maximum enhancement factor $G_0 = \exp B$ occurs for a spatial frequency $\omega_0 = 140\sqrt{(B/l)}$, where the B-integral, $B \approx 0.1\ n_2\ Il$.

Analysis of the near field beam distribution before and after the silica plate provides a measurement of G_0 and ω_0 and hence two ways of calculating B and hence n_2.

Fig B3.20 plots the intensity distribution across the two near-field profiles and clearly shows the enhancement of certain spatial frequencies. The 'worst' spatial frequency ω_0 was measured to be $125cm^{-1}$ and its enhancement G_0 to be x 10. These both gave values of $B \approx 2.5$ and using an estimated intensity-length product in the silica plate of 50 GW/cm, n_2 was estimated to be 0.5×10^{-13}esu.

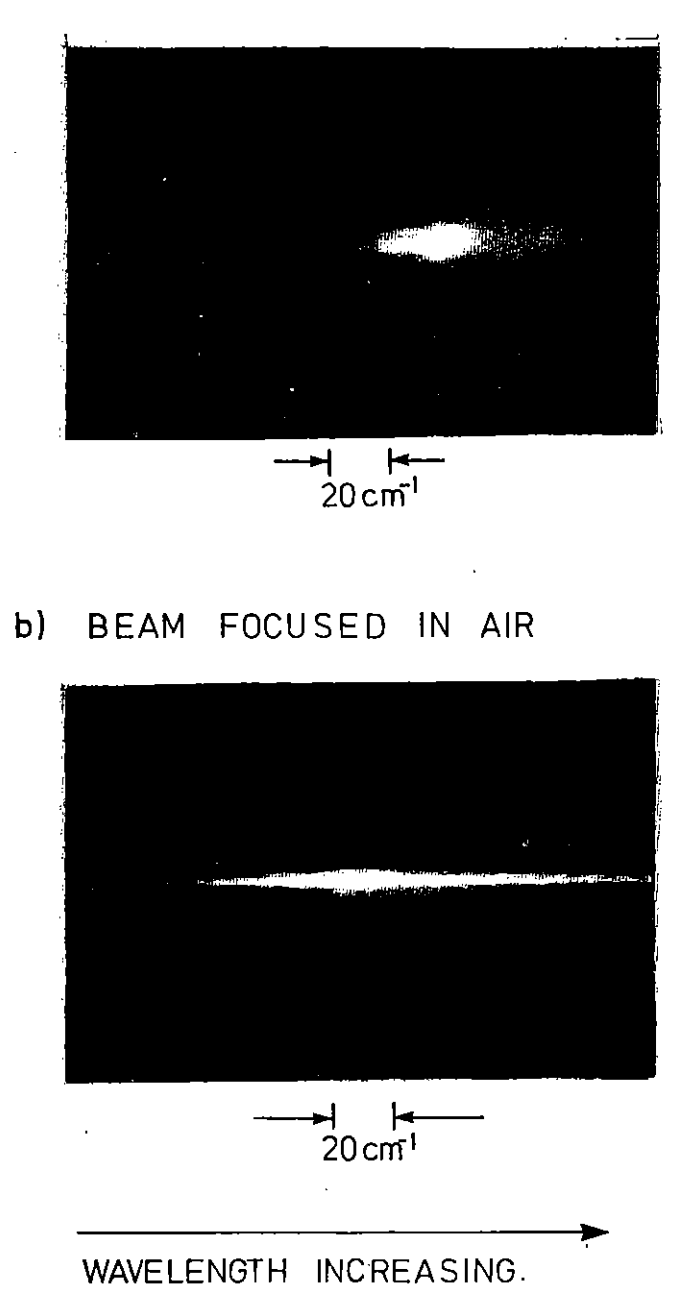

Fig B3.19

d) Spectral Broadening

The non-linear index leads to a positive rate of change of phase $d\phi/dt$ or a positive frequency shift on the rising edge of a short pulse and to a negative $d\phi/dt$ and hence a negative frequency shift on the trailing edge of the pulse. Consequently there will be a broadening of the spectrum. For a transform-limited Gaussian pulse at a wavelength of 249nm, an approximate expression for the spectral broadening at the 1/e intensity level is given by:

$$\frac{\text{Broadened linewidth}}{\text{Input linewidth}} - 1 \approx 0.44B^2$$

Fig B3.21 plots the intensity distribution across the spectra of the front and back reflections from the silica plate. The spectral broadening is evident and measurement of the width of these curves at the 1/e points together with the above equation gave an estimate for the B-integral (B) = 0.8.

But $B = 0.1 n_2 I.l$ and in this instance Il was 9GW/cm.

$\therefore n_2 \approx 0.9 \times 10^{-13}$

One must be sceptical of the low measured values for n_2 when it was expected that n_2 would increase rather than decrease into the ultraviolet. It may be that the pulse length is greater than the assumed 5ps. However one can be optimistic that n_2 is not significantly larger than that measured at visible wavelengths.

The spectral broadening technique was more sensitive than the near field spatial frequency measurement but cannot give as accurate values for n_2 unless the temporal profile is known and the pulse is transform limited. It does make a good monitor for the onset of n_2 effects.

Spectral changes in the generation of 249nm

Measurement of the single shot spectra at 324nm (doubled dye laser) and 249nm indicates the performance of the final nonlinear mixing

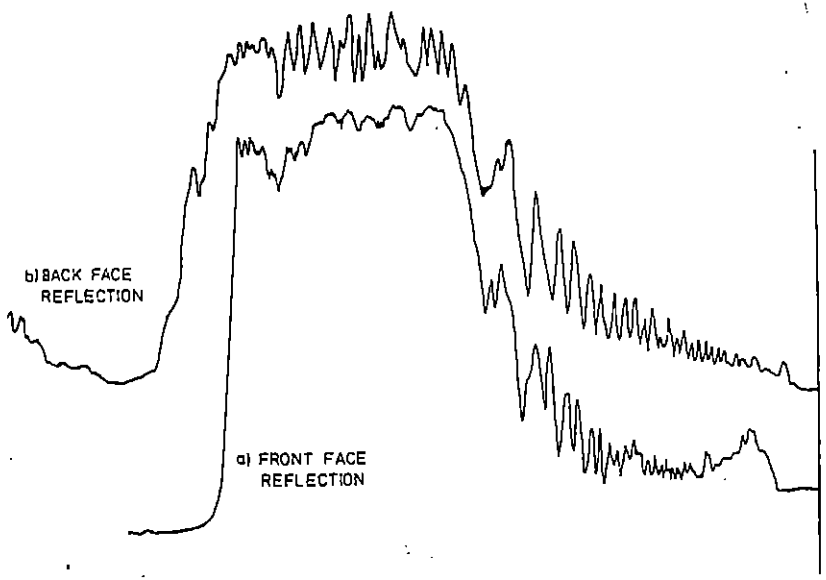

Fig B3.20

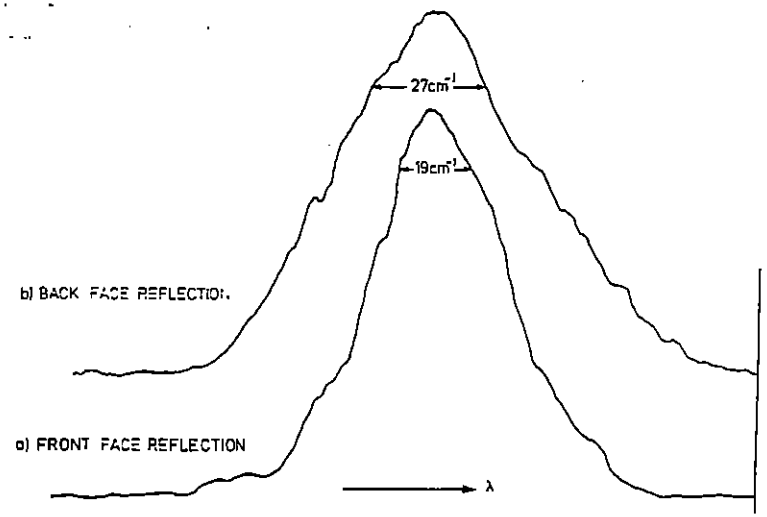

Fig B3.21

process which converts 324nm to 249nm. If the relative spectral distributions are predictable without invoking a crystal bandwidth limit then it is reasonable that the temporal profile is predictable and not lengthened by the nonlinear process.

Fig B3.22 shows typical spectra at 324nm and 249nm as recorded on photodiode arrays (but not for the same pulse). The 249nm linewidth was slightly larger than the 324nm linewidth whereas, since the mixing pulse at 1064nm is a long pulse with a narrow spectral line, it is expected to be the same. The difference is not significant due to the considerable shot to shot changes in spectral width, and it is concluded that the pulse duration does not change significantly in the wavelength conversion processes under the conditions of these experiments.

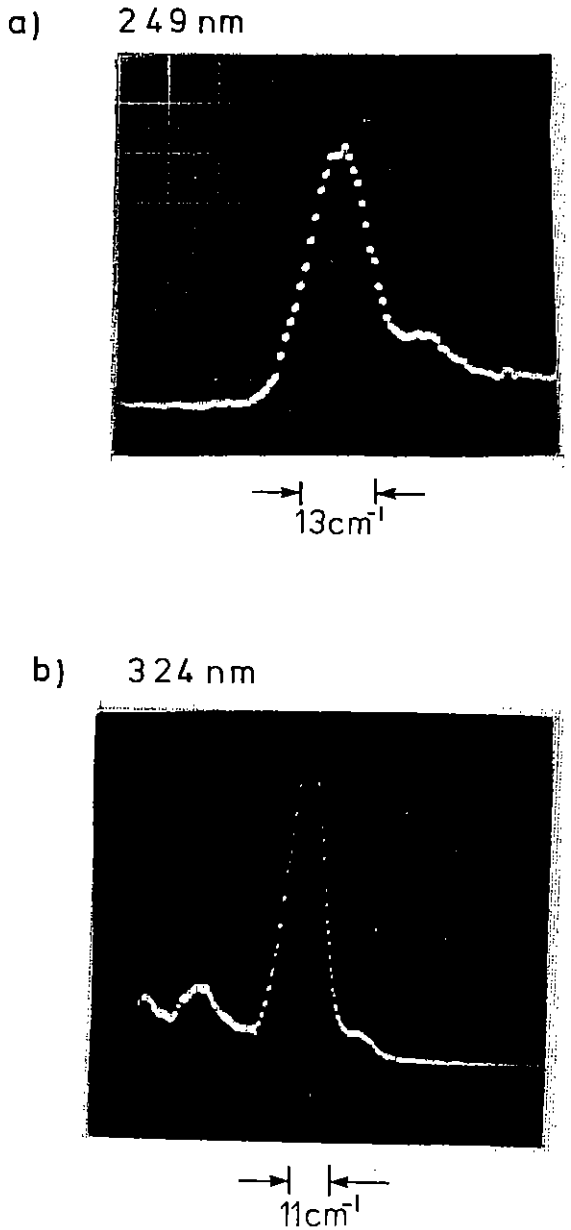

Fig B3.22

References

B3.1 I T F Gillan, D J Denvir, J Bechara, H F J Cormican, I Duncan, W D McGrath and T Morrow, Rutherford Appleton Laboratory, Laser Division Annual Report, Report No. RAL-85-047, Sec B.3.4, B53 (1985).

B3.2 I T F Gillan, D J Denvir, D G Cunningham, H F J Cormican, I Duncan, W D McGrath and T Morrow, Rutherford Appleton Laboratory, Laser Division Annual Report, Report No. RAL-86-046, Sec B3.3, B3.4 (1986).

B3.3 M D Burrows, S L Baughcum and R C Oldenborg, Appl Phys Lett 46, 22 (1985).

B3.4 Aa S Sudbø and M M T Loy, J Chem Phys 76, 3646 (1982).

B3.5 T Ebata, M Mikami and M Ito, J Chem Phys, 78, 1132 (1983).

B3.6 M Asscher and Y Haas, J Chem Phys, 76, 2115 (1982).

B3.7 M W Wilson, M Rothschild, D F Muller and CK Rhodes, J Chem Phys, 76, 4452 (1982).

B3.8 J E Hesser, J Chem Pys, 48, 2518 (1968).

B3.9 K L Wray, J Quant Spectrosc Radiat Transfer, 9, 255 (1969).

B3.10 A B Callear and M J Pilling, Trans Faraday Soc, 66, 1618 and 1886 (1970).

B3.11 H Scheingraber and C R Vidal, J Opt Soc Amer, B2, 343 (1985).

B3.12 S Cieslik and M Nicolet, Planet Space Sci, 28, 105 (1973).

B3.13 M C Lin, IEEE J Quant Elect, QE10, 516 (1974).

B3.14 G Fasol, A D Yoffe and E A Davis, J Phys C15, 5851,(1982)

B3.15 Z Sobiesierski and R T Phillips, Solid State Commun 60, 25, (1986).

B3.16 G Fasol, J Phys C18, 1729, (1985).

B3.17 E A Wilson and T P Kerwin, Phys Rev B25, 5276, (1982).

B3.18 S Depinna and B C Cavenett, J Phys C16, 7063 (1983).

B3.19 W C Chen, B J Feldman, J Bajaj, F M Tong and G K Wong, Solid State Commun 38, 5923, (1983).

B3.20 For a different approach see F Boulitrop and D J Dunstan, Phys Rev B28, 5923, (1983) and D J Dunstan and F Boulitrop, Phys Rev B30, 5945, (1984).

B3.21 M Kastner, J Non-Crystalline Solids 35 and 36 807 (1980).

B3.22 Z Sobiesierski and R T Phillips, Proceedings of the International Conference on Non-Crystalline Semiconductors, Balatonszeplak, Sept 1986, to be published in Journal of Non-Crystalline Solids.

B3.23 B A Wilson, P Hu, T M Jedju and J P Harbison, Phys Rev B28, 5901, (1983).

B3.24 R Jones, Private Communication.

B3.25 "Multiphoton Ionisation of Atoms" edited by S L Chin and P Lambropoulos (Academic. New York, (1984).

B3.26 "Rydberg State of Atoms and Molecules" edited by R F Stebbings and F B Dunning (Cambridge University Press, Cambridge, (1983).

B3.27 E W Thulstrup and A Andersen, J Phys B 8, 965 (1975).

B3.28 A L Robinson Science 232, 1193 (1986). P Lambropoulos Physics Today 40, S25 (1986).

B3.29 U Johann, T S Luk, H Egger and C K Rhodes, Phys Rev A 34, 1084 (1986).

B3.30 K Codling, L J Frasinski, P Hatherly and J Barr, J Phys B to be published.

B3.31 A K Sood, J Menendez, M Cardona and K Ploog, Phys Rev Lett 54, 2111 (1985).

B3.32 J R M Barr, I N Ross, W T Toner, RAL Annual Report to the Laser Facility Commitee RAL-86-046 C3.3 (1986).

B3.33 J H Glournia, G Arjavalnigam, P P Sorokin, J E Rothenburg, Opt Lett 1, 79 (1986).

B3.34 W T White, D Milam, Lawrence Livermore National Laboratory Annual Report, 7-39 (1982).

Editor: W Toner

B4.1 RAL BASED OPERATIONS

J Szechi, J R M Barr, S Tavender, W T Toner, RAL

4.1.1 Nanosecond Laboratories

The major acquisition during the past year for the in-house nanosecond program has been a Lumonics HX460 excimer laser. This laser operates at 308 nm and can be used in two configurations: a) up to 200mJ/pulse at up to 200 Hz; or b) up to 400mJ/pulse at up to 80 Hz, with 30 watts maximum average power. It is being used to pump a new Lambda Physik FL3002 dye laser, and replaces the old EMG101E/FL2002 excimer pumped dye laser, which has joined the pool of loan lasers. Another new FL3002 dye laser has also been purchased, for use either as another loan laser or to add flexibility to the in-house program (for example, see B3.1).

The performance of the Triplemate spectrometer has been enhanced by the addition of a new 3600 g/mm UV grating in the spectrograph stage, and a new sample stage for solid samples is currently under development (see section B1.6). After the extensive work by Dr Chittock described in section B4.3, the new OSMA-SI intensified diode array is now working well, and some very interesting results have been obtained using it (for example, see section B2.5). The LSF Sample Preparation Laboratory has recently taken delivery of a laminar flow cabinet to be used for clean preparation of samples and a gassed incubator.

At the end of 1986, the EMG150ETS excimer laser, which is now four years old, was taken out of service for ten weeks and a major overhaul was carried out. This resulted in improved locking efficiencies, gas lifetimes at least 30% longer, and higher laser energies. The stability of the line-narrowed KrF source was investigated, and the main problem found to be variations in room temperature. Measuring the temperature of the prisms, the line shift is in the region of 3.3 cm^{-1} per degree C. Improved operating procedures to minimise temperature fluctuations are now in effect. The linewidth of the injection locked system was measured as 0.45 cm^{-1} averaged over 20 shots, and over a period of twenty minutes during which the room temperature remained constant this did not increase and the wavelength did not alter appreciably. Several mechanical improvements have also been recommended and these will be carried out as soon as possible.

Six weeks of Division Head's time on the dye laser in early 1987 were not assigned due to staff shortages.

B4.1.2 PICOSECOND LABORATORY

During the year, nine separate experiments ran in the picosecond laboratory for a total of 45 weeks and 5 weeks were devoted to facility development. The CW mode-locked YAG laser operated for 2500 hours and there were just two days lost due to a minor electronic problem. Four flashlamp changes were made. For the last six months the laser has been run to produce 1 watt average power at 532 nm and its output has been divided between the sync-pumped dye laser operating for scheduled LSF experiments and a second sync-pumped system in the adjacent development laboratory. No difficulties were experienced on either side in achieving reliable operation at full specification.

Part of the facility development time was spent investigating the cause of the substantial pulse-to-pulse fluctuations of the amplified output at 10Hz. This was found to be largely due to mode beating in the DCR Q-switched YAG laser which pumps the dye amplifier and appears to be an intrinsic consequence of the design of the system. A potential but very expensive cure would be the injection of a single mode seed pulse from a diode laser; in the meantime users have adapted to the varying output pulse energy (see, e.g., section B1.12).

Time was also devoted to the installation and optimisation of the cavity dumper and pulses 3 picoseconds in length were produced through the addition of a saturable absorber to the laser dye. Up to 760µ watts of average power were produced in the frequency doubled UV output, at 4 MHz (see section C3.3). Further extensions were made to

the wavelength coverage (see section C3.1). The remaining facility development time was used to prepare the laser for the multiphoton experiment (B3.3) and characterise its output and optics. The single shot analyser, developed off-line (section C3.2) was used for some of this work.

Experimental diagnostics were further developed during the normal scheduled runs. Improvements to the pump and probe system described in B1.12 now enable experiments to run under full computer control.

Streak camera runs in the second half of the year were hampered by various faults, some due to misuse. These have been repaired and the trigger system can now operate through a constant fraction discriminator to give reduced jitter. UV sensitivity has been improved by an order of magnitude and a fully two dimensional CCD camera readout has replaced the Vidicon OMA (section B4.4).

Staff shortages prevented work beginning on the photon counting system, equipment for which is on hand.

B4.2 LOAN POOL OPERATIONS

A J Langley RAL

During its second year of operation the Laser Loan Pool has continued to provide lasers and diagnostic equipment to users within their own laboratories. A total of 16 laser loans and 4 diagnostic loans, of approximately 3 months duration, have been made to 1 polytechnic and 13 University research groups. Work carried out by these groups have so far resulted in 10 publications - scientific results are presented in sections B1.7, B1.8, B1.9, B1.10, B1.11, B1.1.5, B1.16, B1.17, B1.19, B1.21, B1.22 and B3.4.

Demand for loan systems continues to be high particularly for the sophisticated Nd:YAG/Dye laser combinations with tunable UV to ir options for which demand often exceeds supply by ∿ 1.5. A list of loan lasers and equipment available in 1987 is given in Table B4.1. (The average duration of loans was three months).

The intensive use and frequent transportation puts a heavy demand upon the reliability of the sophisticated loan lasers. The experience during the past year has been that the frequency of laser malfunction is only marginally more than might be expected for similar static systems. Maintenance and repair are usually carried out by LSF staff or where necessary by Laser Manufacturers who generally respond efficiently to problems.

B 4 . 3 DEVELOPMENT OF OSMA DETECTOR SYSTEM

Dr R Chittock, Dept of Biochemistry, University of Birmingham

B4.3.1 Analytical Software Development

During the year we have developed and extended the software of the OSMA diode array detector and its computer control system. Programs have been written in the BASIC dialect of this computer. The most useful addition has been an implementation of Savitsky-Golay smoothing, since the smoothing routine supplied with the system has been found unsuitable for use with our data and that of several other groups.

Other programs written include improved calibration, background subtraction and interfacing software for the RS232 port of the OSMA terminal. This communication facility has been used to transfer files to a BBC microcomputer for which we have written a suite of data analysis programs, including interactive graphics with hard copy, smoothing, data handling and background subtraction routines. Although the limitations of the BBC make this software inferior to that available on the OSMA in many respects, it allows the lengthy process of data analysis to be conducted 'at home' rather than during scheduled laser time. In addition, data can be analysed while the OSMA is performing another experiment. This system is still under development (current version 1.2).

B4.3.2 Resolution, Sensitivity and Integer Arithmetic

We have found that the sensitivity and resolution of the OSMA system is limited by its use of integer arithmetic. This causes problems with small signals obtained during data accumulations involving several scans of thediode array. The final spectrum produced is

Table B4.1

	Laser system	Operational from	Loans to date
LL1	JK 2000 Pulsed Nd:YAG 500mJ at 1064nm, 130mJ at 532nm and 50mJ at 355nm. JK 2000 dye laser 0.1cm^{-1} line width at 30mJ at 560nm. 10Hz	April 85	10
LL2	Quantel Datachrome 5000. Nd:YAG 700mJ at 1064nm, 250mJ at 532nm and 80mJ at 355nm. 20Hz. Quantel Dye Laser. 0.08cm^{-1} width and 50mJ at 560nm	May 85	9
LL3	(a) J K Hyperyag 750 Nd:YAG 800mJ at 1064nm, 300mJ at 532nm, 170mJ at 355nm and 100mJ at 266nm	Jan 87	2
	(b) Quanta-Ray PDL dye laser and WEX with full range of doubling and mixing options. 60mJ at 560nm	March 87	1
LL4	Lambda Physik EMG101 Excimer (chlorides) 6.5W at 40Hz. FL2002 dye laser with computer controlled scanning and frequency doubling	May 86	4
LL5	Lambda Physik FL3002 dye laser	May 86	RAL based so far
LL6	Spectra Physics 2025 UV/VIS Ar Ion laser 5W vis/.4W UV. Single line (.2cm^{-1}) and single frequency		
	(10^{-4}cm^{-1}) options Spectra-Physics 375 Dye Laser Optics for 550-800nm operation 700mW at 590nm with min 20GHz line width	Jan 87	1
LL7	Lumonics Hyper Ex 460 Fluoride excimer laser	June 87	
Diagnostic loan equipment			
LD1	Imacon 500 S-20 streak camera Film readout	June 86	1
LD2	2 gated integrators (SR250), 1 fast sampler (SR255), 1 computer interface (SR245), 1 analogue processor (SR235), 1 gate scanner (SR235), 1 gate scanner (SR200), 1 main frame (SR280)	May 86	2
LD3	2 gated integrators (SR250), 1 computer interface (SR245), 1 gate scanner (SR200), 1 main frame (SR280)	March 87	1

the average signal from the scans, rather than the total signal. Since the computer only deals in integers, all fractions produced by this averaging are dropped or rounded up, causing weak signals to appear as spikes or to disappear completely. An example of this effect is shown in Fig B4.1a.

This problem may be overcome by using the 'Asynchronous Sequential Scans' option of the OSMA initialisation software, which enables each scan to be stored separately rather than as a single averaged spectrum. These spectra can be summed at the end of the run to produce a single total large enough to overcome loss of resolution. This can be done by hand using the the OSMA data handling software or using a BASIC program we have written. The improvements possible by using this technique can be seen by comparison of Fig B4.1a (normal) with Fig B4.1b (addition of sequential scans).

This problem may also arise due to the reduction in height of weak signals during smoothing. Here it can be overcome by multiplying the spectrum by a scaling factor prior to smoothing.

B4.3.3 Noise Analysis of the OSMA Detector

We have used the BBC microcomputer to analyse the background noise of the diode array in cooled and uncooled operation. Two types of analysis have been performed. The first method examined the distribution of dark diode noise from a single background spectrum. Any overall slope was removed by subtracting the best straight line fitted through the points by linear regression. The distribution of dark noise was represented as a histogram. Fig B4.2a shows such a distribution from an array operated without water cooling. Two separate normal distributions can be seen, corresponding to two separate populations of diodes within the array. When the original spectrum is expanded a 'saw-tooth' pattern is seen (Fig B4.2b), showing that the two populations correspond to the odd and even numbered diodes of the array. Figs B4.2c and B4.2d show the corresponding spectrum and noise distribution when the array is water cooled. The difference in noise between the two populations is supressed. We conclude that the performance of the diode array is improved by water cooling.

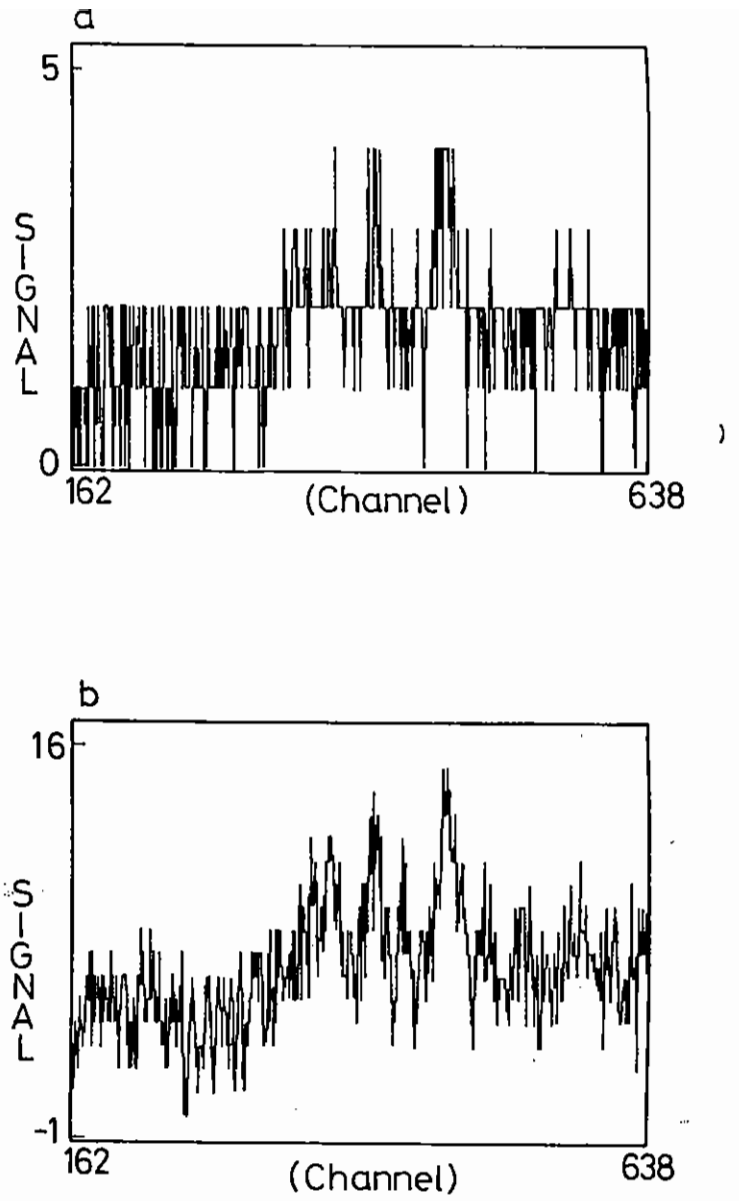

Fig B4.1 Resonance Raman spectra of 350μM NAD. (a) Total of 2 runs each consisting of 125 exposures of the diode array. (b) Total of 2 runs each consisting of 5 sequential scans comprising 25 exposures of the diode array.

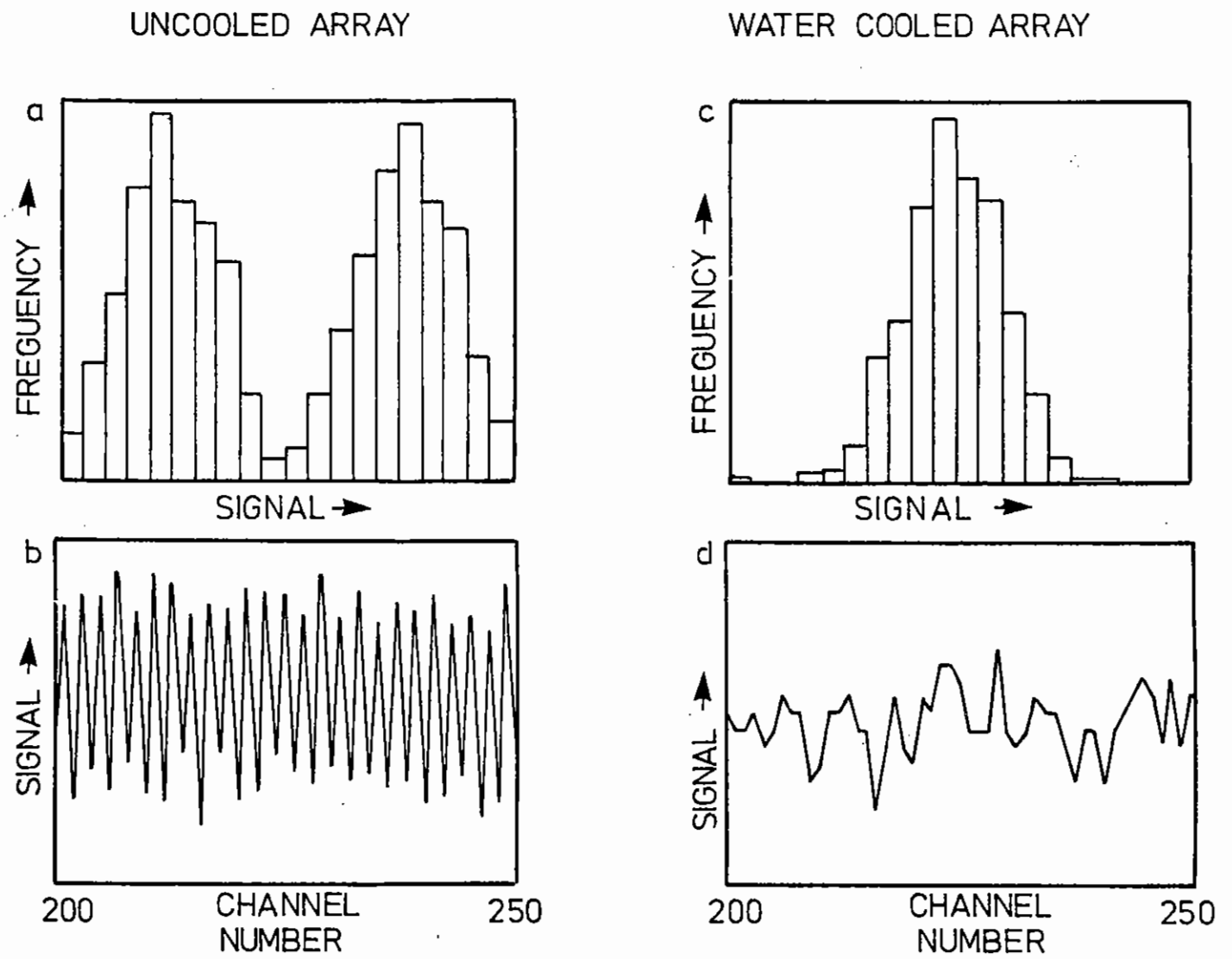

Fig B4.2 (a) Noise distribution of dark spectrum from an uncooled diode array. (b) Expanded dark spectrum from uncooled diode array. (c) and (d) as (a) and (b) but from a water cooled diode array.

The two diode populations may also become apparent in very strong signals such as those produced by a high sample fluorescence or when using poorly matched signal and background spectra. This effect is seen as an excessively broad trace, which on expansion of the x-axis will reveal the characteristic 'saw-tooth' pattern. It arises from the differing light sensitivities of the odd and even numbered diodes. Such spectra can be improved by separating signals from odd and even diodes and filling in gaps by interpolation. Alternatively, the spectrum can be smoothed in the conventional manner.

The second method of noise analysis employed was the 'double y' plot. This uses 2 dark spectra and plots the signal for each diode in one spectrum against the signal from the corresponding diode in the second spectrum. Thus if the background noise arises from random sources the plot will be an uncorrelated scatter of points. However, if noise level is a function of diode position, then the plot will show a positive correlation. Fig B4.3a shows a 'double y' plot between two dark spectra. The high positive correlation coefficient indicates that the observed background signal is a function of diode position, i.e., each diode has its own particular background noise level. In Fig B4.3b both spectra of Fig B4.3a have had separate background spectra subtracted as would be done in a normal Raman experiment. The 'double y' plot now appears as a random distribution with a very low correlation coefficient, i.e., by subtracting a background from a signal spectrum the contribution of differential diode dark activity is removed. The remaining signal is due to random sources, such as thermal noise. We conclude that a dark background spectrum should always be subtracted from a signal spectrum.

B4.3.4 Conclusion

From the foregoing it is clear that the OSMA system is now usable for Raman spectroscopy experiments, though some software development remains to be done.

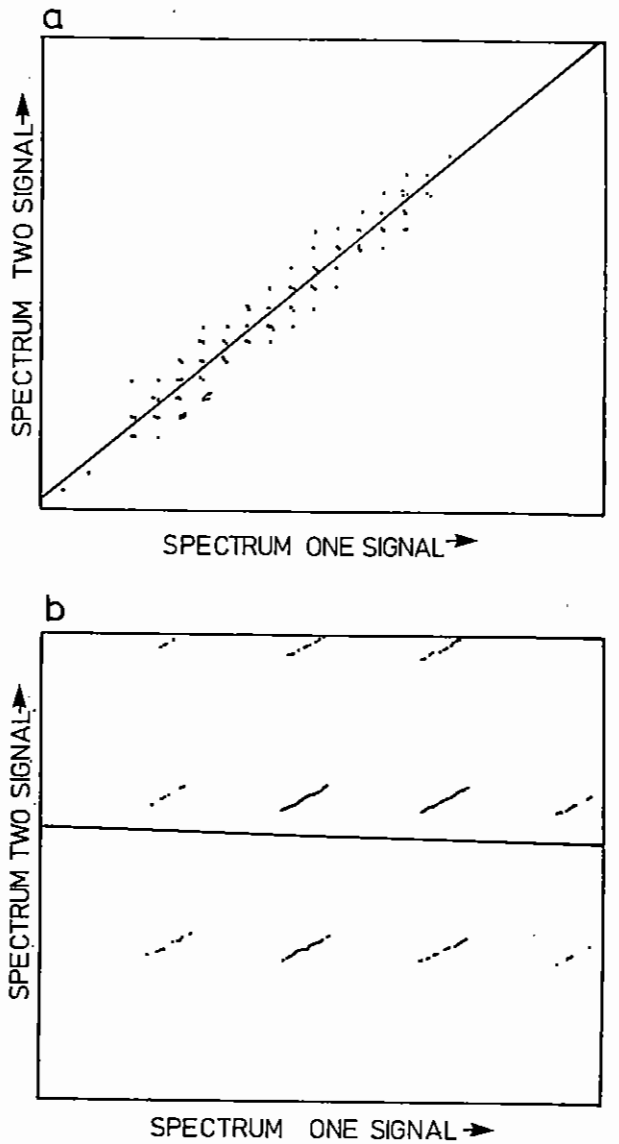

Fig B4.3 (a) 'Double y' plot of two single dark spectra, showing high positive correlation coefficient (r = 0.9786). (b) Double y plot of two 'signal minus background' spectra, showing no significant correlation (r = 0.0266). Drifting of points into lines is caused by removal of overall slope from the two spectra prior to plotting.

B4.4 STREAK CAMERA DEVELOPMENT

M Coulter, A J Langley, C Reason, I N Ross, W T Toner (RAL)

Introduction

The S25UV Delli Delti streak camera has been equipped with a new input optic and with a two-dimensional CCD readout (Hadland Photonics). Preliminary operating data have been obtained. New software has been written for the rapid acquisition of high resolution fluorescence decay data.

The input optic is constructed of four reflecting elements and is therefore fully achromatic. The design is discussed in more detail in section C4.2. Slit to photocathode magnification is unity and the acceptance angle is ∿0.2 steradians (ie is equivalent to an f:1 lens at unit magnification). Resolution is better than 30 line pairs/mm. This represents a more than one order of magnitude improvement in UV throughput, compared with the small aperture fused silica/CaF lens used previously, and also a significant improvement in resolution.

The CCD camera detector is a Peltier cooled CCD (EEV) which is coupled to the streak camera intensifier by a reducing fibre optic taper and can read a 17 x 25mm image in 385 x 576 pixels with 12 bit resolution. The 68000-based data acquisition system has facilities for real-time subtraction of a background image and multiplication by an efficiency correction image. It takes 0.28 seconds to digitise a full frame image and a further five seconds to store and display it. Some image analysis software exists and more is being developed both at Hadlands and at RAL.

Data correction for distortions and efficiency variation

The subtractive and multiplicative correction memories and software supplied with the camera, which operate in real time, make correction for the very substantial distortions and efficiency variations found in streak cameras quite straight forward.

If there are $F(x,y)dxdy$ counts in the bin dx,dy at x,y after subtractive correction only and the original signal is $G(\lambda,t)$ then

$$F(x,y)dxdy = G(\lambda,t) \left\{\frac{\partial(\lambda,t)}{\partial(x,y)}\right\} \eta(x,y)\ dxdy$$

where $\left\{\frac{\partial(\lambda,t)}{\partial(x,y)}\right\}$ is the Jacobian determinant of the transformation, $\eta(x,y)$ represents efficiency variations and $\lambda = \lambda(x,y)$, $t = t(x,y)$ is understood.

The Hadland software permits one to pre-record data from a reference signal $G_0(\lambda,t)$ giving

$$F_0(x,y)dxdy = G_0\ \lambda,t)\left\{\frac{\partial(\lambda,t)}{\partial(x,y)}\right\} \eta(x,y)dxdy$$

F_0 is stored in the multiplicative memory and when data is subsequently taken the value of $F_{corr}(x,y)$ is calculated in real time and stored.

$$F_{corr}(x,y) = \frac{F(x,y)}{F_0(x,y)} = \frac{G(\lambda,t)}{G_0(\lambda,t)}$$

G can easily be found if G_0 is known.

For synchroscan operation a torch bulb uniformly illuminating the slit will give G_0 = constant. For pulsed operation, a long time constant single exponential fluorescence uniformly illuminating the slit will give $G_0 = A \exp - t/\tau$, provided the initial rise of the fluorescence is off screen. (Timing jitter in recording the sixteen consecutive data frames required by the software is unimportant as

$\sum a_i \exp -(t/\tau - \delta_i) = \exp - t/\tau \sum a_i \exp \delta_i)$. It then remains to find the values of F_{corr} at suitable t,λ values and redisplay the data. The coordinate transformation can be found by recording data through a slit equipped with a comb illuminated with short pulse light transmitted through an etalon to give a pattern of spots on the detector.

A simple one-dimensional correction routine has so far been written at RAL to correct for sweep non-linearity. The number of bins chosen for the t-coordinate display is the same as the number of bins in the x-coordinate data. The t-coordinate display contains the values of F_{corr} found by interpolation between the two x-bins adjacent to each t-bin.

System performance

The data so far obtained are preliminary and were taken with two stages of channel plate intensification between the streak output tube and the detector, with fibre optic coupling throughput. The 18mm diameter intensifier maps to 410 x 410 pixels on the CCD. The static slit width is 3.5 to 4 pixels FWHM giving ∿ 110 resolution elements across the screen. Dynamic resolution is worse but no attempt has yet been made to optimise the system or to control the input light level.

System sensitivity at intensifier gain of 2.4×10^4 is 185 counts per photoelectron from the streak photocathode whereas readout noise per pixel is ≤ 2 counts RMS. At this level of gain and at very low input light intensity it is easily possible to identify clusters of bright pixels ∿ 3 pixels in diameter corresponding to single photoelectrons.

Rapid data acquisition

Sequential frames can be added to memory at five second intervals to improve statistical precision, but time resolution is then limited by streak camera jitter. At present, with care, this can be held to 20psec if a constant fraction discriminator is included in the triggering chain.

The system also includes rapid data acquisition facilities (not yet fully operational) and software has been written at RAL to use them.

The operating system enables one to select any rectangular area within the image and to digitise it in bins ν pixels high, μ wide. If the image is n x m bins the area is A = n x m x ν x μ (pixels)² and 385 x 576/A images may be acquired and stored without pause. "Framelet" images of this type can be acquired at 10Hz rates (up to 30Hz).

A typical use would be to record the $\perp_r$ and ∥ components of a fluorescence decay together with a laser reference pulse in three traces each fifteen pixels high, each containing 192 time bins 2 pixels wide. 385 such images could be acquired in 38 seconds. The software written at RAL performs the following tasks:

(1) Find next framelet in store
(2) Correct for streak non-linearity
(3) Find peak of laser pulse to establish jitter
(4) Sum framelet data into composite image after jitter corection.

It can also correct the "roll-off" produced in the composite image at the extremeties of the picture due to jitter to take advantage of the slightly extended time-window that trigger-jitter produces.

The programme is written in Pacal.

This should enable data with high statistical precision to be acquired while preserving single-shot time resolution.

Editor: P T Rumsby/C B Edwards

C1.1 SHORT PULSE OSCILLATOR DEVELOPMENT

C Danson, RAL

Oscillator pulses shorter than 20 ps. will be required for future experiments on Vulcan. The oscillator development during the period was concerned with the generation of these pulses. The method chosen was to generate the pulses directly using active/passive mode-locking (ref.1) rather than to compress the pulses already available. A layout of the experimental oscillator used is shown in Fig C1.1. The active medium used was Nd:YLF selected to lase on the 1.053 µm line by polarization discrimination. This system is designed to generate short-pulses via passive mode-locking but eliminate satellite pulses or double pulsing (ref.2), by adding the active mode-locker to the cavity.

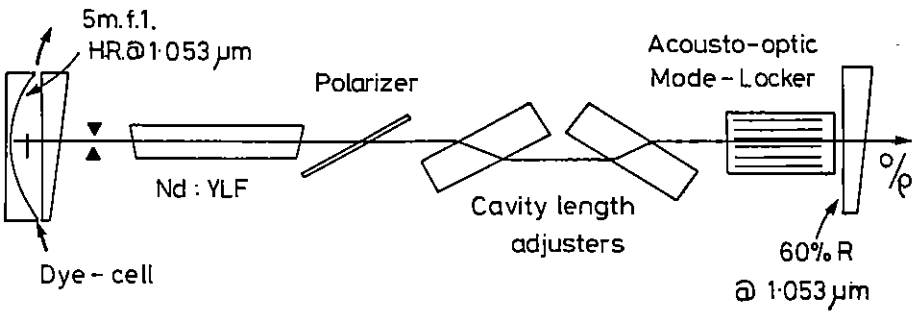

Fig C1.1 Active-Passive Cavity Configuration

The saturable absorber chosen was Kodak 9740 dye dissolved in 1,2 dichloroethane. A concentration was prepared to give a c.w. transmission through the dye of 65% at 1.053 µm. To ensure that the acousto-optic mode-locker was operating satisfactorily the cavity was initially aligned with pure solvent in the dye cell. The solvent ensured that any wedge in the dye cell was compensated, and losses within the cavity reduced. The dye was then introduced. With the current pulse to the lamp set to a width of 3.5 ms and the lamp current adjusted to be above lasing threshold, two Q-switched pulses separated by approximately 1.2 ms were observed. As the current pulse-width was reduced to 1.5 ms a single Q-switched pulse was generated.

The structure of the Q-switched envelope was monitored using a vacuum photodiode and a Tectronix 7104 oscilloscope. The Q-switch consisted of a series of pulses each separated by the cavity round trip time (Fig C1.2). The half width of the pulse train was about 80ns. The pulse shape was not symmetrical with a slower rising edge than fall, which can best be seen in Fig C1.3. This data was recorded after the dye had been in operation for about a week. The number of pulses in the pulse train significantly increased giving a pulse width of about 230ns. When investigating the reason for this it was discovered that the transmission of the dye had increased to 84.2% from an original transmission of 67.4%. The rapid deterioration in dye behaviour was due to contaminants in the dye pump/cell; when the experiment was repeated no such deterioration was observed.

The pulse-width of the individual pulses in the pulse train was measured using a Hadland 675 streak camera. The streak rate of the camera was calibrated by splitting the pulse to be measured and introducing a known delay between them before combining them at the input to the streak-camera. The streak camera records have shown that pulses as short as 16 ps have been generated (Fig C1.4), more typical results give a pulse-width of 16 - 24 ps.

Several data sets were taken to observe how the cavity responded as the pumping to the lamp was varied. Figure C1.5 shows the decrease of Q-switch build up time as the pump level was increased and the decrease in jitter in the Q-switch build-up time as the cavity is

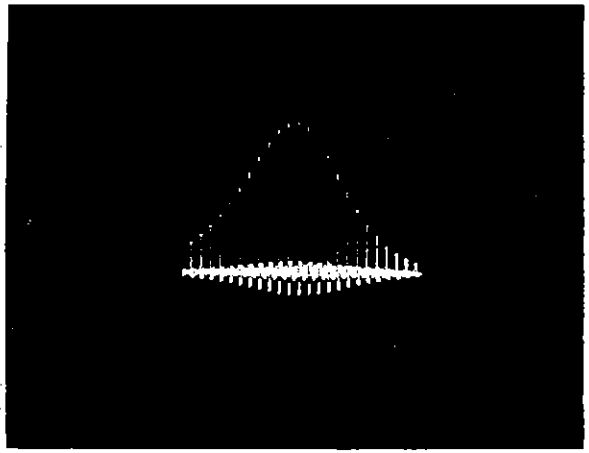

Fig C1.2 Active/Passive short pulse oscillator output

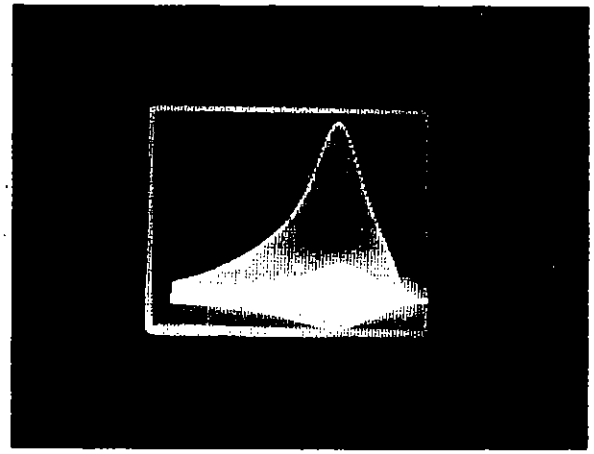

Fig C1.3 Active/Passive oscillator output following one weeks operation

operated further above threshold. No satellite pulses or double pulsing were observed when operating this cavity; a problem which has previously been reported when a purely passively mode-locked cavity was employed (ref 2).

Further work will investigate the possibilities of synchronising this oscillator with the long pulse oscillator currently in operation. Other work will include operating the cavity with different dyes; one such dye recently reported should produce pulses of about 8 ps (ref 3).

C1.2 HIGH-POWER OPERATION TESTS

C B Edwards, RAL

During the past reporting year, an experimental programme was conducted to investigate the operational limits of the forthcoming laser upgrade, to take place in early 1988.

The scheme involves driving the six 108 mm output disc amplifiers to higher fluence and using expanding vacuum spatial filters at the output of the system to improve the fill factor of the existing optical chains to the target chamber. Anti-reflection coating of the doubling crystals and target chamber optics using the colloidal silica scheme, are an essential part of the scheme to reduce losses.

The conversion efficiency to second harmonic is a most important factor in the optimistion off system performance, and studies were made of the crystal performance at increased fill factor and at high average fluence using a single beam with modified drive to give infra-red output energies up to 300 J in 1ns pulses.

i) Enhanced fill-factor.

A fundamental limit on the laser energy available from VULCAN is the damage threshold of optical components. This is related to an energy or power fluence dependent upon pulse duration, and it is thus imperative for cost-effective operation that the system be used at high fill factor. Since total image relay is not employed on the system, apodisers are used to control the spatial profile of the beam, and prior to the work reported here, rather poor use was made of the available aperture.

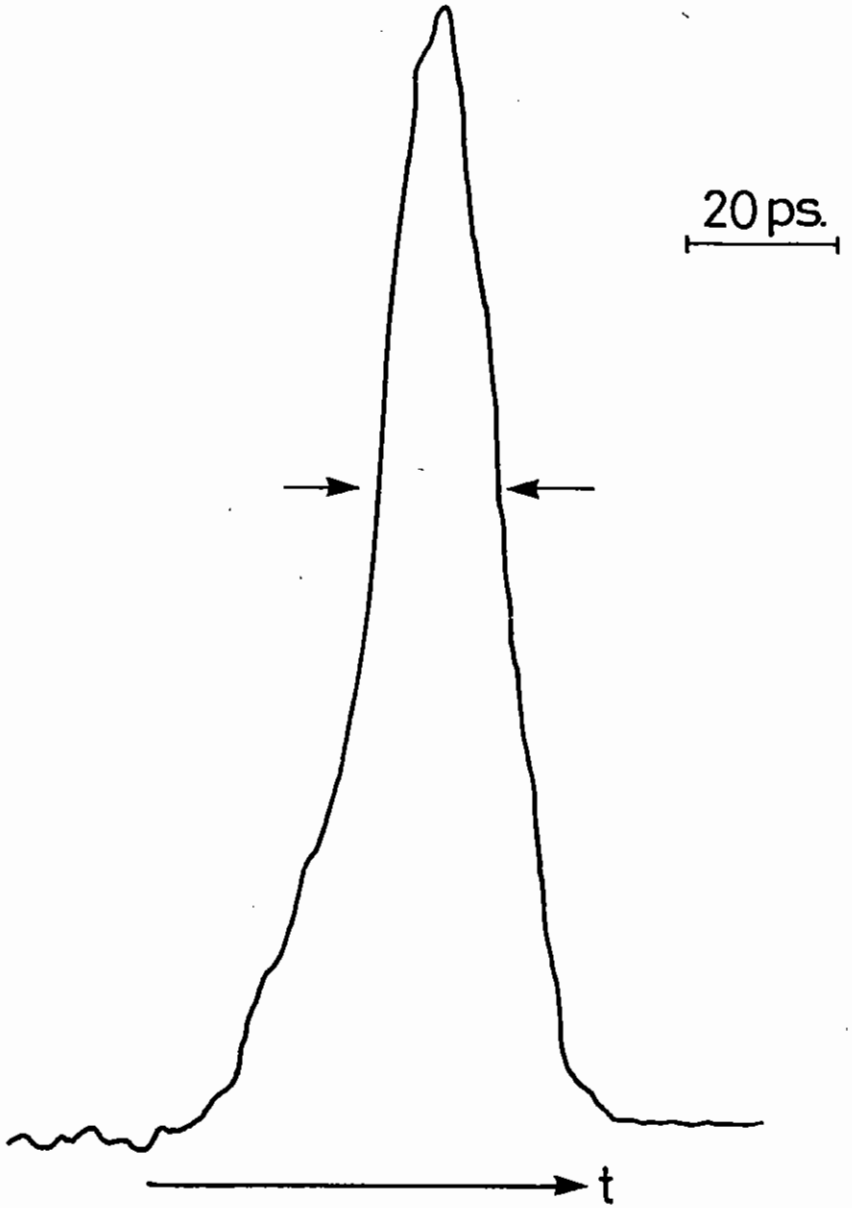

Fig C1.4 16 ps pulse generated from the Active-Passive short pulse oscillator

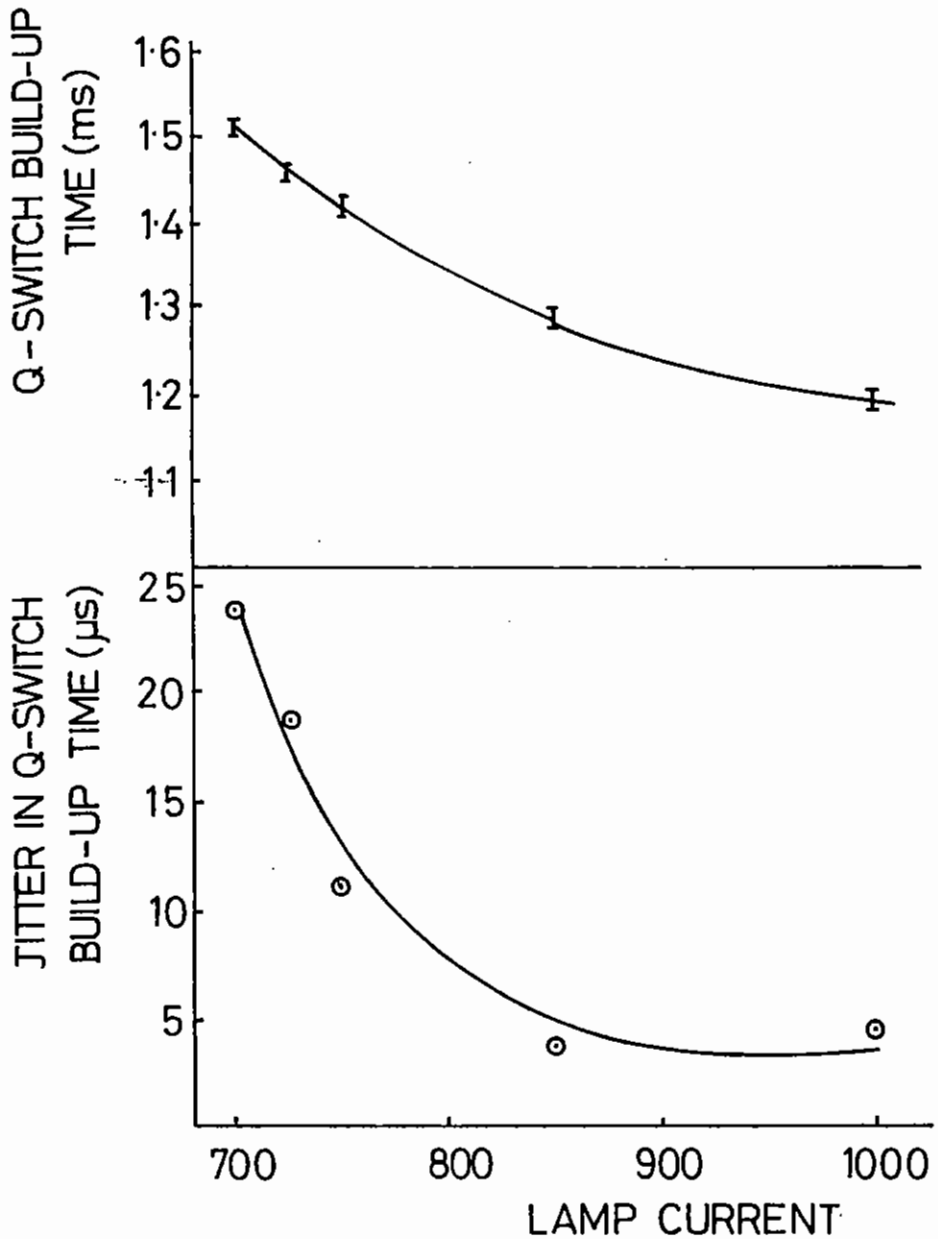

Fig C1.5 Graphs showing the variation in Q-switch build-up time and the jitter in that build up time as the lamp current is increased

The development work on solid state apodisers, reported in an earlier section, has resulted in improved control of the beam profile with the result that the system can be operated at increased fill factor. The recent series of experiments used additional apodisation at the input to the final vacuum spatial filter stage in conjunction with an expansion ratio of 1.23, and gave a fill factor approaching 90%. No problems were experienced in the propagation characteristics of the resulting beam, and an impressive increase in energy on target was achieved.

ii) Conversion efficiency

Using the configuration outlined above, conversion efficiencies in excess of 70% were consistently observed at an infra-red input of 2GW/sq cm. The highest green energy recorded was 217 J, with a conversion of 75%, using a bare crystal with colloidal silica anti-reflection coatings. The green energy recorded at the target chamber during this run was in excess of 200 J in a single beam of 100 mm diameter.

In order to operate reliably at such power levels without serious damage it was necessary to take particular care in aligning the beam to avoid clipping on mirror mounts, and to ensure that all downstream optics were in good condition. The studies show that in principle 1KJ of green energy could be available at the target chamber using six beams at a fluence slightly below those reported here, though penalties would be incurred in shot set-up time and cleaniness requirements.

iii) Optical coatings

Both conventional multi-layer evaporated coatings and colloidal silica coatings were exposed to fluence levels approaching 5 J/sq cm during the progress of this work. The only significant damage was to the coated pellicles in the target chamber, which were replaced after each shot.

Coatings directly on the crystals were satisfactory, though a preferred technique may be the use of coated windows without index matching fluid. This scheme has the important advantage that the crystal is isolated from the local enviroment with obvious advantages in the requirements on humidity and contamination control. In conclusion, it has been demonstrated that improvements in fill factor and conversion efficiency coupled with the use of anti-reflection coatings where appropriate can give significant improvements in the performance of the system at relatively low cost. In particular, 1 KJ operation in long pulse mode is feasible provided the reduced shot-rate and higher standards of cleanliness required in the target areas is acceptable.

References

1. IEEE J of Q.Elec., Vol QE-19, No.4, p578. April 1983.
2. Applied Optics. Vol 21, No.16, p2897. 15 Aug 1982.
3. Optics Comm. Vol 61, No.3, p208. 1 Feb 1987.

Editor: M J Shaw

C2.1 NANOSECOND PULSE AMPLIFICATION IN THE SPRITE LASER SYSTEM

C J Hooker, N J Everall and M J Shaw RAL

Efficient energy extraction from the Goblin laser by short (5 ns and 12 ns) pulses was reported last year. The experiment used the long pump time of Goblin to provide two stages of amplification in the one laser module. This arrangement has been incorporated into the multiplexer design as described in section A5.1. In the same section, modifications to the oscillator pulse switch-out system to reduce the duration of the pulse are also detailed. In this section we report some preliminary observations on the performance of Sprite as a pulse amplifier system.

The gain staging of the Sprite system is shown in Fig C2.1. A short (2-5 ns) pulse is sliced out of the beam of an unstable resonator oscillator and undergoes amplification and beam expansion in 4 stages. The first stage is a single pass of the amplifier section of the EMG 150. A2 and A3 are successive double passes of the Goblin laser with a maximum single-pass gain factor $g_oL = 3.5$. The output stage (Sprite) has a maximum $g_oL = 10$. The system was designed to saturate A4 heavily and thus obtain the maximum output energy. To do this, the A3 stage is also saturated and provides up to 1 J per beam so that A4 is running with a stage gain of about 20.

The net small signal gain in the system is very large ≈ exp (37) and is sufficient to amplify spontaneous emission from the front of the amplifier up to saturation levels. This effect was investigated by measuring the output energy as various stages of the amplifier were blocked.

The results were as follows:

	Energy per beam at Sprite output
1. Pulse injected at input	14 J (signal)
2. Input to A1 blocked	10 J (ASE)
3. Input to A2 blocked	4 J (ASE)
4. Input to A3 blocked	0.1 J (ASE)

Thus in the absence of any input (i.e., between pulses) and if the amplifiers have chance to fully repump, then ASE will be amplified to levels close to that of the signal. The above figures tend to suggest that the ASE output from Sprite itself was very small. This is actually not the case and the low energy recorded with the input to A3 blocked was because the Joulemeter was situated many meters away from Sprite. In a separate measurement close to the Sprite output, ASE energies of 1.4 kJ/StR in single pass and 16.8 KJ/StR in double pass were measured. These figures correspond to 56 J and 128 J for the whole output aperture of Sprite. Thus left to itself, Sprite will radiate nearly 70% of its maximum output energy as ASE.

The effects of the high system gain were apparent when short pulses were attempted to be amplified in the system. Fig C2.2 shows the change in pulse shape as it is amplified firstly in Goblin and then

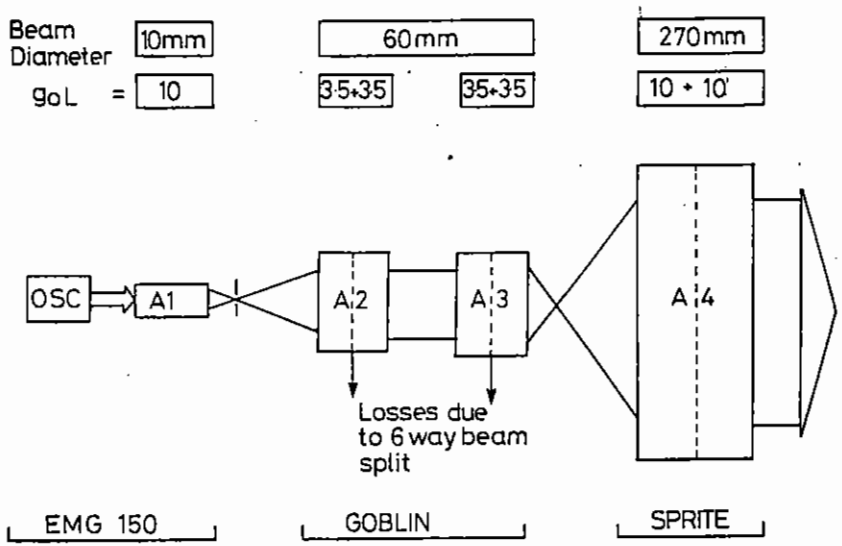

Fig C2.1 Gain staging and beam sizes in the Sprite multiplexed amplifier system.

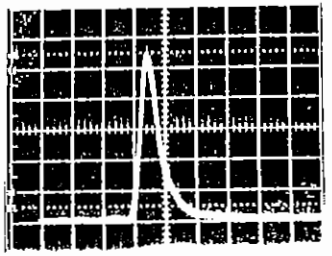

Goblin input

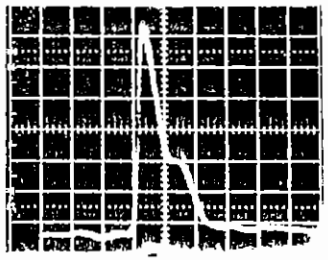

Sprite Input

Sprite Output

5ns

Fig C2.2 Changes in temporal profile due to gain saturation as a pulse propagates through the Sprite system.

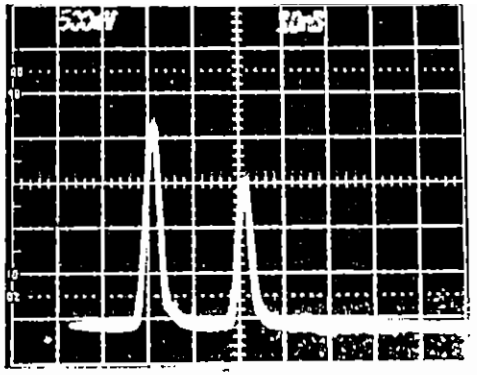

(a)

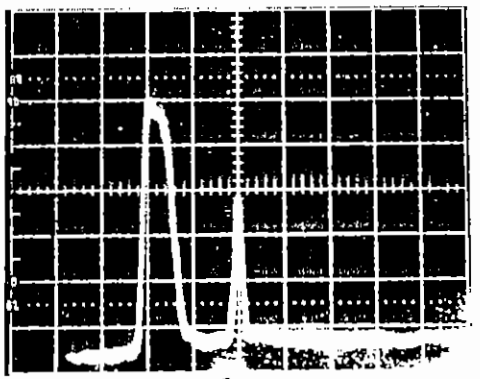

(b)

10ns

Fig C2.3 The effect of pinhole closure of the Goblin output.
(a) shows two input pulses
(b) shows the same two output pulses the second pulse having passed through a 300μm diameter pinhole.

in Sprite. The effects of gain saturation are quite apparent. The final output pulse is truncated at 10 ns by the input of the next highly saturating pulse in the multiplexer train. In order to attempt to improve the pulse performance we have investigated saturable absorbers and have concentrated on anthracene solutions which were previously reported (C2.1) to saturate well at 248 nm.

Preliminary experiments showed the the transmission of a 10^{-6}M solution of anthracene in hexane (2cm path length, $\sigma_{abs} \approx 10^{-16}$ cm²) increased from ca 10% to 50%, when the incident laser fluence (5 ns FWHM pulse) rose from 30 mJ/cm² to 130 mJ/cm². Furthermore the transmission of the ASE background signal was <1% at the highest fluence. However, the transmission figures relate to total pulse energy rather than instantaneous intensity, and so give no information on the dynamics of the saturation process. Although saturation was clearly exhibited, the absorber failed to shorten the pulse risetime, which implies that several nanoseconds are required to significantly populate the non-absorbing state. This appears to be a common problem with organic absorbers, where the lowest excited singlet state may have a significant absorption cross section at 248 nm.

We are currently evaluating the potential of inorganic saturable aborbers, in particular utilising charge-transfer transitions of transition metal complexes. These transitions give rise to strong absorption in the UV, and yield a reduced metal-ion complex which is unlikely to absorb strongly at the primary excitation wavelength. These materials do not appear to have been previously investigated for this purpose.

Another pulse shortening technique which did prove effective was the use of pinhole closure at the output of the Goblin laser. Fig C2.3(a) shows two input pulses on separate beam lines to the Goblin amplifier and the same two output pulses after amplification, one pulse having passed trough a 300μm pinhole at focus. The plasma shutter effect is quite apparent and very short ≈ 1 ns FWHM pulses can be produced by this method. Unfortunately with the present system it was found that the pinhole required constant alignment attention and since short pulses per se were not required for the target run in progress, further investigation and amplification of these pulses was not investigated.

C2.2 MODELLING MULTIPLE PULSE AMPLIFICATION IN KrF LASERS

C J Hooker, I N Ross, M J Shaw (RAL)

The fact that KrF is a high gain medium seriously limits its performance as a high energy amplifier of single short pulses. Firstly, the high gain coefficient means that the saturation fluence, $E_s = h\nu/\sigma$ is small (2mJ/cm²) and thus very large apertures are required for high energy. Secondly, the output fluence is limited by ASE (Amplified Spontaneous Emission) which effectively limits the stored energy in the system by self de-pumping and finally, the short storage time of KrF (2-4ns) leads to large pumping inefficiency where the pump time is much longer than the storage time.

In this section we will show that the main difficulties outlined above can be overcome by the amplification of a series of short pulses rather than just one. If the pulses are sufficiently close together, energy is extracted from the amplifier in a quasi-CW manner and the efficiency should approach that of a CW amplifier. Furthermore, the gain is kept suppressed and ASE is much reduced. The performance of such multi-pulse amplifiers has been modelled for the case where the pulse duration is long compared to the dephasing time i.e., the rate equation approach is valid. We first consider the case of a single-pass amplifier in the steady-state and assume that the pulse duration is short compared to the storage time of the medium.

The gain in normalised pulse fluence $f=E/E_s$ is given by the Franz-Nodvik equation:-

$$\frac{df}{dx} = g_o\,(1 - e^{-f}) - \alpha\, f \qquad (1)$$

where g_o is the small signal gain coefficient and α is the non-saturable loss coefficient. The gain coefficient is directly related to the population inversion n via $g = n\,\sigma$ where σ is the gain cross section. The effect of the passage of a short pulse of fluence f through a point in the amplifier is to rapidly reduce the population inversion and hence the gain at that point by a factor exp(-f). After the passage of the pulse the inversion repumps according to:-

$$\frac{dn}{dt} = R - n/\tau \qquad (2)$$

where R is the pump rate into the upper laser level and τ is its collisionally quenched lifetime. If the initial inversion is n_1, then the inversion after a repumping time t is given by:-

$$n(t) = R\,\tau + (n_1 - R\,\tau)\,\exp\,(-t/\tau) \qquad (3)$$

Multiplying this equation by the gain cross-section σ and using the fact that the undepleted small-signal gain is given by $g_o = R\,\sigma\,\tau$ we find that the gain in the amplifier repumps as:-

$$g(t) = g_o + (g_1 - g_o)\,\exp\,(-t/\tau) \qquad (4)$$

Figure C2.4 shows how the gain (or inversion density) at a point changes as a train of pulses enter the amplifier. After a time, which depends upon the pulse separation, a steady-state situation is reached in which the gain depleted by the passage of a pulse is equalled by the gain recovery in the time between the pulses. The gain depletion is given by:-

$$g_1 = g(t)\,\exp\,(-f) \qquad (5)$$

Eliminating g_1 between (4) and (5), the value for the gain just before the arrival of the pulse can be expressed in terms of known parameters and used in (1) to obtain a new differential equation for the pulse fluence:-

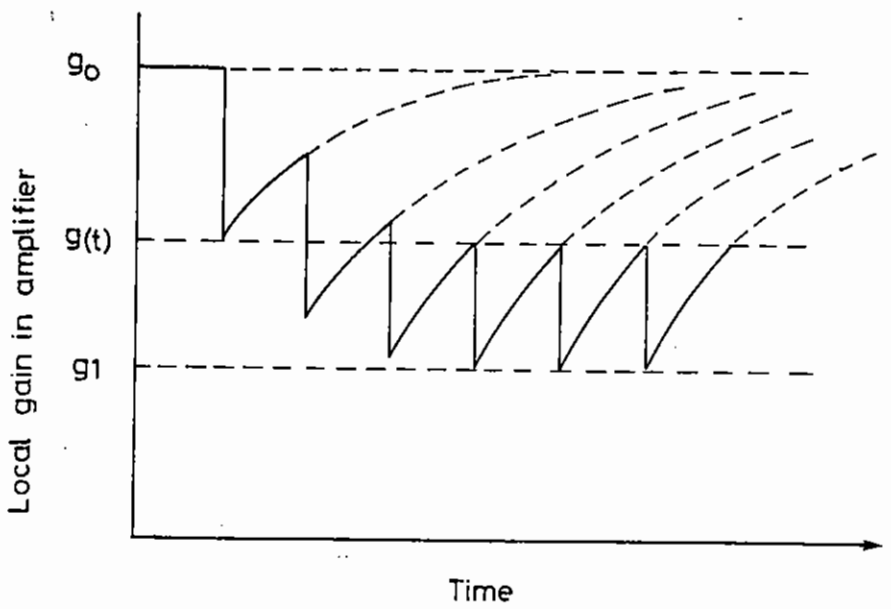

Fig C2.4 The effect of gain depletion and repumping as a pulse train propagates past a point in a repumped amplifier.

$$\frac{df}{dx} = g_o \frac{(1 - e^{-t/\tau})(1 - e^{-f})}{(1 - e^{-f} e^{-t/\tau})} - \alpha f \qquad (6)$$

where t is now the pulse separation. This equation is simple to integrate numerically to obtain the output fluence per pulse f_{out} as a function of the input fluence f_{in}. The steady-state extraction efficiency of such a multi-pulse amplifier is simply the net output power divided by the pump power into the upper laser level and is given by:-

$$\eta = \frac{f_{out} - f_{in}}{(t/\tau)\, g_o L} \qquad (7)$$

Solutions to (6) are easy to obtain and are useful in showing the broad features of multi-pulse extraction. In practical cases, however, a more sophisticated model is required to take account of double-pass amplification, amplifier transit time, finite pulse length and ASE.

We have developed a computer model of multiple-pulse extraction which takes these additional factors into account. The model simulates the extraction by a train of equal pulses of a double-pass amplifier of length L. The amplifier is represented by the exactly equivalent bidirectional amplifier of length 2L, extracted by two identical pulse trains travelling in opposite directions. Since the model is essentially one-dimensional, no attempt was made to include ASE effects.

The amplifier is subdivided into a number N of segments, typically 50. The time step in the code is the transit time of one pulse in the extracting train through a segment of the amplifier; the pulses are considered as infinitesimally short. Each segment of the amplifier has two stored values associated with it: the number t_e of the time step at which the segment was last extracted, and the gain $g(t_e)$ which remained after extraction.

At each time step, the two pulse trains are moved by one segment in their respective directions. After accounting for any pulses that enter or leave the amplifier, each pulse that is currently inside the amplifier is considered in turn. First, the stored values associated with the occupied segment are used to calculate the current value of gain, using a form of the repumping equation (4):-

$$g(t) = g_s + (g_1(t_e) - g_s) \exp(-(t-t_e)/\tau)$$

Here $g_s = g_0/N$ is the small-signal gain of one segment, and t is the number of the current time-step. The value of gain thus calculated is substituted in equation (1), which is solved numerically by a Runge-Kutta technique to yield the fluence increment, Δf, of the pulse as it traverses the segment in question. The fluence in the amplified pulse is then $f_{out} = f_{in} + \Delta f$. Finally, the gain depletion is calculated, using equation (5) with an average value of fluence $f_{av} = (f_{in} + f_{out})/2$ in the exponent. The new value $g_1(t)$ and the current time step t are stored, replacing $g_1(t_e)$ and t_e.

The first version of the code was used to investigate steady-state extraction of a continuously-pumped amplifier by an infinite train of pulses. The normalised fluences of pulses emerging from the amplifier were tested until they converged (after initial oscillations) to a constant level within a pre-defined narrow range. After the steady state had been reached, equation (7) was used to calculate the extraction efficiency. Important parameters of the model could be varied from run to run, in particular the gain-length product g_oL and the gain-to-loss ratio g_o/α of the amplifier, the

initial fluence of the pulses in the extracting trains and the spacing between them. The results of many runs are summarised in Fig C2.5, which is a plot of extraction efficiency against normalised output fluence for $g_0L = 5$ and $g_0/\alpha = 15$. The figure shows five curves corresponding to different pulse spacings t, normalised to the collisional lifetime τ of the upper laser state. Each point is the steady-state output for a given input fluence, starting on the left of each curve at $f_{in} = 0.001\ E_{sat}$ and doubling for each successive point. As the time between pulses is increased the output energy is driven to higher values but the efficiency decreases as expected. For pulse separations < 0.5 τ the efficiency is essentially the same as the CW efficiency under the same conditions. It is interesting to note that the gain at peak efficiency is similar for all pulse separations and depends only on g_0L. Preliminary investigation of the effects of ASE have shown that the problem becomes serious for pulse separations greater than τ.

In conclusion, this analysis has shown that high overall efficiency can be achieved from a continuously pumped pulse amplifier by extracting energy in a series of pulses with separation about the gain lifetime (typically 2–4 ns in KrF).

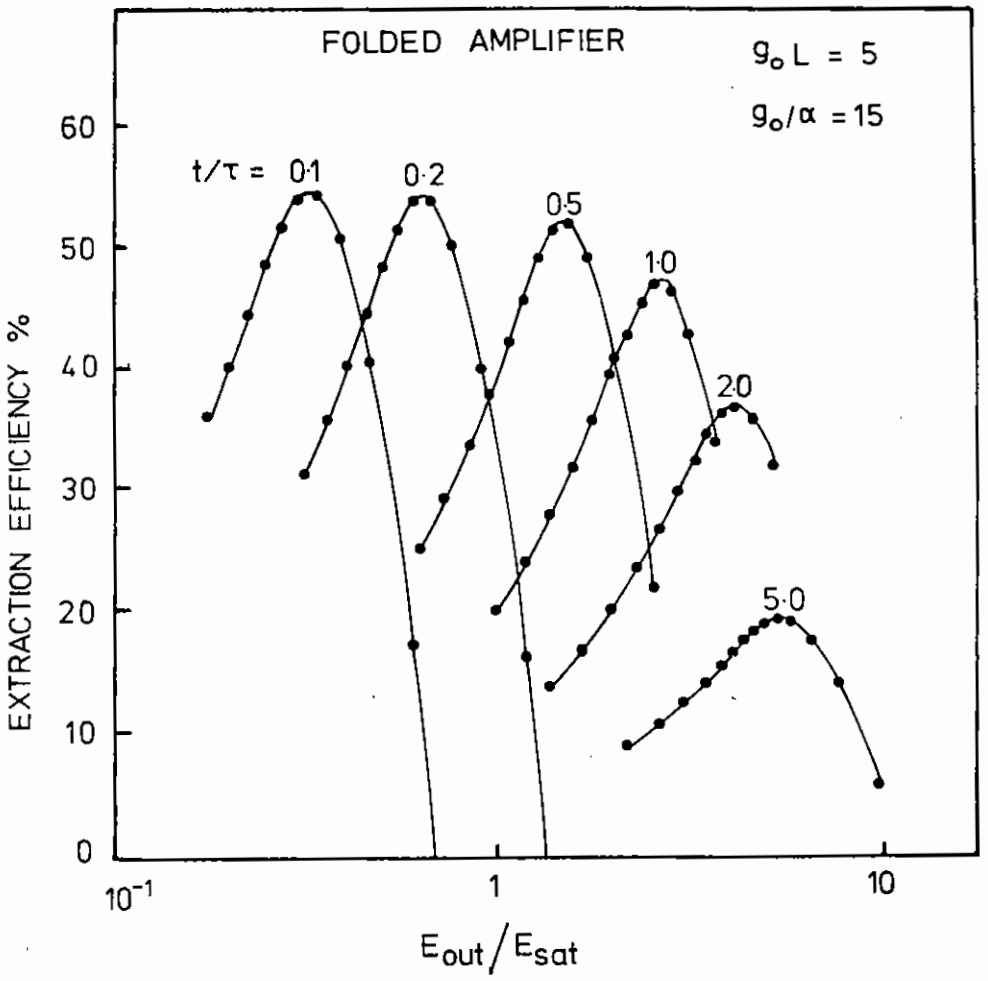

Fig C2.5 Average extraction efficiency versus output energy per pulse for continuous pulse trains amplifier in a folded amplifier with g_0L = 5 and gain to loss ratio g_0/α = 15. Points are for different input fluences starting at 0.001 E_s and doubling for each point.

C2.3 A SINGLE-MODE KrF OSCILLATOR

J P Partanen, RAL

Krypton fluoride and other excimer lasers have become very useful sources of high peak and average power coherent radiation in the ultraviolet. The linewidths of free-running excimer lasers are, however, too wide for many applications in nonlinear optics, spectroscopy and holography. A method widely applied for controlling the linewidth of these lasers is injection-locking. In this technique a low intensity beam of narrow linewidth from a master oscillator is injected into the cavity of a high power oscillator. This forces the power oscillator to lase with a narrow linewidth. The master oscillator laser in this method frequently uses the same excimer gain medium with linewidth selective elements in the laser cavity. The linewidth of a master oscillator laser can be effectively controlled by inserting elements into the laser cavity which make the feedback a function of wavelength. Tilted intracavity Fabry-Perot etalons, gratings and prisms have been used in excimer laser cavities for line narrowing.

Single-mode operation has never been achieved with a discharge-pumped KrF laser. The main difficulty in mode control with discharge-pumped excimer lasers arises from the fact that gain exists in the medium for only a short time, due to the discharge collapse. With a longer excitation time, lower gain may be employed, increasing the number of cavity roundtrips to reach saturation. The line narrowing elements are passed more often and their selectivity is increased. Long excitation times with excimer lasers can be achieved using electron-beam pumping. We have designed and constructed a small table-top co-axial electron-beam-pumped KrF laser. Using a short excitation length we were able to keep the single-pass gain small and allow many roundtrips during the excitation time. Using this laser and intracavity etalons for line narrowing we have demonstrated single-mode operation of a KrF laser for the first time.

The design of the electron-beam diode and preliminary experiments with the high voltage charging circuit has been described in last year's annual report. As shown in Fig C2.6 the charging circuit is based on the autotransformer to provide a 200 kV 150 ns voltage pulse. To protect the thin walled (30μm of stainless steel) anode tube from post closure current heating the series resistors R_1 and R_2 and the vacuum spark gap have been added to the secondary circuit. The vacuum spark gap diverts most of the post closure current away from the anode. Without this protection the anode tube broke through after every shot.

The anode tube containing the laser gas mix is connected to a large reservoir volume and the gas can be circulated between shots. The laser mix used in experiments was 4 torr of F_2, 100 torr of Kr and 1350 torr of Ar.

Because the single-pass gain is low, the laser requires high reflectivity cavity mirrors (99% and 80%). Reflection losses in the windows are avoided by having the windows at Brewster angles. Fig C2.7 shows a photodiode trace of a broad-band laser pulse together with a trace of the cathode voltage. The length of the laser pulse is about 80 ns. The time required for the laser beam to grow from noise can be estimated from the design value of 5 for the single-pass gain and is about 40 ns. This is consistent with the pulse shape and voltage waveforms of Fig C2.7. This build-up time, added to the pulse length, gives the excitation time of 120 ns. The pulse shape and the voltage waveform changed slightly from shot to shot. The pulse energy of a broad-band laser shot was about 1 mJ.

The advantage of long excitation time and many round trips for line narrowing can be explained using Fig C2.8 where the transmission function of a line narrowing element has been plotted after single, 4 and 40 passes. In the case of a Fabry-Perot etalon the linewidth after n passes is

$$\Delta\nu_n = (2^{1/n} - 1)^{\frac{1}{2}}\, \Delta\nu_1 \qquad (J1)$$

where $\Delta\nu_1$ is the single pass linewidth.

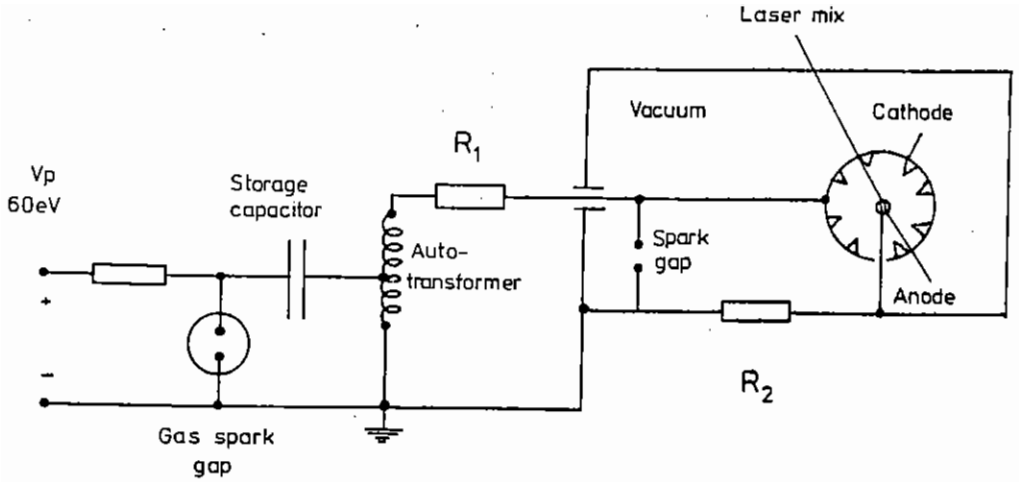

Fig C2.6 The high-voltage transformer circuit for the electron-beam diode.

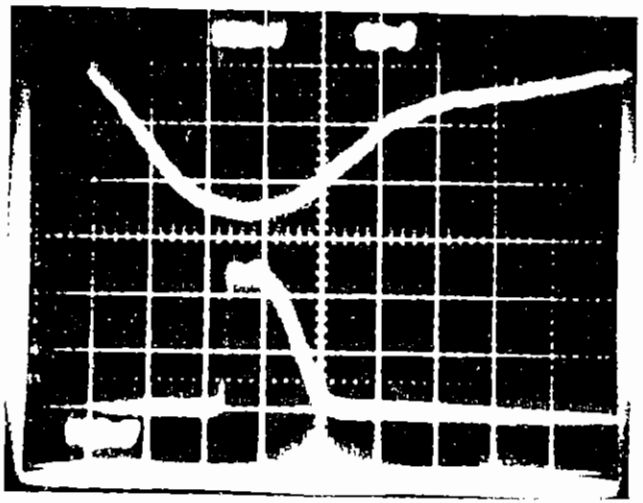

Fig C2.7 Oscilloscope trace of the cathode voltage waveform (top, kV/div) and the laser pulse shape without line narrowing (bottom). The time scale is 50 ns/div.

The linewidth of the laser using a cavity without any line-narrowing elements was measured with a 70 μm air-spaced Fabry-Perot etalon and found to be 20 cm^{-1}. This can be compared to the values of 60-100 cm^{-1} measured on other electron-beam and discharge pumped KrF lasers. The smaller linewidth observed here can be attributed to the lower single-pass gain (here 5 compared with typically 10^4) and the larger number of roundtrips to reach saturation for our laser. In the case of a free-running laser, narrowing occurs because the gain profile is itself a function of frequency.

Single-mode operation was achieved using the cavity shown in Fig C2.9. The line narrowing was done with two intracavity Fabry-Perot etalons: a 70 μm air-spaced etalon giving a free spectral range of 70 cm^{-1} and a 3 cm thick solid quartz etalon giving a free spectral range of 0.11cm^{-1}. The finesse of both of the etalons was 15. The intracavity etalons were slightly tilted with respect to the axis so that the reflections were lost from the laser cavity. The line narrowing is then determined purely by the transmission properties of the etalons. A 1 mm diameter pinhole was inserted into the cavity for transverse mode selection. The length of the cavity was 50 cm.

Single-mode operation was verified by two independent diagnostics. Firstly, a photodiode connected to a fast oscilloscope was used to record the laser pulse shape. With a few longitudinal modes lasing, the pulse shape shows strong mode-beating, whereas with a single mode the output pulse is smooth. Secondly, the linewidth of the laser beam was studied using a 5 cm air-spaced Fabry-Perot etalon with a finesse of 20 having a resolution of 0.005 cm^{-1} which was small enough to resolve the longitudinal mode structure. Fig C2.10 shows both the photodiode trace of the laser pulse and the ring pattern from the diagnostic etalon recorded on the same single-mode laser shot. In contrast, Fig C2.11 shows the same diagnostics from a multimode laser shot which was produced when the solid intracavity-etalon was changed for another having a thickness of 3 mm. With the cavity of Fig C2.9 single-mode operation was observed with about every second shot.

It was observed that without the pinhole in the cavity, single longitudinal mode operation could not be achieved. This is because the peak transmission of the etalon is a function of the angle, and different transverse modes have different angular structures inside the laser cavity. The 1 mm pinhole gives a cavity Fresnel number of

2 which is probably small enough to select a single transverse mode. The energy of the single-mode laser pulse was estimated to be about 1μJ using a calibrated photodiode. This is still sufficient for injection locking of KrF power oscillators.

Figs C2.8, A6

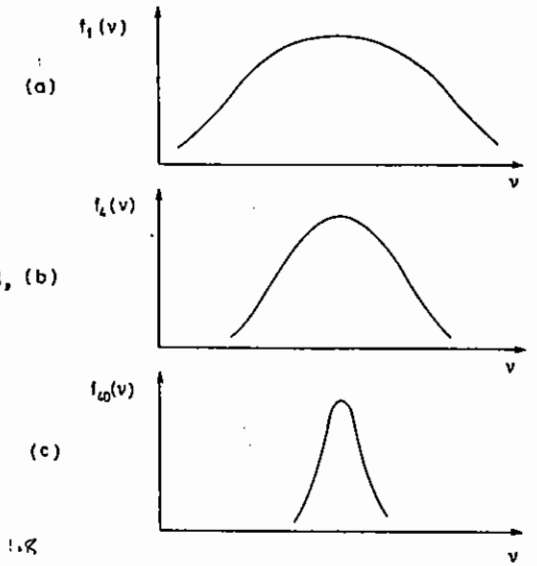

Fig C2.8 A transmission function f(ν) of a line-narrowing element
(a) single pass
(b) 4 passes
(c) 40 passes

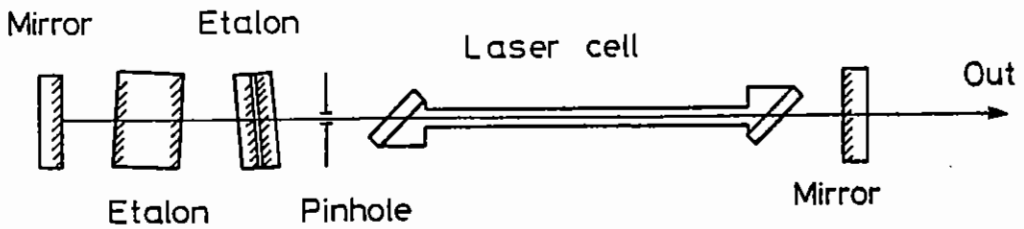

Fig C2.9 The optics of the single-mode KrF laser cavity.

(a)

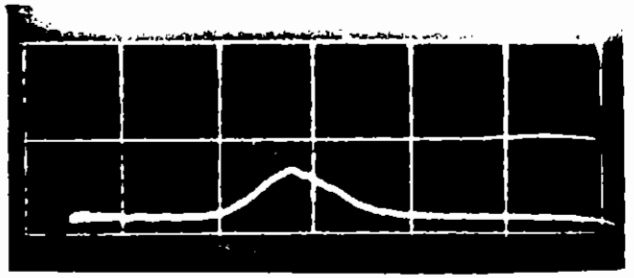

(b)

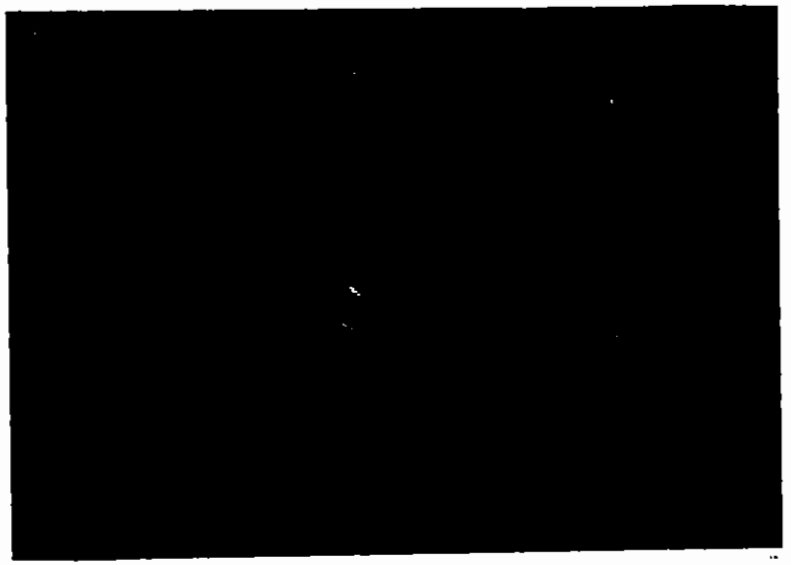

Fig C2.10 (a) Oscilloscope trace of the pulse waveform (20 ns/div)
(b) fringes obtained from the diagnostic etalon (FSR = 0.1cm^{-1}) in a single-mode laser shot.

(a)

(b)

Fig C2.11 (a) Oscilloscope trace of the pulse waveform (20 ns/div) (b) fringes obtained from the diagnostic etalon (FSR = 0.1cm^{-1}) in a laser shot where a few modes were oscillating.

Editor: J Barr

C3.1 WORK TO EXTEND THE WAVELENGTH RANGE OF THE PICOSECOND LASER SYSTEM

J Barr, I N Ross, W Toner

The wavelength coverage of the picosecond laser system achieved by frequency doubling and mixing is described here. Information on Raman generation or continuum generation may be found in the CLF annual report 1986, section C3.2 or in reports on experiments using these techniques. The major improvement to the wavelength coverage has been the extension of the synchronously modelocked dye laser operation from 680nm to 760nm.

The general relation between three frequencies in sum frequency generation is:-

$$\omega_3 = \omega_1 + \omega_2$$

In the degenerate case when $\omega_1 = \omega_2$ the process described is frequency doubling. When frequency mixing the fundamental Nd:YAG wavelength λ_1 = 1.064μm is mixed with either an amplified picosecond pulse or with a frequency doubled amplified picosecond pulse.

The fundamental range of the synchronously pumped dye laser is from 560nm to 760nm. Amplified energies approaching 500μJ are available over most of this range with up to 1mJ at certain wavelengths, eg 590nm. By frequency doubling the wavelength range 280mm to 380nm can be reached. Typical conversion efficiencies are ∿ 10% giving normally 1 ∿ 50μJ per pulse. Mixing an amplified picosecond pulse with the ∿ 3ns fundamental Nd:YAG wavelength is possible since the peak powers are comparable (∿ 100MW). This enables the range 366nm to 443nm to be reached. Up to 25μJ has been generated at 435nm and better than 15μJ over 425nm to 442nm. By frequency doubling the amplified picosecond pulse and mixing with 1.064μm the wavelength range 222nm to 280nm can be reached. To date only 248nm has been generated by this method giving between 10-20μJ. The above information is summarised in figure C3.1.

Further extensions to the tuning range are possible if required. The synchronously modelocked dye laser wavelength coverage could be extended to perhaps 880nm (Styryl 9M). In this way the frequency doubling range would be 280nm-440nm while the mixing range could be 366nm to 482nm. Recent improvements in the range of nonlinear optical crystals available could help to improve conversion efficiencies. For example to reach the shortest wavelengths around 220nm requires the use of potassium pentaborate which is very inefficient. The new crystal Beta Barium Borate (BBB) can reach wavelengths as short as 201nm by mixing doubled dye at 651nm with 532nm. BBB has a high damage threshold (10GWcm^{-2} for 20ps ruby pulse) and is transparent down to 190nm. The relevant nonlinear coefficient is $d_{11} = (4.10 \pm 0.2)d_{36}$(KDP) from reference (C3.1) promising efficient conversion for phase match angles far from the 90^0 phase match angle.

C3.2 A SINGLE SHOT SPECTRUM ANALYSER

J R M Barr (RAL), P Zirngast (Portsmouth Polytechnic)

Many optical experiments require measurements of the spatial distribution of laser intensity. This may be the spatial profile of the laser beam or the spectral power distribution after the beam has been dispersed by a diffraction grating. In this work a prototype system was developed, using photo-diode arrays, which was capable of recording the spatial distribution of a repetatively pulsed laser system on a single shot basis.

The prototype system was designed to demonstrate that a pulsed laser can be synchronised with a photodiode array and the output of the array digitised and stored on a computer. The design finally adopted is shown in Figure C3.2. The mode of operation was constrained by the available ADC (SR245) which operated at a maximum 2kHz digitisation rate. Since ADC's which operate at rates up to ∿ 100kHz are commercially available the final system will probably be limited by the memory to disc storage time of the computer. A master

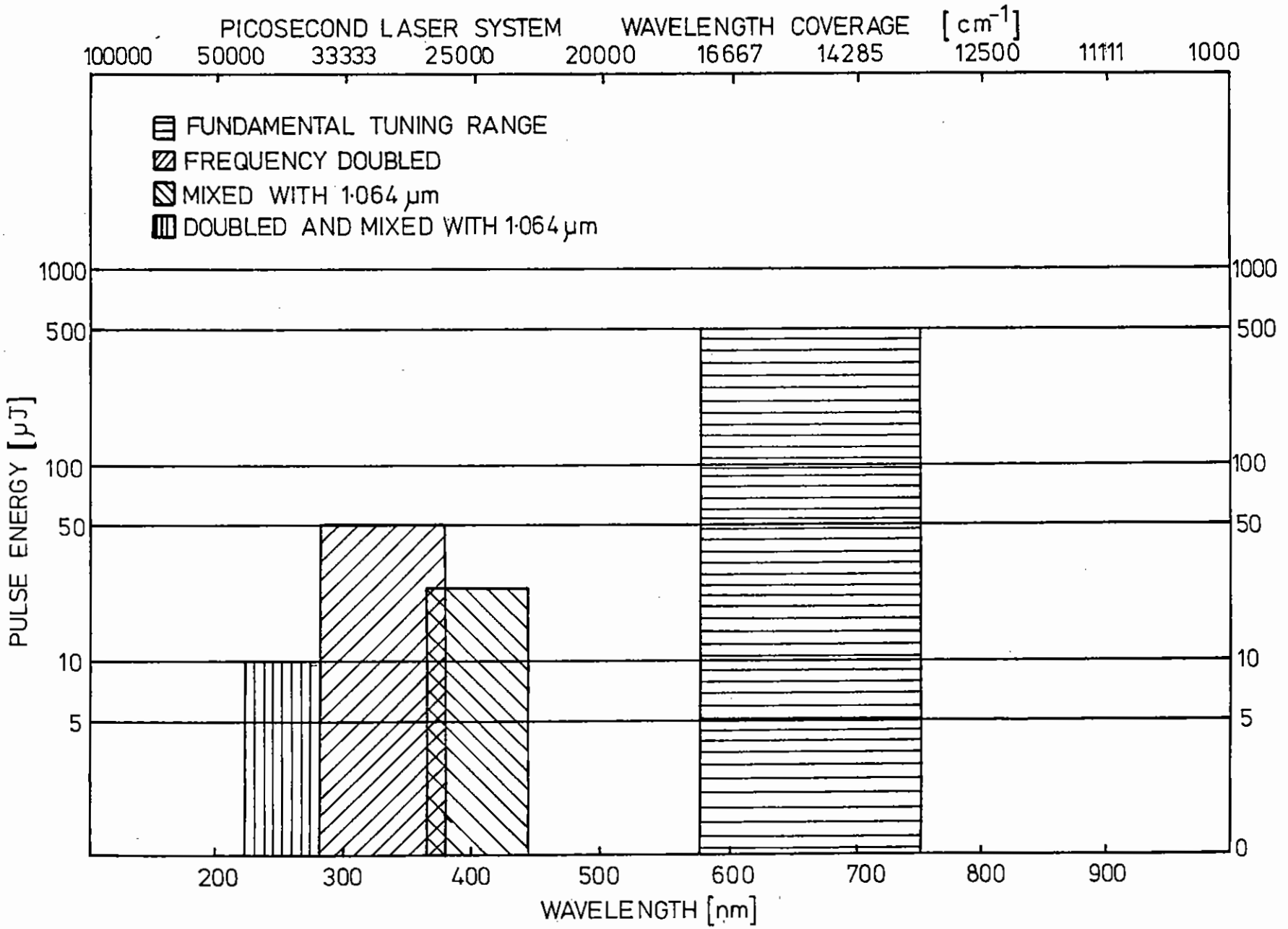

C3.1 The wavelength regions accessible to the LSF picosecond laser system.

oscillator at 6kHz controlled the whole system. The diode array (EG&G Reticon RL128G) was clocked at 6kHz and the data was output serially via a sample and hold also at 6kHz. A divide by 3 circuit provided a 2kHz signal to drive the ADC synchronously with the diode array output. Thus only the output from 1 in 3 diodes from the array was digitised. This restriction could be removed by utilising a faster ADC. The 6kHz signal was also counted down to 40Hz and 10Hz. The 10Hz signal (with appropriate delays) was used to fire the laser system just before a diode scan start signal which occurred at 40Hz. The diode array was scanned four times to each laser shot to reduce the dark leakage current noise to below 1%.

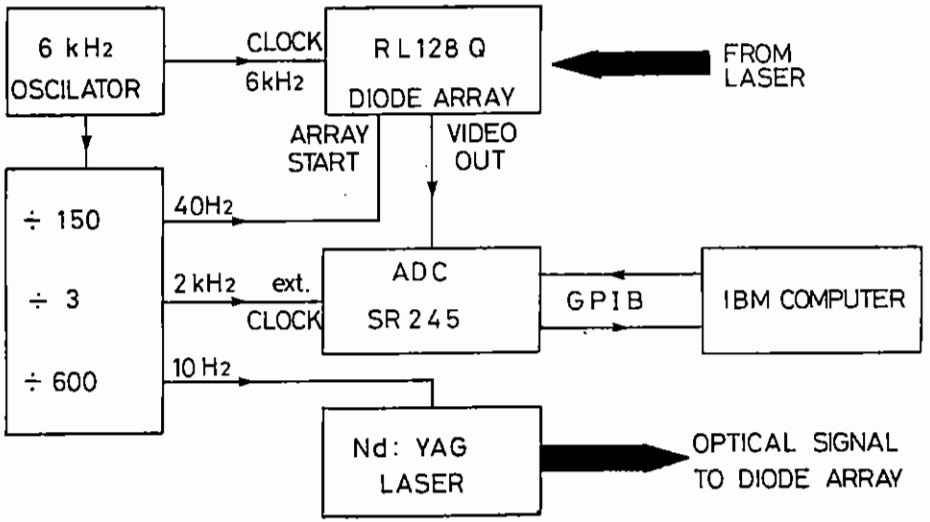

C3.2 Schematic diagram of the diode array data acquisition system.

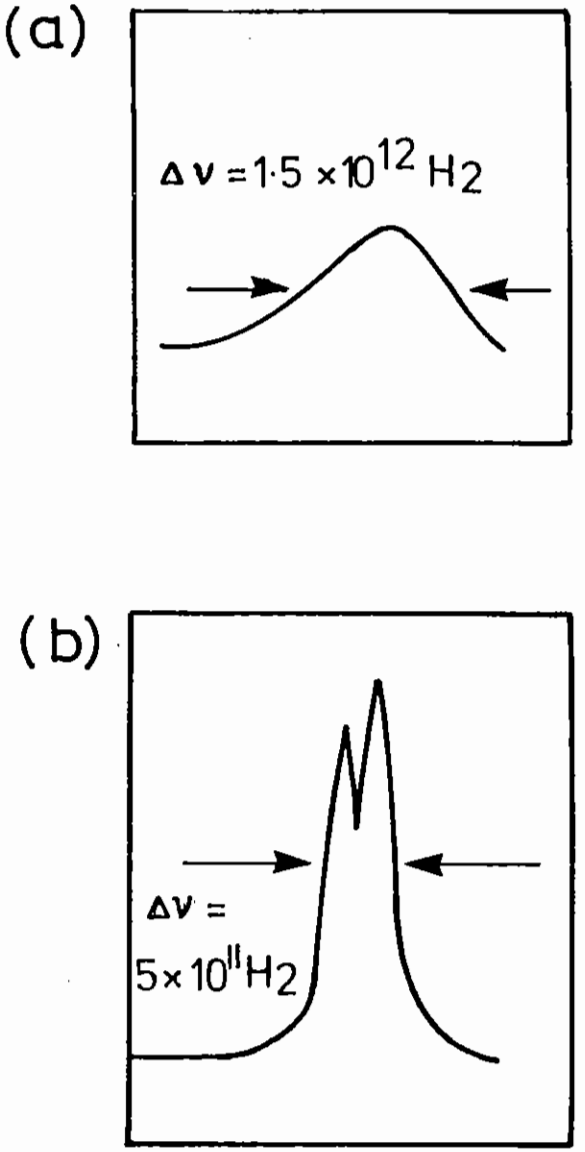

C3.3 (a) The spectrum of the hybridly modelocked dye laser operating at 600nm. The spectrum is averaged over approximately 2x10^6 pulses.

(b) The spectrum of a single pulse from the hybridly modelocked dye laser acquired as described in the text.

To demonstrate the usefulness of such a system the spectrum of a hybridly modelocked dye laser was examined on a single shot basis. Normally such a system produces an 82 MHz train of pulses so spectral measurements involve an average over the response time of the detector and involve many thousand pulses. In order to isolate a single pulse that pulse was amplified to several hundred μJ at 10Hz in a dye amplifier. The spectrum of such a pulse is shown in figure C3.3b while figure C3.3a shows an average over ∿ 2 x 10^6 pulses. Clearly the single shot spectrum is radically different from the average.

To completely characterise a pulse from a modelocked laser both the spectral and temporal profiles should be measured. Such a system based on the single shot data acquisition system described here is under development.

C3.3 PULSE SHORTENING TECHNIQUES

J Barr, I N Ross

Hybrid modelocking provides a simple method to shorten the pulse length from a synchronously modelocked dye laser. With the methods described here pulses as short as 300 ± 50 fs have been obtained using a linear cavity uncompensated for dispersion. Additionally a small quantity of a saturable absorber added to a cavity dumped synchronously modelocked dye laser shortens the pulse length from ∿ 12ps to ∿ 3 ps with near transform limited performance.

In the hybrid modelocking scheme adopted here the gain medium (R6G, 2 x 10^{-3}M) and the saturable absorber (DQOCI 10^{-5}M) were added to ethylene glycol in the same circulator. The dye laser was an unmodified spectra physics 375B with 30% output coupling at 600nm. The bandwidth selecting element was a tuning wedge (Spectra Physics 570B) which in the standard synchronous modelocking case enabled pulses as short as 4ps to be generated. These pulses were distinctly non transform limited indicating that shorter pulses should be achievable. Adding the saturable dye (DQOCI) enabled pulses with autocorrelation function durations of 0.5ps to be produced when the cacity length was correctly adjusted. The deconvolved pulse length is in the range 250fs to 350fs assuming respectively either a single sided exponential pulse shape or a Gaussian pulse shape. A typical autocorrelation trace is shown in figure C3.4. With an average pump power of 550mW the output was 60mW at 600nm. The subpicosecond pulse duration was maintained over a tuning range 585nm - 616nm. This was limited at the short wavelength end by the appearance of satelite pulses and at the long wavelength end by the laser output becoming unstable.

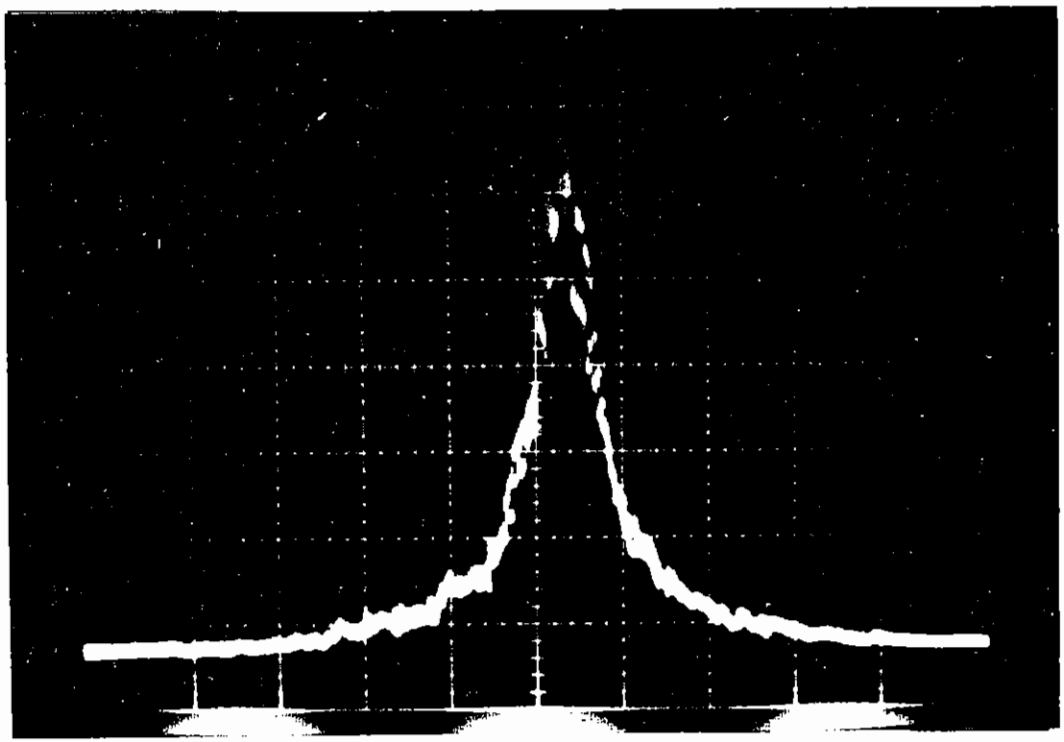

C3.4 The autocorrolation trace of a hybridly modelocked dye laser. One large division represents 0.625 ps. The deconvolved pulse length is 350 fs assuming a Gaussian pulse shape.

In a separate experiment the spectral characteristics of a hybridly modelocked dye laser operating at 600nm with an autocorrelation function of 0.875ps was investigated. The time averaged spectrum was measured and is shown in figure C3.3(a). It was assymetric indicating either a frequency chirp or fluctuations in carrier frequency. The laser bandwidth (FWHM) was 1.5×10^{12}Hz and assuming Fourier transform limited behaviour the corresponding pulse widths are displayed in table C3.1. Clearly none of these pulse lengths correspond to the measured value which was in the range 437fs to 613fs. The problem is partially resolved by generating the single shot spectrum of the hybridly mode locked dye laser. This was done by amplifying a single pulse in a dye amplifier at 10Hz so that most of the average power was contained in the amplified pulse rather than the CW background. Thus the spectrum observed corresponded to a single pulse. An example is shown in figure C3.3(b). The FWHM of this trace was 0.5×10^{12}Hz. Other values observed ranged from 0.375×10^{12}Hz to 0.75×10^{12}Hz with a mean of $(5.5 \pm 1.2) \times 10^{11}$ Hz. Table C3.1 shows the various pulse lengths as a function of pulse shape which have bandwidths corresponding to this value. The only agreement occurs if a $sech^2$ shape is assumed for both spectrum and bandwidth. Averaging the spectra over many shots results in a similar shaped curve to figure C3.3(a) so the assymetry is assumed to result from frequency jitter. The problem is only partially resolved because the autocorrelation trace is composed of an average over many shots which can lead to the measured pulse length being too short. To investigate this feature of synchronously modelocked lasers more fully single shot measurements of pulse length and spectrum will have to be made. The cause of the frequency fluctuations is probably related to the instabilities in pulse formation in synchronously modelocked lasers due to spontaneous emission as predicted by Catherall and New (C3.2).

Table C3.1

bandwidth	Pulse length (fs)		
	single sided exponential (0.441)	$sech^2$ (0.315)	Gaussian (0.159)
1.5×10^{12} H_z	294	210	106
5.5×10^{11} H_z	802	573	289 fres

Pulse length in femtoseconds corresponding to various pulse shapes. The time bandwidth product is in brackets.

C3.4 A SECOND PICOSECOND DYE OSCILLATOR

J R M Barr, I N Ross, Li Ming Zang

Typically 400-500 mW average power at 532 nm is required to pump a synchronously modelocked dye laser. The spectra Physics modelocked Nd:YAG laser can provide up to 1.1 W average power at 532 nm. A logical method of pumping a second modelocked dye laser is simply to divide the available pump power between two dye lasers. An increased experimental workload could be achieved for example, by carrying out a two wavelength pump probe experiment simultaneously with a streak camera experiment using a cavity dumped dye laser. Alternatively experiments requiring two synchronously pumped modelocked dye lasers such as time resolved inverse Raman spectroscopy could be carried out. At present the second synchronously pumped dye laser is being used for development work.

The schematic of the the laser systems is shown in figure C3.5. A nominal 50% beam splitter divides the beam from the Nd:YAG laser into two. The original dye laser operates normally. The second oscillator is sited in an adjacent laboratory and the output of the frequency doubled Nd:YAG laser is image relayed to the dye oscillator using an f = 1.0 m lens. While a pump power of up to 550 mW has been used, normally 500 mW is adequate.

Various dyes, (R6G, 2×10^{-3}M; DCM, 1.5×10^{-3}M; Pyridine 2, 1.9×10^{-3}M) have been tried in the synchronously pumped dye laser in order to test its performance. In each case average powers of 100 mW and typical pulse lengths ∿ 3 ps were obtained. No cross corrolation measurements between the two synchronously pumped dye laser has been carried out so the relative timing jitter is unknown.

A dye amplifier designed to operate at 746 nm has been built. This is intended to provide sufficient energy at 248.7 nm by efficiently frequency tripling 746nm to seed a KrF excimer amplifier. The amplifier layout is shown in figure C3.6. The amplifier is pumped by a Lumonics excimer laser (70 mJ, 6ns). Three dye cells (Lambda Physik) are transversely pumped by 5 mJ, 4 mJ, and 28 mJ respectively. The dye is Rhodamine 700 in each cell with concentrations of 500mg l^{-1} in stages I and II and 50mg l^{-1} in the final stage. ASE rejection is achieved using a combination of spatial and spectral filters. A 100 µm pinhole isolates the first stage from the second stage while a dichroic filter transmitting at 746 nm rejects most of the ASE which peaks at ∿ 720 nm. A single ∿ 3 picosecond, 1 nJ pulse from the synchronously pumped dye laser injected into the amplifier can be amplified to approximately 330 µJ per pulse with an ASE background of ∿ 30 µJ. Frequency doubling to 373 nm yields 25 µJ/pulse and mixing 373 nm with 746 nm gave ∿ 5 µJ per pulse at 248.6 nm.

References

(C3.1) Chen Chuangtian, W u Buchang, Jiany Aidung, You Guiming, Scientia Sinica (B) 28 235 (1985).

(C3.2) J M Catherall and G H C New, IEEE Elect QE22 1593, 1986.

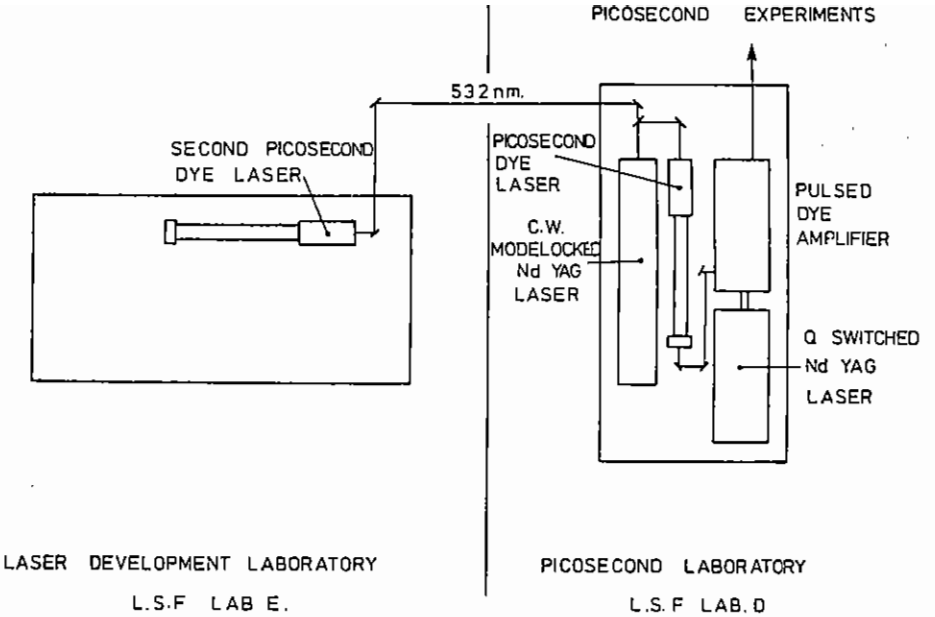

C3.5 Schematic of the layout used to pump two synchronously modelocked dye lasers using a single pump source.

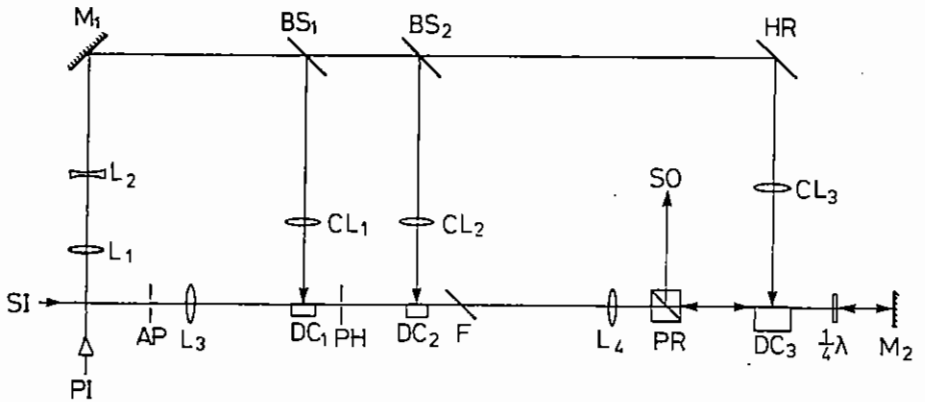

Fig C3.6 Layout of the picosecond dye amplifier system. SI-input; SO-output; PI-pump input; L_1 , ..., L_4 lenses of focal length 400mm, -300mm, 200mm, 500mm respectively; M_1, M_2 mirrors; BS_1, BS_2 beam splitters; HR high reflector; CL_1, CL_2, CL_3 cylindrical lenses of focal length 100mm; DC1, DC2, DC_3 dye cells; AP aperture; PH pinhole Φ = 100µm; F dichroic filter; PR polarising prism; ¼λ - quarter wave plate.

Editor: I N Ross

C4.1 SPIN COATING DEVELOPMENTS

I N Ross and A Bergey

C4.1.1 Introduction

A new and especially simple technique for antireflection coating has recently been developed at the Lawrence Livermore National Laboratory (C4.1). It is deposited from colloidal silica suspension using a spin or dip technique and results in a low average density (effective refractive index ≈ 1.23) coating which is an almost ideal single layer antireflection coating for materials with refractive indices in the range 1.45 to 1.55. This includes silica, many glasses, crystals such as water soluble KDP and plastics. The particle size of the normal colloidal silica is about 20 nm making it useable (without excessive scatter) down to the wavelength of the ArF laser (193 nm) and the damage threshold has been shown to be as high as that of the substrate in many cases. This section reports a programme of work which has been directed towards proper assessment of the COLSI coating and development of its potential.

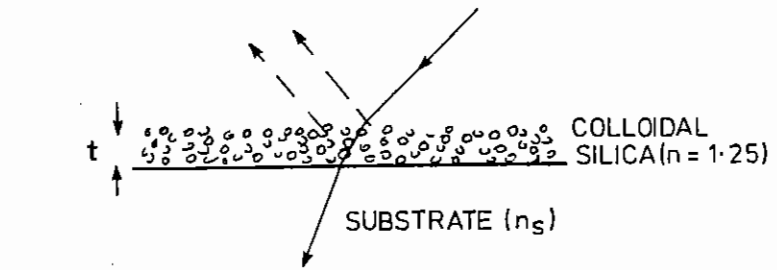

FOR ZERO REFLECTIVITY, $n = \sqrt{n_S} = 1.25$

$\longrightarrow n_S = 1.56$

AND $nt = \lambda/4$

C4.1 Colloidal silica antireflection layer.

C4.1.2 Assessment of the basic coating

A spin coating facility has been established and we now have considerable experience in COLSI coating techniques. Figure C4.1 shows a schematic of the COLSI coating while Fig C4.2 demonstrates its performance on different substrates and at different wavelengths. Typical residual reflectivity on quartz and glass is 0.2% per surface. Table C4.1 shows a variety of damage threshold measurements demonstrating the high power capability of these coatings. We note in particular that COLSI has damage thresholds higher than conventional evaporated coatings by a factor of 2 at 1μm and a factor of 3-4 at 0.25μm.

Table C4.2 lists the advantages and disadvantages of COLSI coatings. Further development has been directed to overcoming the disadvantages and investigating some possibilities for generating high reflection coatings using COLSI.

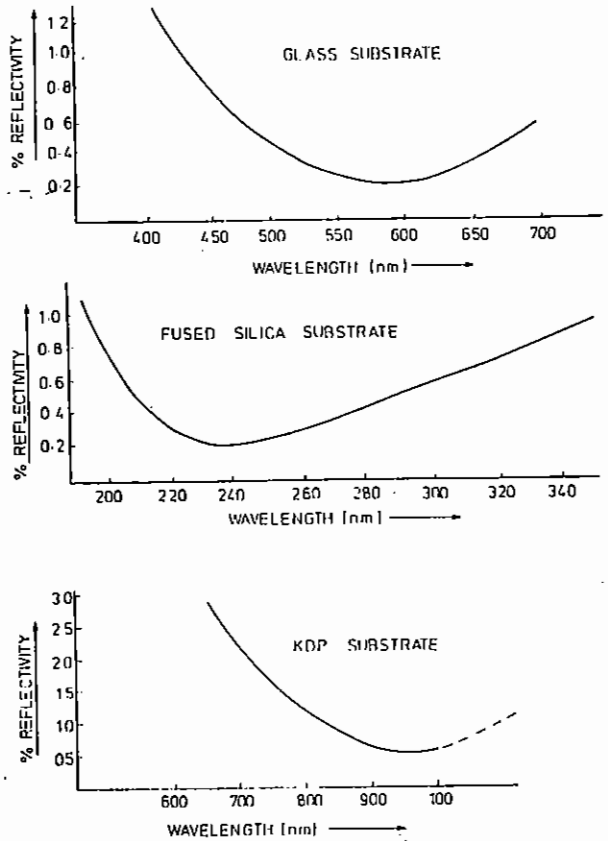

C4.2 Performance of colloidal silica antireflection coating on glass, fused silica and KDP substrates.

DAMAGE THRESHOLD MEASUREMENTS	DAMAGE THRESHOLD J/cm²		
	λ = 1μm		λ = 0·25μm, t = 10ns
	t = 1ns	t = 0·4ns	
BK7 Substrate. (Uncoated)		12	
Evaporated AR coating on BK7 (cryolite)		7	
COLSI coating on BK7		13	
Uncoated KDP	13		
COLSI coated KDP	10		
Fresh COLSI coating on glass (BK7)	20		
COLSI coating on BK7 - after 6 months	20		
Silica substrate (Uncoated)			17
COLSI coating on silica using undistilled material			2
COLSI coating on silica using distilled material			8
Evaporated AR coating on silica (various)			1→2·5
COLSI + overcoating : on BK7 glass			
ZnS	1·5		
Al_2O_3	5		
ThF_4	10		
MgF_2	1·5		
ZrO_2	<1		
COLSI coated, contaminated and baked 2hr @ 110° C	15		

ADVANTAGES	DISADVANTAGES
1) Low reflectivity single layer coating for glass, silica and KDP	1) Fragile - no mechanical contact possible.
2) High damage threshold	2) Vulnerable to contamination in vacuum systems
3) 200nm to >1100 nm	
4) Broad bandwidth - 30%	
5) Low cost spin process	
6) Easily removed and recoated	
7) Useable on any well polished substrate including water soluble crystals.	

C4.1.3 Spin Overcoating

A 'half-wave' overcoating of any transparent dielectric material with a continuous structure will improve the abrasion resistance of the coating and prevent contaminants getting into the COLSI layer without increasing the surface reflectivity. A number of materials have been investigated for spin overcoating. A suitable material must be hard and insoluble in one of the normal cleaning solvents, have low absorption and high damage threshold, must not give a porous coating, must not sink into the underlying COLSI layer and must spin coat to a uniformly thick layer with controlled thickness and low scatter. The most successful results to date have been for PM10, a proprietry electron beam resist material. This material is spun coated and baked, the baking process resulting in a cross-linked polymer which is hard and is insoluble in alcohol. Figure C4.3 shows the performance of COLSI with PM10 overcoat. The small increase in reflectivity is caused by slight incursion of the PM10 into the COLSI layer and this, together with some absorption in the ultraviolet (∿ 1% per surface @ 250nm) make PM10 unsuitable for use below 300nm.

Damage threshold measurements have been made at a wavelength of 1 μm and for 1 ns pulses. Single shot thresholds of $18J/cm^2$ and multiple shot thresholds of $20J/cm^3$ indicate very little reduction due to the overcoating. A three week contamination test in one of the main target chambers increased the reflectivity by only 0.3 → 0.6% per surface showing the effectiveness of the protective overcoating.

C4.1.4 Water film deposited overcoating

We have not found a material which is both suitable for ultraviolet operation and will spin coat onto COLSI without degrading the antireflection properties of the coating. A promising material has been found (a commercial glass resin GR650) which has very low absorption at a wavelength of 250 nm but which sinks into the COLSI during the spin coating process. An alternative technique has been tried and looks promising. This is a technique , already used for generating thin polymer films, in which a droplet of polymer solution spreads out on a water surface and dries to form a uniform thin film. This film can then be transferred onto the substrate by raising the substrate through the water surface. Fig C4.4 shows that such an overcoating is possible onto COLSI and does not increase the surface reflectivity for a 'half-wave' layer.

C4.1.5 KDP protective coating

As a water soluble crystal KDP suffers atmospheric degradation over a period of time. Due to this degradation and the difficulty in polishing such a soft crystal there is generally a considerable scatter loss. A protective spin coating will in principle eliminate both of these defects by sealing the surface against attack by atmospheric moisture and if it has the same refractive index as the crystal, by 'filling up' the surface microstructure to produce a smooth interface. The proposal was tested using PM10 resist as the protective coating. A good quality KDP crystal was coated and placed in a high humidity environment. No increase in scatter was observed over a four week test period. A second crystal with high scatter loss (20%) was coated. The scatter loss was reduced to ∿ 10%, showing a factor of two improvement.

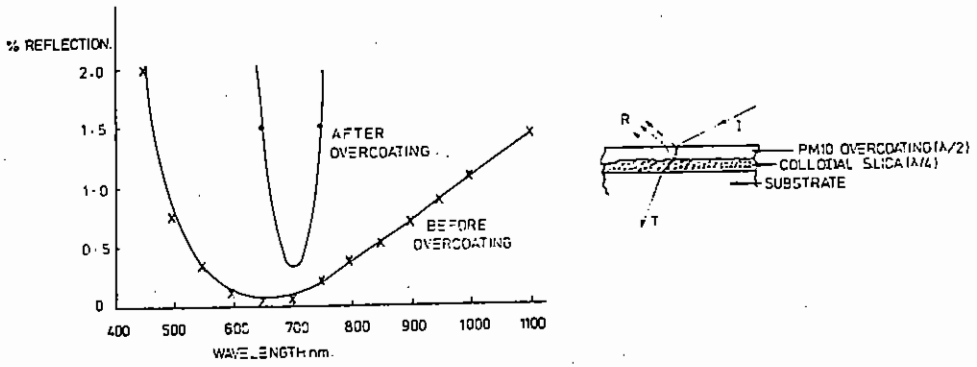

C4.3 Performance of PM10 protective overcoating.

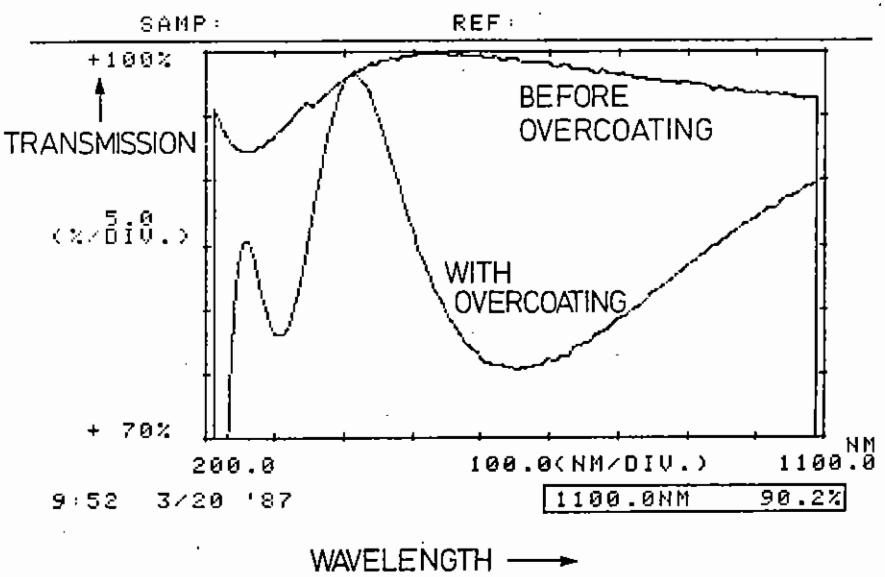

C4.4 Performance of GR650 protective overcoating.

It has also proven possible to overcoat this PM10 coating with COLSI to reduce the surface reflection losses and enable a stand-alone crystal with low loss and high environmental durability. Crystals coated in this way had surface reflectivities between 0.5 and 1% and damage thresholds at 1 μm of 10J/cm^2 single shot and 20J/cm^2 multiple shot (low level working up in power).

C4.1.6 Multilayer reflectors using COLSI

The uniquely low effective refractive index of colloidal silica (n ≈ 1.23) coupled to the high indices of evaporated coatings would seem to offer high potential for efficient high reflection coatings. A number of COLSI-coated plates were overcoated by evaporation to generate a simple two layer reflecting stack for normal incidence, and a four layer stack for normal incidence. Fig C4.5 shows that the measured reflectivities of these coatings come very close to what is achievable theoretically. We note in particular that more than 50% reflectivity was achieved at normal incidence with a two layer coating and more than 75% was achieved with a four layer coating.

C4.2 ACHROMATIC F/2 STREAK CAMERA IMAGE RELAY OPTICS

I N Ross, W T Toner, E M Madraszek

C4.2.1 Introduction

A streak camera has formed an essential part of the picosecond laser facilities especially for experiments using fluorescence spectroscopy. Such experiments may require simultaneous time resolution of an ultraviolet pump pulse and a broad band fluorescence spectrum at visible wavelengths. Existing streak camera input optics were not able to provide sufficient resolution over such a spectral spread and were very inefficient at ultraviolet wavelengths. The objective of this design study was to find a suitable scheme for imaging a slit onto a streak tube with a simultaneous resolution of ≤ 20μm for all wavelengths from 250nm to 800nm and with as high a numerical aperture as possible. It was also felt to be desirable to have good resolution along the slit.

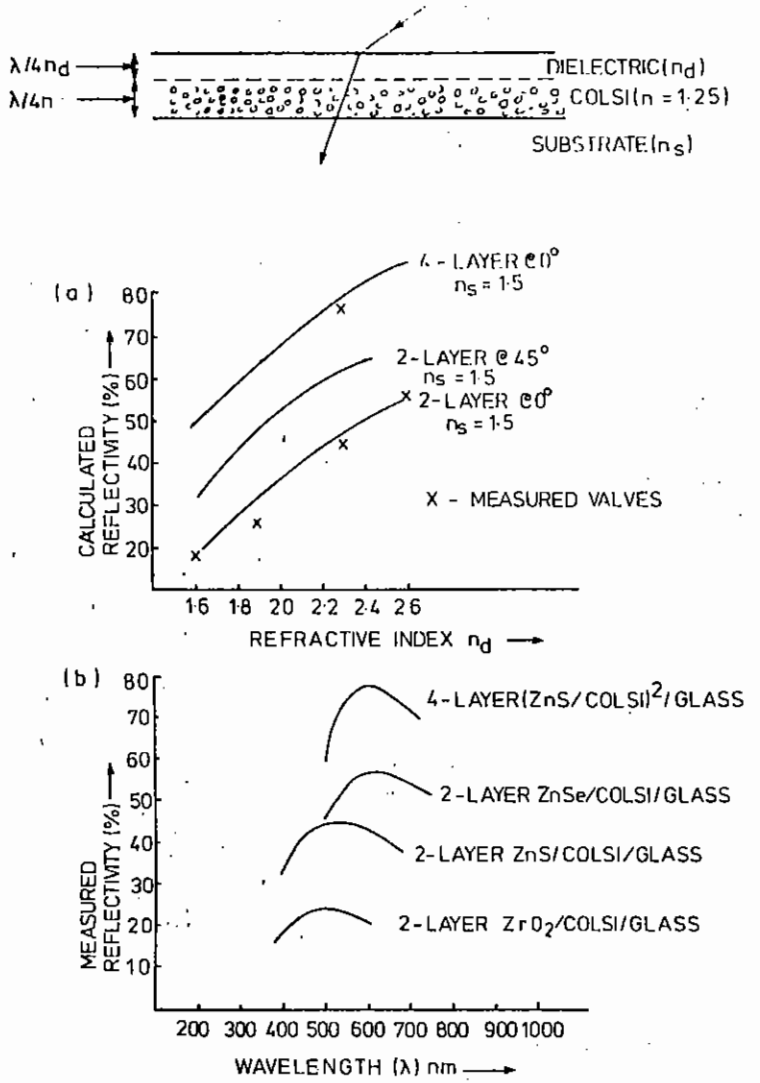

C4.5 Reflecting coatings using COLSI and evaporated materials.

(a) Variation of the reflectivity of two and four layer coatings with the refractive index of the evaporated layer

(b) Measured wavelength dependence of multilayer coatings.

C4.2.2 Design

The requirements called for an all mirror design, while the requirements for a line focus with 1 to 1 magnification suggested the possibility of an off-axis mirror system, already shown to be effective as a generator of high quality line foci for X-ray laser studies.

The selected scheme follows the principal represented in Fig C4.6. Ray tracing calculations were carried out to optimise the scheme. If the image width corresponding to the geometrical parameters a, R, N.A. is $\Delta(a,R,N.A.)$ then, to a reasonable approximation:-

$$\Delta(a,R,N.A.) \approx 0.3\ R\ (NA)^6$$

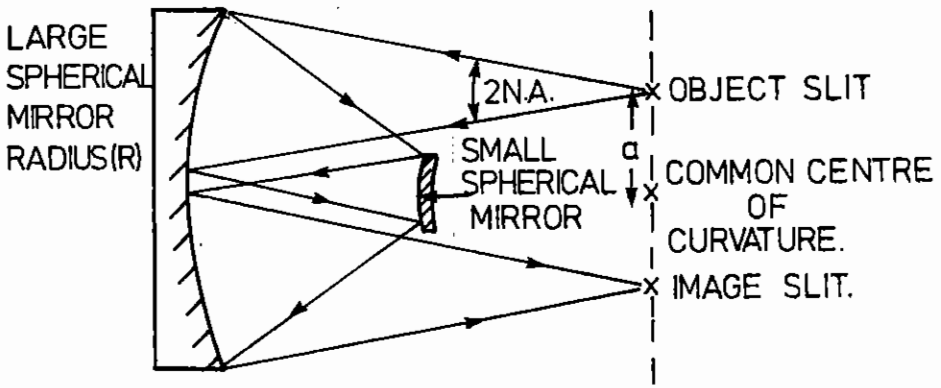

C4.6 Design schematic for streak camera image relay optics.

where for minimum Δ, a is reduced to a minimum compatible with the geometry, and this minimum value of a is given by: $a = R.(N.A.)$

and where the small mirror radius is kept optimum.

For a requirement that $\Delta \leq 20$ μm for all points along a straight slit of length 20 mm, and for geometries that were compatible with the Dellistreak camera, the maximum useable numerical aperture was found to be ≈ 0.25. Having established the feasibility of the proposed arrangement and the basic geometry calculated for optimum performance, a mechanical design was sought to integrate the optics into the streak camera in a way which would allow adjustment and assessment of the optics prior to its attachment to the camera. Fig C4.7 indicates the scheme as used for the prototype assembly.

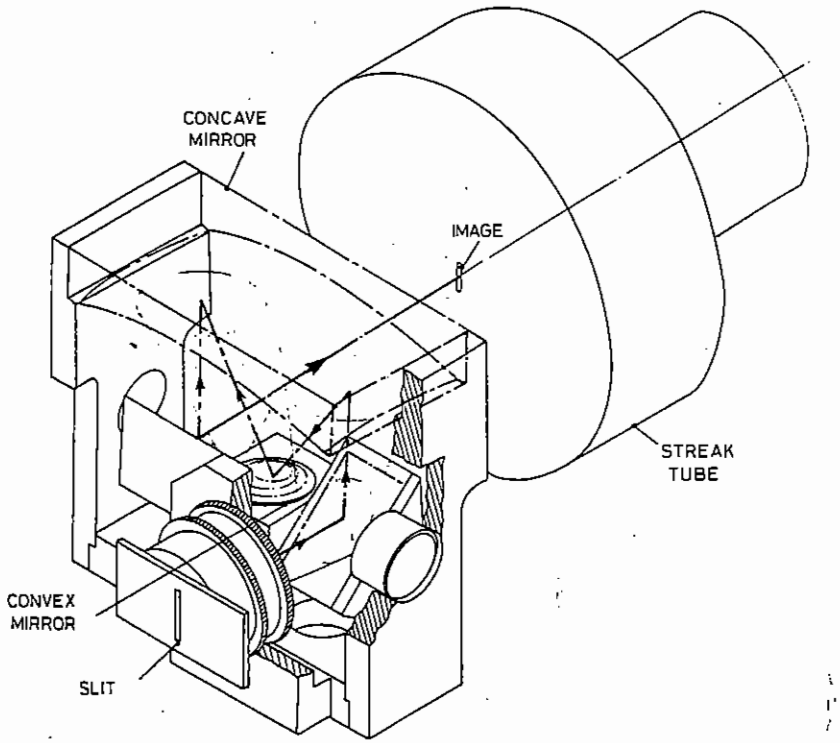

C4.7 Prototype assembly for streak camera image relay optics.

C4.2.3 Assessment of performance of prototype

C4.2.3 A

Prior to its use on the streak camera the optics were set up for best performance in the design mount. A resolution of ≤ 20μm was observed, using a He Ne laser illuminating the full numerical aperture, over a field size ∿ 1 cm in the transverse and axial directions and a field size of ∿ 2 cm in the vertical direction (along the slit direction). Because of the inherent astigmatism of the system, focussing could be optimised for best resolution transverse to or along the slit but not both. At the best compromise focus the resolution was ≈ 20 μm in both vertical and horizontal directions.

The final design involved five mirror reflections, two having been added to provide a convenient geometry. MgF_2 overcoated aluminium was used on all mirrors to give best integrated reflectivity from 250nm to 800nm. This design did not of course give maximum throughput for a particular wavelength. The measured transmission was approx 50% which was as expected for the type of reflectors used.

C4.2.3 B

The new input optical system was transferred to a Dellistrique streak camera and tests carried out to assess the resolution of the complete system. Fig C4.8 shows a streaked image of a very short duration pulse (∿ 5ps) together with an intensity profile in the streak direction. The secondary pulses are time markers from an etalon. Measured pusle width was ≈ 250μm corresponding to an input slit width of 100μm. Static focussing tests demonstrated that this was limited by the camera not the input optics.

References

C4.1 I M Thomas, Applied Optics 25, 1481 (1986).

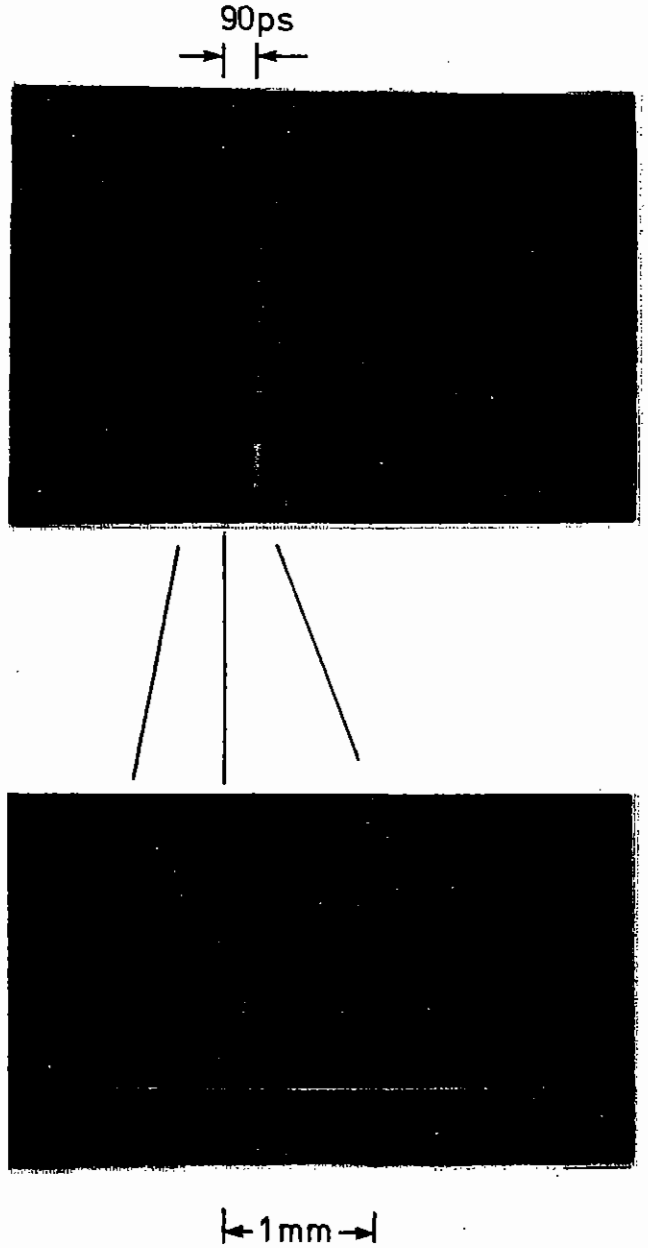

C4.8 Performance of streak camera with new image relay optics. Secondary pulses are time markers generated by etalon reflections.

Editor: A Ridgeley

C5.1 MONOCHROMATIC X-RAY PINHOLE STREAK CAMERA

P Norreys (Royal Holloway and Bedford New College), A Cole, A Ridgeley, A Damerell (RAL)

Two-dimensional monochromatic imaging of X-rays can be achieved by combining an X-ray pinhole camera with a multilayer mirror (C5.1, C5.2). The advantages of using a multilayer mirror over a crystal for monochromatic imaging with a pinhole are:

1. The mirror has a low resolution - this 'smooths out' out fine structure in the spectrum.

2. The mirror has a higher integrated reflectivity coefficient than crystals (x10) giving much brighter images.

3. Correct choice of layer thickness can lead to a very compact instrument which is important in a 12 beam target chamber.

The greatly improved contrast between the X-ray emitter and the background emission from the plastic allows a direct observation of the burn through to a buried layer if time resolution is incorporated into the monochromatic pinhole camera.

Figure C5.1 shows the monochromatic X-ray pinhole streak camera. The multilayer mirror used was a tungsten/carbon mirror consisting of 50 layers with a 2d spacing 43.2Å. The resolution of the mirror has been measured and found to be $\lambda/\delta\lambda = 45$ (C5.3).

The mirror has a range of motion of 5-35 mm from the direct optical axis of the instrument, giving a range of incident angles from 1.7° → 12.0° to the mirror surface. This corresponds to a wavelength range of 1.3 - 9.0Å for this multilayered structure. The mirror motion is independent of the pinhole assembly, so that movement of the pinhole does not affect the position of the dispersed spectrum at the streak camera photocathode plane. The holder has two manual tilt adjustments to position the mirror correctly.

The slit jaws have independent motions allowing one slit to be placed on the desired part of the spectrum and the other closed down on it.

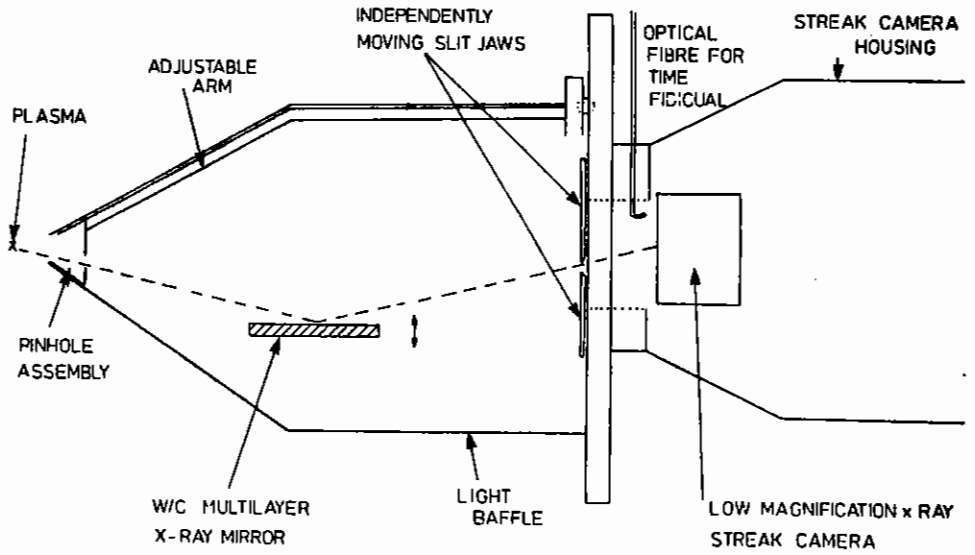

C5.1 A time resolving monochromatic X-ray imaging device.

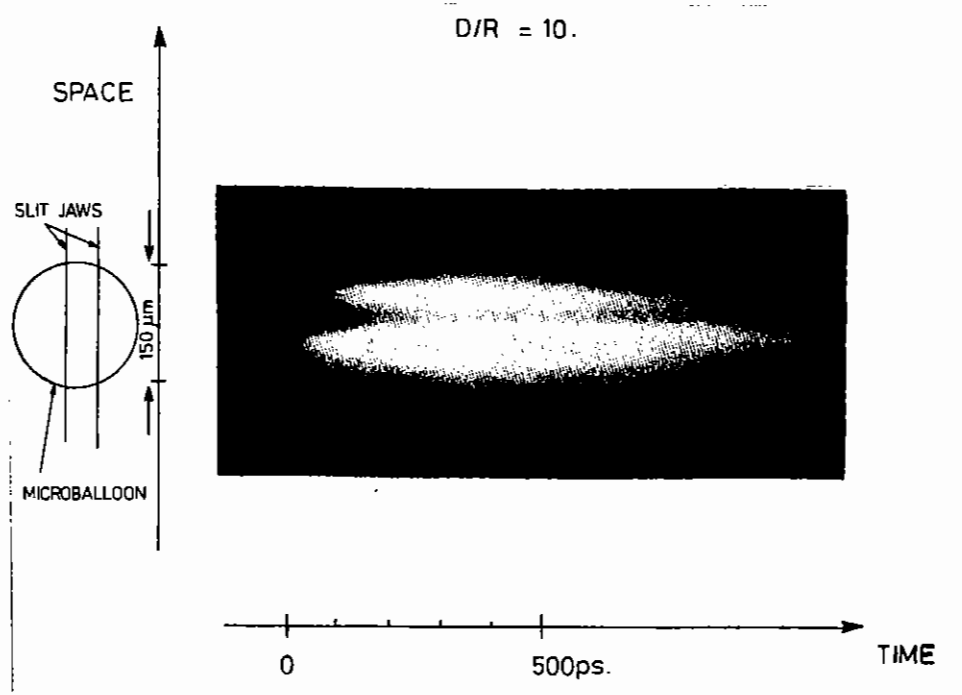

C5.2 Streak camera image of aluminium coated balloon with a plastic overcoat of 1.5μm thickness.

The instrument needs to be light tight and this is provided by the light baffle.

A test was conducted on VULCAN's 12 beam target chamber to determine if the instrument could resolve spatially non-uniform ablation and whether any commissioning changes were necessary.

The instrument was aligned by the following procedure. The streak camera was removed from its housing and a mercury lamp was set up to illuminate the slit jaws. The pinholes were removed and the virtual image of the slit jaws from the multilayer mirror was imaged by a Questor telescope. The jaws had previously been positioned over the correct spectral region. The telescope was adjusted so that the slit jaws, target and the cross wires in the telescope eyepiece were in the same plane. The pinholes were then reinserted and positioned in exactly this plane. The technique was found to be reliable and extremely accurate.

Two types of X-ray emitters were selected for the experiment. They were Selenium which has a bright L shell emission from 7 → 8Å and Aluminium which has Heα and Lα lines at 7.8 and 7.1Å respectively.

Figure C5.2 shows a monochromatic streaked image of an aluminium coated solid plastic microballoon. There was 1.5 μm of N paralyene overcoated onto the aluminium. The diameter of the balloon was 150 μm and the absorbed irradiance was 1 x 10^{14} Wcm^{-2}. The horizontal beams were blocked in this shot so only the top and bottom of the balloon showed any burn through. Figure C5.3 shows a microdensitometer tracing of the streaked image.

Selenium was found to be a more suitable material for imaging because the broad L-shell emission allowed the image to be positioned very easily, whereas the aluminium targets just had the emission line visible.

After this experiment, the mirror motion was increased, light baffling improved and a timing fidicual added to give the uniformity of the mass ablation rate.

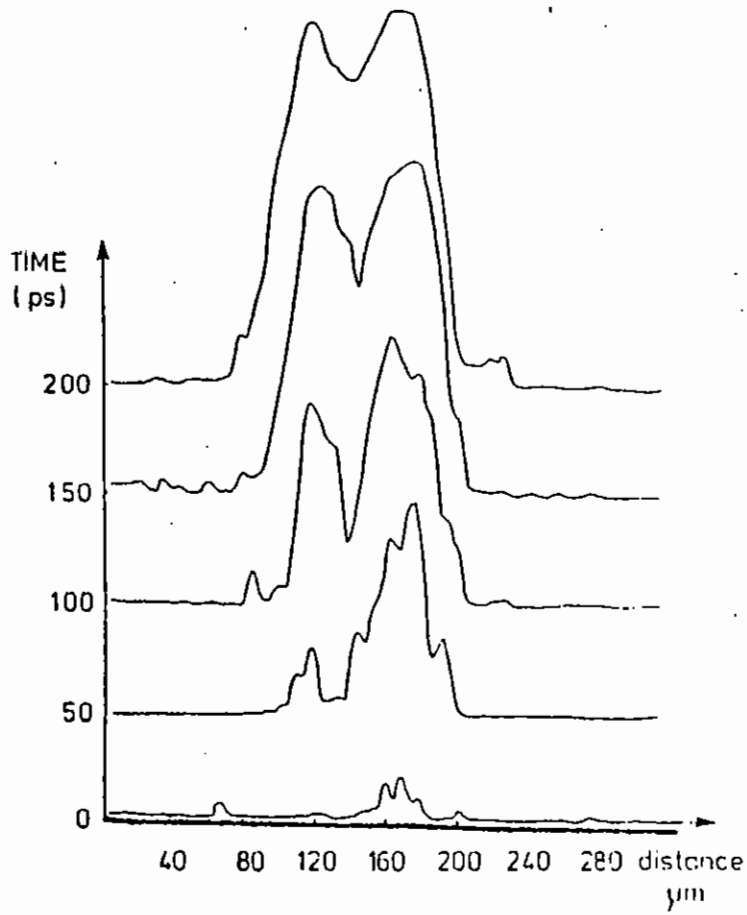

C5.3 Densitometer tracings through the image in fig C5.2 at various times.

C5.2 SPACE RESOLVED X-RAY SPECTROSCOPY

B S Fraenkel (Hebrew University of Jerusalem)

The purpose of this research is to obtain monochromatic images of the laser produced plasma, in the X-ray wavelength. The images would be undistorted two dimensional pictures of the plasma, a separate picture for each emitted wavelength. Such images can give the time integrated ion distribution of each of the species of the variously ionized and excited ions in the laser produced plasma, providing that those species emit X-rays.

Two ways are known to obtain such images, the double reflection method in a single crystal (C5.4), and the double reflection through two crossed cystals, in series (C5.5, C5.6).

The double reflection method in a single crystal is explained in the following way: Assuming an X-ray point source is placed above a plane horizontal crystal, with the plane being a crystal reflection plane, a cone of reflection will be formed for each wavelength emitted from the source. However, there exist crystal planes which are forbidden planes, and will not reflect radiation for crystallographic reasons. There exist, however, crystals of special symmetries, which would reflect in this case along one or several sharply defined directions in the cone. This effect, called the Renninger effect (C5.7), would yield a sharp beam reflected from the point source. Such a beam would be seen as a point on a film held perpendicular to it. A point would thus yield a point, a line would yield a line, and a monochromatic source of any form will yield in this process the same two dimensional form on the film. A polychromatic source will yield a series of images, showing the distribution of each of the X-ray emitting ions in the source. The whole process is possible when a double reflection in the crystal simulates the forbidden reflection, along sharp predetermined directions (C5.4). Involved are, therefore, two allowed reflection planes, and a forbidden reflection plane.

The spatial resolution is of interest. A good crystal at a short wavelength has a diffraction width of two seconds of arc. This would yield a resolution of one micron when the distance from the source to the film is 10 cm.

Spatial resolution of laser produced plasmas has been achieved (C5.8), but in the wavelength range from 1 to 5 Å only. This has been done with Ge and Si crystals. The longest wavelength with double reflections which may be reached with these crystals is about 5.3Å.

There exists an interest to extend the wavelength range to longer wavelengths, where high X-ray intensities may be obtained from the 1.p.p. - e.g., the He-like resonance lines of Al.

Working at long wavelengths calls for crystals of small absorption factors - e.g., organic crystals. It is quite a task to find appropriate crystals for the one crystal double reflection method, while it seems to be easier to work with two crossed crystals with well known big "d" -s. However, the advantage of using the one crystal method is the potential of locating the single crystal and the detector closer to the X-ray source, with attendant improved spatial resolution[2]. Also, "surface broadening" would be half that of the two crystal method.

The double reflection in two crossed crystal method involves two planes of relection, each containing the incoming and the outgoing beam. Usually the term "crossed crystals" means that the planes of reflection are perpendicular to each other. However, this would diminish intesity in many cases because of the polarization factor. This may be avoided by varing the angle between the planes of reflection, with some loss of spatial resolution. It has been found that for a given diffraction broadening $\Delta\theta$ the following broadenings would be expected as function of the angle between the planes of reflection.

Angle	90°	42°	30°	19°	14°
Broadening	$\Delta\theta$	$1.5\Delta\theta$	$2\Delta\theta$	$3\Delta\theta$	$4\Delta\theta$

In this range of angles the broadening will be independent of the Bragg angle, except for the value of the $\Delta\theta$ itself.

Crystals were prepared for the two experiments.

Potassium Hydrogen Phthalate (KAP) has two strong reflections: (0,1,0) and (1,1,1). The reflection (1,0,1) is forbidden. But this reflection is the sum of (1,1,1) and (0,-1,0), which is the same reflection as (0,1,0). Therefore double reflections of considerable intensity should be obtainable. We calculated that this double reflection can extend to 10Å. A crystal was prepared, with its surface parallel to the (1,0,1) plane. It is intended to work with it on the Al highly ionized lines.

The two crystal experiment is being prepared with two Beryllium Alumininium Metasilicate crystals (Beryl) which can give reflections up to 15Å.

The adjustment experiments did not succeed on the laser source itself, and the crystals are now being tested and adjusted in the laboratory of X-ray and V.U.V. spectroscopy at the Racah Institute of Physics, the Hebrew University in Jerusalem.

C5.3 MONOCHROMATIC IMAGING USING A DOUBLE CRYSTAL SPECTROMETER

C Lewis, Queen's University Belfast

Introduction

The basic geometry associated with a double crystal spectrometer providing 2-D spatial resolution at each emission wavelength of an X-ray source is described. The advantages and disadvantages of such a device compared to double reflection in a single crystal, single crystals with a space-resolving slit and pinhole cameras with broadband multilayer filter reflectors will be discussed elsewhere. The present device is expected to be most useful when the source is large ($\geq$ 100μm) and $\geq$ 10μm resolution is adequate. The final image is comparable to the source size and typically requires a black-body equivalent emission temperature of 100-200 eV for recording on DEF X-ray film at an imaging photon energy of $\approx$ 2 keV assuming the emission line width does not significantly degrade the spatial resolution.

Principle of Instrument

The spectrometer is based on the principle that a Bragg X-ray crystal reflects radiation at a particular wavelength emitted by a quasi-point source only over a narrow angular range determined by the crystal rocking curve (typically $\Delta\theta \sim 10^{-4}$ rad). Using two crystals in tandem but each reflecting in orthogonal planes only a narrow bundle of rays with solid angle $\Delta\Omega \sim \Delta\theta^2$ can reach the detector at a total ray path length distance 1. The quasi-point is recorded as a feature of scale length $1\Delta\theta$ and other emitting points are recorded as displaced features in a 1:1 mapping with a 2-D spatial resolution of $\sim 1\Delta\theta$ in the object plane. If the emission line width $\Delta\lambda$ is large then spectral smearing through dispersion can degrade the resolution further. Using wavelengths close to the crystal d-spacing this limit sets $\Delta\lambda \leq d\Delta\theta$. An analysis of the geometry shows that the orientations of the crystals can be arranged such that a wide wavelength coverage is simultaneously possible with small crystal dimensions and hence the possibility of designing a compact instrument.

Geometry of Instrument

The geometry is illustrated in Fig C5.4 where S is the X-ray emission source, one Bragg crystal lies with a reflecting surface in the xy plane and a second crystal has its reflecting surface rotated an angle α out of the xy plane. A ray representing wavelength λ_0 is incident o the first crystal at point C and lies in the xz plane. It is described by the unit vector I_0 and will be referred to as the central ray. After Bragg reflection at an angle θ_0 given by $\lambda_0 = 2d \sin\theta_0$ it travels in the unit vector T_0 direction. T_0 can lie anywhere on the surface of a cone determined by the azimuth angle Φ_0. We define $\Phi_0 = 0$ if the second crystal normal n_2 lies in the same plane (xz) as the first crystal normal and has a positive k

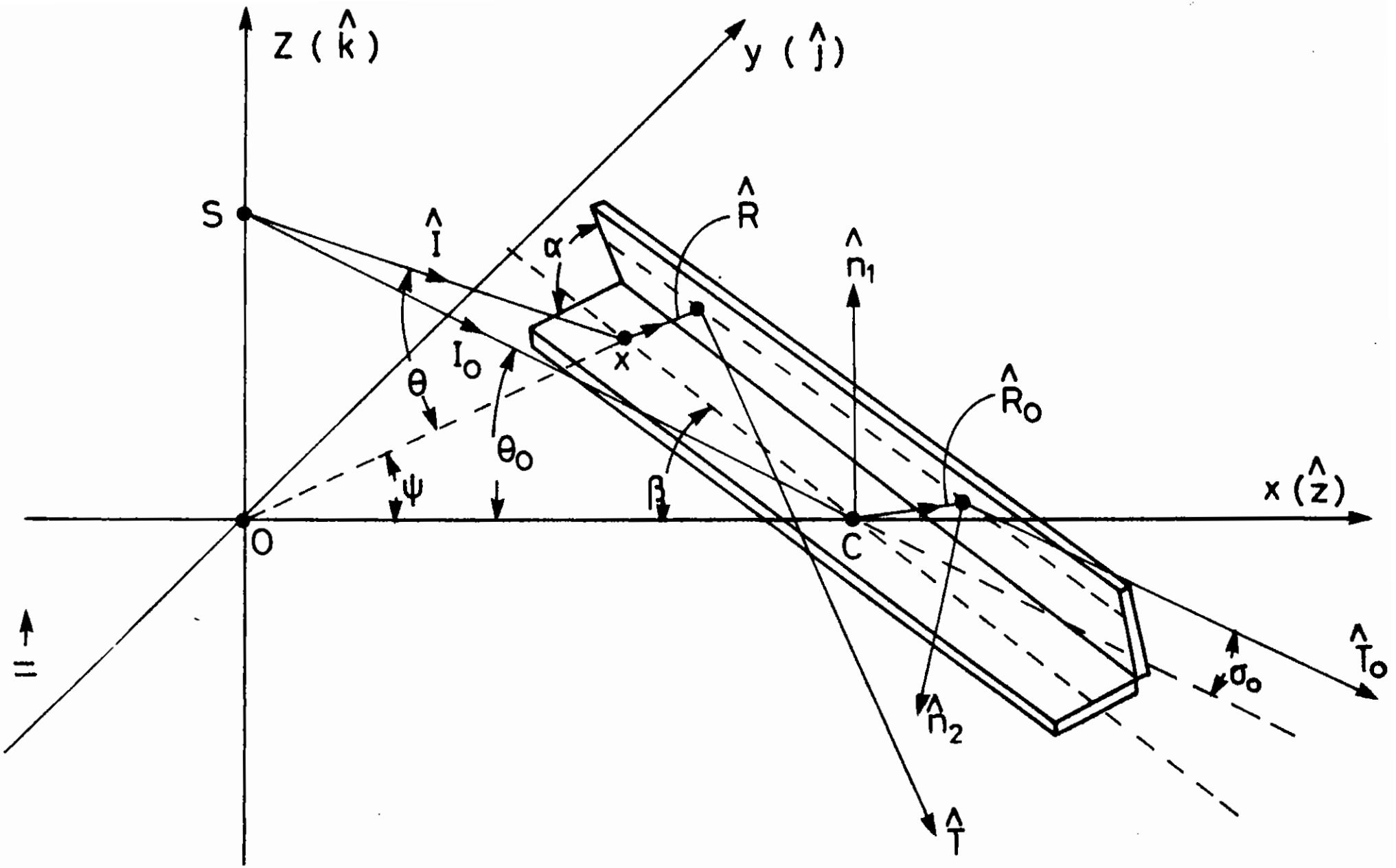

C5.4 Basic geometry and symbols discussed in text where S is the plasma source to be imaged by the two folded crystals.

component. For the special case $\Phi_0 = 90°$ the dispersion planes for each reflection are orthogonal and space resolution of the source S in a plane perpendicular to I_0 is possible for the wavelength λ_0 in orthogonal directions. To satisfy the general case we can write:-

$$I_0 = \cos\theta_0\, i - \sin\theta_0\, k$$

$$n_1 = k$$

$$\text{and } n_2 = [-\sin\theta_0\cos\theta_0(1 + \cos\Phi_0)]i - \cos\theta_0\sin\Phi_0 j +$$

$$[\cos^2\theta_0(1 + \cos\Phi_0) - 1]\, k$$

Then $R_0 = I_0 + 2\sin\theta_0 n_1$ and $T_0 = R_0 + 2\sin\theta_0 n_2$. The folding angle α between the crystal surfaces is then given by $\cos\alpha = -n_1.n_2 = 1 - \cos^2\theta_0(1 + \cos\Phi_0)$ and the deviation angle of the emergent ray bundle σ is given by $\cos\sigma_0 = I_0.T_0 = 1 - \sin^2 2\theta_0(1 + \cos\Phi_0)$. Thus two crystals can be folded for any central ray wavelength λ_0 to undergo two reflections although in practice $\theta_0 \leq 45°$ is a condition that must be satisfied for the emergent ray to escape without striking the first crystal again. Referring to Fig C5.4 we can now examine what happens to a ray I representing $\lambda = \lambda_0$ which is incident on the first crystal at an angle θ defined by $\lambda = 2d\sin\theta$. We can specify this point, X, on the xy plane with the angles θ and Ψ. The incident ray direction is

$$I = (\cos\theta\cos\Psi)i + (\cos\theta\sin\Psi)j - \sin\theta\, k$$

and the reflected ray direction is $R = I + 2\sin\theta n_1$ with $n_1 = k$. If the ray R is to reflect of the second crystal also we must have $\sin\theta = -R.n_2$ where n_2 is as before for θ_0. This condition implies that θ, Ψ and θ_0 are connected through $\tan\theta = (\sin\theta_0\cos\Psi + f\sin\Psi)/\cos\theta_0$ where $f = \sin\Phi_0/(1 + \cos\Phi_0)$. Inspection of the triangles defined by SOCX

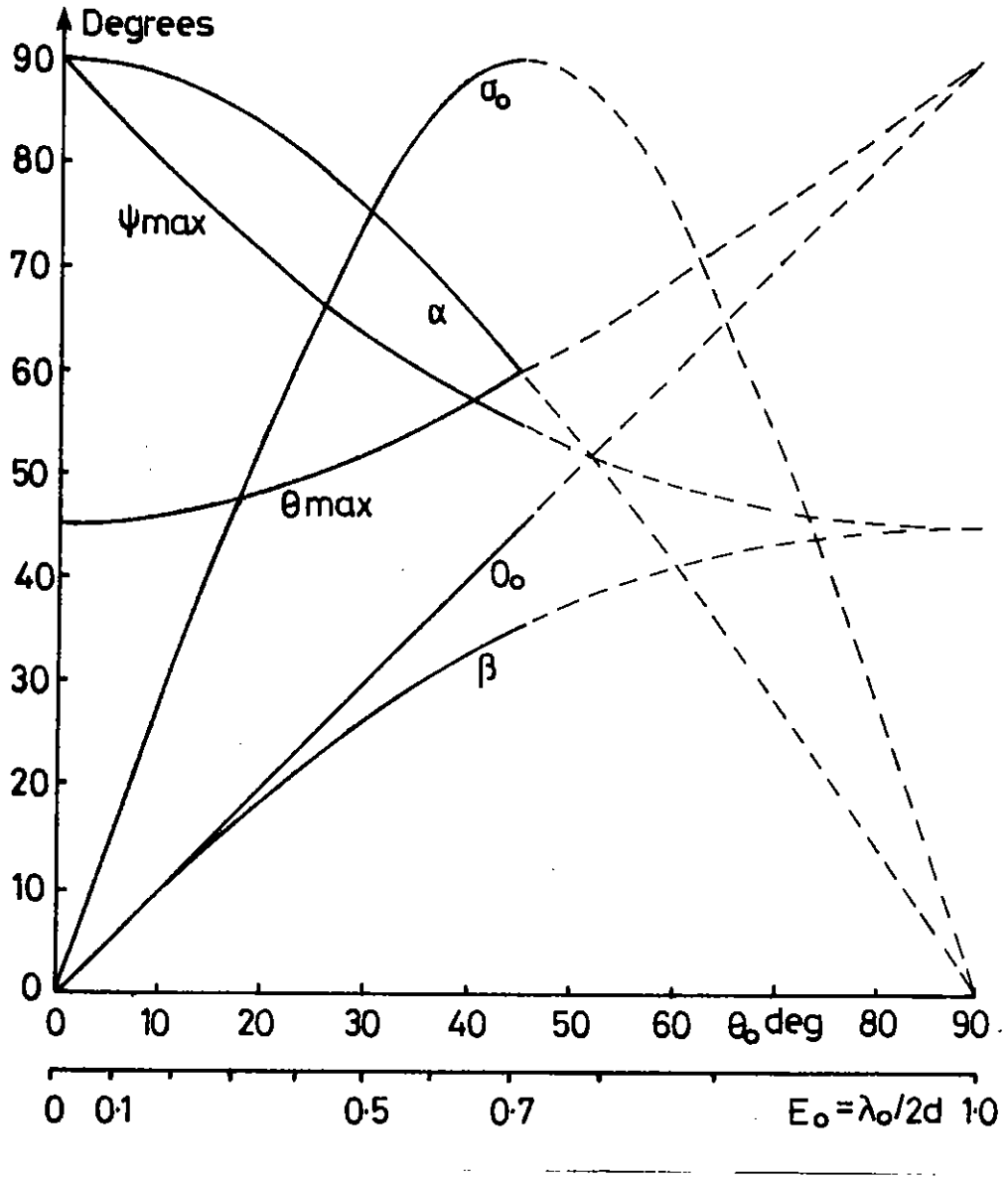

C5.5 Generalised angles appropriate to design of instrument for any $\lambda_0/2d$ ratio.

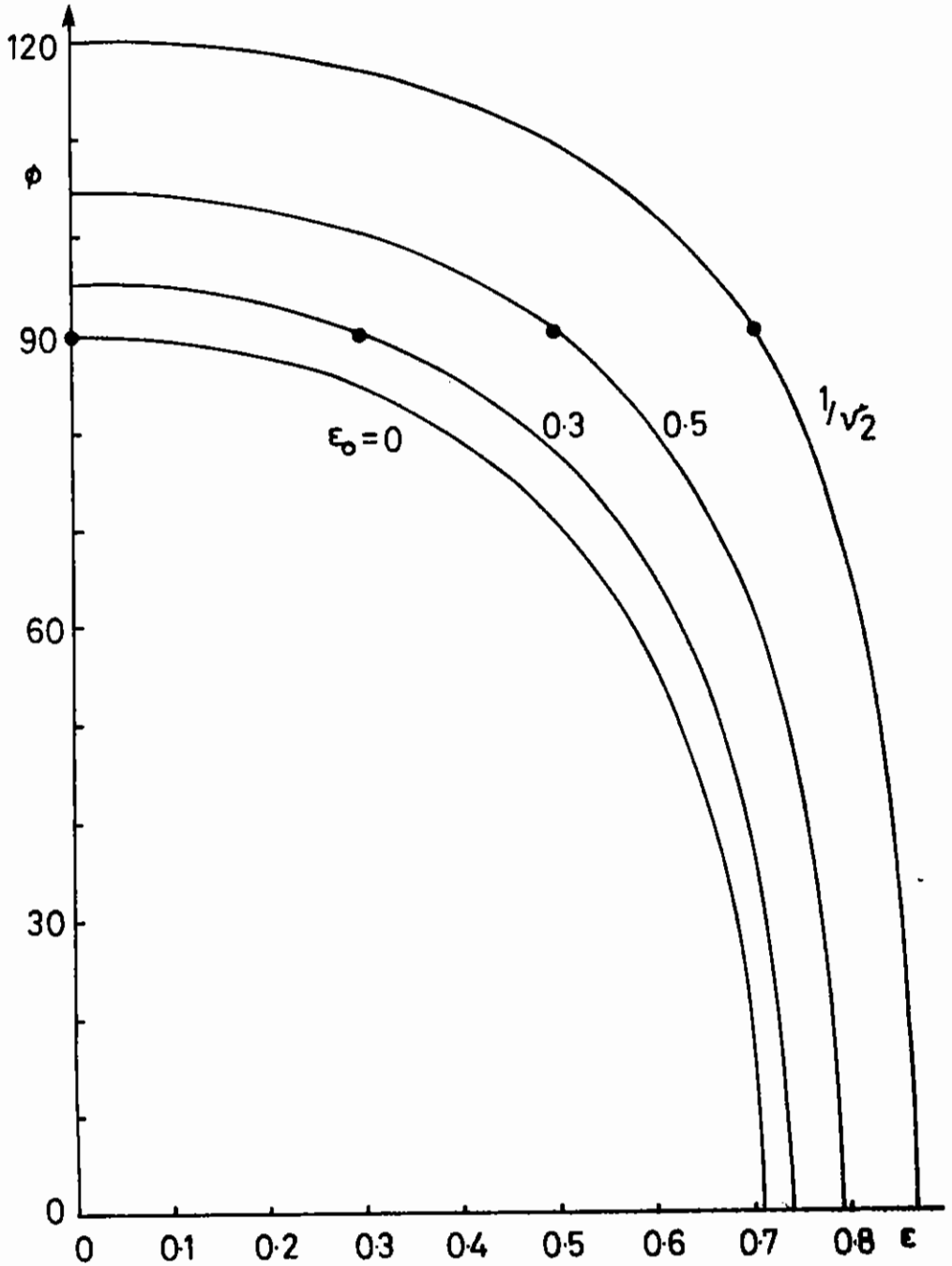

C5.6 *Departure of azimuth angle from 90° for wavelength 2dε, not equal to the central design wavelength 2dε, not equal to the central design wavelength* $2d\varepsilon_0$.

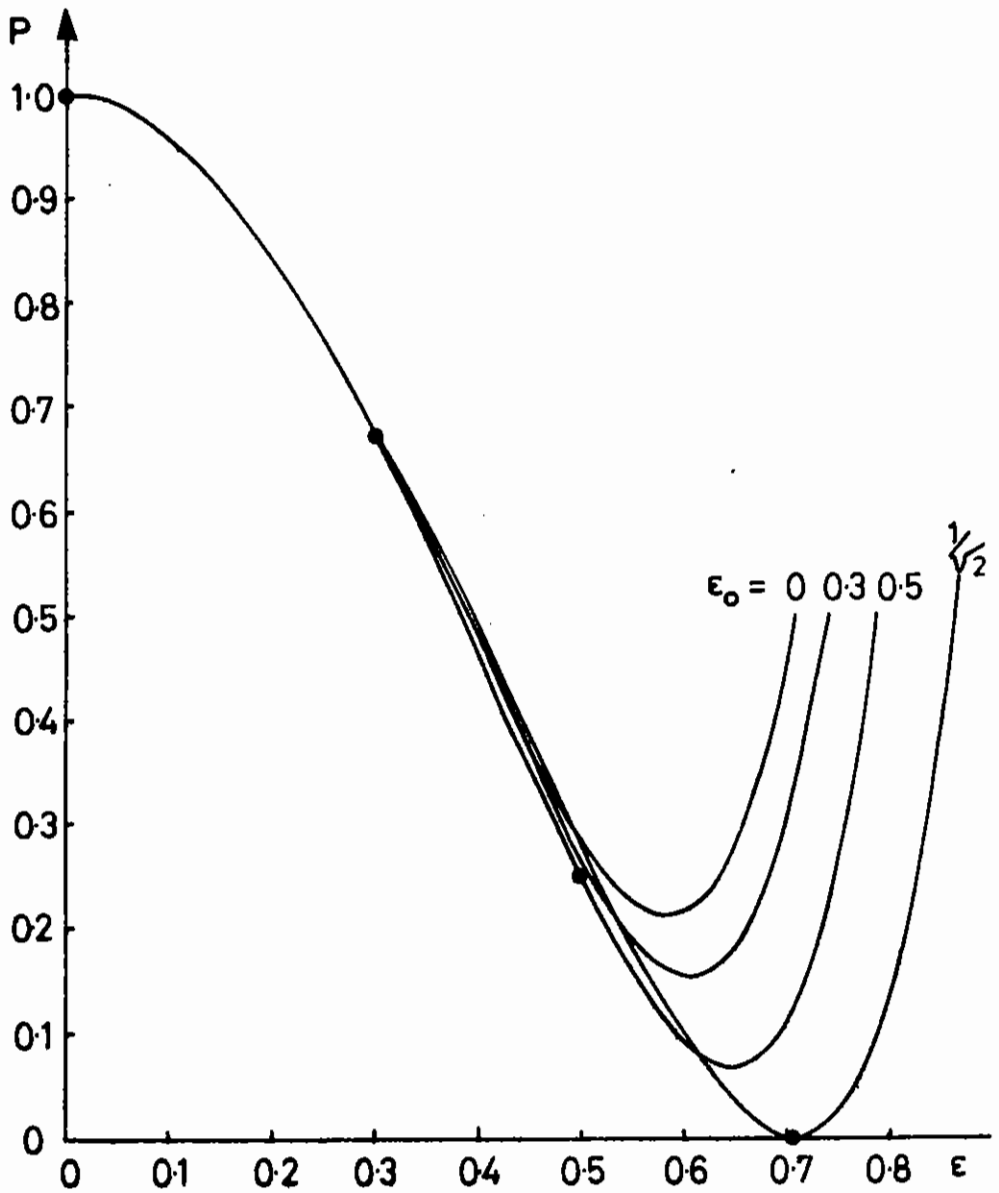

C5.7 *Variation of polarisation factor at different wavelengths 2dε for different central design wavelengths* $2d\varepsilon_0$.

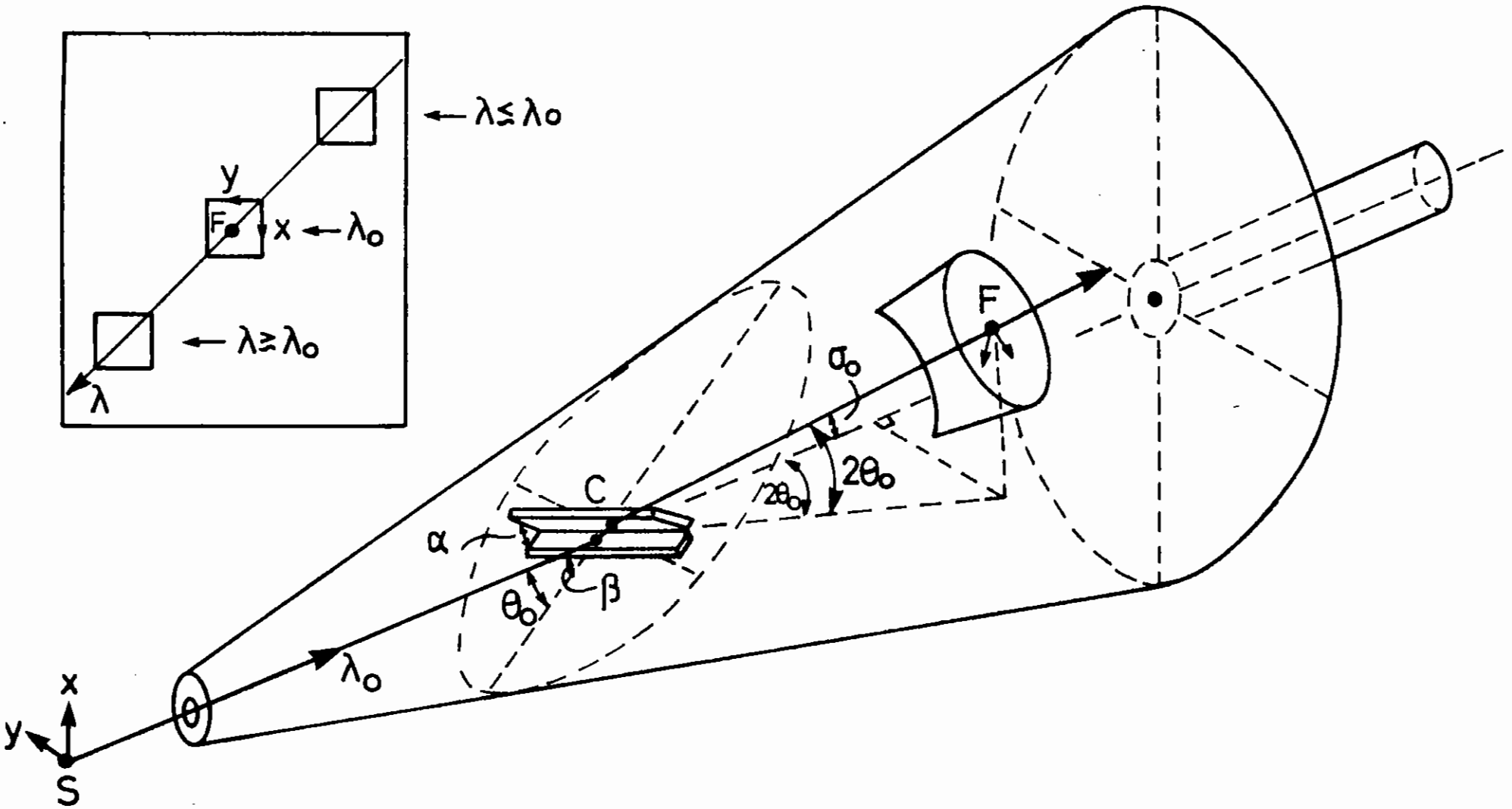

C5.8 *Schematic of possible practical device. The film plane F is contained in a part which does not see the plasma source directly and is normal to the emergent central ray of wavelength* λ_o. *Distance S-C-F is typically ∿ 10cm. Insert depicts image positions of a square source emitting at 3 different wavelengths the azimuth angle* $\phi_o = 90°$.

in Fig C5.4 shows that this is equivalent to making the angle β, which defines the first crystal useful surface points in the xy plane, such that $\tan\beta = \sin\theta_{0max} = [(f^2 + \sin^2\theta_0)/(f^2 + 1)]^{1/2}$ is a straight line and that physically the two crystals require one dimension to be not much larger than the source itself. The long dimension is determined by the wavelength coverage required.

The argument can be made for any pair of crystals with the same 2d spacing and so the geometry can be described in terms of the parameter $\epsilon_0 = \lambda_0/2d = \sin\theta_0$. Then for the special case of orthogonal dispersion planes at λ_0 (ie, $\Phi_0 = 90°$) we have $\beta = \tan^{-1}\epsilon_0$, $\alpha = \cos^{-1}(\epsilon_0^2)$ resulting in $\sigma_0 = \cos^{-1}[(1-2\epsilon_0^2)^2]$ and a maximum wavelength possible given by $\epsilon_{max} = \lambda_{max}/2d = \sin\theta_{max} = [(1 + \epsilon_0^2)/2]^{1/2}$. This corresponds to $\Psi_{max} = \pi/2-\beta$. These general angular relationships are illustrated in Fig C5.5 with the proviso that only $\theta_0 \leq 45°$ is useful in practice.

Although the azimuth angle can be set to $\Phi_0 = 90°$ for λ_0 it will change for other wavelengths. The azimuth angle Φ for other wavelengths can be found from $\cos\theta_0/\cos\theta)^2 - 1 = (\epsilon^2 - \epsilon_0^2)/(1 - \epsilon^2)$. The dependence is illustrated in Fig C5.6 for three central wavelength designs. The changing azimuth angle Φ effects not only the space-resolving component directions but also the efficiency of the instrument. This arises due to the consideration of polarization effects in the two incident E-vectors at each reflection point with the reflected amplitudes of unit incident vectors being 1 and $\cos^2\theta$ for s and p polarizations at a Bragg angle θ. In the general case of two different crystals with Bragg matching angles θ_1 and θ_2 for a given λ and an azimuth angle Φ as defined before the intensity transmitted, or the polarization factor P, is given by

$$P = \tfrac{1}{2}(\cos^2 2\theta_1 + \cos^2 2\theta_2 + \cos^2\Phi \sin^2 2\theta_2)$$

In the particular case of the double reflection spectrometer with $\theta_1 = \theta_2 = \theta$ and $\cos\Phi = (\cos\theta_0/\cos\theta)^2 - 1$ we have

$$P = (1 - 2\epsilon^2)^2 + 8\epsilon^4(\epsilon^2 - \epsilon_0^2)^2$$

for $\epsilon \leq \epsilon_{max} = [1 + \epsilon_0^2)^2/2]^{1/2}$ and $\epsilon_0 \leq 2^{1/2}$. The polarisation factor effect is illustrated in Fig C5.7 and indicates the advantage of having ϵ_0 as low as possible, ie, using a crystal with as large a 2d spacing as possible for the required wavelength range.

Design of Instrument

A possible instrument configuration is illustrated in Fig C5.8 with all angles as discussed above. The solid angle needed is small and the film plane F is located on a side port of the main cone such that the central ray λ_0 is incident normally on the film. In this mode it can be shown that the spectral dispersion direction on the film lies on a line at 45^0 to the orthogonal space-resolving direction for any λ_0 design if $\Phi_0 = 90^0$. The insert indicates what the 2-D image might look like if the source is square and emits at three quasi-monochromatic wavelengths. Preliminary tests of such an instrument have produced images from plasma and CW X-ray sources and appear encouraging.

C5.4 MONOCHROMATIC IMAGING USING SPHERICALLY BENT CRYSTALS

A Rodin, (Lebedev Physical Institute, USSR)
P Norreys (Royal Holloway and Bedford New College)

Two dimensional monochromatic X-ray imaging is of considerable potential for the diagnosis of energy transport in laser produced plasmas (C5.9).

We report here a method of producing a monochromatic X-ray image from a spherically curved crystal with the source at near normal angle of incidence. The crystals produce images which have a small spectral bandwidth and excellent spatial resolution. This technique was developed some time ago in the Lebedev Physical Institute in Moscow (C5.10).

Take the crystal described in fig C5.9.

Then $\Delta\lambda = 2d\ (\sin\theta_{max} - \sin\theta_{min})$.

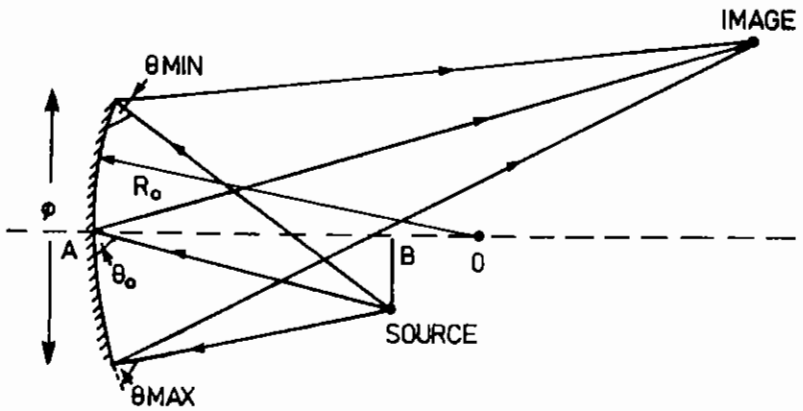

C5.9 Spherically curved crystal imaging a plasma source.

The magnification γ of the image is given by:

$$\gamma = \frac{R_0}{2AB - R_0}$$

Where R_0 is the radius of curvature of the mirror and the distance AB is shown in the diagram.

Fig C5.10 gives an indication of the spatial resolution expected for a set of crystals with a radius of curvature of 500 mm and a magnification of 4. The four curves represent the different diameters ϕ of each crystal.

Below is a list of crystals, some of which are on loan to the Rutherford Laboratory (those marked *)

Plane		R_0(mm)	2d Å	R_c (rad)
Quartz	[10$\bar{1}$0]	150	8.509	42 x 10^{-6}
Quartz	[10$\bar{1}$0]*	300	8.509	42 x 10^{-6}
Si	[111]	300	6.271	33 x 10^{-6}
Si	[111]*	500	6.271	33 x 10^{-6}
Quartz	[13$\bar{4}$0]*	500	2.36	2.2 x 10^{-6}
Si	[400]	500	2.71	∿2 x 10^{-6}

The advantages of using these crystals over a monochromatic X-ray pinhole camera is that the crystal subtends a much larger solid angle to the source and the image is consequently very much brighter. However, the magnification of the image is small (for the present set of R_0) typically x 5. By imaging the continuum with two different crystals an absolute temperature measurement can be obtained as a function of position.

The main disadvantage of this technique is that monochromatic imaging can only be achieved at a wavelength equal to the 2d spacing of the crystal.

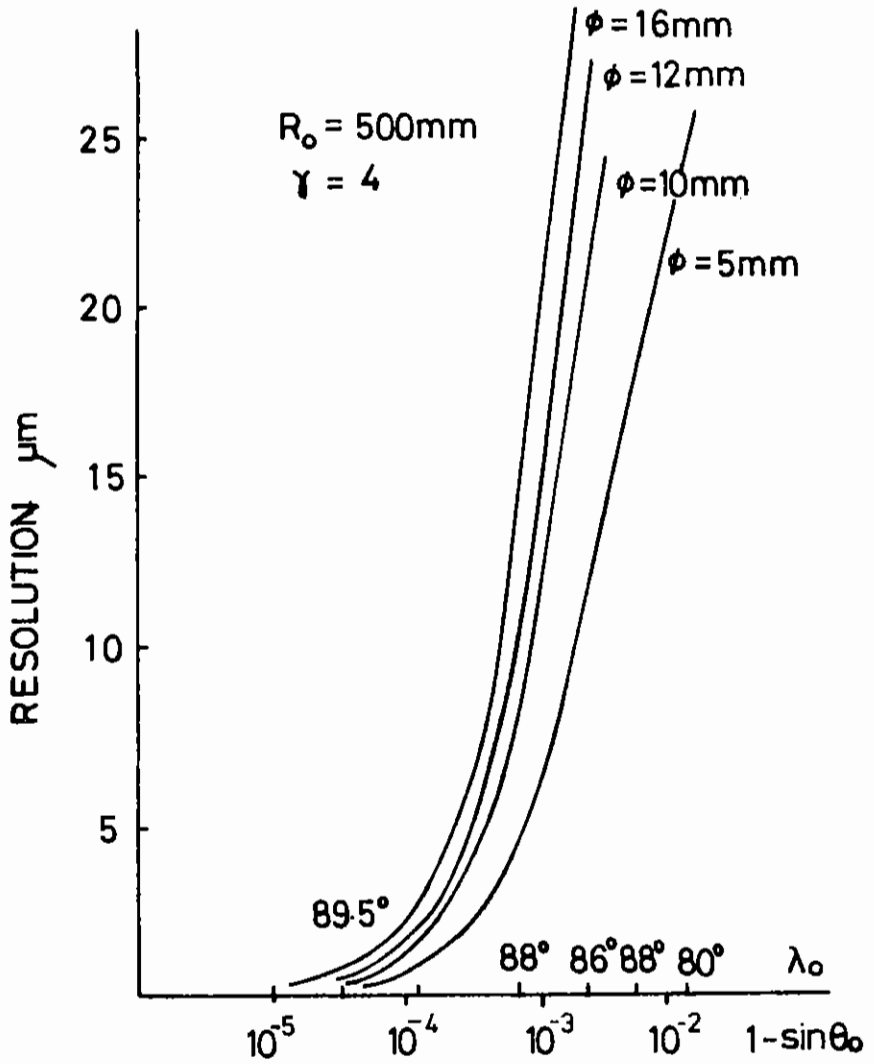

C5.10 Expected spatial resolution plotted against incident angle.

We can conclude by saying that with an increase in the magnification (to say x15), time resolved X-ray imaging is possible. The technique can provide absolute temperature measurements and with the advent of multilayered mirrors any spectral line or region can be imaged provided the 2d spacing is chosen correctly.

C5.5 MONOCHROMATIC IMAGING USING A TRANSMISSION GRATING

T Tomie (Electrotechnical Lab., Japan)
E Fill (Max-Planck, Garching)
M Grande and M H Key (RAL)

When carrying out XUV laser experiments on the Vulcan laser (see section A.1) information concerning the uniformity of the plasma produced in the line focus is indispensible in the analysis of data on the amplification produced. Monochromatic images can give us a great deal of information on the plasma conditions; harder x-ray wavelengths could reveal temperature non-uniformities in the original plasma column, while at longer wavelengths there is information available on the uniformity of electron density during the plasma expansion.

We constructed an x-ray pinhole camera with a transmission grating (XTC) and tried to obtain plasma images at various x-ray wavelengths. High quality transmission gratings of 1000 lines/μm were fabricated by etching in gold at Max-Plank Institute, Garching and have the form of strips 1mm long and 50 μm wide. They were glued to a centre holed disk for easy handling and mounted in the pinhole holder of a conventional x-ray pinhole camera. Spectra were recorded on Kodak 101 film; by rotating the holder, several shots can be recorded on one film without opening the vacuum chamber.

Fig C5.11, shows a schematic diagram of the XTC. In our implementation, the values of a and b, the distance of the source and film from the grating were 10 cm, the grating period d, was 1 μm and the grating width w was 50 μm, giving a number of grating periods N in the aperture of 50 and a diffraction limited resolution of $\Delta\lambda_N = \lambda/N = 2$ Å for 100 Å x-rays. In practice the resolution is limited by the source collimation to $\Delta\lambda_G = wd\ (\frac{1}{a} + \frac{1}{b}) = 10$ Å. The spectral dispersion of the film plane was 100 Å/mm. The length, L, of the grating was decided exprimentally from a compromise between the

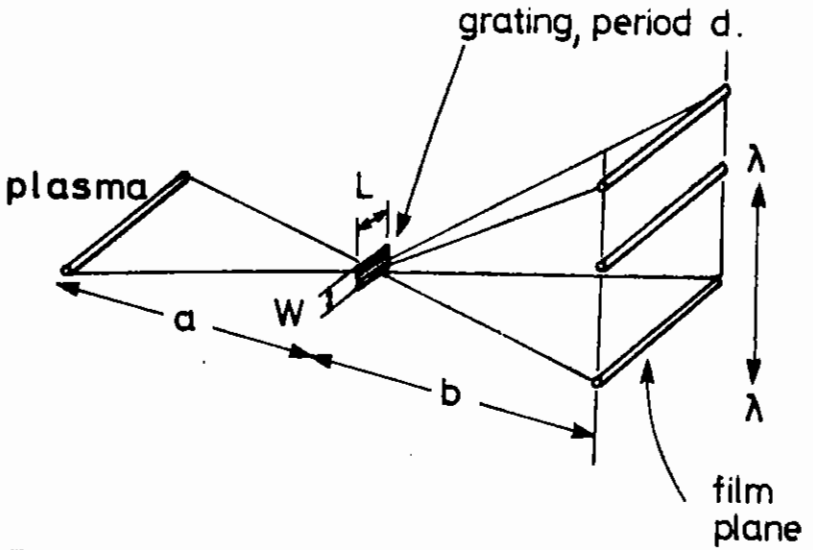

C5.11 Schematic of X-ray pinhole camera with a transmission grating.

spectral brightness and the spatial resolution along the plasma axis. As shown below, clear spectra were obtained by limiting the length, L, to 200μm. The spatial resolution of the monochromatic plasma image was 0.4 mm.

Figure C5.12 shows an example of images recorded by our XTC. Six beams were focussed onto the target to 8 mm length. Two shots were recorded on the film. Targets were SrF_2 and CaF_2 coated on a thin carbon fibre. Total laser energies in the green were 70 J and 80 J. Figure C5.13 shows the spectrum of SrF_2 shown in Figure C5.11. Peaks at 25 Å and 91 Å are assigned as band emissions to M and N shells of Sr ions, respectively. Figure C5.14 shows the intensity distribution of 91 Å emission along the fibre axis, indicating a very good uniformity of emission.

Although filter was used, there was no clear indication of any damage to the grating by plasma blow-off or stray light fogging. In conclusion, as we have demonstrated here, a line focussed plasma can be imaged at various x-ray wavelengths, and this will make possible a better understanding of the plasma conditions in XUV laser schemes. By increasing the grating line density it may be possible to obtain information on the emission perpendicular to the plasma axis.

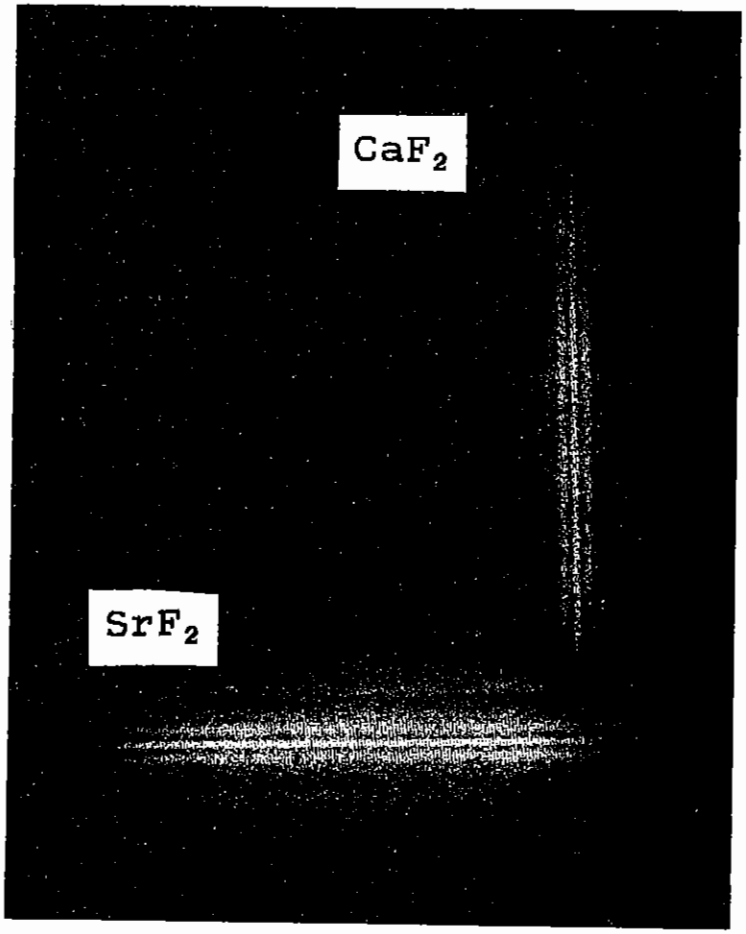

C5.12 Spectrally resolved plasma images. Two shots were recorded.

Fig C5.

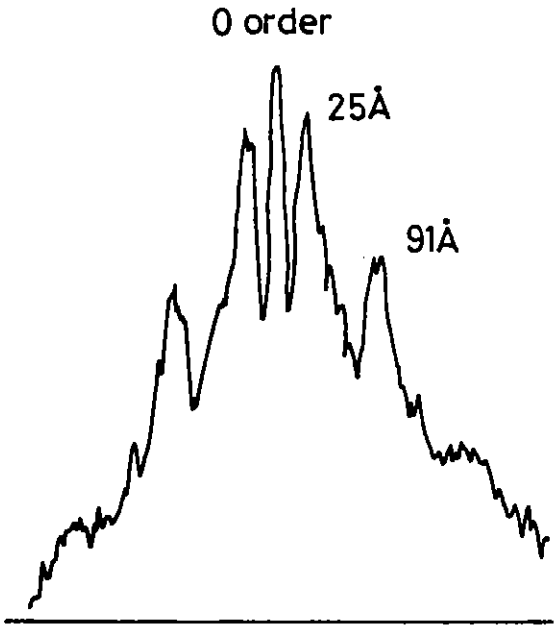

Fig C5.

C5.13 Spectrum of SrF_2.

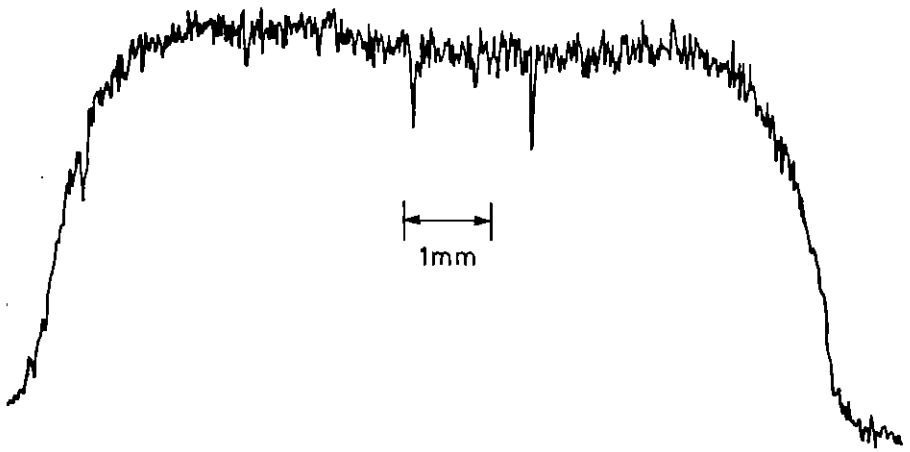

C5.14 Intensity distribution of 91Å X-ray along plasma axis.

C5.6 TIME FIDUCIALS FOR X-RAY STREAK CAMERAS

P Norreys (Royal Holloway and Bedford New College)
A J Cole, A Ridgeley, E Turcu (RAL)

When conducting time resolved experiments it is important in many cases to have an absolute measurement of the timing of the events recorded on the streak camera with respect to the incident laser pulse.

By way of a particular example, the interpretation of laser ablation rate studies, involving the observation of the X-ray emission history from multilayered targets, requires a precise correlation of laser intensity with the onset of spectral line emission.

One very good method of achieving this correlation is to incorporate a time fiducial of the actual laser pulse onto the cathode of the streak camera. The problem with using this technique at 1.06 μm or 0.53 μm (frequency doubled) neodymium laser wavelengths is that the photocathode materials used for X-ray detection are insensitive to the laser wavelengths. The 0.53 μm wavelength has been used for a time fiducial (C5.11) but usually a frequency quadrupled beam is used (C5.12) at which wavelength it is possible to use volume emission photocathode materials which retain some residual sensitivity in the non-vacuum ultraviolet. With a KrF laser there is the advantage that the laser wavelength is short enough to be used for the fiducial beam. This solution was adopted by Papil et al (C5.13) who directed a proportion of the laser beam through an optical fibre onto the photocathode.

This method of producing a time fiducial has now been incorporated into the SPRITE target area. The optical arrangement is shown in Figure C5.15. The first turning mirror is 99% reflecting and the 1% transmitted beam through the mirror is used for the time fiducial. This way the total beam is sampled to avoid any possible errors due to one part of the beam having a different time history to another part. This beam is focussed down from 80 mm diameter to 4 mm diameter using a 1.25 m focal length lens. This 4 mm diameter beam is then sampled by a fibre optic of diameter 600 μm and the beam is transmitted through 2 m of optical fibre into the tank through a vacuum feed-through and to the front end of the streak camera. Here

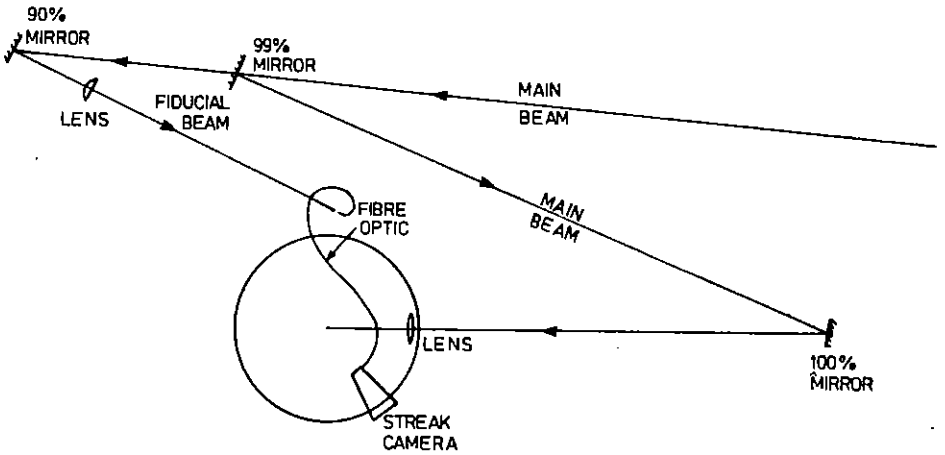

C5.15 Schematic of time fiducial optical arrangement on SPRITE.

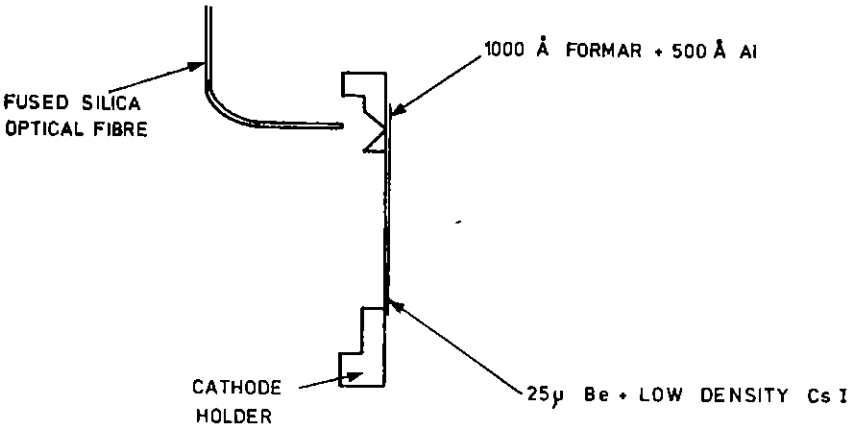

C5.16 Cathode assembley for incorporation of time fiducial.

the fibre is optically linked to a shorter optical fibre which enters the casing of the streak camera from the side. This fibre is directed at a subsidiary photocathode by means of the optical arrangement show in Figure C5.16. The fibre is elastically bent through 90° around a channel in a rigid perspex structure and terminates at a distance 2-3 mm from the subsidiary photocathode. This consisted of 500Å of aluminium evaporated onto 1000Å of formvar but gold has subsequently been found to be a much more sensitive photocathode material. The formvar covers a 1 mm diameter hole in the cathode holder. For a typical 20 J laser pulse it is estimated that approximately 5 mJ is injected into the optical fibre about 50% of which appears to reach the photocathode. The synchronisation of the fiducial laser pulse and the main laser pulse was achieved by equalising the optical path length of the two beams. This was checked by streaking images of bare Se targets where the X-ray emission should coincide with the arrival of the laser pulse.

Figure A2. shows an example of the time fiducial together with a streaked monochromatic image of a selenium target with and without parylene coating.

A time fiducial for the VULCAN laser has now been set up in TAW using the technique of frequency quadrupling a proportion of the incoming laser beam for use as a timing fiducial.

C5.7 A CALIBRATED DETECTOR FOR MEASURING WATER-WINDOW X-RAY YIELD FOR X-RAY MICROSCOPY APPLICATIONS

I C E Turcu, F O'Neill, U Zammit, P T Rumsby, C Brown (RAL)

In this past 2-3 years there has been a considerable amount of research at the CLF on the use of laser-plasma X-ray sources for contact biological microscopy. As these microscopy experiments become more sophisticated there will be a need for more quantitative information on the characteristics of the X-ray source. It will be particularly useful to know the absolute yield of water window X-rays in order that the imaging experiments can be made more quantitative and reproducible and also so that the laser energy can be minimised. In section A1.6 above we have described the results of an experiment to measure the absolute conversion efficiency from KrF laser light to water window X-rays.

The calibrated detector used in the experiment described in section A1.6 was a vacuum X-ray diode (XRD) with an aluminium cathode which viewed the plasma through an energy sensitive filter consisting of a 0.5μm vanadium layer on 0.3μm polystyrene (CH) film. A diagram of the XRD and filter system is shown in Fig C5.17.

The X-ray filter materials were selected so that the XRD would as near as possible see only water window X-rays. Thus two filters were chosen viz a V/CH layer filter and a 30μm Be filter. Fig C5.18 shows the method of constructing the V/CH filter. The starting material consisted of a 0.5μm V layer on 3.5μm mylar. After adding a 0.3μm polystyrene layer the mylar was laser-etched off through a fine grid mask. Complete removal of the mylar was easy to observe as the smooth V layer could then be clearly seen under an optical microscope. The final filter assembly had a total area of 20mm^2 and consisted of the V/CH layer supported on a 3.5μm thick mylar grid. The transmission factor of the grid for water window X-rays was ≈ 32%.

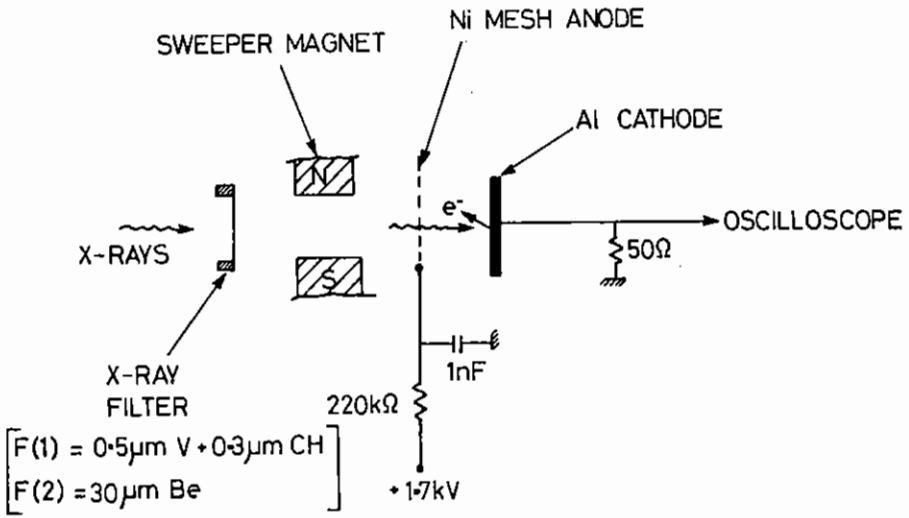

C5.17 XRD and filter arrangement used to detect water window X-rays from KrF laser-plasma X-ray source. The sweeper magnet prevents photoelectrons liberated from the filter from reaching the XRD. With filter F(1) the XRD is sensitive to water window X-rays as well as X-rays at hν>700eV. With filter F(2) the XRD is sensitive only to X-rays at hν>700eV. Subtraction of the two signals gives the water window component.

For X-ray measurements this filter was placed in front of the XRD which had a diamond-turned cathode and was made to a Lawrence Livermore National Laboratory (US) design (manufactured by EG&G, cathode code No VO-58). This XRD was placed in the target chamber to measure the X-ray emission from the plasma and immediately after the experiments it was recalibrated against an NBS standard Al vacuum XRD over the photon range of interest using a continuous wavelength scan (resolution ≈ nm) on the SERC synchrotron radiation source at the Daresbury Laboratory (UK). It was not possible to calibrate the transmission of the V/CH filters in combination with the XRD at the water-window wavelengths using the CW synchrotron source because the signal levels were too low. A measurement was however made at the wavelength of the Al absorption K-edge (7.7Å) where a higher flux from the synchrotron is obtained and also because the filter is more transmitting and the XRD exhibits an enhanced sensitivity. This transmission agreed with the value calculated using published mass absorption coefficient tables to within 15% thus verifying the thickness of the V and CH layers of the filters.

The sensitivity curve of the XRD as measured using the synchrotron source is shown in Fig C5.19. The upper curve shows the sensitivity of the NBS reference detector. Since calibration data for this detector was only available at photon energies $h\nu \leq 280eV$ some assumptions had to be made for the range $h\nu \geq 280eV$. In the range 280eV - 1000eV the NBS diode was assumed to have the same sensitivity as the origonal surface of the diamond-turned cathode. Calibration data for the fresh VO-58 diamond- turned cathode as measured at LLNL had been supplied with the detector. At photon energies $h\nu \geq 1$ keV reference sensitivity data was taken from Fig 2 of Ref C5.14.

The calibration run on the VO-58 cathode shows that there has been a considerable loss of sensitivity at all photon energies which we believe is due to contamination of the photoemissive surface in the target chamber vacuum system. There is also a sharp drop in sensitivity at $h\nu \leq 280eV$ which corresponds to the carbon K-edge.

The overall recalibrated response function at low photon energies of the VO-58 XRD and the V/CH filter is shown in Fig C5.20 where in constructing the curve we have used measured values of XRD sensitivity (lower curve in Fig C5.19 and calculated values of filter

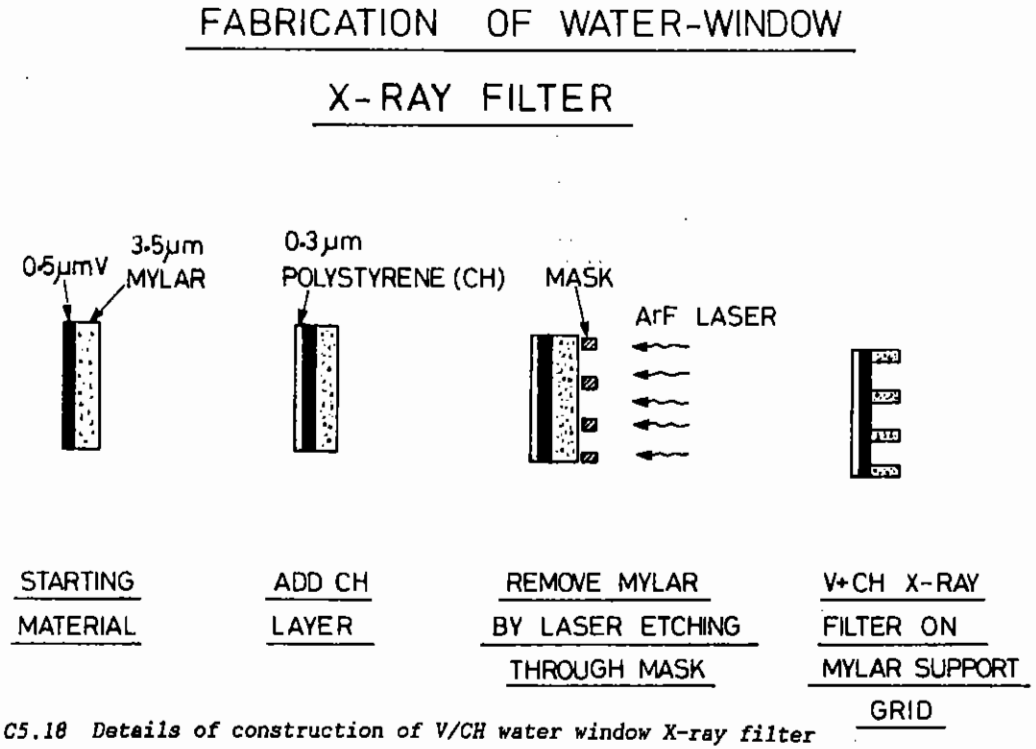

C5.18 Details of construction of V/CH water window X-ray filter (filter fabricated by Exitech Ltd to RAL specification).

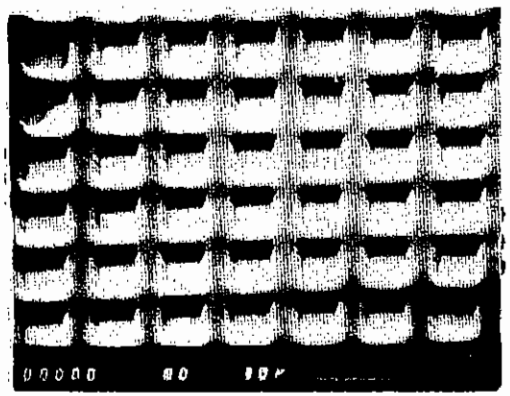

SEM PICTURE SHOWING MYLAR SUPPORT GRID

transmission. This curve shows that the low energy response of the XRD/filter combination used in the target chamber matches the water-window almost exactly except that it cuts off at 510 eV instead of 530 eV. This only introduces a small error in the measurements.

The response of the XRD/filter combination used in the target chamber is different to that of the standard XRD (also shown in Fig C5.20 due to the disappearance of an unwanted second peak in the sensitivity on the low energy side of the carbon K-edge. This effect is caused we believe by organic/carbon contamination of the XRD photoemissive surface in our target chamber. The disappearance of the unwanted peak in the detector response function makes the V/CH filter + contaminated Al cathode a particularly good combination for detecting water-window X-rays. For future work it is intended to use an Al cathode with a thin evaporated layer of carbon to try and make this response function more reproducible. The response curve also shows that the detector begins to respond to radiation at $h\nu \geq 0.7$ keV and thus in a separate experiment the high energy signal ($0.7 \text{ keV} \leq h\nu \leq 1.4$ keV) was measured using the same XRD filtered by 30μm Beryllium (filter F(2) in Fig C5.17 and this was subtracted from the signal recorded with the water window filter.

The results obtained in measuring water window X-rays using this calibrated detector system have been described above (sect A1.6).

C5.8 CALIBRATION OF CCD AND FILM RECORDING OF IMAGE INTENSIFIER AND STREAK CAMERA OUTPUTS

V Platonov, General Physics Institute, Moscow,
A Ridgley, RAL
S Majumdar, Delli Delti Ltd

Introduction

The recording of streak camera and image intensifier outputs can at present be carried out using film, SIT vidicon cameras or CCD cameras. One of the main drawbacks of most streak cameras is that the instruments are not properly calibrated photometrically. Thus the results are mainly time resolved relative intensity measurements.

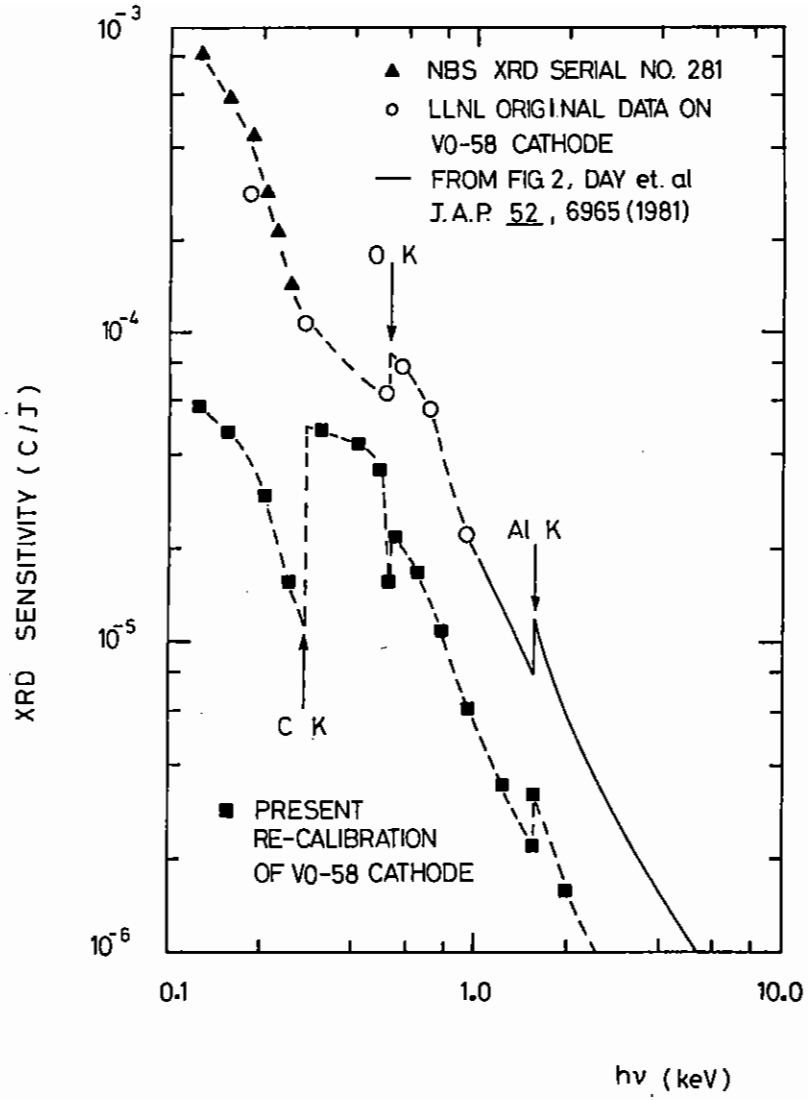

C5.19 Sensitivity of XRD detectors versus photon energy. Upper Curve: sensitivity of reference detector, NBS Al-cathode XRD serial No 281.

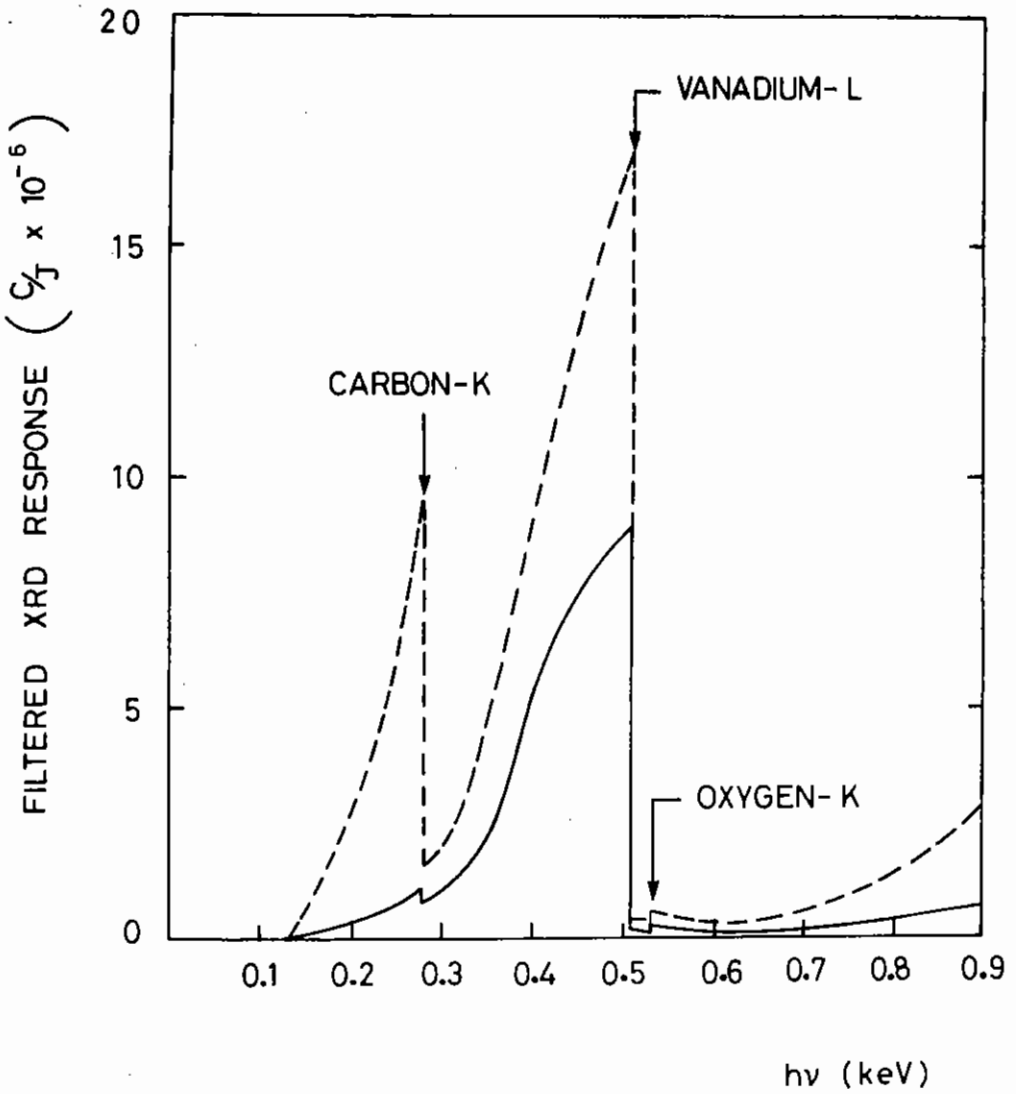

C5.20 Detector responces of filtered XRDs as a function of photon energy. Dashed line = NBS standard XRD + 0.5μm V/0.3μm CH filter. Solid line = recalibrated VO-58 XRD used in present experiment +0.5μm V/0.3μm CH filter.

Film has a very large storage capacity and high resolution but suffers from various nonlinearities and its photometric calibration is difficult as it is susceptible to variations between batches of film. The processing and analysis times are long. Photoelectric optical multichannel analysers have been in use for more than a decade, but until recently, most of them used SIT vidicon cameras which suffered from readout nonlinearities.

Charge coupled solid state detectors, or CCDs are the most recent imaging detectors and they offer both good sensitivity and resolution. The CCDs appear to offer the most satisfactory solution to the problem of image analysis of a streak camera output both for time resolution and quantitative photometry. The CCD has a well defined pixel size and is arranged in a two dimensional matrix and therefore an be used to store a two dimensional image with a pixel resolution around 20 microns square. It is therefore comparable to a film, except that the size of the pixel or "grain" in the case of a film is less than 20 microns.

This report details preliminary results of tests of a liquid nitrogen cooled CCD camera, used to record the images from the output of a Streak Camera, and two intensifier systems. The CCD is compared with Ilford HP5 film in terms of SNR, linear dynamic range and sensitivity. Preliminary results for the sensitivity of the intensified streak camera and the CCD camera recording system are presented.

A Dellistrique DS3 streak camera with high gain intensifier was used and the output was recorded on the Liquid Nitrogen Cooled CCD camera.

Experimental

A. CCD experiments with and without intensifier

Figures C5.21 and C5.22 describe the experimental systems. Fig C5.21 is the schematic diagram for the CCD calibration experiments. Fig C5.22 is the schematic for the total system using a generation 2 channel plate intensifier from EEV and a LN-AT1 liquid nitrogen cooled CCD camera.

The light sources used were a green light emitting diode (LED), type TIL232 from Texas Instruments, with peak output at 560 nm and a 100 picosecond long (FWHM) pulsed diode laser (Hamamatsu type C1308) with

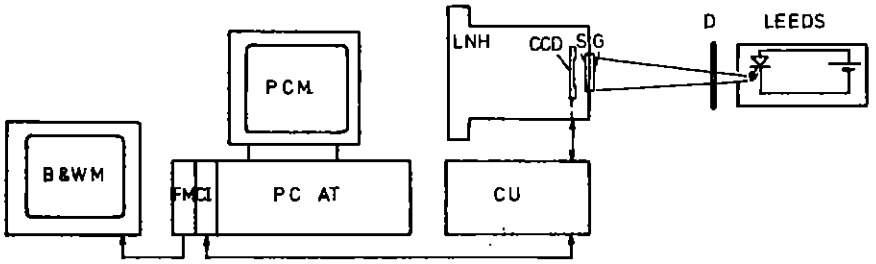

NOTATION : LEDS- LIGHT EMITTER DIODE SOURCE, D- DIFFUSER
LNH - LIQUID NYTROGEN HOUSING, CCD - CHARGE COUPLED DEVICE,
S - MECHANICAL SHUTTER, G - GLASS WINDOW,
CU - CCD CAMERA CONTROL UNIT,
PC - PERSONAL COMPUTER, M - MONITOR, CI - CCD CAMERA INTERFACE,
FM - FRAME MEMORY BOARD.

C5.21 A schematic for CCD dynamic range measurements.

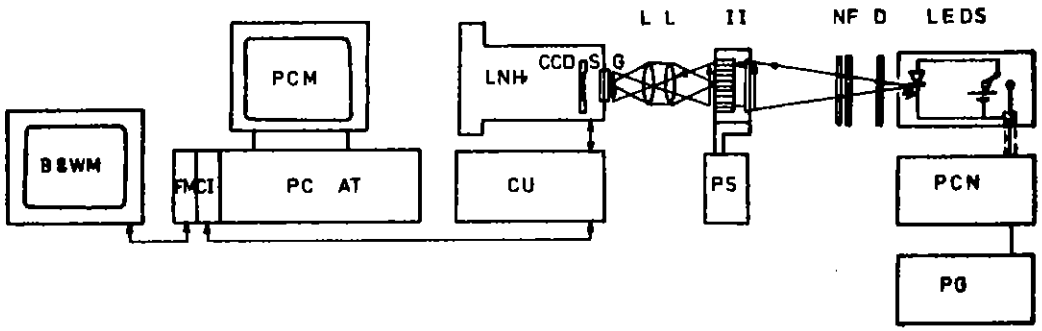

NOTATION: PG - PULSE GENERATOR, PCN - PULSE COUNTER
LEDS - LIGHT EMMITTING DIODE SOURCE, D - DIFFUSER,
NF - NEUTRAL FILTERS, II - IMAGE INTENSIFIER PS - POWER SUPPLY
L - LENS , G - GLASS WINDOW, S - MECHANICAL SHUTTER,
CCD - CHARGE COUPLED DEVICE, LNH - LIQUID NYTROGEN HOUSING,
CU - CCD CAMERA CONTROL UNIT PC AT - PERSONAL COMPUTER,
M - MONITOR, CI - CCD CAMERA INTERFACE BOARD
FM - FRAME MEMORY BOARD

C5.22 A schematic for image intensifier dynamic range measurements.

The specifications of the LN-AT1 cooled CCD camera are as follows:

CCD type	EEV full format P8600
Format	576 by 385 pixels
Pixel size	22ux22u, 23um between centres
CCD Temperature	-125 K
Sensitivity	2 electrons per count at full gain
Quantum efficiency	
at 550 nm	14%
at 820 nm	33%
Read out noise	less than 1.5 electrons per pixel
Fixed pattern dark current	<< 0.5 electron per pixel per min.

Fig C5.23 shows the linearity of the CCD with the led and the laser diode. Figs C5.24 and C5.25 shows the same transfer functions using an image intensifier, lens coupled to the CCD. The image intensifier had an automatic gain control circuit which limited the system dynamic range with the CW LED source. The pulsed 100 psec laser

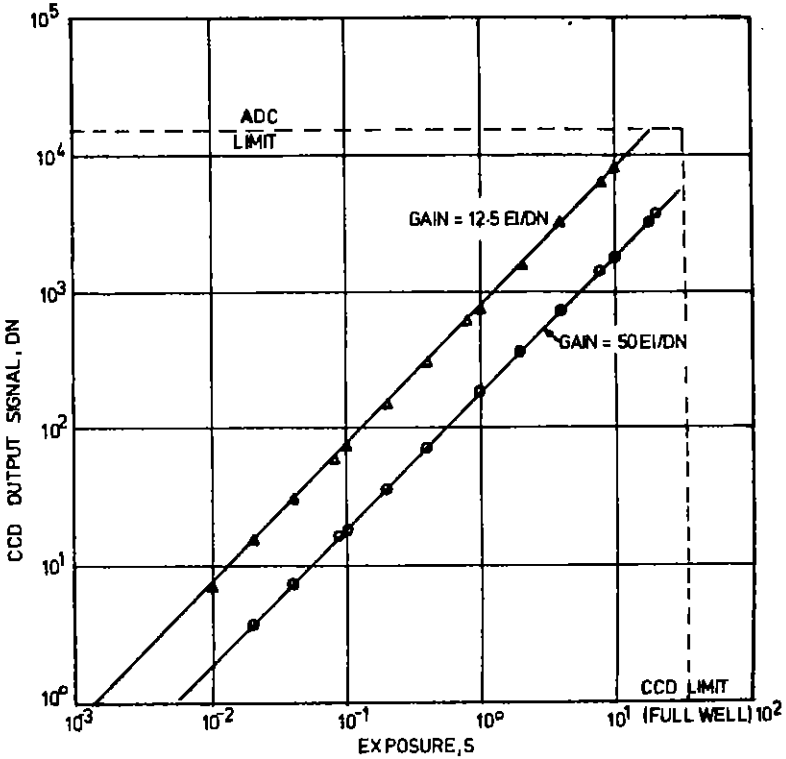

C5.23 CCD output versus CCD exposure.

diode did not show this gain saturation. The nominal gain of the intensifier was 10,000 to white light. The threshold illumination level is 14 electrons on one CCD element. This is equivalent to 100 green photons per pixel, and 42 photons of 820 nm wavelength. These figures are equivalent to a photon flux of 7.5 picojoules per sq.cm for 2.5 ev photons (green and 0.21 picojoules per sq. cm for 1.5 ev photons (800 nm).

The linear dynamic range of the combined CCD and the Image intensifier system was 500 with the laser diode and 300 with the LED. The collection efficiency of the relay lens between the intensifier and the CCD was 2.5%. The photon gain of the intensifier is approximately 1500 at 880 nm and 3000 at 560 nm, due to the higher quantum efficiency of the intensifier at 560 nm. Thus, the effective intensifier gain was 37.5 at 800 nm and 75 at 560 nm. With this gain, the CCD will be able to record two photo-electrons per image point at the input of the intensifier. A relay lens with one stop larger F number would have allowed the detection of a single photoelectron from the intensifier photocathode.

B. DS-3 plus CCD system calibration

Fig C5.26 shows the system schematic, using the Hamamatus laser diode as the light source, and with single exposure recording of the image on the CCD. The DS-3 streak camera has a cascaded intensifier system for single photo-electron detection on negative films of single shot events from the streak camera. The intensifier system has a gain control switch which allows the gain to vary from 100 to 60,000. There is no automatic gain control in the system.

The streak camera is capable of recording a single laser pulse streaked at 35 psec/mm, on HP5 film with a density in excess of 2, using fibre optic coupling (Re: Calibration at RAL during installation).

In this experiment, the image was not streaked: a static 100 picosecond laser pulse was recorded by the CCD.

Fig C5.27 shows the results. The photon transfer curve of fig C5.27 shows that the gain of the system is too high at gain setting of 7 or

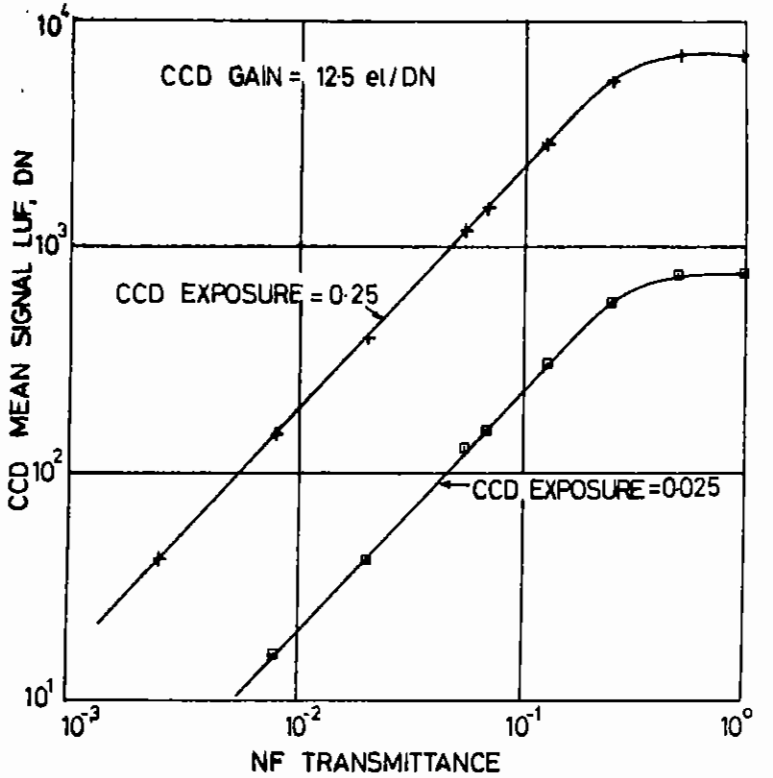

C5.24 (Image intensifier + optics + CCD) transfer function. Using LED.

above. The maximum overall gain of the system compared to the data is shown in fig C5.23 where no streak camera or intensifier was used, was 1500. The linear dynamic range of the whole system was 200, with the threshold level well above the CCD readout noise.

C. Comparison with HP5 Film

The most commonly used detector for streak camera diagnostic work at RAL is Ilford HP5 film developed in D19 developer at 20°C. The H and D curve for HP5 film developed this way is given in fig C5.28.

Granularity measurements were made by scanning uniformly exposed areas of film using a 50 μm scanning aperture with the joyce-loebl densitometer.

Typically about 150 density points were used for each granularity measurement. The granularity measurements were used to compute the signal/noise ratio appropriate to a pixel size of 22μm² shown in fig C5.29.

The film characteristics could not be evaluated on an absolute scale as the led was not calibrated. Shaw and Shipman (C5.15) have published data for HP4 film developed in ID11 and other fine-grain developers. This data would indicate that the threshold for HP4 film is about 5 photons/μm² (or 2×10^{-10} J/cm²), the threshold being defined as the intersection of the linear portion with the density axis. HP4 and HP5 emulsions are very similar.

Taking this as the threshold for development in D19 developer the peak SNR is achieved at an exposure level of about 30 ph/μm² (~10^{-9} J/cm²) at density 0.6.

The SNR is unity for the film at about 6×10^{-11} J/cm² compared with 2.5×10^{-12} J/cm² for the cooled CCD.

The data from Shaw and Shipman would indicated a peak SNR of about 17 for HP4 developed in ID11 as opposed to 6.6 for D19 developed in D19. This would appear to indicate that development in D19 produces an appreciably lower DQE than the value of 2.4% obtained for HP4 in ID11.

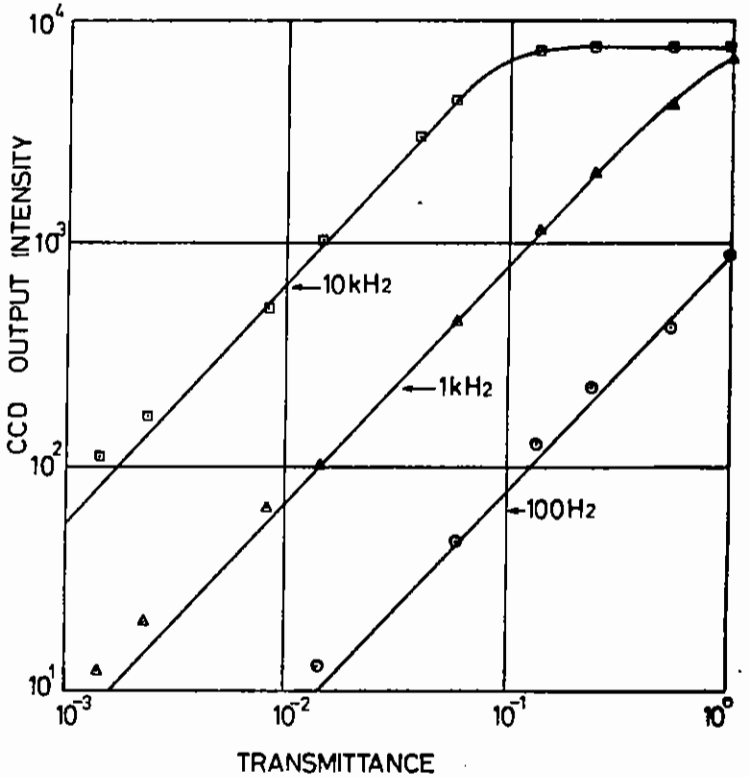

C5.25 (Image intensifier + optics + CCD) response on laser diode 31308 illumination.

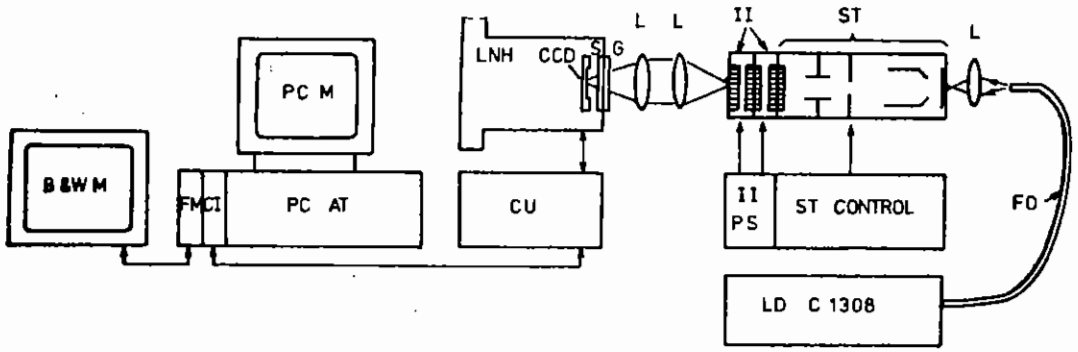

NOTATION: LD - LASER DIODE, FO - FIBRE OPTIC, L-LENS ST STREAK IMAGE TUBE
II - IMAGE INTENSIFIER, G - GLASS WINDOW, S - MECHANICAL SHUTTER, CCD - CHARGE COUPLED DEVICE, LNH - LIQUID NITROGEN HOUSING, CU - CCD CAMERA CONTROL UNIT, PC - PERSONAL COMPUTER, M - MONITOR, CI - CCD CAMERA INTERFACE, FM - FRAME MEMORY BOARD

C5.26 A schematic for (ST + 2II + optics + CCD) dynamic range measurements.

The CCD camera was exposed with the same amount of exposure which produced a density of 0.6 on HP5 film. The area illuminated was 10 pixels and it produced 1790 counts at full gain (12.5 electrons per count). This is equivalent to 1.35×10^{-9} J/sq.cm.). This figure is close enough to the calculated photon density of $1.0 \times 10 \times 10^{-9}$ J/sq.cm for the film exposure.

The useful exposure range on HP5 film for an SNR of 2 or above, is only over an exposure range of $\sim$ 300. Hence both sensitivity and the linear operating range are better for the CCD systems.

Conclusion

The cooled CCD camera was found to be an order of magnitude more sensitive than the Ilford HP5 film. This was mainly due to the very low noise figure of the cooled CCD and its greater quantum efficiency than the film in the spectral region considered.

The other additional advantages of the CCD camera is its linear response and its precisely defined pixel dimension, which makes it

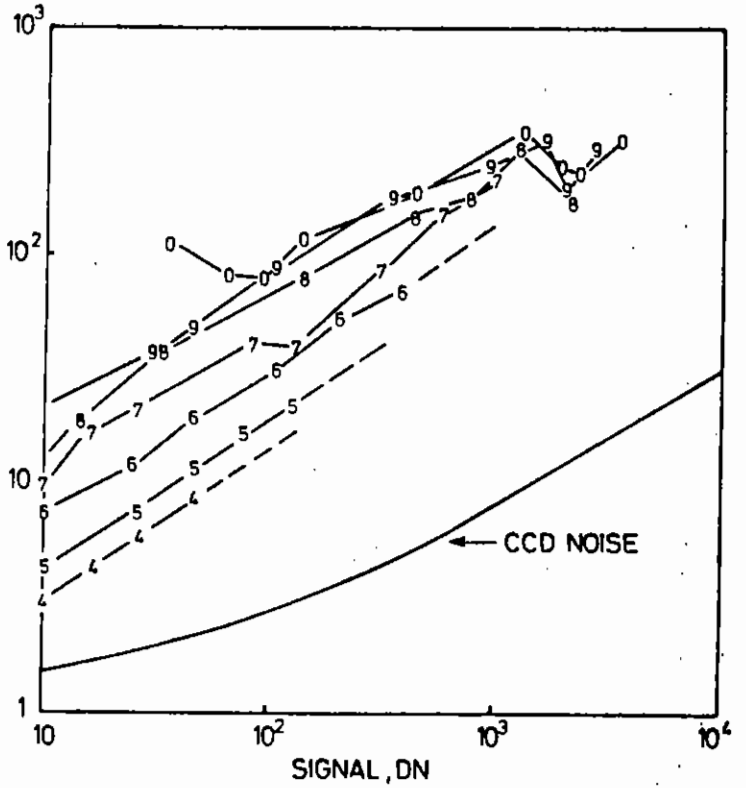

C5.27 Photon transfer curves (streak image tube + 2II + optics + CCD)

very suitable for signal digitisation for computer analysis of the images. The long and labour intensive processing of the film is also eliminated together with the film to film variation of the detector characteristics.

The intensifiers used to show a lower dynamic range than the CCD camera. However, for streak camera operations, the use of intensifiers reduces the sensitivity threshold from 12.5 electrons per count to 1 electron per count or lower.

A fully calibrated streak camera and CCD system would allow us to do quantitative picosecond photometry with the system rather than the relative intensity measurements usually taken with these instruments.

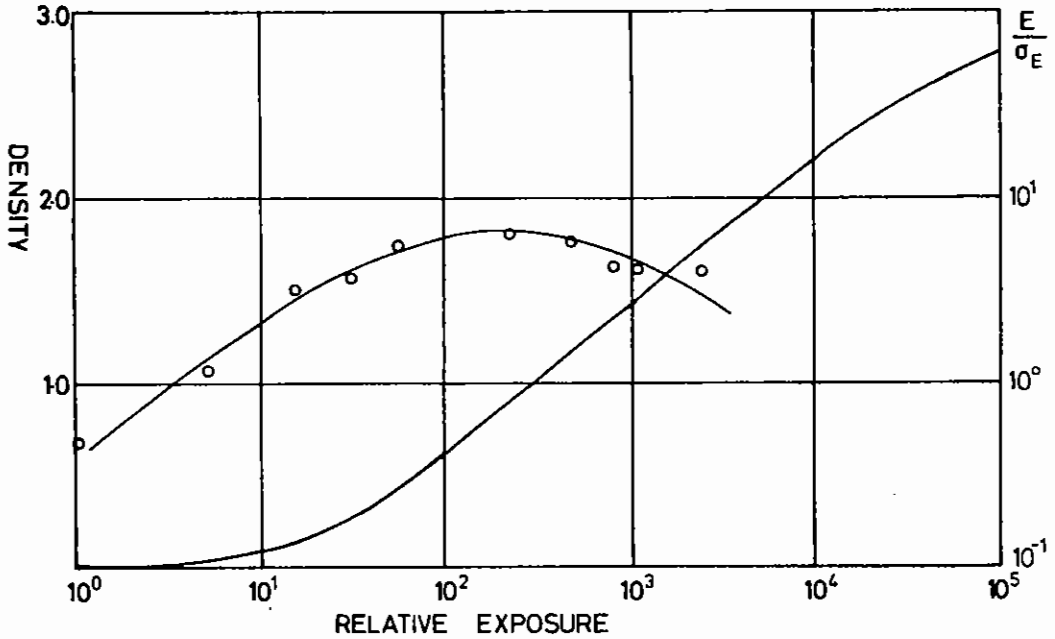

C5.28 Characteristic curve for HP5 film developed 5 min in D19 developer and a plot of SNR versus relative exposure for HP5 film developed in D19.

C5.9 XUV DIAGNOSTIC CALIBRATION

G P Kiehn, R A Smith, O Willi, T Garvey, A Damerell (RAL)
I West (Daresbury Laboratory)

The XUV time resolved spectrographs used as the primary diagnostics in the XRL program were absolutely calibrated during an Imperial College instrumentation initiative. The synchrotron radiation source (SRS) at the Daresbury Laboratory was used to provide a continuous source of monochromatic radiation between ~70 - 300 Å.

The first order efficiency of the 1200 1/mm flat field diffraction grating used in the spectrographs was measured by recording the XUV flux with and without the grating in place. An XUV Al photodiode was used to monitor the flux levels. The radiation from the synchrotron is highly polarized in the plane of the storage ring and consequently the grating efficiency was measured with the grating both parrallel and perpendicular to the ring.

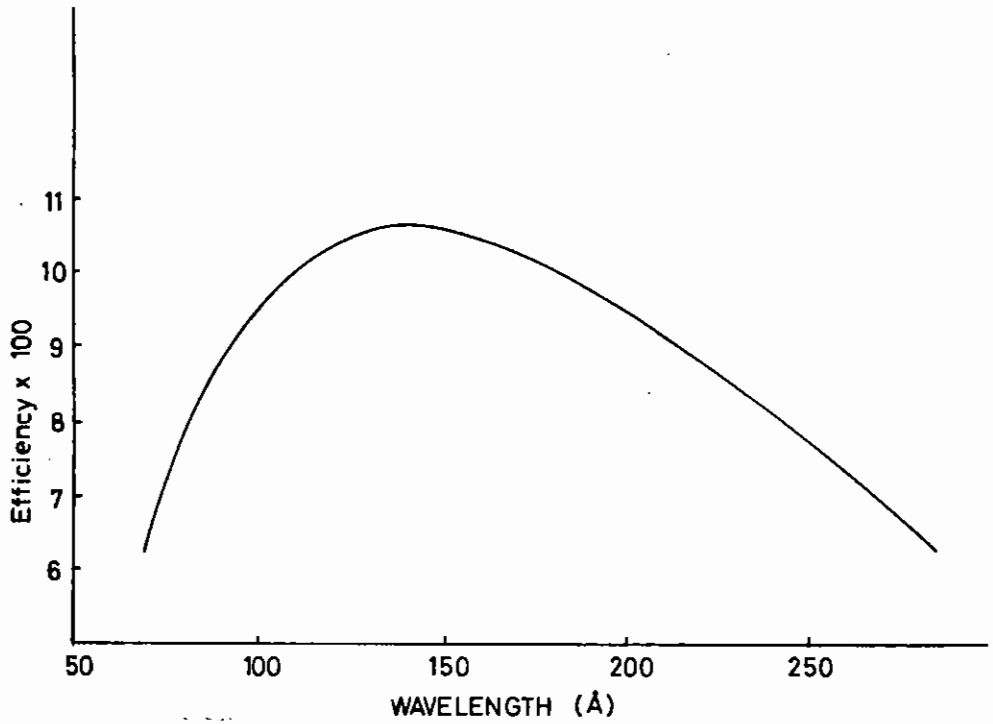

C5.29 1st order efficiency 1200 1/mm flat field grating.

The measurements were averaged to produce the grating efficiency in first order for wavelengths between 70- 300Å shown in figure C5.29. An average efficiency of approximately 10% is noted.

The transmission of various filters to XUV radiation was measured using the same technique as the grating efficiency investigations. Fig C5.30 compares the measure transmission of a 1000Å Formar filter with the calculated values. The excellent agreement between the curves indicates the precision achieved in manufacturing the filters.

The absolute characterisation of the streak camera was performed with reference to an absolutely calibrated photodiode manufactured by the U.S. National Bureau of Standards. The spectrograph steak camera was exposed to the synchrotron beam and its response recorded on film. The exposures on film were corrolated to the flux levels measured by the NBS photodiode to provide the absolute spectral response of the streak camera when a low and high density CsI photocathodes are used. The analysis of this data is currently being carried out and will be reported in the future.

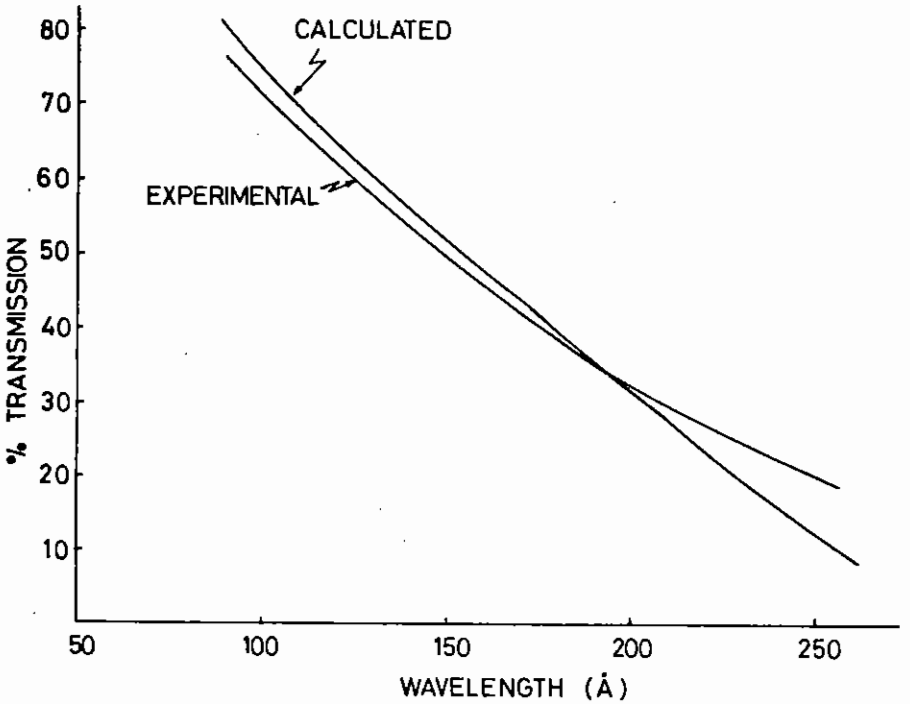

C5.30 1000Å formvar filter.

SECTION C5 - REFERENCES

C5.1 P Norreys, B Brown, E Wooding, A Cole, M H Key, A Ridgeley, Laser Division Annual Report, Section C5, (1986) RAL-86-046

C5.2 A J Cole, M H Key, A Ridgelely, D A Brown, P A Norreys, E R Wooding, T W Barbee. Optics Comm, 62, no 1, p1.

C5.3 K Evans, A Cole, Laser Division Annual Report, Section A6, (1985) RAL-85-047.

C5.4 B S Fraenkel, Appl. Phys. Lett. 36, P341, (1980).

C5.5 R R Whitlock and D J Nagel, AIP Conference Proc No.75, Low energy X-ray Diagnostics, 1981, Ed. by D T Atwood and B L Henke page 334.

C5.6 B S Fraenkel, Z H Kalman and C L S Lewis, V U V VIII Int. Conference, Lund, 1986, abstracts page 666.

C5.7 M Renninger, Z. Phys. 141, P106 (1937).

C5.8 B S Fraenkel, Appl. Phys. Lett. 41, P234 (1982).

C5.9 R Benatter, J Godart, Optics Comm. 59, NO 4, P272 (1986).

C5.10 L M Belgaev, A B Gil'vary, Yu A Mikhailov, S A Pikuz, G V Sklizkov, A Ya Fanov and S J Fedotov. Sov J Quant. Elec. 6, No 9, P1121 (1976).

C5.11 D G Nilson and B J MacGowan, Rev. Sci. Inst. 57, 8, P2187 (1986).

C5.12 P A Jaaning, L de Silva, G G Gregory, C Hestdalen, C K Kiikka, R Kotmel, M C Richardson. Rev Sci. Inst. 57, No 8, P2189 (1986).

C5.13 P Popil, R Fedozejers and A A Offenberger. Rev. Sci. Inst. 57, No 6, P1049 (1986).

C5.14 R H Day, P Lee, E B Saloman and D J Nagel. J Appl. Phys, 52, P6965 (1981).

C5.15 R Shaw and A Shipman. J Phot Sci. 17, P205 (1969).

Editor: F O'Neill

C6 LASER PLASMA X-RAY SOURCE GENERATION USING LOW ENERGY EXCIMER LASERS

C6.1 PLASMA X-RAY SOURCES AT PHOTON ENERGIES ABOVE 1keV GENERATED BY A 0.5J KrF LASER

F O'Neill, M C Gower, I C E Turcu, M Lawless, M Williams (RAL)

In section C6 of the 1986 Annual Report to the Laser Facility Committee we described our first experiments on the generation of plasma X-ray sources using KrF lasers of energy ≤ 1J. These plasma sources generated X-ray photons at energies as high as $h\nu \approx 400$ eV and were successfully used for preliminary studies in X-ray lithography (C6.1) and X-ray microscopy (C6.2).

In this reporting year we have concentrated on experiments to use low energy KrF lasers to generate laser-plasma X-ray sources at photon energies ≥ 1 keV. To achieve this with high efficiency requires a target irradiance $\sim 10^{12} - 10^{14}$W/cm² to give a higher plasma temperature which can be achieved by focussing the low energy laser to a very tight spot (≈ 10μm). X-rays at photon energy ≥1keV are of interest at the CLF for application to X-ray lithography and also for the study of DNA repair mechanisms following radiation damage. Experiments this year have been carried out using a new purpose-built transportable target chamber. This chamber has been designed to facilitate rapid installation on any available excimer laser so that experiments of short duration (1-2 weeks) can be performed.

The experiment reported here was carried out using a Lambda Physik EMG150 KrF laser which delivered ~ 0.5J pulses of 25ns duration. The experimental set-up is shown in Fig C6.1. The beam from the EMG150 laser was measured to be ~ 3-4 times diffraction limited (full angle divergence ≈ 80μRad) so the power on target had a maximum of 1.2×10^{12}W/cm² when using a focussing lens of 9cm focal length. Nevertheless X-rays at $h\nu \geq 1$ keV were easily generated and detected using a filtered Si PIN diode detector. The X-ray filter was either 1.2μm Al (e^{-1} transmission at $h\nu = 0.7$ keV) or 10μm Be (e^{-1} transmission at $h\nu = 1.0$ keV). The X-ray pulse duration was ≈ 20ns.

Fig C6.2 shows the conversion efficiency to X-rays as a function of

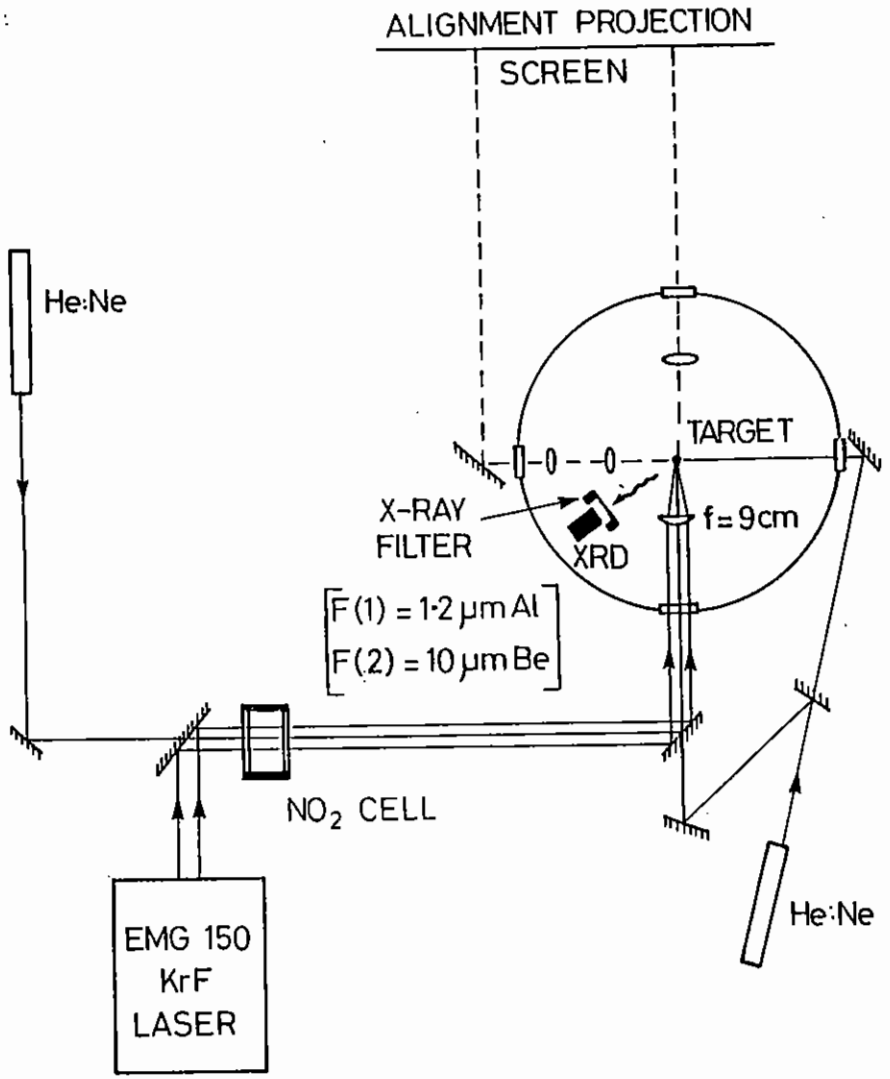

Fig C6.1 Experimental arrangement used to generate a laser-plasma X-ray source at $h\nu \geq 1$ keV using a 0.5J KrF laser.

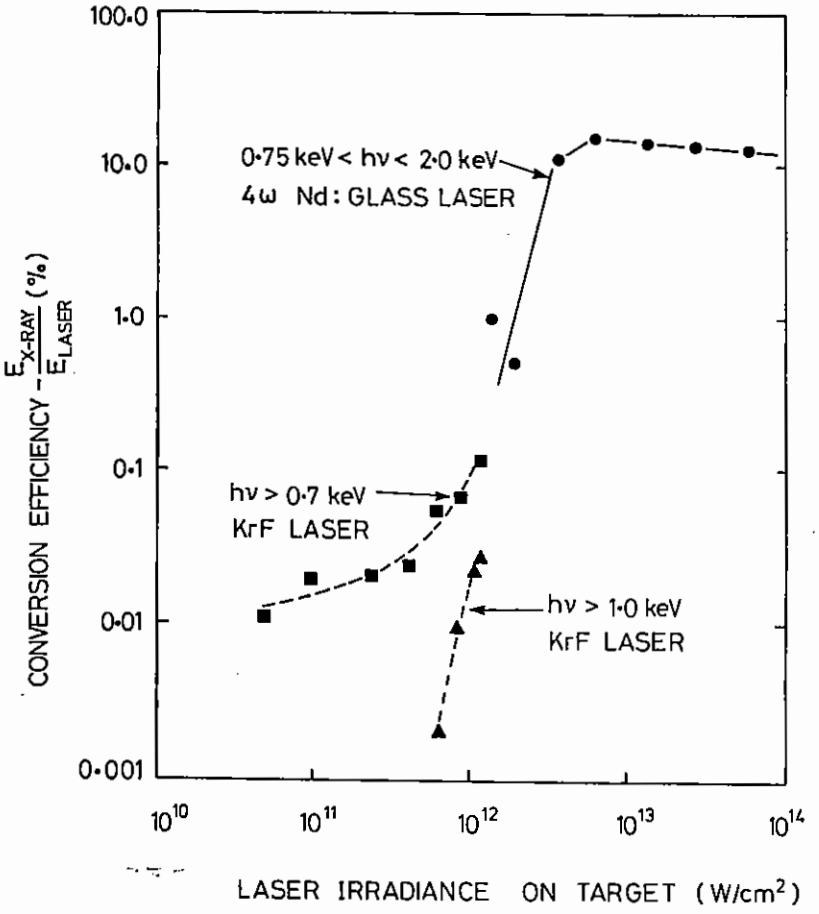

Fig C6.2 X-ray conversion efficiency versus laser irradiance on target. 4ω Nd:Glass laser data is from Ref C6.3. KrF data is from the present experiment.

laser irradiance when using 25μm diameter Cu wire targets. The laser irradiance was varied using the NO_2 gas absorber cell. In this figure we compare the results from the present experiment with efficiency data recorded by other workers using the high power (0.5ns, 15J) 4ω Nd:Glass laser at Ecole Polytechnique (C6.3). It can be seen that the conversion efficiency achieved with the KrF laser is consistent with the Nd:laser data when allowance is made for the different level of irradiance in the two experiments.

With the 0.5J KrF laser at a target irradiance of 1.2×10^{12}W/cm² we have achieved a maximum conversion efficiency of 0.1% for X-ray photons at $h\nu \geq 0.7$ keV and 0.03% for $h\nu \geq 1.0$ keV. Experiments are now underway to improve the beam quality of the EMG150 KrF laser and thus achieve a target irradiance $\approx 10^{13}$W/cm² at which level it is expected that the conversion to X-rays will exceed 10%.

C6.2 GENERATION OF 100psec PULSES AT 308nm FOR AMPLIFICATION IN XeCl LASERS

M H R Hutchinson, W Pang, D Xenakis (Imperial College)
F O'Neill (RAL)

As described in section C6.1 above there is now an interest in generating X-rays of photon energy ≥ 1 keV from high repetition rate laser-plasma sources produced by low energy excimer lasers. In order that a high conversion efficiency to X-rays can be obtained (Fig C6.2) it will be necessary to achieve an irradiance $\sim 10^{13} - 10^{14}$W/cm² on target. A typical commercial high power excimer laser emits ~0.5 - 1.0J pulses of 25ns duration and thus a target irradiance of $\geq 10^{13}$W/cm² can only be achieved by focussing the beam to a spot size ≤ 10μm using a short focus lens of focal length ≤ 40cm (this assumes a 249nm KrF beam, 2cm diameter of beam divergence twice diffraction limited). This focussing geometry is quite acceptable for experimental purposes but would not be suitable for a high average power operational XUV source. With a high repetition rate source, problems could arise in keeping a continuously rotating target in focus because of the small depth of focus of the lens. Also the short stand-off distance of the lens could result in it (or any shielding system) being coated rapidly with target debris. Both of these problems are minimised if long focal length focussing lenses

are employed but then the power on target would be too low if standard commercial excimer lasers are used.

Another approach to increasing the irradiance on target using standard commercial excimer lasers would be to operate the laser with short pulses. For example by using subnanosecond pulses one would increase the peak power of the laser by up to two orders of magnitude so focussing lenses of long focal length (f≥ 100cm) could be used and still achieve high irradiance on target. It is perhaps not advisable to make the pulse duration too short because the X-ray conversion efficiency can drop for pulses ≤ 50psec (the lower limit on the usable pulse duration is not yet clear). It seems that for initial experiments a good compromise would be pulses ≈ 100 psec duration.

100psec pulses have therefore been generated at 308nm using a frequency doubled distributed feed-back dye laser (DFDL) at Imperial College with the aim of amplifying them in an XeCl laser for use in laser-plasma studies. The experimental set-up of the dye laser system is shown in Fig C6.3. A Lambda Physik EMG101 XeCl laser (100mJ, 8ns) is used to pump a DFDL and two dye amplifiers. The DFDL, shown in detail in Fig C6.4, produces a single pulse at a wavelength of 616nm which is amplified first in a transversely pumped amplifier and then in a Bethune cell amplifier. The output pulse from the Bethune cell has an energy ∿ 300 μJ and is frequency doubled in ADP to give ∿ 50μJ at 308 nm. Fig C6.5 shows a streak camera time record of the 616 nm pulse and corresponding Fabry-Perot line-width patterns. The pulse is seen to have a duration of 112 psec and the linewidth measurement shows it to be approximately bandwidth limited ($\Delta\nu.\Delta t \approx 0.3$).

Experiments are now underway to amplify this 30μJ, 308nm pulse in a discharge excited XeCl laser amplifier and to test its capability for generating plasma X-ray sources.

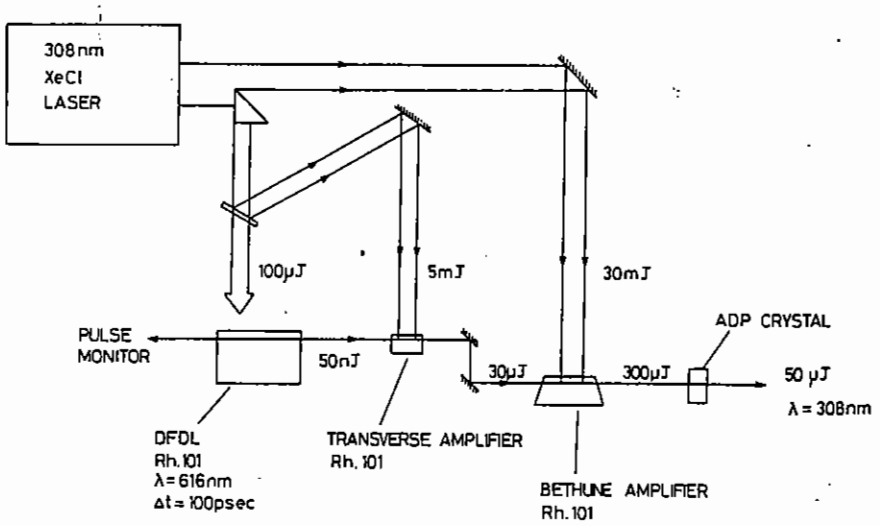

Fig C6.3 100 psec pulse generator at 308nm.

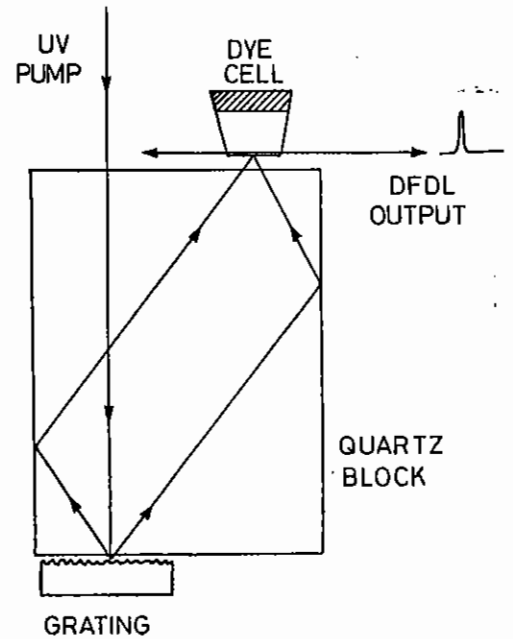

Fig C6.4 Distributed feed-back dye laser (DFDL).

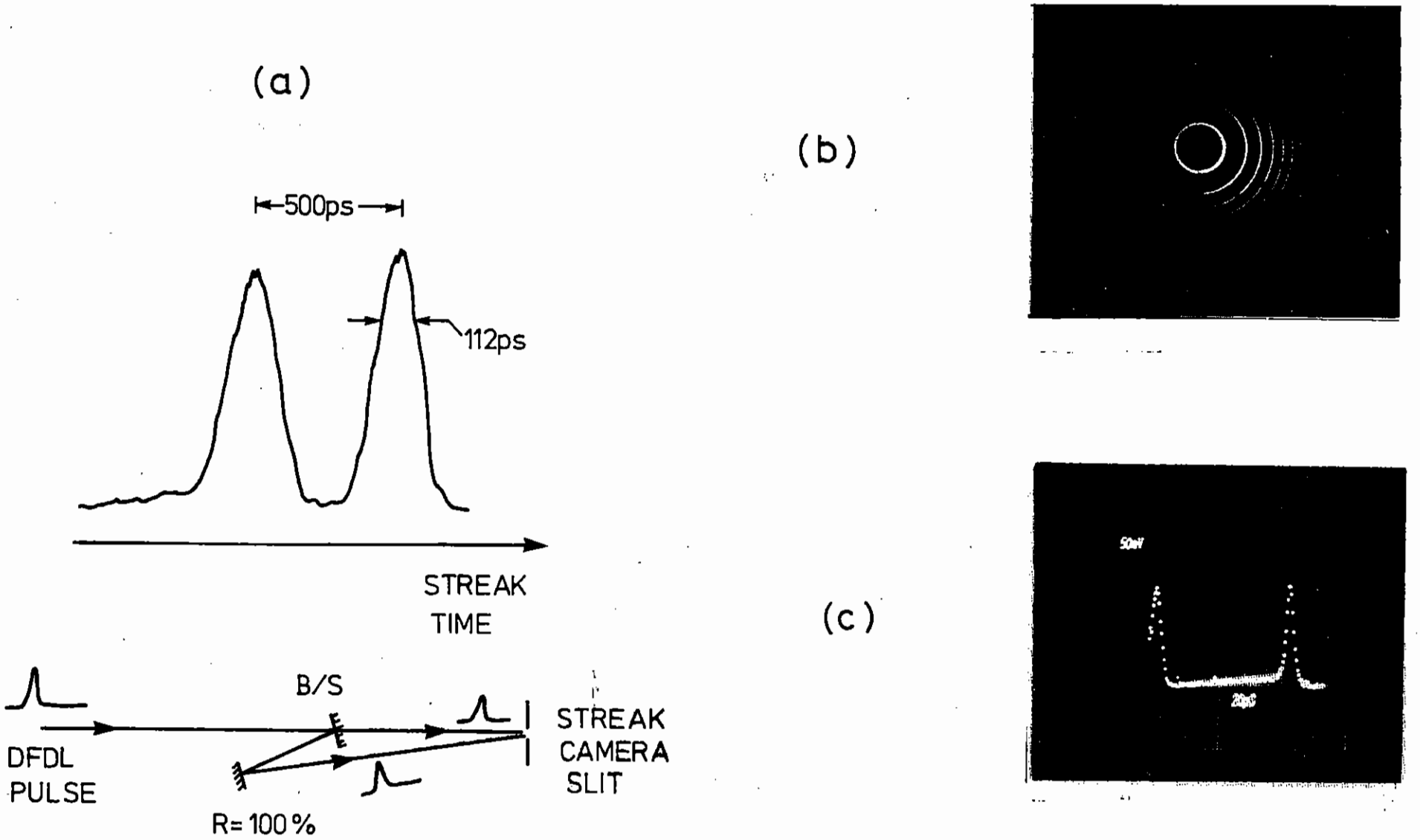

Fig C6.5 (a) Streak camera trace of output pulse of DFDL (616nm)

(b) Fabry-Perot ring pattern of pulse spectrum. Free spectral range = 30 Hz

(c) Expanded view of two fringes of (b) using RETICON diode array. FSR = 30 GHz again.

References

C6.1 F O'Neill, M C Gower, I C E Turcu, and Y Owadano, Appl Opt 25, 464 (1986)

C6.2 F O'Neill, Y Owadano, I C E Turcu, A G Michette, C Hills, and A M Rogoyski, 3rd Topical Meeting on Short Wavelength Coherent Radiation: Generation and Applications, AIP Conf Proc No 147, eds D T Attwood and J Bokor (AIP, NY, 1986), p354

C6.3 M Chaker et al, Proc SPIE Conf on X-Ray Optics and Technology, Berlin (1986), SPIE Vol No 733

Editor: P T Rumsby

D CENTRAL LASER FACILITY PUBLICATIONS April 1986 - March 1987

D1 JOURNALS AND BOOKS

T Afshar-rad, A I Bailey, P F Luckham, W MacNaughton and D Chapman
Direct measurement of the force between lipid bi-layers
Gen discussion Farad Soc 81, 1987 (in press)

T Afshar-rad, A I Bailey, P F Luckham, W MacNaughton and D Chapman
Forces between poly-l-lysine of molecular weight range 4000 - 75000 absorbed on mica surfaces
Colloids and Surfaces (1987) in press

T Afshar-rad, A I Bailey, P F Luckham, W MacNaughton and D Chapman
Forces between basic proteins absorbed on mica surfaces
Biochimica et Biophysica 1987 (in press)

T J Barker, R G Denning and J R G Thorne
Applications of 2-photon spectroscopy to inorganic ions
Inorganic Chemistry 1987 (in press)

H C Barr, T J M Boyd and G A Coutts
Stimulated Raman Scattering in the presence of filamentation in underdense plasmas
Phys. Rev. Lett., 56, 2256 (1986)

J N Bechara, S E J Bell and J J McGarvey
Time resolved resonance Raman spectroscopy of photogenerated transients in the metal carbene complex $CO_5(W{=}C)\ OM_ePh$
Ricerca Scientifica and Educazione Permanente, (1986), Suppl. 50, 83

J N Bechara, S E J Bell, J J McGarvey and J J Rooney
Ligand field photolysis of Fischer complex $CO_5(W{=}C)\ OM_ePh$: Time resolved resonace Raman spectroscopic evidence for alkyl-metal interaction following co-photo dissociation.
J Chem Soc Commun 1785, (1986)

J N Bechara, S E J Bell and J J McGarvey
Resonance Raman spectra of charge - transfer excited states of CuI complexes.
Inorg Chem 25, 4325 (1986)

A R Bell, D J Nicholas and W T Toner
The uniformity of energy deposition on a spherical target using six or twelve laser beams
J Phys D:Appl Phys 19,1869 (1986)

R Bingham, R A Cairns and R G Evans
Saturation of plasma beat waves and de-tuning of relativistic Langmuir waves
Plasma Physics and Controlled Fusion 28, 1735 (1986)

D K Bradley, A Rankin, J S Wark, J Lunney, J Armstrong, R W Eason, A Hauer, J D Kilkenny, A Cullis, V Zammit
Time resolved X-ray diffraction from Silicon during pulsed laser annealing
Bull.Am. Phys. Soc. 31, 1986, p1460

C Chenais-Popovics, R Corbett, C J Hooker, M H Key, G P Kiehn, C L S Lewis, D A Pepler, G J Pert, C Regan, S J Rose, S Sadaat, R Smith, T Tomie,O Willi
Strong XUV laser amplification at 18.2nm (C VI Balmer α) in recombining plasma from a laser irradiated carbon fibre
Phys Rev Letts. (in press)

P C Cheng, R Feder, D M Shinozaki, K H Tan, R W Eason, A Michette, R J Rosser
Soft X-ray contact microscopy
Nuclear Instruments and Methods in Physics Research. A246, 668 (1986)

A J Cole, M H Key, A Ridgeley, D A Brown, P A Norreys, E R Wooding, T W Barbee
A pinhole camera for monochromatic X-ray imaging
Opt Comm (1987) (in press)

R Corbett, C Lewis, E Robertson, S Saadat, P Cunningham, A Cole, E Turcu, M H Key and S Rose
Laser Driven compression of CH shell targets and the effects of increasing aspect ratio
Laser and particle beams 4, 573 (1986)

A E Dangor, A Dymoke-Bradshaw, A Dyson, T Garvey, I Mitchell, A J Cole, C N Dawson, C B Edwards, R G Evans
Generation of uniform plasmas by multiphoton ionisation
IEEE Transitions on plasma Science 1987 (in press)

J R Darwent, C D Flint, P J O'Grady
Observation of photoluminescence from the $^6D_1$ state of the europium decatungstate anion in aqueous solution
Chem Phys Letts, 127, No 6 (1986)

G M Davis and M C Gower
Wavelength dependence of the excimer etching characteristics of polymeric resists
Appl Phys Letts, May 1987 (in press)

G M Davis and M C Gower
Time resolved transmission studies of PMMA films during UV laser ablative photodecomposition
J Appl Phys, March 1987 (in press)

G M Davis and M C Gower
Excimer laser lithography: intensity dependent resist damage
IEEE Electronics Dev Letts EDL-7, 543 (1986)

R W Eason, P C Cheng, R Feder, A G Michette, R J Rosser, F O'Neill, Y Owadano, P T Rumsby, M J Shaw, I C E Turcu
Laser X-ray microscopy
Optica Acta 33, 501 (1986)

R W Eason, A M C Smout
Bistability and non-commutative behaviour of multiple beam self-pulsing and self-pumping in $BaTiO_3$
Optics Letts 11, (1987) p51-53

G H Evans, R W Sparrow, R G Brown, D Shaw, J Barr, M J C Smith, W Toner
Fast flourescence and absorption measurements of photosystem I from a cyanobacterium
Progress in Photosynthesis research, ed J Biggings, Vol 1 p99-102

R G Evans
The basic physics of laser fusion
Canad J Phys 64, 893 (1986)

R G Evans
Magnetic fields generated by the Rayleigh Taylor instability
Laser and particle beams 4, 325 (1986)

R G Evans
The influence of Self-Generated Magnetic Fields on the Rayleigh Taylor instability
Plasma Physics and Controlled Fusion 28, 1021 (1986)

F G Godwin et al
2-photon VUV laser induced fluorescence detection of I* ($^2P_{1,2}$) and I($^2P_{3,2}$) from alkyl iodide photodissociation at 248nm
Chem Phys Letts 135, 163 (1987)

M Golombok, M C Gower, S J Kirby and P T Rumsby
Photoablation of plasma polymerised polyacetylene films
J Appl Phys 61, 1222 (1987)

M C Gower
The razor edge of excimer laser
Spectrum 203, 5 (1986)

M C Gower
Photoinduced voltages and frequency shifts in a self-pumped phase conjugating $BaTiO_3$ crystal
Optics Letts, 11, 458 (1986)

M Grande and W Burton
Aluminium minor coatings in space
Surface and interface analysis 9, 518 (1986)

R J Harrison, B Pearce, G S Beddard, J A Cowan and J K Sanders
Photo-induced electron transfer in pyromellitimide-bridged porphonis
Chem Phys 1987 (in press)

R E Hester
Raman spectroscopic studies of transient chemical species, in time resolved laser Raman spectroscopy Eds D Phillips and G H Atkinson
Harwood Academic Publishers, London, 5 (1987)

M P Irvine, R J Harrison, G S Beddard, P Leighton and J U M Sanders
Detection of the inverted region in the photo-induced intra-molecular electron transfer of capped porphorins
Chem Phys 104, p315 (1986)

F Kannari, M J Shaw and F O'Neill
Parametric studies of an electron-beam-pumped krypton-rich KrF laser
J Appl Phys, Jan 1987 (in press)

M H Key, J E Boon, C Chenais-Popovics, R Corbett, A R Damerell, P Gottfeldt, C J Hooker, C P Kiehn, C L S Lewis, D A Pepler, G J Pert, C Regan, S J Rose, I N Ross, P T Rumsby, S Sadaat, R Smith, T Tomie, and O Willi
Study of X-ray laser schemes using new experimental facilities at the Rutherford Appleton Laboratory
J de Physique Colloque, C6 Suppl. 10,47, pC6-71 (1986)

G P Kiehn, O Willi, A R Damerell and M H Key
Novel time resolved VUV spectrograph for X-ray laser research
Appl Optics 26, 425 (1987)

J G Lunney, J D Hares, P Dobson, S D Tabatabaei, R W Eason
Time resolved X-ray diffraction from silicon during pulsed laser annealing
Opt Commun 58, 269 (1986)

M R S McCoustra, J A Dyet and J Pfab
Photodissociation of methyl and t-butyl thionitrites near 450nm
Chem Phys Letts 1987 (in press)

J A Dyet, M R S McCoustra and P Pfab
The visible spectrum of jet-cooled CF_3NO
Chem Phys Letts 1987 (in press)

M R S McCoustra, J A Dyet and J Pfab
Laser photo-fragment spectroscopy of jet-cooled $CCl\ F_2NO$
Chem Phys Letts 1987 (in press)

I McCubbin, D Phillips and R E Hester
Time-resolved resonance Raman spectroscopy of the triplet state and semi-reduced form of Duroquinone
J C S Faraday Trans 2, 83, (1987) in press

J N Moore and D Phillips
Photophysics and photochemistry of sulphonated derivatives of 9,10 anthraquinone 'strong' versus 'weak' sensitisers.
J C S Faraday Trans 2, 83, (1987) in press

J N Moore, D Phillips, P M Killough and R E Hester
Resonance Raman studies of transient Intermediate in photoreactions of Anthraquinone and Flavone species, in time-resolved vibrational spectroscopy, Eds A Laberau and M Stockburger, Springer-Verlag
Heidelberg, 136 (1985)

J N Moore, D Phillips, N Nakashima and K Yoshihara
Photochemistry of 9,10-anthraquinone-2,6 disulphate
JCS Faraday Trans 2, 82, 745 (1986)

J N Moore, D Phillips, R E Hester, G H Atkinson and P M Killough
Time-resolved resonance Raman spectroscopy of sulphonated Anthraquinone derivatives, in time-resolved laser Raman spectroscopy, Eds D Phillips and G H Atkinson,
Harwood Academic Publishers London, 23 (1987)

J N Moore and D Phillips
Time-resolved resonance Raman spectroscopy of electronically excited species, in time-resolved laser Raman spectroscopy, Eds D Phillips and G H Atkinson
Harwood Academic Publishers London 23 (1987)

F O'Neill
Research boundaries widen with new laser
Spectrum 199, 5 (1986)

F O'Neill
The first KrF target facility
Phys Bull, 37, 286 (1986)

F O'Neill, I N Ross, D Evans, J U D Langridge, B S Bilan and S Bond
Colloidal silica coatings for KrF and Nd:Glass laser applications
Appl Opt 26 (1987)

D J Nicholas and J E Boon
The manufacture of aspheric focussing lenses for high-power multi-wavelength laser systems
J Phys D:Appl Phys 20, 182 (1987)

J P Partanen
Multipass grating interferometer applied to line narrowing in excimer lasers
Appl Opt, 25, 3810 (1986)

J P Partanen and M J Shaw
High power forward Raman amplifiers employing low pressure gases in light guides I-Theory and applications
J Opt Soc Amer B 3, 1374 (1986)

G J Pert et al
Expansion recombination lasers in the XUV
Proceedings of the SPIE, 664, 258 (1986)

D Phillips and R E Hester
Time-resolved resonance Raman spectroscopy applied to anthraquinone photochemistry
J C S Faraday Trans 2, 82, 1093 (1986)

R T Phillips, Z Sobiesierski, W T Toner, J Barr and A J Langley
Initial photoluminescence decay rates in Amorphous Phosphorus
Solid state comm 1987 (in press)

S J Rose
The effect of orbital relaxation on transition energies in radiative opacity calculation
J Quant spectrosc Rad Transfer 36, 389 (1986)

I N Ross, J E Boon, R Corbett, A R Damerell, P Gottfeldt, C J Hooker, M H Key, G P Kiehn, C L S Lewis and O Willi
Design and performance of a new line focus geometry for X-ray laser experiments
Appl Optics 1986 (in press)

M J Shaw, J P Partanen, Y Owadano, I N Ross, E M Hodgson, C B Edwards and F O'Neill
High power forward Raman amplifiers employing low pressure gases in light guides II - experiments
J Opt Soc Amer B 3, 1466 (1986)

C J S M Simpson, J P Hardy
Laser-induced thermal desorption of atoms and molecular physisorbed onto a metal surface
Chem Phys Letts, 130, 175 (1986)

A M C Smout, R W Eason
Analysis of mutually incoherent Beam coupling in $BaTiO_3$
Optics Letts 1987 (in press)

A M C Smout, R W Eason, M C Gower
Regular oscillations and self-pulsating in self-pumped $BaTiO_3$
Optics Commun 59, 77-82 (1986)

I C E Turcu, F O'Neill, U Zammit, Y Al-Hadithi, R W Eason, A M Rogoyski, C P B Hills and A G Michette
Characterisation of KrF laser-plasma X-ray sources in the 280-520 eV photon enegy range
Appl Phys Lett 1987 (in press)

F Wilkinson, C J Willsher, P A Leicester, J R M Barr, M J C Smith
Picosecond diffuse reflectance laser flash photolysis
J Chem Soc Chem Comms, 1216 (1986)

D2 PUBLISHED CONFERENCE PROCEEDINGS

D K Bradley, A Rankin, J S Wark, J Lunney, R W Eason, A Hauer, J K Kilkenny, A Cullis, U Zammit
Time-resolved X-ray diffraction from silicon during pulsed laser annealing
Presented at 28th Annual Meeting of American Physical Society 1986.

A J Cole et al
Direct drive laser compression experiments at the Rutherford Appleton Laboratory
4th International Conference on Emerging Nuclear Energy Systems. G Velarde and E Minguez World Scientific Publishing Co plc Ltd

A E Dangor et al
Generation of uniform plasmas by multiphoton ionisation
Proceedings of the Advanced Accellerator Concepts Meeting
Dangor et al
Wisconsin 1986

J A Dyet, M R S McCoustra and J Pfab
Single and two photon dissociation of $CClF_2NO$ in the visible
J A Dyet, M R S McCoustra and J Pfab paper E14, Abstracts of 9th International Symposium on Gas Kinetics, Bordeaux, July 1986

R W Eason, D K Bradley, J D Hares, J Rankin, S D Tabatabaei, J G Lunney, P C Cheng, R Feder, A G Michette, R J Rosser, F O'Neill, Y Owadano, P Rumsby, M J Shaw
Recent applications of laser-produced plasma X-ray sources
Proc SPIE Vol 664
Proceedings of Conference on High Intensity Laser Processes, Quebec, June 1986

R W Eason, A M C Smout and M C Gower
Self pulsation and incoherent beam coupling effects in self-pumped $BaTiO_3$
Proceedings of Summer School on Photorefractive Materials, Erice, Sicily, Italy (1986) Springer-Verlag

E H Evans, R Sparrow, R G Brown, D Shaw, J Barr, M J Smith, W T Toner
Fast fluorescence and absorption measurements of photosystem I from a cyanobacterium
Proc 7th Int Cong Photosynth, Brown University, Rhode Island

M C Gower
Voltages and frequency shifts in a self-pumped phase conjugating $BaTiO_3$ crystal
XIV Int Quantum Elect Cong, San Francisco (1986)

M G Haines et al
Progress in inertial confinement in the UK.
XI Int Conf on Plasma physics and controlled nuclear fusion research
Kyoto Japan Nov 1986
Paper IAEA - CN - 47 / B-11-1

F Kannari, M J Shaw and F O'Neill
Parametric studies of an electron beam pumped krypton-rich KrF laser

Conf on Lasers and Electro-optics, San Francisco (1986)

M H Key
X-ray lasers, a summary of progress worldwide
Invited paper at Cong on Lasers and electro-optics, San Francisco (1986)

M H Key
Energy transport in laser-produced plasmas
Proc XVII Int Conf in Phenomena in Ionised Gases
Invited papers J Bakos, Z Sorlei
Eds Publ Hungarian Academy of Sciences (1986)

M H Key
Laser produced plasmas
Proceedings of the Royal Institution,
Published Science Rev Ltd 58, 215 (1986)

M H Key
X-ray lasers, a summary of progress worldwide
Proc Conf on Lasers and Electro Optics OSA/IEEE, 68 (1986)

M H Key, C Brown, R G Evans, P Gottfeldt, C J Hooker, D A Pepler, S J Ross, I N Ross, P T Rumsby (RAL), R Corbett, C L S Lewis, C Regan, S Sadaat (QUB), G P Kiehn, R Smith, O Willi (IC), G J Pert, S Ramsden (Hull)
XUV laser action in recombining laser-produced plasmas
Proc OSA 1986 Annual Meeting, 97 (1986)

F O'Neill
Laser-plasma XUV sources generated by KrF lasers
Proc SPIE Conf on soft X-ray optics and technology, Berlin
SPIE Vol 733 (1986)

F O'Neill, I N Ross, D Evans and J U D Langridge
Colloidal silica coating for KrF and Nd:glass laser applications
Conf on Lasers and Electro-Optics, San Francisco (1986)

F O'Neill, Y Owadano, I C E Turcu, A G Michette, C Hills and A M Rogoyski
Low power pulsed laser-plasma sources of soft X-rays
Proc 3rd Topical Meeting on Short Wavelength Coherent Radiation, Monterey, March (1986)

F O'Neill, M C Gower, I C E Turcu, Y Owadano and R Feder
X-ray lithography using a KrF laser-plasma source
Conf on Lasers and Electro-optics, San Francisco (1986)

I N Ross, O Willi, G P Kiehn, M H Key and C J Hooker
Performance of a new X-ray laser line focus geometry
Conf on Lasers on Electro-Optics, San Francisco (1986)

Z Sobiesierski and R T Phillips
Time resolved photoluminescence in Amorphous Phosphous
Proceedings of the International Conference on Non-Crystalline Semiconductors
Balatonszeplak Sept 1986, Published in Journal of Non-crystalline Solids Vol 90 p457-460, 1987

M J Shaw, I N Ross, F Kannari, E M Hodgson, J Partanen, I C E Turcu and F O'Neill
Progress on the SPRITE multiplexer
Conf on Lasers and Electro-Optics, San Francisco (1986)

W T Toner et al
Fusion related experiments at the Central Laser Facility
Proc 12th European Conf on Contr Fusion and Plasma Physics, Budapest 1985
Plasma Physics and Controlled Fusion, 28, 235 (1986)

F Wilkinson, C J Willsher, P A Leicester and M J C Smith
Picosecond laser flash photolysis of opaque materials
Proc of XIV IUPAC Symposium on Photochemistry, Lisbon, 155 (1986)

O Willi et al
X-ray laser research at the Rutherford Appleton Laboratory
Proc SPIE Annual Int Tech Symp, San Diego, USA, 2 (1987).

PART II

PART II LASERS FOR MICROCIRCUIT FABRICATION

Editor: M C Gower

PART II LASERS FOR MICROCIRCUIT FABRICATION

Introduction

M C Gower (RAL)

This section of the Laser Division annual report covers the progress of work undertaken by Laser Division staff working on the 'Microcircuit Fabrication using Lasers' project. This project took place between November 1983 and March 1987 and was jointly funded on a 50:50 basis by the Engineering Board of the SERC and the Department of Trade and Industry (DTI). It involved a collaborative effort between the Laser and Technology Divisions of RAL.

The aims and scope of the programme were to carry out an investigative study of the potential novel uses of lasers in microcircuit fabrication with particular emphasis being placed on the use of laser sources in photolithography. More specifically, it is hoped that results arising from the programme will eventually show that laser sources can provide cheap, high throughput photolithography for device sizes between 0.2 → 1μm.

This report covers only that part of the project undertaken in the Laser Division, namely, investigations of novel methods of high resolution image projection using lasers. This activity involved 2 man years of RAL Laser Division staff effort supplemented by research sandwich student and consultative support. A parallel effort, which studied high resolution imaging using conventional optical materials and methods with excimer laser sources has been undertaken by staff from Technology Division and the results are not included in this report.

The three novel techniques for image projection described in this report all involved the use of either 'real' or 'lapsed time' phase conjugate mirrors (PCM's). The first method made use of a thermally-induced optical nonlinearity in liquid solutions to produced real-time phase conjugate reflections by degenerate four-wave mixing of ultraviolet excimer laser radiation at 249nm and is described in Section 1. Also in this section are descriptions of investigations of the use of holographic techniques to high resolution image projection. While the results of the use of self-pumped photorefractive $BaTiO_3$ crystals for high resolution image projection are fully described in the 1985 Annual Report, further studies of the self-pumping mechanisms which produce such phase conjugate beams from these crystals are also reported in Section 1. Several patent applications arising from the work described in this section have been made.

In Section 2 we describe fundamental studies of the processes which affect the fidelity (and hence the resolution for projecting images) of phase conjugate mirrors produced by stimulated Brillouin scattering (SBS).

Finally in Section 3 we report on the first observations of direct excimer laser etching of GaAs. We believe these results could have great commercial potential for the future fabrication of integrated optical, quantum well and laser diode devices.

One of the main objectives of this project has been to feed into UK industry for possible commercial exploitation the more promising results of the research. Several companies are currently assessing these results with a view to future exploitation.

SECTION 1 IMAGE PROJECTION USING PHASE CONJUGATE MIRRORS

1.1 IMAGING BY DEGENERATE FOUR WAVE MIXING AT 249nm

G M Davis, A F Gibson and M C Gower (RAL)

The size of the minimum resolvable element, ∇, of an image is related to the wavelength, λ, and the numerical aperture, NA, by

$$\nabla = C\lambda/NA \qquad (1)$$

where C is a numerical constant of about 0.8 and depends on such factors as the coherence of the light source. Similarly the depth of focus, δ, is given by

$$\delta = C\lambda/(NA)^2 \qquad (2)$$

so that, for a given NA, ∇/δ decreases with λ. Research on the use of KrF (249 nm) and ArF (193 nm) lasers as UV sources for high resolution image projection and photolithography, primarily using conventional but complex lens systems, is being actively pursued worldwide (including at RAL). Alternative imaging techniques worthy of consideration are UV holography (see Section 1.2) and degenerate four wave mixing (DFWM).

DFWM at 249 nm was first observed by Caro and Gower[1]. The mechanism in the working medium was thermal: energy absorbed by the dye Rh6G dissolved in ethanol modulated the local temperature and hence refractive index. Imaging and photolithography using the Caro and Gower technique was demonstrated by Levenson[2] using a tripled Nd:YAG laser (λ = 355 nm) as his source. For some of our experimental work we used the experimental arrangement shown schematically in Figure 1. It is essentially the same as that used by Levenson (except for the shorter wavelength) and can be considered the basic minimum required for DFWM. In the following sections we describe the factors influencing the choice of component parameters in a DFWM structure for use at 249 nm, how the basic structure might be improved and our experimental results.

The source of 249 nm radiation was a Lambda-Physik type EMG 150 laser. The linewidth of this laser was measured to be $\sim 0.3\text{cm}^{-1}$. The irreducible beam divergence was no greater than twice the diffraction limit so that the transverse coherence length, ℓ_T, was more than half the actual beam width, w. The laser pulse duration was about 20ns.

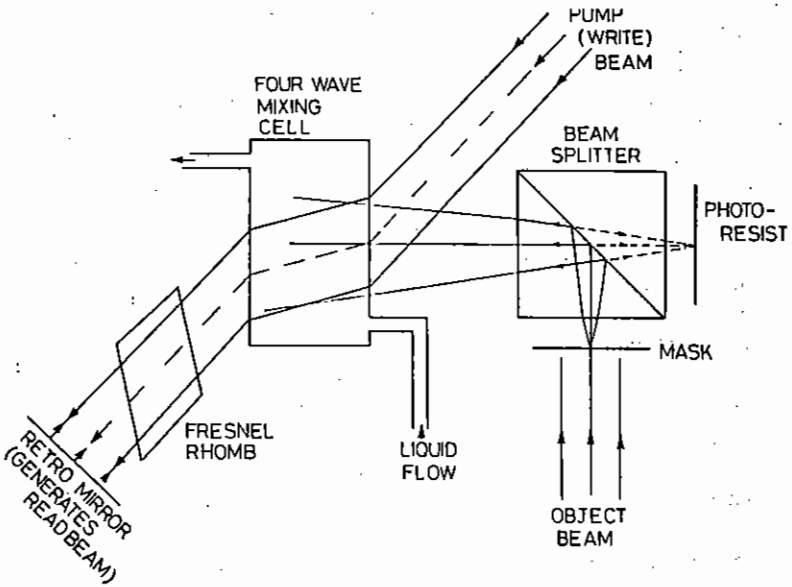

Fig 1 Equipment for degenerate four-wave mixing (DFWM).

The very high gain of KrF necessitates protection of the laser from the retro-reflected or "Read Beam" pulse. To do this a gap of several metres was left between the laser and imaging apparatus so that the amplifier gain had subsided before the read pulse returned to the laser. In addition, isolation of the laser was obtained by using a Fresnel rhomb which was inserted between the interaction cell and the retromirror (see Figure 1) to rotate the plane of polarisation by 90° in double pass, and a polarizer stack interposed between the laser and apparatus (not shown in Figure 1). This type of polarisation isolation also gave two other advantages. The polariser stack eliminated half of the amplified spontaneous emission from the KrF amplifier. Also a polarisation sensitive beam splitter cube could be used in the set-up shown in Figure 1 (object and image beams must have the same polarisation as the write and read beams respectively). Such protection was not used with Levenson's tripled YAG source.

Single shot photolithography suffers from irreproducibility of dose problems. We therefore wish to deliver the required total dose ($\sim$ 100mJcm^{-2}) to the photoresist in a few tens of pulses. However the energy, E_1, delivered to the photoresist per pulse should be maximised since this allows for the maximum field size coverage. Clearly E_1 is the product of the pulse energy in the object beam, E_o, the efficiency, e, of the beam splitter and the reflectivity, R, of the conjugator. Since the intensities of the pump beams are orders of magnitude greater than those of the object or image beams, the former are the prime source of scattered light, or "noise" in the system. Hence the product of the three parameters, $E_o \epsilon R$, per unit pump intensity is of critical importance in obtaining an adequate signal to noise ratio at the photoresist. We consider these three parameters separately.

The object beam pulse energy, E_o, is limited by the risk of damage to either the mask or the beam splitter. An uncoated quartz plate at 45°, thick enough to sufficiently separate the wanted and unwanted reflections, can provide a high damage threshold beam splitter and its relatively low efficiency (9%) can be compensated for by increasing E_o to the limit set by the mask. The astigmatism which such a component produces can be compensated for by inserting an equivalent plate between mask and beam splitter, as shown in Figure 2. It might be thought that, arranged as in Figure 2, the astigmatism of each plate would add. In fact the phase conjugate reflector reverses the astigmatism caused by the first (compensator) plate so that cancellation is achieved in the second (beam splitter) plate. Cancellation requires that the nett astigmatism be less than the depth of focus. For quartz (n = 1.5) plates of thicknesses t_1 and t_2 at angles ϕ_1 and ϕ_2 to the optic axis where $t_1 \approx t_2 = t$ and $\phi_1 \approx \phi_2 = 45°$ this requires

$$\delta = \frac{C\lambda}{(NA)^2} > .0.27\ (t_1 - t_2) + 1.37\ t(\phi_1 - \phi_2) \qquad (3)$$

so that, if $t_1 > t_2$, the thinner plate must be tipped at a greater angle ($\phi_2 > \phi_1$) to compensate. For NA $\sim$ 0.25 and t $\sim$ 1 cm this requires thickness accuracies of a few tens of microns and angular accuracies around 100 μradians. A beam splitter to this design has been made, tested and patented.

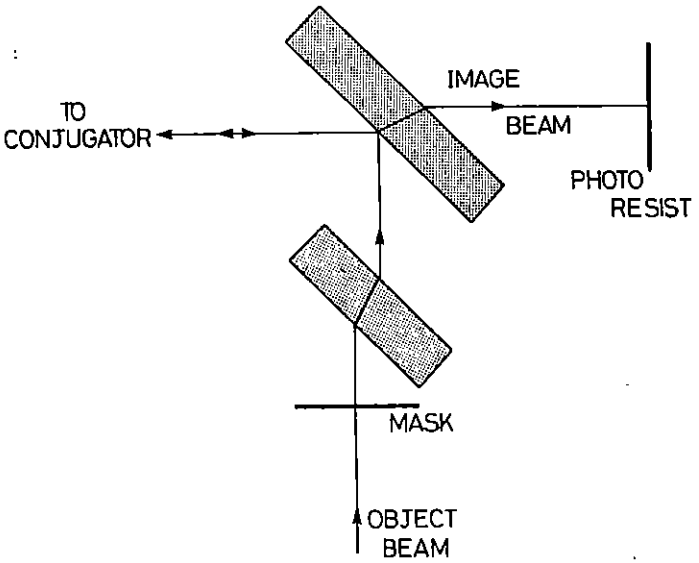

Fig 2 Damage-resistant beam splitter

A beam splitter cube is not astigmatic (provided it is truly cubic) but, unlike the above two plate system, no adjustment can usually be made after assembly. Furthermore, we have found that it is not possible to reach the theoretical 25% efficiency at 249 nm with thin metallic coatings. Absorption of ∿10% was typical in such coatings which have damage thresholds of ≤ 5mJ/cm². However, we have obtained high efficiencies (∿ 40%) using polarisation sensitive multilayer dielectric coatings. Provided the number of layers is kept small (≤ 3) a cubic beam splitter can still be produced for which a strong dependence of efficiency on angle (which could limit NA) was avoided and an adequate damage threshold (> 20 mJ/cm²) was obtained.

For $R < 1$ the reflectivity is proportional to the product of the write and read beam intensities and hence, for a given laser power, varies as w^{-4} where w is the pump beam diameter. For $R > 1$ the dependence is even steeper. Since $R \sim 1$ requires pump powers $\sim 25\ MWcm^{-2}$ [1], some beam diameter compression using a telescope is necessary and we have generally used a diameter compression factor of x3 of the output beam from the laser. However, far more important than the absolute value of R, is the fact that the image to scatter energy ratio, and hence the signal to noise ratio at the photoresist, also varies as w^{-4} or steeper. This is because, for a given laser pulse energy, the scattered energy is independent of w. A consequence of reducing w, to increase signal to noise at the photoresist is to reduce the numerical aperture and hence resolution (see above).

Compared with w the variation of R (and hence signal to noise ratio) with other parameters is comparatively slow. Caro and Gower confirmed that R varied with the absorption coefficient, α, of the liquid filling the cell as

$$R = C \exp(-2\alpha L/\cos\psi)\ [1 - \exp(-\alpha L)]^2 \qquad (4)$$

where L is the cell thickness and ψ the angle between write and object beams in the liquid. This function passes through a broad maximum at $\alpha L \sim 0.7$, or less if ψ is large.

Even when not multiplied by α the cell thickness also influences R. A hologram is only formed in the cell if the write and object beams not merely overlap but are mutually coherent. Inspection of Figure 1 shows immediately that this sets an upper limit to L. For the central, unscattered, object ray the reflectivity will fall when

$$L \geq \ell_T/\tan\psi \qquad (5)$$

where ℓ_T is the transverse coherence length and, in our equipment with a beam diameter compression of 3 is only a few millimetres.

When the write and read beams became misaligned, L appears indirectly through the fall in R which occurs if the phase matching condition is not met. For a small misalignment, θ, the object and image beams also become misaligned by a small angle, Δψ, given by

$$\Delta\psi = \theta \cos\psi \qquad (6)$$

so that aberration correction of any double passed components, the hallmark of phase conjugate systems, will not normally be achieved. There remains, however, an uncorrectable wavevector mismatch, Δk, given by

$$\Delta k = \theta k \sin\psi \qquad (7)$$

and R falls off when Δk exceeds the uncertainty in k due to the finite linewidth of the laser and the thickness of the cell. We can roughly estimate the uncertainty in k to be of order

$$\left[\left(\frac{1}{nL}\right)^2 + \left(\frac{1}{\ell_L}\right)^2\right]^{1/2} = \frac{1}{L_c}, \quad \text{say} \qquad (8)$$

where ℓ_L is the longitudinal coherence length of the laser. The reflectivity is then given by

$$R = \sin^2 x/x^2$$

where (9)

$$x = 2\pi L_c \theta \sin\psi / L_c$$

and hence pump beam alignment is much more critical in the plane of Figure 1 than perpendicular to it, although of course $\psi \neq 0$ in any plane due to the finite beam divergence of the laser. For L_c = 5mm and sin ψ = 0.5, $x = \pi/2$ gives R = 0 at θ = 25μradians. Confirmation of this conclusion is provided by Levenson[2], who with L_c = 2cm and a more coherent laser noted "The direction of the retroreflected beam was exceedingly critical; a deviation of a few microradians .... reduced .... the reflectivity essentially to zero". The roles of the thermal properties of the solvent in determining R have been studied by Hoffman[3]. The constant of proportionality in equation(4) contains a solvent figure of merit, Q, given by

$$Q = \frac{2\pi n}{\lambda \rho C_p} \left(\frac{dn}{dT}\right) \quad (10)$$

where ρ is the density and C_p the specific heat. Within the limited range of available solvents which are transparent at 249nm, Q does not vary greatly between materials. Rh6G is not a good choice as absorber due to its high fluorescence efficiency and so acetone was used as the working medium.

The time constant τ, for washout of the thermal hologram formed by write and image beams in the liquid depends on the grating spacing and hence the angle between them

$$\tau = \frac{\rho C_p \lambda^2}{n^2 K (4\pi)^2 \sin^2(\psi/2)} \quad (11)$$

where K is the thermal conductivity. Since R decreases when τ is a less than the laser pulse duration (about 20 ns) equation (11) sets an upper limit to ψ in ethanol of 36° corresponding to an angle of 53° between write and image beams external to the cell. Eq (11) similarly sets an upper limit to equation (4).

If τ is greater than the laser pulse duration the conjugator reflectivity can be enhanced by delaying the read beam and we have observed an enhancement of up to a factor of 2 by this method.

The image quality obtainable from a phase conjugate reflector is intrinsically limited by the finite spread in wavevector of the reflected beam (equation (8)). In practice, however, at least in our experiments, the resolution is limited (as in conventional optical instruments) by half the angular aperture, φ, subtended by the conjugate reflector at the photoresist or the mask. Then

$$NA = n' \sin\phi \quad (12)$$

where n' is a composite refractive index since part of the optical path is through quartz and part through air.

In the structure shown in figure 1, sinφ and hence the resolution is obviously determined by the effective radius of the conjugator divided by the distance between the cell and photoresist. As noted above, the former is limited by the pump beam width, w, or the transverse coherence length, ℓ_T, and is constrained by the need to maintain a high reflectivity per unit pump power. Reducing the cell-photoresist separation requires either reducing w, which is counterproductive, or increasing the angle, ψ, between write and object beams subject to the constraints imposed by equations (4), (5) and (9) but particularly the limit set by equating τ (equation (11)) and the laser pulse duration. We, like Levenson, have used a value of $\psi \sim 35°$ in the geometry of Figure 1. If a major improvement in resolution is to be obtained a new structure must be devised. Two novel geometries have been tried.

In the arrangement shown in Figure 3 a lens images the mask within the mixer cell with unit magnification. Being double passed the aberrations of the lens are, in principle, cancelled. Three consequences follow:

(a) $\sin\phi$ and hence the resolution is determined by the aperture of the lens. For unit magnification

$$NA = \frac{1}{4F} \qquad (13)$$

where F is the "f number" of the lens.

(b) The width of the pump beam determines the area of mask included in the image, not the resolution. Hence w can be decreased, with the advantages discussed above without a loss in resolution.

(c) Provided the object beam is inverted twice, as in Figure 3, each ray of the object beam at the cell is pumped by a near equivalent ray in the write beam. Mixing is then much less sensitive to the transverse coherence of the laser.

From equations (1) and (13) a lens of $F \leq 1$ is required for submicron resolution. While no single lens was available when this scheme was tested experimentally a two lens combination of, plano-convex lenses (F=2 and 1.5) were used and where tilted to deflect unwanted Fresnel reflections from the surfaces impinging upon the photoresist. A result, using a 1 mm thick cell, is shown in Figure 4. It is likely that the aberrations caused by tilting of these lenses were too large to be fully corrected for by the thin conjugator particularly in areas of the large angle used between write and image beams.

Two beams at right angles to one another can be combined at a 45° quartz prism (n = 1.5, critical angle 42°) as shown in Figure 5. The angle between the two beams in the mixing cell can then be quite modest (∿15°) which then allows a thick cell to be used. Most important, the use of such a prism allows the beam splitter to be brought very close to the cell: the layout in Figure 5 gives

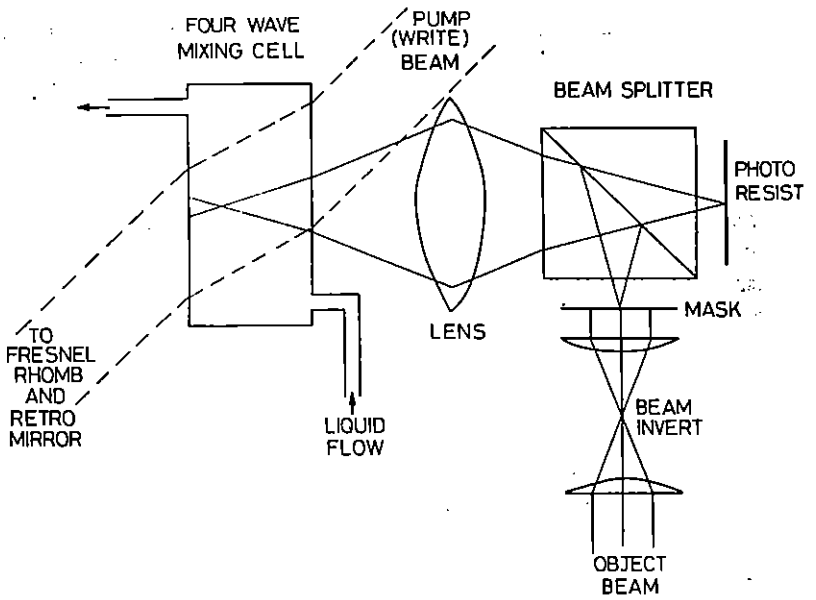

Fig 3 Equipment for DFWM with image relaying

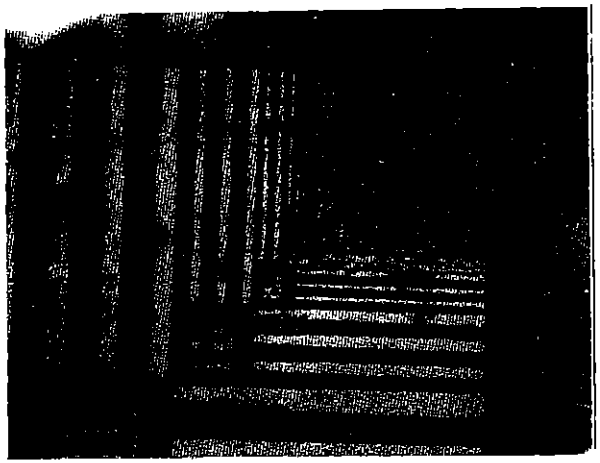

Fig 4 Optical microscope pictures of 3μm features produced by the setup shown in Fig 3.

N.A. = 0.28. The NA can be further enhanced - theoretically at least - to 0.6 or 0.7 by guiding the object beam by using mirrors. Such a design has be patented. Finally, a simple rectangular layout can be achieved when using this arrangement. This simplifies the achievement of the mutual coherence requirements between write and object beams.

A photograph of apparatus using this principle is shown in Figure 6 and a test image recorded in photoresist in Figure 7. High resolution appears to be achievable but clearly there is an unacceptable amount of "fogging" of the photoresist due to scattered pump light. This scattered light was found to arise from (non-total), total internal reflection at the prism surface. The image shown in Figure 7 was obtained with a pump beam diameter compression factor of 3, a relatively low (∿10%) efficiency beam splitter and no enhancement of the reflectivity by read beam delay (possible with $\psi = 15°$). However, the improvements achievable

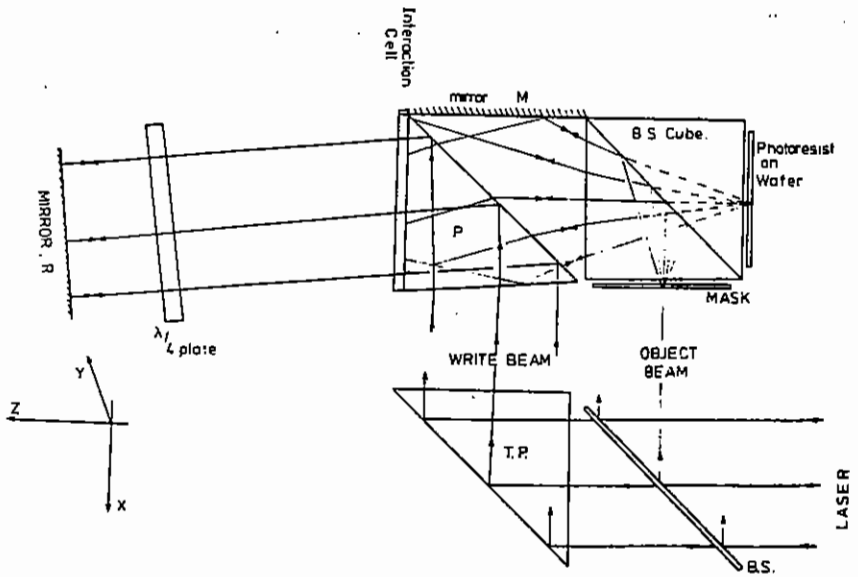

Fig 5 Equipment for DFWM with beam combining prism

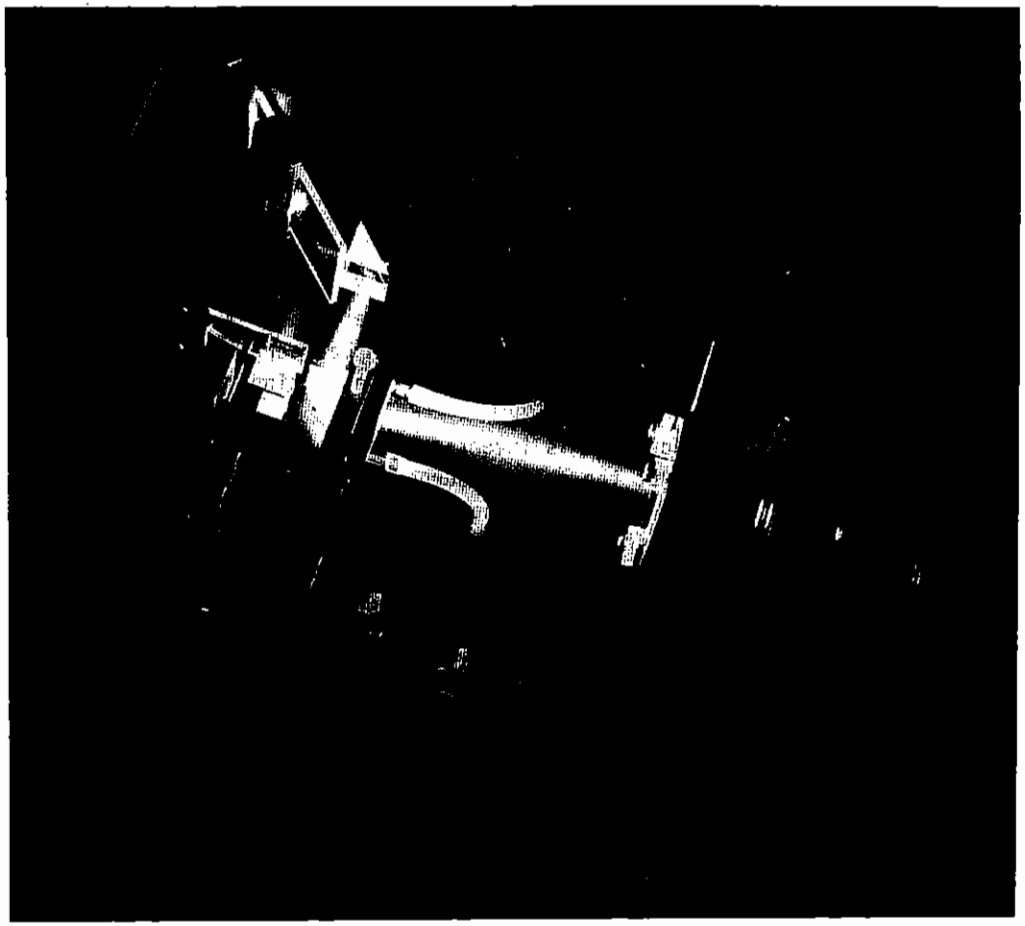

Fig 6 Photograph of set-up drawn in Fig 5.

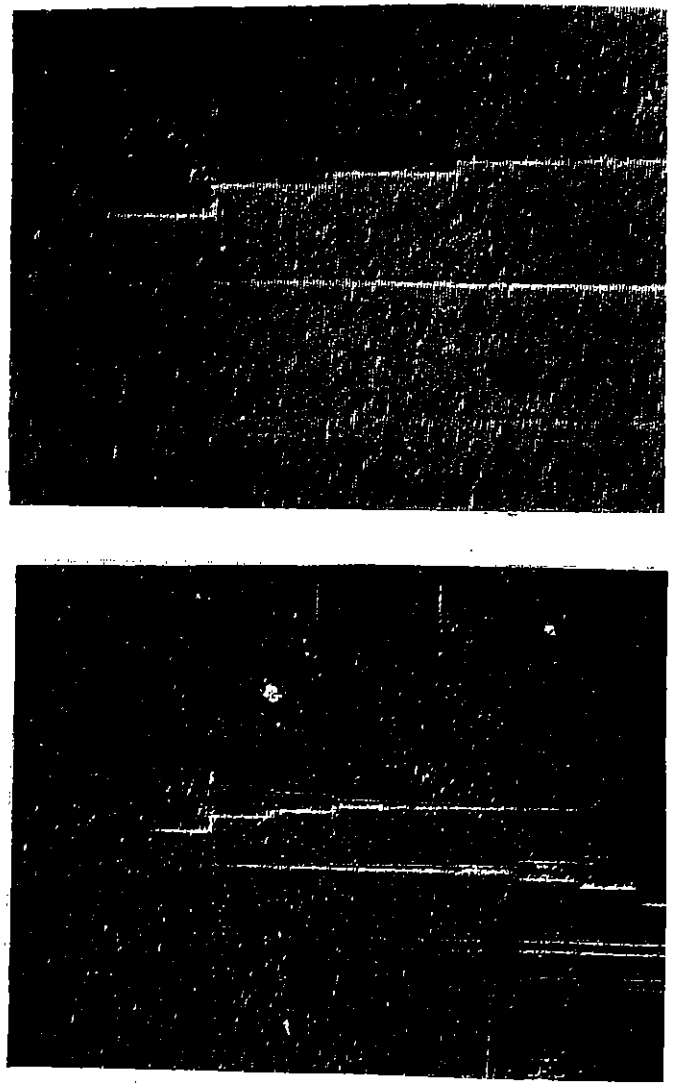

Fig 7 SEM pictures of images produced by set-up shown in Figs 5 and 6. The smallest lines are 1μm wide.

through these factors would not be sufficient to produce an acceptable image to scatter ratio. Investigation showed that the intensity of the light scattered at the prism surface was substantially omnidirectional so that no reduction in the amount reaching the beam splitter by adjusting the prism orientation was possible. Furthermore, scattered light which would normally have missed the photoresist was guided to it by total internal reflection within the beamsplitter cube so that the effective NA for the scatter was greater than that for the signal. Extensive studies were made of the effect of prism surface quality and cleanliness and of alternative geometries (eg 60° prisms) but it was finally concluded that an adequate image to scatter ratio was not obtainable at 249 nm with currently available conjugate reflectivities per unit pump power. Success might be achieved at the longer wavelength using an XeF laser at (351 nm) for which scattering is less.

For the nonlinear optical materials which have been studied thus far for use as active media in the ultraviolet, the high pump intensities required for efficient DFWM will always be a handicap for an potential applicability of phase conjugate image projection to photolithography. Further research on this application should concentrate on the search for more efficient conjugator materials.

1.2 HOLOGRAPHIC IMAGE PROJECTION AT 248 nm.

G M Davis and I N Ross (RAL)

The work reported in this section describes the use of surface relief reflection holograms fabricated on photoresist to produce speckle-free reconstructions of micron-sized mask features recorded directly into photoresist. Other than the information of holographic diffraction gratings[4] to our knowledge these are the first holograms produced by an excimer laser operating at a wavelength of 249 nm, In addition, this work describes the most practical demonstration to date of microcircuit replication from a hologram of a microcircuit.

The basic experimental recording geometry is shown in Figure 8(a). The hologram was formed by the interference between an aberrated image of the mask and a plane reference beam. There are a number of features of this chosen geometry which require comment:

(a) The hologram is located close to the image plane of the mask giving a balance to the need minimising transverse coherence and beam quality requirements during recording and reconstruction, and the need to minimise the effect of hologram surface defects. In addition, for this near image plane geometry the fidelity of the reconstructed wave is relatively insensitive to the bandwidth of the reconstruction wave[5] as well as the optical quality of the medium and substrate.

(b) All beams are specular and care is taken to reduce scatter to a minimum. Reconstructed images should then be near speckle-free.

(c) For reference and object beam with matched path length at the centre of the hologram, the longitudinal coherence length, L, required during recording is given by:

$$L \approx \frac{W}{2} (\sin\theta - \sin\beta) \qquad (1)$$

where W = width of hologram, θ = the angle between the normal to the hologram and reference beam and the β = the angle between the normal to the hologram and the object beam. Both angles are measured from the same side of the hologram normal. For all of our holographic experiments $\theta \leq 50°$, $|\sin\beta| \leq 0.25$ and $W \leq 1.3$cm. Thus the longitudinal coherence length, L, of the laser needed to be more than 0.66cm which corresponds to a bandwidth $\Delta\bar{\nu}$(FWHM)=0.4cm^{-1}. This bandwidth can relatively easily be produced from an excimer laser.

(d) During recording, the interference fringes illuminating the holographic resist plate must remain stationary. However, if the hologram is recorded using a single laser pulse of 9ns (FWHM) duration the effect of the mechanical stability of the mounts and air

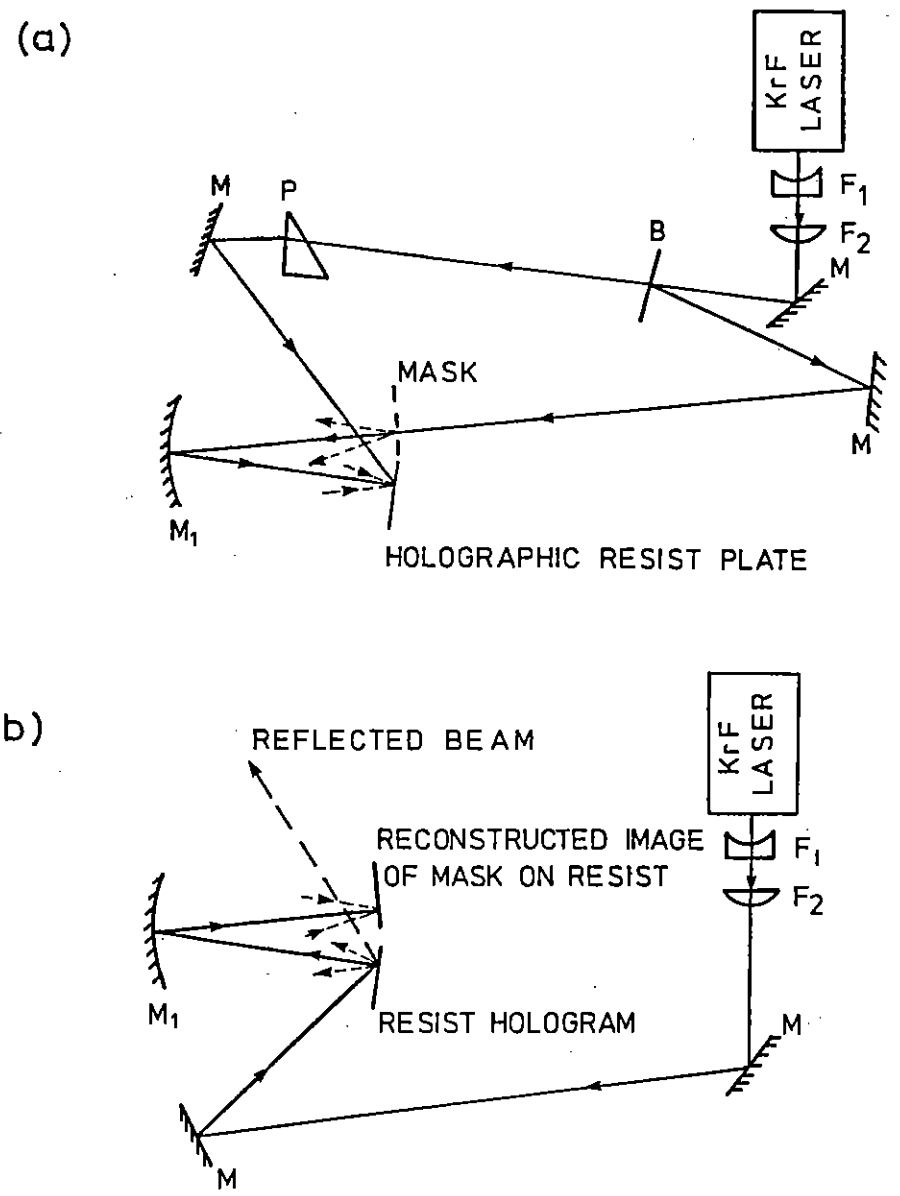

Fig 8 Experimental arrangement used for:
(a) recording the holograms, (b) reconstruction from a reflection hologram. Dielectric turning mirros, M, beam compressing prism, P, beam splitter, B, curved imaging mirror, M_1, of diameter 10cm and radius of curvature 20cm, beam expander consisting of two lenses F_1 = 25cm and F_2 = +50cm.

turbulance can be ignored. To achieve this single pulse exposure while minimising the fluence on the mask during recording and on the hologram during reconstruction, unit magnification was used in the imaging system. This choice of magnification also minimises mirror aberrations on the hologram.

(e) A mirror was used to image the mask onto the hologram since such a system is inexpensive and is achromatic. This latter property reduces the requirements on the bandwidth of the reconstruction wave. For the chosen geometry the 10cm diameter mirror of radius of curvature of 20cm had a numerical aperture NA of 0.25 giving a limit of resolution, ∇, for this coherent illumination system of

$$\nabla = 0.77\lambda/NA \qquad (2)$$
$$= 0.8\mu m$$

at a wavelength a 248nm. In addition the recording geometry resembles the imaging optics of some current commercial VLSI projection printers.

(f) These experiments used an 850Å thick chromimum-on-quartz mask which contained feature sizes as small as 1µm.

The 1Hz KrF excimer laser used for these experiments was a line-narrowed oscillator, single-pass amplifier system. This laser provided a fluence of about 60mJ/cm² at a wavelength of 248nm over the central 0.17cm² of the collimated output beam. This beam had a divergence of 47µrads and an elliptical cross-section with major and minor axes of 1.1cm and 0.4cm respectively. By replacing the line-narrowing optics of the oscillator with a plane mirror the linewidth of $0.3cm^{-1}$ could be increased to $50cm^{-1}$ without affecting the beam quality. The oscillator output was plane-polarised and using a half-wave plate positioned between the oscillator and the amplifier, the electric field vector of the amplifier output was rotated perpendicular to the plane of incidence at the mask.

A x2 beam expander was used to improve the beam uniformity over the central area of the hologram. The mask and holographic plate were placed approximately normal to the optic axis of the incident object beam. The distance of the holographic plate from the imaging mirror was adjusted for the best overall focus of the mask image on the plate. Prism P in Fig 8(a) compressed the beam laterally until its width was equal to that of the object beam on the hologram. When the mask was absent form the experimental arrangement, the object to reference wave fluence ratio was 1:3 at the hologram plane. For a fixed average exposing fluence, this ratio was a compromise between achieving sufficient resist depth modulation for a high diffraction efficiency while simultaneously exposing all regions of the hologram sufficiently to achieve material linearity.

By choosing the angle θ between the reference beam and the normal to the hologram to be 50°, the unwanted first order reflection from the hologram was eliminated. Thus, the hologram efficiently diffracted energy into the required real image. Negligible energy was diffracted into higher orders. In addition, for θ=50°, the planes of interference of the two beams are at a substantial angle to the recording plane so that the processed hologram may have exhibited blazing which would further increase the efficiency of image reconstruction[6].

The holograms were recorded on positive photoresist. There were several reasons for this choice of photosensitive medium:

(a) Positive photoresist is capable of recording the high spatial frequencies of several thousand cycles/mm which are typical of our holographic recordings[7].

(b) Unlike commercial fine grain emulsions, where the dimensions of the developed silver grains can range from about 0.2µm to several microns, the positive photoresist remaining after development is virtually identical to its unprocessed form and hence is non-granular. Therefore, the speckle, so prominent in reconstructions from photographic holograms should be negligible when positive photoresist is used as the recording medium.

(c) Thin layers of positive photoresist are highly stable materials and show little dimensional change after exposure and processing[8].

The holographic fringe pattern illuminates the photoresist which has been coated onto a suitable substrate. The solubility of resist in developer depends on exposure so the variations in intensity of the fringes become variations in resist thickness. Therefore the resulting hologram is primarily a surface relief phase hologram, although when used in transmission there is also a contribution from absorption variations due to the thickness variations.

The choice of photoresist for recording the hologram was determined by the requirements that the resist be sufficiently sensitive at the laser wavelength to allow single-pulse recording, and that it should have an absorption depth large enough to ensure reasonably uniform exposure to the depth of the surface modulation of the hologram. Of the photoresists readily available Shipley AZ2400 seemed the most suitable since at the KrF excimer laser wavelength of 248nm it has an absorption depth of 0.31±0.03μm[9]. In addition, Jain et al[10] have already successfully employed this resist for conventional lithography using a KrF excimer laser as the exposing light source.

The hologram efficiencies were measured using a photodiode and an oscilloscope to record the incident power, I, and the power, S, diffracted into the image. Although the experiments were not exhaustive, our results indicated that in general greater efficiency (S/I) was achieved for holograms recorded at higher fluences. However, the damage threshold of AZ2400 resist when exposed to high pulsed fluences of 9ns duration from the KrF excimer laser limits the maximum exposure fluence to about 5mJ/cm². Thus, in order to achieve the highest hologram diffraction efficiency using single-pulse recording, it was necessary to use recording beam fluences which were as close as possible to the resist damage threshold.

Transmission holograms on quartz substrates and reflection holograms on glass or quartz substrates were recorded on Shipley AZ2400 resist using single laser pulses. The development conditions were varied to produce holograms which had the optimum surface quality and diffraction efficiency for the given exposure of about 5mJ/cm². Development for 30 seconds in a 4:1 water to Shipley AZ2401 developer solution provided the best results. Even so, these holograms produced diffraction efficiencies of less than 2%, images which were unacceptably degraded by scatter noise, and reconstruction exposure times which were sufficiently long to cause image blurring due to mechanical instabilities.

To achieve higher diffraction efficiencies, of about 10%, the holograms were coated with a nominal 600Å thick layer of aluminium by thermal evaporation. An additional advantage of coating the holograms with aluminium was that the damage threshold of the holograms was increased from the 5mJ/cm² resist damage threshold to more than 20mJ/cm². Thus higher fluences could be used during reconstruction to further shorten the exposure time of the image. For the same reason AZ2400, the most sensitive resist available to us, was used to record the reconstructed images even though the absorption depth of 0.31±0.03μm of this resist is probably too small to easily achieve vertical wall profiles in the 1μm thick layer of resist[9].

As mentioned above, reconstructions from uncoated photoresist holograms suffered from background speckle noise. Since there was no source of grain scatter in this experiment the main source of speckle was assumed to be dust on the optics. Thus to minimise speckle in the holographic images, where possible the optical components were cleaned and removed as far away as practicable from the hologram, both during recording and reconstruction.

Having made these improvements several holograms were recorded, developed and aluminised. In the plane of the hologram the reconstruction beam had a fluence of 14mJ/cm². To fully expose a 1μm thick layer of resist to the smallest image features required about 60 laser pulses for 1 minute development in a 4:1 water to Shipley 2401 developer solution. Figures 9 and 10 are scanning electron micrographs of these smallest features and show little evidence of speckle.

The mechanical stability of the experimental arrangement was limited to a few microns and since no interferometric technique was used to reposition the hologram after development the best image fidelity was sought by 'trial and error' focusing. The hologram was moved along a line normal to the hologram in steps of a few microns, and the holographic image recorded at each new setting. As shown in Figure 11, translation of the hologram by about 5μm produced a noticeable deterioration in the image fidelity. This observation is in agreement with the depth of focus, δ, as calculated from the numerical aperture, NA, of the imaging system, where

$$\delta=\lambda/(NA^2) \qquad (3)$$
$$=4\mu m.$$

Since perfect relocation was not possible by this method even the best images obtained (Figures 9 and 10) show features not present in the mask and which may be due to positioning errors of the developed hologram and the resist plate.

Exchanging the line-narrowing optics on the laser oscillator for a plane 100% mirror produced a broad bandwidth (50cm^{-1}) laser output

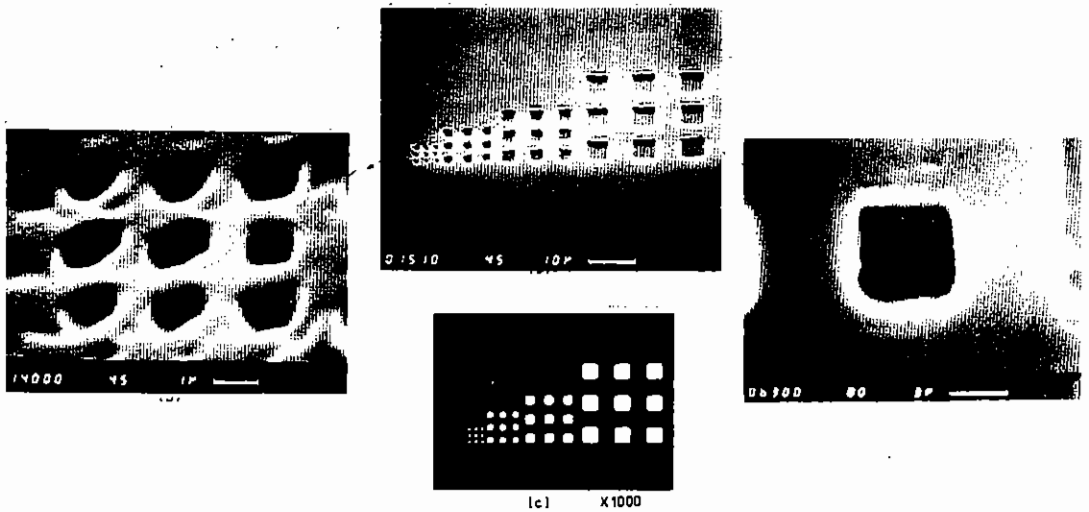

Fig 9 (a), (b) and (d) are scanning electron micrographs of the smallest square features present in the mask reconstruction. The exposure dose of about 180mJ/cm² was delivered in 60 laser pulses. The images were recorded on a 1μm thick layer of AZ2400 resist spun on a glass substrate. Development was for 1 minute in a 4:1 water to Shipley 2401 developer solution. (c) An optical transmission micrograph of the corresponding area of the mask.

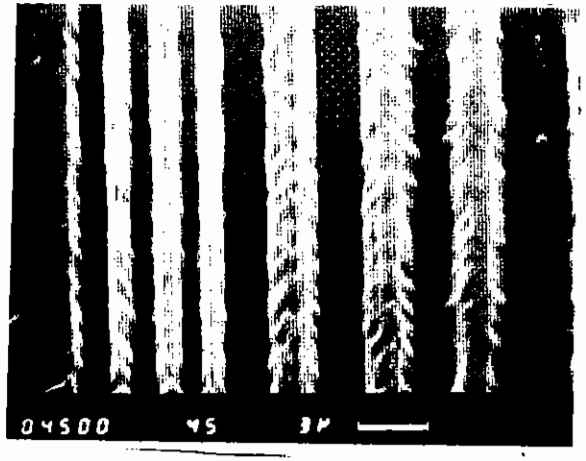

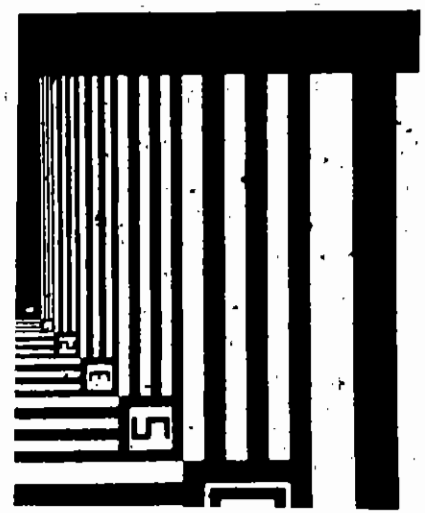

X400 (b)

Fig 10 (a) Scanning electron micrographs of the smallest lines and spaces present in the mask reconstruction. The exposure dose of about 180mJ/cm², was delivered in 60 laser pulses. The images were recorded on a 1μm thick layer of AZ2400 resist spun on a glass substrate. Development was for 1 minute in a 4:1 water to Shipley 2401 developer solution. (b) An optical microscope transmission photograph of the same area of the mask. The numbers refer to the nominal widths of the lines in microns.

without affecting the spatial beam quality. Using the 'trial and error' focussing technique described above it was demonstrated that increasing the linewidth from 0.3cm^{-1} to 50 cm^{-1} blurred the holographic image by less than 1μm (Figure 12).

In conclusion this series of experiments has successfully demonstrated that using a KrF excimer laser, a simple projection geometry and an aluminised photoresist hologram, speckle-free images of micron-sized features can be recorded in photoresist.

Preliminary experiments using a proximity holographic system and a KrF excimer laser were also undertaken. The details of this system are described in the following section. Figure 13 shows scanning electron micrographs of the smallest features in a reconstruction of the mask from one of these proximity holograms. Although the 1μm features are clearly visible, the images are severely degraded by speckle noise due to significant scatter from nearby surfaces.

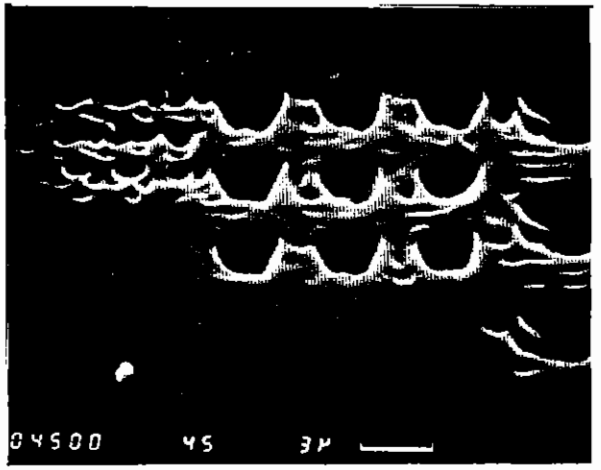

(a)

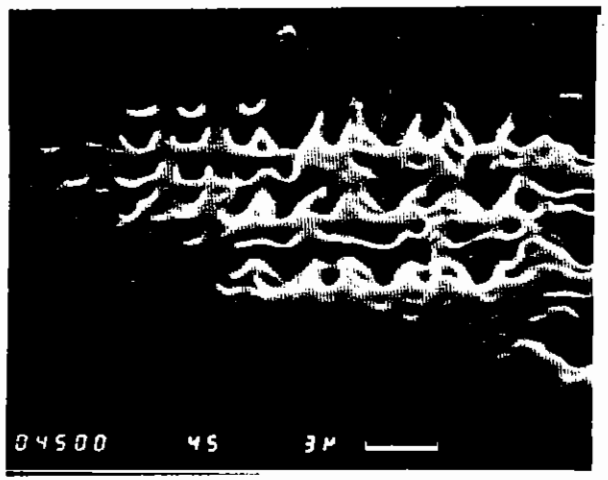

(b)

Fig 11 (b) Scanning electron microscope of the image produced when the hologram position was translated by 5μm from the position used to obtain the image shown in (a).

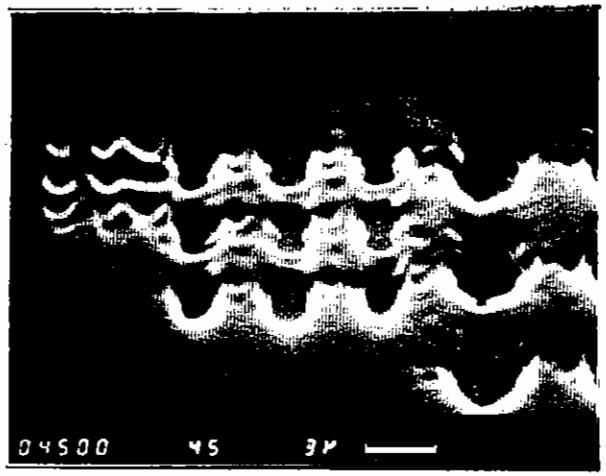

(a)

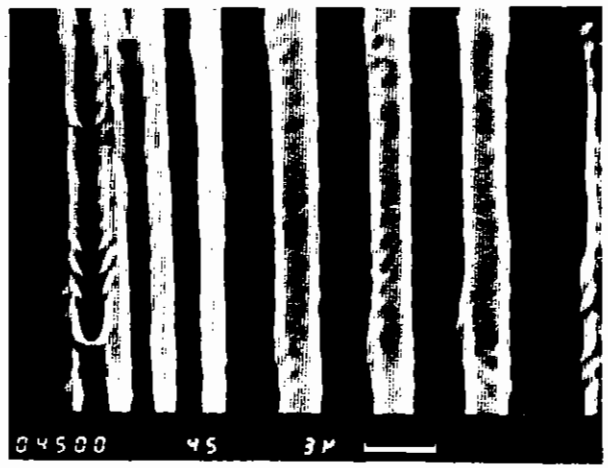

(b)

Fig 12 (a) and (b) are scanning electron micrographs of the image produced by illuminating the hologram with a broad-band ($50cm^{-1}$) KrF excimer laser.

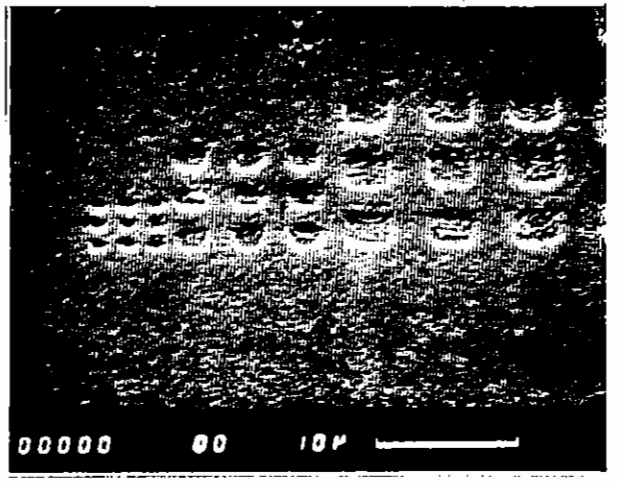

(a)

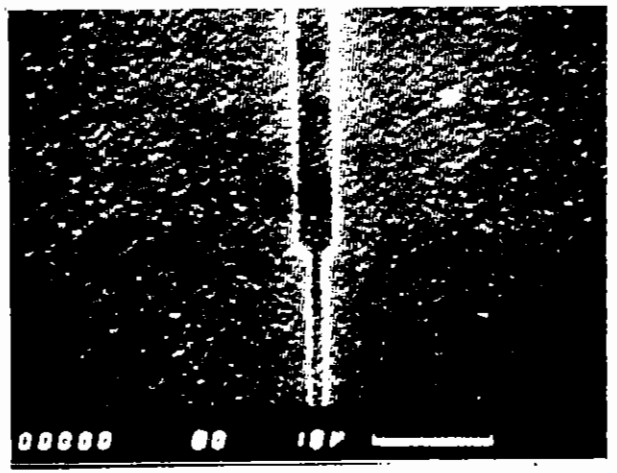

(b)

Fig 13 Scanning electron micrographs of reconstructions from a proximity hologram. Shipley AZ2400 resist was used to record both the holograms and the reconstruction of the mask.

1.3 HOLOGRAPHIC IMAGE PROJECTION AT 458 nm

D Klemitz and I N Ross (RAL)

Holography is a two stage or time lapsed imaging process, the work here is looking at the possibility of employing this unconventional technique in microcircuit lithography. During recording of the hologram and subsequent reconstruction of its image, our chosen scheme involves three significant light waves being present. The reference wave is made to reflect internally giving two components while the subject wave creates a third; Fig 14 (a) and (b).

Fig 15 shows the optics used in the hologram recording mode. The light source is a c.w. argon ion laser at 458 nm (visible) operating in the single transverse mode T.E.M_{00}. The prism arrangement amplitude divides the incident beam forming the subject and reference beam arms directed by mirrors M_1 and M_2 respectively. Both path lengths are matched through the optics to within the coherence length of the laser light (0.2 $cm^{-1} \equiv \Delta \upsilon$ = 6GHz). Internal reflection of the reference wave allows the subject - here a resolution test mask - to be brought in close proximity to the recording plane. This small distance between the two planes relaxes the normally stringent requirements for positioning the hologram for faithful image reconstruction.

AZ 1350 photo-resist (0.3 μm deep) on a glass plate serves as a material for recording the hologram. The resist is exposed to the laser light through the transparent features of the resolution mask in the subject beam. Subsequent development of the resist realises the optical interference effects of the subject and reference beams in the surface relief of the remaining resist. During reconstruction in the presence of the reverse direction or phase conjugate of the reference wave, the surface relief of the acts as a resist diffraction grating to create the conjugate of the original wave and subject hence reconstruct the transparent and opaque features of the resolution mask.

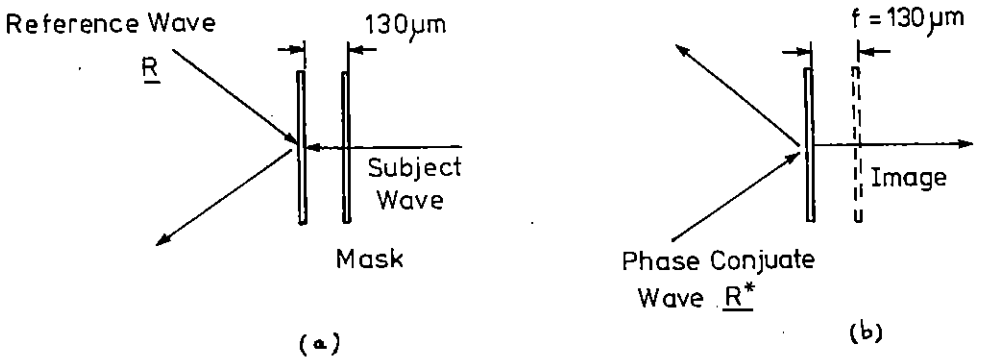

Fig 14 (a) Recording of the hologram of a resolution test mask. The reference wave is totally internally reflected,
(b) Reconstructing the resolution test mask image with R^*.

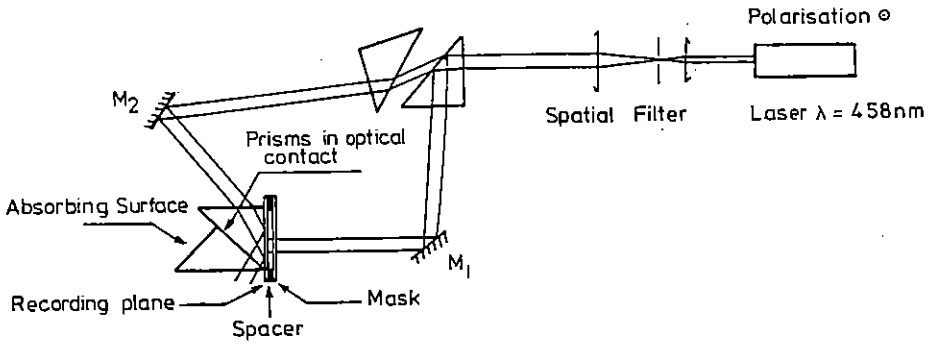

Fig 15 Optics for recording the proximity hologram.

To record these features from the reconstructed image a similar glass plate spin coated with photo-resist is placed in the image plane (Fig 14(b)) and exposed. The image distance of the reconstruction is fixed during the recording stage by a spacer (in this case 130 μm) separating the recording plane and resolution test mask. It should be emphasised here that the physical nearness of the test mask and recording plane does not constitute a contact print. Observation of the hologram after development under white light shows a colour spectrum indicative of its diffractive nature. Further, reconstruction as in Fig 14(b) shows the image to appear as expected 130μm away from the plane of the hologram.

Fig 16 is the image generated from the hologram. These holographic images are 'lensless' and are derived during reconstruction from the phase conjugate wave only. As such the image suffers from none of the associated Seidel aberrations when imaging with spherical lenses and mirrors. One problem, however, is the amount of background scatter giving rise to 'speckle' inherent with coherent imaging. Light from the laser also causes specular reflections within the prisms in optical contact. These were eliminated by the absorbing surface shown (Fig 15) preventing these reflections from degrading the image.

Scattered light is also caused by the microscope objective used in photographing Fig 16 (x40 NA = 0.65). The multiple reflections scattered within the objective lens are superimposed on the image to give a worst case figure of signal to noise ratio in the image of -15dB or 32:1. The scanning electron micrograph (S.E.M.) shown in Fig 17 is obtained by exposing the features of the reconstructed image (Fig 16) to AZ photo-resist placed in the image plane of the hologram. Subsequently developed, the resist is etched in the exposed regions leaving the required delineations as shown.

With simple optics and a laser source we have shown better than 1 μm resolution from an image generated via a hologram. Resolution is dependent upon wavelength and numerical aperture and in our case the limit fixed by diffraction is ≈ 0.23μm. The image delineations shown on the S.E.M. show edge imperfections of only ≈ 0.1μm and result from residual scatter which gives rise to a low level of background speckle on the image.

Since AZ 1350 photo-resist has limited useful absorption at 458nm, an energy of 150 mJ cm^{-2} was the required exposure to achieve the etch shown in Fig 17. Further work using a Helium Cadmium laser source emitting at 351 nm could reduce this exposure level.

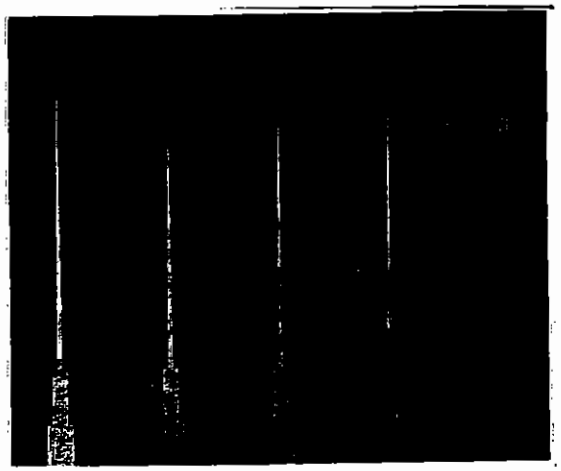

Fig 16 The reconstructed holographic image produced by the proximity hologram.

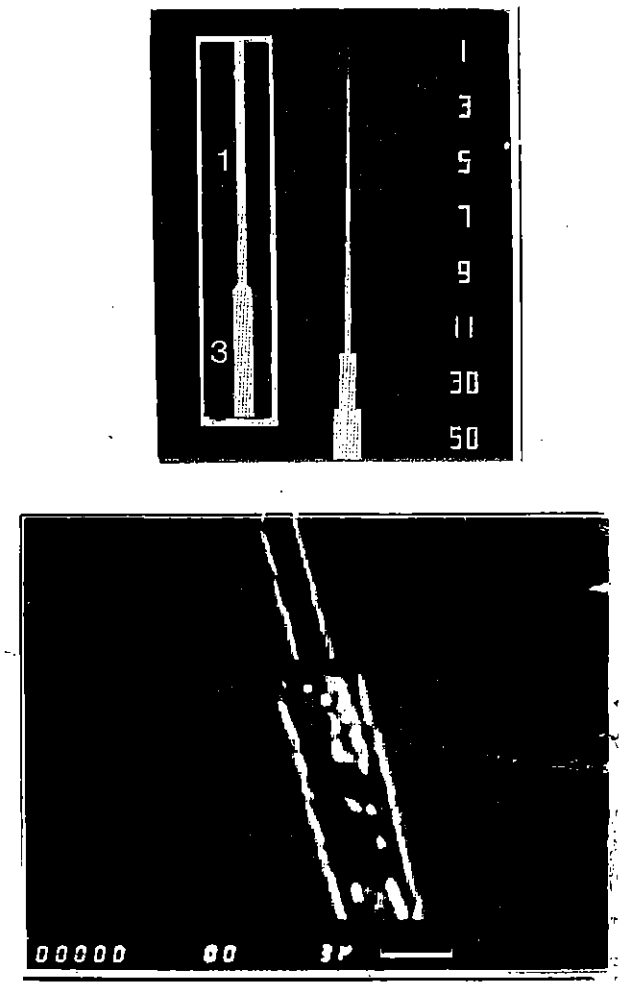

Fig 17 Micron features etched in photo-resist produced by the proximity hologram.

1.4 MECHANISMS FOR INTERNALLY SELF-PUMPED PHASE CONJUGATE EMISSION FROM $BaTiO_3$ CRYSTALS

M C Gower (RAL) and P Hribek (Technical University of Prague)

Since the first discovery of self-pumped phase conjugate mirrors (SPPCM's) created by internal reflections in crystals of $BaTiO_3$[1], there has been much interest in trying to understand the mechanisms responsible for the process. The simplicity and ease of obtaining efficient self-pumped phase conjugate reflections (SPPCR's) of low power continuous wave (CW) lasers using this photorefractive material is contrasted by the great difficulty in understanding how it works. Much of this difficulty arises because both the length and direction of the beams within the crystal are governed by beam fanning and coupling effects which optimise themselves and leave the experimenter with little external control. This frustration would be greatly reduced if many crystals of different dimensions but identical in all other respects were available for study. At present this is not the case. Thus of the few experimental and theoretical studies which have addressed the problem of understanding the mechanism responsible for SPPCE, there is little agreement between them. Although degenerate four-wave mixing in coupled interaction regions[11,12], in ring cavities[13] and stimulated photorefractive scattering[14,15] have been suggested as possible mechanisms, great difficulty arises when trying to explain all of the observed beam paths within the crystal and phenomena such as the frequency shifts[16,17], oscillations and pulsations[18,19] of the phase conjugate wave. Despite the great interest in using and observing SPPCE in $BaTiO_3$, progress on its understanding has advanced little since its first observation by Feinberg five years ago. In this section we report precise measurements of some of the processes which help to clarify some of the mechanisms involved.

Two poled single domain $BaTiO_3$ crystals of dimensions 7x7x7 and 6x4x5 mm having measured absorption coefficients at 488 nm of

1.8 cm^{-1} and 4.2 cm^{-1} respectively were used for this study. Both apertured and expanded extraordinary polarised beams from a multi-longitudinal mode 488 nm CW Ar^{+} laser were used to study the response of the SPPCE. A Michelson interferometric arrangement with the SPPCM as the mirror in one arm is used to monitor any spatial or temporal frequency shifts of the SPPCE relative to the pump beam.

Small beam measurements

(a) Stable emission $2.3 < x < 3.2$ mm

In Fig 18 we show photographs of the familiar beam focussing, bending and total internal corner reflections which occur inside the 7 mm cube crystal and are characteristic of the self-pumping process. By carefully studying many enlarged photographs of this crystal as a small 0.4 mm diameter beam is scanned horizontally across the front face, we have drawn a scaled diagram in Fig 19 of the paths of the most intense beams observed. Consider the behaviour as the input beam is moved from right to left in Figs 18 and 19. The SPPCE begins $\sim$ 2.5 mm from the right face of the crystal. In the steady state the fringes were spatially uniform and stationary in this region indicating stability and no grating movement within the crystal. A drop of index matching oil placed sequentially in each corner of the crystal destroyed the SPPCE only when placed on the top right hand corner. As shown in Figs 18 and 19, two intense parallel beams separated by 0.16 mm were observed to propagate towards adjacent faces of the top right hand corner at an angle of incidence θ_1 to the top face almost exactly equal to the critical angle of $BaTiO_3$, $\theta_c \sim 25°$. Both parallel beams had similar intensities. Since the maximum value of the two-beam coupling parameter

$$\gamma = \frac{\omega}{2nc}\,\frac{r_{eff}E}{\cos(\theta/2)} \qquad (1)$$

occurs at $\theta \sim 25°$ when the crystal is illuminated at near normal incidence[11], the optimum bending angle of the beam into the corner occurs for $\theta \sim \theta_c$ for which case $\gamma \sim 0.65\ mm^{-1}$. In Eq (1) E, r_{eff}, n and ω refer to the light induced space charge field amplitude, the effective electro-optic coefficient, the light frequency and background refractive index respectively

of $BaTiO_3$ and are defined further in Ref(11). Geometric considerations of the diagram in Fig 19 shows that the length of the loop of light which is reflected in the corner is given by:

$$\ell_1 = \frac{2x_1}{\sin\theta_1} = \frac{L - h}{\cos\theta_1} + \frac{d_1}{\sin\theta_1} \qquad (2)$$

for light incident normal to the entry face. Thus for a given x_1, ℓ_1 is a maximum if simultaneously θ_1 is as small and d_1 is as large as possible. If light is to stay within the crystal by total internal reflection, the smallest value which θ_1 can have is θ_c. The requirement that $h \geq 0$ in Fig 19 means that light can only couple into this critical angle loop when

$$x_1 \leq \frac{L\tan\theta_c + d_1}{2} \qquad (3)$$

Hence the maximum value of x_1, x_1^{max}, for which the critical angle loop can still form occurs when d_1 is maximised to be $\sim x_1$. Hence

$$x_1^{max} \sim L \tan\theta_c \sim 3 \text{ mm for our 7 mm cube crystal}$$

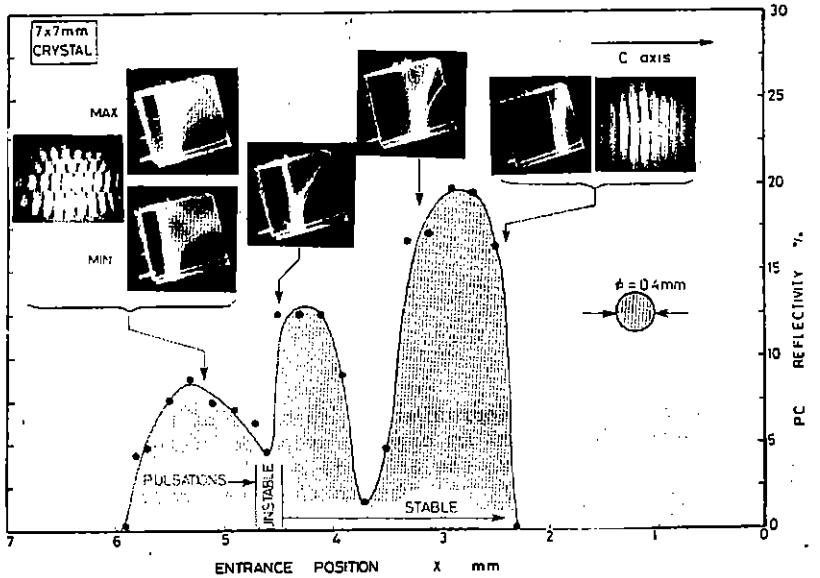

Fig 18 SPPCR versus horizontal entrance positions of a 0.4 mm diameter beam on the 7x7 mm cube crystal. The angle of incidence of the pump beam to the entrance face = 8° and the laser power was 0.9 mW $\sim 6P_{th}$. Photographs of the beam paths within the crystal are shown at the entry position indicated. The spatially resolved interference fringes produced between the SPPCE and the pump beam are also shown for the extreme positions at each side of the crystal.

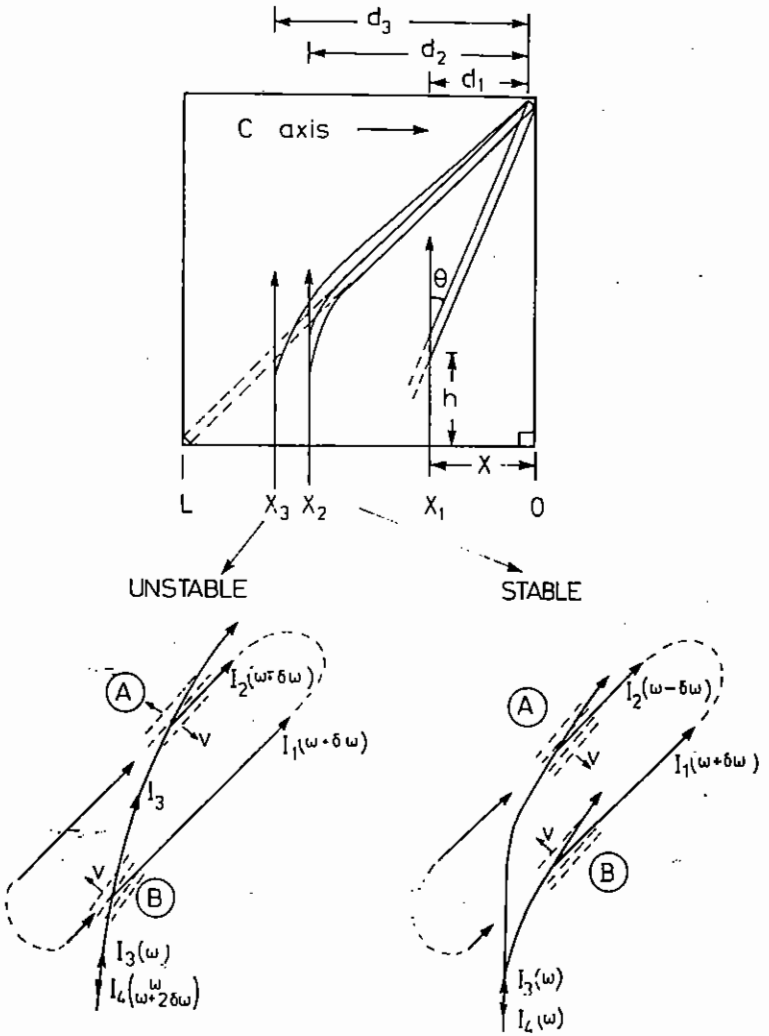

Fig 19 A sketch drawn approximately to scale of the strongest beam paths observed in the 7x7 mm crystal at three different entry positions x_1, x_2, x_3. At x_1 and x_2 the SPPCE is stable and spatially uniform without a frequency shift relative to the pump frequency. At x_3 the emission is unstable and shows pulsation characteristics Also shown are sketches at positions x_2 and x_3 of the observed beam paths as they couple into the ring of light which propagates between diagonal corners.

Since we see exactly this behaviour in Figs 18 and 19, ie that a critical angle loop of minimum area is created in the region $2.3 < x_1 < 3.2$ mm, we conclude that in this region of the crystal the process causing SPPCE arranges its path so as to maximise its length into and out of the corner. With the beam at this input position, feedback by coupling to form ring cavities between corners other than the top right was never observed. For the power and beam diameter shown in Fig 18, the minimum length of the loop which still produced SPPCE was $\ell_{min} \sim 1$ cm and corresponded to the input beam position $x_1 \sim 2.3$ mm. For this case the minimum coupling strength around the ring, $\gamma\ell_{min} \sim 6.5$. This value should be compared with calculations of the threshold coupling strengths of 2.34, 1.24 and 0.5 for the self-pumped two interaction region model[11,12], the external ring and semi-linear cavities[20], respectively.

Four-wave mixing in coupled interaction regions alone does not self-maximise the path length of light around the loop[11,12]. On the other hand, stimulated photorefractive scattering of a single beam by itself leads to a decreasingly intense beam as the backscattered light depletes the pump, and does not self-optimise by producing minimum area loops of light[14]. Maximisation of the loop length so that each side of the loop had similar intensities would be consistent with a four-wave mixing mechanism occurring within the loop itself rather than at the coupling regions which intersect the pump beam. To achieve high gains, the four-wave mixing around the loop may possibly be enhanced by stimulated photorefractive scattering in a manner analogous to Brillouin enhanced four-wave mixing in liquids for which high gains have been observed[21].

(b) Stable emission $3.1 \leq x < 5.0$ mm

When the incident beam is moved further to the left to $x_2 \geq 3.1$ mm the geometry of the crystal no longer allows coupling into a critical

angle maximum path length loop. However, as shown in Fig 18 stable SPPCE without frequency shifts was also observed in this region. The (undepleted) pump is now able to efficiently two-beam couple into a ring cavity formed between diagonal corners of the crystal[13]. Confirmation that this diagonal ring cavity provides feedback for the process was obtained by placing a drop of oil on either the top right or bottom left hand corner of the crystal and observing that in both cases no SPPCE occurred.

For the diagonal ring in the cube crystal shown in Fig 19, $\theta_2 = 45°$ and the path length around the whole ring is fixed at $2\sqrt{2}L$ while that around the loop to the right of the pump beam is

$$\ell_2 = 2\sqrt{2}x_2 = \sqrt{2}(L+d_2-h) \qquad (4)$$

We observe that after turning on the beam, in the steady-state the most intense beams maximise ℓ_2 by maximising d_2 to form rings containing minimum area. Presumably as in position x_1 this behaviour enhances the four-wave mixing processes which occur around the ring.

The value of γ that describes the strength of the coupling into the top right hand corner is reduced to $\sim 0.5\ mm^{-1}$ when θ is increased to 45°[11]. However this smaller value of γ is clearly compensated for by the extra feedback provided by light which propagates around the ring. The requirement that $h \geq 0$ means that for coupling into the diagonal loop we must have

$$x_2 \lesssim \frac{L+d_2}{2} \qquad (5)$$

which as $x_2 \to L$ implies $d_2 \to x_2$. Hence in agreement with our observations as x_2 becomes larger then rings of smaller area are created. On the right hand side of the crystal when $x \lesssim 3$ mm, since $\theta_c < 45°$, h is smaller for and light can be more efficiently coupled into the critical angle loop. Thus in this region the pump becomes depleted before it can reach and couple into the diagonal ring. The maximum value of x_2 for coupling into the diagonal ring is given by

$$x_2^{max} = (L-h) \qquad (6)$$

For several crystals we have found empirically that the minimum beam bending radius for turning into the corner is such that $h_{min} \sim 2$ mm. Thus when $x_2 \lesssim 5$ mm light is less efficiently coupled into the ring because the beam radius of the fanned light is too large to do so. As sketched at the bottom right hand side of Fig 19, we found that the beam entering the crystal in this region tended to split into two or more beams before coupling into both sides of the ring. This allowed for independent bidirectional coupling of energy by two and four-wave processes into and out of the ring. Light can then be fed into the ring by two beam coupling with scattered light, amplified and then extracted by four-wave mixing in the interaction regions A and B in Fig 19. Since a frequency shifted writing beam of a few hertz optimises the (frequency shifted) phase conjugate emission produced in photorefractive media by four-wave mixing[22], and since similar frequency shifts are produced to enable the phase to reproduce after a transit around the ring[13], the most likely configuration which leads to optimised stable SPPCE in this region is shown in Fig 19. Counterpropagating beams $I_1(\omega + \delta\omega)$ and $I_2(\omega - \delta\omega)$ of equal and opposite frequency shift $\delta\omega$ are set up in a bidirectional ring to act as pump waves for the probe wave $I_3(\omega)$ which produces an unshifted phase conjugate wave $I_4(\omega)$ by four-wave mixing. Since efficient extraction of energy from the ring leaves little energy circulating to the left of the pump beam, the phase conjugate waves produced from the different regions, A and B combine independently of each other to form a single stable unshifted phase conjugate beam $I_4(\omega)$.

A pair of additional parallel beams which arose by total internal reflection in the lower right hand corner of the crystal and which couple energy out of the diagonal ring were destroyed by placing a drop of oil on this corner with the result that the SPPCR in the region $x_2 \sim 3.7$ mm increased by 30% from that shown in Fig 18. These interfering beams could be eliminated entirely and the reflectivity greatly increased in this crystal by increasing the angle of incidence of the pump beam to greater than 16°. After taking into account the Fresnel reflection losses of the light entering and exiting the crystal when the angle of incidence was increased to 28° we found that the crystal produced a SPPCR ∿ 45%. Power measurements around the rest of the crystal showed that in the steady state only 1.4% of the pump power was lost from the crystal as a non-phase conjugate beam. Thus the remaining 53% of the pump power is dissipated within this crystal.

(c) Frequency shifts and instabilities $4.5 \leq x < 6.0$ mm

Increasing x above 4.5 mm produced instabilities and pulsations of the SPPCE. The frequency of the pulsations was roughly linearly dependent on the incident laser intensity[18,19]. The photographs on the left of Fig 18 show the beams in the crystal at the peak and dark periods of the PC pulsations. Also shown in this figure are the spatial frequency shifts which were simultaneously observed to occur across the PC beam. Such spatial shifts in the vertical direction were accompanied by horizontal fringe movement corresponding to frequency shifts of a few hertz. The fringes were found to move in both the same and in opposite directions to each other across the beam. The fringes moved slowly at the beginning of each pulsation and reached their maximum velocity at the peak just as the emission was extinguished. As shown in the left hand sketch at the bottom of Fig 19, in the position x_3 only a single pump beam was found to couple into both sides of the ring - presumably because unlike in position x_2 the dimension of the crystal allowed insufficient space ($h_3 \sim 2$ mm) for the pump beam to split into two before coupling into each side of the ring. As shown in Fig 19 in this case the counterpropagating beams I_1 and I_2 may have frequency shifts of the same or opposite signs to produce either an unshifted $I_4(\omega)$ or a frequency shifted beam $I_4(\omega+2\delta\omega)$ respectively. However, because the two interaction regions into and out of the ring are now additionally coupled together by the same (single) pump beam $I_3(\omega)$, the SPPCE now becomes unstable.

Unlike the situation at x_2, the contribution to I_4 which arises from region A can now mix with beams I_1 and I_2 in region B to produce an additional contribution to $I_3(\omega)$ which arrives at region A and can in turn produce an additional component to I_4 in region B (and so on). The gratings for coupling into and out of the ring at B must adjust themselves accordingly. If the PCR's, from regions A and B are not perfect then new gratings must continue to be formed in these regions. Beams I_3 and I_4 become partially trapped between the two interaction regions. This explanation for the instability observed at the position x_3 is supported by the observation that at the peak of each pulsation a beam which bent into the top right hand corner was produced from a position beyond the diagonal ring such that $\theta \sim 58°$ (see the photograph and sketch in Figs 18 and 19 respectively). We believe that this beam is the contribution to I_3 which arrives at A and which has undergone at least two imperfect phase conjugation processes from A to B and back again. Its imperfect match to the original wave I_3 arriving at A causes it to be transmitted through region A and subsequently bent round into the top right hand corner. Broadly speaking the more efficient the production of a phase conjugate beam from A then the more efficient the destruction of the gratings coupling into and out of the ring at B. New gratings are created at a rate determined by the photoconductivity of the crystal. Thus the period of the pulsations will be approximately inversely proportional to the laser intensity[18,19]. This type of unstable behaviour would then explain our observation that gratings move most rapidly at the maximum and during the decay period of each pulsation. The spatial phase shifts in the vertical direction shown in the photograph in Fig 18 are presumably created by geometric inhomogeneities of the crystal (imperfect corners, etc), which allow for the counterpropagating waves in the ring to have frequency shifts of the same sign in some vertical regions and opposite signs in other regions.

The spatially resolved near threshold SPPCR measurements shown in Fig 20 for the 6x4 mm crystal are qualitatively similar to those shown in Fig 18 for the 7x7 mm crystal. However the SPPCR was less and the near threshold power for self-pumping occurs over a more restricted region of the crystal. We also show in Fig 20 the buildup and temporal characteristics of the SPPCE. Most of the behaviour can be explained by the observations and arguments presented above for the 7x7 mm crystal. An additional region that gave a reflection with an oscillatory amplitude on the right hand side of the crystal was observed. These sinusoidal oscillations may arise from beating between SPCCE's which arise by different mechanisms within the crystal.

Full aperture illumination

In Fig 21 we show the crystal and fringes when the whole entrance face was illuminated at a power several times that required for self-pumping. Both the critical angle loop and the diagonal ring regions are clearly evident in the 7 mm crystal shown in Fig 21(a) for $x_1 \leq 3$ mm and 3 mm $< x_2 <$ L respectively. Fig 21(b) shows that when the entrance face to the crystal is fully illuminated the SPPCE which arises from these two regions are phase-locked together. In the steady state these fringes were found to be both stable and stationary, without any frequency shift. However, as shown in Fig 21(c) if a small $\lesssim$ 200 μm wide slit of light was allowed to spill over from the front face and illuminate the left hand face around the left hand corner, a new phase conjugate beam appeared from this region. The phase of this additional reflection was unrelated to that of the SPPCE from the front face. Since this new emission disappeared when the front face was not illuminated we conclude that it arose from four-wave mixing between beams entering the front face and the light refracted into and across the crystal via the left hand side face. If light was allowed to spill over to cover all of the left hand face then all SPPCE from the front and side faces was extinguished. When a 1 mm diameter hole was made in the screen which stopped light from falling on the left face, SPPCE occurred through the hole and a dark 1 mm wide strip at the same height as the hole appeared on the SPPCE across the entire front face. Clearly light which enters the left face can greatly affect the full aperture

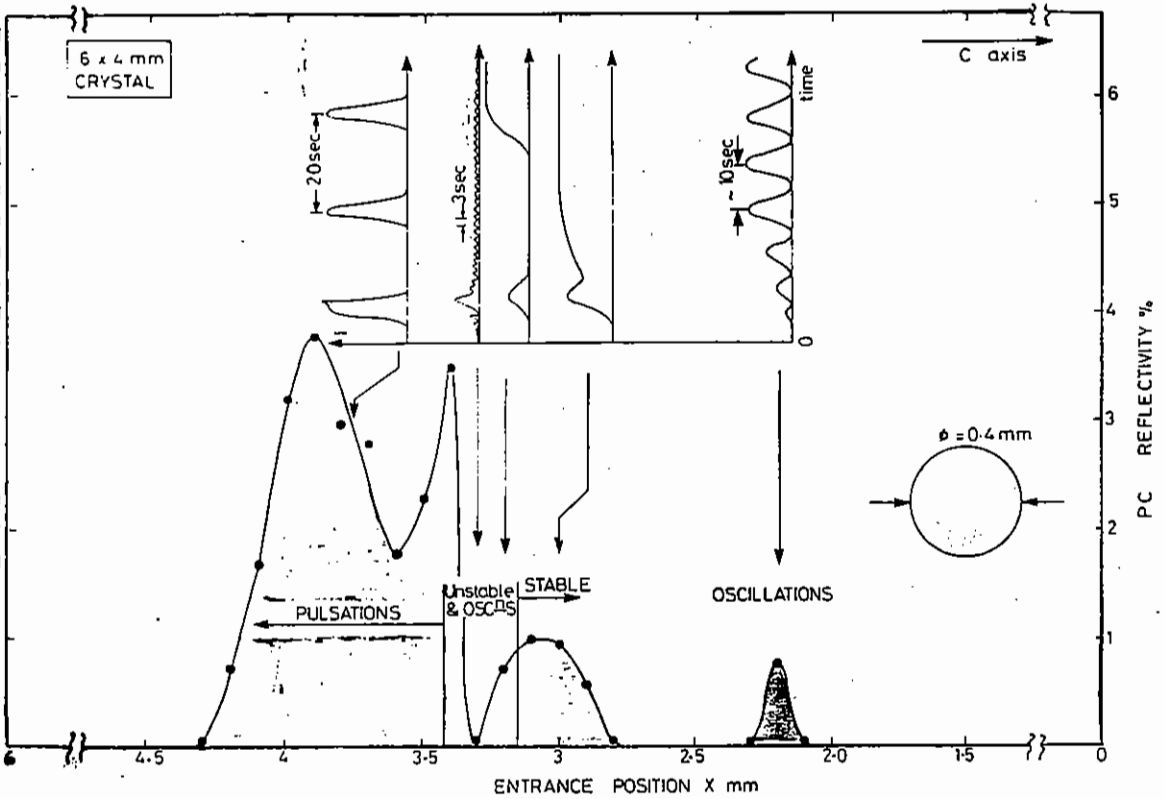

Fig 20 SPPCR versus horizontal entrance position of a 0.4 mm diameter beam on the 6x4 mm crystal. The angle of incidence was 16° and the laser power was 3.6 mW ∿ 1.4P_{th}. The temporal behaviour of the SPPCE is shown for different entry positions of the pump beam following the initial illumination of the crystal at t = 0.

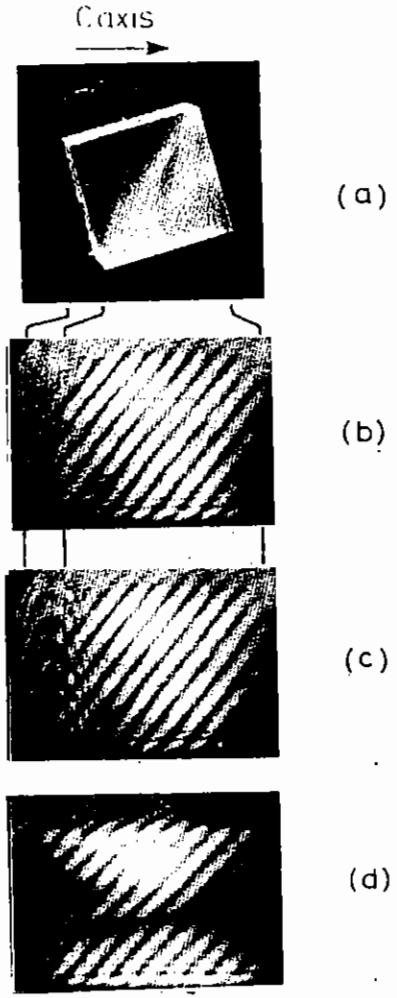

Fig 21 (a) Picture of beam paths in the 7x7 mm crystal with illumination by the pump beam of the full entrance aperture of the crystal. Note the two distinct beam paths of the critical angle loop and the diagonal ring.

(b) Uniform and stationary interference pattern produced across the entire aperture of the 7x7 mm crystal.

(c) If a 200 μm wide slit of light also illuminates the left hand face at the left hand corner an additional SPPCE is created in this region which has an unrelated phase to the emission which arises through the front face.

(d) Spatial phase shifts in the vertical direction are created in the 6x4 mm crystal when the full aperture is illuminated. The top half of the pattern also moves horizontally corresponding to frequency shifts of a few Hz.

emission from the front face. The importance of the left hand face to the process was underlined by measurements on the 6x4 mm crystal. In this crystal, which had a larger absorption coefficient than the 7 mm crystal, SPPCE of a 2 mm diameter beam which entered the front face did not even begin unless some small amount of scattered laser light entered the left hand face of the crystal. Hence depending on the size and entry position of beams, light which enters the left face can either favourably or unfavourably couple with the pump beam to help establish or extinguish the diagonal ring. Since the light travelling in the direction of the top right hand corner initially becomes amplified by the pump beam to establish the ring, the left face is crucial to the establishment of the SPPCE process. Painting this face with white[18] or black[13] paint to enhance or inhibit the light in this direction is known to alter the behaviour of the process. As described earlier we find that a drop of oil placed only at the bottom left hand corner can prevent the building up of SPPCE altogether.

In Fig 21(d) we also show the SPPCE and fringes produced for full aperture illumination of the 6x4 mm crystal. As can be seen, for this crystal there was a phase shift of the SPPCE between the top and bottom halves of the crystal. While the fringes in the bottom half were stationary, in the top half their horizontal movement corresponded to a frequency shift of a few hertz. Depending on the vertical position in some crystals it appears that beams can simultaneously counterpropagate in rings with both the stable and unstable coupling arrangements shown in Fig 19. As discussed previously for the 7x7 mm crystal, this behaviour presumably results from the geometrical variations of the crystal in the vertical direction. Progressively masking the crystal from the left hand edge slowed down the fringe movements in the upper half of the 6x4 mm crystal. The fringes across the full aperture became stationary when light was prevented from entering the crystal $\sim$ 1 mm from the left hand corner. It appears that this masking can transfer the coupling into the ring from the unstable position at x_3 to the stable position x_2 in Fig 19.

When the full entrance aperture of the 6x4 mm crystal was illuminated as in Fig 21(d), we found that obscuring the region around x ∿ 3.5 mm with a 1 mm diameter wire prevented the buildup of any SPPCE from the rest of the entrance face. Hence the 1 mm wide strip of light entering the crystal around x ∿ 3.5 mm is crucial to the setting up of the ring resonator that allows four-wave mixing to occur with light across the rest of the aperture. It is this same region in this crystal which the near threshold small beam measurements presented in Fig 20 emphasised in the establishment of the diagonal ring.

Power and intensity measurements

We have found that the crucial parameter for reaching the threshold for SPPCE is the power P_{th}, rather than the intensity of the beam incident upon the crystal (0.14 and 2.5 mW for the 7x7 and 6x4 mm crystals, respectively). Even though the threshold intensity changed by two orders of magnitude, the measurements in Fig 22 show that P_{th} is independent of the diameter of the incident pump beam. In Fig 23 we show measurements of the SPPCR and the buildup time of the SPPCE for both crystals as a function of the incident laser intensity which was varied by separately changing either the laser power for a fixed incident beam diameter or the beam diameter for a fixed incident laser power. Somewhat surprisingly we found that both the SPPCR and the delay time to the start of SPPCE were relatively insensitive to the incident laser intensity at constant power. From these results we conclude that a crucial parameter which determines if threshold for self-pumping is reached is the threshold energy, E_{th}, accumulated on the entrance face of crystal (∿ 35 mJ and 200 mJ for the 7x7 and 6x4 mm crystals respectively). This behaviour can be understood qualitatively by arguing that once inside the crystal, beams adjust themselves to keep fixed the volume of the interaction regions containing the holograms which produce the SPPCE - independent of the size of the input beam. The threshold power of the incident beam determines only if sufficient charge carriers are generated for the gratings to be formed in the fixed volume. As shown in Fig 23(b), keeping the diameter of the beam fixed and increasing the incident beam intensity by increasing its power reduces the delay time for the appearance of self-pumped emission in a near linear fashion. Since the time with which the gratings are written is determined by the photoconductivity of the crystal, which itself is inversely proportional to the light intensity, this behaviour is not surprising and has been known since the original study of Feinberg[11].

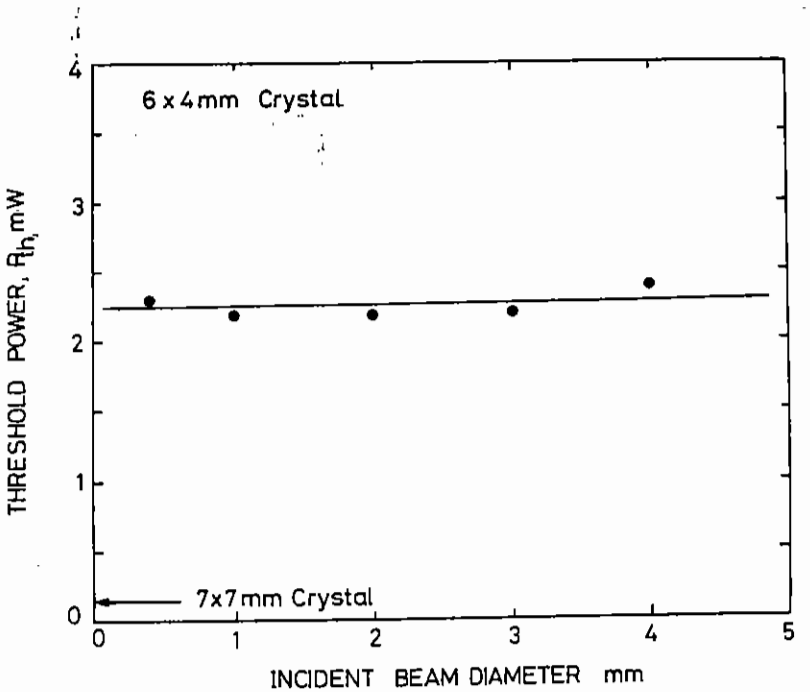

Fig 22 Threshold power for SPPCE as a function of the incident laser beam diameter on the 6 x 4 mm crystal. Angle of incidence was 8°.

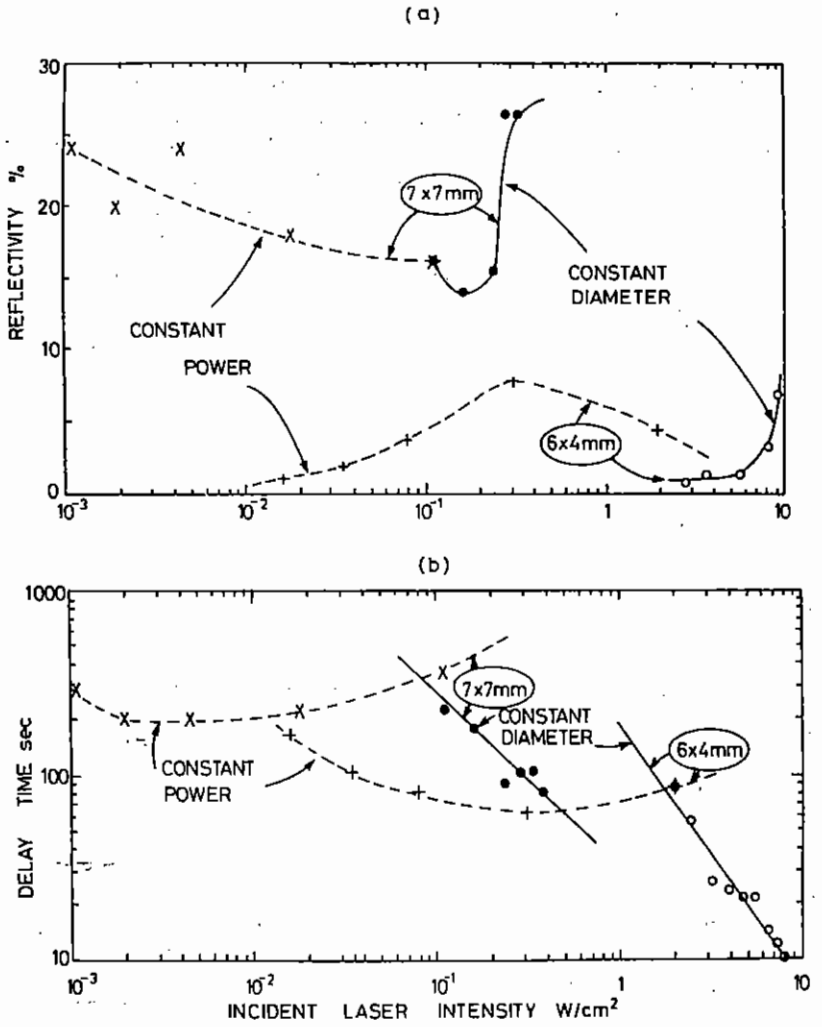

Fig 23 (a) SPPCR and (b) delay time for buildup of SPPCE versus incident laser intensity. The laser intensity was changed by varying both the beam diameter at constant power and the power at constant diameter. Data is shown for both 7x7 and 6x4 mm crystals.

In summary, we have identified two types of pathways which can simultaneously produce SPPCE in crystals of $BaTiO_3$. By total internal reflection at a corner, two parallel beams of roughly equal intensity are created in the form of a loop such that the angle of incidence to the c-axis is equal to the critical angle and the total path length around the loop is maximised. Self-pumped phase conjugation is most likely produced by four-wave mixing around the entire length of this loop of light and may possibly be enhanced by stimulated photorefracted scattering. The second mechanism producing SPPCE couples light into and out of ring cavities which contain counterpropagating beams and are set up in the crystal between diagonal corners. The path length around the ring between coupling regions maximises by creating rings which contain minimum area. If the pump beam can separately couple into either side of the ring independently by splitting before it reaches the ring, then the SPPCE is stable without frequency shift relative to the pump frequency. On the other hand, if the pump beam couples into both sides of the ring without splitting, then both coupling regions couple to each other by the pump beam itself as well as through the ring. Frequency shifts, instabilities and pulsations of the SPPCE then occur. For some crystals both stability and instability can be observed to occur simultaneously depending on the vertical position. Light entering the crystal such that a component travels along the positive c-axis direction can be crucial to starting up the SPPCE process. On the other hand, when the full aperture is illuminated strong beams which propagate with a component along the c-axis can extinguish the SPPCE.

Rather than laser intensity, the power and energy of the incident beam determine the threshold characteristics for SPPCE. The volumes of the gratings which produce SPPCE appear to be fixed independent of the diameter of the input beam.

By modelling bidirectional ring resonators in photorefractive media in a similar way to the ring resonator calculations of Yeh[23,24] and including the coupled interaction regions, many of the observations presented here can be more formally predicted.

SECTION 2 SBS PHASE CONJUGATE MIRRORS

2.1 FIDELITY OF SBS PHASE CONJUGATE MIRRORS

G M Davis and M C Gower (RAL)

There has been relatively little detailed study of the phase conjugate fidelity of the Stokes beam produced by a weakly aberrated pump beam of limited coherence length when focussed directly into an SBS medium without the use of a lightguide. Although high phase conjugate fidelities (PCF) for such systems have been reported[25,27], there is evidence that for beams of sufficiently high intensity the PCF degrades during the laser pulse[28]. The experiments reported in this section used a KrF excimer laser to study the SBS efficiency and PCF as a function of the focal length of the focusing lens, linewidth and intensity of the pump beam.

Fig 24 shows the experimental arrangement used for this investigation. The laser was a home made excimer laser system composed of an oscillator and single-pass or double-pass amplifier. By changing the optics of the oscillator it was possible to operate the laser with a variety of linewidths ranging from about $50cm^{-1}$ to as narrow as $0.035cm^{-1}$. As shown in Fig 24 two separate focusing systems were employed to enable simultaneous monitoring of the focal-plane spatial intensity profiles of the pump and SBS beams. Each focusing system comprised of two lenses of focal lengths f_1 = +50cm and f_2 = +5cm which were used in a telescopic arrangement equivalent to a single lens of 15m focal length. The pressure in two NO_2 absorption cells, C_1 and C_2, was adjusted until the fluences of these beams in the focal plane were suitable for recording by a diode array (1024 pixel EG&G G-series Reticon) orientated vertically so that the vertical profiles of the laser beam could be recorded. Using a suitable Fabry Perot etalon the linewidth of the laser was also simultaneously monitored on the same diode array. The signal from the diode array was monitored by three storage oscilloscopes enabling the two spatial profiles and the Fabry Perot rings to be recorded separately with higher resolution than could be achieved by using a single oscilloscope.

The temporal profiles of the pump and Stokes beams were simultaneously monitored using the beam splitters BS_1, BS_2, photodiodes PD_1, PD_2, and fast oscilloscopes. Using calibrated glass attenuation filters the signals incident on these photodiodes were reduced to a level suitable for recording on the oscilloscopes. The filters were placed sufficiently far from the photodiodes to ensure that any occurrence of laser-induced fluorescence in the filter glass would not affect the recording of the temporal profiles of the laser pulses.

Care was taken to ensure that the pump beam was uniformly polarised in front of the focusing lens, L_1. For each laser linewidth one of a range of focal length lenses was used to focus the pump beam into either a 30cm or a 100cm long SBS cell. In each case, the pump beam was focused to a position in the liquid sufficiently far from the input face of the cell so as not to cause damage to the fused silica window. Provided that window damage was avoided the quality of the SBS beam did not appear to be affected by the precise position of the focus in the SBS cell. However, in order to maximise the SBS

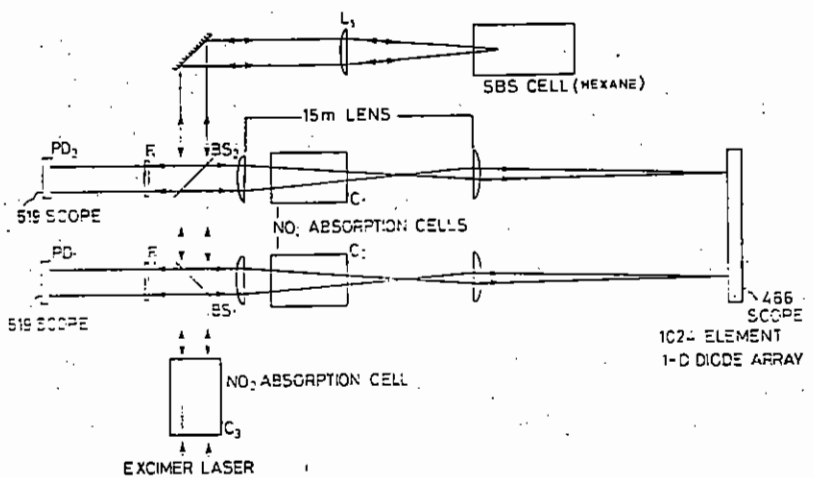

Fig 24 Experimental arrangement for the SBS fidelity measurements.

reflectivity the length of the active medium was minimised so that the absorption in the liquid was kept to a minimum.

A third NO_2 absorption cell, C_2, was used to vary the power of the incident pump beam. For each laser pulse, the variation with pump power of the spatial and temporal characteristics of the pump and SBS beams was recorded. Using a joulemeter to simultaneously record the energy incident on the SBS cell and the signal from the photodiode PD_1, it was possible to calibrate this photodiode in terms of the instantaneous power of the pump beam at the input window of the SBS cell. Calibration of the reflectivity of the SBS mirror was achieved by replacing the SBS mirror with a normal incidence fused silica flat of known reflectivity. In calculating the reflectivity of the SBS cell account was taken of the Fresnel losses of the focusing lens, L_1, and the SBS cell input window.

Fig 25 shows the variation of the SBS energy reflectivity with the pump laser coherence length for an incident pump power of 10^5W. Each curve is for a focusing lens of different focal length. We see that for the longer coherence lengths the SBS reflectivity is insensitive to the focal length of the lens. For long coherence lengths, growth of the Stokes wave can take place coherently over the full focal region[29,30]. This behaviour can be further understood by noting that for several simple spatial beam profiles the integrated intensity-length product ($\int_{-\infty}^{+\infty} I.dl$) is independent of the focal length of the lens. As the laser coherence length decreases the length of the active medium over which the Stokes beam can efficiently grow becomes smaller due to the lack of mutual coherence between the Stokes and pump waves. Thus as shown by the data in Fig 25 as the laser coherence length decreases the SBS energy reflectivity depends more and more strongly on the focal length of the focusing lens. Similar trends were observed for all pump powers between 10^4 and 10^6W.

Fig 26 shows representative pictures of the variation with pump power of the far field spatial profiles of the SBS beam compared with that of the pump beam profile as recorded by the diode array at the focal

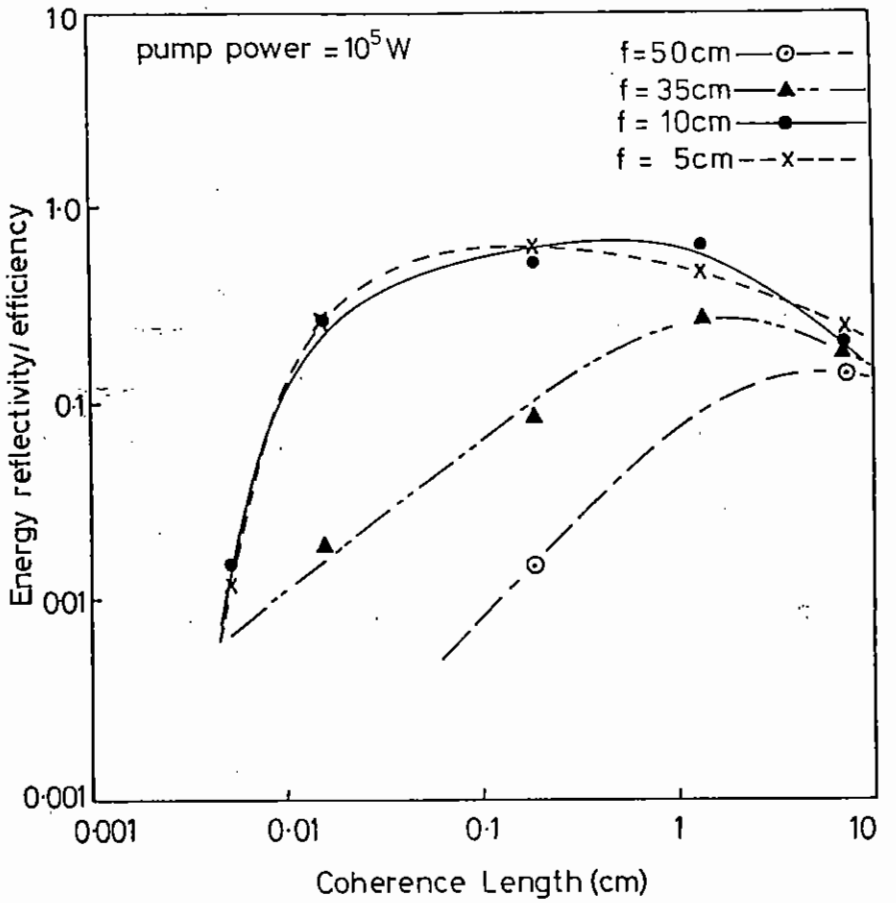

Fig 25 Variation of the SBS energy reflectivity as a function of the pump laser coherence length.

plan of the 15m telescope shown in Fig 24. We see that as the pump power increases the profile of the SBS beam becomes wider and has more random intensity variations than the pump beam.

To examine the dependence of the SBS PCF as a function of laser linewidth and pump power it is convenient to define the fidelity as the full width at half maximum (FWHM) of the focal plane spatial profile of the pump beam divided by that of the corresponding smoothed SBS profile. Fig 27 shows that for a fixed pump power the variation of the SBS PCF as a function of the laser coherence length. The insensitivity of fidelity on coherence length is representative of additional data taken using other laser powers and focusing lenses to those shown in this figure.

In Fig 28 we show the variation of SBS PCF as a function of the pump power for different focusing lenses. These data are taken by averaging results obtained at several different coherence lengths at each value of pump power. We see from Fig 28 that as the pump power increases above the SBS threshold the trend is for the PC fidelity to decrease from values near unity. Since the SBS focal plane spatial profile has an increasingly random intensity distribution at higher pump powers (see Fig 26) we attribute this decrease in fidelity at higher pump powers to the onset of electrostrictional self-focusing. It then appears from the data shown in Figs 25 and 27 that, compared to the SBS reflectivity, the onset of such self-focusing is less dependent on the laser coherence length.

In conclusion we have shown that provided the laser coherence length is longer than the length of the focal region over which the SBS wave grows rapidly (approximately 1.5 times the Rayleigh range for a Gaussian beam[30]), reflectivities of > 20% can be obtained and are independent of the focal length of the focusing lens. Using long coherence lengths high SBS reflectivity can be produced. For laser powers close to the threshold for SBS values of the PCF near unity can be obtained. However, as the laser power is increased the trend is for the PCF to decrease. We attribute this decreasing PCF to electrostrictional self-focusing which splits up the pump beam into

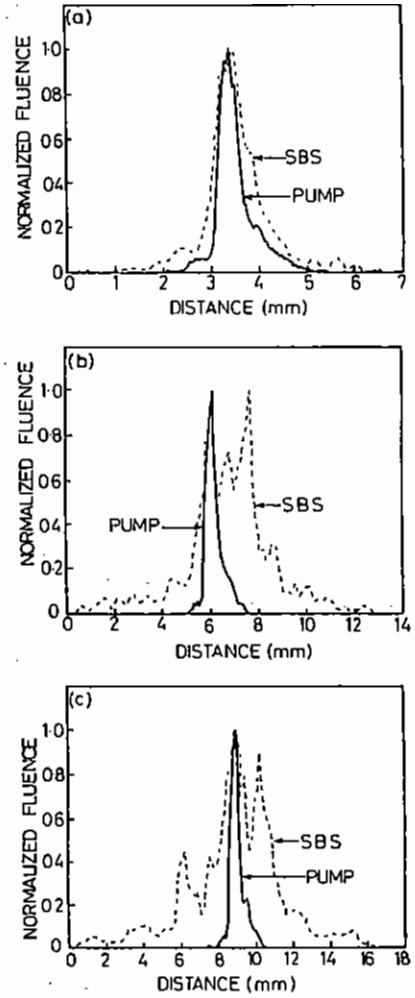

Fig 26 Focal plane spatial fluence profiles of the SBS and pump beams for three pump powers. In each case the laser linewidth was 0.2cm^{-1} and a 10cm focal length lens was used to focus the pump beam into the liquid.

(a) pump power of 10^{4}W, SBS energy reflectivity of 24%, SBS fidelity of 0.59.

(b) pump power of 2 x 10^{5}W, SBS energy reflectivity of 74%, SBS fidelity of 0.18.

(c) pump power of 10^{6}W, SBS energy reflectivity of 100%, SBS fidelity of 0.17.

Note that (a), (b) and (c) have different horizontal scales.

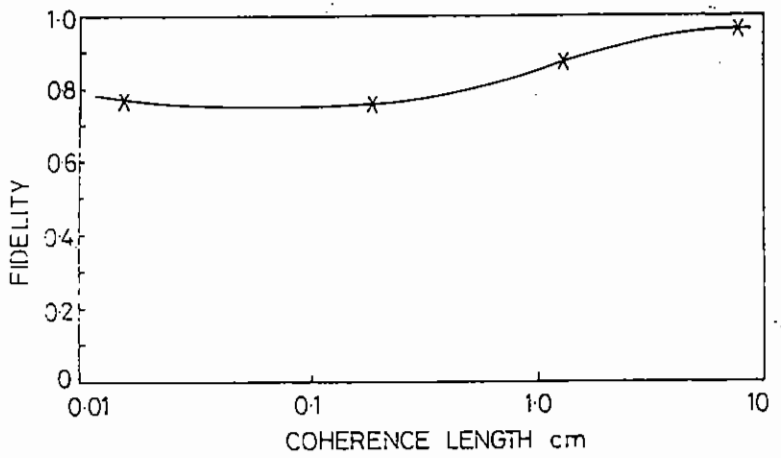

Fig 27 Variation of SBS fidelity as a function of pump laser coherence length. The laser pump power was 2.5 x 10⁴W and a 35cm focal length lens was used to focus the laser into the SBS liquid.

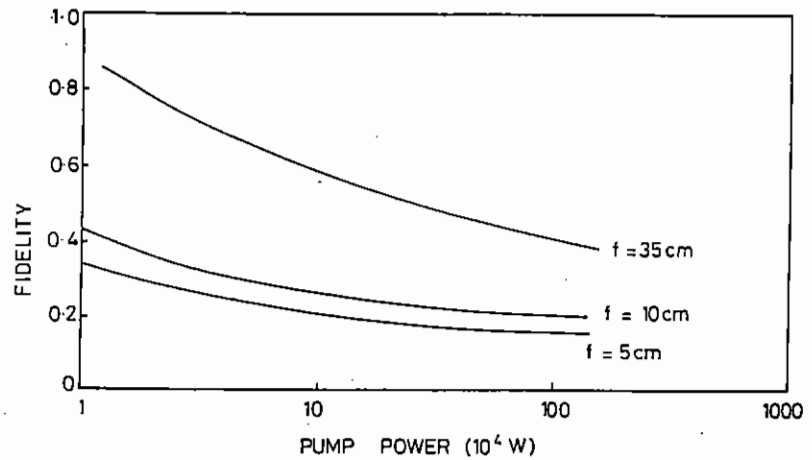

Fig 28 SBS fidelity versus pump power for three different focusing lenses. Each curve represents an average of the data for several different laser linewidths.

filaments that can each produce a Stokes wave. Since each of these filamentary SBS waves will originate with an arbitrary phase, the PCF of the total generated SBS wave is expected to degrade.

2.2 PULSE SHORTENING OF A KrF EXCIMER LASER USING TRUNCATED SBS

M C Gower (RAL)

Stimulated Brillouin scattering in gases and liquids, is an established technique for generating phase conjugate mirrors[31] and in particular has been used to generate such devices at 249 nm[32,33]. While some pulse shortening of the backscattered beam is observed, well above the intensity threshold for SBS the backscattered light has approximately the same temporal characteristics as the pump beam. However, if the focussed pump beam is allowed to break down and produce a plasma in the Brillouin active medium (at the surface of a liquid, for example) then it is known that the stimulated backscattered light becomes truncated and can be of a considerably shorter duration than the pump beam[34,35]. When using this method of truncated stimulated Brillouin scattering (TRUBS) backscattered pulses as short as ∿ 100 psec and ∿ 20 psec can be produced when using XeCl and dye laser pump sources respectively[34,35]. In the work described here we present results on pulse shortening at 249 nm using TRUBS with a high energy KrF laser source and liquid hexane as the active Brillouin medium.

In Fig 29 we show the experimental set-up. The amplifier section of a Lamda Physik EMG 150 laser was used to amplify on a single pass the output from the line narrowed oscillator section. The linewidth of this pump radiation was ∿ 0.2cm^{-1} and had an energy of ∿100mJ. Shown in Fig 29 is the SBS signal in cases when no breakdown occurred at the scattering liquid and when breakdown occurred on its surface. As can be seen the pulse is shortening from ∿6 nsec FWHM for SBS to ∿1.7 nsec for TRUBS. However, in the case for TRUBS the trailing edge of the pulse does not rapidly drop. By comparison the trailing edge of

TRUBS when using XeCl and dye laser sources can be as short as 50 psec and 20 psec respectively[34,35]. This incomplete truncation of the backscattered light at 249 nm may be a result of the plasma spark created at the liquid-air interface being insufficiently dense so that the plasma frequency is too low for strong attenuation of wavelengths shorter than ∿300 nm. Partial truncation of the SBS return at this wavelength could still occur by refractive effects in the plasma although these effects would tend to scatter rather than attenuate the beam. Because of the poor contrast of the TRUBS pulse shown in Fig 29, this technique is of limited use when further amplification of the pulse in high gain excimer amplifier modules is contemplated.

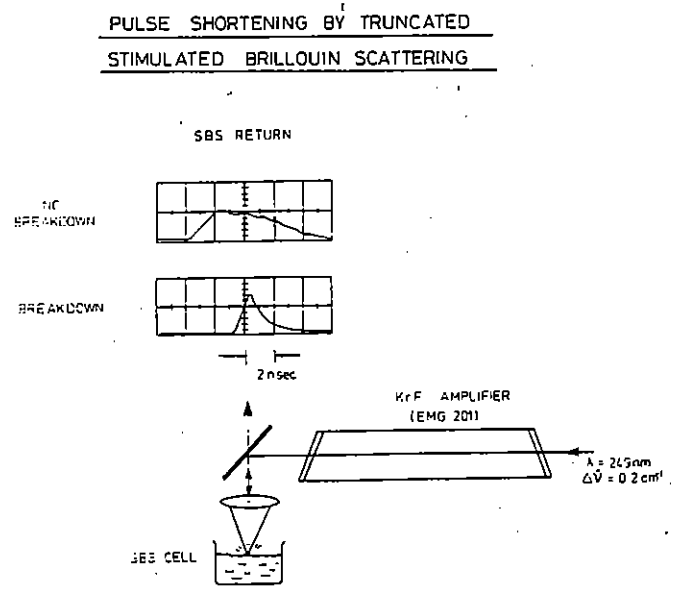

Fig 29 Pulse shortening by truncated stimulated Brillouin scattering in hexane at 249nm.

SECTION 3 EXCIMER LASER PHOTOABLATION OF SEMICONDUCTOR MATERIALS

3.1 HIGH RESOLUTION DIRECT LASER ETCHING OF GaAs

D W Thomas (Portsmouth Polytechnic)
G M Davis and M C Gower (RAL)

In this section we describe the direct laser etching characteristics of GaAs substrates at wavelengths of 193nm (ArF) and 248nm (KrF). This work differs from that described previously[36-38], in that the etching was performed in air without the assistance of special gas or liquid phase reactants. To our knowledge there has been no detailed study of the direct etching of compound semiconductors when exposed in air to excimer laser radiation. It is generally assumed that such etching by ablation of material will leave rough and damaged surfaces so that the technique is often dismissed as unsuitable for high resolution etching of III-V semiconductors[36,38,39]. In this paper we show that high resolution direct etching of GaAs is possible using excimer lasers. Such a process may have applications in the area of device fabrication for microelectronics and integrated optics. The measurements of the threshold at which damage or etching occurs to compound semiconductors may also be useful for determining the limiting laser fluence acceptable for laser-assisted processing techniques such as laser chemical vapour deposition.

A pulsed excimer laser (Oxford Lasers Model KX2) which was operated on either KrF (248nm) or ArF (193nm), illuminated the GaAs substrates through 200μm square apertures of a free-standing copper mask pressed into contact with the substrate. For both wavelengths the laser pulse duration was about 20ns full width at half maximum. The substrates were undoped (100)-oriented, 420μm-thick, polished GaAs wafers.

A 1mm diameter aperture was used to select a uniform portion of the laser beam and to measure the laser fluence incident upon the substrate. The exposing fluence was varied by changing the distance of the substrate from a 50cm focal length lens used to focus the laser beam. During each etch the fluence illuminating the mask was

monitored by recording the reflected signal from a beam splitter. For each fluence the substrate was exposed to 1000 laser pulses at a repetition rate of 1pps. Prior to measurement of the etch depths, the substrates were cleaned in an ultrasonic bath of alcohol to remove most of the surface debris that resulted from the etching process. The etch depths were measured to an accuracy of ±0.05μm using an interference microscope.

In Fig 30 we show measurements of the variation of the average etch depth per pulse as a function of the incident exposing fluence. The variation in etch depth over all of the exposed 200μm square apertures was measured and is indicated by the root mean square (rms) deviation error bars shown in Fig 30. For this figure the fluences shown are the values averaged over the 1000 laser pulses and the error bars indicate the rms deviation in fluence during the exposure. It is immediately apparent from this figure that removal of GaAs material by the direct etching of the sample occurs at much lower fluences (<1J/cm²) than has hitherto been observed for KrF and ArF excimer laser sputtering of metals[40] or etching of silicon[41] or of diamond[42]. The quantity of material removed by each laser pulse by this direct etching of GaAs is comparable to that removed by ArF excimer laser-induced gas phase chemical etching of GaAs[36,37] although the laser fluences used in our experiments were typically an order of magnitude higher than those employed for photochemical etching at 193nm.

Since only those photons which are absorbed in the GaAs can cause etching of the substrate, one important parameter for this process is the fluence, $\xi=E(1-R)$ absorbed by the GaAs. R is the reflectance of the GaAs, which has values of 0.507 and 0.668 at wavelengths of 193nm and 248nm respectively[43], and E is the fluence incident upon the substrate. The fluence absorbed at the threshold for etching of GaAs, $\xi_T=E_T(1-R)$, was 23mJ/cm² and 33mJ/cm² at 193 and 248nm respectively. We note that while these fluence thresholds are similar to those encountered in the excimer laser ablative photodecomposition of polymers, once above threshold the etch depths per pulse are approximately two orders of magnitude less than for polymers[44].

The morphology of the etched regions was examined using Nomarsky and scanning electron microscopes. Figs 31(a) and (b) show typical etches for fluences close to the thresholds at 193nm and 248nm respectively. For exposures at both of these wavelengths the undulating diffraction pattern etched into the substrate is clearly visible. At these low fluences the depths measured were spatial averages of these undulations. As shown in Figs 31(c) (ArF) and (d) (KrF), at higher fluences the etched regions become more smooth. It appears that at these higher fluences the surface temperature of the GaAs is raised sufficiently to cause melting of the substrate. From calometric considerations[45] we estimate that the surface temperature of the GaAs at the end of the laser pulse is increased by ΔT where $\Delta T=E(1-R)/C\rho\delta$, and the heat penetration depth $\delta=\sqrt{K\tau/\rho C}$ where C, ρ, τ and K are the specific heat capacity, density, laser pulse length and thermal conductivity respectively. With τ=20ns and values of the thermal parameters at a temperature of 900K taken from Ref (46), we calculate that for the 300mJ/cm² fluences used in Figures 31(c) and (d) the surface temperature reaches about 1800K and is comparable to the melting point of GaAs (=1500K).

Further experiments have shown that when irradiating the substrate at wavelengths of 193nm and 248nm in both vacuum (10^{-2} torr) or N_2 (1 atm) environments the etch depth per pulse is less than a quarter of that observed when exposure takes place in air. In addition, very little etching of GaAs occurred in either an air or N_2 environment when irradiation was performed using an XeF excimer laser at the longer wavelength of 351nm. Hence it appears that for the shorter wavelength excimers some etching occurs by photochemically induced reactions of the atmospheric oxygen with the GaAs substrate.

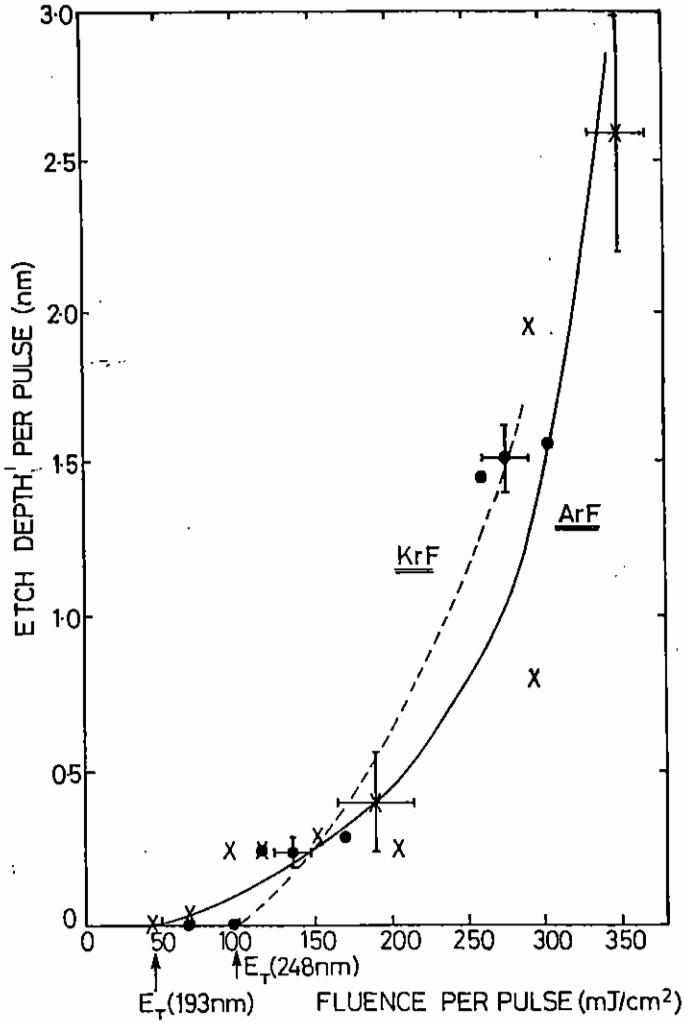

Fig 30 Average etch depth per pulse versus incident exposing fluence for GaAs (100) substrates using ArF and KrF excimer lasers. The average etch depth per pulse shown in this graph represents the total depth of GaAs which has been etched divided by the number of laser pulses (1000). For 193nm and 248nm the threshold fluences, E_T, are shown.

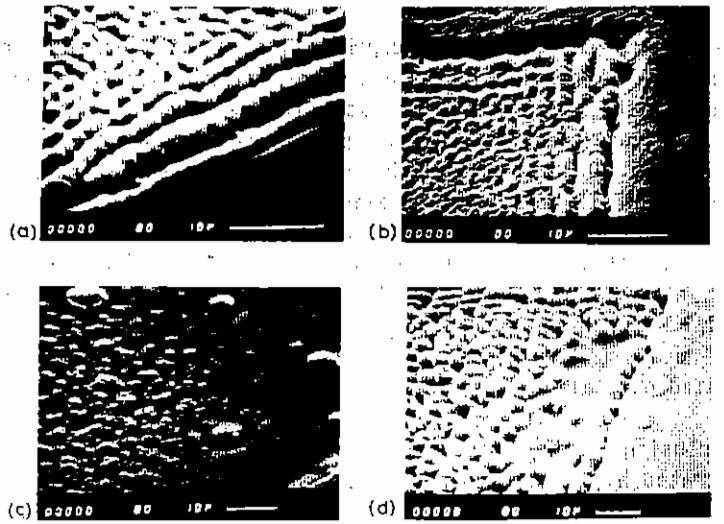

Fig 31 Scanning electron micrographs of a GaAs substrate directly etched by excimer laser pulses each of (a) 150mJ/cm² at 193nm, (b) 190mJ/cm² at 248nm, (c) 290mJ/cm² at 193nm, (d) 300mJ/cm² at 248nm.

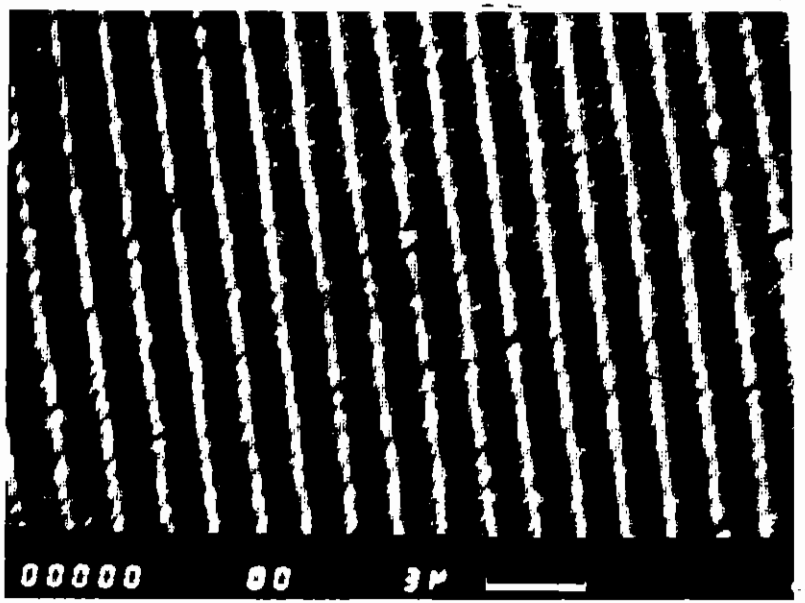

Fig 32 Scanning electron micrograph of a 1.5μm-period grating etched into a GaAs substrate. This grating pattern was produced by the interference of two mutually coherent KrF excimer laser beams at the surface of the substrate. Each laser beam had a fluence of about 160mJ/cm² and 100 laser pulses were used at a repetition rate of 2pps.

To investigate the resolution capabilities of this etching process the substrates were illuminated with the sinusoidal fluence variation produced by the interference of two mutually coherent excimer laser beams. After travelling equal path lengths two beams from a line-narrowed (0.3cm^{-1} linewidth) KrF excimer laser (Lambda Physik model EMG 150EST) were made to overlap at the GaAs substrate. The sinusoidal pattern produced at the sample then caused ablation. From the scanning electron micrograph shown in Fig 32 1.5µm-period grating etched into the substrate is clearly visible and demonstrates the potential resolution capability of this direct etching technique. Such sinusoidal structures in GaAs are of interest as couplers in integrated optical devices[47] .

In conclusion, using UV excimer lasers at 193 and 248nm we have demonstrated high resolution direct etching of bulk samples of GaAs. The threshold fluence, ξ_T, for the process depends slightly on the wavelength and is between 20 to 30mJ/cm^2. By using a two beam interference pattern to directly etch the substrate. 1.5µm-period sinusoidal gratings in GaAs were produced. This (low temperature) direct etching technique may find applications to the fabrication of integrated optical devices, laser diodes and microcircuits.

References:

1. R G Caro and M C Gower, IEEE Journal of Quant Elect QE-18, 1376 (1982).

2. M D Levenson, J Appl Phys 54, 4305 (1983).

3. H J Hoffman, JOSA B, 3 253 (1986).

4. M Murahara, Y Kawamura, K Toyoda and S Namba, Oyo Buturi (Japan) 52, 83 (1983).

5. G W Stroke, Phys Lett 23, 325 (1966).

6. N K Sheridon, Appl Phys Lett 12, 316 (1968).

7. A M Hawryluk, H I Smith, R M Osgood and D J Ehrlich, Opt Lett 7, 402 (1982).

8. M J Beesley and J G Castledine, Appl Opt 9, 2720 (1970).

9. G M Davis and M C Gower, IEEE Electron Dev Lett EDL-7, 543 (1986).

10. K Jain, C G Wilson and B J Lin, IBM J Res Develop 26, 151 (1982).

11. J Feinberg, Opt Letts 7, 486 (1982).

12. K R MacDonald and J Feinberg, JOSA Am 73, 548 (1983).

13. M D Ewbank and P Yeh, SPIE 613, 59 (1986).

14. T Y Chang and R W Hellwarth, Opt Letts 10, 408 (1985).

15. J F Lam, Appl Phys Letts 46, 909 (1985).

16. W B Whitten and J M Ramsey, Opt Lett 9, 44 (1984).

17. J Feinberg and G D Bacher, Opt Lett 9, 420 (1984).

18. P Gunter, E Voit, M Z Zha and J Albers, Opt Comm 55, 210 (1985).

19. A M C Smout, R W Eason and M C Gower, Opt Comm 59, 77 (1986).

20. M Cronin-Golomb, B Fischer, J O White and A Yariv, IEEE. J Quant Electr. QE-20, 12, (1984)

21. N F Andreev, B I Bepalov, A M Kiselev, A Z Matveev, G A Pasmanik and A A Shilov, JETP Lett 32, 625 (1980).

22. K R MacDonald and J Feinberg, Phys Rev Letts 55, 821 (1985).

23. P Yeh, JOSA B, 2, 1924 (1985).

24. P Yeh, Appl Opt 23, 2974 (1984).

25. M C Gower, Opt Lett 8, 70 (1983).

26. E Armandillo and D Proch, Opt Lett 8, 523 (1983).

27. E Armandillo, Opt Comm 49, 198 (1984).

28. M C Gower, SPIE 476, 72 (1984).

29. V M Rysakov, Sov Phys JETP 34, 383 (1972).

30. V M Rysakov, Yu V Aristov and V I Korotkov, Opt Spectrosc (USSR) 47, 412 (1979).

31. M C Gower, Prog in Quantum Electronics 9, 101 (1984).

32. M C Gower and R G Caro, Optics Letts 7, 162 (1982)

33. M C Gower, Opt Lett 7, 423 (1982)

34. O L Bourne and A J Alcock, Appl Phys B37, 15, (1985)

35. Y S Huo, A J Alcock and O L Bourne, Appl Phys B36, 125 (1985)

36. P Brewer, S Halle and R M Osgood Jr, Appl Phys 45, 475 (1984).

37. P D Brewer, D McClure and R M Osgood Jr, Appl Phys Lett 47, 310 (1985).

38. P D Brewer, D McClure and R M Osgood Jr, Appl Phys Lett 49, 803 (1986).

39. G Koren, F Ho and J J Ritsko, Appl Phys Lett 46, 1006 (1985).

40. R Kelly and J E Rothenberg, Nucl Instr and Meth B7, 755 (1985).

41. G B Shinn, F Steigerwald, H Stiegler, R Sauerberg, F K Tittel and W L Wilson Jr, J Vac Sci Technol B4, 1273 (1986).

42. M Rothschild, C Arnone and D J Ehrlich, J Vac Sci Technol B4, 310 (1986).

43. D E Aspnes and A A Studna, Phys Rev B 27, 985 (1983).

44. R Srinivasan and B Braren J Polymer Sci:Poly Chem Ed, 22, 2601 (1984).

45. W W Duley, CO_2 Lasers: Effects and Applications, Acad Press, London, 139 (1976).

46. J S Blakemore, J kAppl Phys 53 123 (1982).

47. A Yariv and M Nakamura, IEEE J Quant Electron QE-13, 233 (1977).

ACKNOWLEDGMENTS

The task of producing the report is considerable and it would not have been accomplished without the dedicated efforts (including overtime working) of many people.

Chris Ayling and Clare Schröder have as usual borne the brunt of the typing effort, ably assisted by Tricia Morgan. Jan Smith has produced the drawings and Nic Allen has looked after the overall production plan. The RAL Reprographic Section have reproduced copies for distribution with their usual efficiency.

Thanks are due also to users of the facility for their willingness to give up time to write reports on their work and to the Section Editors for persuading them to do it in time for the press deadline, and for editing the manuscripts.